



**UNIVERSITÀ
DEGLI STUDI
DI TRIESTE**

UNIVERSITÀ DEGLI STUDI DI TRIESTE

XXXVI CICLO DEL DOTTORATO DI RICERCA IN
Scienze della terra, fluidodinamica e matematica. Interazioni
e metodiche

Borsa MUR/Ateneo

ANALYSIS OF A MORPHODYNAMIC ANOMALY LINKED WITH DIVERGENT BEDFORM SYSTEMS: THE MULA DI MUGGIA NEARSHORE SAND BANK, NORTHERN ADRIATIC SEA, ITALY

Settore scientifico-disciplinare: **GEO/02**

DOTTORANDO
Saverio Fracaros

COORDINATORE
PROF. Stefano Maset

SUPERVISORE DI TESI
PROF. Giorgio Fontolan

ANNO ACCADEMICO 2022/2023

CONTENTS

Abstract	3
1 Preface & objective	4
2 Introduction	5
2.1 Coastal environment	5
2.2 Relative Sea Level Rise & human impact	5
2.3 Shoreface and wave processes	6
2.4 Sediment transport dynamics	7
2.5 Morphology	9
2.6 Analysis & methodologies	11
2.6.1 Sedimentological mapping	12
2.6.2 Sediment budget and transport computation	13
3 Study area	16
3.1 Geographical setting	16
3.2 Wind regime	16
3.3 Wave regime	18
3.4 Sea level rise	19
3.5 Extreme storm events	21
3.6 Precipitations	24
3.7 Morphological set-up	24
3.8 Historical trends	26
3.9 Coastal area management	28
4 Materials and methods	29
4.1 Surveys and data	29
4.1.1 Bathymetric Survey	29
4.1.2 Aerial photogrammetry with Unmanned Aerial Vehicle	31
4.1.3 Sediment samples	31
4.2 Data analysis	33
4.2.1 Digital Terrain Model (DTM) & DTM of Differences (DoD)	33
4.2.1.1 Sediment budget	34
4.2.1.2 Position indexes & Residual method	35
4.2.1.3 Landforms position evolution	36
4.2.2 Sedimentological maps	37
4.2.3 Total mercury distribution and analysis	42
4.2.4 Modelling	42
4.2.4.1 Storm events of 2023	48
4.2.4.2 Not-extreme events	51
5 Results	53

5.1	<i>Geomorphology & sediment budget</i>	53
5.1.1	Front of the Mula di Muggia Bank & High Intertidal Bank	54
5.1.1.1	Geomorphological set-up	54
5.1.1.2	Short-term geomorphological changes	61
5.1.1.3	Sediment budget	70
5.1.2	Isonzo river delta	71
5.1.2.1	Geomorphological set-up	71
5.1.2.2	Short-term geomorphological changes	71
5.1.2.3	Sediment budget	75
5.2	<i>Sedimentology</i>	76
5.2.1	Dataset analysis	76
5.2.2	Distribution maps	78
5.2.2.1	Mz distribution: geostatistical vs Semi-Automatic Interpolation Method	79
5.2.2.2	Sorting & normalized sorting	83
5.2.2.3	Texture.....	85
5.3	<i>Provenience analysis: Hg proxy (Geochemical)</i>	86
5.4	<i>Modelling</i>	90
5.4.1	Bora multi-event: 25/02 – 03/2023	90
5.4.2	Southern wind multi-event: 27/10 – 05/11/2023	94
5.4.3	Models' summary	101
6	Discussion	108
6.1	<i>Methodological analysis: Geostatistical vs SAIM</i>	108
6.2	<i>Morphodynamic interpretation</i>	113
6.2.1	Isonzo River delta	113
6.2.2	Longshore transport pathway	116
6.2.3	The Deep Mula Muggia Bank	119
6.2.4	Front of Mula Muggia Bank & High Intertidal Bank.....	122
6.3	<i>Natural dynamics vs urban planning: conflicts and perspectives</i>	129
7	Conclusions	131
8	Bibliography	134
9	Acknowledgements	151

Abstract

The coastal environment is the most densely populated location on the planet, as well as one of the most complex because of the presence of both marine and terrestrial forcings. In particular, the small-scale landforms are usually rapidly changing as a result of the modification of the forcings such as waves, tides, the sea level rise (SLR), fluvial solid discharge and anthropic activities. An analysis of the geomorphological aspects, sediment budgets and characteristics, marine forcings, and their evolution over time is a basic requirement for coastal management. In this work, we analysed a nearshore depositional system made up of active and relict sand banks characterized by the presence of a fluvial sediment source of sediments characterized by mercury contamination, a bimodal wave regime made up of long southern and short north-eastern waves, and divergent landforms, intrinsically related to the delicate balance of hydrodynamic conditions and grain-size characteristics of the sediments. This environment is situated in a coastal area with significant human impact, where the hardening of the shoreline has increased its vulnerability and reduced its ability to adapt to natural evolutionary processes. To investigate its short-term evolution and place it within the context of long-term trends, a multidisciplinary approach was used, incorporating topo-bathymetric, sedimentological, and geochemical data, along with hydrodynamic and wave motion modeling. By combining all the data together, processed both with standard methodologies and with algorithms developed during the PhD, it was possible to derive the complex evolutionary pattern of the area, in which the subcoastal dynamics linked to the transport of sediments along the longshore transport pathway in a westward direction combines with the deep dynamics linked to the relict sedimentary body, made up of landforms with opposite vergence compared to the longshore drift. In this context, the bimodality of wave motion has proven to be the most important morphodynamic agent although the presence of the sedimentary source is of fundamental importance for the constant recharge of sediments and the evolution of ongoing processes. Finally, using an approach that combines morpho-sedimentological and geochemical evidence with the modeling of meteorological and marine forces allowed for cross-validation of the results. This provided a robust morpho-evolutionary foundation, which is also valuable for managing an area with significant tourist activity.

1 Preface & objective

The study of coastal environments is becoming increasingly relevant especially in the global context of sea level rise. Rapid process-driven morphological and sedimentological changes, high anthropic pressure and an intricate network of habitats due to the rapid transition between the terrestrial and marine environments are concentrated on the narrow coastal zone. The vulnerability of such a delicate environment has recently been exacerbated by the threat of human-induced sea level rise, putting both economic and ecological value at serious risk. Furthermore, the rigidity established by human infrastructures and the depletion of fluvial solid discharge caused by dams and dredging have further reduced its resilience. The study and understanding of coastal dynamics are therefore of fundamental importance for predicting future evolution at different time scales, providing a knowledge base from which to then develop the most appropriate adaptation strategies.

In this work the Mula di Muggia sand bank (hereinafter MMB) is studied, a nearshore depositional system made up of active and relict sand banks that extends up to 2 km seawards from the touristic beaches of Grado (Northern Adriatic Sea, Italy). While erosion and sand loss are always key issues for the tourism business, managing rapid morphological changes linked to large quantities of moving sediments is the challenge here. The morphodynamic analysis becomes even more important if, within the study area, there are both depositional anomalies represented by active sedimentary bodies, such as river deltas, and relict ones characterized by patterns of bedforms whose geometry is intrinsically related to the delicate balance of hydrodynamic conditions and grain-size characteristics of the sediments. The study of this complex coastal system, the secular evolution of depositional bodies, the current dynamics, and the morpho-sedimentary responses to ongoing climate change requires a broad and multidisciplinary approach.

The objective of this PhD project was to clarify the complex morphodynamics of this area combining data of different source in order to furnish a basis for future accurate planning and re-evaluation of coastal management choices to balance environmental protection and tourist use.

2 Introduction

2.1 Coastal environment

The coastal environment represents a dynamic interface where terrestrial, marine, and atmospheric systems converge, giving rise to complex and diverse ecosystems that are crucial for global biodiversity and human well-being. Despite their ecological importance, coastal environments face numerous threats stemming from human activities and natural processes. Understanding the complexities of the coastal environment is essential for devising effective conservation and management strategies to mitigate these threats and ensure the long-term sustainability of coastal ecosystems. Due to its geographical, hydrographic, administrative characteristics and the various stakeholders present, the coasts are difficult to manage, and the different needs of the interested parties often compete (Longhorn, 2005), creating critical situations. Through interdisciplinary research and collaboration, scientists strive to unravel the intricate interactions between physical, biological, and socioeconomic factors shaping coastal environments, with the aim of promoting resilience and adaptation in the face of environmental change.

The coast, by its nature, is a geographical area in constant morphological evolution. Among the factors that influence the morphological changes of a coastline we can list marine forcings, sediment supply, changes in sea level, subsidence, extreme storm events and human activities. Currently, erosion, drowning and increased vulnerability involve sedimentary bodies such as beaches, coastal dunes, barrier island systems and deltas (Van Rijn, 2011).

Common anthropogenic effects that influence coastal environments are a reduction in the solid load transported by rivers, induced land subsidence (Galloway et al., 2016; Gatto and Carbognin, 1981; Holzer and Johnson, 1985; Zanchettin et al., 2021) and sea level rise (Carbognin et al., 2010; Church and White, 2011; FitzGerald et al., 2008; Friedrichs et al., 1990; Griggs and Reguero, 2021; Nienhuis and Lorenzo-Trueba, 2019; Palmer et al., 2019; Zanchettin et al., 2021).

2.2 Relative Sea Level Rise & human impact

The increase in mean sea level is among the main factors to take into consideration in the evolutionary context of coastal systems and adaptation to global climate change represents a current and future challenge for populations and ecosystems directly connected to the coastal environment (Palmer et al., 2019). Relative sea level rise refers to the local change of sea level (Gregory et al., 2019) under the effect of global sea level rise due to global warming and local effects that could reduce the global signal (e.g. the isostatic rebound) or exacerbate it (e.g. land subsidence). Subsidence can be driven by both natural and human processes. The main components of natural subsidence are tectonic and sediment compaction while human-induced subsidence is related to mining (Bell et al., 2001, 2000; Yavuz, 2004; Zhengfu et al., 2010), urbanization and fluid withdrawal (Carbognin et al., 2010; Gatto and Carbognin, 1981; Nicholls, 1995; Shen et al., 2014;

Stramondo et al., 2008; Tosi et al., 2010; Zanchettin et al., 2021). Hence, human-induced subsidence can amplify the effect of relative sea level rise thus increasing flood risk (Antonioli et al., 2017; Umgiesser et al., 2021; Zanchettin et al., 2021), as well as the accommodation space, responsible for the submergence and drowning potential of littoral systems (De Falco et al., 2015; Sanders and Kumar, 1975). Venice represents one of the most famous examples of exacerbation of natural subsidence by groundwater withdrawal which have caused a human-induced exacerbation of SLR of about 10 cm compared to other coastal areas in the northern Adriatic Sea (Gatto and Carbognin, 1981; Zanchettin et al., 2021).

The transgressive trend resulted from relative SLR is exacerbated by the simultaneous severe anthropogenic influence on sediment supply and longshore transport, as well as on coastal dynamics and subsidence (Anthony et al., 2014; Besset et al., 2019; FitzGerald et al., 2008; Maselli and Trincardi, 2013; McManus, 2002; Syvitski and Saito, 2007). Further human actions such as the construction of river dams, embankments or the dredging of sand and gravel on riverbeds contribute to the modification of sedimentary flows from rivers to the sea (Anthony, 2015; Otvos, 2018; Ritchie et al., 2018; Rubin et al., 2015).

In shallow environments, the dynamics of sea level rise interact with tides, waves and sediment transport, making the response of the environment more complex (Friedrichs et al., 1990; Palmer et al., 2019). These complex interactions between hydrodynamics, sediment transport and morphological changes over variable time scales make it difficult to produce quantitative predictions of future geomorphology with certainty (Coco et al., 2013; French et al., 2016; Van Maanen et al., 2016).

2.3 Shoreface and wave processes

The shoreface is the surface that develops from the low-tide shoreline to the depth where wave action interacts with the seabed. The term shoreface, introduced by (Barrell, 1912) with a stratigraphic meaning, has successively been updated from a clear hydrodynamic/morphodynamic point of view (Cowell et al., 2003; Galloway and Hobday, 2012; Hinton and Nicholls, 2007; Niedoroda et al., 1984; Swift et al., 1985; Wright, 1995).

The shoreface can be separated into two zones (Anthony and Aagaard, 2020): the upper shoreface is the most morphologically active zone at annual timescale while in the lower shoreface the morphological changes due to wave motion are much smaller at annual timescale (Aagaard, 2014). These two zones are separated by the inner closure depth defined by (Hallermeier, 1981) with respect to the significant wave height that exceeded for 12 hours per year. The seaward boundary of the lower shoreface is usually defined by wave base, i.e. the depth where seabed and wave start to reciprocally affect. Hence, within the lower shoreface the morphological features are mostly wave-dominated while, beyond, current became dominant (Anthony and Aagaard, 2020).

The shallow bathymetry in the upper shoreface induce the process of wave breaking that produces important morphological changes at annual timescale (Aagaard, 2014; Ruggiero et al., 2016; Ruiz De Alegría-Arzaburu et al., 2022). During breaking, part of the energy and momentum of wave motion is converted in a turbulent flow, generating nearshore currents, increase in the water level (wave set-up) and sediment resuspension. Such energy and momentum transfer from waves to currents and seabed and consequent morphological dynamicity perdures throughout the surf zone.

On the other hand, in the lower shoreface, except during storm wave conditions, the wave shoaling, the change in wave shape due to reduction in water depth, is the most active process (Anthony and Aagaard, 2020). The energy flux is maintained during shoaling, with a consequent increase in energy density due to the progressive reduction of wave speed. The consequence of energy flux conservation is the almost morphodynamic stability of lower shoreface at annual timescale (Aagaard, 2014; Hallermeier, 1981).

A consequence of shoaling and wave-speed reduction due to depth is refraction, a process in which the wave direction tend to parallelize with the bathymetric contours. Due to refraction, wave fronts tend to converge around headlands and to diverge entering bays, with a consequent increase or decrease in wave energy respectively. In coastal areas characterized by a complex bathymetry refraction could lead to patterns in wave energy that significantly influence coastal dynamics.

2.4 Sediment transport dynamics

Wave motion, jointly with tides, currents, bathymetry, type and availability of sediments drives sediments dynamics such as erosion, transport and deposition, which involve upper and lower shorefaces at a range of spatial and temporal scales, from local and event-scale to regional and longer time integrated changes (Anthony and Aagaard, 2020).

In the study and management of sandy and flat coasts, a fundamental factor is the evaluation of sediment dynamics and budget, that becomes even more important considering the potential changes in coastal forcing due to the anthropogenic factors (Anthony, 2005; Pilkey and Cooper, 2014). Sediment transport is commonly divided into components: the alongshore transport is the sediment transport parallel to the shoreline, while cross-shore transport is the component normal to the shoreline itself.

Longshore transport, the sand movement in the nearshore parallel to the shoreline (Seymour, 2005a), is among the most important processes in the coastal evolution and largely determines whether a shoreface is stable, eroding, or accumulating (Leont'yev, 2014). Occurring mainly within the surf zone, longshore sediment transport is a critical process affecting beach morphology and plays a major role in determining whether coastlines erode, accrete, or remain unchanged. It is crucial for coastal morphodynamics to incorporate a thorough understanding of this process. Net annual transport can range from essentially zero to large

quantities, estimated at one million cubic meters of sand per year for some coastal sites (Rosati et al., 2002; Seymour, 2005a). It is the result of seabed resuspension by waves and consequent transport by longshore currents, usually generated by waves and enhanced or reduced by tidal or wind-driven currents (Seymour, 2005a). As firstly suggested by (Eaton, 1950) and subsequently explained by (Komar, 1976), the longshore transport is driven by waves approaching at the shoreline obliquely and, theoretically, the maximum value is associated with an angle of 45°.

In addition to longshore transport, sediments can also be transported perpendicular to the shoreline, producing so-called cross-shore transport. A wave motion perpendicular to the beach has the ability to rearrange the sediment perpendicular to the shoreline while the movement of the sediments in a direction parallel to the shoreline is minimal. Cross-shore sediment transport can lead to major morphological changes even at daily timescale and is particularly associated with beach erosion (Seymour, 2005b).

The cross-shore transport mechanics are associated with wave asymmetry approaching the beach. As hypothesized by (Cornish, 1898) and subsequently verified by (Bagnold, 1940), the orbital motion under Stokes-type waves induces a shoreward transport of coarser sediments and a corresponding seaward transport of finer particles. In fact, Stokes-type waves are characterized by forward motion of short duration but high velocity able to produce a shoreward transport of both coarse and fine sediments, and a backward motion slower but longer that is able to carry fine particles only, producing a seaward net transport of the latter (Dean, 1973; Rafati et al., 2022).

Once the net particle transport is null, it reaches an equilibrium among fluid forces, gravity force (related to seabed slope) and grain-size characteristics called null-point hypothesis, concept introduced by (Cornaglia, 1889) and subsequently modelled by (Bailard, 1981; Bowen, 1980) on the basis of (Bagnold, 1966) sediment transport model. Under the null-point hypothesis, the shoreward increase in wave energy due to shoaling, lead to an onshore coarsening gradient (Ippen and Eagleson, 1955). Moreover, (Dean, 1991) proposed the concept of equilibrium profile of the shoreface as a function of the grain-size distribution along the profile expressed by the equation:

$$h(y) = Ay^{0.67}$$

where $h(y)$ is the depth at distance y from the shoreline and A is a scale factor related to grain-size distribution.

Even though null-point equilibrium and equilibrium profile are useful theoretical models to understand cross-shore sediment dynamics, the complexity of coastal environments can't be fully described. The equilibrium profile is intrinsically correlated with the temporal and spatial timescale chosen (Osborne and Simpson, 2005). For example, at seasonal timescale, the difference between winter and summer wave climate can

produce significant effects on the cross-shore sediment transport and then a modification of the shoreface profile (Seymour, 2005b).

Moreover, major storm event can have a significant impact on the cross-shore profile and sediment transport (Anthony and Aagaard, 2020; Casagrande et al., 2023; Shepard, 1950; Wright et al., 1985), often causing the seaward migration of nearshore sandy bars (Ruessink et al., 2003; Ruiz De Alegría-Arzaburu et al., 2022; Seymour, 2005b). In fact, the larger and more energetic waves exacerbate sediment transport dynamics: they produce stronger longshore currents capable of resuspending coarser sediments at greater depth, speeding up the sediment transport, with consequent significant morphological changes at short timescales.

The erosive trend often recorded in the upper shoreface due to extreme storm events is progressively recovered over longer timescale by the sediment supply from the lower to the upper shoreface during not-extreme conditions (Aagaard, 2014; Aagaard et al., 2004; Anthony and Aagaard, 2020; Guillén et al., 2024; Stive and de Vriend, 1995; Thom and Hall, 1991): such mechanism could be significative even in the adaptation to RSLR (Guillén et al., 2024).

Extreme events and RSLR have a significant influence also on the beach, establishing a transgressive regime and often producing beach erosion and retreat (Bezzi et al., 2021b; Emery et al., 2019; McBride et al., 1995). Low-lying coastal barriers are particularly exposed to such treats (Nienhuis and Lorenzo-Trueba, 2019). In fact, during storm events associated with storm surges, the whole barrier can be flooded resulting in overwash, the landward movement of sediments due to overtopping (Casagrande et al., 2023; Nienhuis and Lorenzo-Trueba, 2019; Pouzet and Idier, 2024). If barrier frequently face overwash, rollover process become dominant with consequent landward migration of the barrier itself (Davis and Fitzgerald, 2004; Lorenzo-Trueba and Ashton, 2014; McBride et al., 1995; Tillmann and Wunderlich, 2013).

2.5 Morphology

The complex interplay of coastal forcings, driving sediment dynamics, are able to reshape the seabed often creating peculiar features such as sand bars, troughs, ripples, megaripples, dunes. Among coastal features, the ones that are organized in rhythmic patterns are particularly interesting because of their relationship and feedback with specific flow conditions (Coco et al., 2022; Masselink et al., 2014). Spatial scale of coastal rhythmic feature ranges from centimetric (e.g. ripples), to decametric (e.g. dunes or megacusps) up to kilometric (e.g. rhythmic spits). Most of these bedforms represent the signature of short time scale processes.

On a longer temporal scale, transverse finger bars are long transverse bars, i.e. sandy bars oriented normally or inclined to the shoreline (Shepard, 1952), found in the subtidal areas of certain beaches, developed up to the depth of few meters (Niedoroda and Tanner, 1970). These features are particularly stimulating to analyze

in the morphodynamic framing of a specific coastal area since they appear to be the signature of longer temporal scale processes in a way not yet entirely clear.

Numerous elongated finger bars can be found on wide, sheltered, microtidal coasts with low to moderate energy wave conditions (Bruner and Smosna, 1989; Falqués et al., 2021; Garnier et al., 2012; Gelfenbaum and Brooks, 2003, 1997; Niedoroda, 1972; Niedoroda and Tanner, 1970). These beaches are ideal for finger bar formation because of their characteristics, such as gently slope, terraces and abundant sediment supply (Niedoroda and Tanner, 1970; Ribas and Kroon, 2007). These long-crested finger bars often stretch far beyond the surf zone, with their length typically being two to five times greater than their width between waves (Ribas and Kroon, 2007). Such bars generally vary in height from 0.2 to 2.1 m (Gelfenbaum and Brooks, 2003) and in a wide range of length: from tens of meters (Carter, 1978) to a kilometer (Goud and Aubrey, 1985), but can reach a length of 3500 m when filled by important sediment supply (Ribas and Kroon, 2007). The heights of the bars are typically lowest at the extremes and greater in the middle section (Gelfenbaum and Brooks, 2003). They vary in cross-shore length between 10 and 200 m and are spaced from 10 m to 360 m (Konicki and Holman, 2000, 1997; Ribas and Kroon, 2007), extending up to relative deep waters (Levoy et al., 2013). These structures are oriented either perpendicularly or at an angle to the shoreline direction (Ribas and Kroon, 2007) and tend to remain relatively stationary, exhibiting very low rates of movement (Ribas and Kroon, 2007).

In more energetic coasts, transverse finger bars tend to have narrower cross-shore extensions and exhibit higher migration rates compared to those found in more protected environments (Konicki and Holman, 2000). Here, finger bars may be connected to the low-tide shoreline or may be “offshore bars”, connected to a shore-parallel inner bar (Gelfenbaum and Brooks, 2003; Konicki and Holman, 2000). Levoy et al. (2013) reported one of the few observations of transverse finger bars in higher tidal range environments.

Finger bars’ orientation may be normal to the shoreline, tilted up-current (i.e. against the alongshore flow) or down-current (i.e. in down-flow direction): such orientation depends on the angle of wave incidence and the depth-integrated suspended sediment concentration (Ribas and Kroon, 2007). Furthermore, they can have opposite directions with respect to the littoral drift (Levoy et al., 2013).

The rates of migration of such bars range from substantial immobility (Bruner and Smosna, 1989; Niedoroda and Tanner, 1970) to tens of meters per year (Gelfenbaum and Brooks, 2003; Goud and Aubrey, 1985; Levoy et al., 2013; Pellón et al., 2014) up to meters per day (Garnier et al., 2012; Konicki and Holman, 2000; Ribas et al., 2012; Ribas and Kroon, 2007).

Transverse finger bars may be almost symmetrical or asymmetrical (Levoy et al., 2013). In case of asymmetry, the steeper slope is a useful indicator of the direction of bar migration (Gelfenbaum and Brooks, 2003).

Although the formation of transverse finger bars seems to be related to multiple factors such as the bathymetry, wave climate, currents and high sediment supply (Falqués et al., 2021, 2012; Levoy et al., 2013; Ribas et al., 2012; Ribas and Kroon, 2007), there is not a clear relationship between the marine forcings and their morphological characteristics (Gelfenbaum and Brooks, 2003; Levoy et al., 2013). Different mechanisms of finger bar formation were proposed. (Niedoroda and Tanner, 1970) supposed that wave shoaling induced by refraction may cause an along-crest sediment circulation that may generate and maintain transverse bars. Other authors suggest the implication of wave-induced longshore currents (Falqués et al., 1996, 1993) and/or wind-wave processes (Garnier et al., 2012; Khabidov, 2001; Pellón et al., 2014), modulating the nearshore wave energy and influencing the coast stability and management (Levoy et al., 2013). Models based on self-organization mechanisms in the surf zone (Caballeria et al., 2002; Falqués et al., 2000; Ribas et al., 2003) are also proposed, some of these based on the instability analysis (Falqués et al., 2021; Levoy et al., 2013; Ribas et al., 2012, 2011) focused on the importance of a sand depocenter in the transverse bar formation. Field measurements showed that no single mechanism seems to explain the heterogeneous formation of bars observed in nature (Gelfenbaum and Brooks, 2003; Levoy et al., 2013).

2.6 Analysis & methodologies

There are various investigation methodologies that can be used to study the coastal environment, and which are often used together in multidisciplinary approaches in order to exploit the strengths of each, making up for the weaknesses that each individual method presents. Topographic and bathymetric surveys using GNSS and echo-sounders (Aouiche et al., 2015; Bezzi et al., 2021a; Fontolan et al., 2007; Psuty et al., 2016) (e.g. Allen et al., 2012; Benninghoff and Winter, 2019; Mitasova et al., 2019; Silva et al., 2019), aerial photogrammetry with Unmanned Aerial Vehicles (UAVs) (Casagrande et al., 2023; Gonçalves and Henriques, 2015; Kandrot et al., 2022; Klemas, 2015; Laporte-Fauret et al., 2019) and sediment sampling (Baux et al., 2022, 2019; Diesing et al., 2020, 2014; Khomsin et al., 2021; Lark et al., 2015) are among the mostly used survey techniques to study the coastal environment.

Once collected, these data are processed to obtain multiple outputs: for example, digital elevation models (DEMs) are produced from topographic, bathymetric, or aerial photogrammetric data, while sedimentological maps are generated from sediment samples. DEMs and sedimentological maps are the basis of further elaborations aimed at analyzing coastal dynamics through, for example, the definition of sedimentary transport, the sediment budget, morphological analysis and its temporal evolution, hydrodynamic modeling etc. etc.

2.6.1 Sedimentological mapping

In coastal environments, in particular, the characteristics and distribution of sediments is one of the most important elements for both scientific and applicative purposes. Sedimentological maps furnish a useful morphosedimentary frame in specific coastal environments (Bezzi et al., 2021a; Bianco et al., 2020; Conti et al., 2012; Jerosch, 2013; Kinsela et al., 2022; Park and Jang, 2014; Watson et al., 2020); it can give the possibility to reconstruct sediment-transport pathways (Baux et al., 2022; Conti et al., 2012; McLaren and Bowles, 1985; Yamashita et al., 2018) and represent a useful basis for coastal and marine engineering and for multidisciplinary and integrated environmental studies (Albertazzi et al., 1987; Longdill et al., 2007; Watson et al., 2020).

Extensive seabed sediment mapping is critical to characterize coastal and marine ecosystems, defining the distribution and extent of benthic habitats (Gaida et al., 2019; McBreen et al., 2008; Meilianda et al., 2015; Molinaroli et al., 2014; Ware and Downie, 2020). It is also crucial to support marine archaeological discipline in creation of predictive maps of archaeological potential and risk (Ward and Larcombe, 2008).

In recent years, the possibility to use indirect integrated methods by means of acoustic data (back scatter of acoustic signal) has offered a great opportunity to map the characteristics of sediment (Diesing et al., 2020; Gaida et al., 2019; Innangi et al., 2022; Khomsin et al., 2021; Watson et al., 2020), but remains substantially limited to the determination of the texture and not the grain size parameters.

The sedimentological maps based on physical ground truthing data remain a fundamental issue due to:

1. The possibility to represent the distribution of grain size parameters (Mean size, sorting, median), which allow to obtain hydrodynamic details about sedimentary processes; to support evaluation of coastal vulnerability to erosion (Bianco et al., 2020); for a correct sediment management, involving the exploitation of submerged sand deposits as strategic sediment reservoirs for beach nourishment (Brambilla et al., 2019; Correggiari et al., 2016; Fontolan et al., 2007); as a basis for numerical modelling of sediment transport and morphodynamics in coast and lagoons (Petti et al., 2018; Yaiche Temam et al., 2024).
2. the needs to reconstruct and digitalize maps based on old samples data, useful to compare data along time (Bianco et al., 2020; Sarretta et al., 2010) and evaluate environmental variation driven by natural or anthropogenic impact.

Sediment sampling with mechanical methods, e.g. grab samplers, is a quest that demands a high and extensive effort (Park and Jang, 2014; Sielski et al., 2017): then, even if geographical information systems provide geostatistical algorithms that allow to generate maps rapidly (Lark et al., 2012), the sparsity of data obtained through sediment sampling becomes an issue for geostatistical interpolation (Jerosch, 2013).

Generally, among geostatistical approaches, kriging-based algorithms work well in case of low data density (Bockelmann et al., 2017) because of the possibility to use auxiliary data in the interpolation. In fact, when

only a few sediment samples are available, using additional, more thoroughly sampled auxiliary data that shares characteristics with grain size data can enhance the accuracy of predictions. (Bockelmann et al., 2017; Davis, 2002; Goovaerts, 1997; Jerosch, 2013; Lark et al., 2012; Park and Jang, 2014; Zananiri and Vakalas, 2019).

The nature of auxiliary data can be various: the most used are acoustic (Diesing et al., 2014; Hasan et al., 2012; Ierodionou et al., 2011; Sielski et al., 2017), bathymetric (Bockelmann et al., 2017; Jerosch, 2013; Koop et al., 2021; Lark et al., 2015; Meilianda et al., 2015; Zananiri and Vakalas, 2019) and secondarily geochemical (Baux et al., 2022, 2019; Li et al., 2019).

The general, hypothetically natural, relationship between the surficial sediment distribution and bathymetry or morphology (Zananiri and Vakalas, 2019) can offer the possibility to improve the quality of surficial sediment mapping (Jerosch, 2013). Using bathymetric data and the consequent morphological evidence in the process for the construction of sedimentological maps was the base for the expert-based manual method used in the past (Zananiri and Vakalas, 2019), when geologist exercised “expert” judgment by interpreting these data in the context of the geological (seabed and sub-seabed) and hydrodynamic environment. This judgement also introduces a level of adaptability and enables the interpreter to map areas where ground-truthing is limited, and to identify questionable, or over-represented sample points (Diesing et al., 2014). Even in geostatistical approaches the performance of interpolation relies to a certain degree on expert knowledge (Jerosch, 2013). In fact, nowadays, expert judgement is often use in the process of data analysis (Neder et al., 2020), parametrization, and quality assessment (Diesing et al., 2014; Lark et al., 2015).

Moreover, the spatial scale is an important factor to take into account when both small- and large- scale landforms are present. To increase the performance of interpolation, a locally adaptive parametrization could improve the detail and the confidence of the final output (Bockelmann et al., 2017).

2.6.2 Sediment budget and transport computation

There are numerous studies that have attempted to quantify sediment transport and obtain information on the type of sediments transported based on different approaches, such as data-driven, sediment budget or modeling e.g. (Baux et al., 2022, 2019; Bhattacharya et al., 2005; Li et al., 2019; Poizot and Méar, 2010; Yamashita et al., 2018). However, the transport mechanism is quite complex and its description, often based on simplified assumptions, is often affected by errors (Bhattacharya et al., 2005; Poizot and Méar, 2010).

Data-driven methods received an important contribution from the work of McLaren (1981) who defined Sediment Trend Analysis. In this method, and in the many methods derived (Baux et al., 2022, 2019; Poizot and Méar, 2010; Yamashita et al., 2018), the objective is to find the sediment transport vectors starting from the grain-size statistical parameters of surficial sediment sampled on the seabed. The spatial variation of

statistical parameters, such as mean-size, sorting, skewness, etc., is related to the type and direction of sediment transport, related to the meteorological and sediment source forcing present. In such methods, auxiliary data analysis such as chemical elements distribution can provide useful information in the assessment of sediment transport. Physical processes leading to sediment resuspension and transport also affect the heavy metal's fluxes (Pavoni et al., 2023b). Since that, some studies integrated the sediment transport analysis based on the grain-size parameters with the distribution of chemical elements (Baux et al., 2022, 2019; Duman et al., 2006; Li et al., 2019).

A widespread method for determining the sedimentary flows and evolutionary trend of a coastal region is the sediment budget quantification. Sediment budget not only describes the sediment transport dynamics but also can provides information about erosion/accretion at different timescales (from daily to multi-decadal). Several authors have used this methodology to determine sedimentary budgets (Anfuso et al., 2011; Aouiche et al., 2015; Giardino et al., 2018; Messaros et al., 2018; Rosati, 2005; Sabatier et al., 2006; Sarretta et al., 2010). A sediment budget quantifies the volumes of sediment entering and leaving the system in a certain time interval in a given area (or cell) (Roberts and Brooks, 2018) and the resulting erosion or accretion in the coastal area under consideration. This way it is possible to determine whether a system has a net increase or deficit of material and therefore whether it is in equilibrium or disequilibrium (Roberts and Brooks, 2018). Sediment budget can be processed both at a local and regional scale and can be developed for short to long-term analyzes (Rosati, 2005). The use of a local scale, compared to the regional scale, simplifies the analysis: however, a regional balance is often necessary to fully understand long-term sedimentary dynamics (Rosati, 2005). The principle underlying the sedimentary balance is simply a condition of continuity, that is, conservation of volume or mass for a defined system (Roberts and Brooks, 2018). In the example of a beach, the continuity may be largely one-dimensional along the shore. Conversely, in wider environments, the paths to establishing continuity can be very complex and multidirectional. The complexity increases further when considering different types of sediments such as mud, sand and gravel which have a different behavior under the hydrodynamic conditions. Furthermore, the time horizon over which the system is observed can determine whether the beach is eroding, accumulating or in equilibrium (Roberts and Brooks, 2018). Generally, the coastal area is divided into cells whose dimensions are chosen following the aim of the study and the loss/gains in volume are calculated for each cell (Rosati, 2005). The objective is to evaluate at different time- and spatial-scale sediment gain/loss, sediment transport and source-to-sink pathways (Anfuso et al., 2011; Aouiche et al., 2015; Patsch and Griggs, 2008; Van Rijn, 2011).

Recently, sediment transport modeling has become quite popular (Aagaard, 2014; Amoudry and Souza, 2011; Aouiche et al., 2015; Chen et al., 2024; Ruggiero et al., 2016) thanks to the ever-increasing computational power and modeling packages (Anthony and Aagaard, 2020) and the high spatial and temporal density of marine and meteorological data (e.g. water level, wave and wind parameters, atmospheric pressure, water

and air temperature, salinity, etc. etc.). Sediment transport modeling is mainly based on the effect of waves and currents in the resuspension and transport of seabed sediments.

Physically, to move the sediment deposited on the seabed, the flowing fluid must produce a shear stress on the seabed greater than a specific threshold. The critical bed shear stress is a key concept in sediment transport and morphodynamics. It refers to the minimum shear stress required to initiate movement and subsequent transportation of sediment particles along the bed of a body of water, such as a river, lake, or ocean. This threshold varies depending on factors such as grain size, density, cohesiveness, and bed's roughness. Critical shear stress is proportional to grain size and density: the coarser and denser the grain, the greater its threshold to start moving. However, cohesiveness plays a fundamental role in sediment motion dynamics. In fact, finer sediment such as muds have usually greater cohesiveness, leading to a complex behavior under the effect of fluid flow.

Understanding and calculating this stress is crucial for managing and predicting sediment transport in various environmental contexts. In the literature there are several experimental works that have tried to understand in detail the behavior of sediments under the effect of a fluid, some of which have focused mainly on non-cohesive sediments (sand and gravels) e.g. (Egiazaroff, 1965; Govers, 1987; Mantz, 1977; Miller et al., 1977), others on mixtures of granular and cohesive sediments, such as sand and mud respectively (Jacobs, 2011; Kamphuis and Hall, 1983; Van Rijn, 2020, 1993).

3 Study area

3.1 Geographical setting

The study area is a coastal area of the northern Adriatic Sea. Entirely included in the municipality of Grado, it is boarded by the Isonzo River's mouth to the east, the Grado Inlet to the west and the Marano and Grado Lagoon to the north which is connected to the study area by the Primero Inlet (Figure 1). The Primero inlet separates the two most significant sedimentary bodies of the study area, the Isonzo's Delta to the east and the MMB to the west. At depths up to approximately -3 m, a system of longitudinal bars develops westwards from the Isonzo's mouth along the entire study area, constituting the longshore littoral drift pathway, punctually interrupted only by the Primero Inlet (Bezzi et al., 2021a). With a drainage basin of 3452 km², the Isonzo River is the main sedimentary source of the study area and at its mouth the average annual flow rate is 196.8 m³/s, with a monthly range between 43.1 and 665.9 m³/s (INTERREG II, 2001) and maximum values that can exceed 2500 m³/s during floods (RAFGV, 1986).

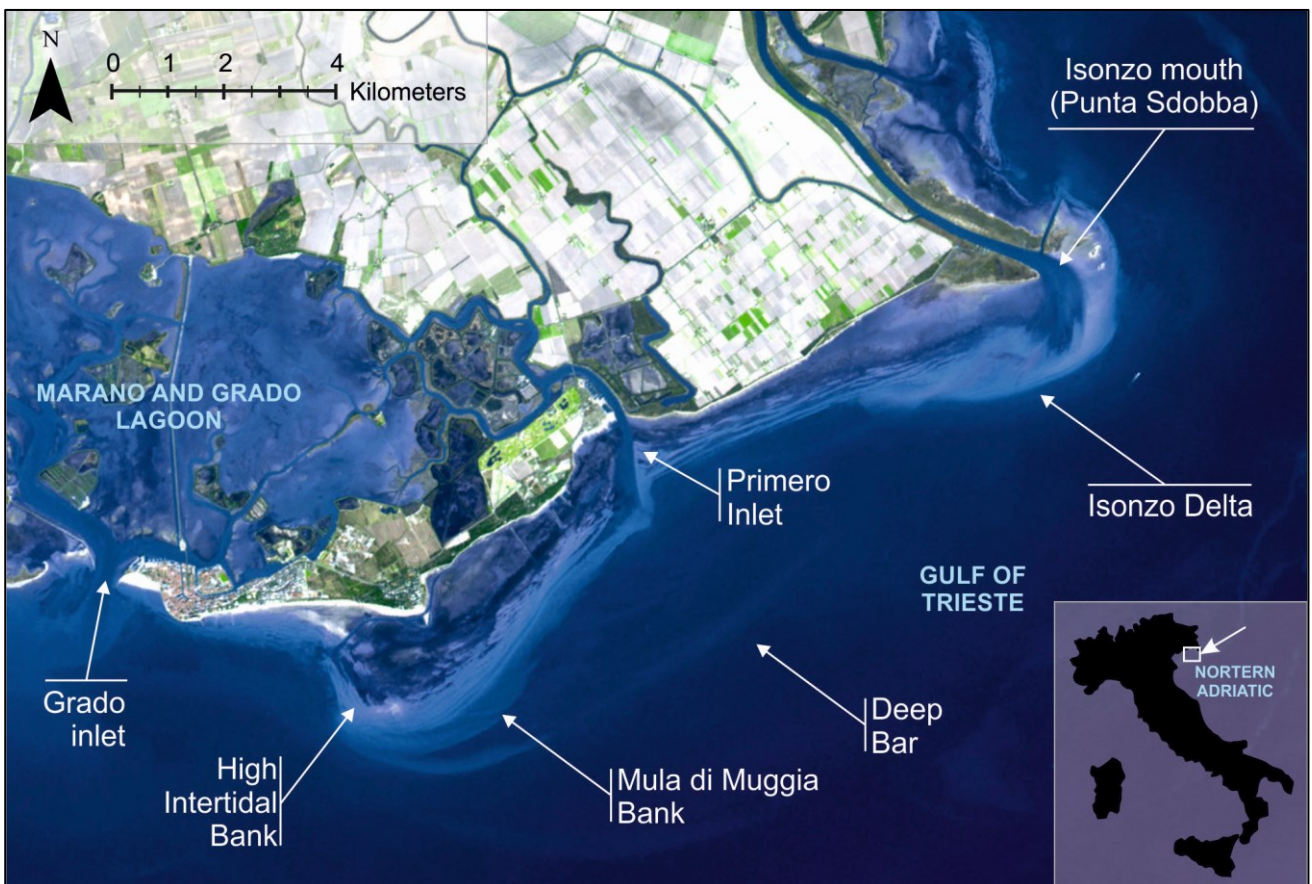


Figure 1 Overview of the study area (Basemap: Landsat, in false-color, modified from RAFVG, 2019).

3.2 Wind regime

The predominant winds in terms of frequency in the northern Adriatic Sea are largely from the first quadrant, primarily from the ENE direction (Bora) (Bezzi et al., 2018; RAFVG, 2019) as shown by the wind-roses of Lignano and Grado (Figure 2) reported by Fontolan et al. (2017). Additionally important are wind from

southern sector (Sirocco) which are secondary in term of frequency, while, regarding the intensity, Sirocco is comparable with Bora-Levante, and wind regime is substantially bimodal.

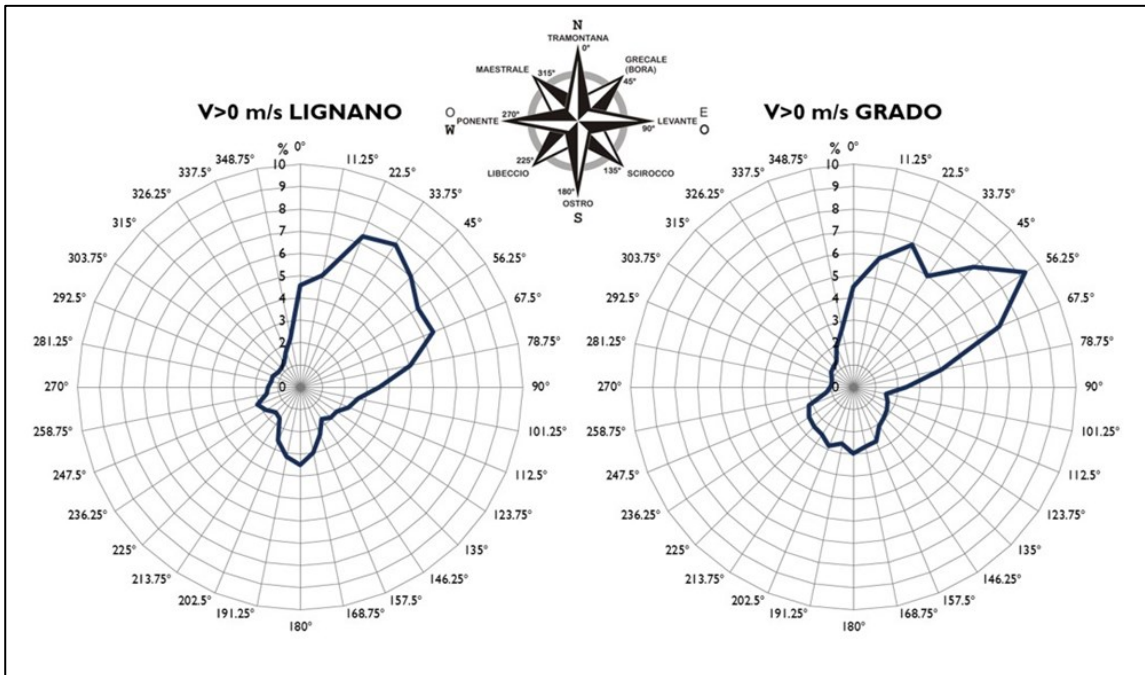


Figure 2 Wind roses of Lignano and Grado (from Fontolan et al., 2017): data relate to the anemometric stations of Lignano Darsena (managed by OSMER-FVG, hourly data relating to the time interval 2000-2014, coord. 13.15°E, 45.70°N) and Grado Meteo (managed by ISPRA, data every thirty minutes of time interval 1998-2014, coord. 13.37°E; 45.68°N).

The anemometric data recorded in the Gulf of Trieste at the Paloma weather station (Figure 3) over the past two years (from July 2022 to June 2024) are consistent with historical data recorded in Grado and show a predominance of ENE winds both in terms of frequency and intensity (Figure 4).

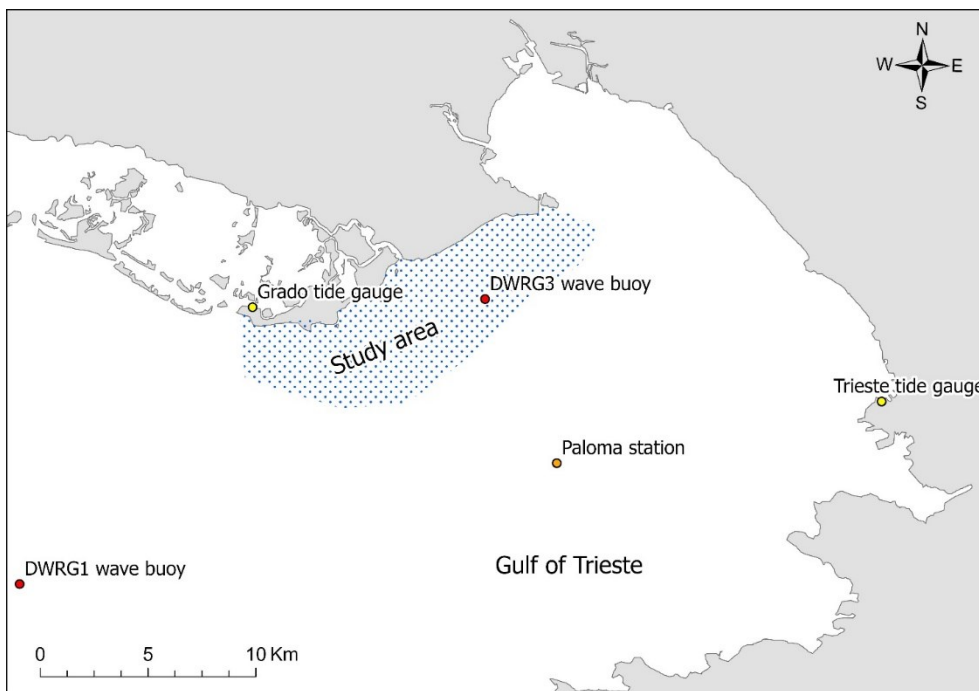


Figure 3 Location of the meteorological and marine forcing measurement instruments in the Gulf of Trieste.

Secondarily to the northeasterly winds, there are Libeccio (SW), more frequent and intense than Sirocco in the center of the Gulf. The maximum values recorded reach 25 m/s in the Bora sector.

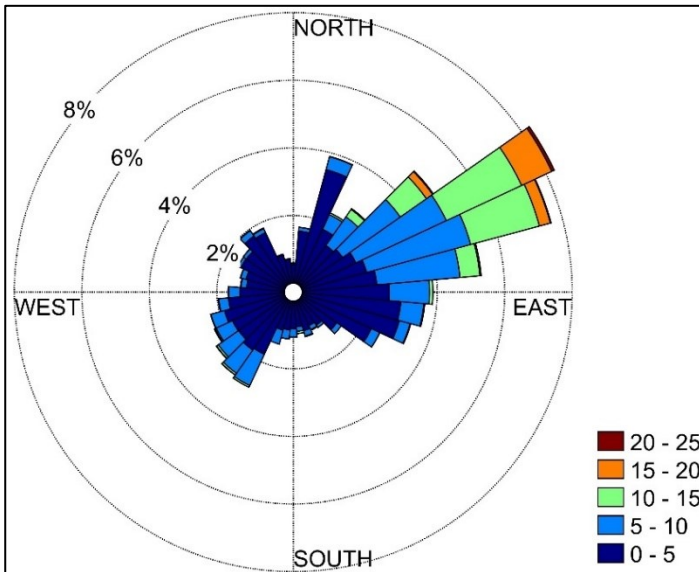


Figure 4 Wind rose of Gulf of Trieste: data relate to the anemometric stations of Paloma Station (managed by OSMER-FVG, hourly data relating to the time interval 07/2022 - 06/2024, coord. 13.57°E, 45.62°N, 10m height).

3.3 Wave regime

The Gulf of Trieste is characterized by anti-clockwise semi-diurnal tides with a mean range of 76 cm (Petti et al., 2019), a mean spring-tide range of 105 cm, and a mean neap tide of 22 cm (Dorigo L., 1965). Bora and Sirocco generate a bimodal wave regime (Figure 5a), with the mean significant wave height (H_s) less than 0.5 m, according to data collected at the wave buoy DWRG1 (placed at the coordinates 13.24°E, 45.56°N, -15.2 m depth) managed by the National Institute of Oceanographic and Applied Geophysics (OGS). Events with H_s greater than 0.5 m represent the 25.2% of the overall record, with prevailing waves from the SSE (10.7%) and ENE (10.5%): even if Sirocco is weaker than Bora, its fetch above 800km, one order of magnitude longer than the Bora's fetch, causes its waves to record the highest H_s values of 4.4 m (RAFGV, 2019). The OGS wave buoy DWRG3 (placed at the coordinates 13.52°E, 45.69°N, -9.7 m depth), located inside of the study area, recorded only 11.5% of events with H_s greater than 0.5 m, also coming from two main directions (Figure 5b). However, waves roses of the two buoys indicate that waves recorded at DWRG3 (Figure 5b) are rotated clockwise with respect to DWRG1 (Figure 5a), coming from E and SSW, and deviate slightly from Bora and Sirocco respectively.

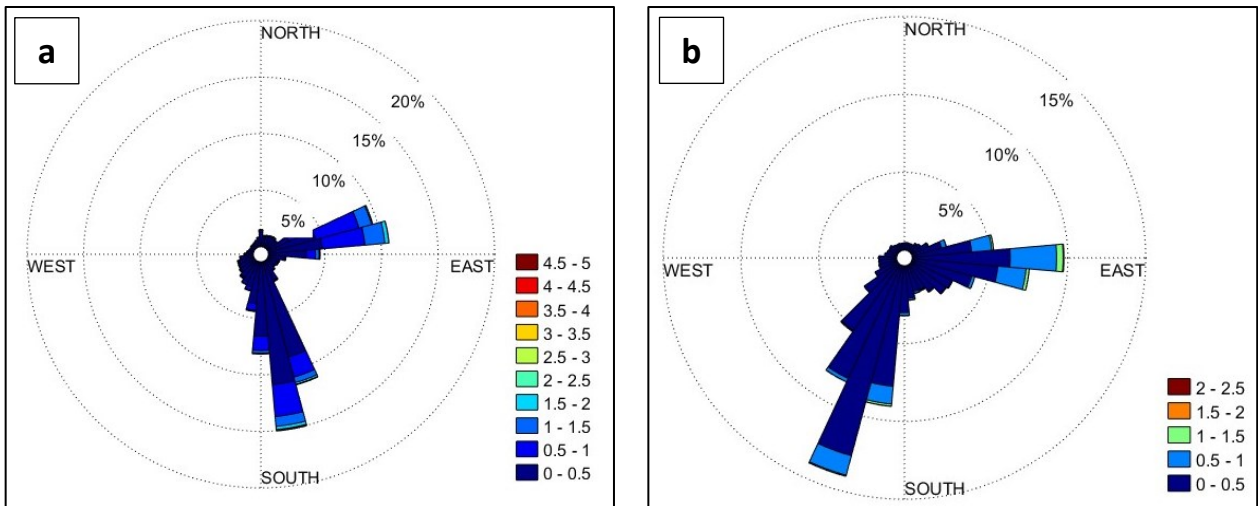


Figure 5 Wave roses of (a) DWRG1 relating to the time interval 2004-2023, and (b) DWRG3 relating to the time interval 2007-2023.

3.4 Sea level rise

Similar to most coastlines worldwide, the study area is also experiencing relative sea level rise. The historical series of the mean sea level recorded at the tide gauge of Trieste – Molo Sartorio (located at 13.76°E and 45.65°N) (Figure 6a) shows how the R-SLR is a secular phenomenon with a rate in the order of +1.4 mm/y, although there are also annual variations of several centimetres and ten-year oscillations (orange line in the graph of Figure 7). In particular, the average levels recorded in 2010 (+10.6 cm) and 2014 (+8.2 cm) are significant when compared with the 2020-2022 average (+0.3 cm). The mean sea level refers to the Italian IGM42 datum.

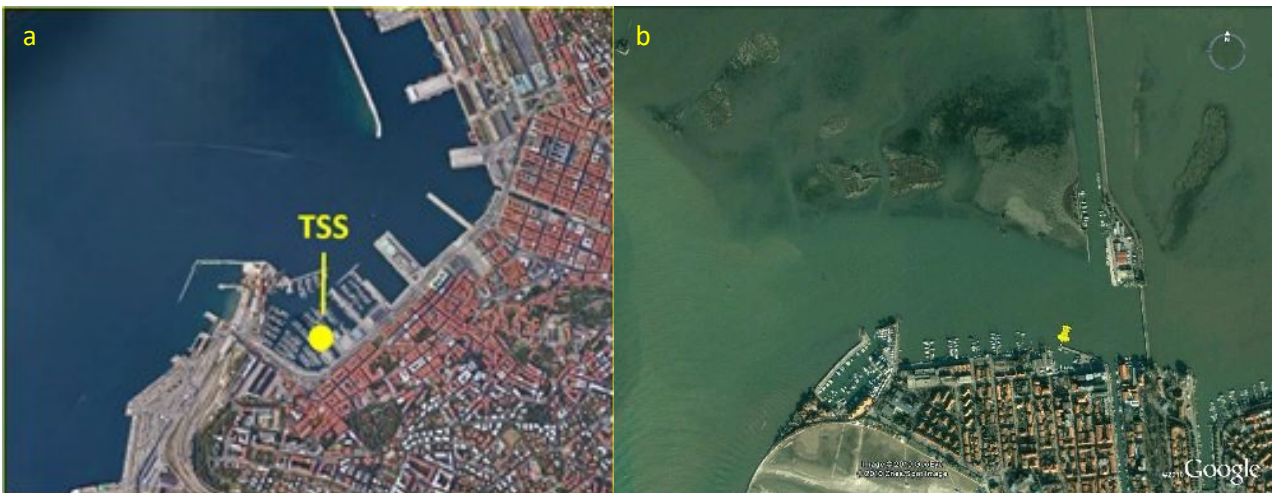


Figure 6 Location of the tidal gauges in (a) Trieste - Molo sartorio and (b) Grado.

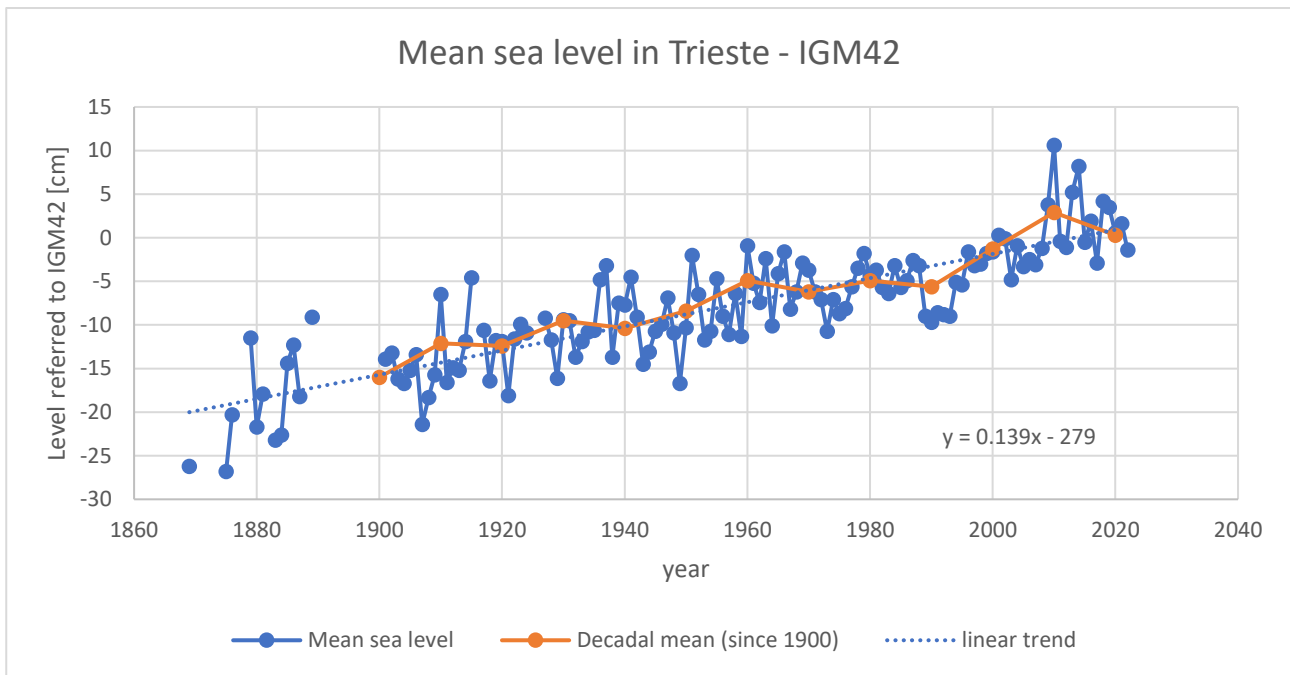


Figure 7 Mean annual water level (blue line) registered at Trieste tidal gauge and decadal mean (orange line).

Since 1991, data from the Grado tide gauge station (located at 13.38°E and 45.68°N), part of the ISPRA Venezia monitoring network, has been available (Figure 6b). The 32-year historical series of mean sea level (Figure 8), measured with respect to the tide gauge zero of Punta della Salute (ZMPS) in Venice (+23.56 cm above the Italian datum IGM42), indicates a progressive increase in mean sea level with a rate of +4.7 mm/y, higher than that recorded in Trieste in the same period (+3.1 mm/y). The Grado tide gauge, the closest to the study area, is located in a territory geologically similar to the study area, characterized by alluvial substrates hundreds of meters thick, more subject to subsidence phenomena than karst-flyschoids substrates of Trieste. In fact, as reported by (Areggi et al., 2023), who analyzed the subsidence using satellite differential interferometry (InSAR), the substrate characterized by Quaternary deposits with thicknesses of hundreds of meters (Tosi et al., 2010) of the Friulian-Venetian plain tends to compact generating subsidence around -2 mm/y in the Grado area, while Trieste is essentially stable or slightly rising due to active Dinaric tectonics. Values similar in Grado (-2.3 mm/y) are also represented by the InSAR data made available by the European Ground Motion Service (EGMS) of the European Environment Agency which used the Copernicus satellite data of the Sentinel 1 in the period 2015-2021 (EGMS, 2022), reported in the technical report (Fontolan et al., 2023b)(Figure 9).

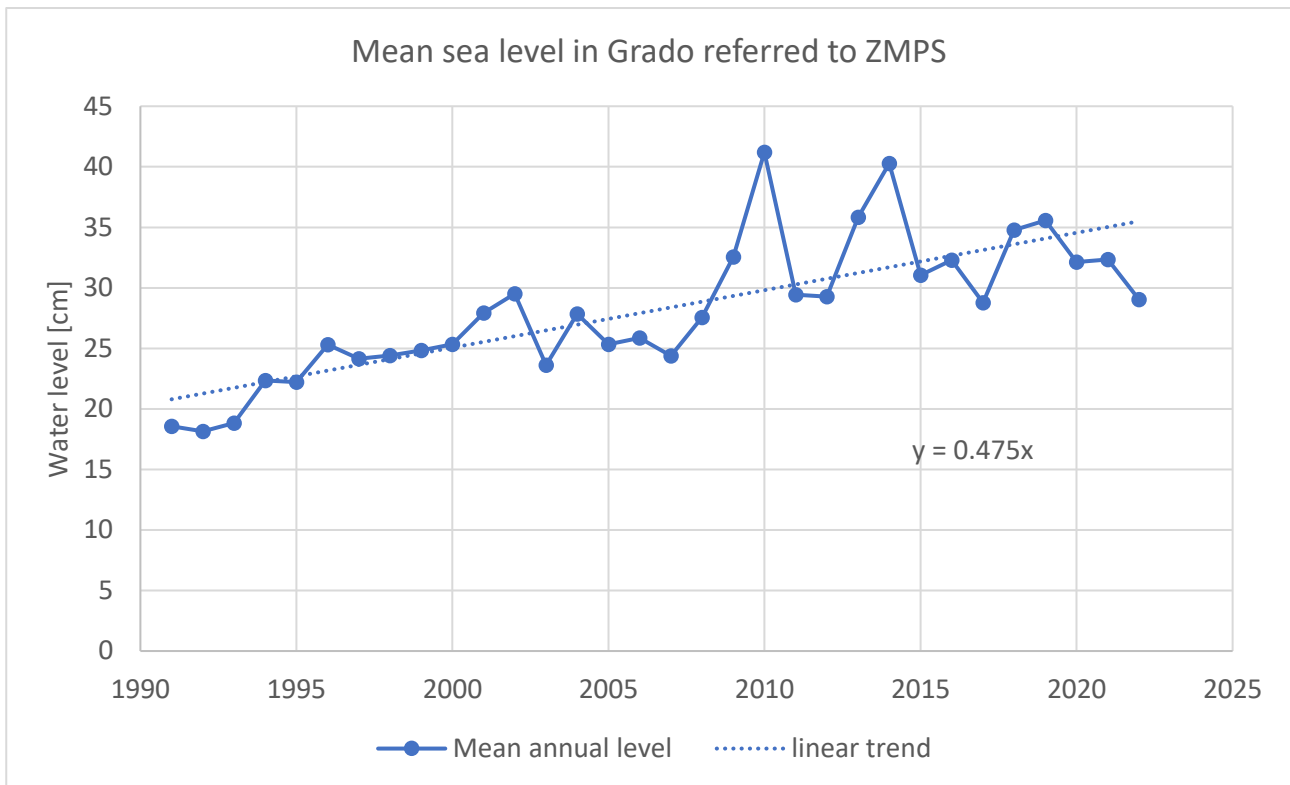


Figure 8 Mean annual water level (blue line) in Grado registered by the ISPRA tidal gauge and linear trend (blue dotted line).

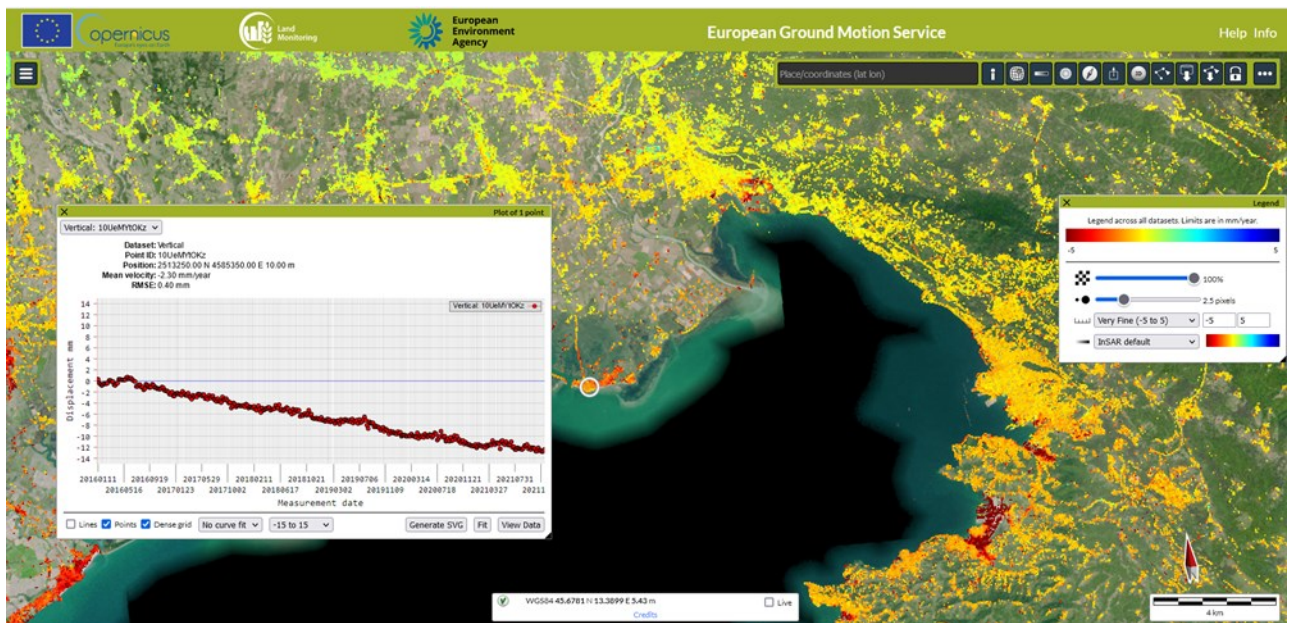


Figure 9 Land subsidence in Grado from EMGS portal (EGMS, 2022).

3.5 Extreme storm events

The combined effects of spring tides, seiches, winds, and low atmospheric pressure can lead to a significant rise in sea level in the northern Adriatic, a phenomenon locally known as “acqua alta”. The parameterization of storm surges in the northern Adriatic is quite variable and site-dependent (Perini et al., 2020). Several authors have defined the minimum threshold for the significant wave height to classify a storm surge event as being between 1.5 m (Armaroli et al. 2007; Boccotti 1997) and 2 m (Bertotti et al., 1996). The storm surges

in the northern Adriatic Sea are mainly related to Sirocco and secondly to Bora due to their different fetches of 800 km (the whole Adriatic basin) and 20 km respectively (Lionello et al., 2012). Numerous scientific studies have focused on extreme storm events in the northern Adriatic due to the presence of the city of Venice and its significant artistic and cultural heritage (Carbognin et al., 2010; Ferrarin et al., 2022, 2021; Fontolan et al., 2023a; Mel et al., 2023; Umgiesser et al., 2021). Fontolan et al. (2023a) created a database of the storm events that had an impact on the coasts of Veneto (the Italian region west of Friuli Venezia Giulia) and found that a total of 79 storm events between 1980 and 2022 (Figure 10), with a significant increasing trend since 2000s, partially due to the greater amount of data available online. The majority of the events occurred in autumn months while only few events occurred in summer (Figure 11).

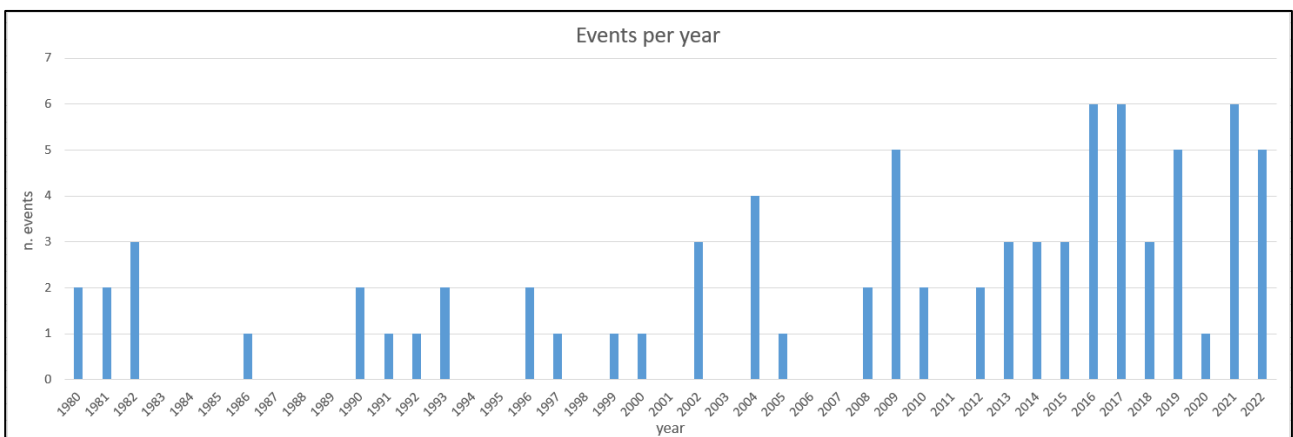


Figure 10 Event per year between the 1980 and 2022 (from Fontolan et al., 2023a).

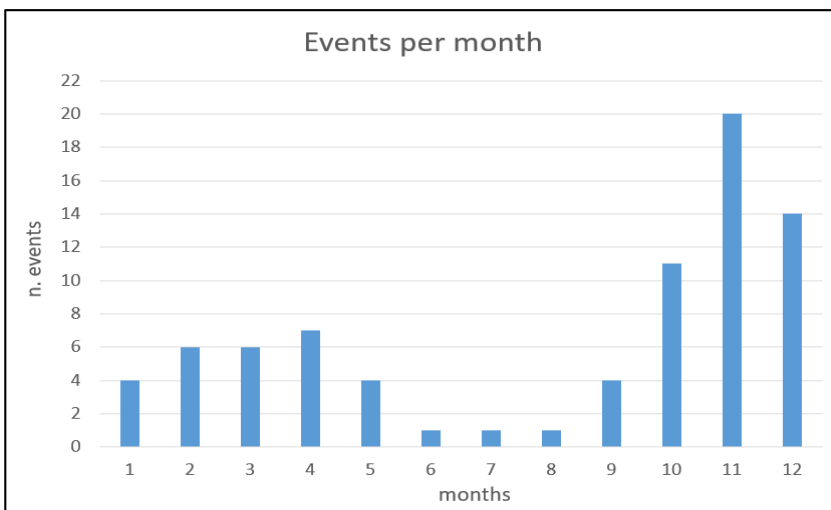


Figure 11 Event per months between the 1980 and 2022 (from Fontolan et al., 2023a).

Most of the events were caused by Sirocco and secondly by Bora (Figure 12a and b): however, since the greater fetch of Bora in Veneto compared to the study area, it can be assumed that Sirocco storm events are even more predominant.

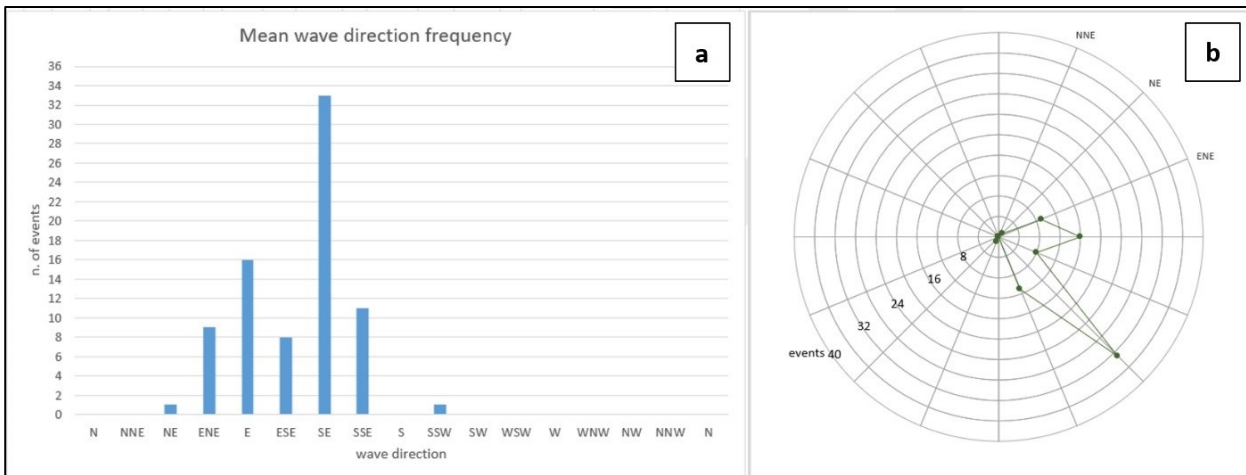


Figure 12 a) Number of events and b) average wave/wind direction frequency for the 79 events identified between 1980 and 2022 (from Fontolan et al., 2023a).

The distribution of maximum Hs (data provided by Pomaro et al. (2017, 2018) recorded at the CNR-ISMAR Acqua Alta oceanographic tower, (coord. 12.508°E, 45.314°N, -16 m depth) and water level (referred to ZMPS) values associated to the 79 events is shown in Figure 13.

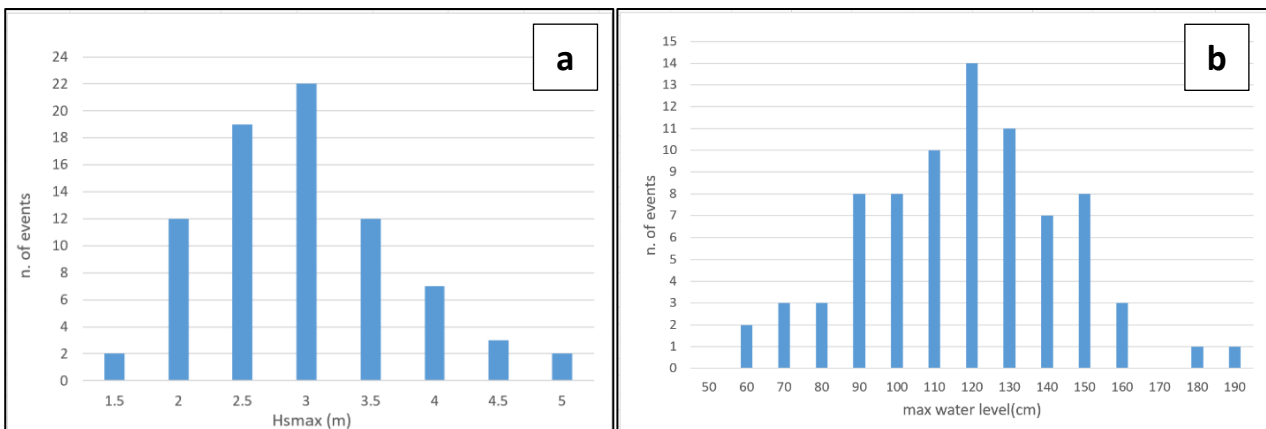


Figure 13 Frequency of the (a) maximum Hs and (b) water level referred to ZMPS for the 79 events selected between 1980 and 2022 (from Fontolan et al., 2023a).

The major storm surges occurred in Venice in last years had distinct characteristics. Two end-members in term of characteristics are represented by the extreme event of 29th October 2018 called “Vaia” and the one of November 2019 which were particularly different: the first was characterized by an extreme storm surge above +150 cm limited by the out-of-phase astronomical tide (Cavaleri et al., 2019) while the second showed how the in-phase concomitance of even non-extreme factors can lead to an exceptional rise in sea level of +182°cm referred to ZMPS (Ferrarin et al., 2021). Finally, during storm events, the barrier islands of the Marano and Grado lagoon, few kilometers west of the study area, are frequently overwashed and breached, evidencing the morphological signature of such extreme events (Casagrande et al., 2023).

3.6 Precipitations

Precipitation does not show a significant change in the last 30 years. In fact, considering the pluviometric stations made available by OSMER-FVG relating to the Isonzo river drainage basin, the average linear variation in precipitation from 1991 to 2023 is +4.1 mm/y which represents an increase of +0.02% (Table 1). Nonetheless, the standard deviation of annual precipitation is significant, in the order of $\pm 20\%$, and annual precipitation can also deviate significantly from the thirty-year average: for example, in 2014, precipitation was +51% higher than the 1991-2023 average values (Figure 14).

Station	annual mean [mm]	Linear annual rate [mm/y]	Linear annual rate (percentage)
Fossalon	1093	+7.2	+0.66%
Faedis	1666	+0.0	+0.00%
Gradisca	1345	-2.6	-0.20%
Cividale	1592	+6.3	0.40%
Capriva	1439	-7.4	-0.51%
Musi	3422	+21.3	+0.62%
Mean	1775	+4.1	+0.02%

Table 1 Annual rainfall statistics recorded by the OSMER-FVG pluviometric stations relating to the Isonzo River catchment area.

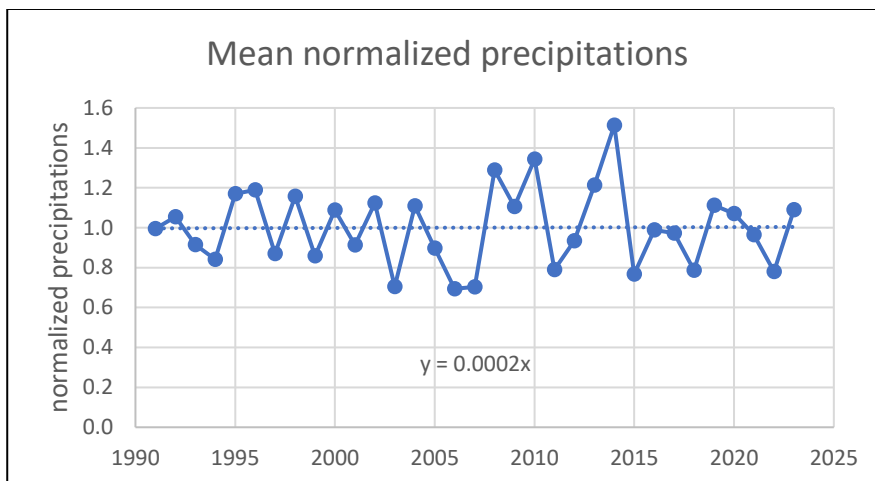


Figure 14 Mean normalized precipitations in the stations referred to the Isonzo River catchment: for each station, the annual precipitation was normalized with respect to the annual mean value.

3.7 Morphological set-up

The digital terrain model (DTM) of the study area (Figure 15) was produced for the Interreg Italy-Croatia ChangeWeCare (CWC) project starting from single beam echo sounder (SBES) bathymetric surveys and GNSS topographic ones acquired in 2019-2020. The characteristics of the surveys are available on the website of the project (Interreg Italy-Croatia CWC, 2021). The bathymetry of the study area (Figure 15) is characterized by the morphological elements of the Isonzo River delta, the Mula di Muggia Bank (MMB) and the deep part of MMB (D-MMB), evidenced in Figure 16. The Isonzo's delta is much more regular and has an almost symmetric prodeltaic lobe, which extends from -4 m isobath, with a marked extroversion of the isobaths, mainly near to the mouth (B-B1 in Figure 16). The delta type is river-dominated according to the classification

of (Galloway 1975) due to the high sedimentary input of the river coupled with a low wave energy at the mouth confirmed by data from the DWRG3 buoy with respect to the DWRG1, located further west (Figure 5).

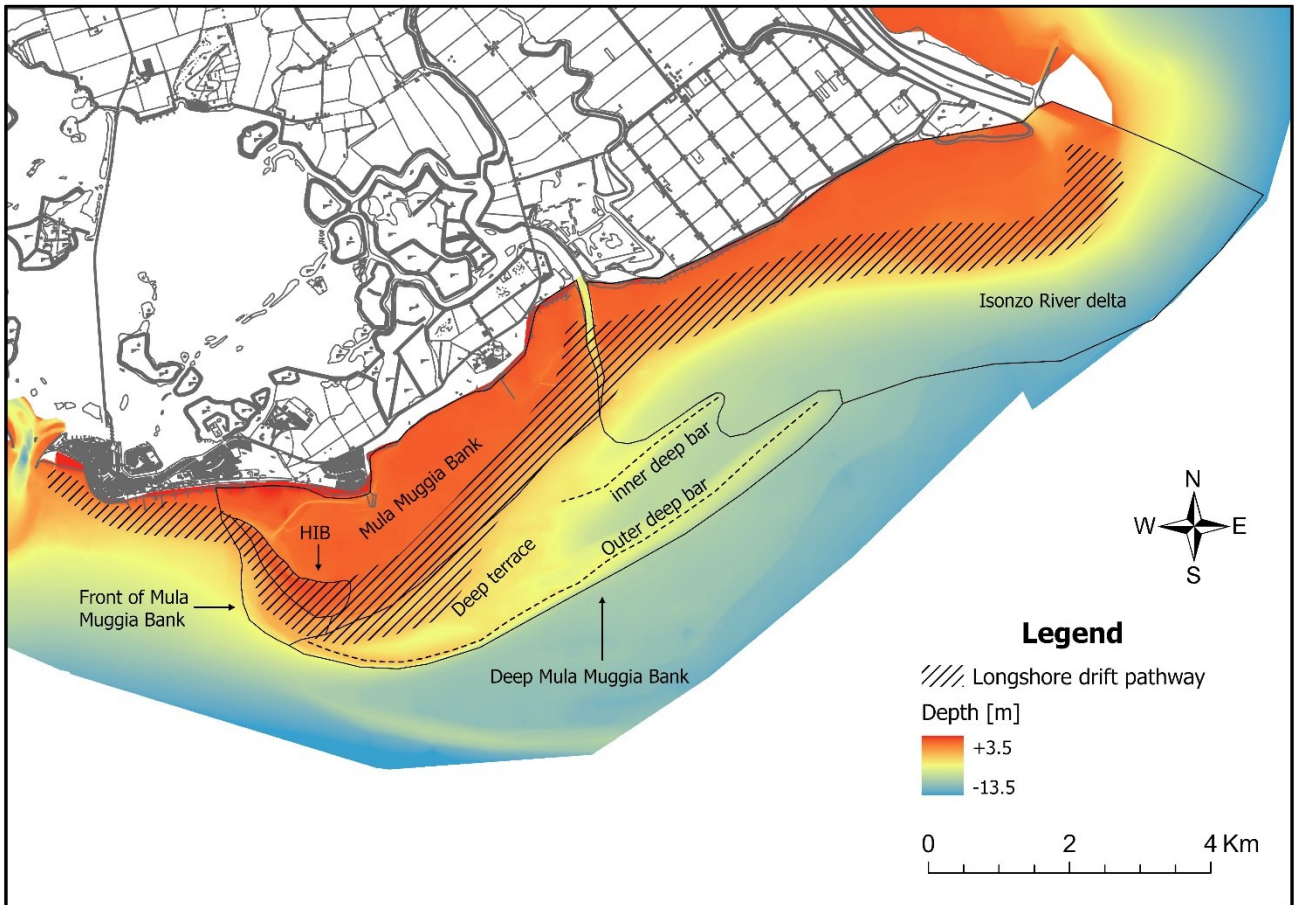


Figure 15 DTM of the study area.

The MMB, on the other hand, is more morphologically complex. In the most superficial part, within -4 m, the sedimentary body has a triangular shape with the base constituted by the shoreline and the greater outpouring coinciding with the southern vertex. According with Bezzi et al. (2021a), the MMB consists of a large flat low-energy backbarrier area, colonized by seagrass meadows, at the border of which extends the longshore littoral drift pathway consisting of a series of bars parallel to the bank boundary. The longshore pathway, as identified by Bezzi et al. (2021a), consists in a long and thin trail characterised by a set of sand bars drifting westwards from the Isonzo river's mouth. It extends to about -4 m. In the area of the southern vertex there is an almost completely crescent-shaped emerged sand bank (High Intertidal Bank, hereinafter HIB). Beyond -4 m, the deep part of the MMB (D-MMB) forms a bathymetric anomaly together with the MMB (A-A1 in Figure 16). Here, three main structures can be identified: (i) a large morphological terrace consisting of a series of finger bars whose direction tends to rotate counterclockwise from west to east and is inclined about 60° to 90° with respect to the edge of the MMB; (ii) two deep bars extending towards north-east, an inner deep bar shoreward and a larger outer deep bar seaward beyond which the D-MMB connects with the Gulf of Trieste; (iii) a deep trough between the two deep bars which extends from about half the length of the bars towards north-east and connects with the area of the Gulf of Trieste in front of the prodelta of the

Isonzo. The whole sedimentary body, made up of MMB and D-MMB, is an anomaly in the regular bathymetric trend of the northern Adriatic Sea and the Gulf of Trieste (Gordini, Caressa, and Marocco 2003) and its marked extroversion of nearshore contour lines corresponds to high sediment thicknesses (up to 8 m) of likely deltaic origin (Brambati, 1985; Marocco, 1989) deposited during the Holocene, following the Last Glacial Maximum (Trobec et al., 2018).

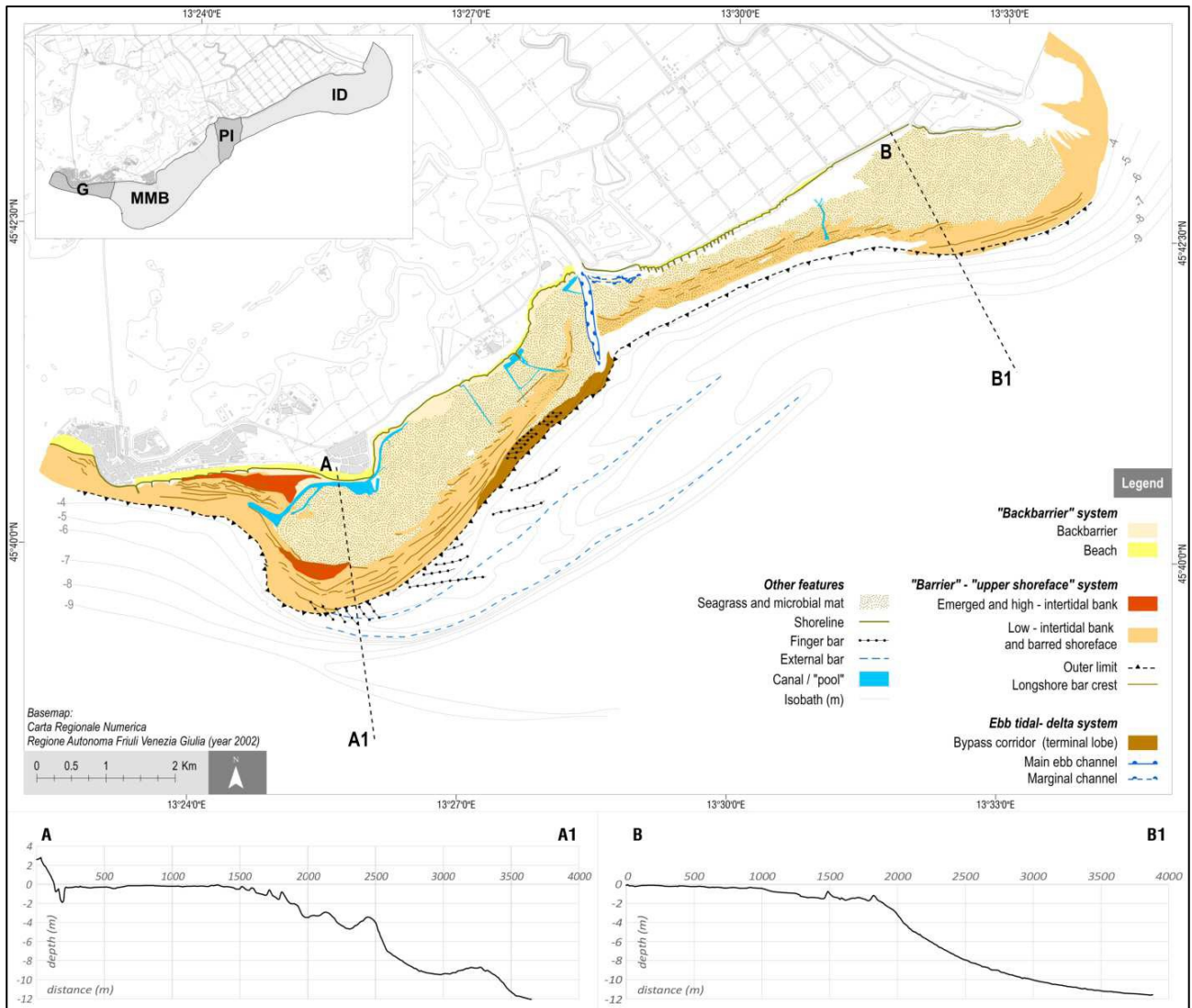


Figure 16 Geomorphological map of the coastal area (from Bezzi et al., 2021a).

3.8 Historical trends

The historical evolution of the study area is described by Bezzi et al. (2021a) and Fontolan et al. (2018). Using historical cartography, aerial photos and topo-bathymetric surveys, they identified two main evolutionary processes. First, the westward migration of the front of MMB (F-MMB) was almost steady throughout the time interval, with a significant rate of about 12.6 m/y (Figure 17). Moreover, from 2007, an aggradation process that leads to an elevation near the emersion at the top of the bank has started.

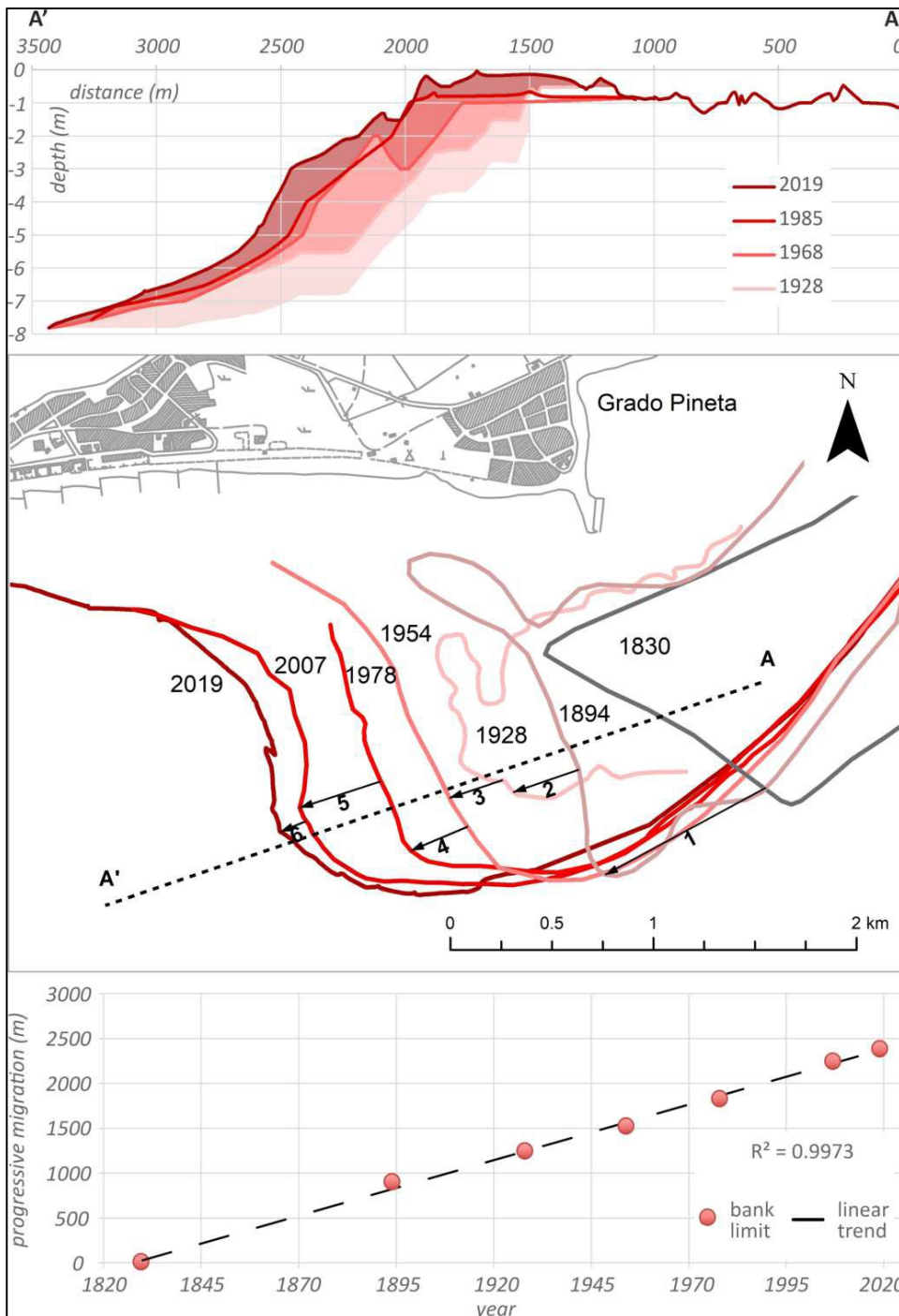


Figure 17 Detail of the bank migration analysed on the western F-MMB (from Bezzi et al., 2021a).

Secondly, the Isonzo river showed to play a primary role as a sedimentary depocenter in the constructive processes of the study area. This letter was particularly clear when, from 1896 to 1937, a new main mouth branch (called Quarantia mouth) opened to the north following a flood breach (De Grassi and De Grassi, 1957) and became more and more important (Desio, 1922) until it was artificially closed (De Grassi and De Grassi, 1957). This period coincided with an erosive phase of the barrier island that had lasted until the mouth was brought back to Sdobba, with a consequent reduction of the erosive effects on the coast. The sediment budget of both the Isonzo's delta and the F-MMB showed to be positive by approximately 50-60 thousand cubic meters per year while the rest of the study area remained volumetrically stable or eroding, evidencing

a possible cannibalization especially on the edge of the MMB from -3 m depth. Finally, the sediments transported by the Isonzo are characterized by a high mercury content due to mining activity in the Idrija district, which is part of the Isonzo drainage basin (Covelli et al. 1999; Gosar, Pirc, and Bidovec 1997). The extraction of cinnabar (HgS) at the Idrija mine lasted for about 500 years (Covelli et al. 2006; Floreani et al. 2023), until 1996 (Pavoni et al., 2023a). Despite the closure of mining activity, recent studies demonstrate the active role of Isonzo in conveying Hg into the Gulf of Trieste and that mercury flows are mainly associated with river floods and the resuspension of sediments by wave motion (Covelli et al., 2007; Pavoni et al., 2023b, 2021).

3.9 Coastal area management

The vast majority of the study area is subject to high anthropogenic pressure (Bezzi et al., 2021a). The area, from Isonzo to Primero, has been largely utilized for agricultural purposes, while most of the coastal territory between Primero and Grado had been rapidly urbanized between the end of the 19th and the 20th century to promote the growth of tourism: new beaches were artificially created using replenishment sands sourced from the nearby seabed (De Grassi and De Grassi, 1957). Such a rapid coastal development led to the creation of a rigid system with no degrees of freedom in terms of possible beach migration to the hinterland. Despite the touristic development, a significant portion of the MMB, along with the mouth of the Isonzo River, has been preserved through the inclusion in the Natura 2000 network (Special Areas of Conservation and Special Protection Area IT 3330006 and IT 3330005). Additionally, the Autonomous Region of Friuli Venezia Giulia has designated both locations as regional geosites.

4 Materials and methods

This chapter is mainly divided into two subchapters. The first concerns the characteristics of the surveys and the first processing of the datasets to obtain the basic products, i.e. DTMs and orthophotos, while the subsequent processing and analyzes are described in the second subchapter.

4.1 Surveys and data

In order to formulate hypotheses capable of explaining the complex dynamics that occur in coastal environments, and in particular to give an explanation to the anomalies present in the study area, it was necessary to set up a multidisciplinary approach consisting of multiple campaigns of topographical, bathymetric, aerial photogrammetric, and sedimentological surveys. These surveys allowed us to (i) obtain information on the morphologies present, (ii) calculate short-term sedimentary budgets in the critical areas, (iii) evaluate the distribution of the sediment characteristics both from the textural point of view and with regard to the grain size, and (iv) determine the amount of mercury in the seabed, the latter thanks to the collaboration with Prof. Covelli, Ph.D. Pavoni, Dr. Petranich and Dr. Makdoud of the MercuryLab (MiGE). Further information regarding meteomarine forcings and physical sea characteristics was obtained from monitoring systems such as wave buoys, tide gauges and satellite data. The whole dataset is summarized in Table 2.

Survey Year	Type of data	Reference	Area
2011	Bathymetric survey with Multi Beam Echo Sounder (MBES)	Gordini et al. (2013)	F-MMB
2019	Bathymetric survey with Single Beam Echo Sounder (SBES)	Coastal Group, Interreg Italy-Croatia Change We Care (2021)	Entire study area
2019	Digital orthophotos (UAV survey)	Coastal Group, Interreg Italy-Croatia Change We Care (2021)	HIB
2020-2021	Sedimentological survey	Coastal Group, Interreg Italy-Croatia Change We Care (2021)	Entire study area
2022	SBES bathymetric survey	University of Trieste – Coastal Group this thesis	Isonzo River delta
2023	SBES bathymetric survey	University of Trieste – Coastal Group this thesis	F-MMB
2023	Digital orthophotos & DEM (UAV survey)	University of Trieste – Coastal Group this thesis	HIB

Table 2 Summary of the entire dataset used for elaboration.

4.1.1 Bathymetric Survey

The bathymetric acquisition campaign was set up with the aim of obtaining information on the short-term evolution of the most dynamic areas. For the CWC project, the evolution of the same study area was analyzed

considering three previous surveys, dated 1968, 1985 and 2007 to which a new bathymetric campaign was added in 2019. In the project, the areas that demonstrated greater dynamism were the F-MMB and the Isonzo River delta. Considering these trends, for this work it was decided to monitor the two most dynamic areas with SBES bathymetric surveys of the F-MMB and the Isonzo's delta. The survey campaign of the delta was carried out in July 2022 (Figure 18a) while that of the F-MMB in May 2023 (Figure 18b). The acquisition system was as follows: Ohmex Sonarmite 3.0 digital depth sounder with a Stonex S9III GNSS in N-RTK mode and CommTec Navigator Professional 6.42 acquisition software. The software saves the data collected by the GNSS and the transducer with the frequency of 1Hz. The digital fish finder operates at a frequency of 235 KHz, with a 10° cone and an accuracy of ±0.025 m RMS. The speed of sound was set to 1500 m/s.

As regards the pre-processing of the data, these were initially corrected with respect to the speed of sound. To estimate the correct speed of sound in the water column, the average sea surface temperature obtained from Copernicus data was considered using the formula proposed by (Coppens, 1981):

$$V(T, S, Z) = 1449.05 + T(4.57 - T(0.521 - 0.00023T)) + (1.333 - T(0.0126 - 0.00009T))(S - 35) + dZ$$

where $V = \text{sound velocity in m/s}$, $T = \text{mean temperature in } ^\circ\text{C}$, $S = \text{salinity in psu (Practical Salinity Units)}$ and $Z = \text{depth in m}$. Salinity and depth were considered constant with values of 35 psu and 0 m respectively: this approximation is still considered acceptable since the maximum error that can be generated is less than ±0.3%, generating a maximum error relating to the depth of around -10 m in the order of ±0.015 m, lower than the accuracy of the echo sounder. The previous surveys conducted in 2019 were also corrected due to the absence of a sound-speed adjustment at that time. Even if 1500 m/s could be a good approximation for temperatures around 13°C (early spring / late autumn), in winter ($T < 10^\circ\text{C}$) and especially in summer ($T > 20^\circ\text{C}$) it could be an over or underestimation respectively, leading to a significative loss of accuracy. In this way it was possible to obtain more reliable data, especially with regards to the comparison between measurements carried out in different seasons. Subsequently, spikes and other errors in SBES data were removed, and then the entire dataset was projected from ellipsoidal coordinates (Ellipsoid GRS 1980) to the geodetic coordinate reference system RDN2008 / UTM zone 33N (N-E) (EPSG:6708) using the IGM (Italian Military Geographical Institute) ConveRgo software. Finally, in presence of oscillation in SBES data due to wave during the survey, a moving average of order 5 was applied.

A MBES survey carried out by the OGS and commissioned by the municipality of Grado was also used in the analyzes (Gordini et al., 2013). This survey, carried out in autumn 2011 (7 September - 3 October), includes the seabed of the F-MMB.

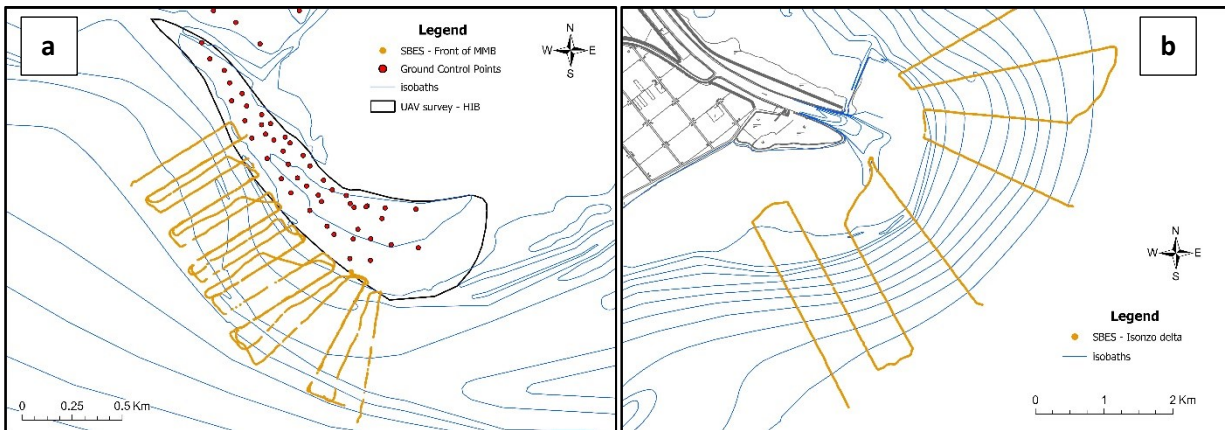


Figure 18 SBES surveys of (a) Isonzo River delta in July 2022 and (b) front of Mula di Muggia Bank in May 2023.

4.1.2 Aerial photogrammetry with Unmanned Aerial Vehicle

The aerial photogrammetric surveys were carried out with the aim of monitoring the emerged and intertidal areas to evaluate the topographic evolution of particularly dynamic areas. During the period 2019-2021, three aerial photogrammetric surveys were carried out with UAV in the area in front of the Grado municipality for the CWC project. In 2019, two surveys were carried out, one on the beach called “al Bosco” and one on the HIB; while in 2021 only the “al Bosco” beach was resampled, leaving out the HIB (Figure 18). Due to accuracy problems, since the ground control points (GCPs) were not materialized, only two orthophotos were obtained from the 2019 surveys while in 2021 the DSM was also obtained. In spring 2023, surveys of both areas were carried out with a DJI Phantom RTK UAV connected to SmartNet's N RTK HxGN correction network. The frames were processed with SfM (Structure from motion) algorithms using the Agisoft Metashape software to obtain georeferenced orthophotos and DSMs. The orthophoto with GSD (Ground Sampling Distance) of approximately 5 cm/px and the DSM were generated from the photogrammetric model. To obtain high precision and accuracy of the georeferenced data, 81 control points were materialized on the ground (detected with the Stonex S9III GNSS system operating in N-RTK mode and connected to the SmartNet HxGN correction network), 34 on the beach “al Bosco” and 47 on the HIB, and used for the georeferencing of the photogrammetric model which allowed obtaining a positional error (RMSE) on the control points of approximately 6 cm.

4.1.3 Sediment samples

During the CWC project, some seabed sediment samplings were performed in 2020 and 2021 along some topo-bathymetric profiles every meter within a depth from -6 m to -10 m depending on the profile (Figure 19). A total of 138 samples were collected: the samples of the seabed were carried out using a 10 litre Van Veen grab sampler while the samples on the emerged areas were collected with a bailer.

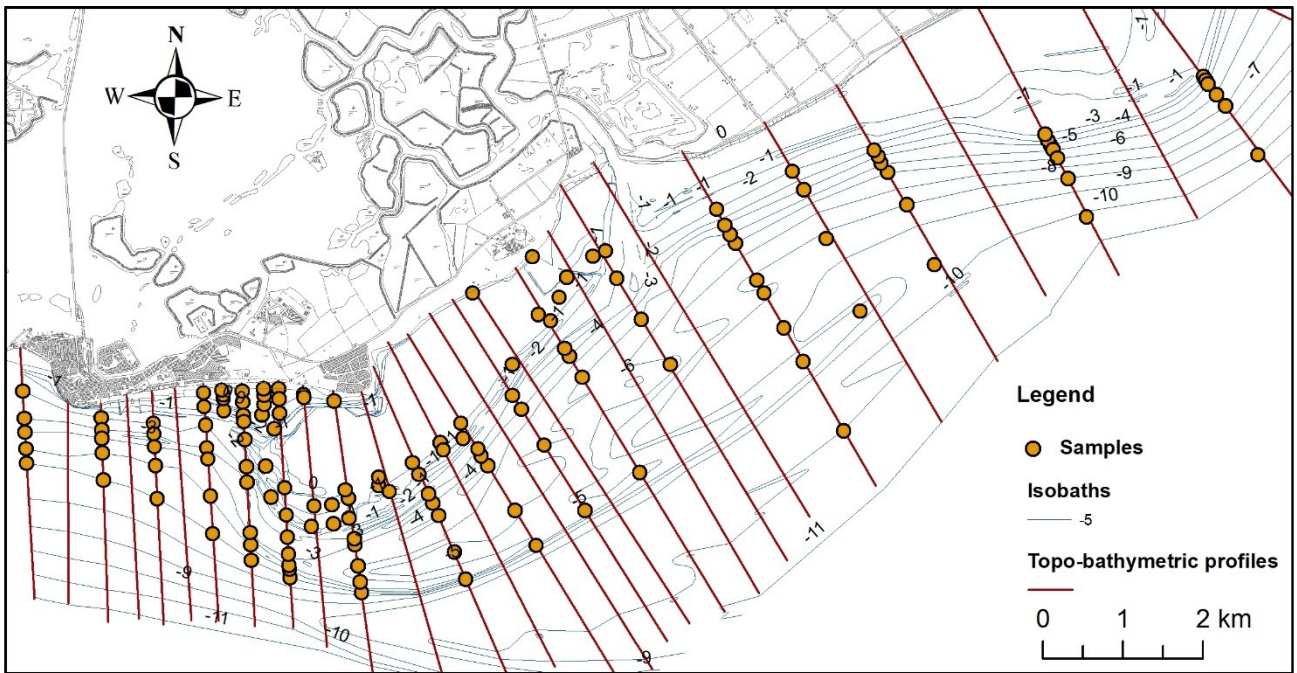


Figure 19 Sedimentological samples distribution.

The entire sample dataset was analysed using Malvern 3000 laser diffraction particle size analyser. The output data consisted in the class distribution with a step of 0.5ϕ from -1.0ϕ to $>11.0 \phi$ and some statistical parameters (mean size M_z , sorting S_r , median M_d , etc etc). A short description of every sample was also provided. Thanks to the collaboration with MercuryLab, the concentration of mercury (Hg) present in the samples was analyzed via atomic absorption spectroscopy (AAS). We should remember that the phi scale, first proposed by (Krumbein 1934), is calculated as the:

$$D_{\phi} = -\log_2 D_{mm}$$

where D_{ϕ} = diameter of the particle in ϕ units and D_{mm} = diameter in millimeters. On this scale, smaller values represent coarser sediments while greater values correspond to smaller diameters. According to the various classifications, the fields of existence of the different grain sizes may vary slightly. For example, (Wentworth, 1922) modified the (Udden, 1914) classification to produce a commonly used classification called the Udden-Wentworth scale where ϕ values of -1, 4 and 8 (2 mm, 62.5 μm and 4 μm respectively) separate gravel from sand, sand from silt and silt from clay respectively. Another widely used classification is that of Kruit-Nota, proposed by (Kruit, 1954) and modified and published by (Nota, 1958) in which the separation between sand and silt is set at 50 μm and between silt and clay at 2 μm . In this thesis we decided to use the (Friedman and Sanders, 1978) classification (Figure 20), similar to the *Udden-Wentworth* but with clays ranged from 9 ϕ (2 μm).

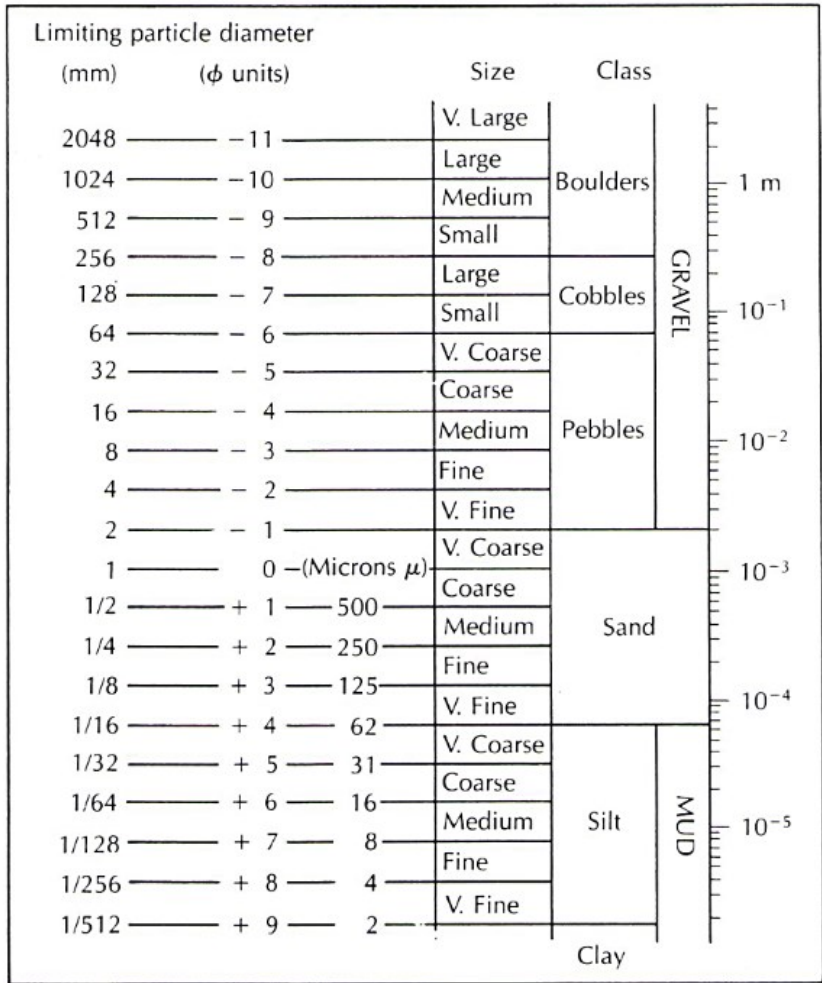


Figure 20 Grain size classification following Friedman and Sanders (1978)

4.2 Data analysis

Both bathymetric, aerial photogrammetric and sedimentological data were put in a Esri ArcGIS projects in order to be elaborated and analysed.

4.2.1 Digital Terrain Model (DTM) & DTM of Differences (DoD)

All topo-bathymetric data were further filtered in a GIS environment to eliminate residual spikes, points with erroneous heights owing to seagrass meadows, and echo-sounder receipt of multiple waves. When filtering in GIS became too time-expensive and complicated, the software BeamworX 2021.1 Autoclean was used. Subsequently, to integrate the bathymetric data, two types of lines were drawn to further constrain the model and improve its quality and fidelity. Initially, the isobaths were drawn with a step of 0.5 m and, subsequently, 3D polylines representing the axes of bars and troughs and other support lines were created in case of evident interpolation errors (Figure 21). These lines were traced following both quantitative and qualitative criteria

derived from expert knowledge of the study area assisted by orthophotos or satellite images regarding the emerged areas and shallow waters.

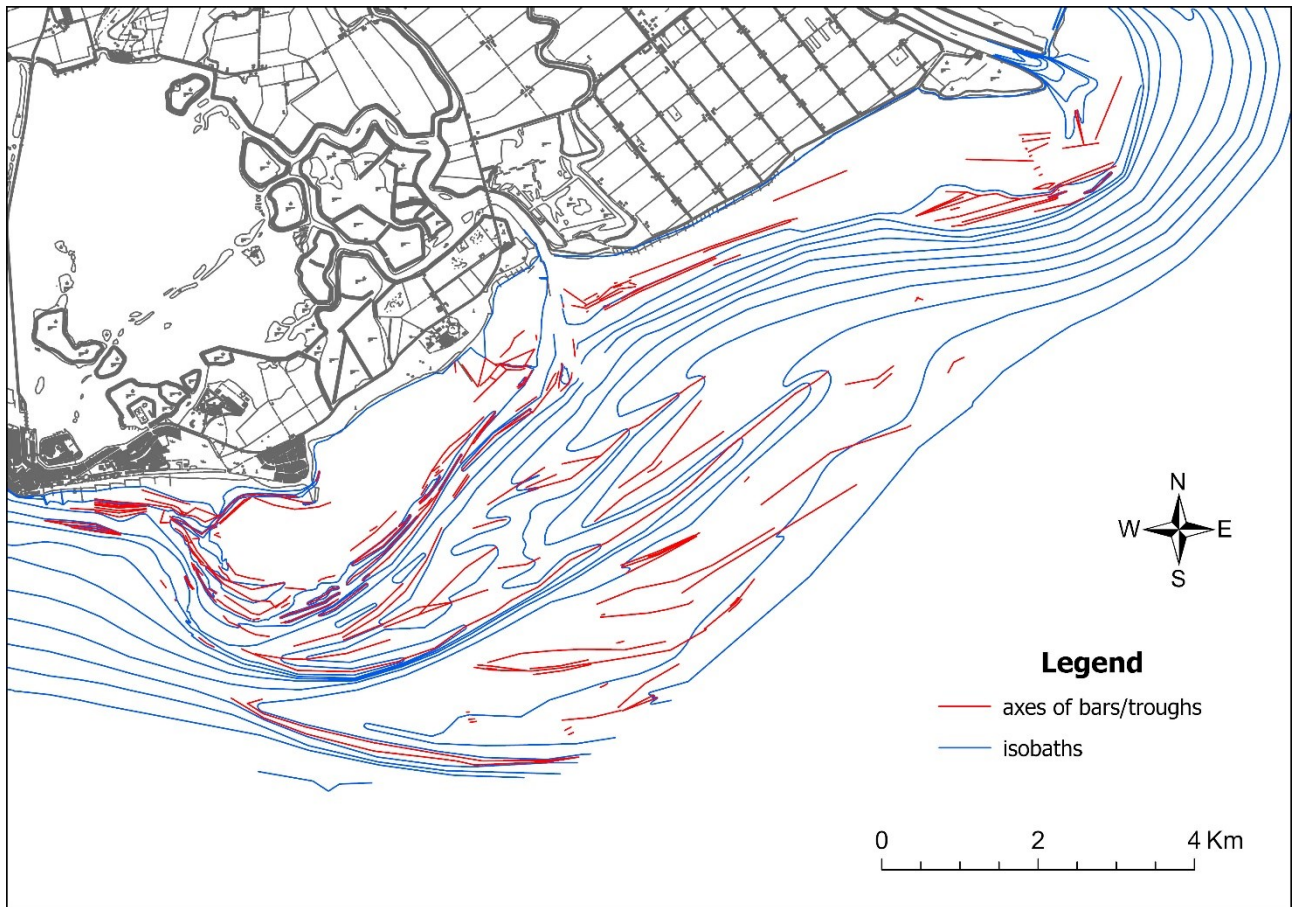


Figure 21 Example of integration of topo-bathymetric data through the tracing of isobaths, and axes of bars and troughs.

The DTMs were obtained by converting the altimetric models generated using the Triangulated Irregular Network (TIN) interpolation technique into raster. The TIN was chosen because it does not modify the depth of the input data, making the DTM faithful to the acquired data points. The obtained DTMs were returned with a resolution of 2×2 m. To calculate the volumetric variations in a given time interval, the DTM of the differences (DoD) were calculated, i.e. the difference between a DTM and a previous one. In this way, each cell represents accumulation or erosion, with positive or negative values, respectively.

4.2.1.1 Sediment budget

The sediment budgets and the comparison of bathymetric sections were used in the CWC project for determining any accumulation/erosion gradients. These methodologies have been taken up in this thesis to evaluate the short-term geomorphological variations undergone by the F-MMB and the Isonzo River delta. In the area of the Isonzo delta, the last two SBES surveys were compared: the one conducted for the CWC project (2020) and the most recent one performed for this thesis (2023). On the F-MMB, in addition to the CWC survey (2019) and the most recent one (2023), a third MBES survey (2011) was also used. The volumetric

budgets were performed by considering the survey transects and extracting these ones from both DTM and DoD. Extracting profiles from the rasters has the advantage to obtain bathymetric profiles composed by equally spaced points (the cell dimension of DTM or DoD), making subsequent data processing easier, maintaining a high degree of reliability since, in TIN algorithm, where profile is close to the surveys, DTM's elevation is close to the surveyed depth. Comparisons on the bathymetric sections were performed taking into consideration the bathymetric profiles both in their entirety and in some localized bathymetric range (e.g. in the Isonzo's delta there will be a focus of the shallow waters within -4 m only).

The profiles extracted from DoDs would be used to compute:

- Linear budget, i.e. the integral of the DoD profile expressed in m³/m.
- Accretion/erosion, i.e. the mean thickness of sediment accumulated (positive values) or eroded (negative) expressed in mm and computed dividing the linear budget for the profile length.
- Sedimentation rate, expressed in mm/y, calculated dividing by the time elapsed between the two surveys considered.

The limit of this methodology lies in the fact that spatial data is not obtained, but linear data only: therefore, the eroded/accreted volumes would be obtained by multiplying the mean sedimentation rate of the transects and analyzed area. Volumetric rates per year are calculated dividing the total volume accreted/eroded for the time period between surveys.

4.2.1.2 Position indexes & Residual method

The bathymetric and topographic Position Indexes (PIs) are parameters often used for morphological analysis (Koop et al. 2021). They measure the depth relative to the surrounding landscape and is defined as

$$PI_r = z - \bar{z}_r$$

where z = the point height and \bar{z}_r = the mean height within a certain radius r . Positive values indicate topographic highs, such as bars, while negative values indicate depressions (e.g., troughs, holes, etc). Using a larger or smaller radius it is possible to identify topo-bathymetric anomalies at different scales: from small to large radii, morphologies from ripples to mega ripples, to bars, to sedimentary bodies can be identified (Figure 22). Furthermore, this parameter is able to highlight the anomaly only, making morphological analysis easier because the local slope is filtered out. There are several authors who have used this parameter for various scientific purposes (Agus et al., 2021; Aiello and Sacchi, 2022; Arosio et al., 2023; Janušaitė et al., 2023; Koop et al., 2021; Lundblad et al., 2006; Walbridge et al., 2018; Weiss, 2001). Depending on the starting product and the size of anomalies to be identified, different radii were used, from 1 m up to 200 m. To obtain the maps of the topographic and bathymetric anomalies, i.e. the spatial distribution of the PI, the difference was

calculated between a DEM (Digital Elevation Model, be it DTM or DSM) and a raster in which each pixel was associated with the average height within a circular buffer of a chosen radius (r).

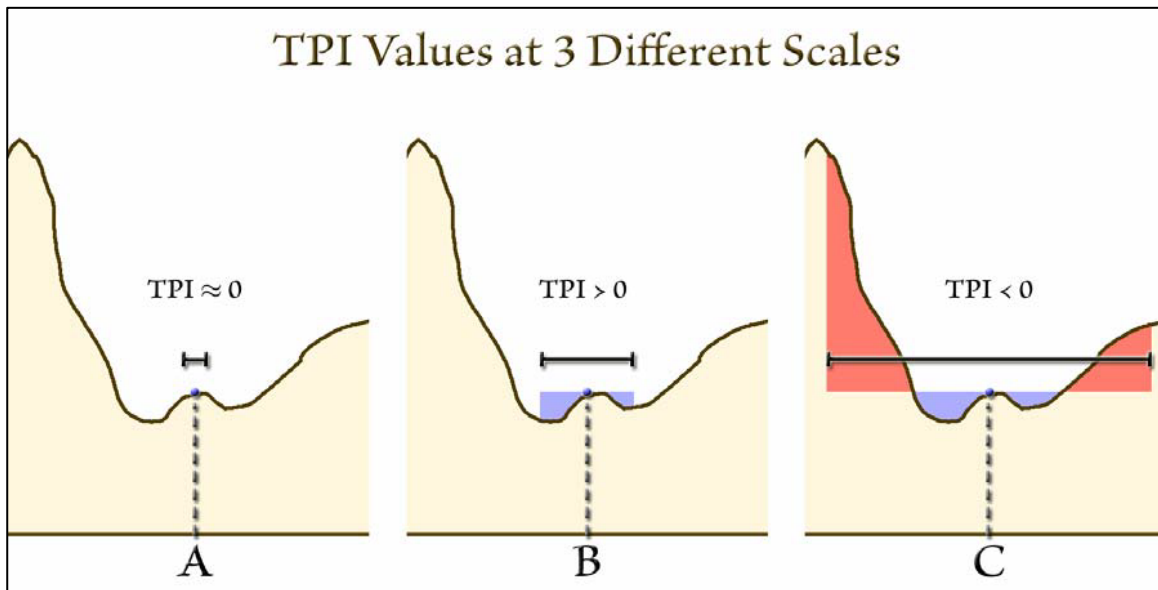


Figure 22 Representation of positioning index at different scales (from Jenness, 2006).

A second method used to obtain depositional anomalies is the Residual Method proposed by Fontolan et al. (2007). This method, developed to calculate the volume of sediments stored at ebb-tidal deltas, consists in subtracting from the DTM of an area the idealized bathymetry without the sedimentological anomalies. The idealized bathymetry is approximated by a polynomial (usually first or second order) of part the seabed with a regular bathymetric profile. The idealized contour lines were manually drawn following both the shoreline and the DTM. The Residual Method, differently from the PI, is more reliable to represent macro-scale anomalies while is not able to represent small-scale one.

4.2.1.3 Landforms position evolution

A further element in support of the morphodynamic analysis is the quantification of the topographic variations of the emerged and semi-emerged areas of the HIB, the area that in the past has proven to be the most dynamic (Bezzi et al., 2021a; Fontolan et al., 2018; Interreg Italy-Croatia CWC, 2021). To obtain this data it was chosen to use the extension for ESRI ArcGIS 10.8 produced by the United States Geological Survey (USGS) called DSAS (Digital Shoreline Analysis System) release v5.1 (Himmelstoss et al., 2021). This extension, designed to evaluate the variation of the shoreline over time, can be applied to any morphological line that has a temporal evolution. In this study, the variation of the landward edge of the HIB will be analyzed (Figure 23) to evaluate its short-term evolution and analyze it in the long-term evolutionary context produced by (Fontolan et al. 2018) and successively by the Coastal Group of the University of Trieste for the project (Interreg Italy-Croatia CWC, 2021). The landward boundary lines of the HIB were manually digitized starting from the orthophotos obtained from the 2019 and 2023 UAV surveys (Figure 23). The DSAS algorithm involves

tracing a baseline that indicates the basic development of the coastline: in this case it has been digitized following the shape of the HIB and positioned towards the land (Figure 23). The DSAS automatically draws transects perpendicular to the baseline with the desired spacing (10 m in this study), with respect to which it is able to obtain various parameters from the intersections with the evolutionary lines. In this thesis, for each transect, the Net Shoreline Movement (NSM), i.e. the total movement perpendicular to the baseline between the two evolutionary lines, and the End Point Rate (EPR), i.e. the ratio between NSM and the interval elapsed between the two lines.

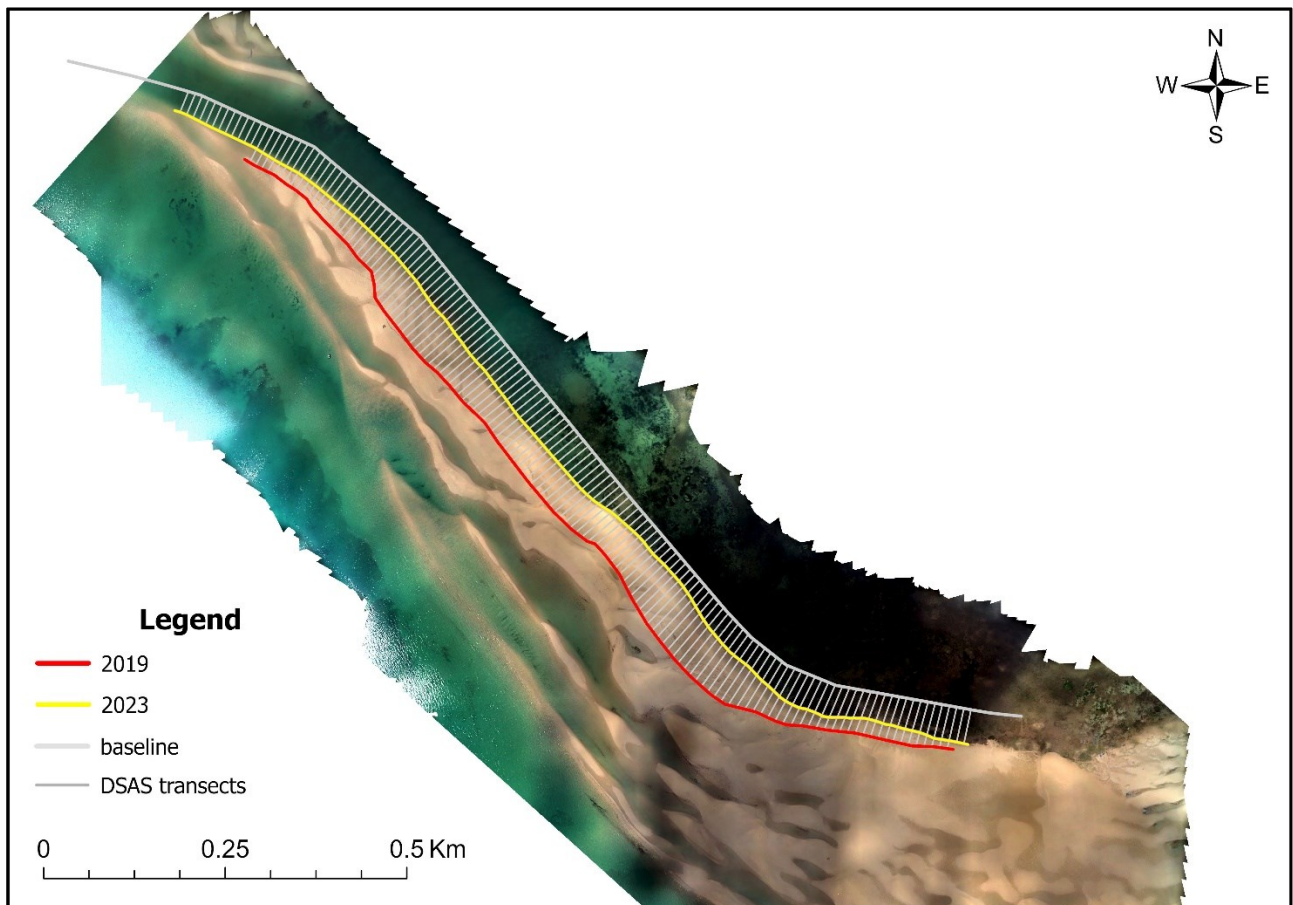


Figure 23 Example of application of DSAS extension. From shore to sea there are a baseline (white), the 2023 (yellow) and 2019 (red) edges of the HIB. Normal to the shoreline, many transect (grey) spaced by 10 m are produced by the algorithm to evaluate the lines' displacement.

4.2.2 Sedimentological maps

The creation of sedimentological maps presents many critical issues: if, on the one hand, the most recent acquisition techniques, such as MBES backscatter, give the possibility of having a very dense distribution of data, on the other hand they are rather expensive both economically and temporally, and not applicable on grain-size parameter distribution. The collection of samples, the most common technique used for many decades, presents some other difficulties. As happens in our study area, it's hard to have a high and regular density of samples because their collection is expensive in time and money. These criticalities may lead, in areas with peculiar landforms like the study area, to problems in interpolation which cannot be solved by only

choosing the best geostatistical algorithm and parameterising it. Hence, the idea of following a Semi-Automatic Interpolation Method (SAIM) based on the expert use of bathymetric information, much easier and faster to acquire and process, and the knowledge of sedimentary morphodynamics to help the automatic algorithms in the interpolation, generating more reliable sedimentological maps. In order to estimate the improvements obtainable by applying the SAIM, it was decided to compare the sedimentological maps obtained through this method with those produced using both the most commonly used automatic geostatistical algorithms (e.g., Simple Kriging, Ordinary Kriging or Empirical Bayesian Kriging) and the more refined ones (e.g., CoKriging, Empirical Bayesian Kriging Regression Prediction), i.e. those which involve the use of secondary variables to be coupled with sediment samples to obtain more reliable maps. The zeroth step was to prepare the datasets to be interpolated, loading both topo-bathymetric and sediment data into an Esri ArcGIS project: a shapefile of points was created with the position of the 138 collected samples and the related grain-size parameters (e.g., mean size, median, sorting, etc.), expressed both in phi units and in μm . Then, we applied the following standard geostatistical approaches to model the sediments' mean size (MZ) distribution on the study area. Firstly, we used geostatistical methods that do not use explanatory variables: these approaches use only one type of data in the interpolation and the model obtained is referred to the spatial distribution of the data used.

Kriging

Kriging is a geostatistical procedure that generates an estimated model from a scattered set of point of any type of data. Kriging, as other geostatistical approaches, is based on statistical models that include autocorrelation, that is the statistical relationships among the measured points. It weights the surrounding measured values to derive a prediction for an unmeasured location not only on the distance between the measured points and the prediction location (as in Inverse Distance Weighting), but also include the degree of spatial autocorrelation and the directional dependency (anisotropy) when predicting measurements. The degree of spatial autocorrelation can be assessed by applying variogram analysis, where semi-variances are calculated for defined distance classes and plotted against the separation distance (Jerosch, 2013). Applying cross-validation, each measurement value is extracted from the dataset and estimated by kriging based on the selected variogram model (Jerosch, 2013). The general formula for both interpolators is formed as a weighted sum of the data:

$$\hat{z}(s_0) = \sum_{i=1}^N \lambda_i Z(s_i)$$

Where $Z(s_i)$ = the measured value at the i^{th} location, λ_i = an unknown weight for the i^{th} measured value at the i^{th} location, s_0 = the prediction location, N = the number of measured values.

Empirical Bayesian Kriging (EBK)

In the EBK, the parameters that are manually adjusted in the standard kriging are calculated automatically through a process of sub-setting and simulations, reducing by far the time spent in the parametrization. Differently from the kriging method, the EBK also accounts for the error introduced by estimating the underlying semi-variogram: in this way the standard error of prediction is less underestimated. The kriging model in EBK doesn't follow an overall mean as kriging does: compared to kriging models, EBK ones are less smoothed but more sensitive to the outlier which may be affected by errors. The main advantages of the EBK are that it requires minimal user interactive modelling, the more accurate standard error of prediction, and it is particularly accurate for small datasets as ours. The main drawbacks are that the processing time increases quickly, the lack of cokriging or anisotropic corrections, and the sensibility to outliers.

Secondly, we tested the methods with explanatory variables. These approaches use secondary variables to be cross-correlated with the main variable. Secondary variables, in particular if denser than main one, may improve the model obtained, filling the information gaps with correlated data.

CoKriging with depth

The kriging method can be used considering information of several variables. In addition to the kriging method, the main variable is cross-correlated with the secondary ones: this process may help to make better predictions at the cost of extra computational effort (ArcGIS manual). We decided to use depth as a secondary variable. The use of a secondary variable (depth) denser than the primary one (mean size) may provide better estimations for the mean size distribution (Davis 2002; Goovaerts 1997).

Empirical Bayesian Kriging Regression Prediction (EBKRP)

EBK Regression Prediction is a geostatistical interpolation method that uses Empirical Bayesian Kriging (EBK) with explanatory variable rasters (in our case, the DTM) that are known to affect the value of the data you are interpolating. This approach combines kriging with regression analysis to make predictions that are more accurate than either regression or kriging can achieve on their own. The overall effect is similar to the CoKriging but with EBK as interpolation method.

Finally, we followed the semi-automatic interpolation method developed during the PhD to produce the grain-size distribution in the study area. The method requires an expert judgement to force the automatic interpolation in order to obtain more reliable and detailed outputs. For the representation of the MZ distribution model of the study area (but also of other parameters, both granulometric and otherwise), both granulometric and topo-bathymetric data are used, as well as the knowledge of the meteomarine characteristics of the study area, in particular way the littoral drift. Figure 24a shows the representative algorithm of the method. The data needed to apply the method are:

- Distribution of samples on the study area

- DTM of the area
- Knowledge of morphodynamics and marine forcings

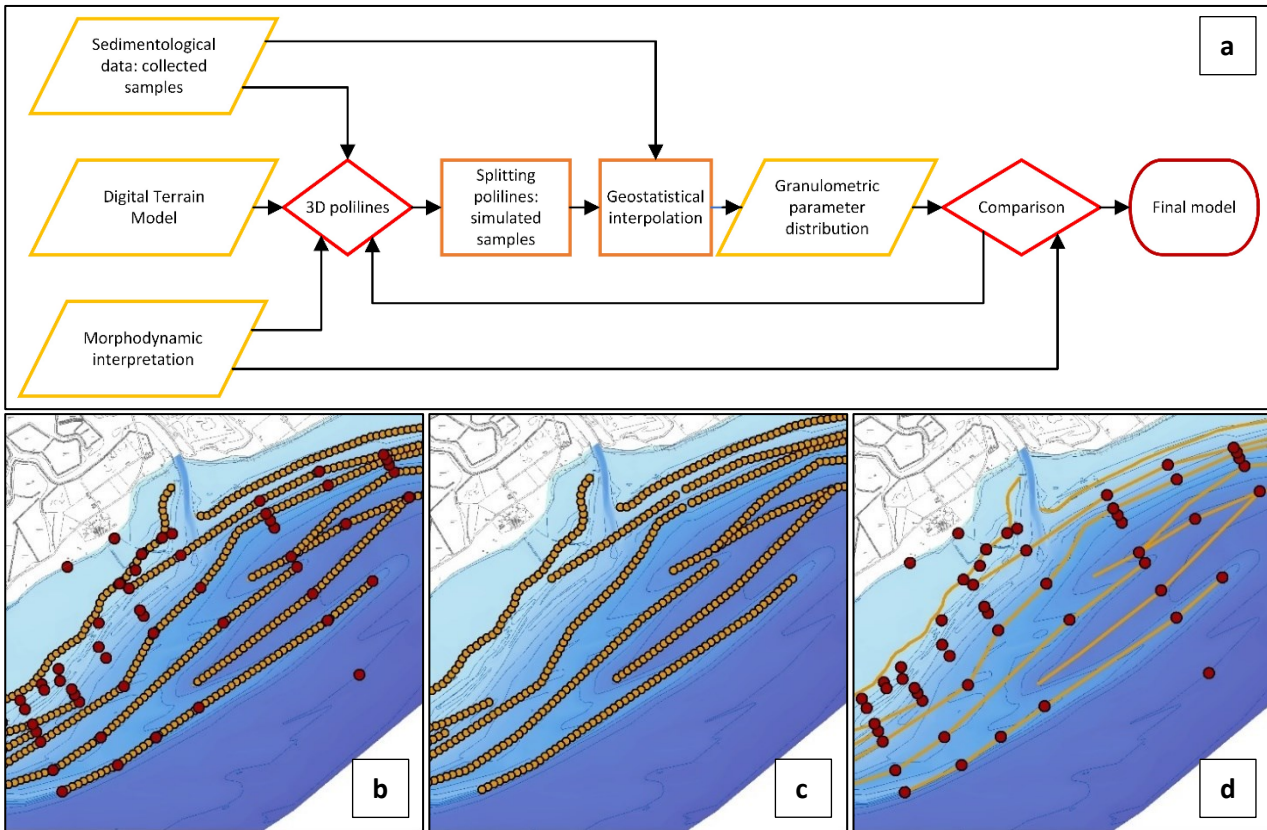


Figure 24 (a) Representative algorithm of the Semi-Automatic Interpolation Method with detail on its steps: (b) creation of polylines; (c) simulated samples generated over the polylines and (d) merge of simulated and collected samples and interpolation with geostatistical algorithm.

The **first step** (Figure 24a) of the method involves the creation of 3D polylines to join sedimentologically correlated samples: this is the most delicate and important step since it requires expertise and knowledge of the bathymetry of the seabed and the derived morphodynamic interpretation. Each polyline is created by joining samples that are consistent with each other (for example samples belonging to the same sandy bar): in this way, at each intermediate point of each segment of the polyline is given a value of the mean size (or any other characteristic desired) intermediate between the 2 extremes (Inverse Distance Weighting or manually assigned value). Through this operation we may simulate the preferential direction of distribution of sediments using morphodynamic interpretation. The **second step** (Figure 24b) is to split the polylines into simulated samples with a certain spacing, which can be wide or narrow: more spaced points will constrain the subsequent interpolation less while denser points on the polylines will give more a preferential direction of interpolation. In this way we generate simulated points that fill the lack of sedimentological data, creating denser and more regular mesh with the aim of increasing the reliability of the final model. The **third step** (Figure 24c) is the interpolation of all samples, both collected and simulated, using standard geostatistical algorithms. The suitable number of samples depends on the characteristics of the study area and the

distribution of the samples and will have to be researched until desired output is obtained. The steps will be tuned together to be able to achieve the maximum degree of reliability of the model.

In order to be able to estimate the error of the Mz prediction, a subset of 10-15% of the whole dataset was extracted as control samples (CS), reducing the data available for the interpolation: such a procedure to the assess the model's accuracy was followed by many authors (e.g., Diesing et al., 2014; Hasan et al., 2012; Ierodiaconou et al., 2011). The reduced dataset may lead to a decrease of the quality of final outputs but is necessary to reliably estimate the criticalities of the different methods and to compare the outputs themselves. Once produced, the outputs were firstly qualitatively analysed and then, at the control samples' location, the MZ values of all models were extracted, and the error was calculated as:

$$\text{Absolute Error} = |Mz_{\text{model}} - Mz_{\text{sample}}|$$

where Mz_{model} is the mean size predicted and Mz_{sample} is the mean size of the sample. Mean and maximum absolute errors, 16th and 84th percentiles, and standard deviation were calculated for the CSs' dataset and used to compare the interpolation methods.

In addition to the methodological analysis of the SAIM developed starting from the distribution of the Mz, three further sedimentological maps were produced representing the sorting (Sr), the normalized sorting (NSr), i.e. the ratio between Sr and Mz, and the textural distribution according to the (Flemming, 2000) classification (Figure 25). The maps of Sr and NSr were obtained applying the SAIM, i.e. following the steps described in Figure 24, while the textural one was manually drawn following the sedimentological dataset.

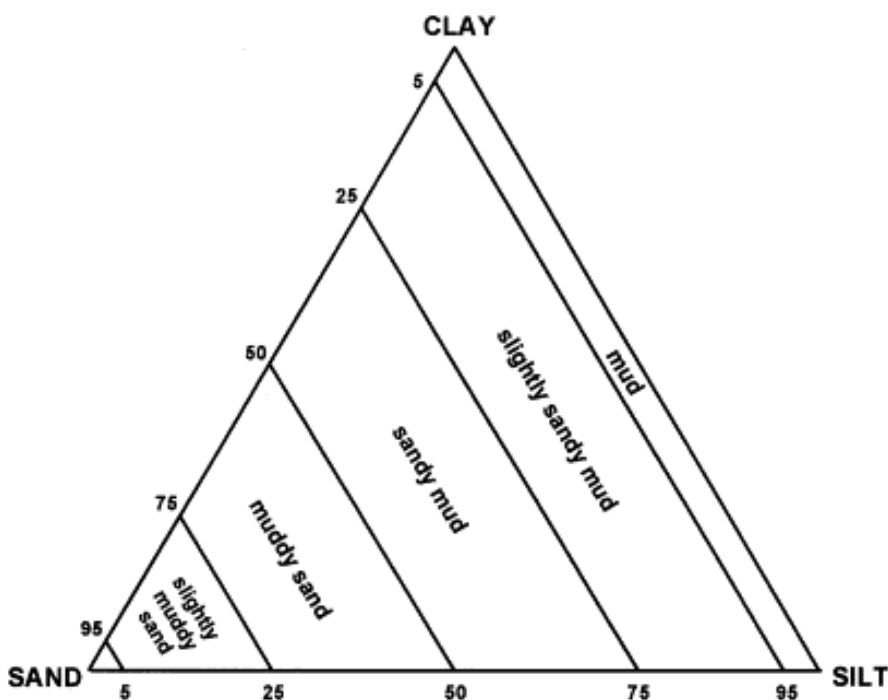


Figure 25 Textural classification diagram proposed by Flemming (2000).

4.2.3 Total mercury distribution and analysis

Due to its historical presence in the study area, mercury represents an excellent tracer both in terms of sediment transport and dating. Mercury may be used as a tracer to assess the age of the sediments, transport's vectors, and the hydrodynamic conditions of the area. The 138 sediment samples underwent an Atomic Absorption Spectrophotometer analysis to calculate their concentration in total Hg (THg). Samples were previously frozen and therefore required a freeze-drying procedure and subsequently drying at room temperature with filter paper after cleaning the salt formed on the walls of the bailers containing the sediment. Successively, they were sieved with a 0.85 mm mesh sieve to remove shell fragments and algal filaments and, finally, they were homogenized with an agate mortar. To measure the mercury concentration, a portion of sediment was taken from each sample and subjected to double manual grinding. The concentration of total Hg was measured using a direct mercury analyser (DMA-80, Milestone, Sorisole, Italy) according to the EPA Method 7473 (EPA, 2007). Before each measurement session, to check quality of the analysis, two measurements of the National Research Council Canada certified marine sediment reference material for total and extractable metal content (PACS-3) were performed. Two or more aliquots were weighed from it to conduct at least two analysis replicates to achieve a relative standard deviation lesser than 10%. In order to obtain as much information as possible from total mercury concentration in the samples, these were processed in various ways. First of all, a distribution map of the THg in the sediments was produced in parallel with the sedimentological maps. Subsequently, the THg was correlated with the different particle size classes in order to identify a correlation between hydrodynamic conditions and tracer transport. All the analyzes and processing of the data relating to mercury were obtained from the collaboration with MercuryLab and were the subject of Makdoud's master's thesis.

4.2.4 Modelling

Modelling is a widely used tool to study coastal dynamics (Amoudry and Souza, 2011; Baldoni et al., 2024; Chaumillon et al., 2017; Chen et al., 2024; Yaiche Temam et al., 2024), acting as a knowledge base both for morphodynamic interpretations and for engineering purposes of designing works on the coast. Furthermore, it is particularly suitable for predicting short-, medium-, and long-term evolutionary scenarios. In this thesis, a spectral and a hydrodynamic wave model were used in conjunction to understand where the wave energy is mostly concentrated, and which currents are generated by the interaction of meteorological forcing during the most important storm events. For this purpose, considering the bimodality of the wave motion, two multi-events were chosen, one generated by the winds of the north-eastern sectors (from 25/02 to 02/03/2023), and one coming from the southern sectors (from 27/10 to 05/11/2023).

The model used is the MIKE21 by ©DHI in the Spectral Wave (SW) and Hydrodynamic (HD) modules. The following description of the model is reported in the MIKE21 software documentation

(https://manuals.mikepoweredbydhi.help/latest/Coast_and_Sea/MIKE_21_Flow_FM_Scientific_Doc.pdf & https://manuals.mikepoweredbydhi.help/latest/Coast_and_Sea/M21SW_Scientific_Doc.pdf).

In both modules, spatial discretization is carried out using the finite volume approach applied to unstructured meshes. MIKE21-SW computational code simulates the growth, transformation and dissipation of wind and swell waves in coastal and offshore areas. The module allowed us to simulate the main processes such as refraction, diffraction, shoaling, background friction, breaking and simple reflection. MIKE21-SW includes two different formulations: directional decoupled parametric formulation and fully spectral formulation. The first is based on a parameterization of the wave action conservation equation. The parameterization is made in the frequency domain by introducing the zeroth and first moment of the wave action spectrum as dependent variables following (Holthuijsen et al., 1989). The second is based on the wave action conservation equation, as described in e.g. (Komen et al., 1994) and (Young, 1999), where the directional-frequency wave action spectrum is the dependent variable. The basic conservation equations are formulated in either Cartesian coordinate for small-scale applications or polar spherical coordinates for large-scale applications. The wave action balance equation developed in Cartesian coordinates is:

$$\frac{\partial N}{\partial t} + \nabla \cdot (\bar{v}N) = \frac{S}{\sigma}$$

where: $N(\bar{x}, \sigma, \theta, t)$ is the density action; t is the time; $\bar{v} = (c_x, c_y, c_\sigma, c_\theta)$ is the group propagation velocity of the waves in the four dimensions phase space. S is the source term for energy balance equation:

$$S = S_{in} + S_{nl} + S_{ds} + S_{bot} + S_{surf}$$

where S_{in} represents the momentum transfer of wind energy to wave generation; S_{nl} is the energy transfer due to non-linear wave-wave interaction; S_{ds} , S_{bot} and S_{surf} are the dissipation of wave energy due to white-capping (deep water wave breaking), bottom friction, and depth-induced breaking respectively. The characteristic propagation speeds are given by the linear kinematic relationship:

$$(c_x, c_y) = \frac{d\bar{x}}{dt} = \bar{c}_g + \bar{U} = \frac{1}{2} \left(1 + \frac{2kd}{\sinh(2kd)} \right) \frac{\sigma}{k} + \bar{U}$$

$$c_\sigma = \frac{d\sigma}{dt} = \frac{\partial \sigma}{\partial d} \left[\frac{\partial d}{\partial t} + \bar{U} \cdot \nabla_{\bar{x}} d \right] - c_g \bar{k} \cdot \frac{\partial \bar{U}}{\partial s}$$

$$c_\theta = \frac{d\theta}{dt} = -\frac{1}{k} \left[\frac{\partial \sigma}{\partial d} \frac{\partial d}{\partial m} + \bar{k} \cdot \frac{\partial \bar{U}}{\partial m} \right]$$

where s is the space coordinate in wave direction θ and m is a coordinate perpendicular to s . The wind input is based on (Janssen 1989, 1991) quasi-linear theory of wind-wave generation, where the momentum transfer from the wind to the sea not only depends on the wind stress, but also the sea state itself. The non-linear energy transfer (through the resonant four-wave interaction) is approximated by the DIA approach

(Hasselmann et al. 1985). The source function describing the dissipation due to white-capping is based on the theory of (Hasselmann 1974) and (Janssen 1989). The bottom friction dissipation is modelled using the approach by (Johnson and Kofoed-Hansen, 2000), which depends on the wave and sediment properties. The source function describing the bottom-induced wave breaking is based on the well-proven approach (Battjes and Janssen, 1978; Eldeberky and Battjes, 1996). The directionally decoupled parametric formulation is based on the parameterization of the wave action balance equation (Holthuijsen et al. 1989) in the frequency domain, introducing the zeroth and first moment of wave action spectrum as dependent variables. The equations are:

$$\frac{\partial(m_0)}{\partial t} + \frac{\partial(c_x m_0)}{\partial x} + \frac{\partial(c_y m_0)}{\partial y} + \frac{\partial(c_\theta m_0)}{\partial \theta} = T_0$$

$$\frac{\partial(m_1)}{\partial t} + \frac{\partial(c_x m_1)}{\partial x} + \frac{\partial(c_y m_1)}{\partial y} + \frac{\partial(c_\theta m_1)}{\partial \theta} = T_1$$

Where $m_0(x, y, \theta)$ and $m_1(x, y, \theta)$ are the zeroth and first order of the action spectrum $N(x, y, \sigma, \theta)$ respectively. $T_0(x, y, \theta)$ e $T_1(x, y, \theta)$ are source functions based on the action spectrum. The moments $m_n(x, y, \theta)$ are defined as:

$$m_n(x, y, \theta) = \int_0^\infty \omega^n N(x, y, \omega, \theta) d\omega$$

The source functions T_0 and T_1 consider the effect of the energy dissipation due to the friction with the bottom and wave breaking, and the wave-currents interaction. Spatial and spectral discretization is performed using a finite volume method with values centered on the single element. The frequency domain can be discretized both linearly and logarithmically. The discretization in the time domain is done through time-steps and the propagation of the “wave action” is done through an explicit multi-frequency method.

MIKE21-HD module simulates water level and current variations in response to the different types of forcings considered. MIKE21-HD allows the simulation of a wide range of hydraulic phenomena that can be used for the representation of any non-stratified free surface current. In particular, the module allows to take into consideration the following aspects: flooding and drying, density gradients, bottom friction; Coriolis force, wind effect, pressure gradients, ice covers, tides, precipitation/evaporation, wave motion (through radiation stress), and punctual sources. The modeling system is based on the numerical solution of the averaged Navier-Stokes equations (Reynolds Averaged Navier-Stokes Equations) under the hypothesis of Boussinesq and under hydrostatic pressure conditions. The model solves the equations of continuity, momentum, temperature, salinity, and density. It uses the finite volume method for the discretization of the flow and transport equations with values centered on the single element. The spatial domain is discretized through the subdivision of the continuum into non-overlapping elements. In Cartesian coordinates, the equations used by the model are:

The local continuity equation:

$$\frac{\partial u}{\partial x} + \frac{\partial v}{\partial y} + \frac{\partial w}{\partial z} = S$$

Horizontal momentum equations for x- and y-component:

$$\frac{\partial u}{\partial t} + \frac{\partial u^2}{\partial x} + \frac{\partial uv}{\partial y} + \frac{\partial wu}{\partial z} = fv - g \frac{\partial \eta}{\partial x} - \frac{1}{\rho_0} \frac{\partial p_a}{\partial x} - \frac{g}{\rho_0} \int_z^\eta \frac{\partial \rho}{\partial x} dz + F_u + \frac{\partial}{\partial z} \left(V_t \frac{\partial u}{\partial z} \right) + u_s S$$

$$\frac{\partial v}{\partial t} + \frac{\partial v^2}{\partial x} + \frac{\partial uv}{\partial y} + \frac{\partial wv}{\partial z} = fu - g \frac{\partial \eta}{\partial x} - \frac{1}{\rho_0} \frac{\partial p_a}{\partial y} - \frac{g}{\rho_0} \int_z^\eta \frac{\partial \rho}{\partial y} dz + F_v + \frac{\partial}{\partial z} \left(V_t \frac{\partial v}{\partial z} \right) + v_s S$$

The calculation of the temperature (T) and salinity (s) exchanges are modeled according to the general transport equations:

$$\frac{\partial T}{\partial t} + \frac{\partial uT}{\partial x} + \frac{\partial vT}{\partial y} + \frac{\partial wT}{\partial z} = F_T + \frac{\partial}{\partial z} \left(D_v \frac{\partial T}{\partial z} \right) + H + T_s S$$

$$\frac{\partial s}{\partial t} + \frac{\partial us}{\partial x} + \frac{\partial vs}{\partial y} + \frac{\partial ws}{\partial z} = F_s + \frac{\partial}{\partial z} \left(D_v \frac{\partial s}{\partial z} \right) + H + s_s S$$

The terms of horizontal diffusivity are defined by:

$$(F_T, F_s) = \left[\frac{\partial}{\partial x} \left(D_h \frac{\partial}{\partial x} \right) + \frac{\partial}{\partial y} \left(D_h \frac{\partial}{\partial y} \right) \right] (T, s)$$

where t is time; x , y , and z are the cartesian coordinates; u , v , and w are the flow velocity components; T is temperature; s is salinity; D_v is vertical turbulent (eddy) diffusion coefficient ; D_h is the horizontal diffusion coefficient ; h is depth ; F_t , F_s , and F_c are the horizontal diffusion conditions; S the magnitude of discharge for point sources; H the thermal source that causes an exchange of heat with the atmosphere. The model produces many outputs such as:

- Spectral wave: Significant wave height (Hs) and its components (u and v), mean wave direction, peak wave period (Tp), zero-crossing wave period (T02), radiation stresses (Sxx, Syy, Sxy), wave power (P) and its components (Px, Py), etc etc.
- Hydrodynamic: surface elevation, still and total water depth, current speed and its components (U and V), current direction, etc etc.

For our purposes, H_s , bed shear stresses, current speed and direction are the most important data because they can be related to sediment transport and morphodynamics. In order to properly simulate littoral currents in the HD module, the radiation stresses from the SW module are necessary. Radiation stresses are defined by Katopodis (2019) as “the excess flux of momentum due to the presence of the waves, and the term stress is used to emphasize that the force is not isotropically distributed”. Water level set-up and alongshore currents are two important phenomena occurring in the shallow waters that are related to gradients in cross-shore and alongshore radiation stresses respectively (Ribas and Kroon, 2007).

The boundaries of the calculation mesh were drawn following the following criteria. The northern border was drawn following the shoreline, giving it directional continuity in the presence of lagoon mouths and river mouths, up to the border with the Gulf of Panzano. The eastern and south-eastern border, from Panzano to Punta Salvore, was drawn parallel to the coastline, however simplifying its course. The border towards the Adriatic was drawn by connecting Punta Salvore to the DWRG1 buoy and going further, in the same direction, for about 3km. Finally, it was closed perpendicularly to the shoreline. For our triangular mesh creation, we set the smallest allowable angle of 28° . The mesh for the SW module was divided into 3 zones with different resolution: offshore it was generated starting from a vertex spacing of 675 m on the edge, in the center from a spacing of 225 m while below the coast the spacing between the vertices was 75m (Figure 26a). In the three zones, the maximum area for the mesh elements was set equal to $\frac{1.25 \cdot (\text{spacing})^2}{2}$. The obtained mesh has a total of 34'585 nodes and 68'426 elements.

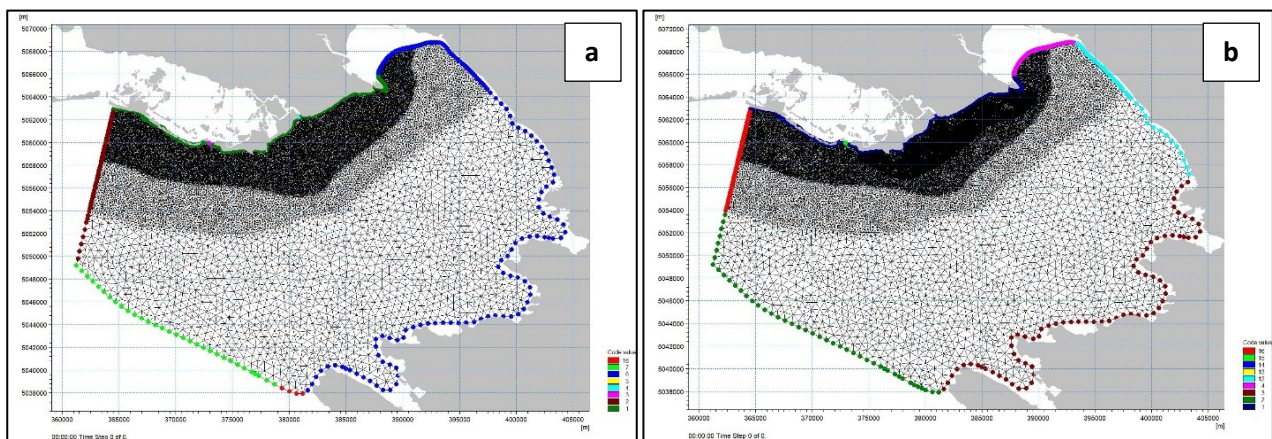


Figure 26 Mesh used for (a) MIKE21-SW module and (b) MIKE21-HD module.

For the hydrodynamic module, an additional area with higher resolution (25 m spacing) was used to discretize the more dynamic areas in greater detail (Figure 26b), obtaining a mesh of 111'843 nodes and 222'487 elements. The mesh was subsequently interpolated starting from a set of bathymetric data: for the subcoastal area the 2019 DTM was used (cellsize 2×2 m) while the offshore bathymetry was obtained from the bathymetric model of the European Marine Observation and Data Network (EMODnet) of 2022 (<http://www.emodnet-bathymetry.eu>) on a grid of $1/16 \times 1/16$ arc minute of longitude and latitude (ca 115×115 m). After having reprojected the EMODnet raster into the RDN2008-TM33 reference system, the buffer

area between the two rasters was analyzed to identify and remove any bathymetric inconsistencies due to the different resolution and source of the rasters themselves. In this area, the EMODnet bathymetry was manually modified to make it congruent with the 2019 subcoastal DTM. Finally, the EMODnet bathymetry was cropped externally compared to the 2019 DTM, and the mesh was interpolated on the basis of the two rasters (Figure 27).

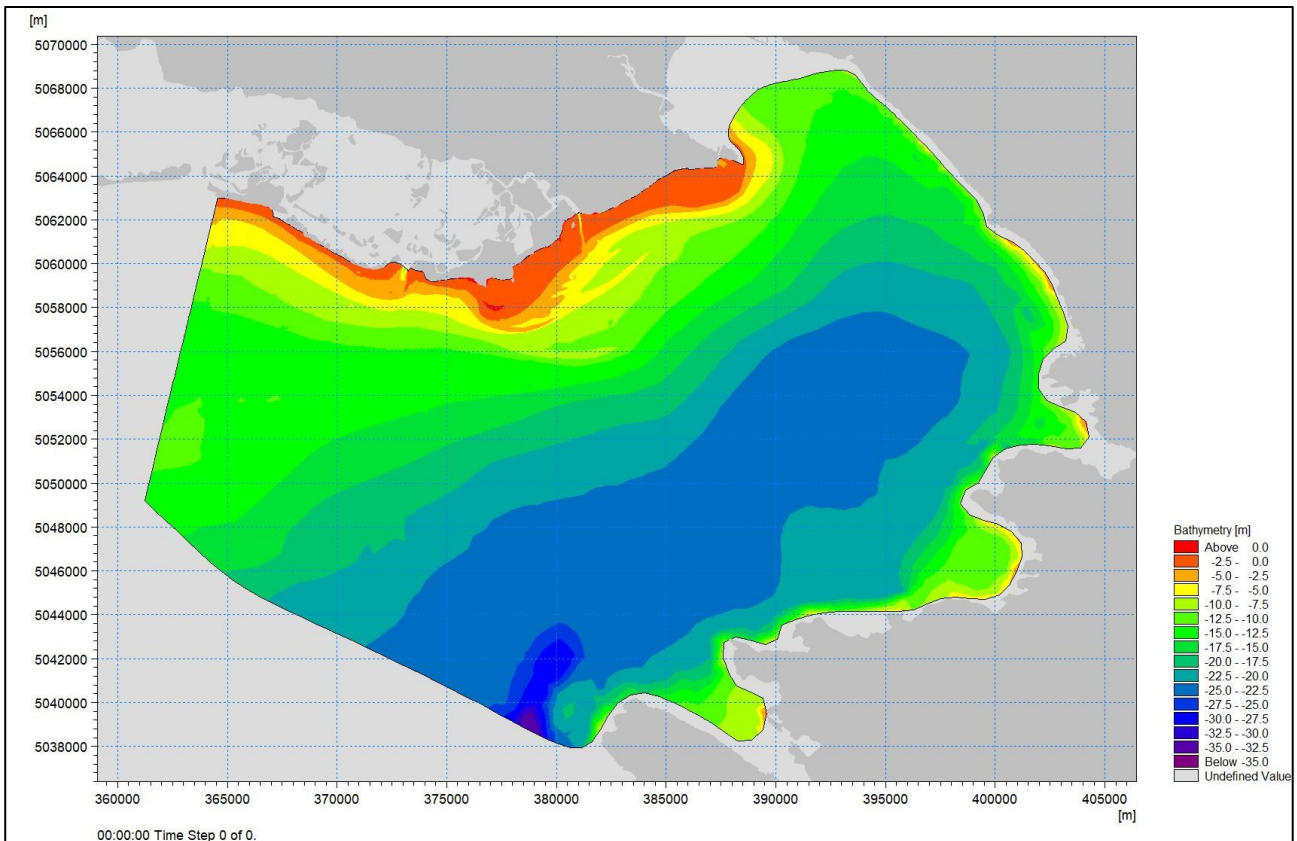


Figure 27 Bathymetry of the mesh used in MIKE21 modules.

To obtain the boundary conditions of the two modules the following data were used:

- Recordings of wave data from the DWRG1 wave buoy: significant wave height (H_s), mean wave direction, peak period, wave spreading.
- Weather data from the Paloma station: wind speed and direction, temperature, precipitation.
- Level data obtained from the Trieste tide gauge (Molo Sartorio).

In both modules, 7 boundaries were defined: land boundary, Grado Inlet, Primero Inlet, Isonzo river, Monfalcone - Punta Salvore, sea boundary, western lateral boundary. The final arrangement of the mesh and the boundary conditions was the result of repeated calibration and analysis of the outputs produced by the model in order to make it as close as possible to the data recorded by the DWRG3 wave buoy, located within the maximum area interest, and the evidence obtained from bathymetric and sedimentological data. For this reason, the first 1.5 km of the sea boundary from Punta Salvatore have been defined as lateral boundary. Once the distribution of bed shear stress is obtained from model simulations, the excess over the critical bed shear stress required for resuspension of seabed sediment will be calculated. The critical bed shear stress for

suspension describes the minimum shear stress level required to not only mobilize sediment particles from the bed of a water body, such as a river or sea, but also to maintain these particles in suspension within the fluid flow. In marine environment, it depends on the characteristics of the sediment (such as grain size and density) and the fluid dynamics of the sea. Once the critical bed shear stress for suspension is reached, sediment particles are lifted into the water column and transported alongshore by the flow. Understanding the critical bed shear stress for suspension is crucial for predicting sediment transport in coastal systems, designing sediment management strategies, and modeling erosion and deposition processes under various sea conditions. To calculate the excess over the critical bed shear stress, a map of the critical bed shear stress for suspension will first be produced following the theory of (Van Rijn, 2020). First, we calculated the dimensionless grain size D^* as:

$$D^* = d_{50} \sqrt[3]{\left(\frac{\rho_s}{\rho_w} - 1\right)g/\nu^2}$$

where d_{50} is the median grain size (in m), ρ_s is the density of the sediment particle (assumed 2.65 g/cm³), ρ_w is the sea water density (assumed 1.025 g/cm³), g is the acceleration of gravity (9.8066 m/s²) and ν is the kinematic viscosity coefficient (1×10⁻⁶ m²/s). Secondly, the shields parameter $\theta_{cr,s}$ was calculated as:

$$\theta_{cr,s} = \frac{0.3}{1 + D^*} + 0.1(1 - e^{-0.05D^*})$$

Finally, the critical bed shear stress for suspension $\tau_{cr,s}$ was calculated as:

$$\tau_{cr,s} = \theta_{cr,s}((\rho_s - \rho_w)gd_{50})$$

Once obtained the map of the critical bed shear stress for suspension, we derived some products. First, we produce, for every timestep of any event simulated event, the map of excess of BSS, i.e. the difference between calculated BSS and critical BSS for suspension, taking care to eliminate negative values. Subsequently, for any event simulated, we calculated the mean excess of BSS, the time of exceedance of critical BSS and the total the excess of BSS, summing the excess of BSS of every timestep of any event simulated event. The latter, although physically it represents the product of stress and time, can be assumed to be proportional to the solid transport that occurs when the BSS exceeds the critical value.

4.2.4.1 Storm events of 2023

Considering bimodality of the wave climate showed by the wave roses of both DWRG1 and DWRG3 buoys (Figure 5), it was chosen to simulate the most significant storm events of 2023 of ENE and southern waves occurred from 25th February to 2nd March and from 27th October to 5th November respectively, whose characteristics are summarized in Table 3.

Event	February – March 2023 (Bora)	October – November 2023 (Sirocco)
Max Significant wave height	DWRG1: 2.31 m	DWRG1: 3.77 m
Mean wave direction	DWRG1: 77.3°N	DWRG1: 182.6°N
Max wind speed (1h data)	Paloma: 82km/h	Paloma: 66 km/h
Max water level	Trieste Molo Sartorio: 0.37 m	Trieste Molo Sartorio: 1.36 m
Duration:	101h	105h

Table 3 Meteorological characteristics of the two major storm events simulated.

Extreme events from Bora and Sirocco are particularly different: Bora, even if it's stronger than Sirocco, is not able to produce particularly high waves due to the short fetch and its storm surges are negative in the Gulf of Trieste, leading to a progressive increase in the storm surge towards south-east. On the other hand, due to the geographical characteristics of the Adriatic Sea, Sirocco extreme events are often related to high values of both storm surges and H_s .

The winter bora event was characterized by several days of intense winds from ENE. Bora winds flowing on the Gulf of Trieste produce a negative surge as highlighted by the comparison between predicted and registered water level in Trieste (Figure 28).

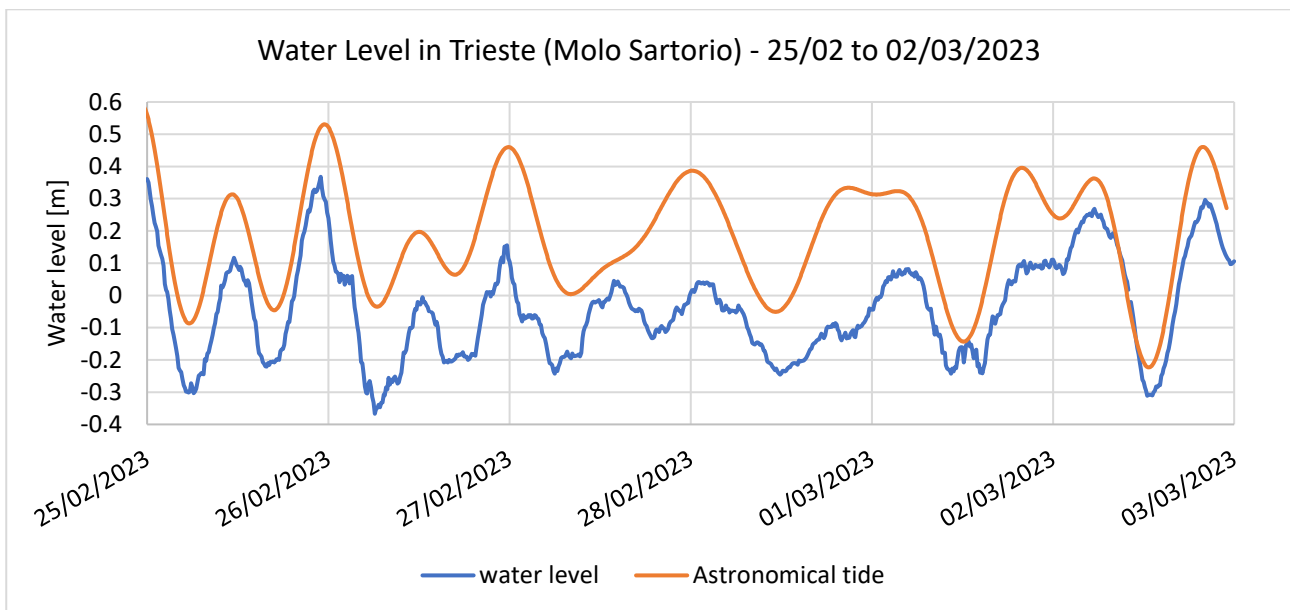


Figure 28 Water level (blue) and predicted astronomical tide (orange) in Trieste during the Bora storm event in winter 2023.

The stability of wind conditions led to the generation of waves with H_s greater than 1 m for four consecutive days, with two main peaks, one just after the start of the event (26/02 at 1:30) and one the last day (01/03 at 10:00) (Figure 29).

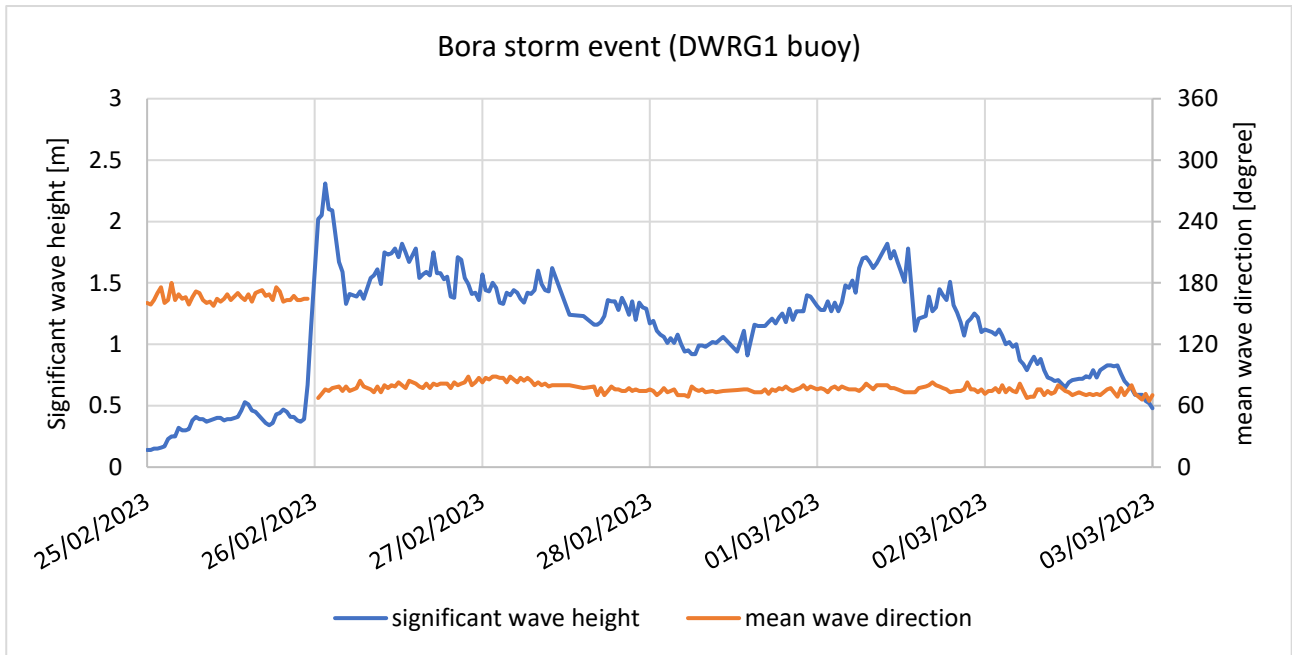


Figure 29 Significant wave height (blue) and mean wave direction (orange) of the winter storm event of 25/02 - 02/03/2023 registered at DWRG1 buoy.

The autumn 2023 multi-event was quite intense and the impact it had on the coastal realities of the northern Adriatic was significant. Both flooding phenomena and damage to coastal structures due to wave motion were recorded in various coastal locations. During these events the hydrometric level reached +1.36 m in Trieste (Figure 30).

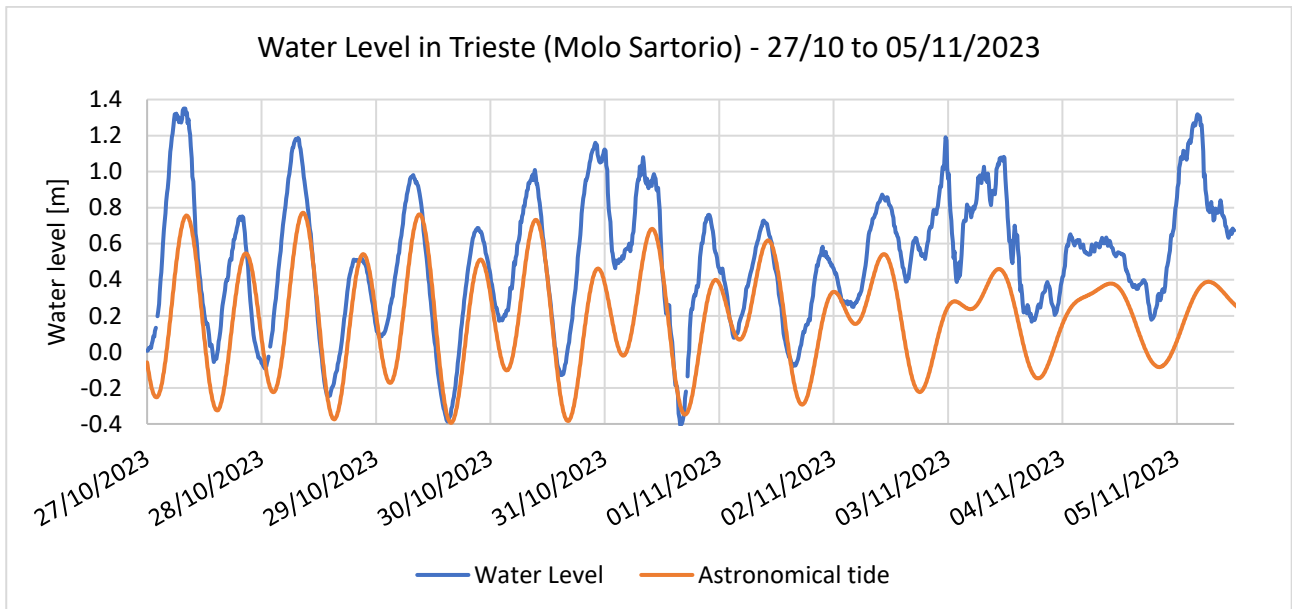


Figure 30 Water level (blue) and predicted astronomical tide (orange) in Trieste during the storm multi-event in autumn 2023.

Waves were quite high during the multi-event, reaching up to 3.77 m of Hs (Figure 31). The six events recorded between 27 October and 5 November by the DWRG1 wave buoy have the following characteristics.

Event peak (date and hour)	Max significant wave height [m]	Mean direction [degree]
27/10/2023 06:00	2.26	170°N (Sirocco)
30/10/2023 20:30	2.28	166°N (Sirocco)

31/10/2023 13:00	2.07	205°N (Libeccio)
02/11/2023 17:30	3.24	175°N (Sirocco)
03/11/2023 14:00	2.72	197°N (Libeccio)
05/11/2023 03:00	3.77	172°N (Sirocco)

Table 4 Wave characteristics of the six peaks of the multi-event of 27/10 – 05/11/2023. Data registered at DWRG1 wave buoy.

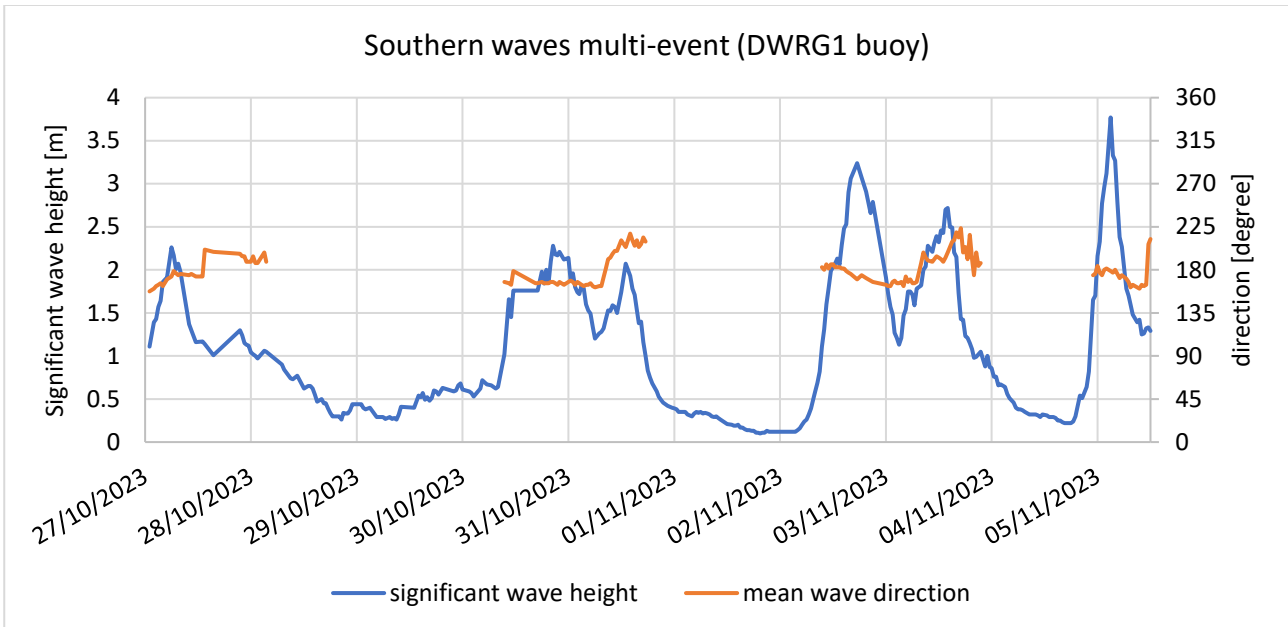


Figure 31 Significant wave height (blue) and mean wave direction (orange) of the multi-event of 27/10 - 05/11/2023 registered at DWRG1 buoy.

4.2.4.2 Not-extreme events

In addition to the two most severe events of 2023, three other events were simulated: the first (from 25/01 to 30/01) characterized by moderate ENE winds and waves, the second (24/03 to 29/03) of moderate southern waves and the third (18/04 to 22/04) of low waves from both south and ENE (Figure 32).

Event	Max significant wave height [m]	Mean direction [degree]
25/01 to 30/01/2023	1.46	83°N (Bora)
24/03 to 29/03/2023	1.10	176°N (Sirocco)
18/04 to 22/04/2023	0.43	Both Bora and Sirocco

Table 5 Wave characteristics of the three not-extreme wave conditions of winter-spring 2023 recorded at DWRG1 buoy.

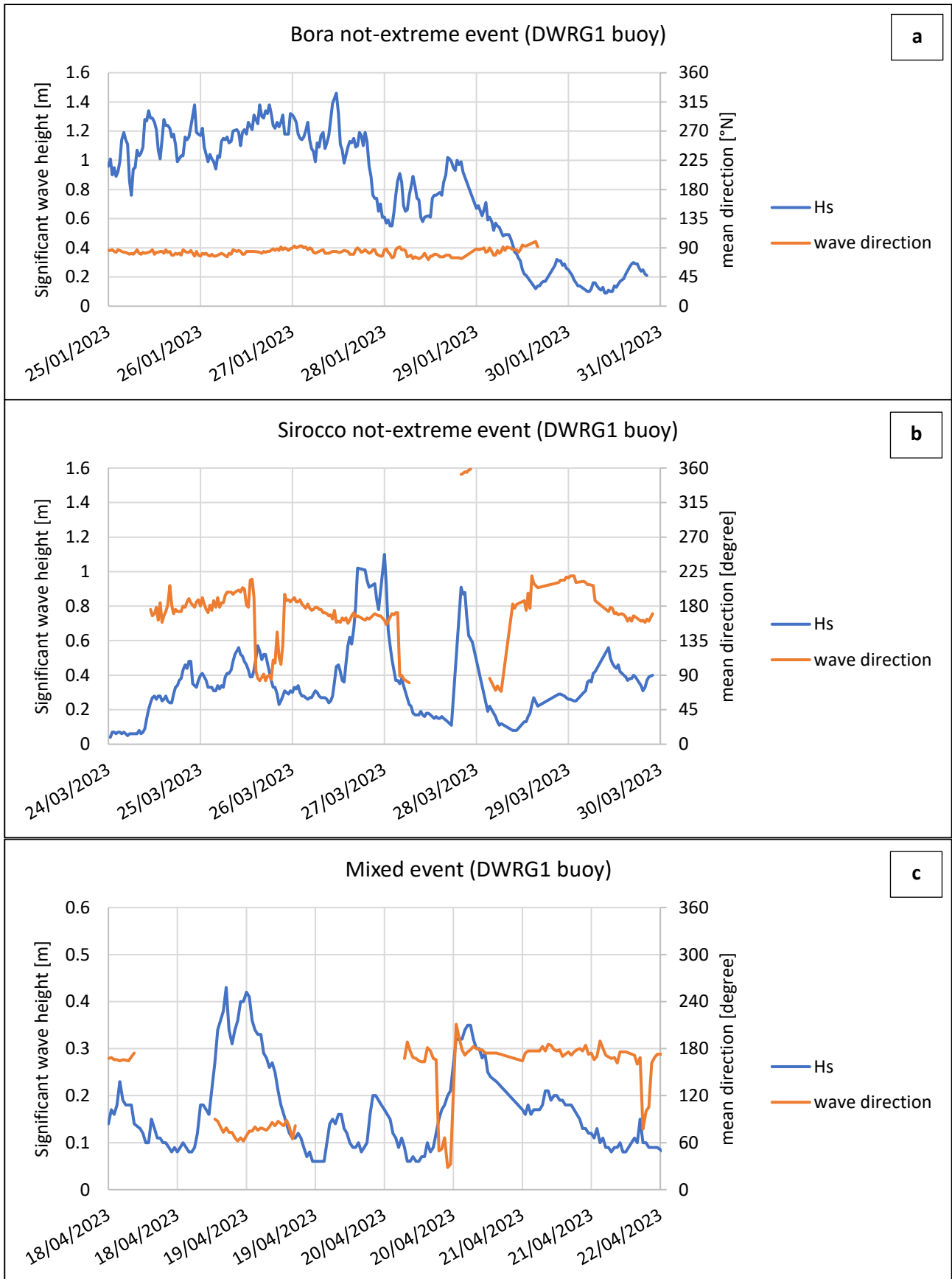


Figure 32 Hs (blue) and mean wave direction (orange) of not-extreme wave conditions of (a) Bora, (b) Sirocco and (c) mixed waves.

5 Results

In the sixth chapter, the results are presented by type, first discussing geomorphological set-up and sediment budgets, followed by the sedimentological and geochemical aspects, and finally the hydrodynamic and spectral wave models. Part of them have already been published by Bezzi et al. (2021a), presented at national (Sponza et al., 2023) and international conferences (Fracaros et al., 2021; Pavoni et al., 2023a), and in technical reports for the regional administration.

5.1 Geomorphology & sediment budget

The residual map in Figure 33 provides an initial tool for identifying the largest depositional anomalies at the spatial scale of the entire study area. It was obtained by applying the method proposed by Fontolan et al. (2007), which involves subtracting the second-order polynomial trend of the DTM of the study area (2019) from the DTM itself. The map highlights the presence of the two sinks of the MMB and the Isonzo River delta. In particular, the most positive anomalies are in the HIB and in the south-central part of the delta.

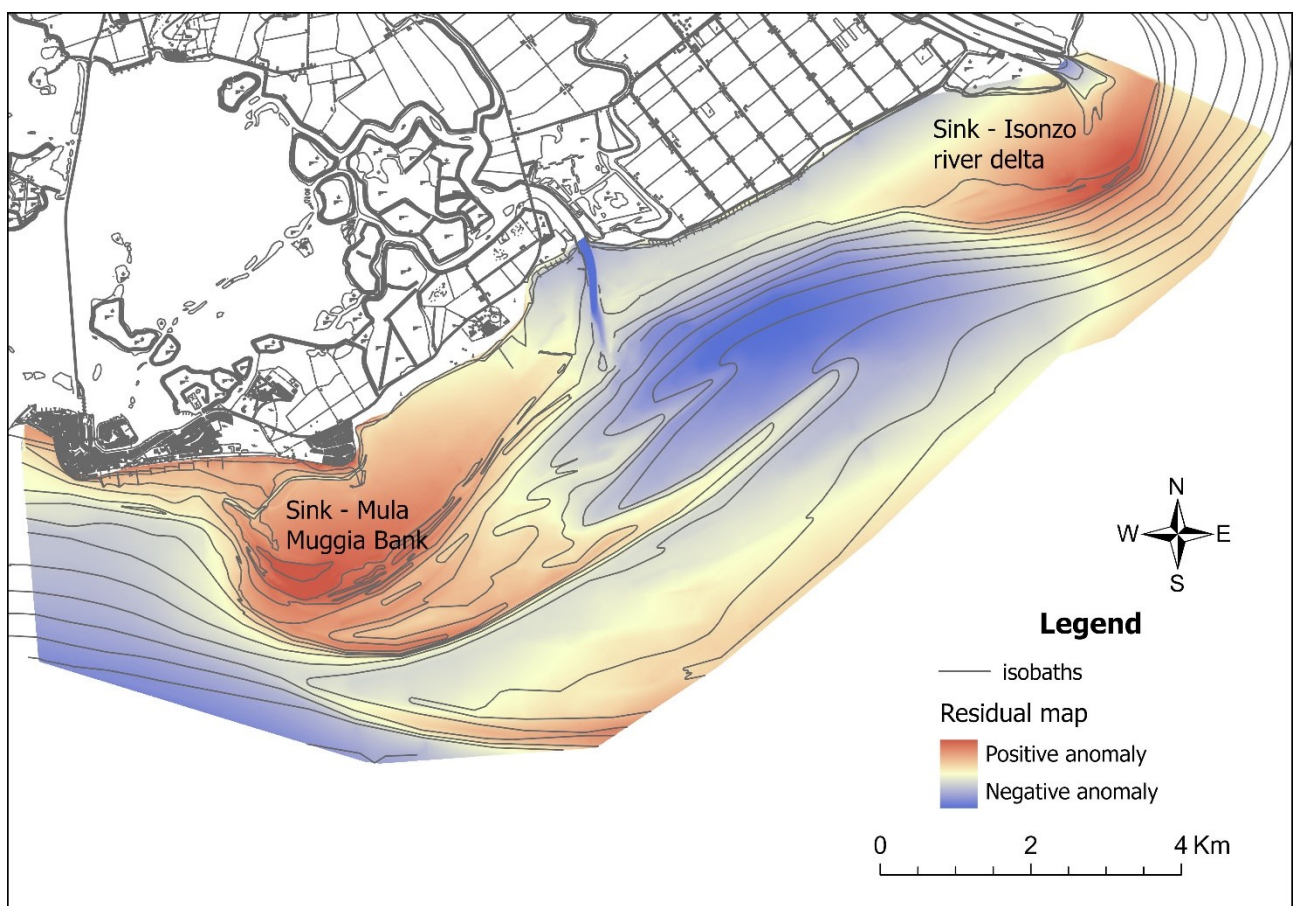


Figure 33 Residual map of second order polynomial. The map emphasizes positive (red) or negative (blue) depositional anomalies.

5.1.1 Front of the Mula di Muggia Bank & High Intertidal Bank

F-MMB and HIB are essentially two parts of the same area, with the former comprising the seabed below the mean sea level and the latter the intertidal zone. The results of the analyses for these two zones are presented separately for convenience, as they were surveyed using different methodologies due to physiographic reasons.

5.1.1.1 *Geomorphological set-up*

The survey of the HIB was carried out in spring 2023 via UAV to evaluate the evolution in the last four years through comparison with a survey dated spring 2019. It is important to point out that only the orthophoto and not the DTM was obtained from the 2019 UAV survey due to the impossibility of using GCPs for height correction, compromising the accuracy in height (error >70 cm).

In 2023 (Figure 34a), considering the HIB in its entirety, the shape of the HIB remained essentially the same as in 2019 (Figure 34b). The extension of the bank continues to follow the SE-NW direction of the F-MMB. Furthermore, the bank can be divided into two areas, the southernmost vertex of the MMB and the F-MMB. In the southernmost vertex of MMB the bank is spatially very extended, around 450 m wide. Here, the bank is made up of a set of crossed bars, part parallel to the side of the MMB (NE-SW), part parallel to the F-MMB (SE-NW). Towards the north-west the HIB gradually becomes narrower and more elongated: here its structure is characterized by a set of four bars parallel to the F-MMB. These bars are not equally long: from sea to shore, the firsts two start from the southern vertex and extend up to the half of the total length of the HIB while the two onshore are essentially a unique bar up to the half of the HIB where the third bar splits from the fourth. The fourth and most onshore bar is wider compared to the other three, with a width is around 80-130 m.

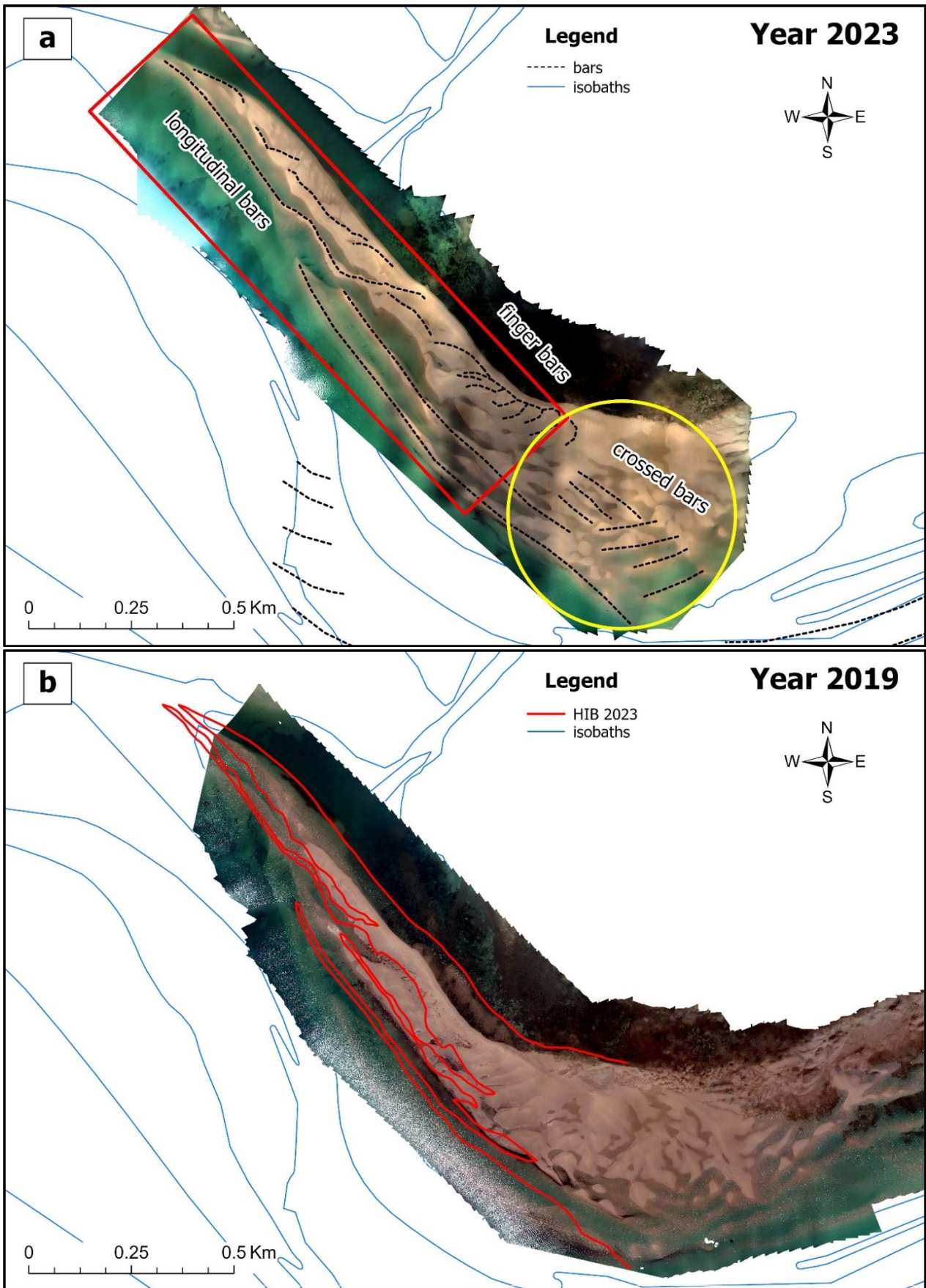


Figure 34 Orthophoto of the High Intertidal Bank obtained from UAV survey in (a) 2023 and (b) 2019. The HIB is made up of the southernmost vertex (yellow circle) and the F-MMB (red rectangle) in 2023 orthophoto (a). In 2019 orthophoto (b) the red line represents the border of the HIB in 2023.

Positioning Index maps are useful tools for identifying geomorphological elements and quantifying their dimensions at different spatial scales. To analyse the UAV survey of the HIB (2023), we tested the PI with multiple radii, from 1 m to 20 m. The map obtained with a radius of 10 m proved to be a good compromise for identifying the structures present (Figure 35). The landward edge of the HIB has a line shape broken into two branches, the first, further west, approximately 1150 m long with a direction of 135°N beyond which the second begins with a direction of 100°N. Starting from the edge of the HIB, a set of finger bars extends, similar to the finger bars present on the D-MMB, with directions that form angles of 30°-50° anticlockwise with the structure of the HIB and which tends to rotate clockwise going from south-east to north-west following the trend of the edge of the HIB. From two of these bars extends one of the 5 parallel branches that form the tip of the bench itself. Finally, in the area of the tip of the HIB, structures parallel to the edge of the bench at angles of 120°-130° in an anti-clockwise direction are visible, albeit less clearly.

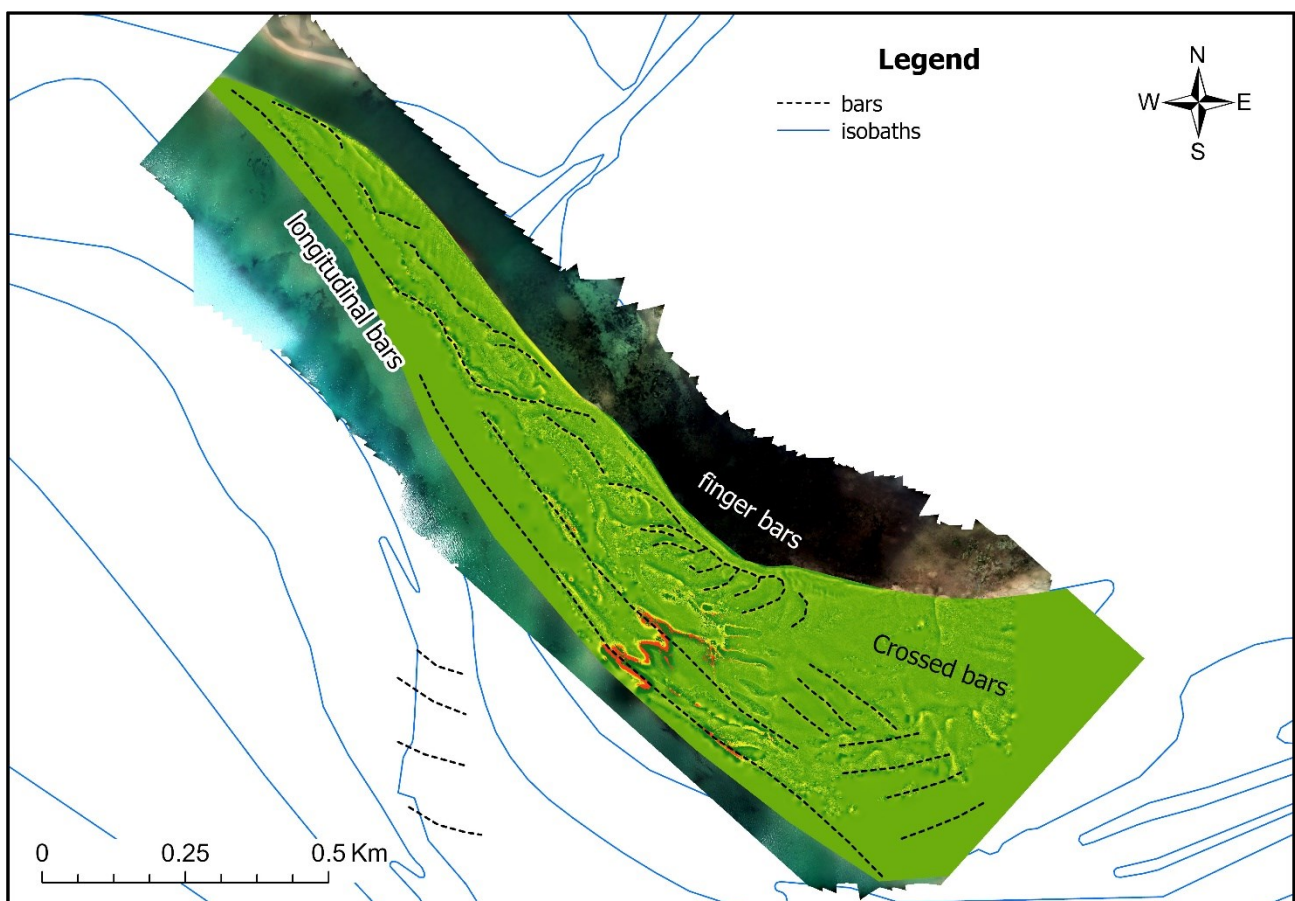


Figure 35 Positioning Index with a 10 m radius of 2023 DTM of HIB.

On the F-MMB, starting from the 2023 SBES surveys, a DTM was produced to be compared with the 2011 and 2019 DTMs with the aim to identify evolutionary trends (Figure 36). The production of the DTM of the area was rather difficult due to the high presence of seagrass meadows which, in the SBES surveys, are particularly difficult to filter if they are very widespread: these plants may reflect the acoustic wave emitted by the echo-sounder before it reaches the seabed, resulting in a lesser depth and, if not filtered out, they may alter sediment budget significantly. From a total of 6129 points sampled, 1003 were removed, partly due to the

presence of spikes or reception of multiples, but mostly due to the presence of seagrasses, managing to use 5126 points for the creation of the DTM, with a loss of data by 16.3%. Moreover, the presence of seagrasses and the consequent loss of data, is not equally distributed: it was highlighted starting from transect 4F, but the greatest filtering was carried out between transects 9F and 13F. Finally, given that the objective of the 2023 SBES survey is to make a comparison on transects, it was decided not to intervene further on the data, using, for example, polylines or axes, since the reliability of the model is sufficiently high in the neighborhood of the transects.

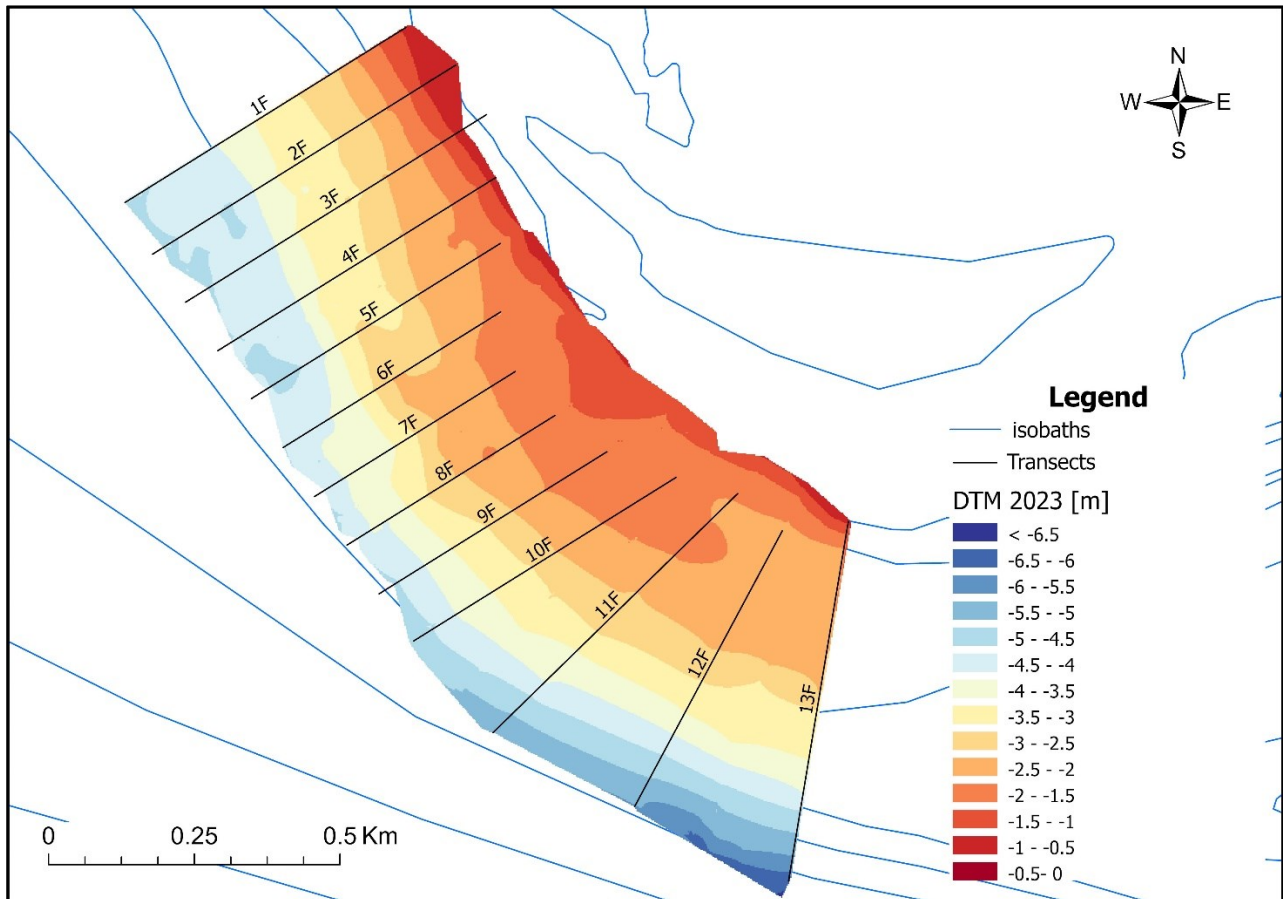


Figure 36 DTM of the F-MMB in 2023.

For the geomorphological analysis of the DTM we therefore chose to analyze the MBES survey dated 2011 (Gordini et al. 2013) which, although older, is much more detailed and more extended than the SBES surveys. Furthermore, the architecture of the method is much less affected by the presence of seagrasses since the disturbance caused by them can be filtered and removed without a loss of data.

The DTM of 2011 (Figure 37a) shows in detail the extroflexion of the isobath of the F-MMB, the presence of the western part of the outer deep bar, the western sector of the deep terrace characterized by the presence of the finger bars and a depressed area in between the latter. A further description of these features was produced by Bezzi et al. (2021a), Fontolan et al. (2018) and Interreg Italy-Croatia CWC (2021).

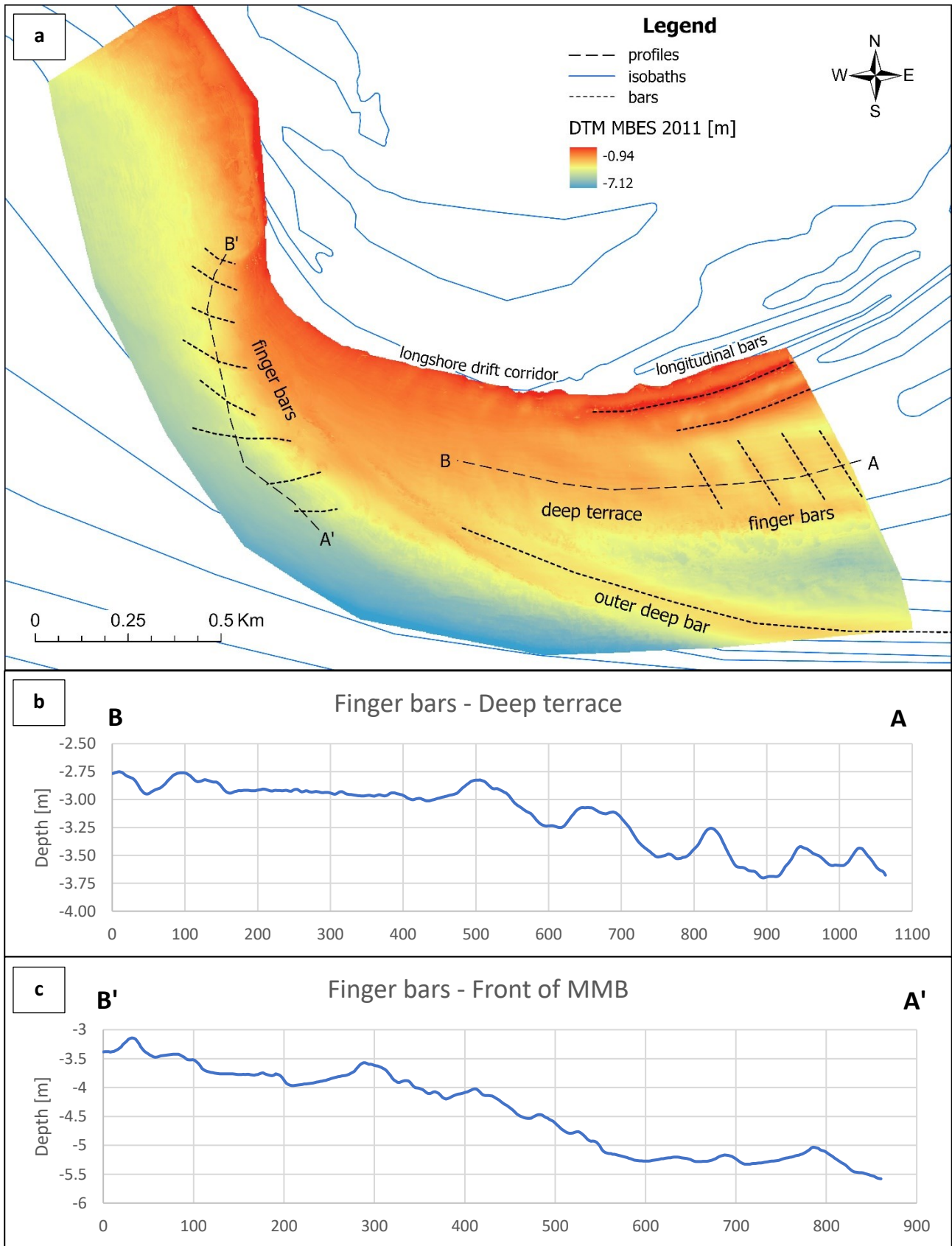


Figure 37 (a) 2011 DTM of the F-MMB from a MBES survey, (b) transect normal to the finger bars on the deep terrace and (c) transect normal to the finger bars on the F-MMB.

Positioning Index was also used on the MBES surveys of the F-MMB carried out by the OGS in 2011 (Gordini et al. 2013), with greater radii (from 10 m to 200 m) compared to those used on the UAV surveys due to the different resolution of the survey and the greater size of submerged structures. Using a radius of 200 m (Figure 38) it was possible to identify the larger structures: you can clearly see, in red, the areas that are higher than the surrounding area, such as the longitudinal sand bars of the littoral drift pathway, the part western part of the outer deep bar, the edge of the F-MMB and the westernmost finger bars can be found. Compared to the DTM of the same area (Figure 37), the Positioning Index manages to highlight the bathymetric anomalies, improving the identification of the structures.

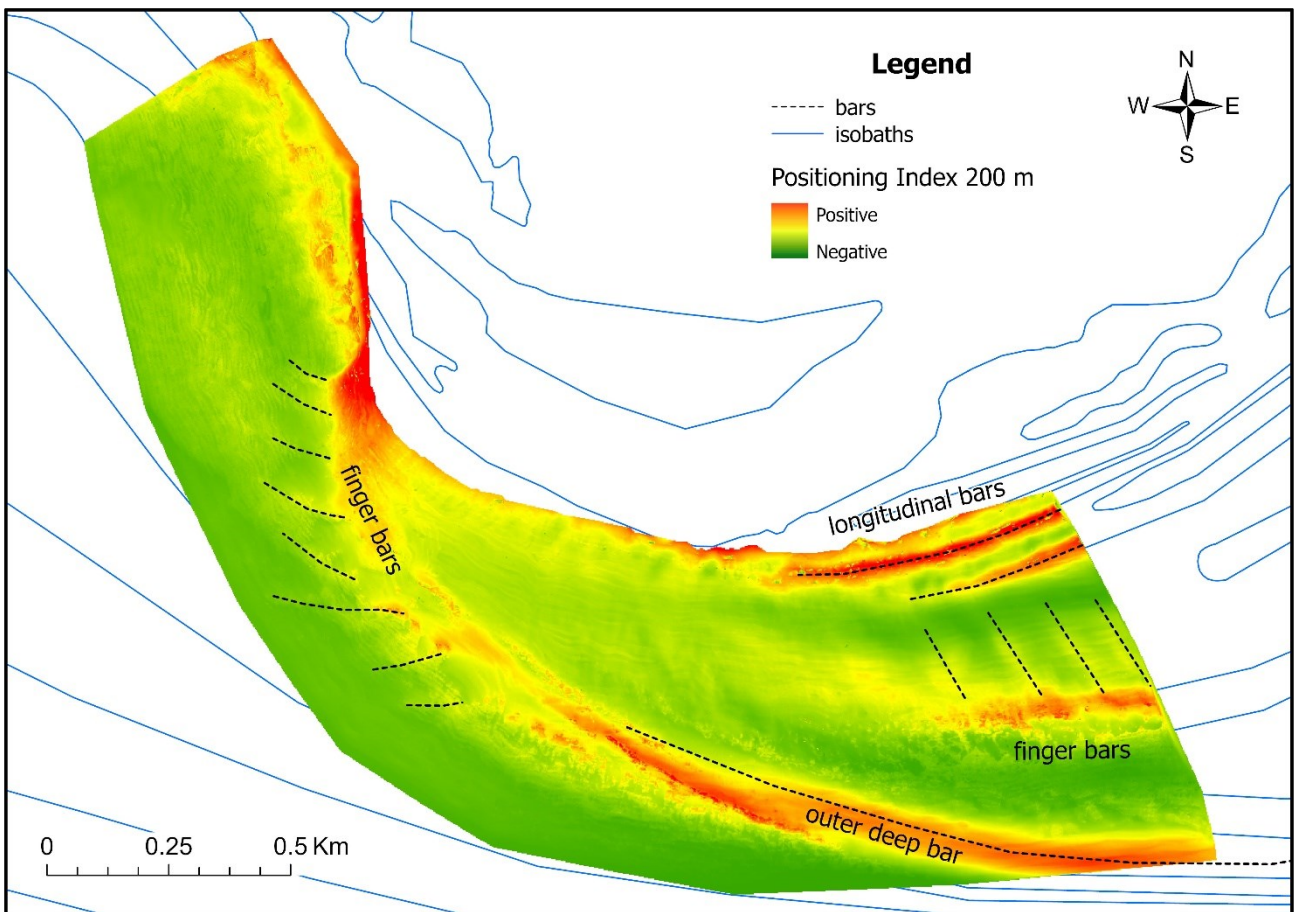


Figure 38 Positioning Index with a 200 m radius of MBES 2011 – F-MMB.

By reducing the radius to 50 m (Figure 39), some smaller scale structures become more visible such as, for example, the finger bars: these bars have a direction rotated with respect to the longitudinal bars (and in general to the trend of the isobaths) by an angle ranging from 50° to 70° clockwise.

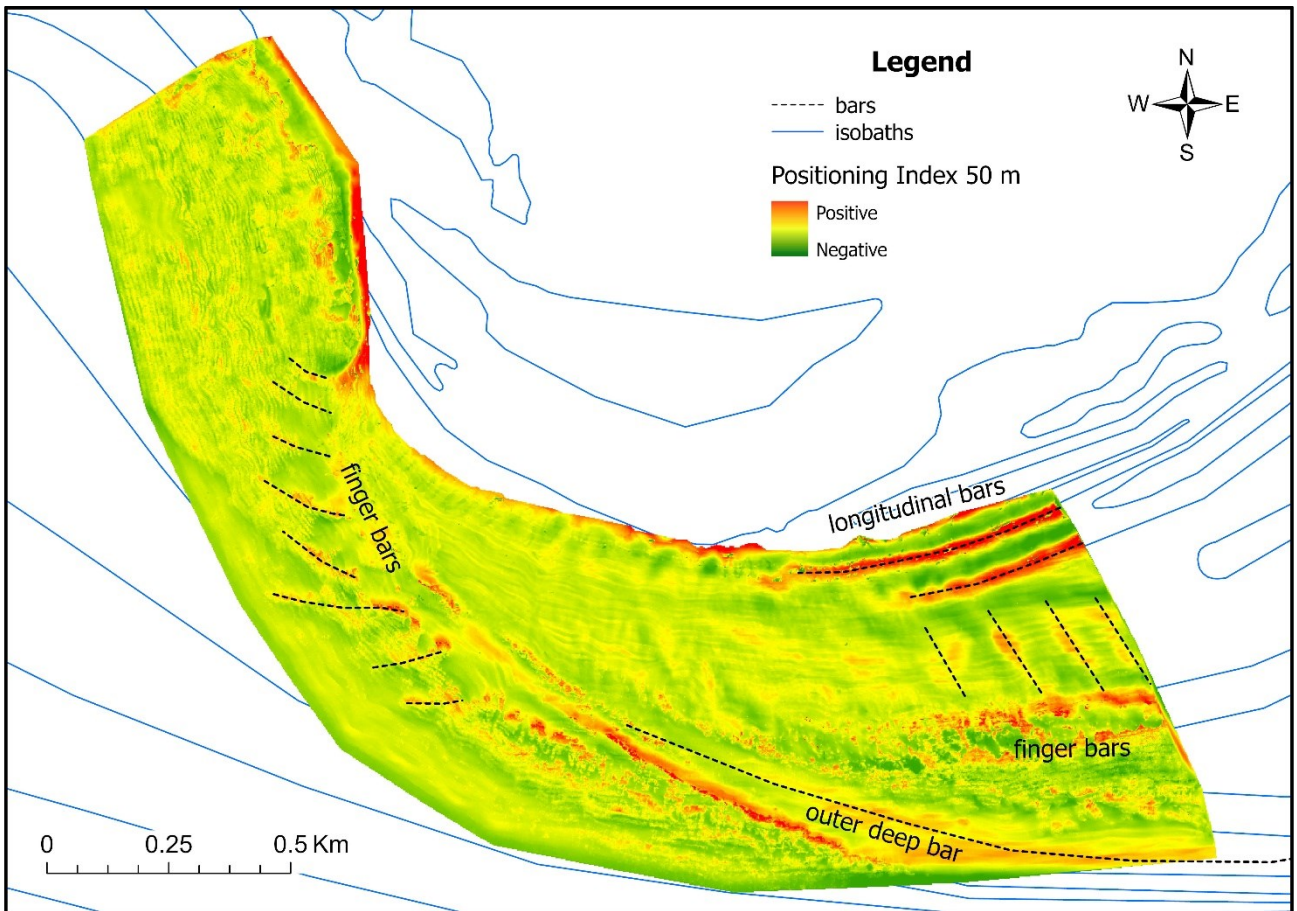


Figure 39 Positioning Index with a 50 m radius of MBES 2011 – F-MMB.

Finally, by further reducing the radius to 20 m, the small-scale structures are more highlighted (Figure 40): it can be seen how there are undulations in the bottom in a direction approximately E-W on the outer deep bar and on the deep terrace on which the finger bars are located, while other N-S directed undulations are located on the F-MMB. Finally, some areas such as the depressed area between the outer deep bar and the finger bars, and the area beyond the outer deep bar present an irregular pattern, characterized by greater noise in the relief.

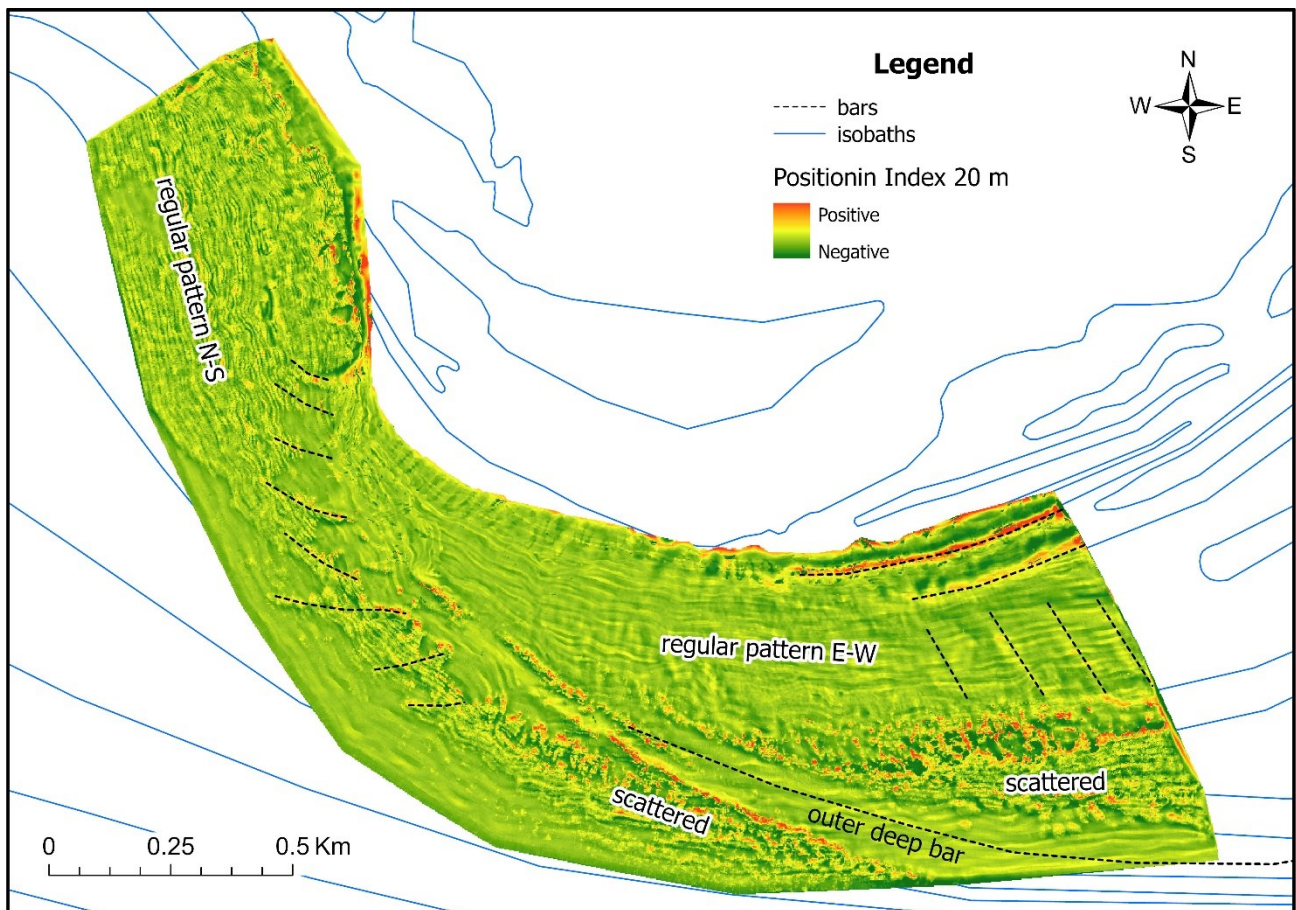


Figure 40 Positioning Index with a 20 m radius of MBES 2011 – F-MMB.

In the areas of the deep terrace and the F-MMB, bathymetric profiles were extracted to obtain information on the characteristics of the finger bars that were identified (Figure 37a). The finger bars of the deep terrace are slightly asymmetric, with the western flank being slightly steeper, spaced about 100-150 m apart, and have a height of about 20-25 cm (Figure 37b). The finger bars of the F-MMB have a more complex symmetry, partly influenced by the fact that they develop along a steeper ramp, which extends from a depth of -3.4 m in the north to -5.6 m in the south over approximately 870 m of the profile's length (Figure 37c).

5.1.1.2 Short-term geomorphological changes

The HIB, even if it has maintained its whole shape, has undergone a clear evolution in the last 4 years (Figure 41). Three significant trends can be highlighted:

- 1) The north-west tip of the emerged bank continues to migrate towards the north-west, bringing gradually due to the blockage of a small channel that connects the backbarrier area with the sea, following the natural littoral drift pathway that from the edge of the MMB tends towards the beaches of Grado.
- 2) The HIB as a whole has undergone a rollover phenomenon towards the north-east for the last four years: in this rollover process, the tendency towards the emergence of this HIB continues the recent

evidence of the period 2007-2019. The analysis through DSAS (Figure 42) quantifies the rollover and highlights its spatial variability. Considering the Net Shoreline Movement of the whole 129 transects spaced by 10 m, each one retreated and the average movement is about -43 m. The central part of the HIB underwent the maximum retreat, with values from -43 m to -72 m, mainly focalized not in the center but at 1/3 and 2/3 of the total length of the HIB (Figure 42). On the other hand, at the extremes of the HIB the net retreat gradually reduces up to -11 m at the southern tip and -18 m at the northern one. Given the 4-year time interval between the two UAV surveys, the annual rate of retreat (EPR) varies from -2.8 m/y up to -17.9 m/y, with an average of -10.8 m/y.

- 3) Last, a further bar has been formed on the external margin of the bank, which also led to the increase in its extension seawards.

Overall, in last 4 years, the HIB has become longer and wider both on and offshore.

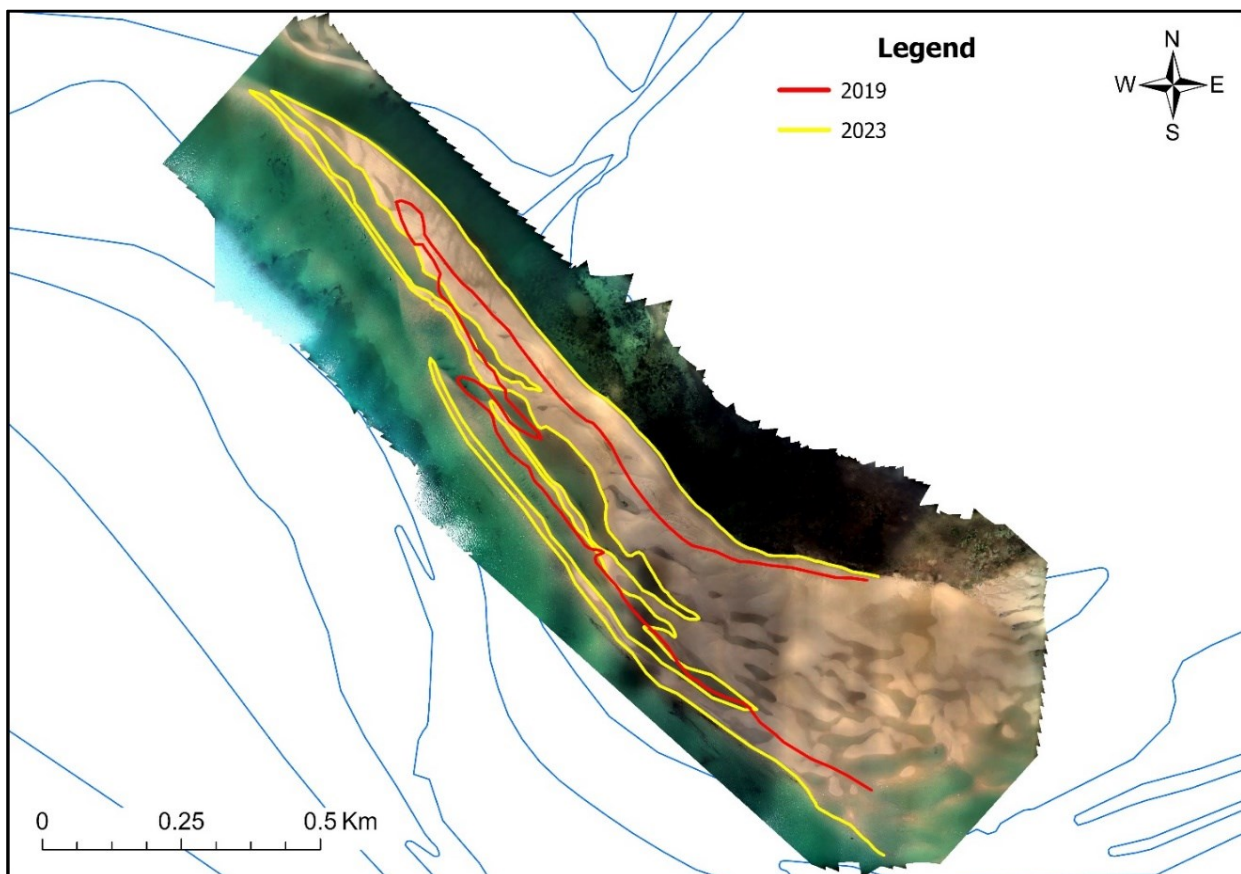


Figure 41 Evolution of the High Intertidal Bank between 2019 and 2023. The tip of the sand bank progressively lengthens north-westwards and the whole bank tends to migrate landwards.

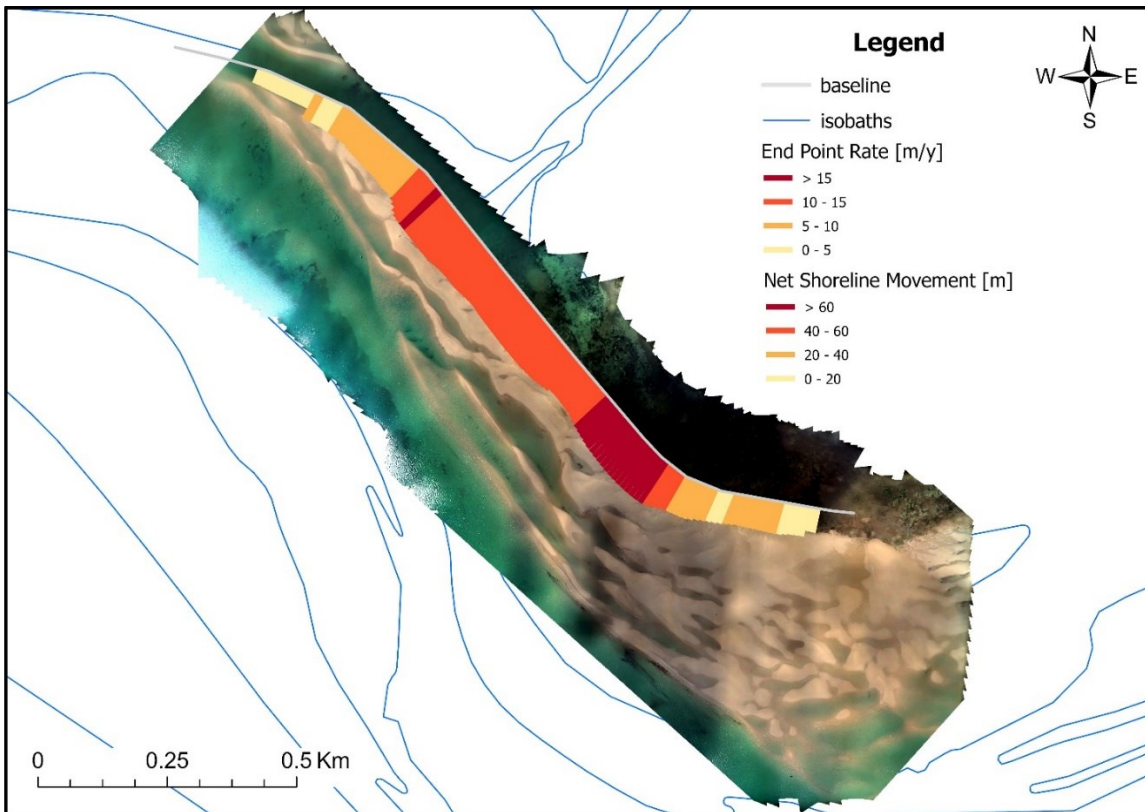


Figure 42 Net Shoreline Movement of the onshore border of the HIB from 2019 to 2023 calculated with DSAS algorithm.

A total of thirteen profiles have been extracted from the DTM of 2011, 2019 and 2023 of the F-MMB (Figure 36). The profiles extracted from transect 1F (Figure 43) show continuous growth over the years, although with some differences. In the period 2011-2019 the deposition is rather constant along the entire profile while in the period 2019-2023 it is concentrated more in the shallower part, within -3.5 m. Furthermore, sedimentation rates show a reduction of about half, going from +88 mm/y in 2011-2019 to +45 mm/y in 2019-2023.

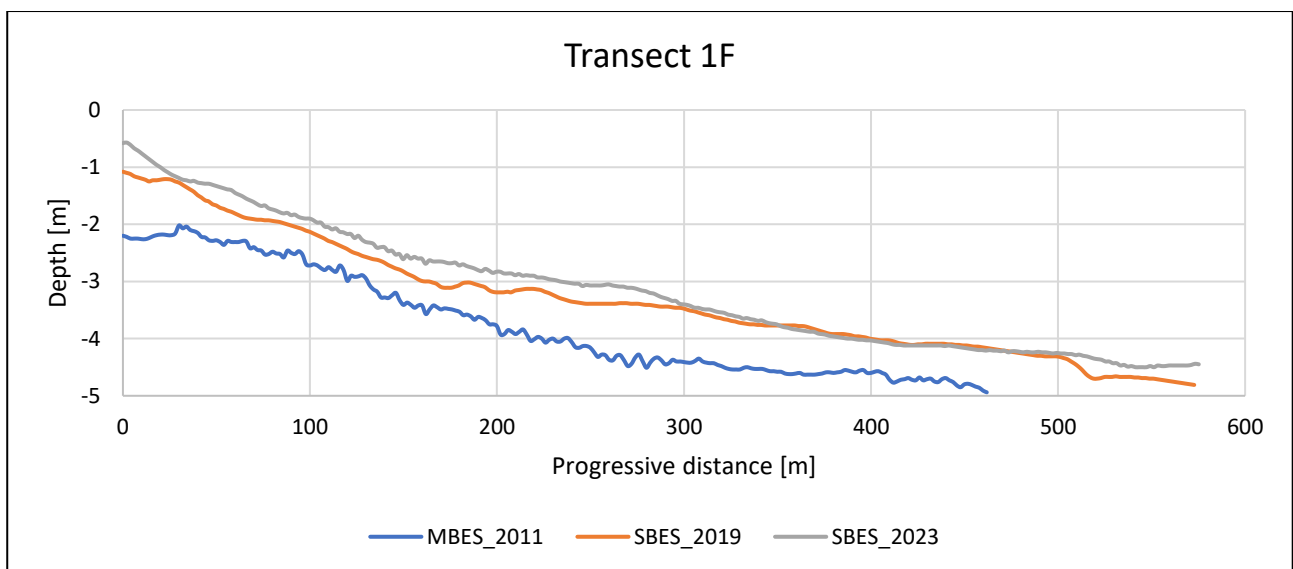


Figure 43 Profile extracted from transect 1F.

Transect 2F (Figure 44) is rather similar to 1F, both from a quantitative and qualitative point of view, although in the period 2019-2023 the growth goes up to approximately -4 m. In 2023 a new submerged bar formed at 52 m.

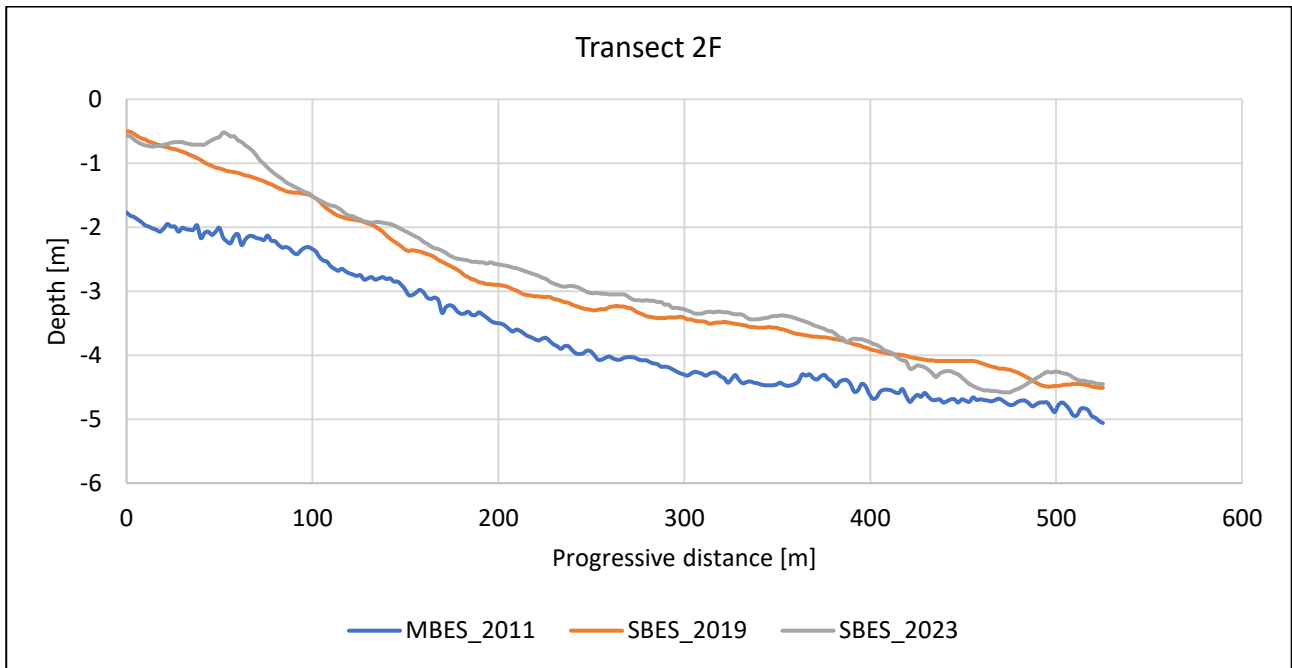


Figure 44 Profile extracted from transect 2F.

Transect 3F (Figure 45) is rather similar to 2F and the main changes from 2019 to 2023 are concentrated in the first 40 m of the profile, where a new bar has formed.

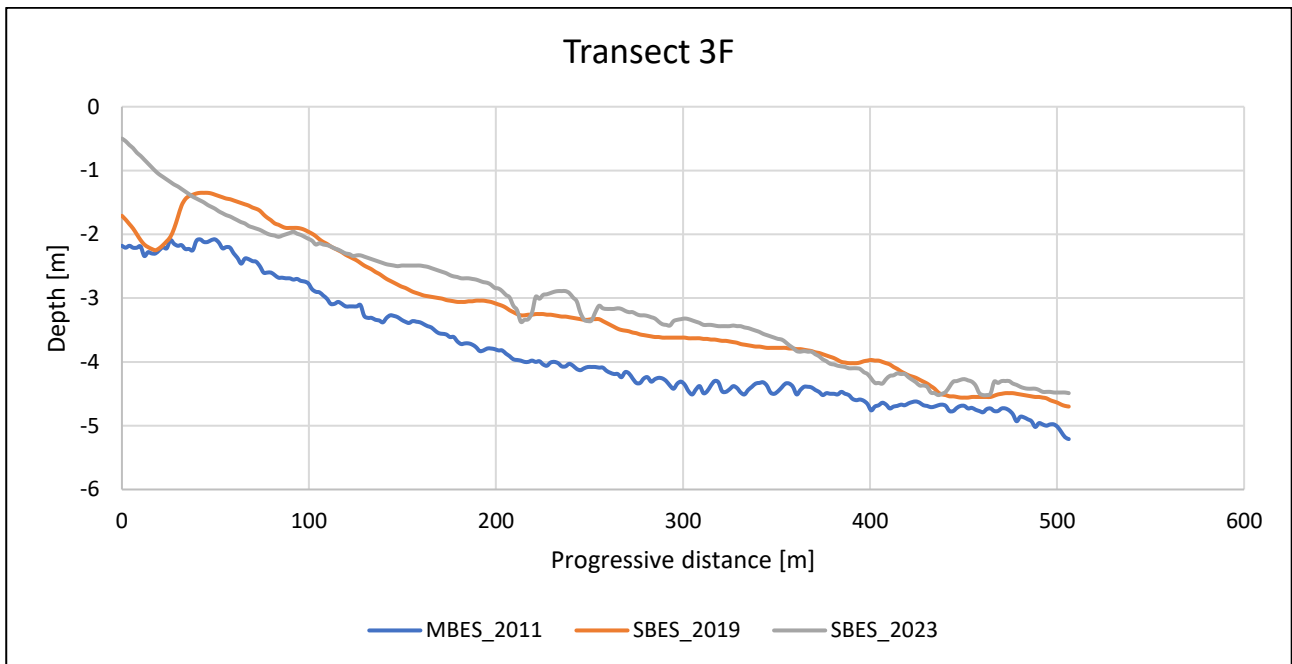


Figure 45 Profile extracted from transect 3F.

The profiles of transect 4F (Figure 46), from 2011 to 2019, show a widespread and rather constant filling up to -4.5 m depth, with the only trend anomaly at the beginning of the profile (at 46 m), while in 2011 the profile begins with what was the HIB still submerged in the emerging phase.

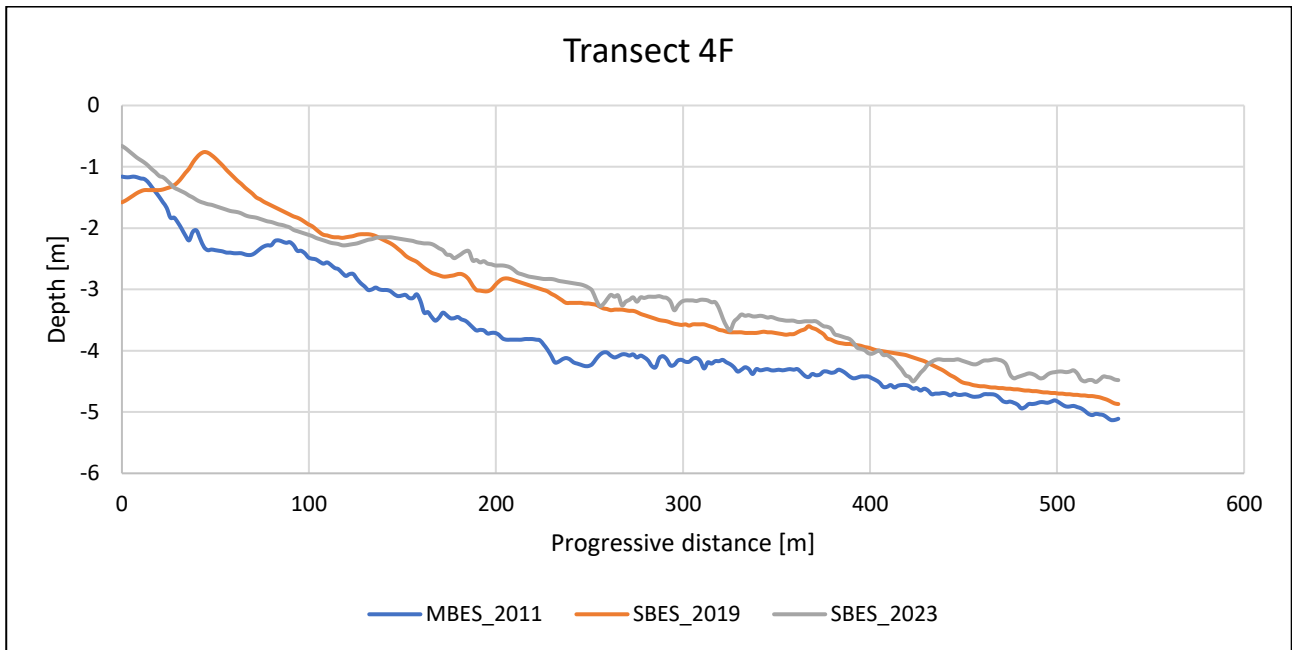


Figure 46 Profile extracted from transect 4F.

In the period 2019-2023 there was a widespread filling from the progressive 130 m but reduced compared to the previous interval, while the shallower part is characterized by a clear retreat of the bar of approximately -50 m which, topographically expresses itself as a migration towards north-east. On traces 5F, 6F and 7F (Figure 47, Figure 48 and Figure 49) the trend is similar to that of trace 4F.

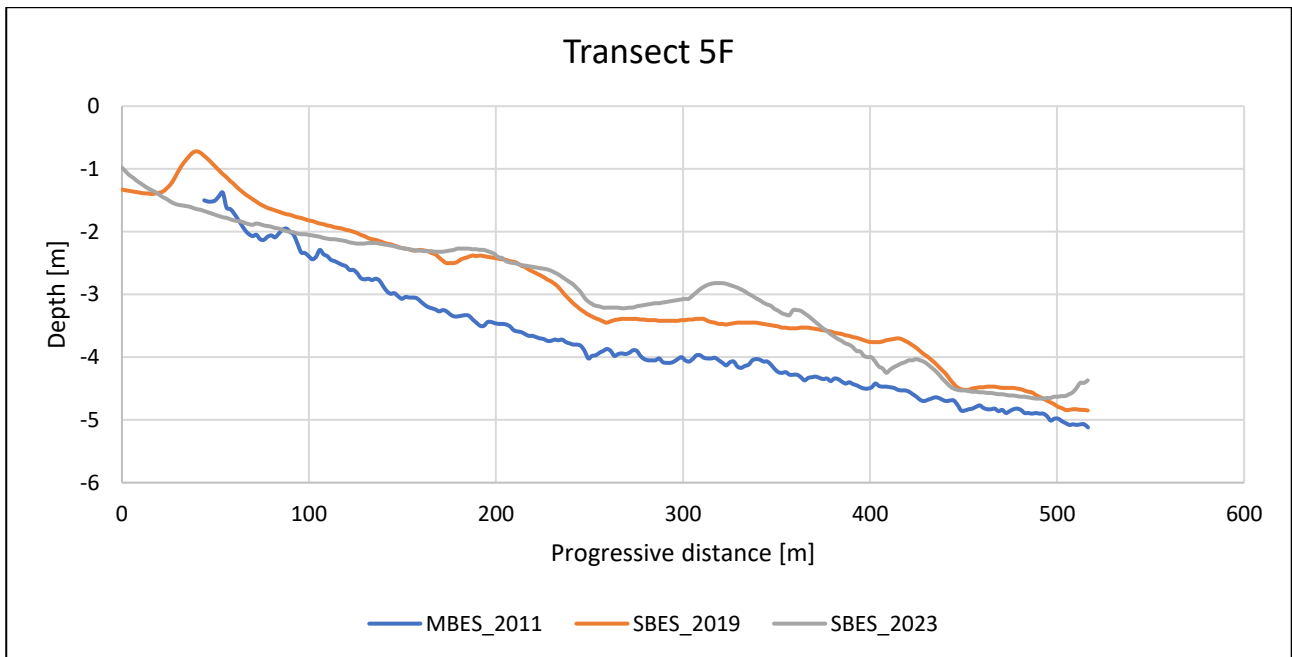


Figure 47 Profile extracted from transect 5F.

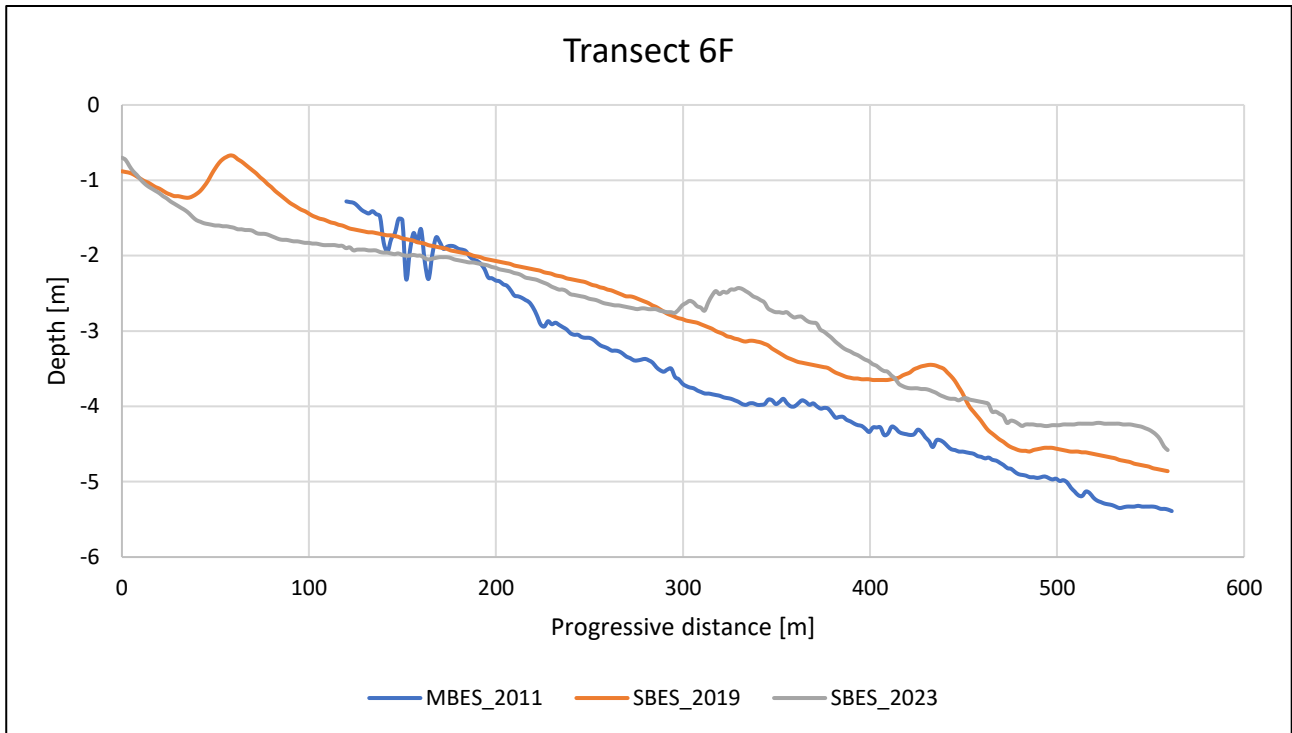


Figure 48 Profile extracted from transect 6F.

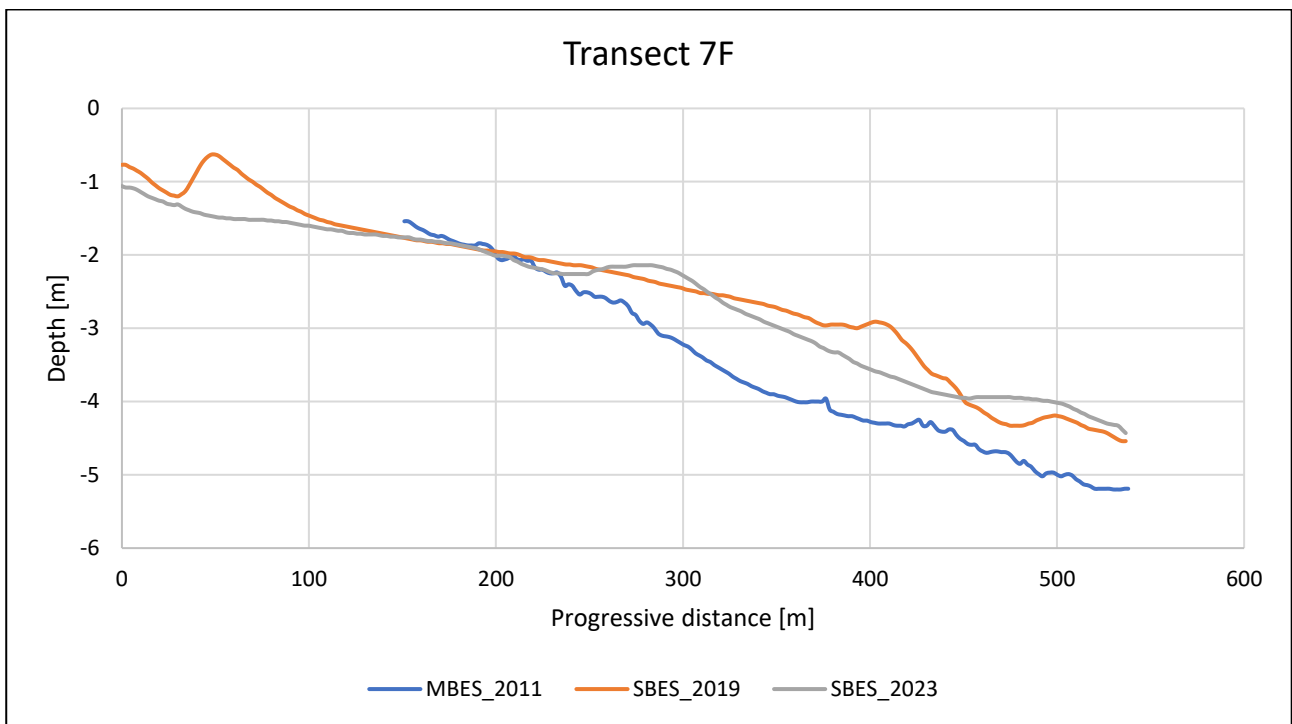


Figure 49 Profile extracted from transect 7F.

On transect 8F (Figure 50) the 2011-2019 interval is characterized by stability up to -2.5 m, beyond which a rather marked growth is highlighted until the end of the profile. From 2019 to 2023 the greatest evidence is the retreat of the bar present in 2019 at the beginning of the profile and of which in 2023 only the seaward side is visible while the remaining profile remains stable.

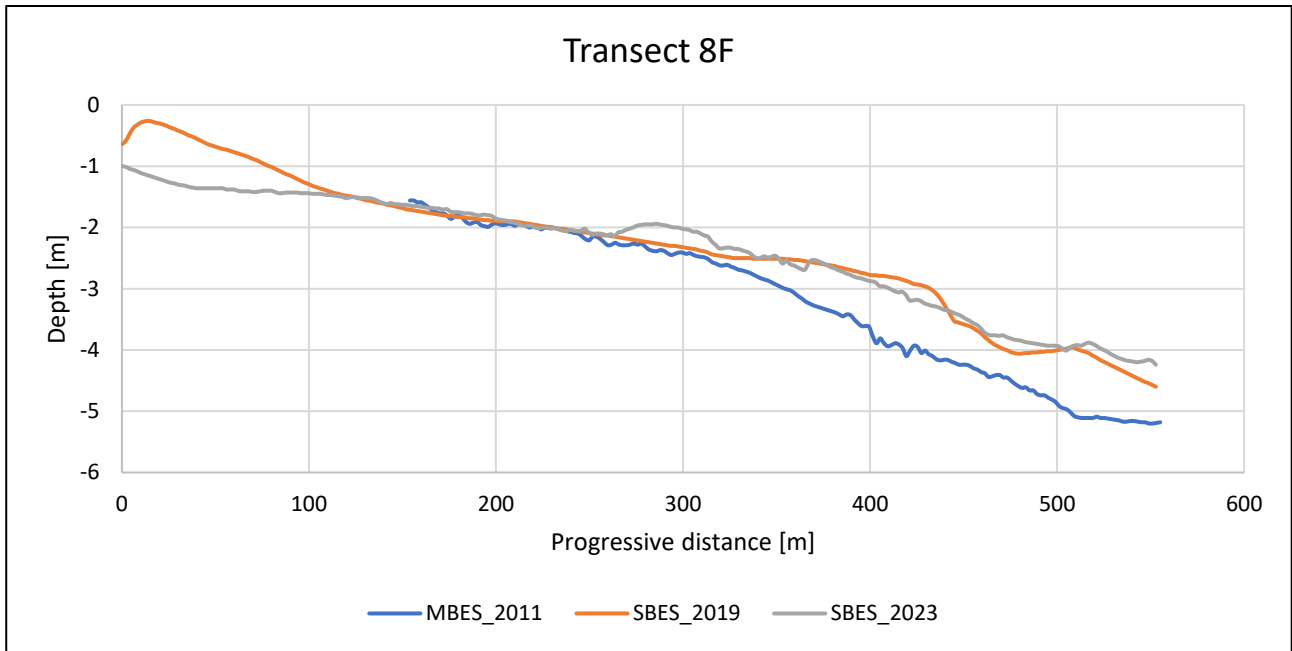


Figure 50 Profile extracted from transect 8F.

On transect 9F (Figure 51) the trend is similar to that of 8F with the only substantial difference between 2019 and 2023 in which, above -2.5 m there seems to be a slight erosion of the profile.

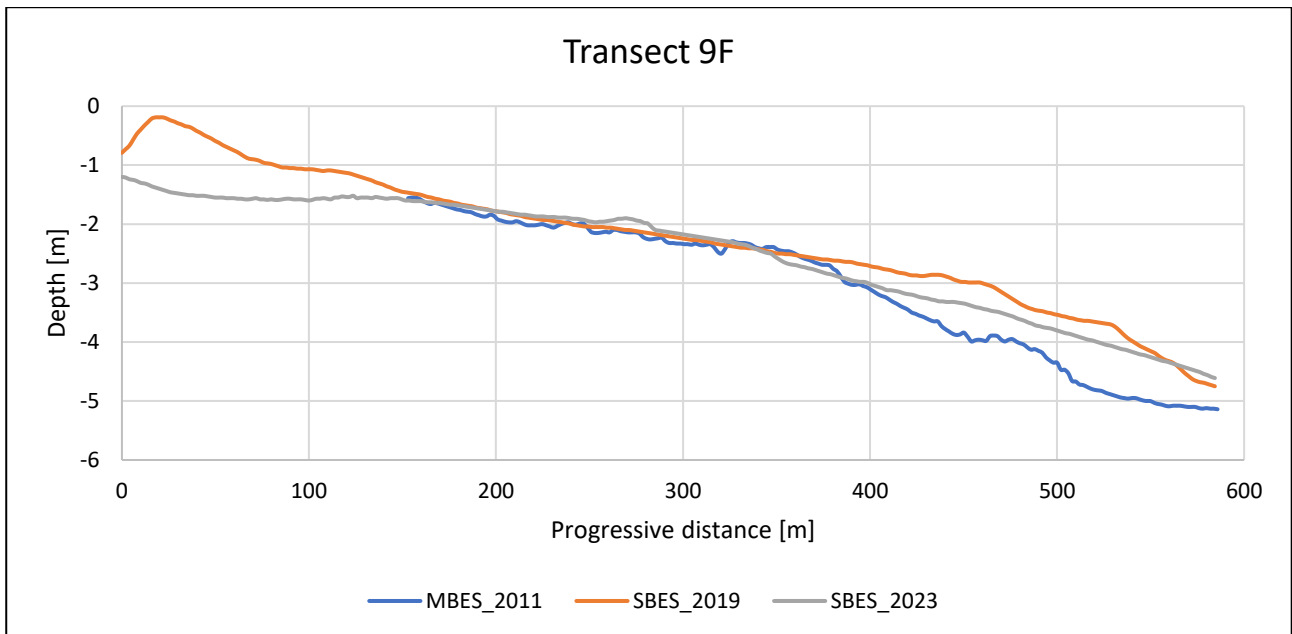


Figure 51 Profile extracted from transect 9F.

On transect 10F (Figure 52) the trend is similar to that of the two previous ones although with some differences. In the period 2011-2019, although the greatest growth was concentrated above -2.5 m, there was sediment deposition even at lower depths. From 2019 to 2023, the retreat of the shallow structures along the transect is evident, within the progressive distance of 200 m.

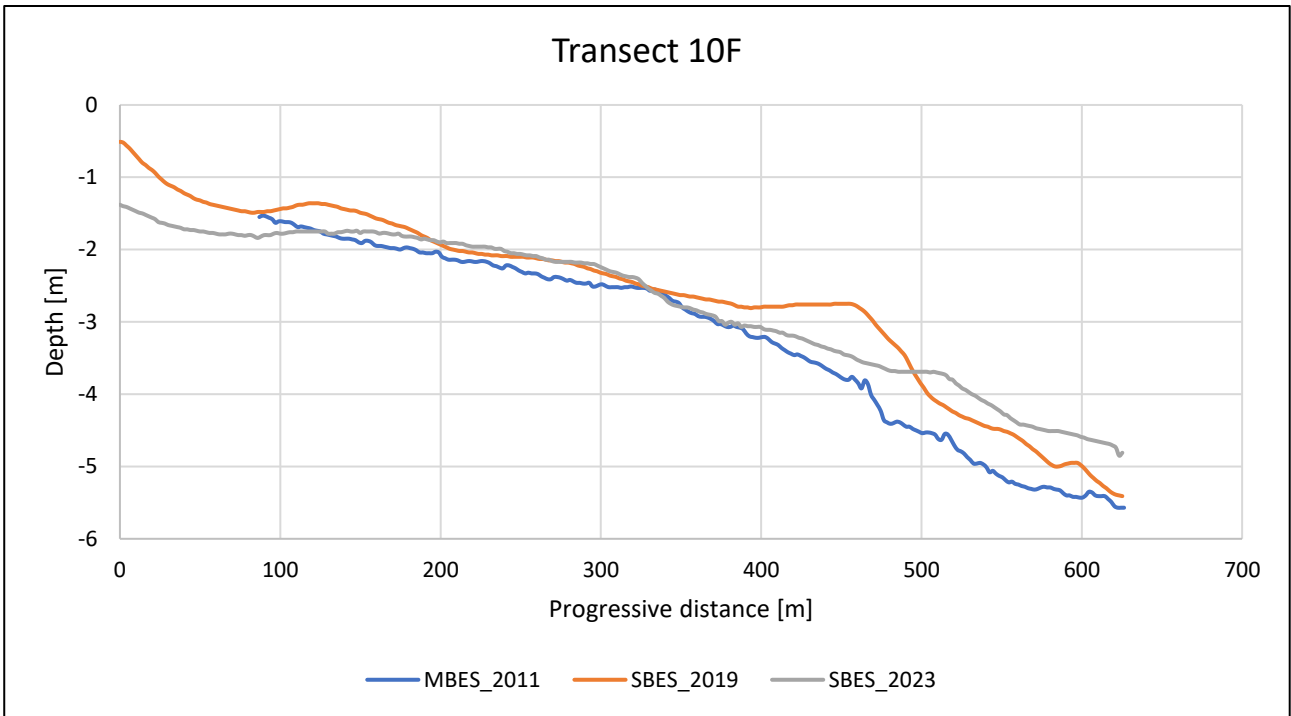


Figure 52 Profile extracted from transect 10F.

Compared to transect 10F, the 11F and 12F (Figure 53 and Figure 54) show the same trend within -3 m while there is a progressive reduction in sedimentation rates in the deepest part of the profile, where, in the 12F, an erosive trend is identifiable in the two periods 2011-2019-2023.

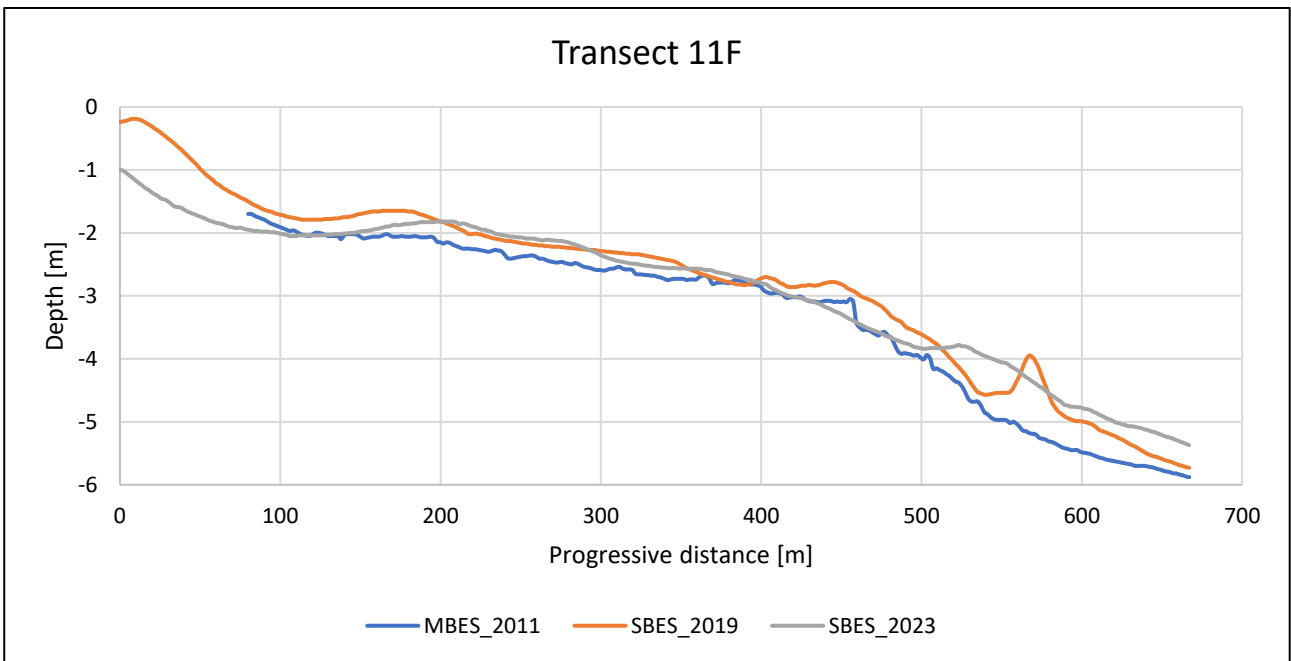


Figure 53 Profile extracted from transect 11F.

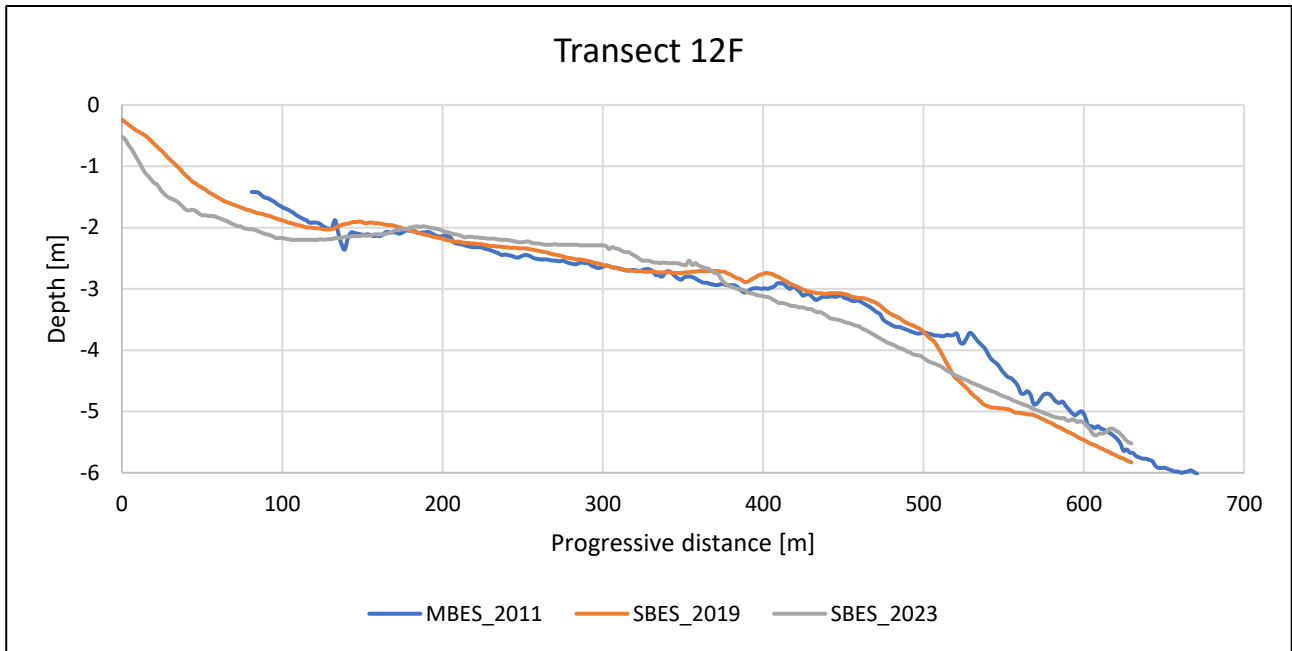


Figure 54 Profile extracted from transect 12F.

The profiles on transect 13F (Figure 55) are quite stable. Between 2011 and 2019 there was evidence of sedimentary accumulation within -3.5 m of depth and a seaward advancement of the edge of the MMB. In the period 2019-2023, however, within -3.5 m the two profiles are substantially stable while there appears to have been erosion beyond this depth up to -5 m. However, the 2023 profile is very similar to that of 2023 above -3.5 m and therefore it cannot be excluded that the accumulation identified in 2019 is the effect of the presence of seagrasses.

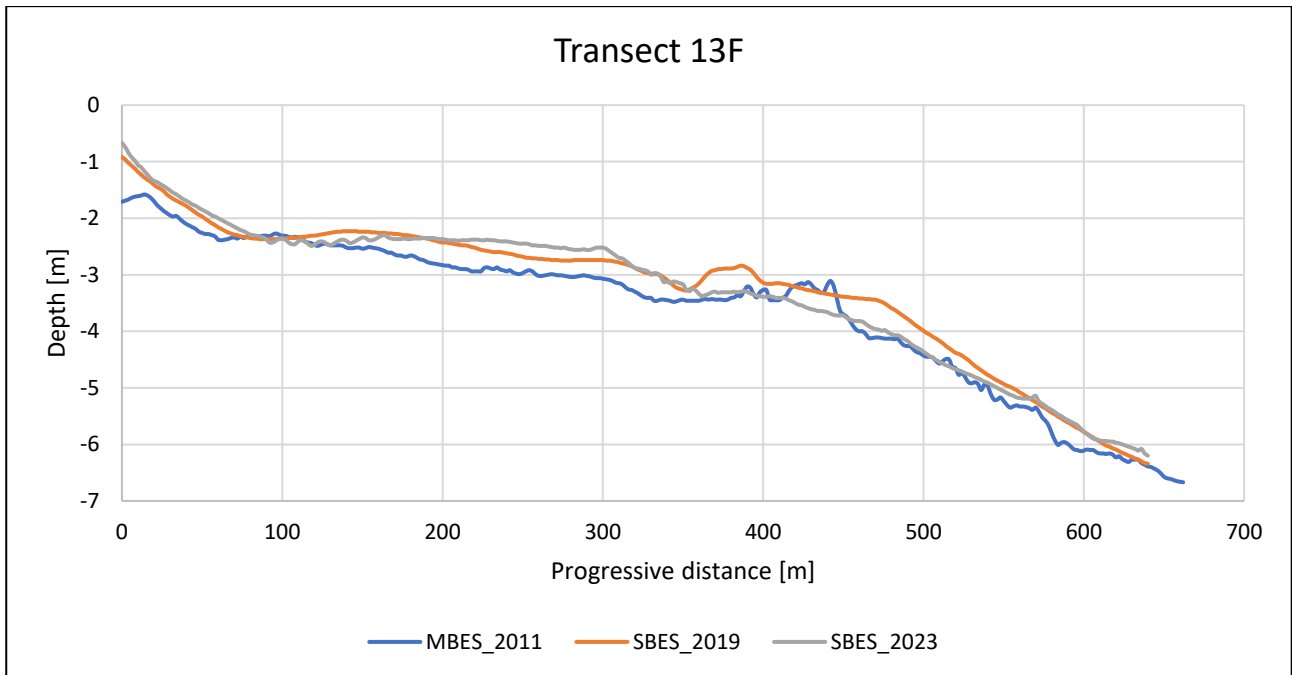


Figure 55 Profile extracted from transect 13F.

5.1.1.3 Sediment budget

As regards of the evolutionary analysis of the F-MMB, 13 transects relating to 2011 (extracted from an MBES survey), 2019 and 2023 were detected (Figure 56, Figure 43-Figure 55). Budgets, accreted/eroded thicknesses, and sedimentation rates were calculated on the parts of the profiles in common, although the profiles of some years may be longer (Table 6).

Transect	Linear Budget [m ³ /m] 2011-2019	Linear Budget [m ³ /m] 2019-2023	Sedimentation rate [mm/y] 2011-2019	Sedimentation rate [mm/y] 2019-2023
1F	+326	+83	+88	+45
2F	+394	+64	+93	+30
3F	+308	+85	+75	+42
4F	+317	+68	+74	+32
5F	+300	-3	+79	-1
6F	+230	+4	+65	+2
7F	+244	-66	+79	-30
8F	+180	-37	+56	-17
9F	+165	-152	+47	-65
10F	+218	-76	+50	-30
11F	+181	-84	+38	-31
12F	-29	-68	-7	-29
13F	+184	-39	+36	-15
Mean	+232	-17	+60	-5

Table 6 Budgets and sedimentation rates of the F-MMB

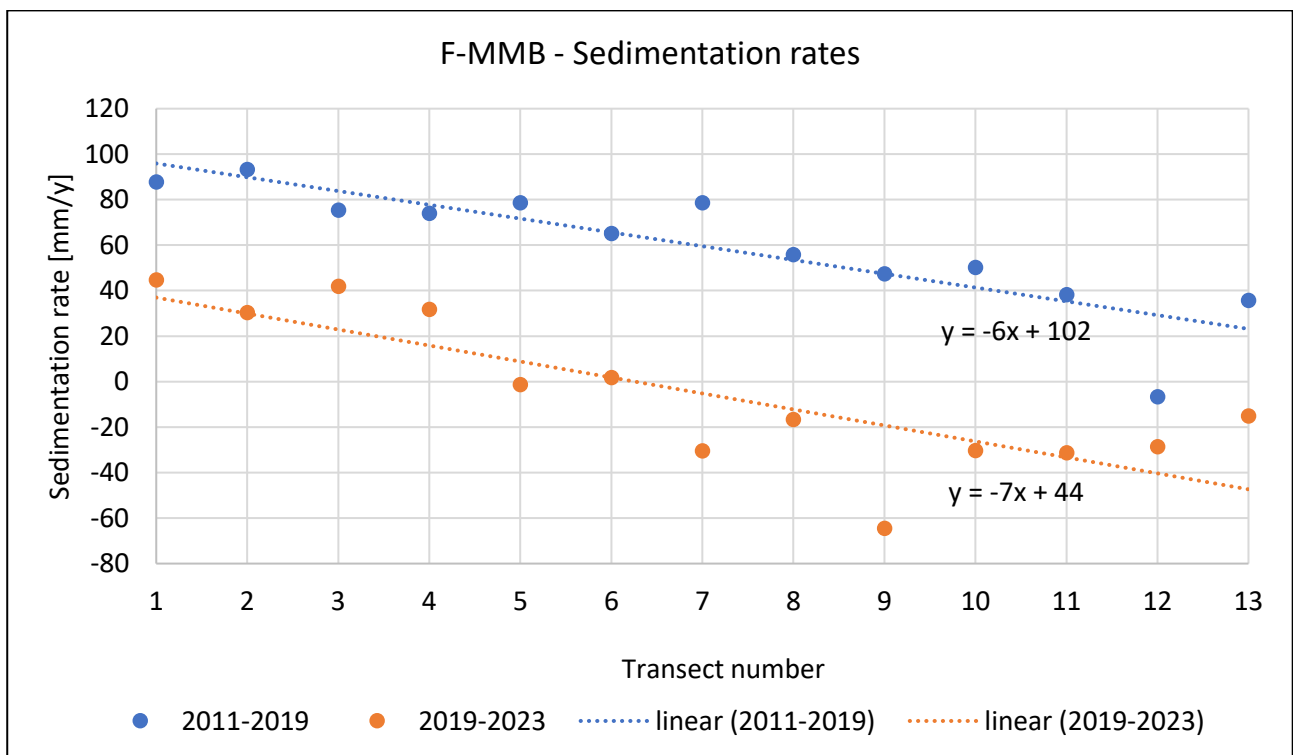


Figure 56 Sedimentation rate in the transects of the F-MMB. The blue dots represent the rate between 2011 and 2019 while the orange the one between 2019 and 2023.

Comparing the sedimentation rates of the F-MMB in the two periods investigated (Figure 56), both series show a progressive reduction from transect 1F to 13F, quantifiable as -6 mm/y per transect in the period

2011-2019 and -7 mm/y in 2019-2023. Furthermore, sedimentation rates decreased consistently for all transects investigated in the period 2019-2023 (mean of -5 mm/y) compared to 2011-2019 (mean of +60 mm/y), with an average reduction of approximately -65 mm/y. In particular, in the period 2019-2023 the F-MMB showed globally a slightly negative budget, with a volumetric accretion localized on the first four transects and an erosive trend in the transects 7-12, while the 2011-2019 a positive sediment budget was recorded and almost every single transect but 12F (-7 mm/y) has accreted.

5.1.2 Isonzo river delta

5.1.2.1 Geomorphological set-up

A DTM of the Isonzo River delta was produced from the 2022 SBES dataset (Figure 57) in order to evaluate the evolution of the area between 2019 and 2022 both from sediment budget and geomorphological point of view.

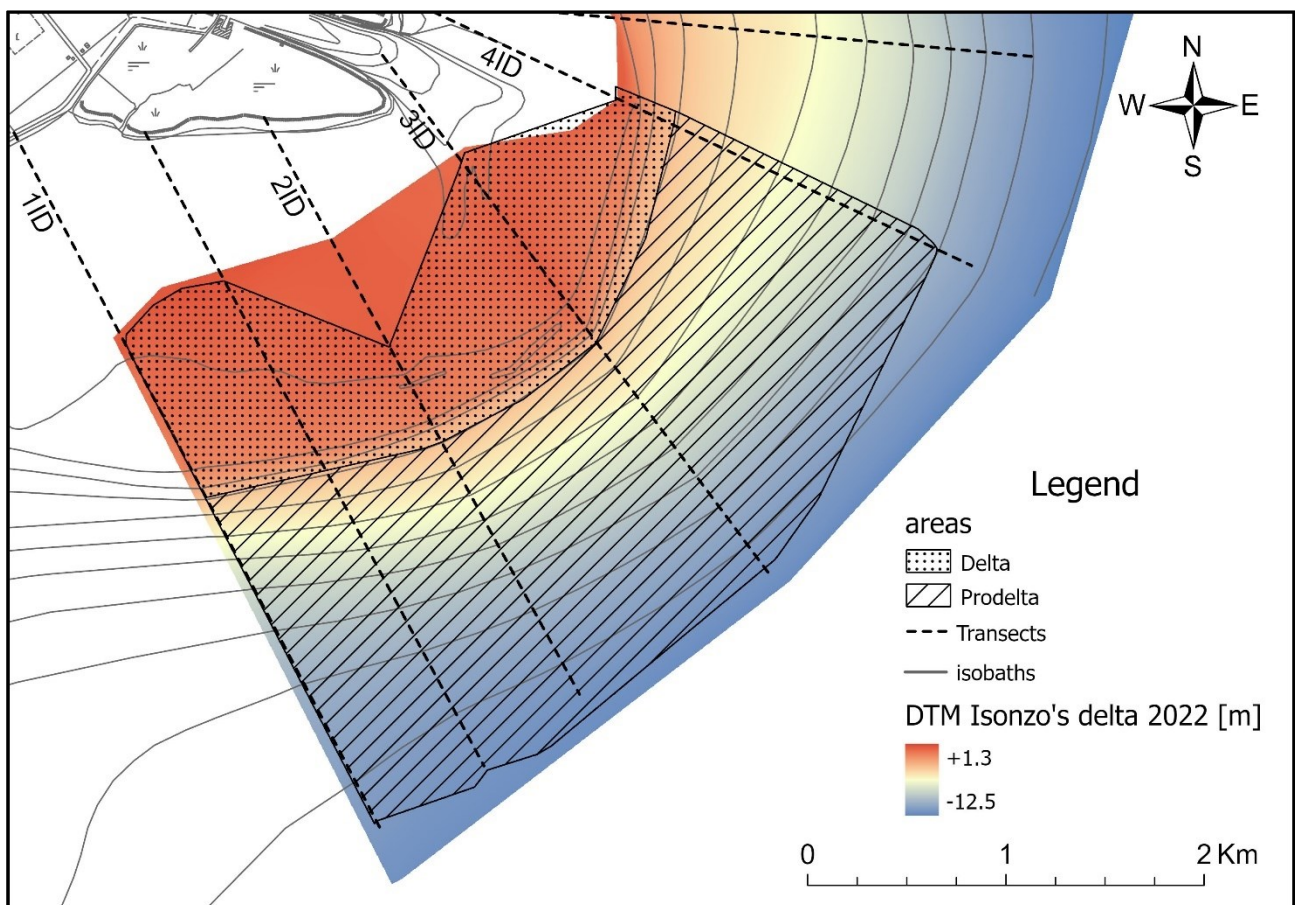


Figure 57 DTM of the Isonzo's delta in 2022 and extracted from profiles 1ID, 2ID, 3ID and 4ID.

5.1.2.2 Short-term geomorphological changes

Four bathymetric profiles (Figure 58-Figure 61) were extracted from the 2019 and 2022 DTMs along the survey transects (Figure 57). In the prodeltaic area no substantial morphological differences can be seen

between 2019 and 2022, while some variations occurred in the shallower part (within -4 m). The profiles will be analyzed from the mouth towards the sea starting from the south-west profile (1ID).

The profiles on transect 1ID (Figure 58), in addition to highlighting some variations in the morphologies due to the dynamism of the deltaic environment, presents the greatest variations in the retreat of three bars during the three years (Figure 58b). The first bar (from the land), located in 2019 at 340 m from the beginning of the profile, in 2022 underwent a retreat of -36 m and an increase in altitude of +25 cm. The second, less prominent and flatter, has moved back by -36 m and the third, just before the break in the slope of the delta structure, retreated by -10 m: these two bars maintained their depth almost unchanged.

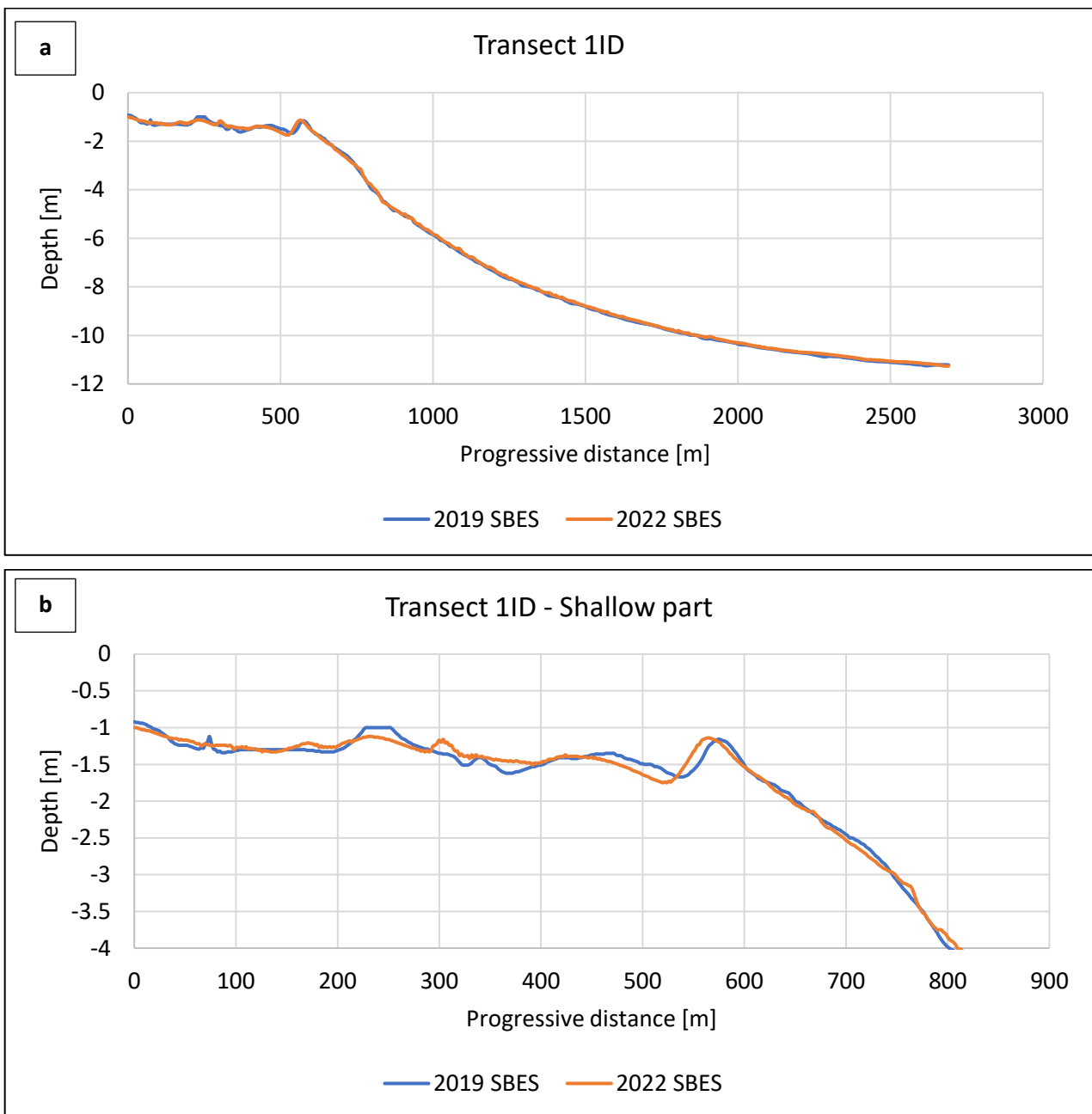


Figure 58 Profiles extracted from (a) the complete transect 1ID and (b) focus on the shallower part within -4 m.

In transect 2ID (Figure 59b) there are mainly two changes in the shallower part of the profiles. The first 150 m of the profiles show a loss of sub-surface landforms in 2019-2022. From 150 m to 400 m in both 2019 and 2022 there is an alternation of five bars and troughs before the slope break. Although these bars were less prominent in 2022, the morphology remains substantially stable but with an average retreat of -25 m.

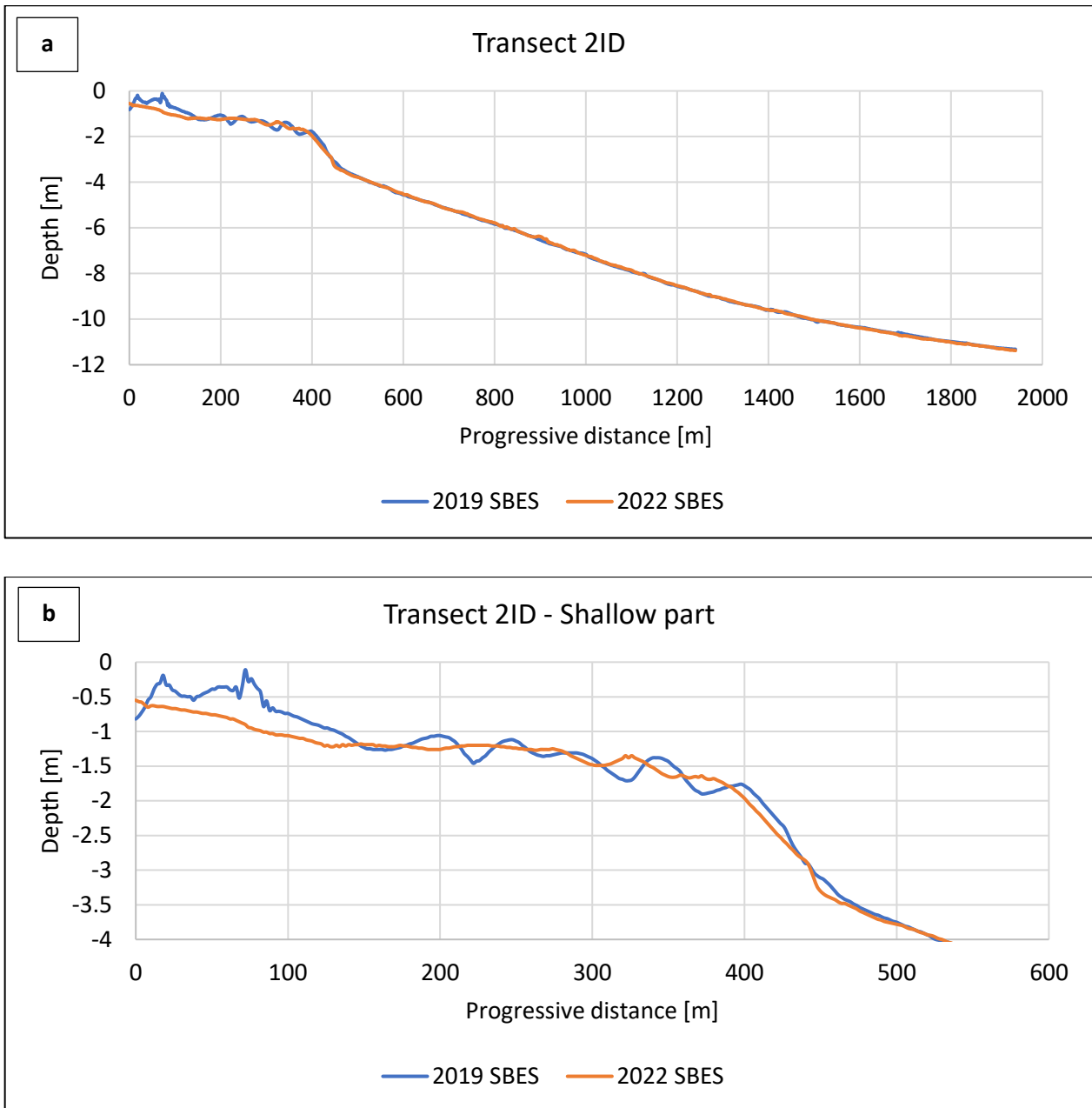


Figure 59 Profiles extracted from (a) the complete transect 2ID and (b) focus on the shallower part within -4 m.

Transect 3ID (Figure 60), unlike the previous ones, does not show retreat of the landforms. There are two most evident changes between the two years: the first concerns the first 180 m in which in 2019 there was an alternation of bars and troughs which in 2022 were obliterated; the second is a widespread erosion in 2022 between 230 m and 900 m on average -87 mm.

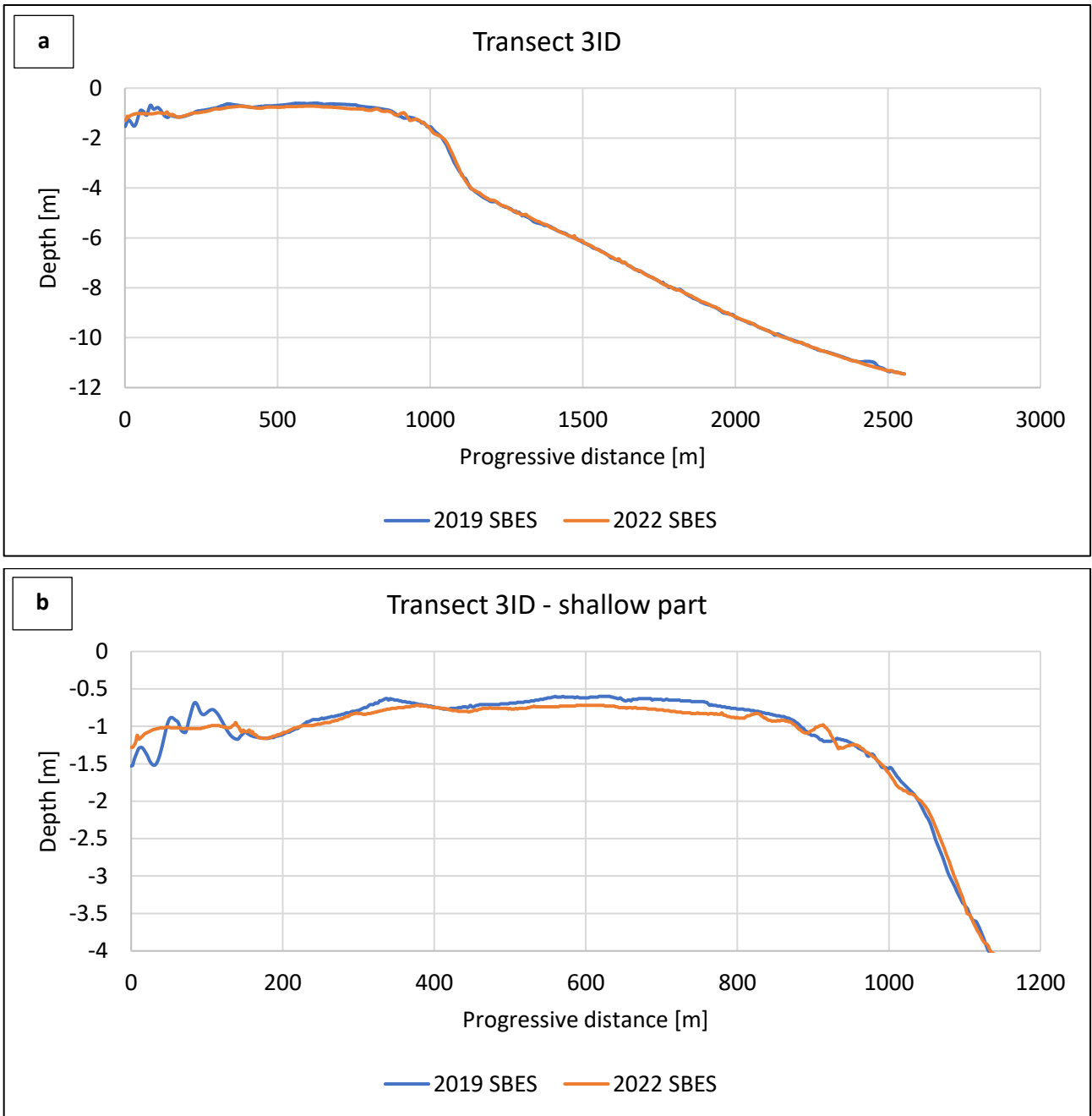


Figure 60 Profiles extracted from (a) the complete transect 3ID and (b) focus on the shallower part within -4 m.

Finally, transect 4ID highlights minor changes over the three-year period. The shape of the profiles is rather regular and there are no obvious structures apart from the change in concavity at the depth of -1.2 m, more marked in 2022, as a result of a slight accumulation between -0.6 m and -1.2 m depth and a more marked erosion between -1.2 m and -2.5 m depth. The rest of the profiles remain rather stable down to -10 m.

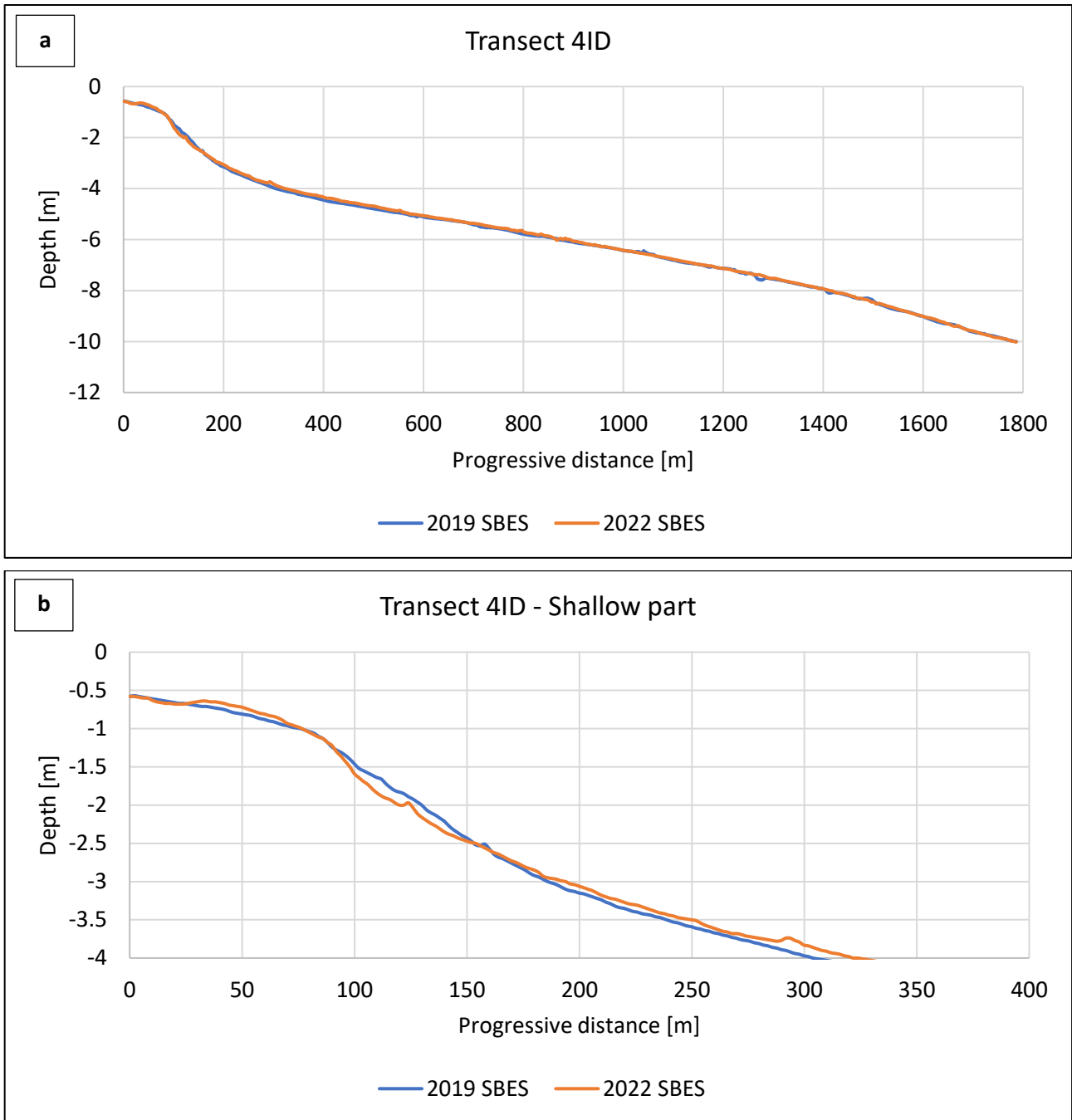


Figure 61 Profiles extracted from (a) the complete transect 4ID and (b) focus on the shallower part within -4 m.

5.1.2.3 Sediment budget

The profiles extracted by four transects in the Isonzo Delta are overall slightly positive from the point of view of the sediment budgets between 2019 and 2022 (Table 7) with an average accretion of +7 mm, even if most of the differences falls within the order of magnitude of the instrumental error of the acquisition. Furthermore, sedimentation rates of +11 mm/y for the external profiles (1ID and 4ID) and -6/-7 mm/y for the internal ones (2ID and 3ID) indicate the lack of a spatial gradient. Considering the area of $8.32 \times 10^6 \text{ m}^2$ between the four transect, the total accretion of the Isonzo River delta in three years can be quantified in around $+55'800 \text{ m}^3$ and the budget per year in $+18'600 \text{ m}^3/\text{y}$, approximately a third of the value registered

between 2007 and 2019. Taking into account depths greater than -4 m, i.e. the prodeltaic area, the sediment budget is quite different (Table 8). Here, each transect shows positive budget, even if the external ones (1ID and 4ID) are more accreting. Considering the prodeltaic area of 5.75×10^6 square meters, the total accretion can be quantified in around $+12'700 \text{ m}^3$ and the volume per year in $+42'400 \text{ m}^3/\text{y}$, value almost comparable with the accretion registered from 2007 to 2019.

Profile	Linear budget [m^3/m]	Accretion/erosion [mm]	Sedimentation rate [mm/y]
1ID	+85	+32	+11
2ID	-41	-21	-7
3ID	-42	-17	-6
4ID	+59	+33	+11
Mean	+15	+7	+2
Total	Area [m^2]	Volume [m^3]	Volume per year [m^3/y]
Value	8.32×10^6	+55800	+18600

Table 7 Budgets and sedimentation rates of the Isonzo delta.

Profile	Linear budget [m^3/m]	Accretion/erosion [mm]	Sedimentation rate [mm/y]
1ID	+85	+45	+15
2ID	+8	+6	+2
3ID	+3	+2	+1
4ID	+53	+36	+12
Mean	+37	+22	+7
Total	Area [m^2]	Volume [m^3]	Volume per year [m^3/y]
Value	5.75×10^6	+127000	+42400

Table 8 Budgets and sedimentation rates of the Isonzo prodelta from -4 m depth.

5.2 Sedimentology

5.2.1 Dataset analysis

The dataset, as often happens for the sampling campaigns, results irregular and sparse. The criterion followed in the survey to locate samples along pre-existing profiles at defined depth generated two irregularities: on the one hand, the mesh is denser in the direction normal to the beach than longitudinally while, on the other hand, along a single profile the samples are closer where the profile is steeper. The result is a greater sampling density on the western side of the study area than in the eastern one, which may lead to interpolation criticalities.

The mean size of the 138 samples analyzed ranges from 1.52ϕ to 7.37ϕ . From the distribution of Mz with respect to depth results that it doesn't seem to follow a normal gradient of seaward-fining or, at least, some other non-standard trends are present (Figure 62a).

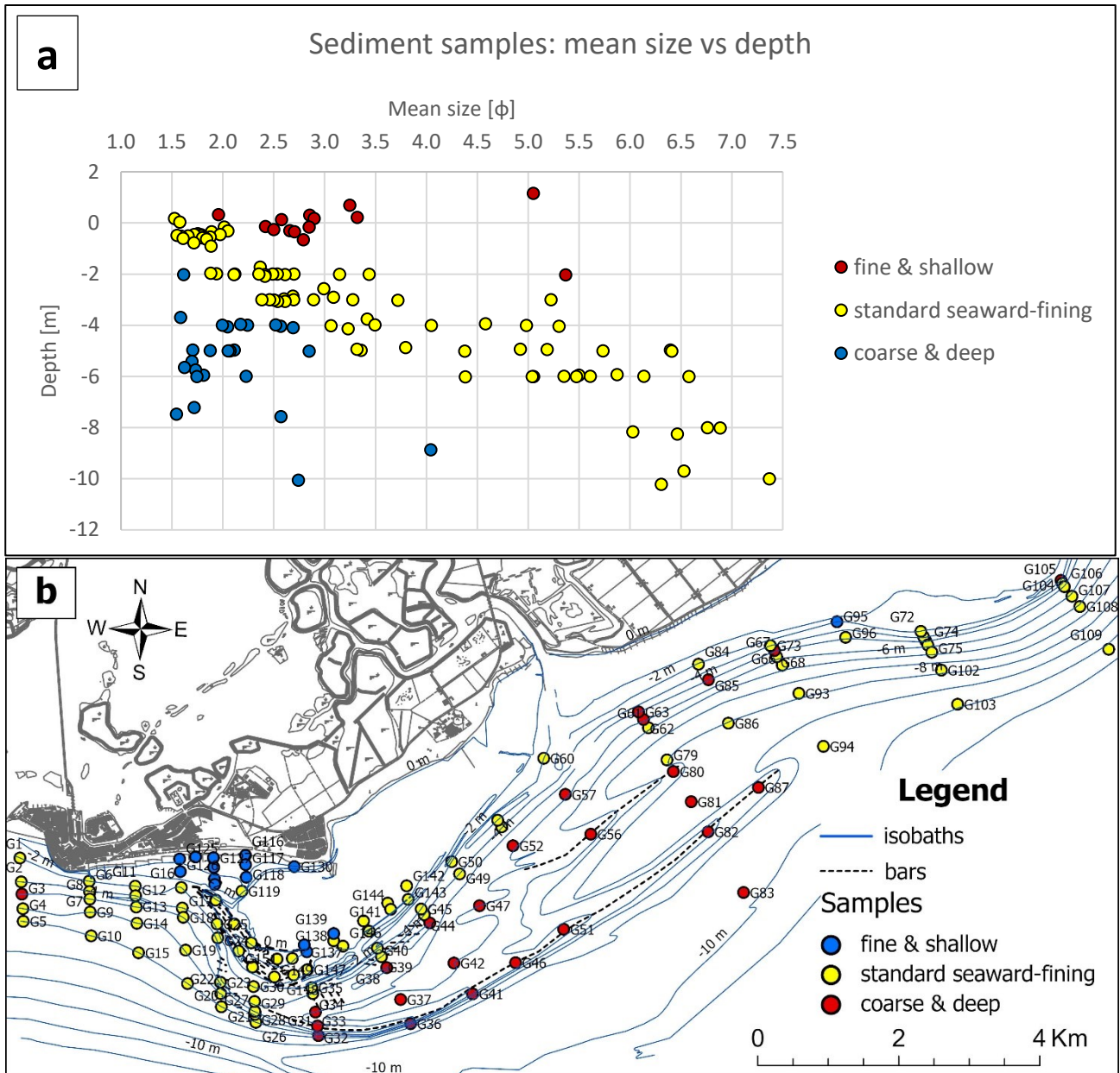


Figure 62 (a) Diagram of mean size versus depth for the dataset and distribution the two sample anomalous groups: (b) coarse samples at various depth and (c) shallow samples with different MZ values.

By analyzing the samples as a whole, it is possible to identify at least three main groups of samples: (1) samples following the seaward-fining gradient, (2) coarse samples at various depths and (3) shallow samples with different values of M_z . Groups (2) and (3) represent sedimentological anomalies with respect to the seaward-fining trend. The group (2) mainly includes samples from the D-MMB, representing an anomaly from both geomorphological and sedimentological point of view. This group can be further separated into two subgroups. The first is made up of the coarsest samples with M_z values between 1.54 ϕ and 1.81 ϕ (samples G32, G36, G41, G46, G51, G82 and G87): these samples are all present on the outer deep bar. The second subgroup is instead formed by the samples present on the deep terrace of the D-MMB where slightly finer samples are also present, with M_z around 2 ϕ . The group (3) consists in the samples at the border of the MMB, where both fine sediments from the backbarrier and coarse sediments from the littoral drift pathway

are present. Focusing attention on the group of samples located in front of the beach “al Bosco”, these represent a widespread anomaly. In this area, in fact, there are both decidedly coarser samples (samples G113 and G118) and much finer samples (e.g., samples G114, G124 and G129) apparently arranged in a sparse manner. This can be explained by analyzing the sampling methods used in that area: here, in fact, during the survey campaign, both clearly sandy samples were deliberately collected, mainly located on the higher areas, and finer samples found in the areas depressed. The choice to carry out this type of sampling was derived from the desire to represent the evident granulometric alternation in a border area between the large rear barrier area and the western limit of the MMB. By deeply analysing some samples/groups it is possible to identify further peculiar characteristics. If we consider the two series of samples from G131 to G142 (excluding G137 and G139) and from G143 to G151 we can notice a very similar trend. These samples are located on the HIB, and, for both series, a double gradient is visible: a westward coarsening gradient is present up to the central area of the HIB, where this curves sharply; subsequently, towards the north-west an opposite gradient, with the samples gradually becoming finer. In both series, the external elements have Mz values around $1.8 \phi - 2 \phi$. If instead we consider the sorting, in both series the samples gradually become more classified towards the west, following the direction of the littoral drift. Considering the MMB and the D-MMB we can see how the finest samples are located in two specific areas: a first group, made up of the samples G137 and G139, is located on the border with the back barrier area; a second group, however, is also located in a border area but in this case it is located on the area of the D-MMB terrace at the edge of the MMB, an area in which the slope of the seabed drastically decreases. On the D-MMB terrace, as you move offshore the samples become increasingly coarser. The Isonzo Delta area is characterized by a seaward fining gradient, with sandy samples located within -4 m. This gradient is disrupted in the presence of structures such as deep bars. In particular, samples G79 to G82, located on the same relief profile, are alternatively finer and coarser: samples G80 and G82 belong to the two deep bars while samples G79 and G81 are located on depressed areas. Furthermore, sample G81 is rather unique because it's bimodal: and the MZ (4.04ϕ) differs particularly from the two main modes and the median (2.71ϕ).

5.2.2 Distribution maps

The sedimentological maps were produced with two main objectives. A first aim, in which we focused on the production of mean size maps, was to find a method that could produce reliable maps both in conditions of standard sediment distribution (seaward fining gradient), and in the presence of anomalies or of irregular and sparse sampling distribution. Secondly, maps of other grain size parameters, such as sorting and normalized sorting, and a textural map with the (Flemming, 2000) classification were developed.

5.2.2.1 Mz distribution: geostatistical vs Semi-Automatic Interpolation Method

A set of sedimentological maps have been created through the use of four automatic geostatistical algorithms (Figure 63): in these maps, in addition to the distribution of the grain size parameter, in this case the Mz, the control samples and the difference between the value estimated by the model and the measured one are identified.

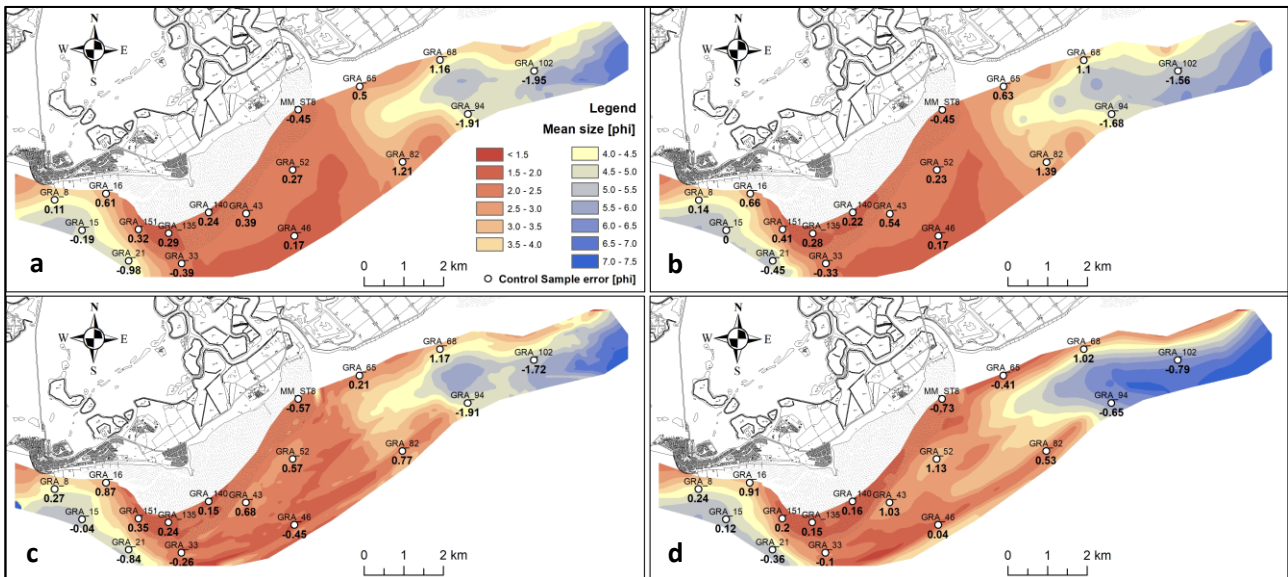


Figure 63 Mean size distribution model created using (a) ordinary kriging, (b) empirical bayesian kriging, (c) cokriging and (d) EBK regression prediction. Control samples and the error between model and sample's MZ are represented.

The first two maps are produced through geostatistical algorithms, ordinary kriging (a) and empirical bayesian kriging (b), that don't take into account explanatory variable. The use of sedimentary data only reduces by far the dataset dimension, leading to a low density of points to interpolate. The maps produced through OK and EBK are very similar: they are characterized by a smooth variation of the Mz, a more or less regular area with coarser sediments in the centre and two areas with finer sediments at the edges, to the south-west and north-east. The longshore transport pathway is not particularly evident, and the two CS located on its present discrepancies between 0.5 ϕ (sample G65) and 1.16 ϕ (sample G68), showing that the model tends to overestimate the Mz value. The Mz distribution doesn't follow the elongated structures such as the deep bars and the trough, and the fine sedimentation area of the prodelta seems to be too coarse: in fact, in the end of the outer deep bar and in the prodelta the greatest errors are present, with Mz discrepancies in phi of 1.39 (EBK) and 1.21 (OK) on the bar (sample G82) and up to -1.68 (EBK) and -1.95 (OK) on the prodelta (samples G94 and G102). The absolute errors of both maps in the western zone are lower than 0.5 ϕ with rare exceptions. Overall, the western part of the map seems to fit better with the CS and the expected model.

In the geostatistical algorithms with explanatory variable, CoKriging and EBK Regression Prediction (Figure 63 c and d respectively), bathymetry was used as an explanatory variable to enhance the interpolation and its signature on the Mz distribution is rather evident. The longitudinal structures, such as the deep bars, the littoral drift pathway, and the deep trough between the bars, are evident from the Mz distribution. The outer

deep bar is characterised by Mz values between 1.0 - 2.5 ϕ , from SW to NE, while the deep trough is different in the two maps: EBKRP predicts a longer structure towards south-west while CK predicts coarser sediments. On the other hand, the inner deep bar isn't completely represented in its full length by the EBKRP while is more evident in the CK model. In the prodelta EBKRP model is way finer than CK and it's confirmed by the error that are decidedly lower for EBKRP, with values of -0.65 ϕ and -0.79 ϕ , compared to -1.91 ϕ and -1.72 ϕ for CK.

The application of the developed semi-automatic interpolation method made it possible to produce three maps of the MZ that differ in the type of geostatistical algorithm used in the third step of the SAIM (Figure 64). The statistical algorithms used are OK (a), EBK (b) and EBKRP (c). The maps are very similar to each other both from mean-size distribution and error values.

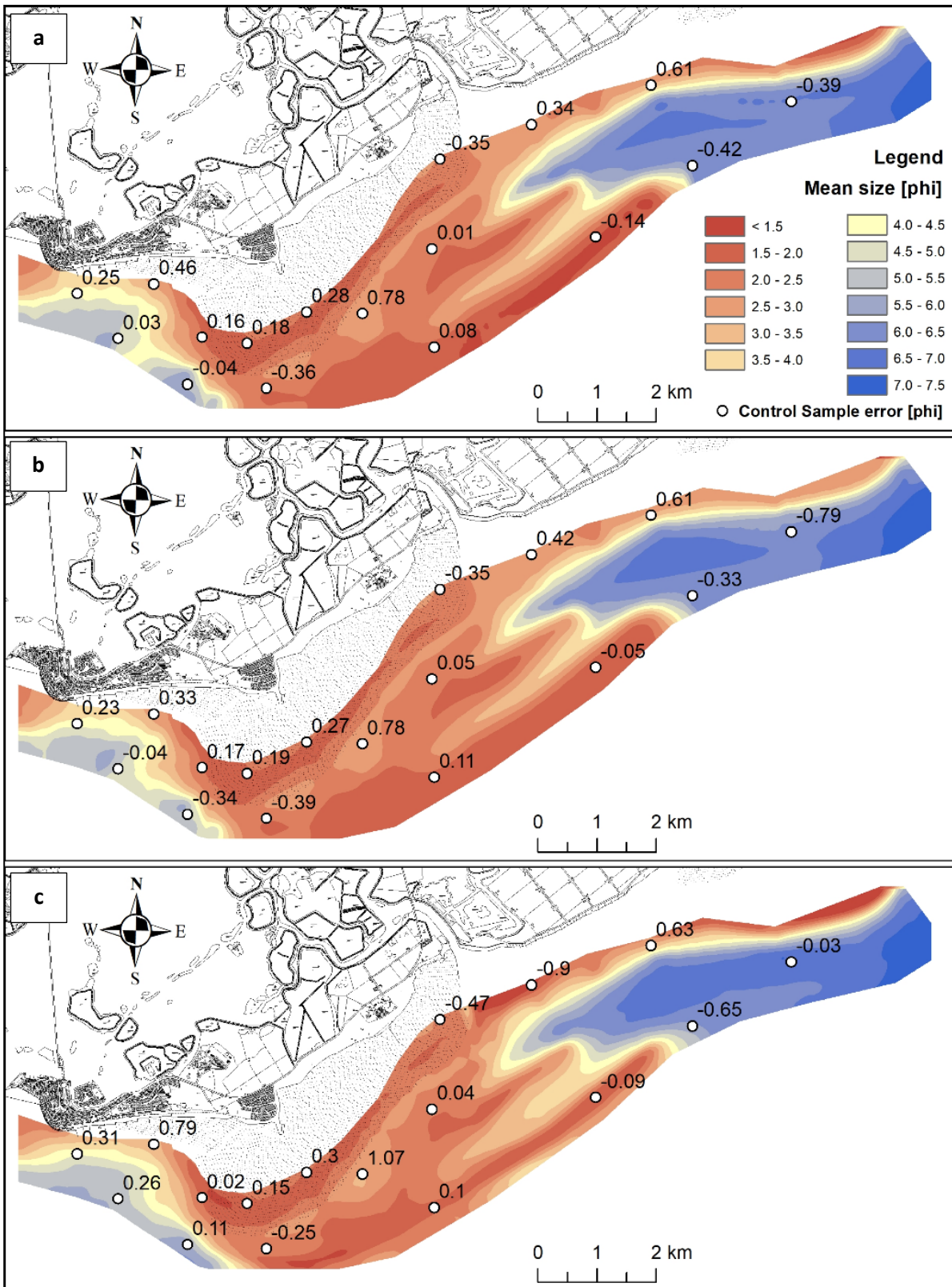


Figure 64 Mean size distribution model created through Semi-Automatic Interpolation Method using (a) OK, (b) EBK and (c) EBKRP as geostatistical interpolation algorithm. Control samples and the error between model and sample's Mz are represented.

The maps are compared with the geomorphological set-up of the study area. With respect to the Mz distribution, the study area can be split into three parts. The western and eastern margins are characterized by a standard seaward-fining gradient, greater in the eastern half of the area and lesser in front of the Grado

beaches. In the central part of the maps, the sedimentary body of the MMB is characterized by the presence of low Mz values corresponding to coarser sediments, almost only sands. However, the Mz distribution does not follow a constant gradient but represents the signature of geomorphological context: each model shows the sedimentological evidence of the two deep bars, the littoral drift pathway from the Isonzo river mouth across the entire study area, the finer sediments in the deep trough and the presence of fine sediment in the prodelta. On the morphological highlands there are mainly coarser sediments with low MZ values. The outer deep bar is characterized by a rounded tail towards north-east and presents MZ values between about 1.5 and 2.0 ϕ . The border area between the inner deep bar and the westernmost branch of the prodelta is characterized by a high MZ gradient: in about 200m the Mz increases by about 3.5 ϕ , going from sandy to muddy sediments. On the contrary, in the deep trough, where sample G81 is located, the transition from the fine sediments' characteristic of the prodelta to the coarse sediments of the D-MMB is decidedly more progressive, as also happens for the bathymetry. In the D-MMB, a corridor of finer sediments (Mz between 2.5 - 3 ϕ) is evident in the area of the deep terrace at the border with the littoral drift pathway. In the HIB the coarser sediments, with ϕ values around 1.5 - 1.6, are concentrated at the point of maximum extroversion of the bank, where the curvature of the isobaths is evident. Finally, the F-MMB, in its deep part just west of the HIB, shows an extrusion of the coarser grain sizes while the grain size of the area in front of the Grado beaches shows a standard seaward fining gradient. Analysing the discrepancies between measured and predicted Mz values they are overall, for all three models, are lower than 1.0 ϕ but only one point in EBKRP. On the other hand, EBKRP model (Figure 64c) predicts a more regular Mz distribution of fine sediment of prodelta.

Through the use of CSs, the absolute interpolation errors and their statistical distribution were extracted. From the graph of Figure 65 it can be seen that the geostatistical methods, both with and without explanatory variables, have a quite regular average mean absolute error between 0.51 ϕ (EBKRP) and 0.65 ϕ (OK and CK), an average maximum absolute error between 1.13 ϕ (EBKRP) and 1.95 ϕ (OK) and the range from the 16th and 84th between 0.77 ϕ (CK) and 1.03 ϕ (EBK). Overall, the EBKRP error statistics are often the lowest for geostatistical approaches. Again, from the graph of Figure 65, now considering SAIMs models, all the error parameters are decidedly lower. The mean absolute error is in the range 0.29-0.36 ϕ while the maximum error is around 0.78-1.07 ϕ , with the greatest values regarding to EBKRP model. The range of plus-minus a standard deviation is around 0.4 ϕ except for EBKRP where it is 0.64 ϕ .

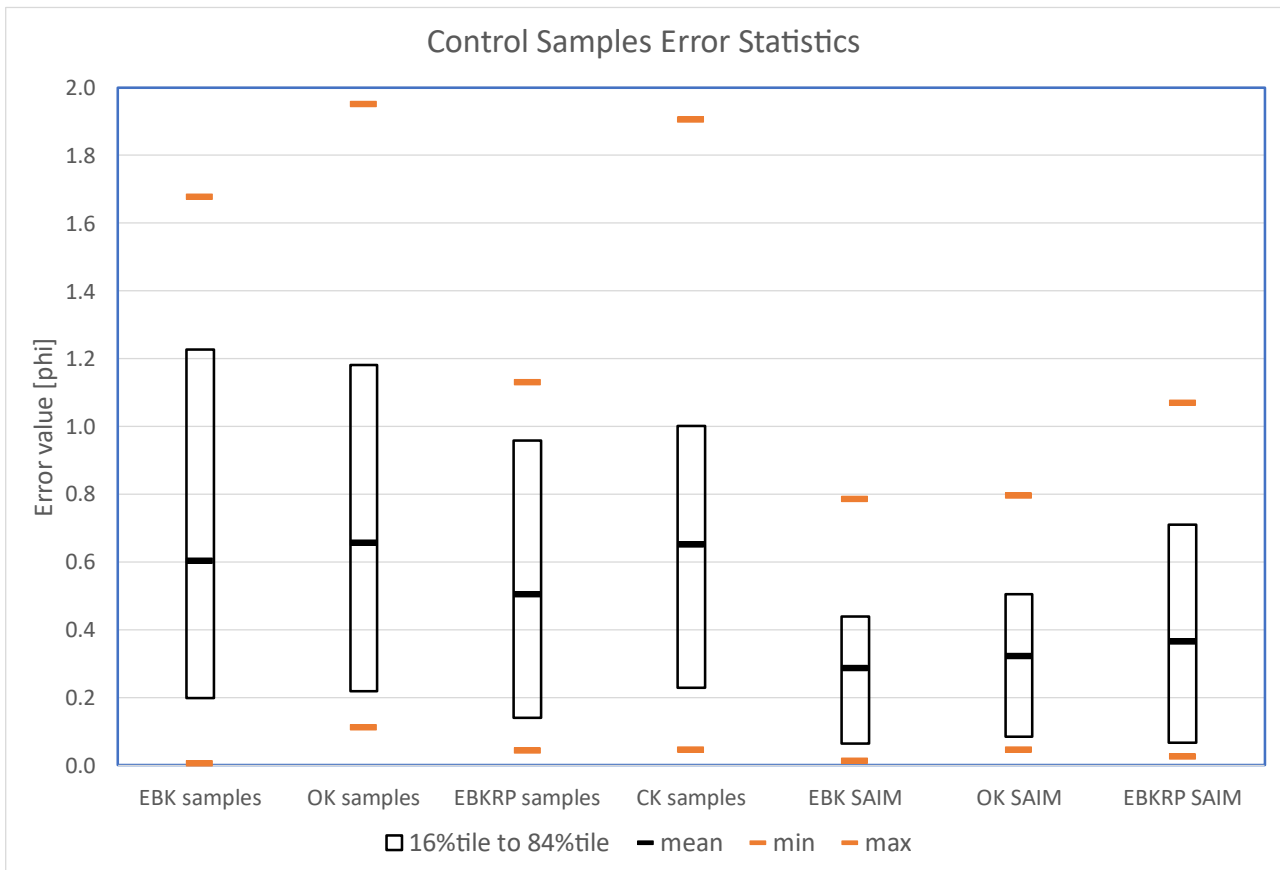


Figure 65 Control samples error statistics.

5.2.2.2 Sorting & normalized sorting

The sorting and normalized sorting maps (Figure 66) provide slightly different information: if on the one hand the Sr is mostly used as a parameter, on the other it has the limit of being correlated with the Mz, therefore producing the NSr map can also cover the information hiatus by increasing the reliability of sedimentological interpretations, especially in environments where there is great variability of the Mz. Both maps were produced with the SAIM method. In general, sorting is a parameter that represents the stability of the sediment selection and deposition agent and therefore can provide complementary information compared to that of the Mz which is more an expression of the energy of the morphogenetic agent. It is important to remember that high Sr values represent poorly sorted sediments and vice versa.

The sorting map (Figure 66a), as expected, reflects the evidence of the Mz distribution very well, with some differences localized in specific areas. In the longshore transport corridor, a gradient of Sr reduction (and therefore better sorting) from east to west is visible and continues up to the tip of the HIB. In the D-MMB the area of the deep terrace of the D-MMB is less sorted while the area of the two deep bars has lower Sr in the center which gradually becomes higher both towards the south-west and towards the north-east. The area with the highest Sr is located in the deep trough while all the areas of fine deposition, e.g., the prodelta of the Isonzo river, are characterized by high Sr values.

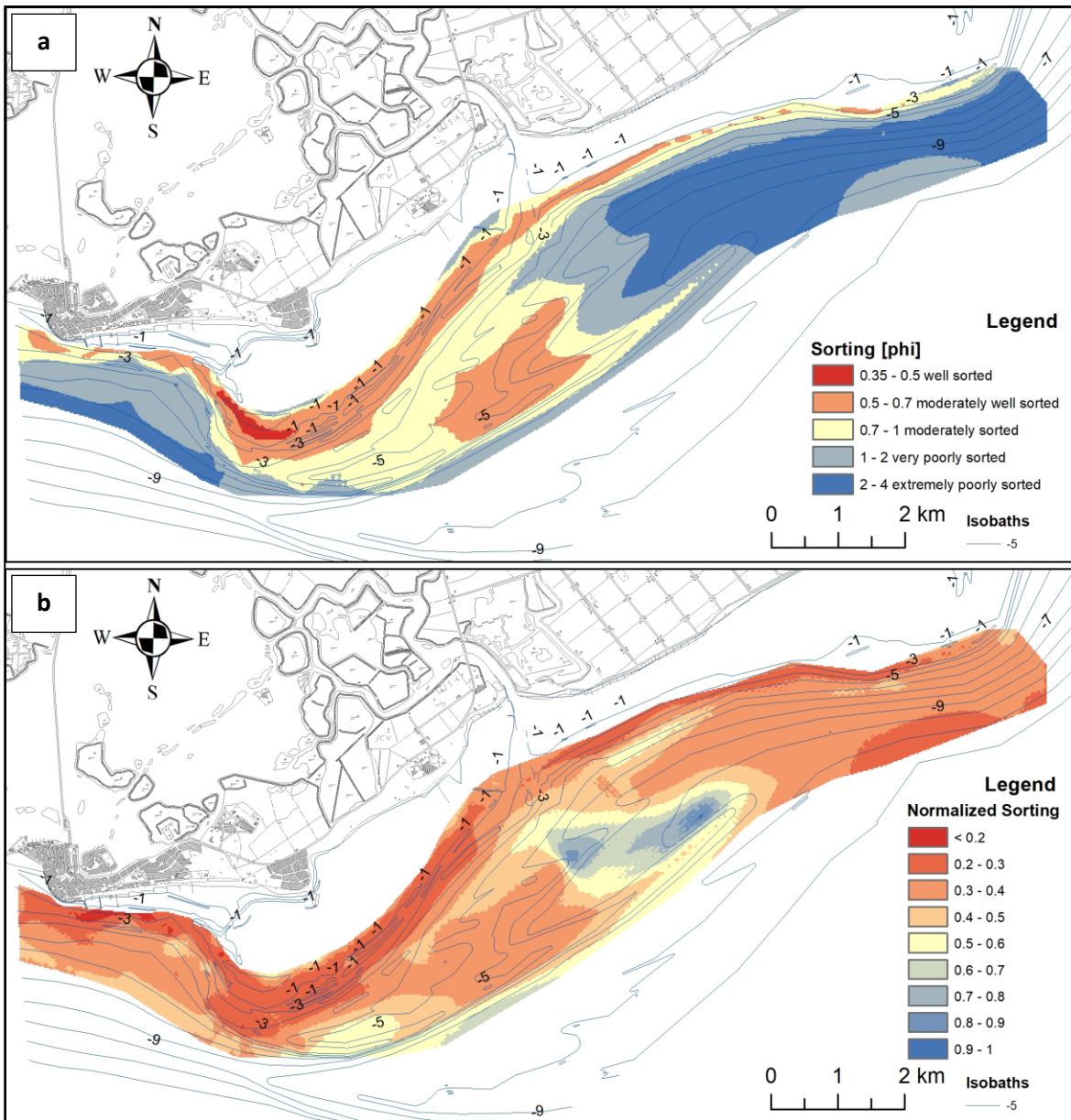


Figure 66 (a) sorting and (b) normalized sorting maps.

The NSr map (Figure 66b), however, manages to further exacerbate the sorting variations even for the coarsest grain sizes, resulting in some cases different compared to pure sorting. The map further highlights the sorting that occurs along the littoral drift pathway, and the only interruption in the continuity of this trend is localized located downdrift of the Primero Inlet, where worse sorted sediments are found. Along the pathway, the extroflexion of the NSr present on the F-MMB is evident. Furthermore, the D-MMB is less sorted than the longshore transport pathway, again showing a reduction in sorting (therefore an increase in NSr) from the center both towards the north-east and towards the south-west. In this map, the worst classified areas are those relating to the deep trough and the border between the inner deep bar and the Isonzo prodelta.

5.2.2.3 Texture

Finally, the last sedimentological map produced is a textural map with Flemming's classification. This map, unlike those concerning the grain-size parameters, is able to provide complementary information which, in part, is identifiable from the interpretation of the Mz and Sr (or NSr) maps but which are highlighted in these maps. In particular, they are able to immediately provide information on the number of sedimentary sources or transport vectors. Furthermore, the contemporary interpretation of this product with the granulometric parameters is able to further increase the knowledge of the sedimentological dynamics, completing the cognitive framework of this aspect. The textural map can be divided into three blocks (Figure 67). The western margin, i.e. the coastal area in front of the beaches of Grado, is characterized by sands in the shallower part which gradually become muddier with increasing depth until they become slightly sandy muds beyond -5 m depth. The central area, composed of the MMB and the D-MMB, is characterized by sands: the only slightly muddy sands are localized in the north-eastern part of the deep bars, where these deepen and border the third zone, i.e. that of the prodelta of the Isonzo. In the third zone, the sediment limit with more than 75% sand varies from -3.5 m near the river mouth to -6 m in front of the Primero Inlet. Furthermore, in front of the river's mouth from a depth of -5 m the muds extend (sand <5%): this boundary is progressively deeper up to halfway between the mouth and the Primero inlet, i.e. up to where the extroflexion of the isobaths due to the deltaic structure. From this point towards the south-west there is an increase in the percentage of sand, more gradual towards the deep trough, while the sandy muds go much further west in the area between the Primero ebb-delta and the inner deep bar.

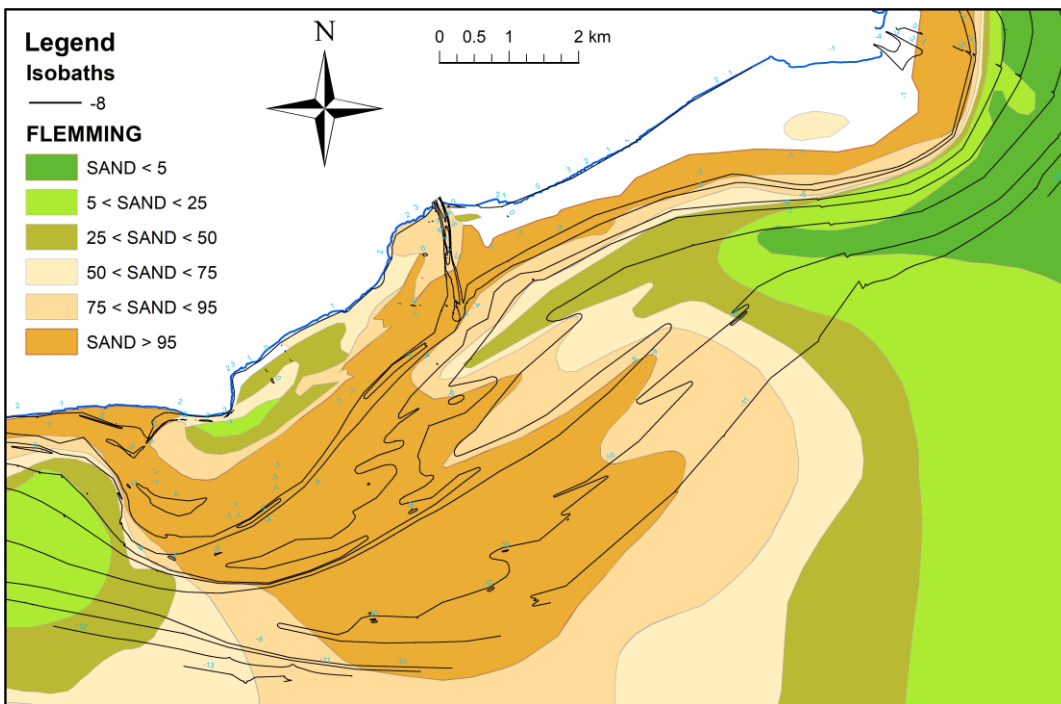


Figure 67 Textural map with Flemming classification.

5.3 Provenience analysis: Hg proxy (Geochemical)

The 138 sediment samples were analysed through an Atomic Absorption Spectrophotometer. The concentration of total Hg in the sediments varies widely, ranging overall from 0.16 to 59.1 $\mu\text{g/g}$. Even though Mz has not an evident signature on the THg, the graph in Figure 68a shows that THg in the coarsest sands (1-2 ϕ) is low, although in 8 on 33 samples THg is greater than 2 $\mu\text{g/g}$. Moreover, sediments with Mz between 2 ϕ and 4 ϕ (mainly composed by fine and very fine sands) are the greatest in THg, showing a positive gradient of THg from medium to very fine Figure 68b. Finally, within the finest sediments (Mz > 4 ϕ), there seems to be a slightly inverse proportionality of THg with respect to Mz.

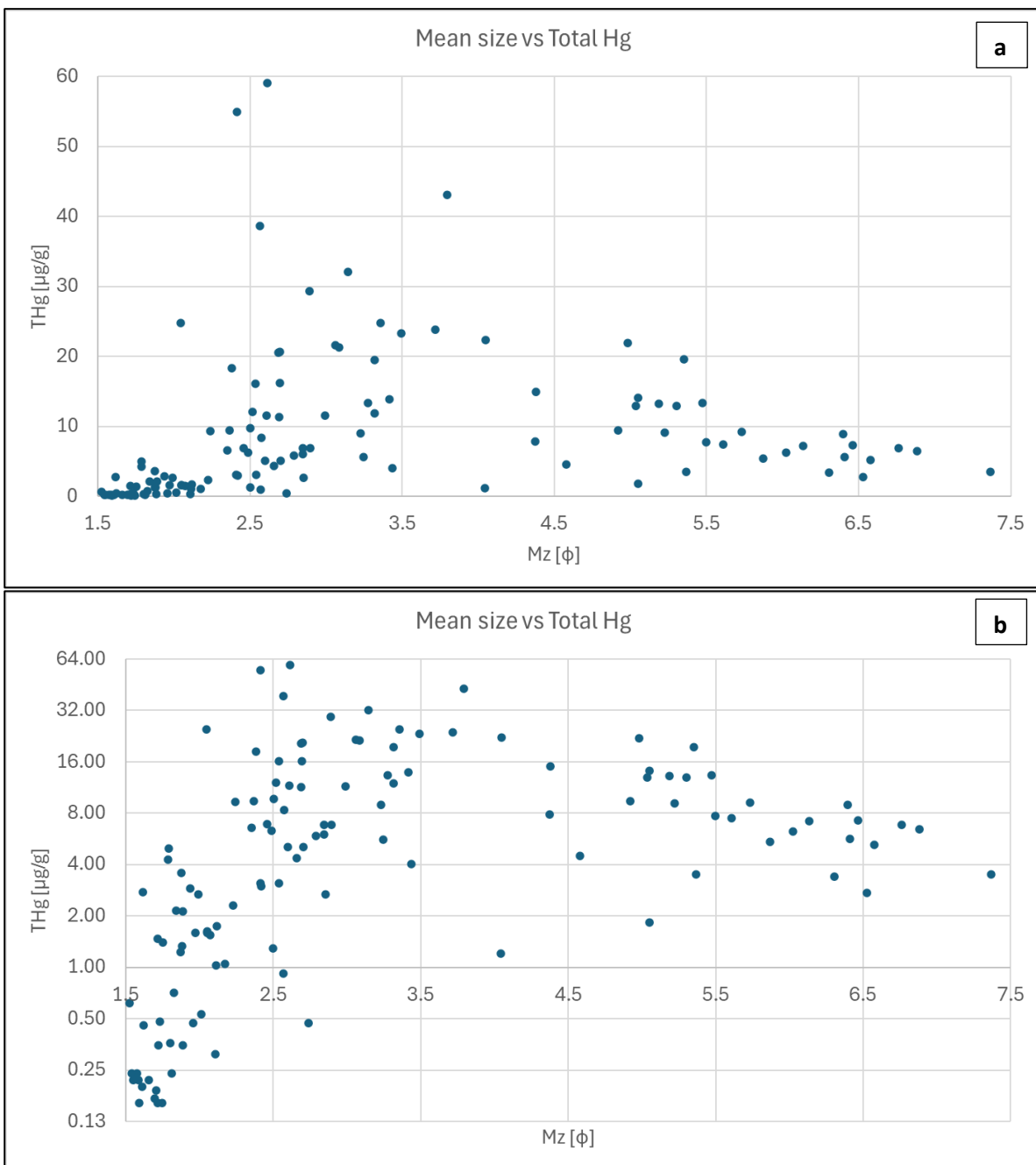


Figure 68 Mean size vs Total Hg concentration using (a) linear and (b) logarithmic scale.

Interpolating the THg concentration of the samples (Figure 69a) through the application of the empirical bayesian kriging algorithm we obtained the map of THg distribution (Figure 69b). Relatively to the range of Hg concentration in the study area, low values are present on the two areas, the HIB and the deep bars, medium ones are located on the deep terrace and the Isonzo River delta, while sediments high to extremely high in Hg are present in the seabed facing the municipality of Grado and in a small area between the Primero Inlet and the Isonzo delta.

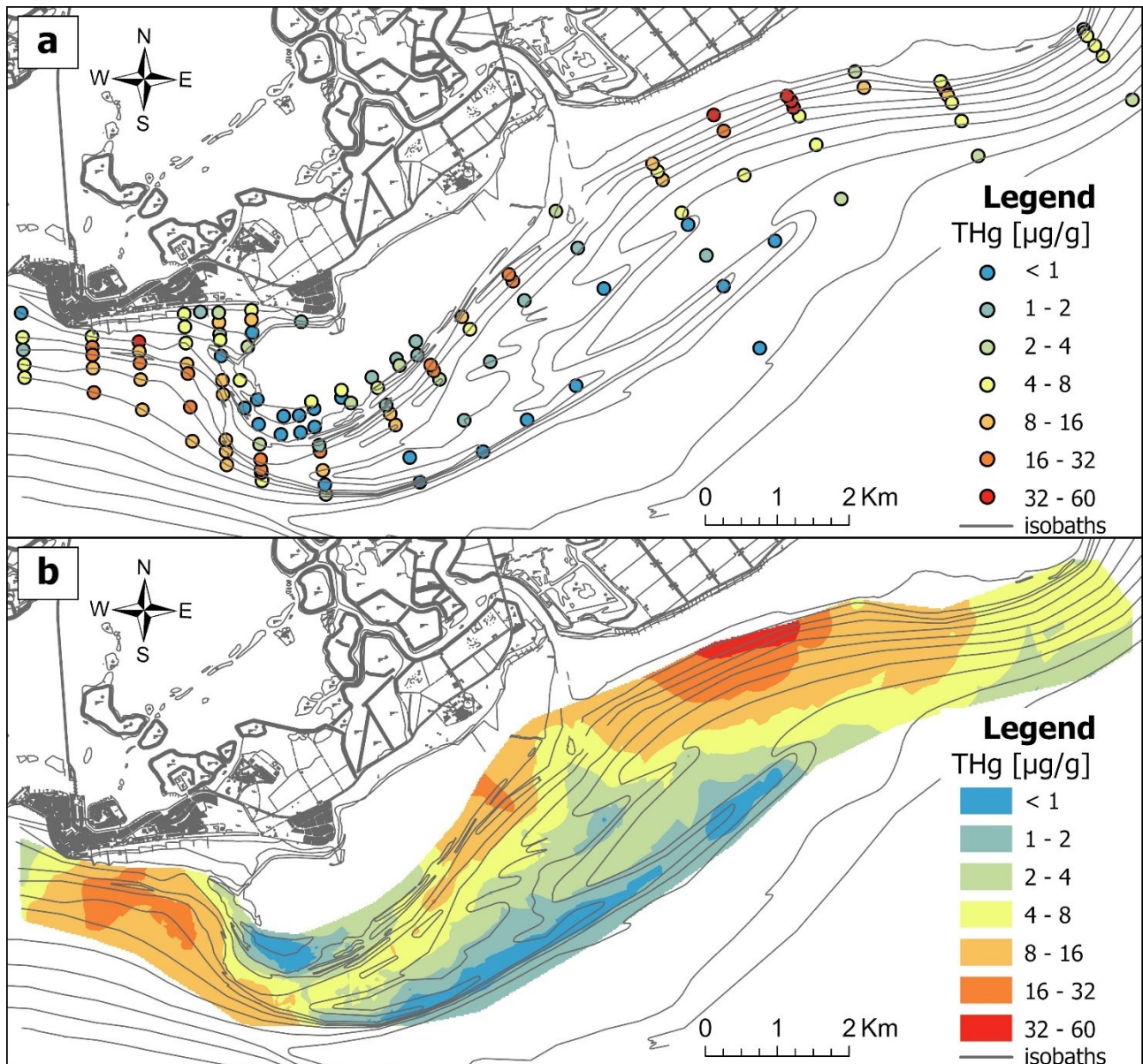


Figure 69 (a) Distribution of THg concentration in the sediment samples and (b) map of the THg concentration.

The sediment samples on HIB are mostly very poor in Hg as shown in Figure 70: everyone but sample G132 ($\approx 5 \mu\text{g/g}$) are lesser than $1 \mu\text{g/g}$. Samples G137 and G139, located just inside the backbarrier, have values of 6.84 and $5.09 \mu\text{g/g}$, greater than closer ones on the HIB. Considering samples G140 - G146, just upstream of HIB on the littoral drift, they are slightly richer in Hg (1.40 to $4.27 \mu\text{g/g}$) than HIB, indicating a negative gradient on this sector of the littoral drift pathway.

Samples on outer deep bar (G32, G36, G41, G46, G51, G82 and G87) are some of the lowest in Hg concentration, ranging from 0.16 to 0.24 $\mu\text{g/g}$, while the ones on inner deep bar are slightly richer (0.46 and 0.92 $\mu\text{g/g}$ for samples G56 and G80 respectively) (Figure 71). The deep terrace is characterized by sediments with a wide range of values of Hg (from 1 to 30 $\mu\text{g/g}$). The richest samples on the whole MMB are concentrated between -2 m and -3 m.

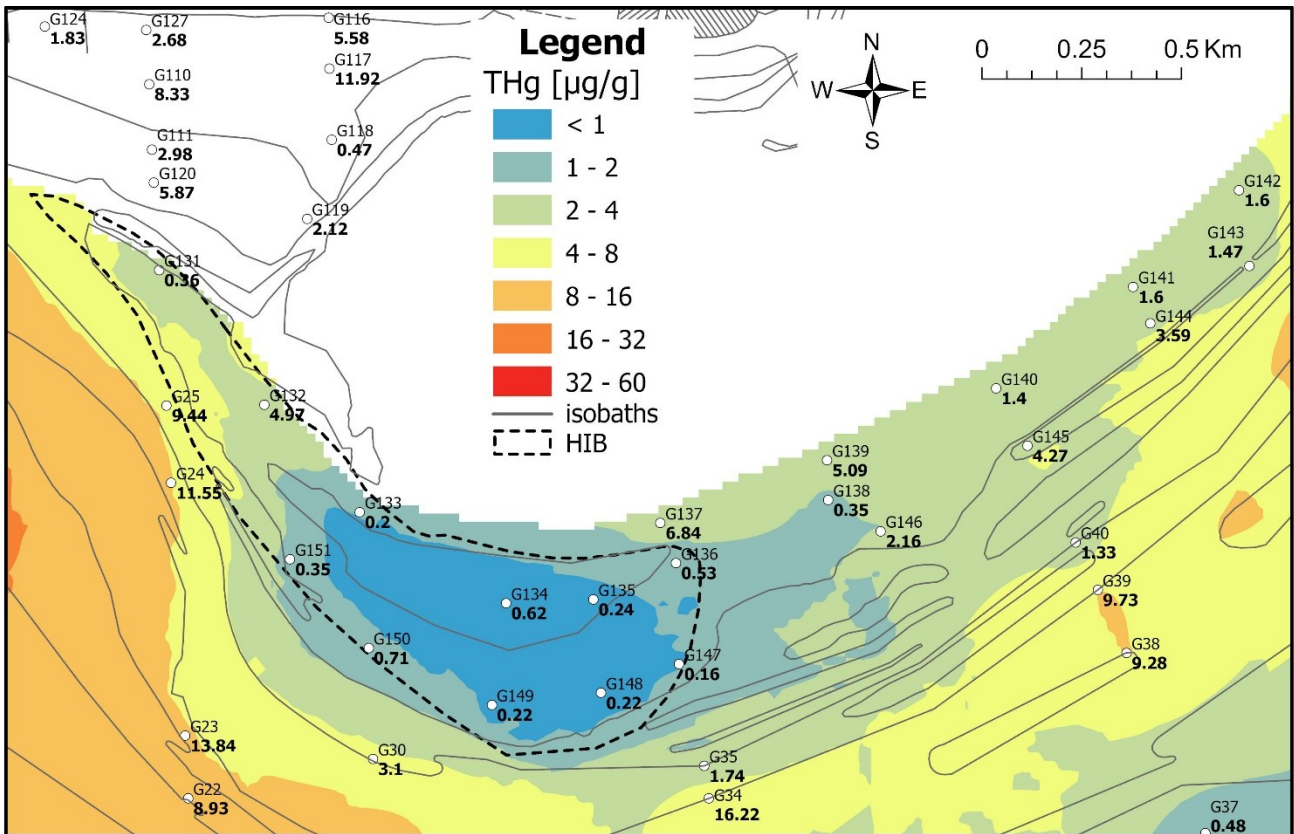


Figure 70 Map of THg concentration: detail of the HIB. Samples' labels represent code and THg concentration (bold) in $\mu\text{g/g}$.

On the Isonzo River delta there is an enriching gradient from the mouth to the west, from values around 3.0 - 5.5 $\mu\text{g/g}$ on the mouth up to 15 $\mu\text{g/g}$ just east from the Primero Inlet (Figure 72). Moreover, the highest values (up to 59.1 $\mu\text{g/g}$) of the whole study area are all located in a relatively small zone between the river delta and the Primero Inlet, at depth within -5 m, with the highest ones between -2 m and -3 m.

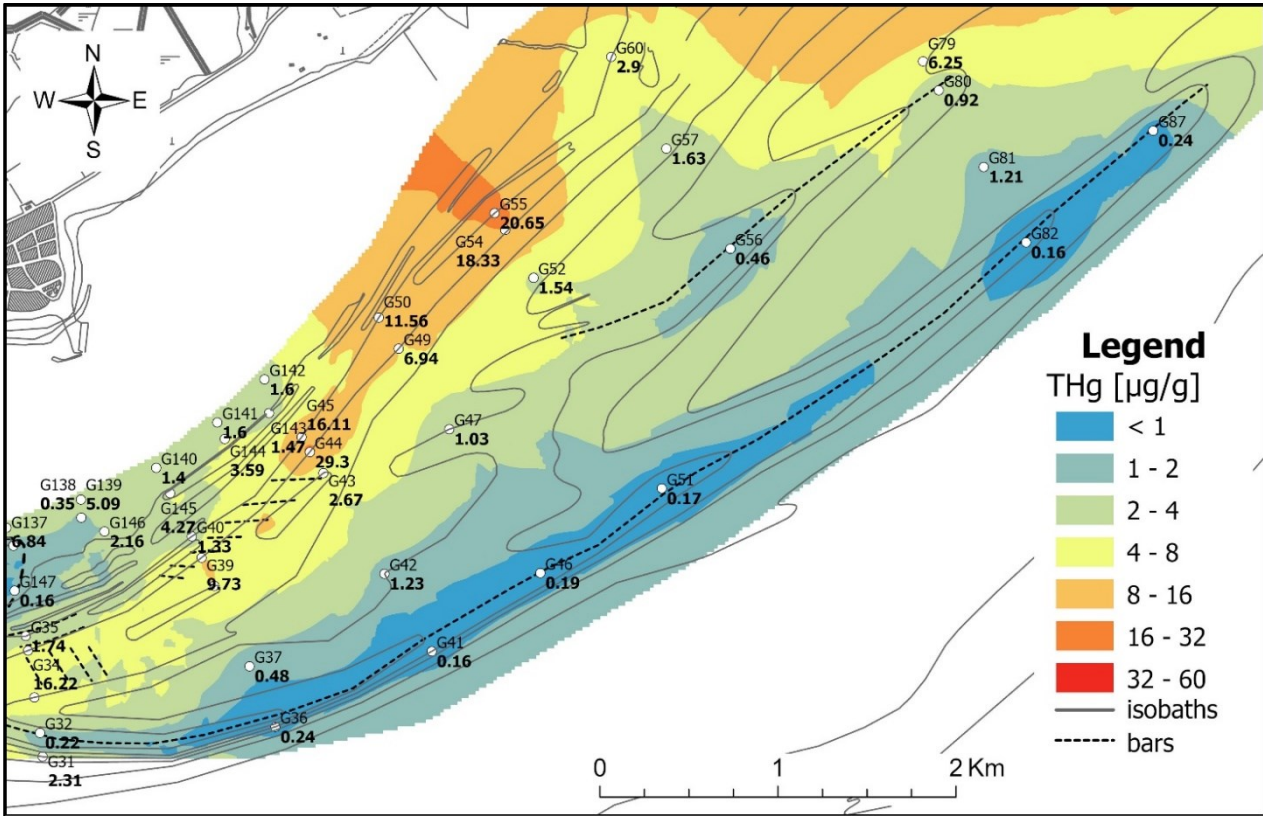


Figure 71 Map of THg concentration: detail of the D-MMB (deep bars and deep terrace). Samples' labels represent code and THg concentration (bold) in $\mu\text{g/g}$.

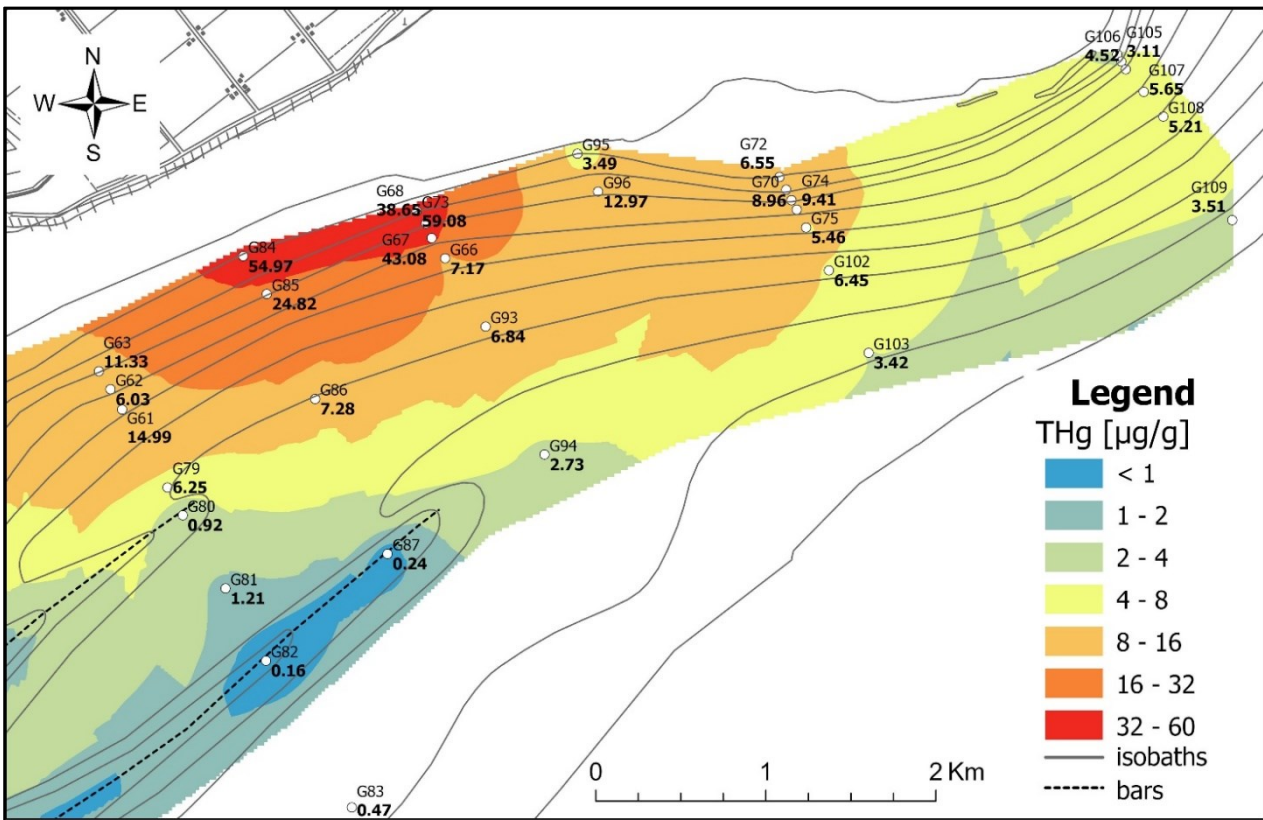


Figure 72 Map of THg concentration: detail of the area between Isonzo River Delta and Primero Inlet. Samples' labels represent code and THg concentration (bold) in $\mu\text{g/g}$.

5.4 Modelling

From Spectral Wave and Hydrodynamic modules of MIKE21 we obtained a total of 10 models. For our purposes, the focus would be on H_s , bed shear stress, current direction, and current speed.

Before analyzing the model outputs, the map of the critical bed shear stress for suspension (Figure 73) were obtained using the granulometric characteristics of the seabed following the theory of (Van Rijn, 2020).

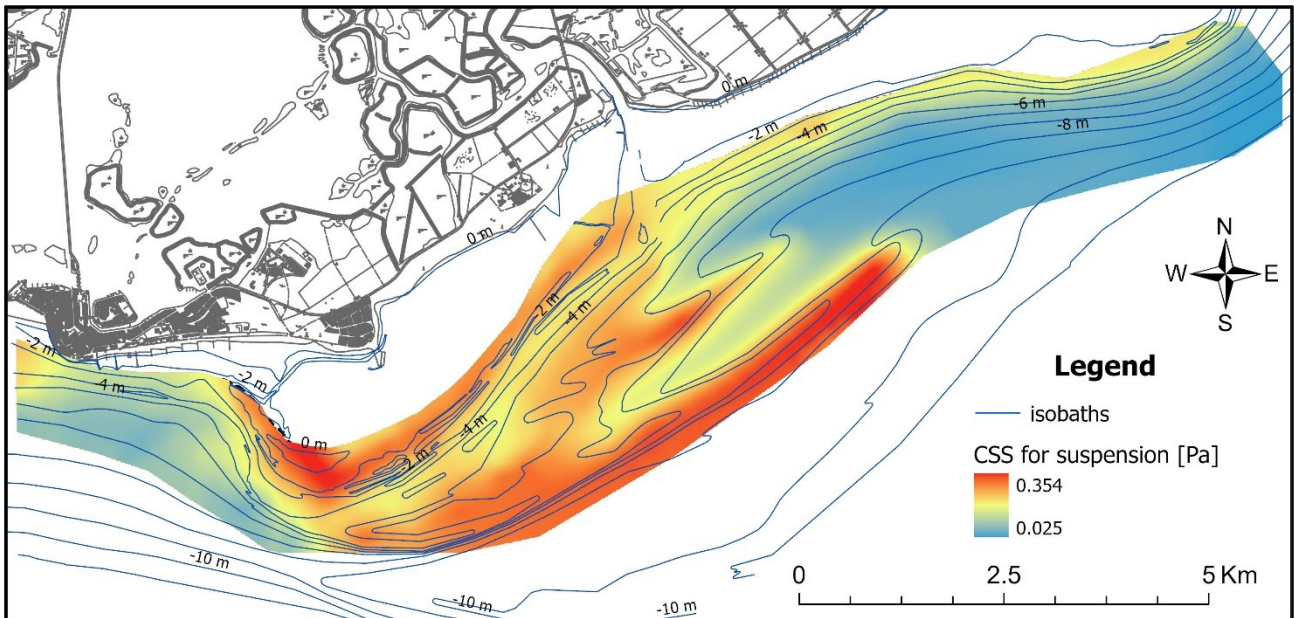


Figure 73 Map of critical bed shear stress for suspension.

Critical BSS is directly related to the d_{50} (median diameter), and it ranges from 0.026 to 0.354 N/m². Coarser sediments, located on the deep bars and the HIB have the highest values of critical BSS. Lowest values are found in the area around the Isonzo's prodelta, below -4 m. Along the longshore transport pathway, from the mount to the HIB there is a positive gradient of critical BSS related to the sediment coarsening. On the deep-MMB, between the longshore transport pathway and the deep bars (from -3 to -5 m), a pathway of average values of critical BSS is present, with values in the range 0.188 – 0.249 Pa.

5.4.1 Bora multi-event: 25/02 – 03/2023

Bora is the dominant wind in the Northern Adriatic Sea. Differently from the waves coming from south, the ENE waves are generated inside the mesh through MIKE21-SW. This way the recorded wave parameters from the two buoys (DWRG1 and DWRG3) were used to assess the reliability of the simulations and, consequently, to calibrate the models. In particular, buoy DWRG1 is very useful to the quality evaluation of the simulations because it is located to the south-western edge of the mesh, where waves reach the maximum H_s . The calibration process allowed us to obtain two calibrated simulations, one using the DWRG1 wave input and one without external wave input, that are represented with recorded data and simulated ones with default parameterization (Figure 74).

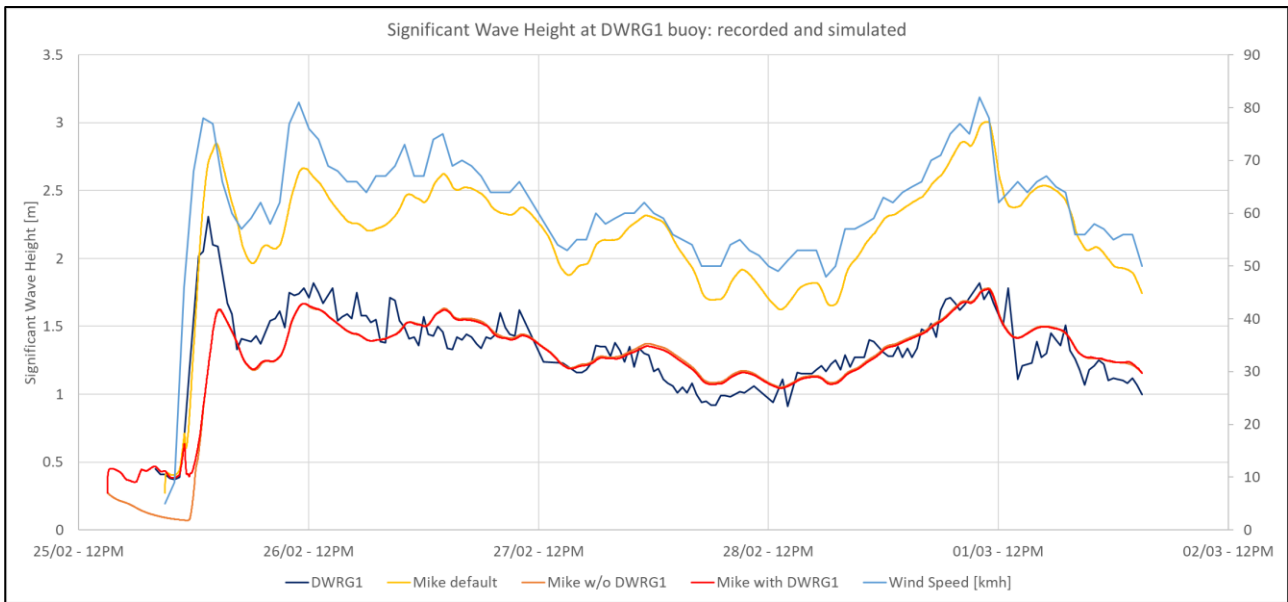


Figure 74 Wind speed at Paloma station buoy (light blue) and significant wave height of the recorded at DWRG1 buoy (dark blue), simulated with default parameterization (orange), and simulated with calibrated parameterization using (red) and not using (dark red) the wave input for the simulation.

The model calibration allowed to reduce the mean difference between recorded and simulated significant wave height from 0.84 m to -0.03 m and standard deviation from 0.27 m to 0.23 m. Calibrated models appear quite faithful with respect to recorded data from 26/02/2023 at 6AM to the end of the simulation, while the first peak of H_s (2.31 m) at 1:30AM on 26/02/2023 is delayed and underestimated in both models. From 6AM on 26/02 to the end of the simulation, the mean difference between recorded and simulated H_s and the standard deviation are reduced to 0.02 m and 0.13 m respectively for the calibrated models. This issue may be found in the wind input: the recorded wind speed at Paloma station buoy has not got a significantly high peak at 1:30AM on 26/02 compared to the rest of the dataset and then the model is unable to produce the desired output. The use of wave input in the ENE storm simulation doesn't improve the reliability of the simulation by far. In fact, the main difference between the two calibrated models is relative to the pre-event when the H_s is lower than 0.5 m. On the other hand, the H_s during the Bora storm is almost the same for the two models. During ENE events, wave develops from ENE to WSW, leading to an increase in H_s from the Isonzo's delta to the MMB (Figure 75). The wave vectors show the refraction due to the bathymetric set-up, in particular around the isobaths' extroflexion of the Isonzo River delta and the MMB. Moreover, the F-MMB is protected by ENE waves, with H_s lower than 0.5 m, while the littoral drift pathway is characterized by stable values of H_s around 1.0 m.

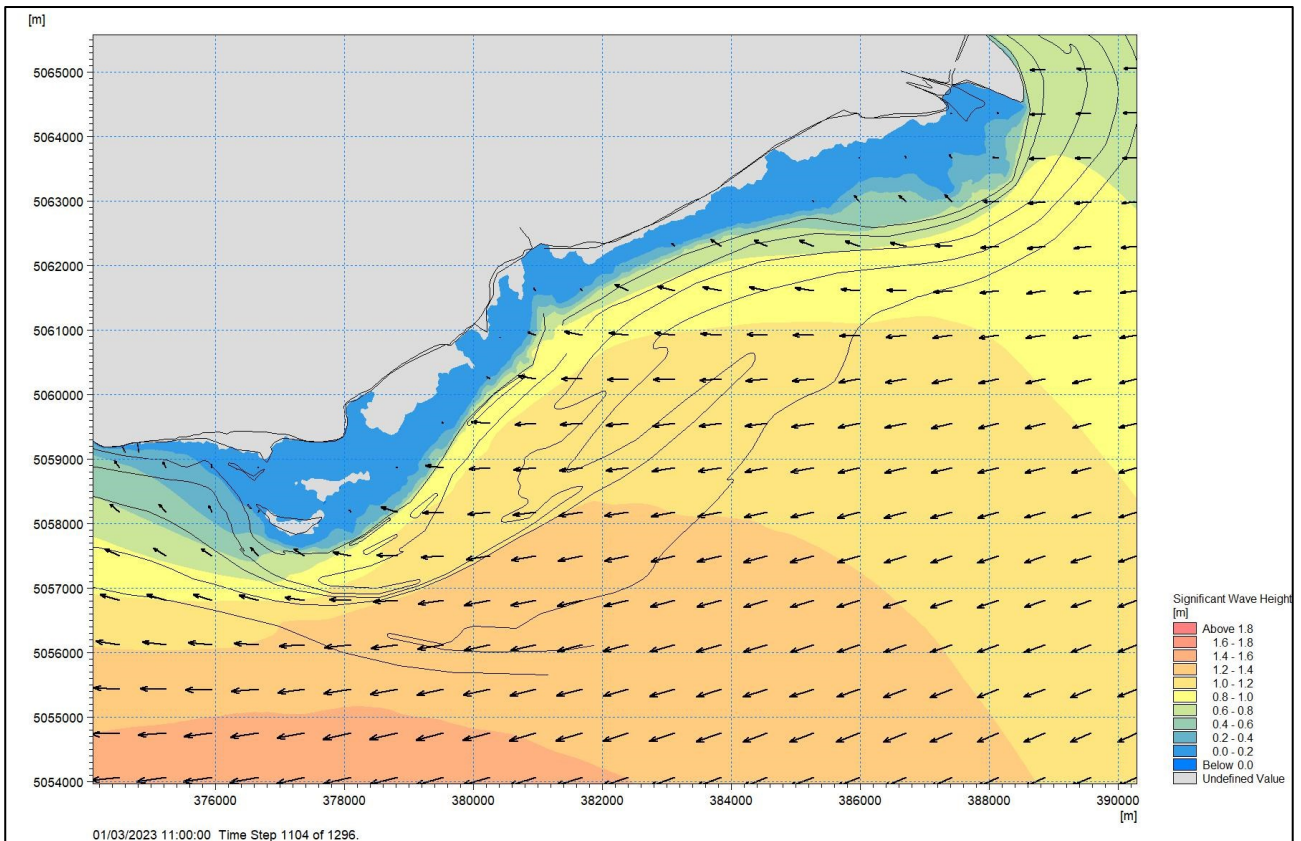


Figure 75 Significant wave height of the calibrated simulation obtained by MIKE21-SW. The step represents the maximum values of the whole event.

With MIKE21-HD we obtained simulations of currents (Figure 76) and bed shear stress (Figure 77). Currents on open sea follows the wave direction (ENE-WSW) while the more the depth is reduced, the more they tend to flow parallel to the isobaths following the longshore transport pathway until -1 m. Current speed ranges from 0.1 to almost 1.0 m/s. Maximum current speed may be found between -2 and -3 m on the longshore transport pathway, in particular around the MMB. Average current speed (≈ 0.5 m/s) may be found just around the Isonzo's river mouth and on the western side of the D-MMB. On the D-MMB there is a positive gradient of current speed from ENE to WSW. On the F-MMB current speed drastically reduces from 0.8 m/s at the southern vertex of MMB to 0.2 m/s towards NE. Bed shear stress distribution is widely correlated with current vectors while is also depends on the bathymetry: the shallower the depth, the higher the bed shear stress. For these reasons, the highest values of bed shear stress are found along the longshore transport pathway, between -1 and -3 m. As it happens for the currents, average values of bed shear stress may be found on the western half of the D-MMB, higher on the raised landforms (bars) and lower on the depressed one (troughs).

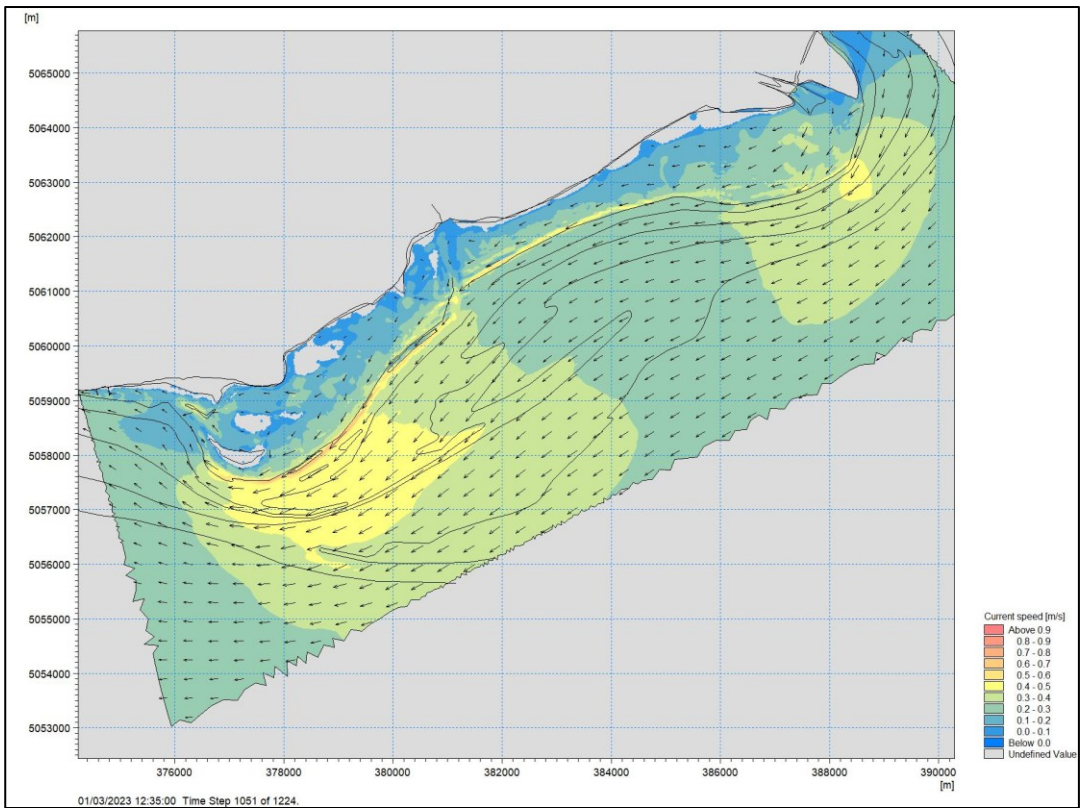


Figure 76 Current speed of the calibrated simulation obtained by MIKE21-HD. The step represents the maximum values of the whole event.

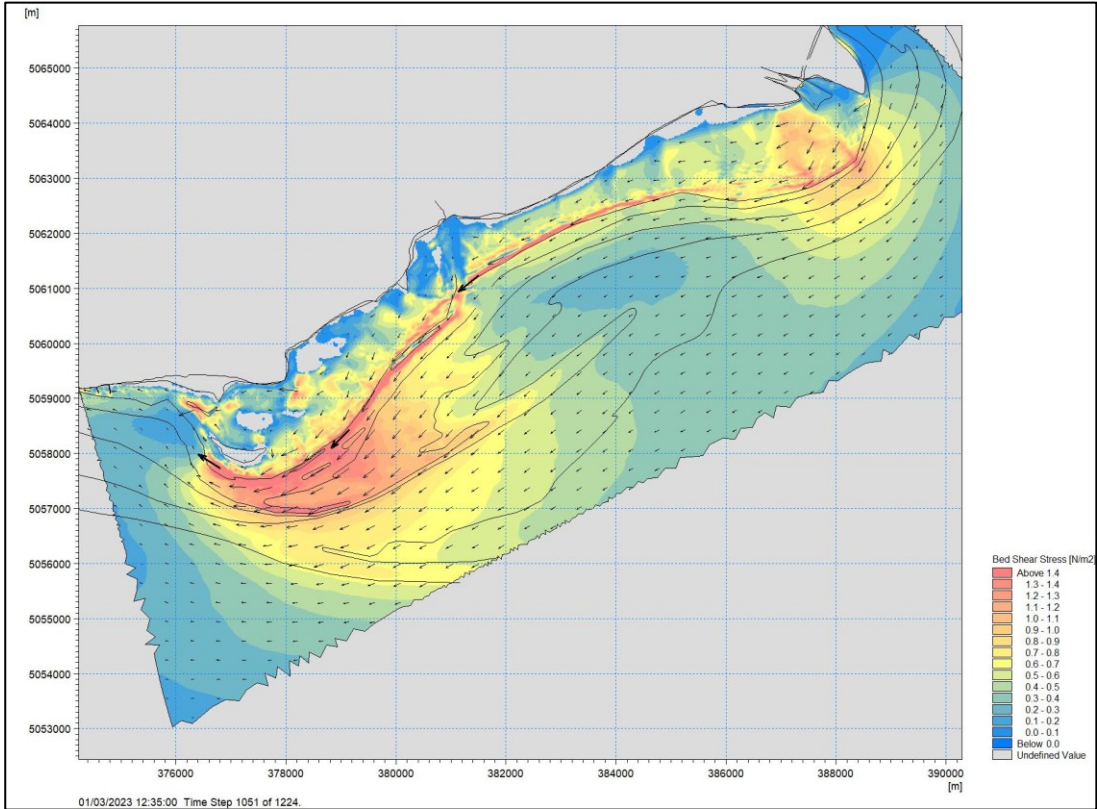


Figure 77 Bed shear stress of the calibrated simulation obtained by MIKE21-HD. The step represents the maximum values of the whole event.

5.4.2 Southern wind multi-event: 27/10 – 05/11/2023

Although the southern winds are less intense and frequent than the Bora in the northern Adriatic (Figure 2), the waves coming from the south are dominant in both buoys present (Figure 5) because they can develop throughout the entire Adriatic Sea basin. In fact, unlike the ENE wave motion which develops entirely within the calculation mesh used in the MIKE21-SW model, in the case of storm surges from the south it is necessary to use the characteristics of the waves as input (H_s , peak period, mean direction and directional spreading) on the boundary defined DWRG1 (Figure 26). The multi-event analyzed is characterized by six main peaks as regards the H_s (Figure 31), some with waves coming from SSE and others from SSW.

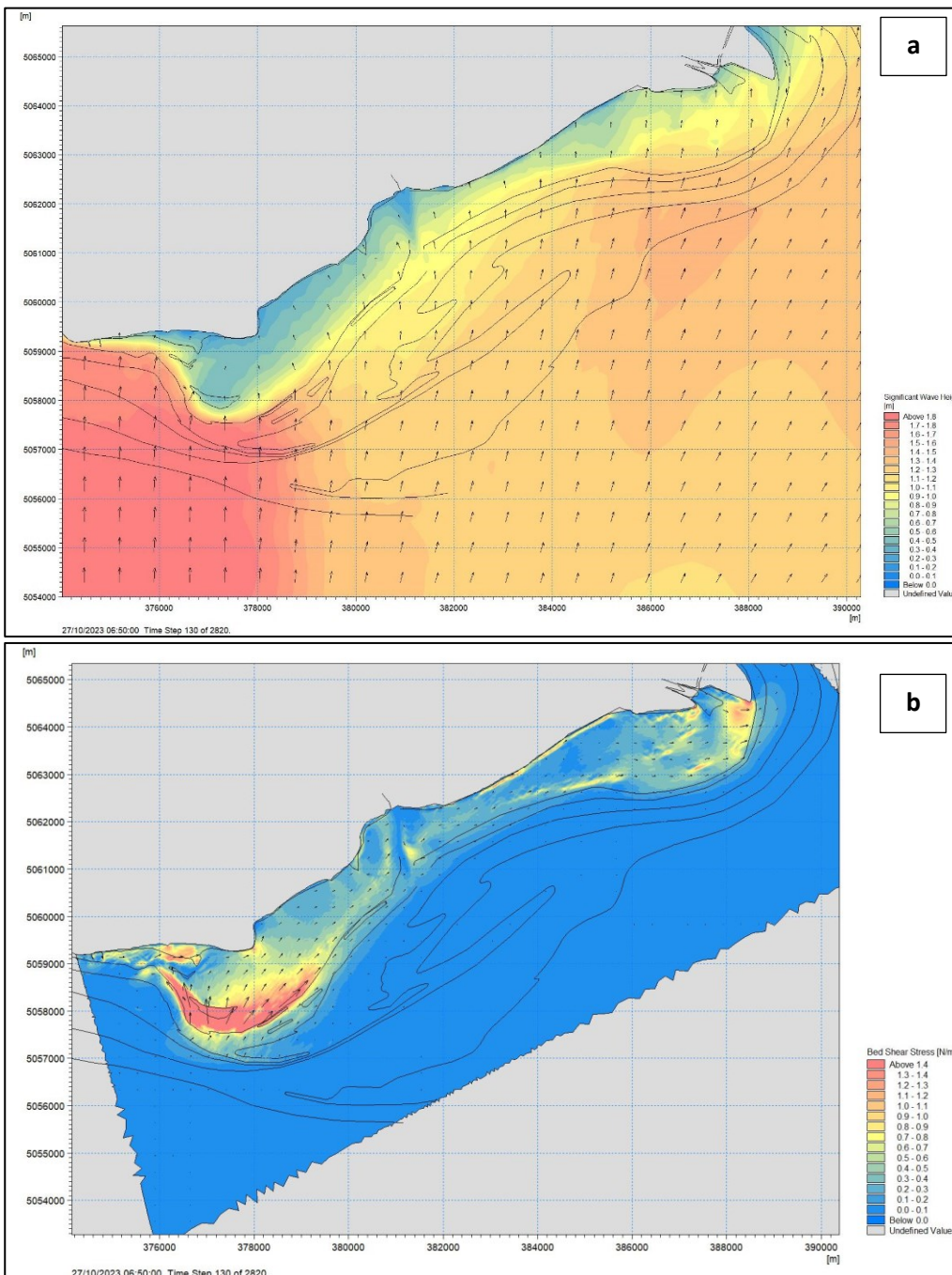
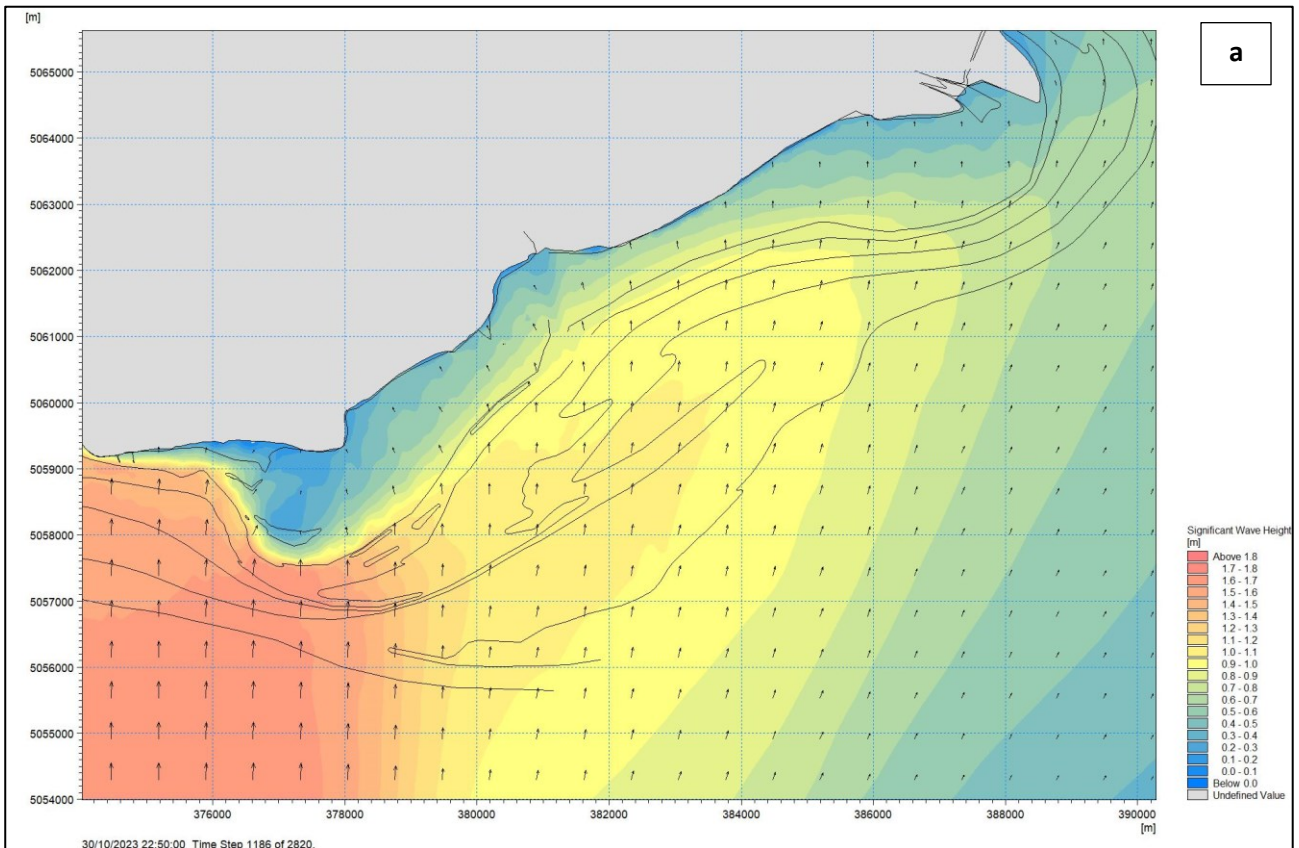


Figure 78 MIKE21 model outputs of the 27/10/2023 event: (a) H_s and (b) BSS.

The H_s distribution during the peak of the first event (27/10/2023 at 6:50), characterized by SSE waves (170°N), is inhomogeneous: the highest values ($>1.8\text{ m}$) are focused on the western side of the area, up to the southern vertex while eastwards the H_s quickly damps to values just above 1.2 m , with a slightly clockwise rotation of wave direction (Figure 78a). Due to the H_s distribution, the BSS is low but in the HIB. Here, BSS is greater than 1.4 N/m^2 and its direction is divergent from the vertex, leading to a northeastward BSS to the east of the vertex and to a northwestward BSS to the west of the vertex, in the F-MMB.



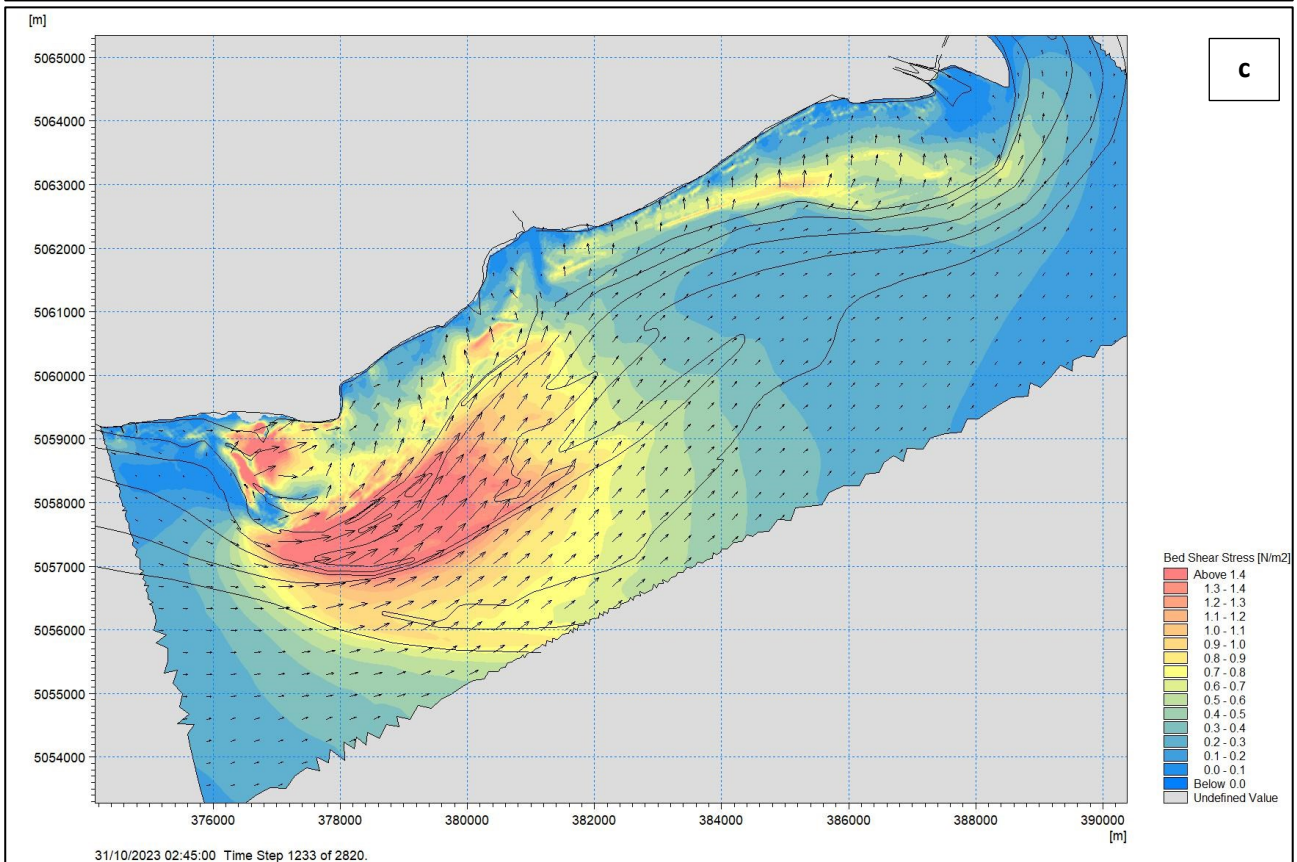
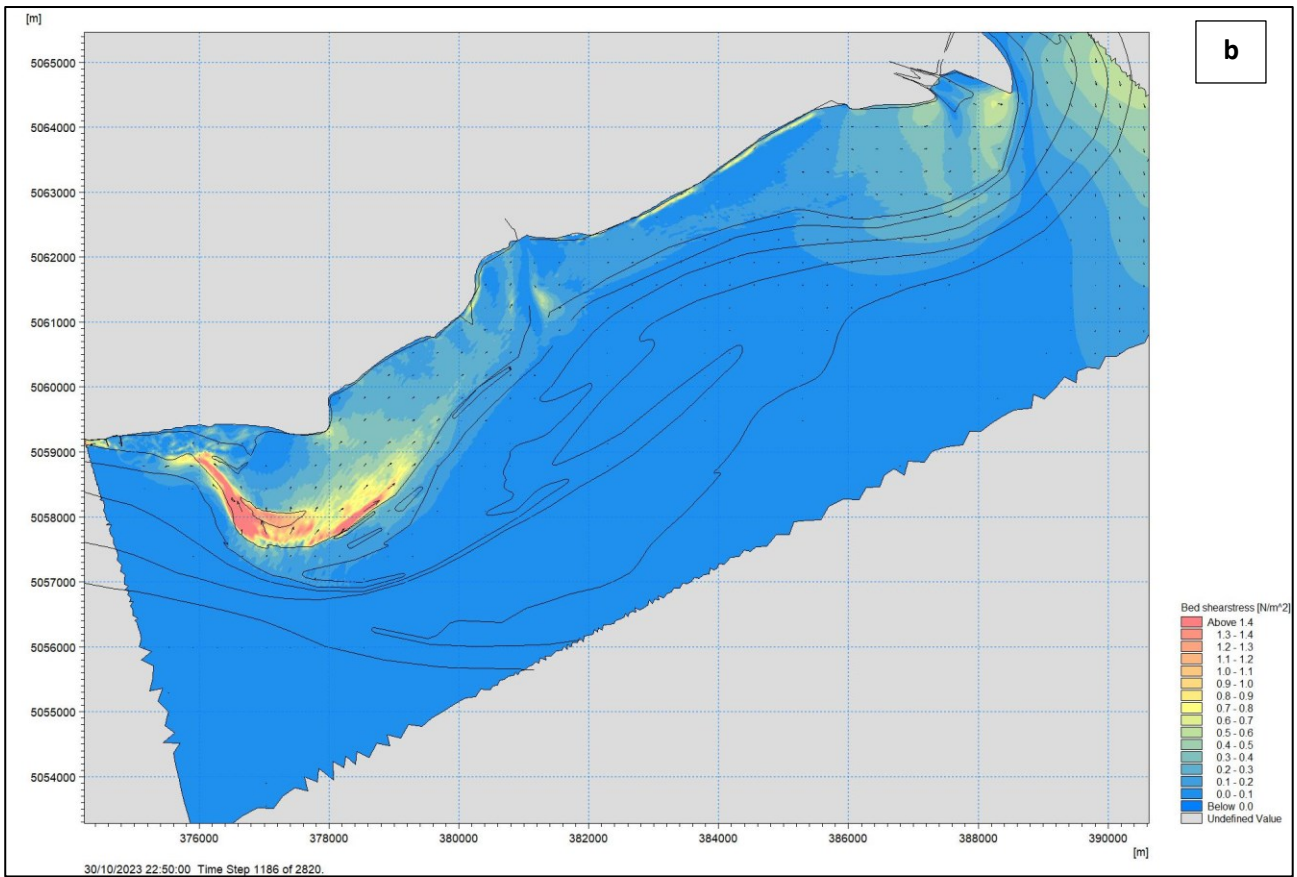


Figure 79 MIKE21 model outputs of the event between 30 and 31/10/2023: (a) Hs and (b) BSS at 22:50 on 30th October and (c) at 2:45 on 31st October.

The 30/10/2023 event is quite similar to the 27/10 event for both H_s and BSS distribution (Figure 79a and b). During the night, wind turned from SSE (166°N) to SSW (210°N) at Paloma buoy, leading to a clockwise rotation of waves on the study area, resulting in a high BSS on the deep-MMB, particularly on the western side. In the area of the deep terrace and the longshore transport pathway the BSS is northeastwards.

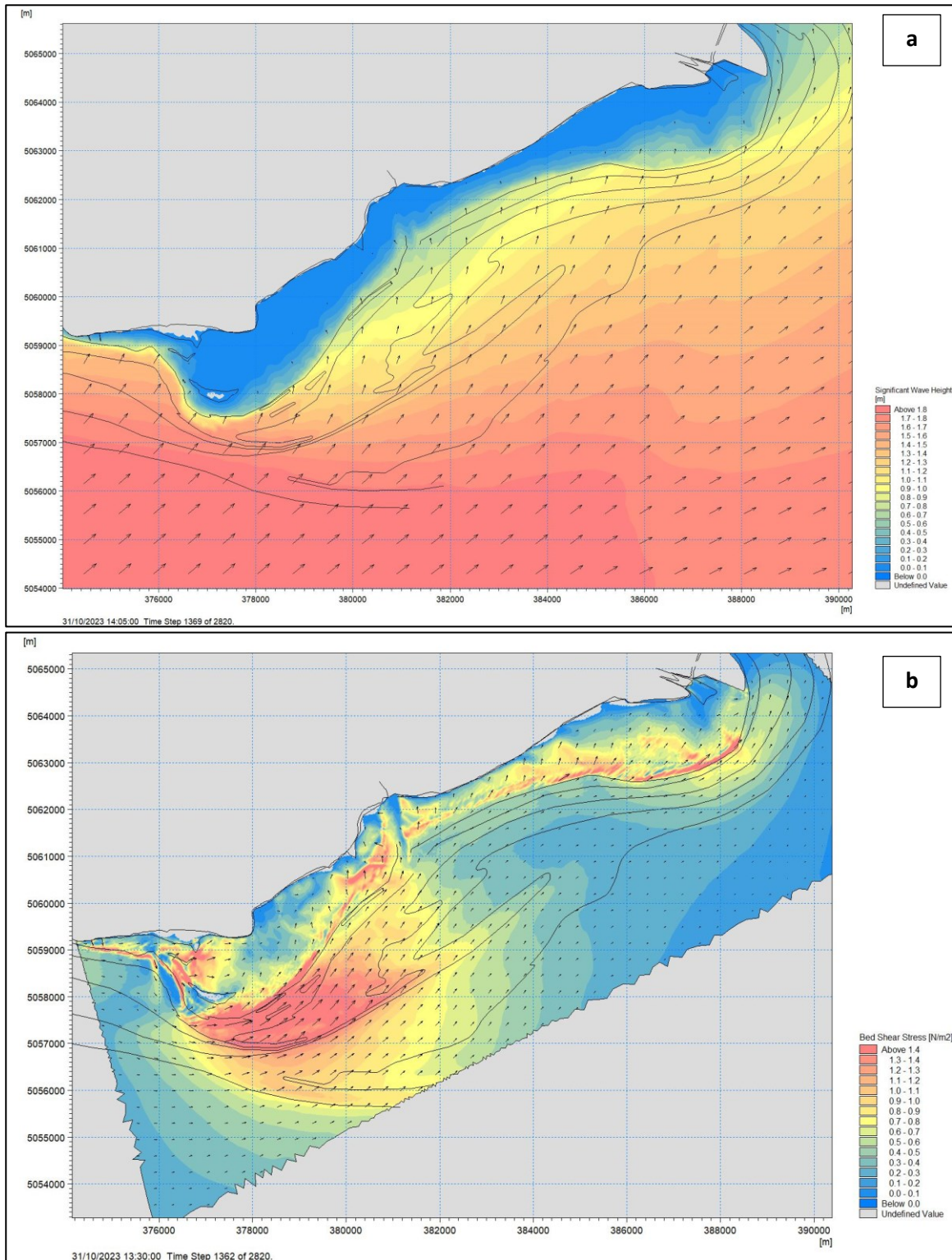


Figure 80 MIKE21 model outputs of the 31/10/2023 event: (a) H_s and (b) BSS.

During the 31/10/2023 event, SSW waves maintain high H_s also east of the southern vertex of MMB, with a progressive landward damping (Figure 80). BSS are high on the D-MMB and the longshore transport pathway while is lower in the F-MMB if compared to SSE events (27-30/10/2023). BSS at 12:35 is very high also on the Isonzo's delta, although the apex of the event did not occur at that time, due to the rapid drop in water level caused by spring tidal cycle.

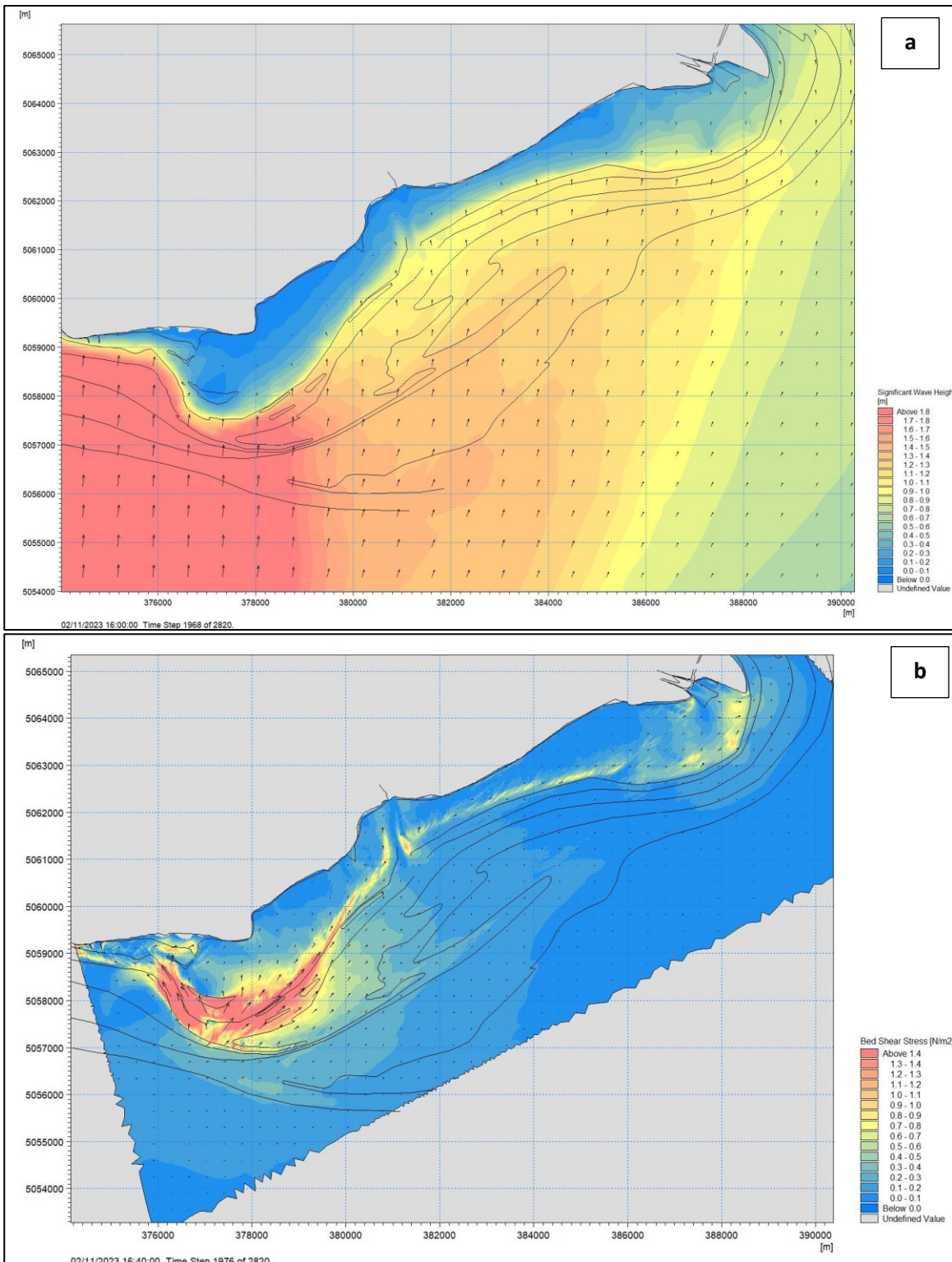


Figure 81 MIKE21 model outputs of the 02/11/2023 event: (a) H_s and (b) BSS.

The event of 02/11/2023 has almost the same characteristics as that of 27/10/2023.

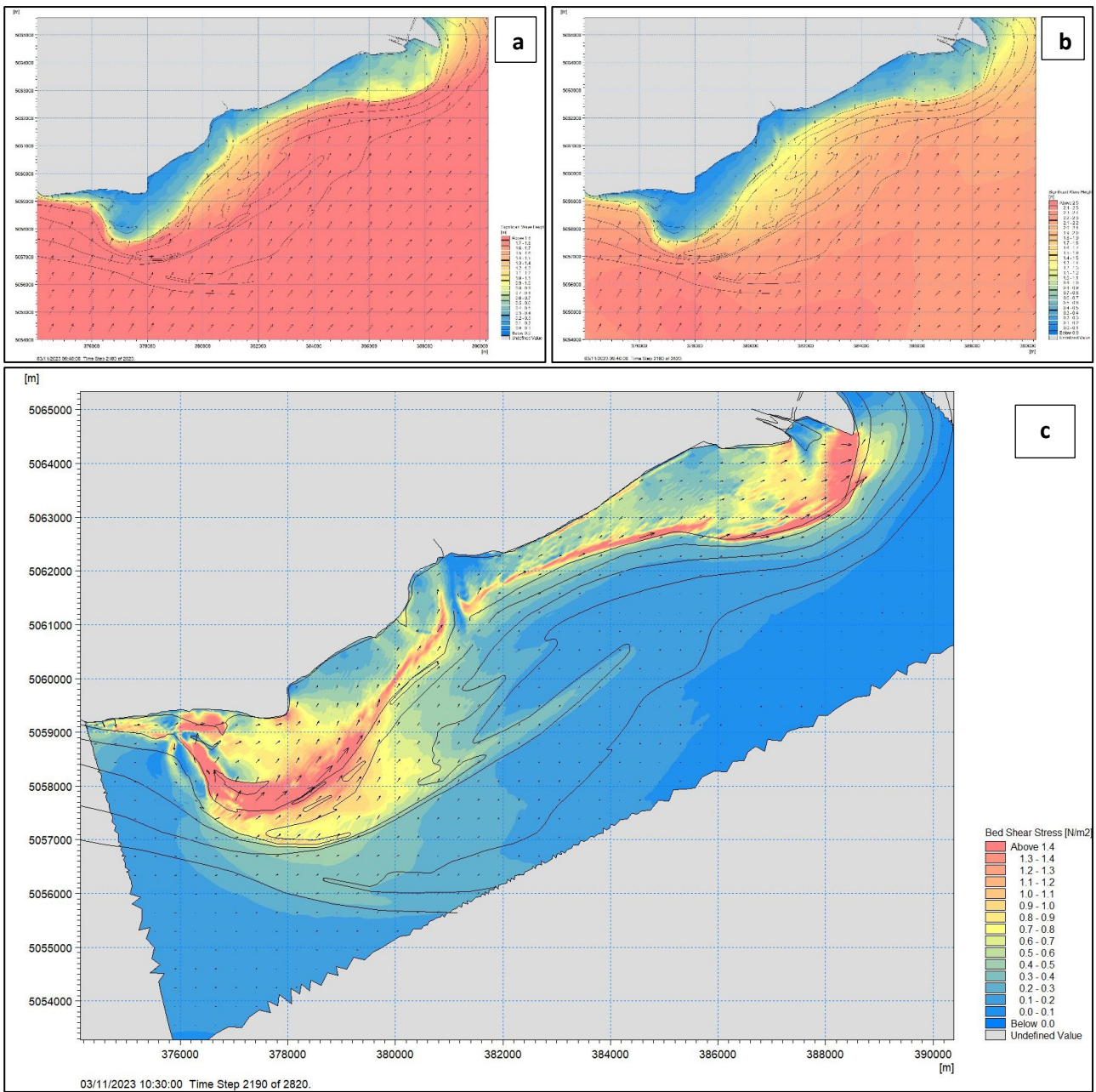


Figure 82 MIKE21 model outputs of the first event of 03/11/2023: (a) H_s with standard palette, (b) H_s with different palette and (c) BSS.

During the first event of 03/11/2023 high H_s values are higher than the previous storm events, leading to the use of a second palette with higher H_s classes. As it happened for the 31/10 event, SSW waves produce a less damping of the H_s towards the east compared to SSE storm events. On the other hand, BSS distribution is a mix between 31/10 and 27/10 events, with average values on the deep terrace area and the highest value on the HIB and the longshore transport pathway. Differently from SSE storms, BSS divergence point on the southern vertex is migrated westwards.

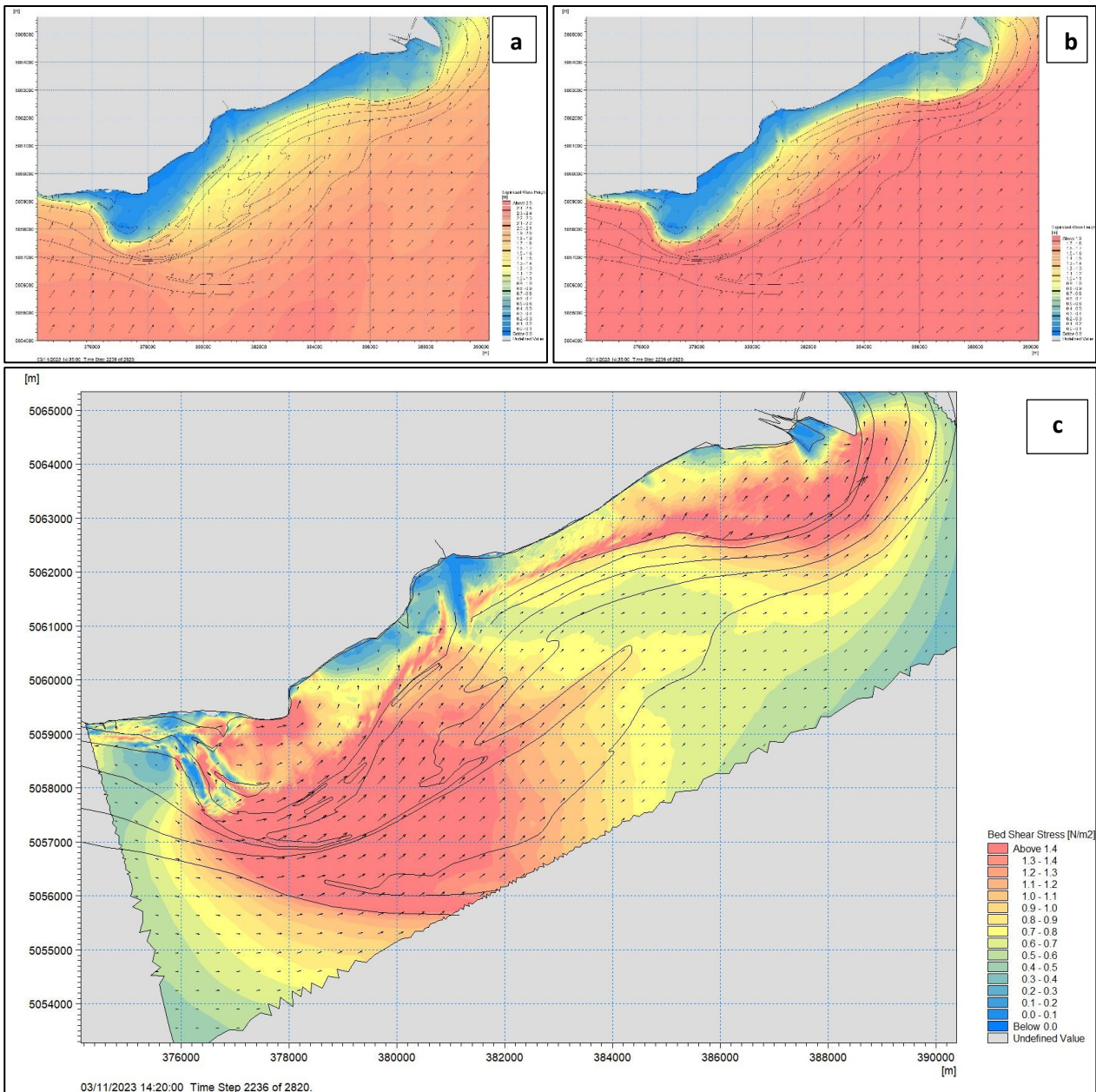


Figure 83 MIKE21 model outputs of the second event of 03/11/2023: (a) Hs with standard palette, (b) Hs with different palette and (c) BSS.

The second event of November 3rd is the main event of the whole series from SSW in terms of Hs (Figure 83a), with values greater than 1.8 m on most of the study area. BSS is greater than 1.4 N/m² on the most part of the D-MMB, damping slightly towards the northeast (Figure 83c). BSS is focalized on the deep bars and decreases a bit in the trough between them. BSS is high on the shallow area of the Isonzo's delta too.

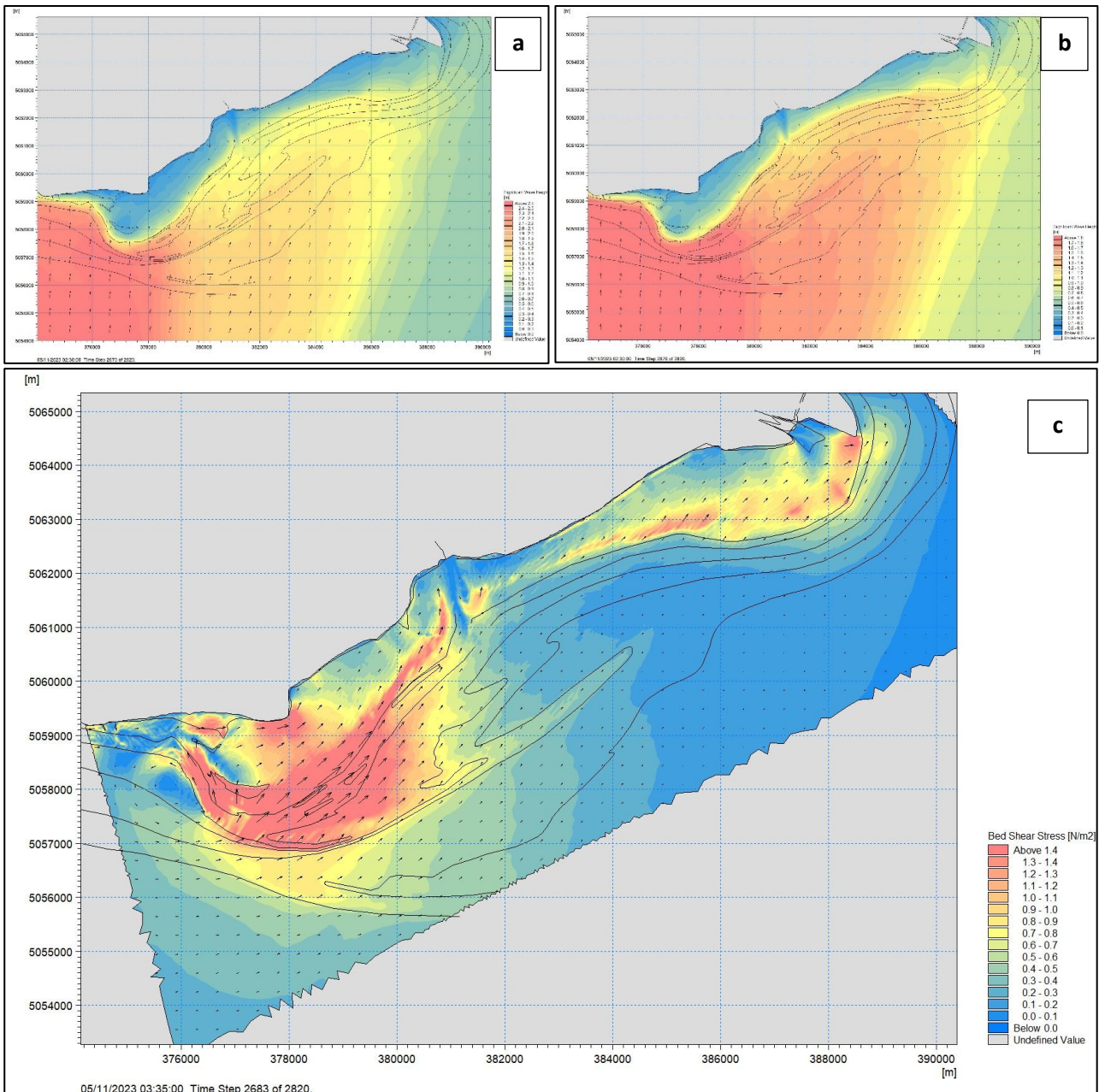


Figure 84 MIKE21 model outputs of the event of 05/11/2023: (a) Hs with standard palette, (b) Hs with different palette and (c) BSS.

The event of November 5th was the greatest in term of Hs recorded at DWRG1 buoy (3.77 m). The Hs is very high in the western sector up to the southern summit and tends to progressively dampen towards the east as happens during other Sirocco events (Figure 84a, 73b). The HIB, the longshore transport pathway and the southwestern sector of the D-MMB are characterized by high BSS, with rather large values in the deep terrace area, between -3 and -5 m while it reduces significantly towards the northeast, although there is a focus on the bars over the morphological lows.

5.4.3 Models' summary

The two main storm events analyzed have rather different characteristics, both in terms of peak intensity and duration. To make their comparison more objective and to be able to estimate the cumulative effect of the

events themselves, the values of excess of BSS with respect to the critical BSS for suspension of sediment were extracted and summed over the entire duration of the events. By doing this, a value proportional to the suspension and transport of sediments on the seabed was obtained, thus being able to identify the most morphodynamically active areas.

The ENE storm proves to be quite active both in the area of the longshore transport pathway and in the deep terrace of the D-MMB while it is less effective in suspension of the sediment in the most north-eastern sector of the deep bars and in the area of the F-MMB and the HIB, particularly to the northwest (profiles 1F-6F) (Figure 85).

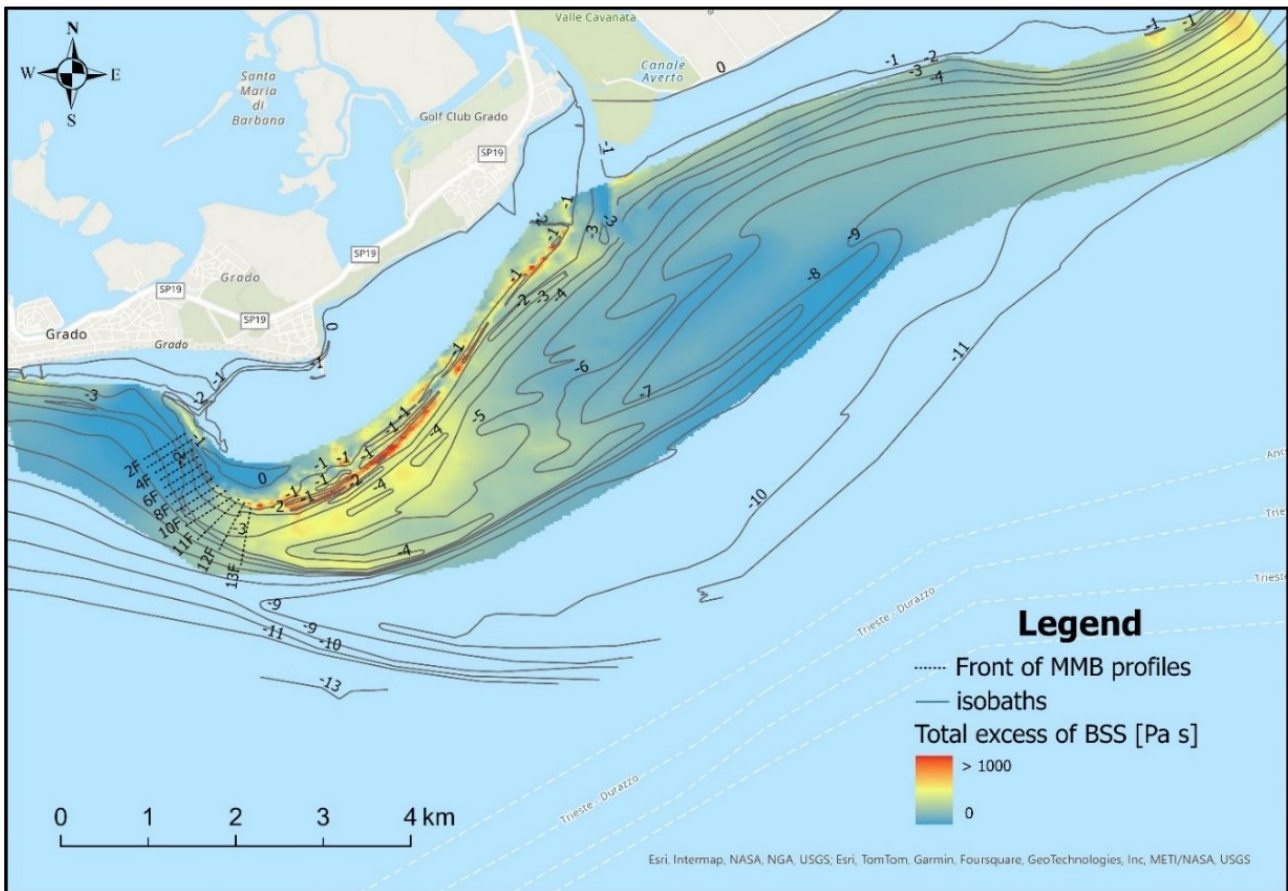


Figure 85 Total excess of bed shear stress during the storm event from ENE (Bora).

During this event, in most of the areas the bed shear stress is above the critical threshold for most of the time. The BSS is often below the critical threshold on the northeastern tips of the deep bars, on the F-MMB and on the HIB (Figure 86).

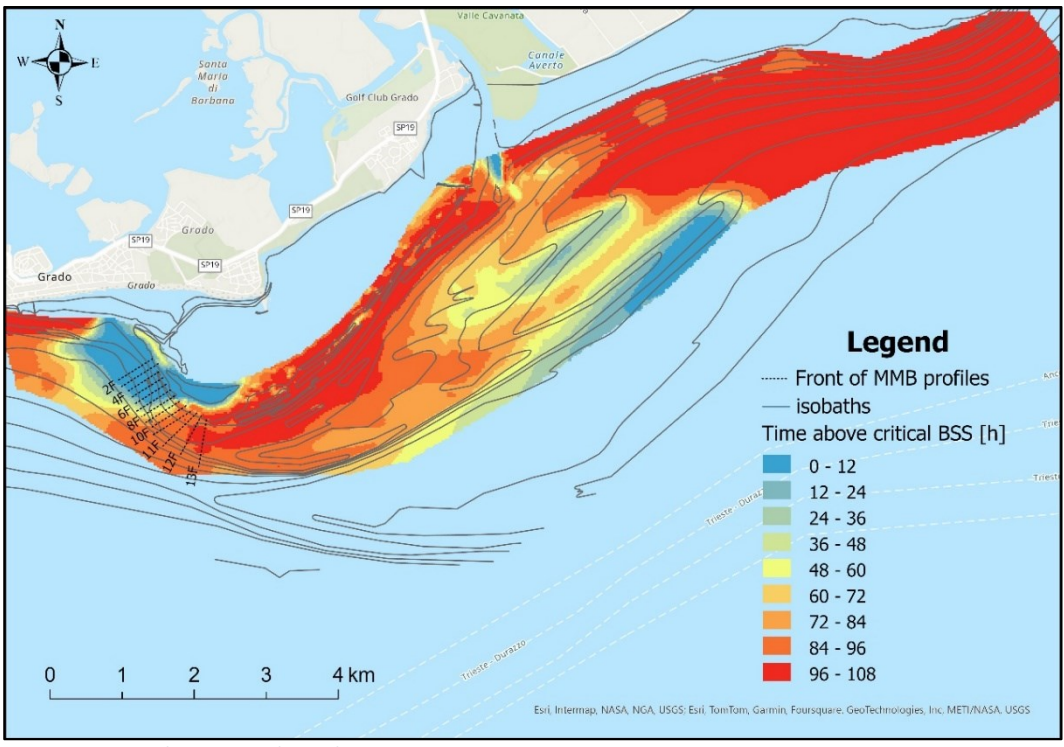


Figure 86 Time above critical BSS during ENE storm event.

The storm multi-event from the south (autumn 2023), characterized by series of intense peaks of H_s , is decidedly active in the area of the F-MMB, the HIB and the western sector of the littoral drift pathway above -3 m, and, while it has a lower impact on the western part of D-MMB (Figure 87).

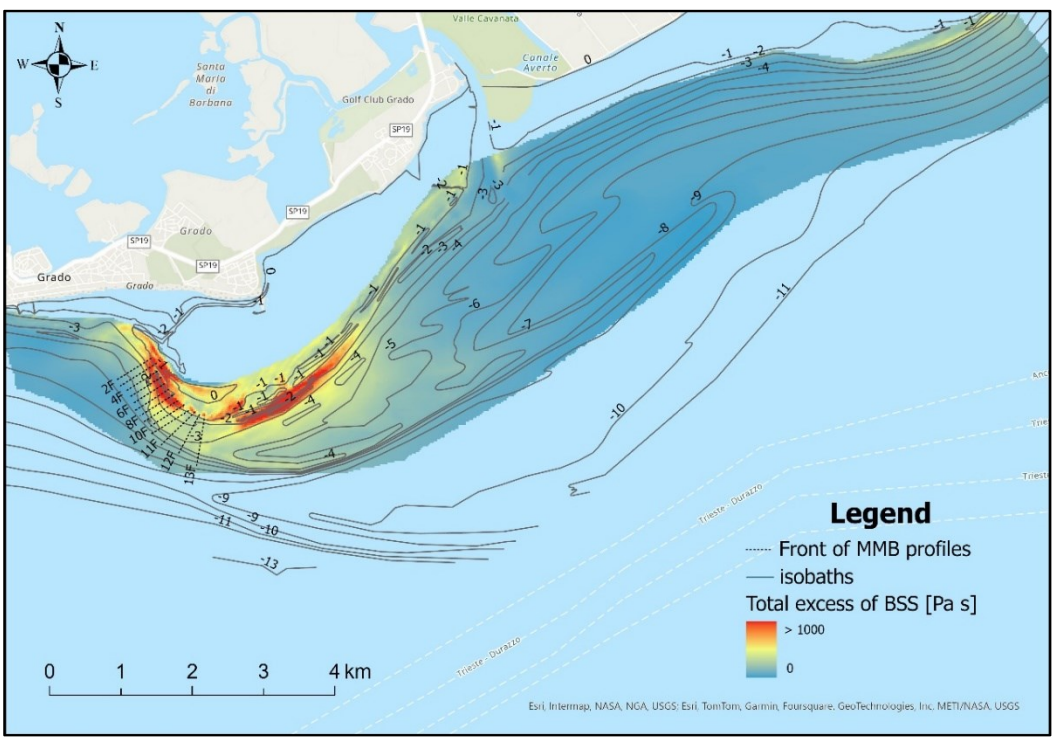


Figure 87 Total excess of bed shear stress during the storm multi-event from south (Sirocco-Libeccio).

Moreover, the BSS exceeded the critical threshold for suspension for most of the time during the event only on the western part of the MMB (F-MMB, HIB and western sector of the littoral drift pathway). On the deep

terrace BSS exceeds the threshold for almost a half of the time while on the tips of the deep bars the BSS is mostly below the critical threshold for suspension (Figure 88).

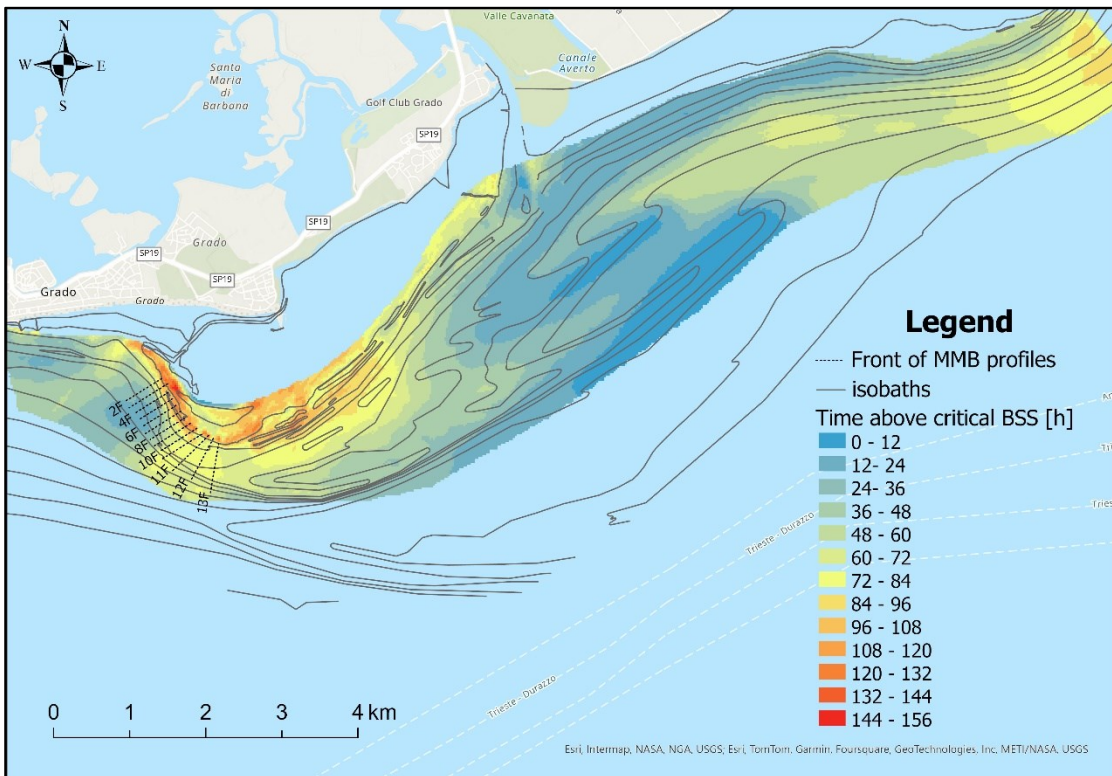


Figure 88 Time above critical BSS during southerly storm multi-event.

In order to compare the total effect of the two events, we calculate the ratio between the total excess of BSS during southerly and ENE events (Figure 89). The total excess of BSS is greater for the Bora event on the Isonzo's prodeltaic area, on the eastern part of the longshore drift pathway and on the western part of the D-MMB while Sirocco and Libeccio waves are more effective on the F-MMB, the HIB and the tip of the deep bars, particularly the outer. On deep bars, the two events have different effects. Analyzing the outer deep bar, the Bora is able to generate an excess of critical BSS mainly in the south-western sector while going towards the north-east the value reduces very quickly. In southerly events the BSS reduction gradient is lower, giving rise to a greater effect on the north-eastern tip of the bar during SSW events. On the inner deep bar, both the Bora and Sirocco hydrodynamic models predict a lower BSS than the outer one, while maintaining the reduction gradient towards the northeast.

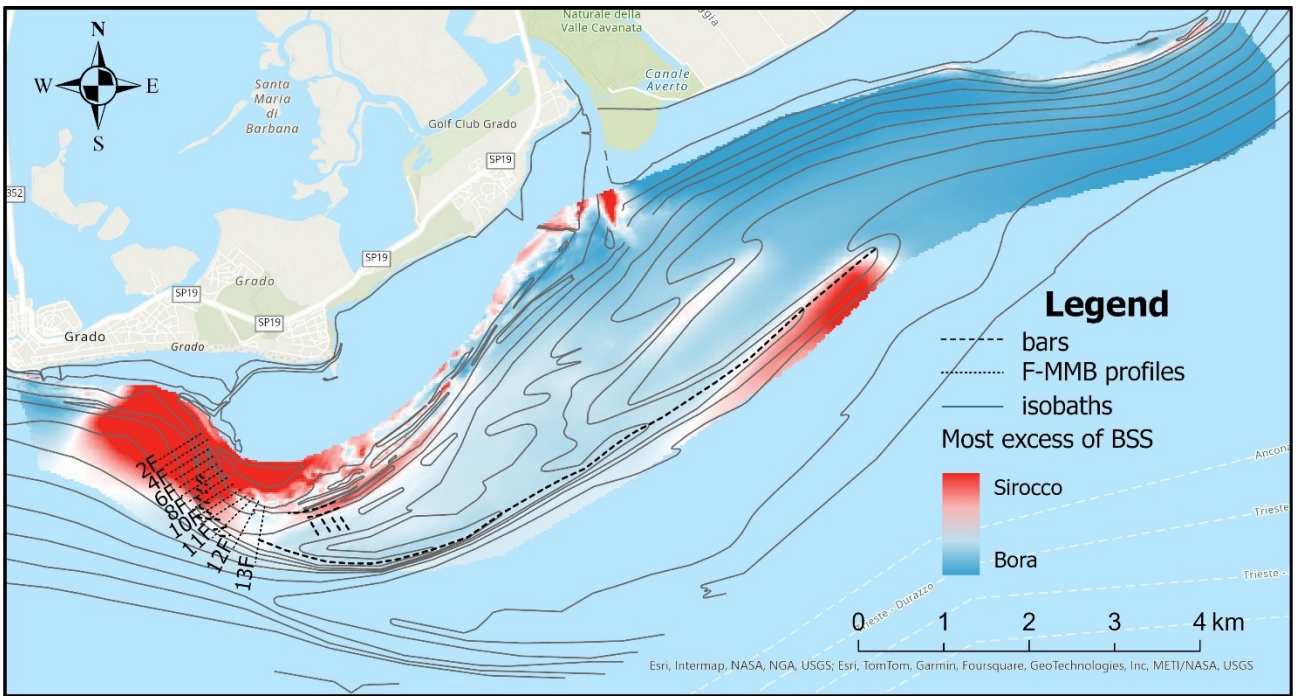


Figure 89 Map of the ratio between the total excess of BSS during southerly and ENE storm events.

In addition to the hydrodynamic models of main storms, further models were developed in non-extreme sea conditions: one event with waves from the ENE, one from SSE and one from both directions. Even in not-extreme wave conditions (H_s max of 1.46 m), the ENE waves maintain the same BSS distribution: the longshore transport corridor is quite active, as is the south-western area of the deep terrace while on HIB and F-MMB the BSS is much lower (Figure 90).

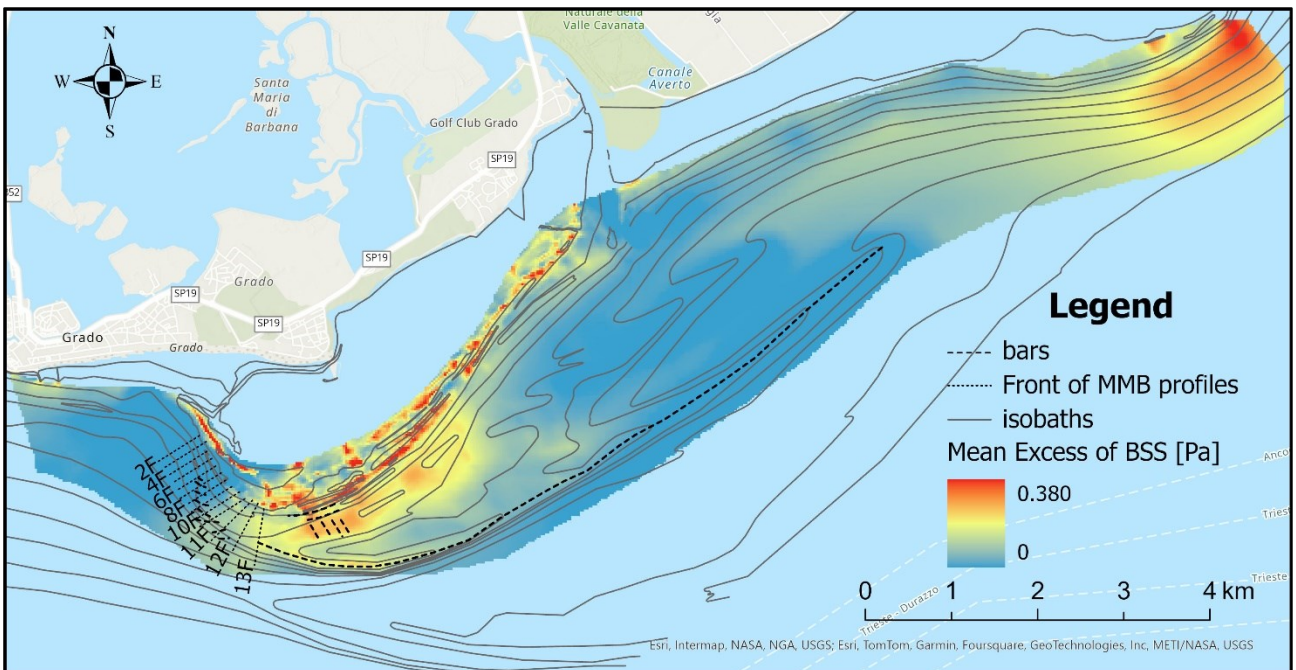


Figure 90 Mean excess of BSS during ENE not-extreme event.

In the case of southerly waves, the model shows different scenarios (Figure 91). The reworking of the sediments due to the exceedance of the critical BSS is active in the south-western portion of the D-MMB and

along the most superficial part (depth below -1 m) of the edge of the MMB, on the border with silty backbarrier.

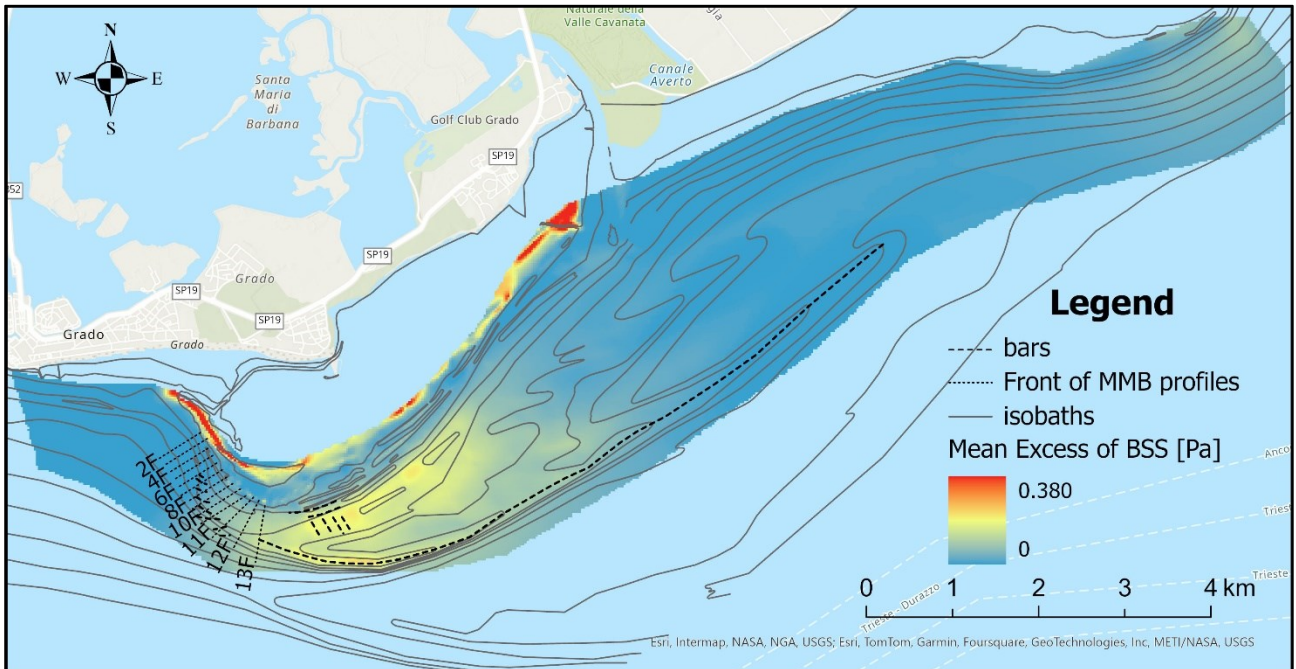


Figure 91 Mean excess of BSS during Sirocco not-extreme event.

When H_s is less than one metre, the critical BSS is exceeded mainly on the north-western tip of the HIB (Figure 92).

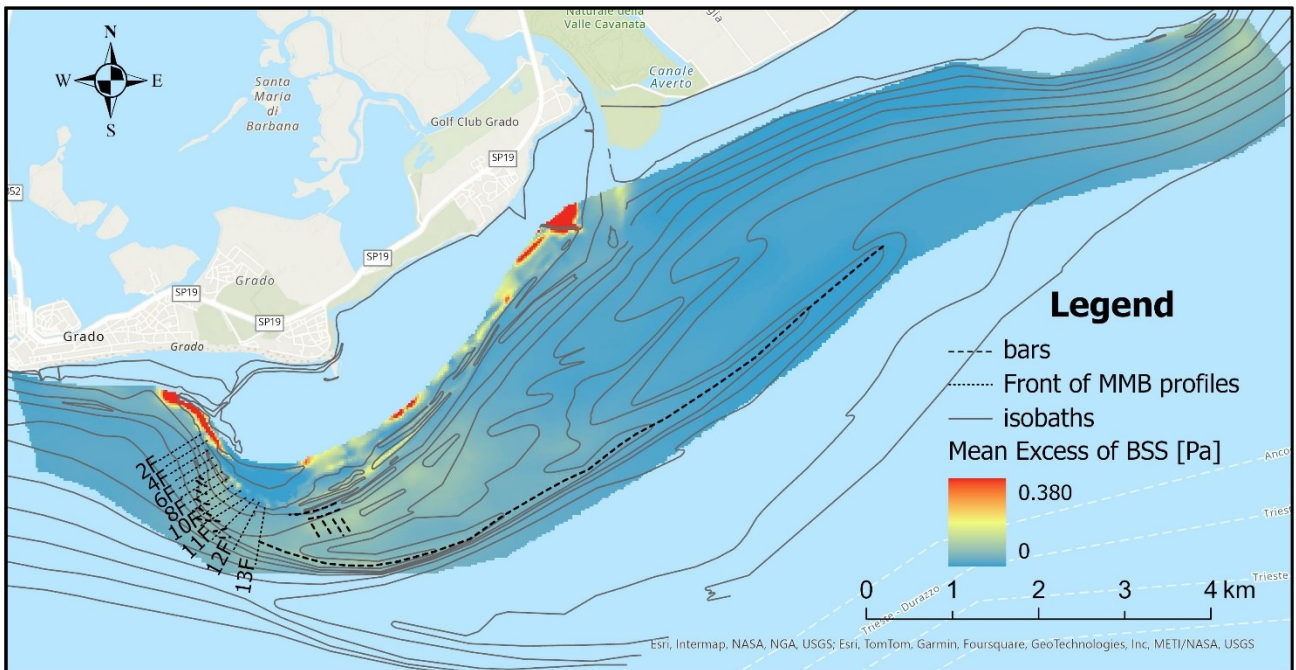


Figure 92 Mean excess of BSS during mixed not-extreme event.

In the map of the ratio between Bora and Sirocco not-extreme storms the dominance of one wave-direction with respect to the other is evident (Figure 93). Bora wave-generated BSS is dominant on the Isonzo's prodeltaic area, on the longshore drift pathway up to the southern vertex and on the deep terrace. On the other hand, Sirocco waves produce a greater excess of BSS on the deep bars, on the HIB and the F-MMB.

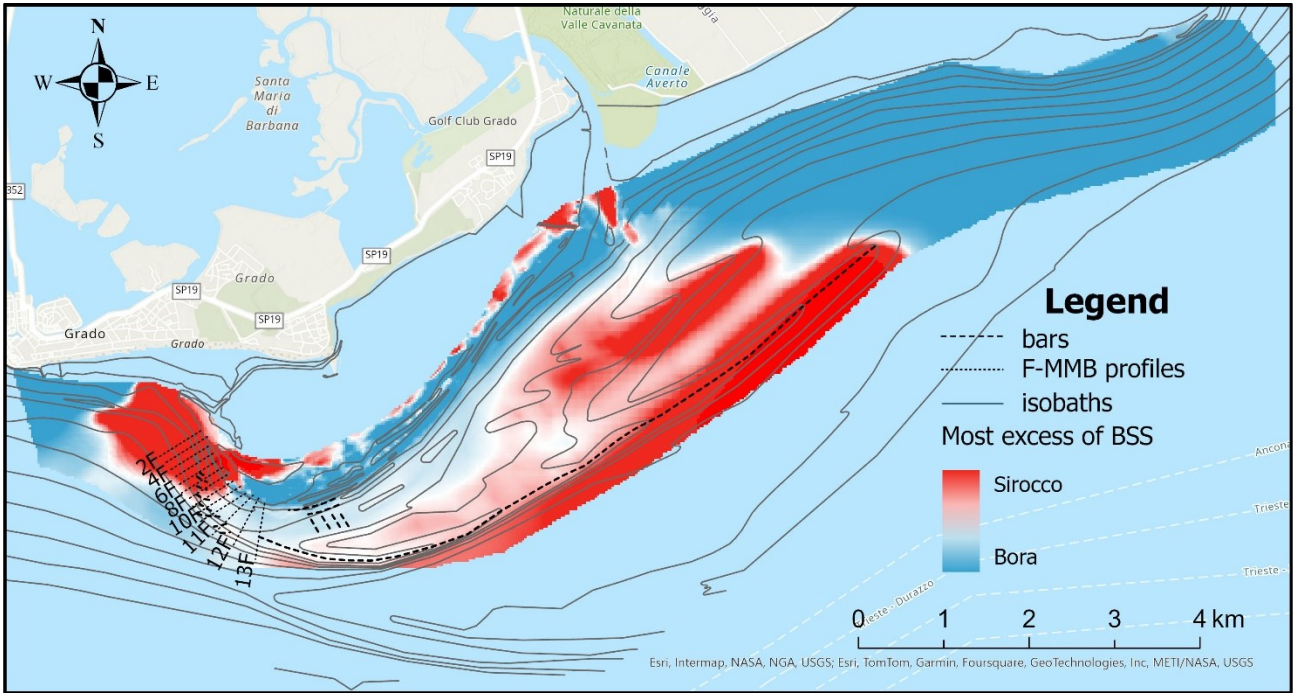


Figure 93 Map of the ratio between the total excess of BSS during southerly and ENE not-extreme events.

6 Discussion

In seventh chapter, the SAIM method for obtaining sedimentological maps will first be discussed and analyzed, comparing it with other geostatistical algorithms. Subsequently, the five most characteristic areas of the study region—namely the Isonzo River delta, the longshore transport pathway, the D-MMB, the F-MMB, and the HIB—will be examined from a morphodynamic perspective, with a focus on the main morpho-sedimentary aspects of each zone. Finally, the interconnection between the knowledge of the morpho-sedimentary dynamics and the urban context will be discussed, analyzing the critical issues in response to changes and potential adaptation strategies.

6.1 Methodological analysis: Geostatistical vs SAIM

Before analysing the sedimentological maps produced, it is necessary to compare the results obtained from the application of automatic geostatistical methods with the semi-automatic SAIM method. The sedimentological maps obtained with standard geostatistical methods present critical issues that cannot be solved through a specific parameterization but require additional adjustments by the operator in order to obtain reliable outputs.

Considering methods that do not provide explanatory variables two are the main criticalities which can be found (Figure 94): (i) the low evidence of longitudinal structures, such as the littoral drift pathway, the deep bars and the trough between the bars (Figure 94a), and (ii) the prodeltaic fine sedimentation area results coarser than expected (Figure 94b). In these areas, high (ii) and low (i) values of Mz are respectively reduced or increased, leading to a significant smoothing of the Mz distribution as found by other authors (Bockelmann et al. 2017; Jerosch 2013). In the presence of high Mz gradients, these methods are not able to produce the desired output. If we focus on samples G79 and G80 (Figure 95), they have significant differences in Mz because they are part of different structures (morphologically low and high, respectively), although very close. EBK and even more OK almost obliterate the information provided by these two samples, mixing the values of Mz and producing very low gradients between them: this way, the inner deep bar and the western branch of the prodelta are badly or no represented.

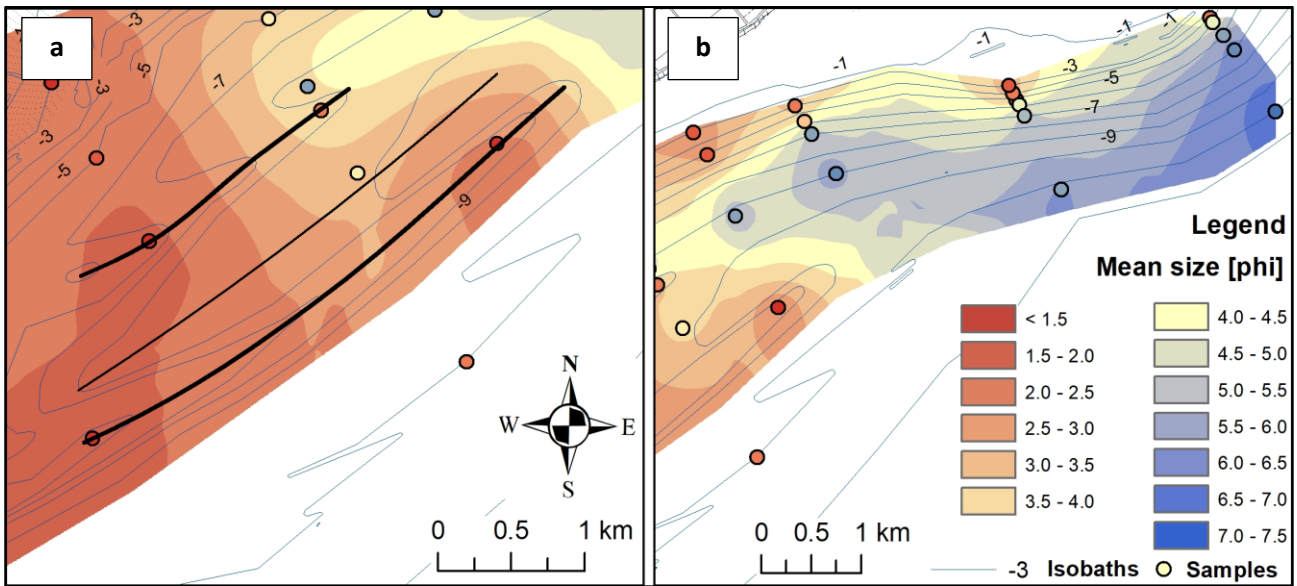


Figure 94 Criticalities in the MZ distribution of pure geostatistical maps. (a) An example of incongruities between MZ distribution and geomorphological set-up and (b) coarser than expected prodeltaic area.

Moreover, even the parametrization has significant impact in the creation of better maps, in particular for kriging algorithm. The two maps proposed (Figure 63 a and b) are the best obtained after many tests to reach the best output. For these reasons, the use of pure geostatistical approach may become critical also from the time-consuming point of view.

On the other hand, the integration of bathymetry in the geostatistical algorithms increases the model's concordance with the morphological set-up (chapter 3.7); moreover, with regard to EBKRP, even the errors, both average and maximum, are significantly lower (Figure 65). That, on the one hand supports the choices made in the SAIM method for the creation of polylines, but on the other it could make the SAIM method itself less necessary. However, CK and even EBKRP are not free from issues, although less relevant. First, the outer deep bar presents a thinning gradient towards the north-east which is not confirmed by the samples that are rather homogeneous as regards the Mz (Figure 95a). Furthermore, even in these models, the inner deep bar, and the western branch of the prodelta just north from the bar are not correctly represented: the Mz gradient between them is lower than expected, producing a smoothing, even if less pronounced than in the OK and EBK. Finally, while models generated only from the sediment sampling dataset are very similar, EBKRP and CK, even if they use the same explanatory variable, are not that alike: if, on the one hand, CK qualitatively better represents the continuity of the deep bars, on the other hand the prodelta seems to be too coarse if compared to the geomorphological interpretation and the continuity of the deep trough towards south-west is not as long as expected.

From a quantitative point of view, the error statistics showed in Figure 65 evidence the improvement obtained using SAIM. The reduction in mean absolute error is about 46% and is similar if compared to geostatistical with (44%) or without (48%) explanatory variables. This trend is confirmed by standard deviation and maximum error reduction, with average improvement of 46% and 47% respectively. In other words, the SAIM

errors seem to be reduced by half with respect to the standard geostatistical approaches. If we do not consider the EBKRP, an advanced algorithm rarely present in GIS software, the reduction obtained with SAIM is on average 52% for the mean absolute error, and 57% for the maximum absolute error and the standard deviation. The greatest goal obtained is about the containment of the maximum absolute error: it is the parameter that most influences the reliability of the model obtained. A certain variability of Mz is intrinsic in the nature of sedimentology even on samples collected in the same place, therefore a certain average discrepancy between sample and model is absolutely natural: the 0.3 ϕ mean absolute error of SAIM is hard to improve. On the other hand, very high maximum errors indicate a significant discrepancy between model and reality, which translates into erroneous interpretability of morphodynamic and sedimentological processes and, regarding to engineering and modelling applications, can lead to significant computational errors. From this perspective, maximum absolute error becomes an indicator for the quality of the model while standard deviation indicates its stability.

If we analyse geostatistical algorithms, they tend to behave in the opposite way when they are applied only to collected samples or in the SAIM. In the firsts, kriging produces the highest errors, while, if used within the SAIM, EBKRP seems to be the worst algorithm. In particular, EBKRP seems to produce maps with similar errors if used within SAIM. This can be explained by considering the nature of the algorithm, which, using the DTM as a secondary variable, continues to maintain the effect of this variable also in the SAIM, making the effect of the simulated samples less impactful on the final model. On the other hand, kriging, which is influenced only by Mz data, is more affected by the forcing generated by simulated samples. One common trend in any model obtained, both with and without SAIM, is the low error values in the western part of the study area (Figure 63 and Figure 64). Here, because of the higher sampling density and the less presence of unique elongated structures, geostatistical algorithms can produce reliable models by themselves, and SAIM forcing is not necessary.

The irregular sample mesh is the main source of disturbance for the interpolation with geostatistical automatic methods. Because of this, many elongated structures are not properly represented by the samples and their evidence may be visible only from other sources of data (e.g., aerial photos and bathymetry).

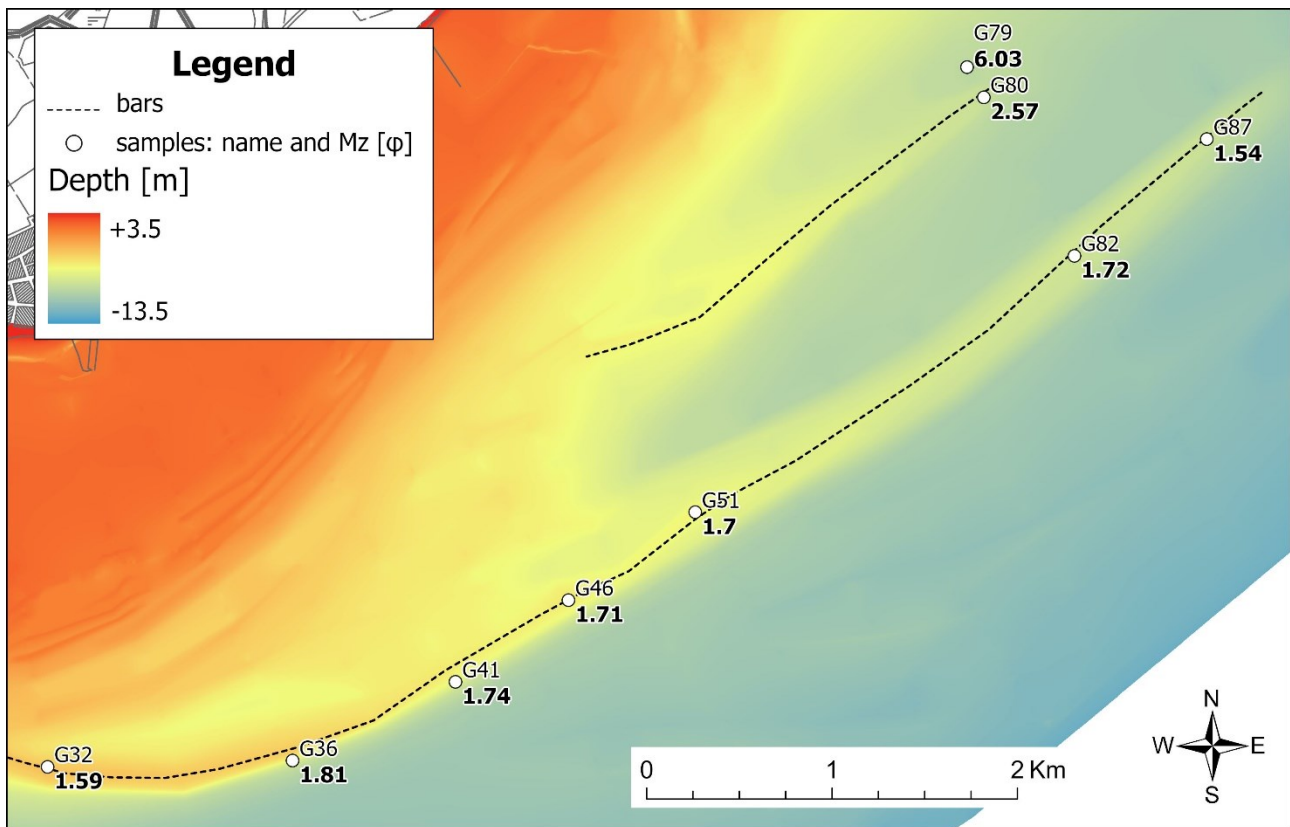


Figure 95 Samples on the outer deep bar: their Mz (bold) is almost homogeneous along the structure.

The effect of the anisotropy of both sample mesh and landforms is the cause of discontinuity of Mz distribution over the longitudinal elongated structures, mainly for approaches without explanatory variables. Over the outer deep bar, also due to one missing sample along the bar between samples G51 and G82, geostatistical approaches without explanatory variables are not able to interpret a uniform structure, as it shows to be from a geomorphological point of view. Despite being widely spaced, the samples aligned along the bar (Figure 95) show substantial Mz uniformity, confirming the geomorphological evidence and the same origin. Even EBKRP and CK models, which use bathymetric information, predict the presence of geomorphological signature on the Mz distribution on the outer deep bar, validating the geomorphological interpretation, although, by interpolating the sedimentological data with the bathymetry, they describe a gradient that is not highlighted by the samples themselves. The littoral drift pathway and the fine sedimentation prodeltaic area present almost the same issue than the outer deep bar, connected to the anisotropy of sample distribution. The inner deep bar issue is related to the presence of two close samples, G79 and G80 (Figure 95), with a Mz of 6.03 ϕ and 2.57 ϕ respectively. Even if they are one closer to the other, the great difference in Mz between them of almost 3.5 ϕ indicates that they have not the same origin. It is confirmed by the geomorphological set-up: sample G79 is located in a depressed area just north from the bar where G80 is located: so, the first is subjected to the prodeltaic fine sedimentation while the latter has a residual origin. Unfortunately, the proximity of these samples causes the automatic interpolation algorithms to homogenize the Mz values, estimating finer sediments over the bar and coarser over the depressed area. Moreover, the trough between the bars has almost no signature on the Mz distribution in OK and EBK. That

is related to the presence of only sample G81 on it. Because of the lack of other samples, it's simply impossible for the automatic interpolation algorithms to produce a Mz-coarsening trend towards south-west as supposed from a geomorphological point of view. This interpretation is only correlated to the geomorphological set-up and the bimodality of sample G81 and not confirmed by other sedimentological evidence, but models with explanatory variables, in particular the EBKRP, depict the same interpretation obtained by expert judgment. A high degree of anisotropy in the interpolation radius could partially solve these two issues, with the side effect to produce issues in areas with no geomorphological anisotropy. If we focus on the EBKRP model, which is definitely the most reliable among the models developed with automatic algorithms, the main issues are all correlated to the side effects given by the DTM. This model tends to produce a gradient following the bathymetry even if the Mz shows to have a different trend: for example, the outer deep bar seems to be homogeneous in Mz while EBKRP model is characterized by a fining gradient towards the deepest depths; or the inner deep bar that seems to be not continuous. Because of this, although mean and max errors are the lowest for automatic algorithms, the standard deviation is quite high and remains so even when EBKRP is applied in SAIM. The SAIM models, due to the very nature of the SAIM, follow better the geomorphologic set-up (chapter 3.7). Furthermore, the error statistics also show a significant reduction in them. This involves two main findings:

1. as also confirmed by the algorithms with explanatory variables, the use of bathymetric information greatly improves the quality and reliability of the model obtained. In our study case, comparing geostatistical algorithms with EBKRP we observed a reduction of mean absolute error, max absolute error, and standard deviation by 21%, 39% and 11% respectively.
2. secondly, further improvement can be achieved by expert assessment of the morphodynamics of the studied area, with a further reduction of mean absolute error (43%), maximum absolute error (31%) and standard deviation (54%) if best SAIM model (EBK) is compared to EBKRP.

Comparing SAIM with the EBKRP, the best automatic geostatistical algorithm, the SAIM method has the great advantage of being able to provide the geomorphological interpretation, not only binding it to the joint effect of parameter distribution and explanatory variable but leaving the interpreter to make the most coherent choice for him. Finally, comparing each SAIM outputs (Figure 64) and their error statistics (Figure 65), they show to be quite similar. In particular, referring to Figure 65, the stability of the mean absolute error and the low magnitude of the maximum one denote a marked robustness of the SAIM on the choice of the geostatistical algorithm, and, indeed, it seems to work slightly better with simpler algorithms. SAIM is therefore flexible and applicable on different GIS software with geostatistical interpolation algorithms.

Summing it up, the SAIM, shows to be an economical and tuneable method in terms of time and costs to produce good sedimentological maps even with a sparse and irregular sampling. Compared to the standard interpolation methods, provides models that better represent the geomorphological imprinting on the

sedimentological data and reduced the error of prediction. None of the maps obtained only by the standard methods was able to adequately represent all the sedimentary dynamics of the study area.

6.2 Morphodynamic interpretation

In order to discuss and highlight the morphodynamic set-up of the study area, we will focus on five important coastal compartments: the Isonzo river delta, the longshore transport corridor, the deep part of the Mula di Muggia bank, the front of the MMB and the high intertidal bank.

6.2.1 Isonzo River delta

Sedimentologically, the distribution of the Mz (Figure 96a) follows the standard trend of deltaic environments, with the sands confined in the upper shoreface (here within -4 m) and the muddy sediments constituting the entire prodelta. Although the sediments of the area are very or extremely poorly sorted (Figure 96b), particularly in the prodelta, due to the correlation with the Mz, the normalized sorting (Figure 96c) is quite good, especially around the river mouth and along the littoral drift corridor (above -4 m). These grain size characteristics confirm the dominance of fluvial forcing in the morphodynamics of the area.

The sediment budget of the Isonzo river delta remained rather stable in the period 2019-2022, unlike what happened in the period 1968-2019, since it has always been accumulating (Interreg Italy-Croatia CWC, 2021). However, already between 2007 and 2019 the delta growth rate had reduced compared to the previous period. In fact, on the only section surveyed in each campaign (transect 1D, Figure 58), the sedimentation rate progressively reduced from +19 mm/y (1968-2007) to +13 mm/y (2007-2019) up to +11 mm/y (2019-2022). The prodeltaic area (below -4 m) behaves quite differently from the shallow area around the mouth: in fact, the total sediment budget, estimated in +42'400 m³/y, is almost 2.5 times greater than the entire delta (+18'600 m³/y) (Table 7 and Table 8). This data highlights the extreme variability of the nearshore budgets, which are strongly influenced by the seasonality of the surveys. Additionally, the very short time interval is significantly affected by the intrinsic measurement error.

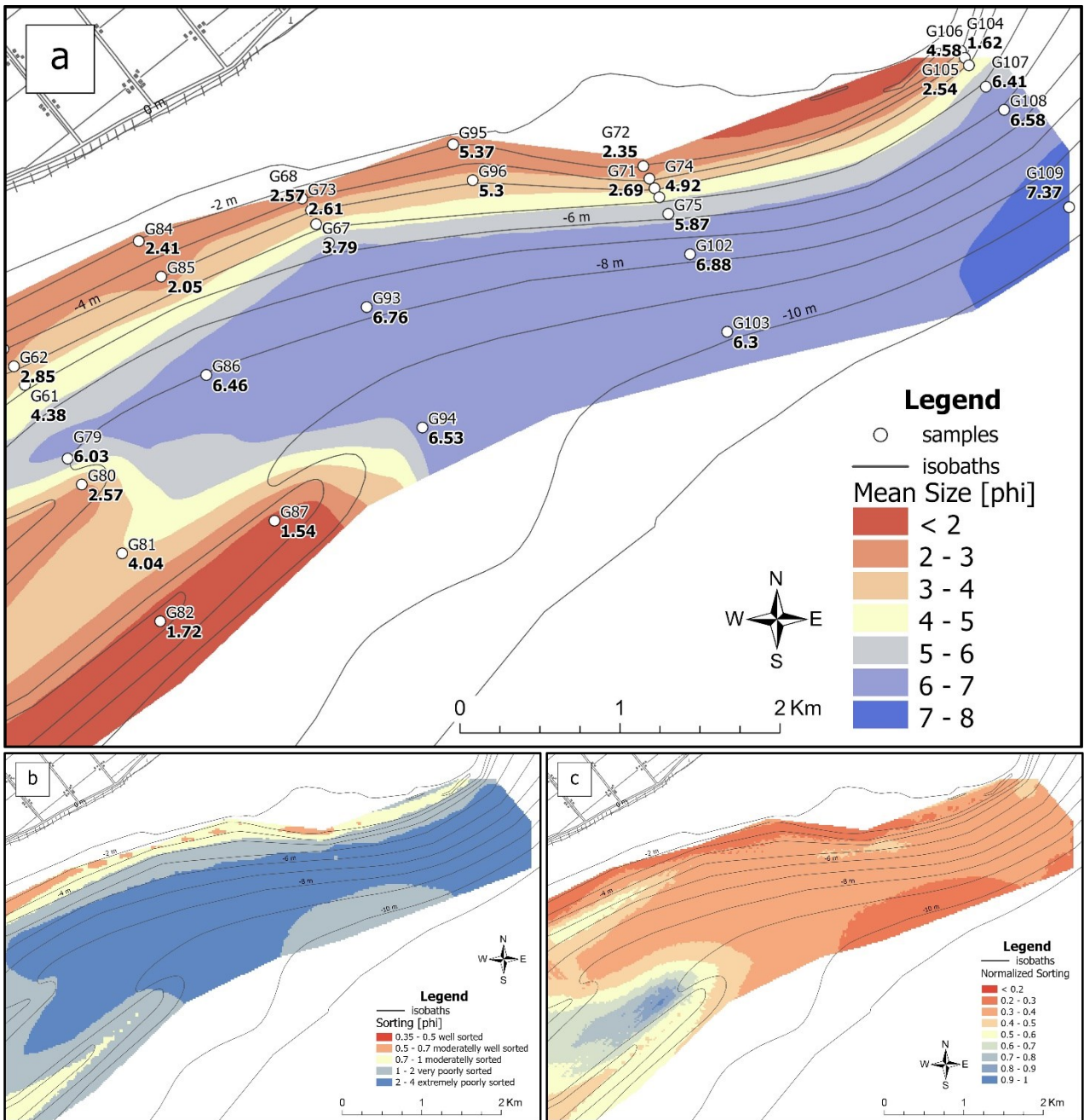


Figure 96 Detail of the (a) mean size, (b) sorting and (c) normalized-sorting maps of the Isonzo River delta.

Precipitation statistics (Figure 14) have shown to be quite stable in last 20 years although a significant annual variability has been observed (standard deviation around $\pm 20\%$). Therefore, although there are no accurate estimates of the solid discharge at the mouth, it can be estimated that there has not been a significant reduction in the sediment supply caused by the reduction of water fluxes. Then, a possible cause for the reduction in the sediment supply in this area can be identified in the achievement of a new condition of stability of the delta following the instability generated by the reopening of the Sdobba branch as the only mouth of the Isonzo starting from 1937 (De Grassi and De Grassi, 1957). Additionally, on a regional scale, the sediments from the Isonzo delta are carried by longshore drift and transported along all the sandy coasts of Friuli Venezia Giulia, establishing a sediment bypass dynamic in the deltaic area. The long-term positive

sediment budget of the F-MMB, estimated in almost $+60'000 \text{ m}^3/\text{y}$ since 1968 (Fontolan et al. 2018), suggest that F-MMB could currently be the main sink in the study area and, more generally, in the coastal context linked to the Isonzo solid discharge. Therefore, our hypothesis is that the volume of sediment taken up by littoral drift may have remained stable also in the short term.

Morphologically speaking, the most dynamic area of the Isonzo's delta is the shallow area around the mouth. In fact, this area underwent a significant geomorphological evolution even though the sediment budget in that area is slightly negative. The SBES survey evidenced a retreat of the sandy bars in the shallow waters within -2 m. Such a similar trend was also identified through the UAV surveys on the HIB as a result of a rollover effect (Figure 41).

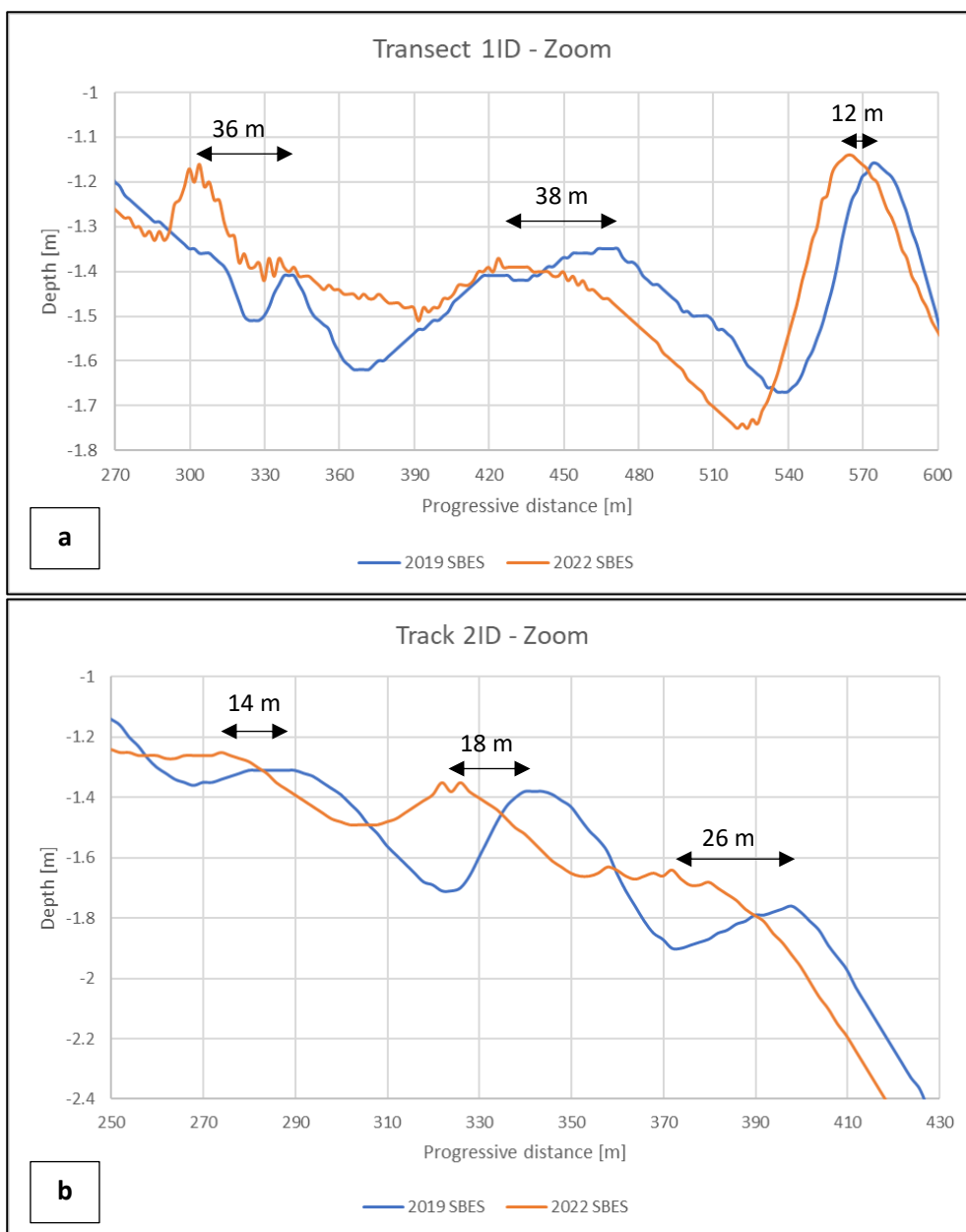


Figure 97 Bar retreat on the Isonzo river mouth at transects (a) 1ID and (b) 2ID.

The sandy bars visible in the two western transects of the Isonzo's delta (1ID and 2ID) migrated averagely -24 m landward in 3 years, with a rate of -8 m/y (Figure 97). The average End Point Rate of -10.8 m/y evaluated through the DSAS tool shows that the HIB behaves quite similarly to the Isonzo's delta, although the rate of retreat ranges from -2.8 to -17.9 m/y is very wide (Figure 42). Marine transgression and consequent retreat of coastal landforms is usually the geomorphological response to some coastal processes such as relative SLR and storm events (Bezzi et al., 2021b; Emery et al., 2019; McBride et al., 1995). However, over a very short time interval, it is more likely that the most impactful geomorphological changes are due to extreme events rather than RSLR, which, by nature, operates on a longer time scale. Additionally, over the past four years, the mean sea level in the northern Adriatic has slightly decreased, as a result of natural fluctuations. Such a geomorphological response, although similar in the two areas in the short term (3-4 years), is however more complex to analyse if contextualized in the medium term, also considering the relationships between marine forcings.

Three are the main differences between the Isonzo's delta and the HIB. First, the Isonzo river is a sedimentary source, with peculiar geomorphological features and dynamics mainly related to the fluvial sediment supply. On the other hand, due to the distance from the sedimentary source, the sediment supply on HIB is less subject to river floods. Second, HIB and the bars around the river mouth are at different depth. The HIB maximum height is just around 0.9 m, and the bank is alternatively emerged and submerged. On the other hand, the bars at the river's mouth extend in the range from -2 m to -1 m and are always submerged. For this reason, the Isonzo's bars are always subjected to the morphodynamic forcings while the HIB is mainly subjected to significant winnowing during high spring tides and storm surges. Third, the waves impacting on the two sites are quite different. The Isonzo's delta is way more protected than the HIB from SSE waves, while the latter is less affected by ENE waves, as shown by the spectral wave models of southern and north-eastern storm events (Figure 75 and Figure 78Figure 84). Only southwesterly waves seem to affect both areas, even though predominantly on the HIB as shown by higher significant wave height.

6.2.2 Longshore transport pathway

The longshore transport pathway is an important feature of the coastal environment because it represents the path where sandy sediment flows. The littoral drift is the movement of sand parallel to the shore driven by the combination of waves and tides' longshore currents (Seymour, 2005a). The whole study area is crossed by a series of longitudinal sandy bars detectable both by the DTM (Figure 15) and by satellite images (Figure 1) with evident vergence towards the west. These bars constitute the longshore transport pathway mainly developed between -1 m and -4 m, bordering the sedimentary bodies of the Isonzo delta and the MMB and locally interrupted by the presence of the Primero inlet. Sediments have a M_z less than 4 ϕ with a coarsening trend towards the west until reaching the lowest values ($\approx 1.50 \phi$) in the HIB area (Figure 98a), at the same

time becoming increasingly sorted, from moderately near the Isonzo's mouth to well sorted on the HIB (Figure 98b). Such evolution in the granulometric characteristics of the sediments indicates the presence of an agent of sediment transport and selection from east to west, confirming the bibliographic data (Bezzi et al., 2021a; Fontolan et al., 2018). The littoral drift pathway shows a continuous process of sediment coarsening and sorting, and a progressive decrease in THg concentrations downdrift of the Primero Inlet (Figure 98c). In the HIB area THg decrease drastically, with very low values coinciding with the coarser sediments located on the southern vertex of the MMB.

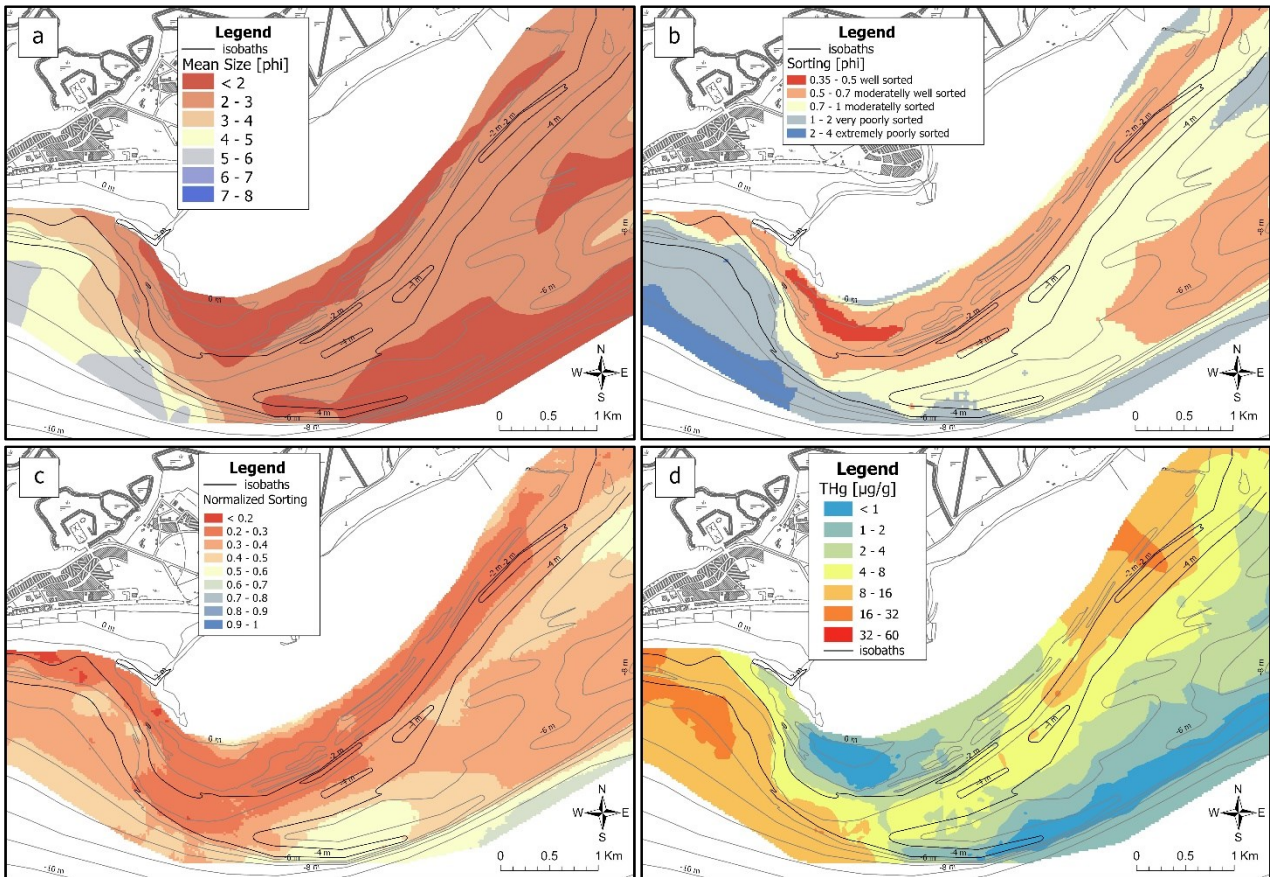


Figure 98 Detail of the (a) Mz, (b) Sr, (c) NSr and (d) THg of the MMB sector of the littoral drift pathway.

In the study area, the fractions of fine and very fine sands, with which THg tends to correlate most (Pavoni et al., 2023a), are unable to settle in the HIB due to the hydrodynamic conditions even during non-extreme events. Probably, the Sirocco wave energy focus on the HIB due to the refraction caused by the extroflexion of the contour lines, leading to the removal of cinnabar particles which, despite being denser than calcareous sand, are likely hydrodynamically more similar to fine and very fine sands.

Hydrodynamic models indicate that the littoral drift pathway is characterized by currents and bed shear stresses of opposed direction during storm surges coming from the north-east (Figure 99a) and south (Figure 99b). During northeastern storm event, currents are directed towards southwest, in agreement with the littoral drift indicated by both bibliographic data and the morpho-sedimentological evidence; while during

southern storms currents have opposite vergence from the HIB to the river mouth, while it remains concordant on the F-MMB, an area which is rather protected from the Bora waves.

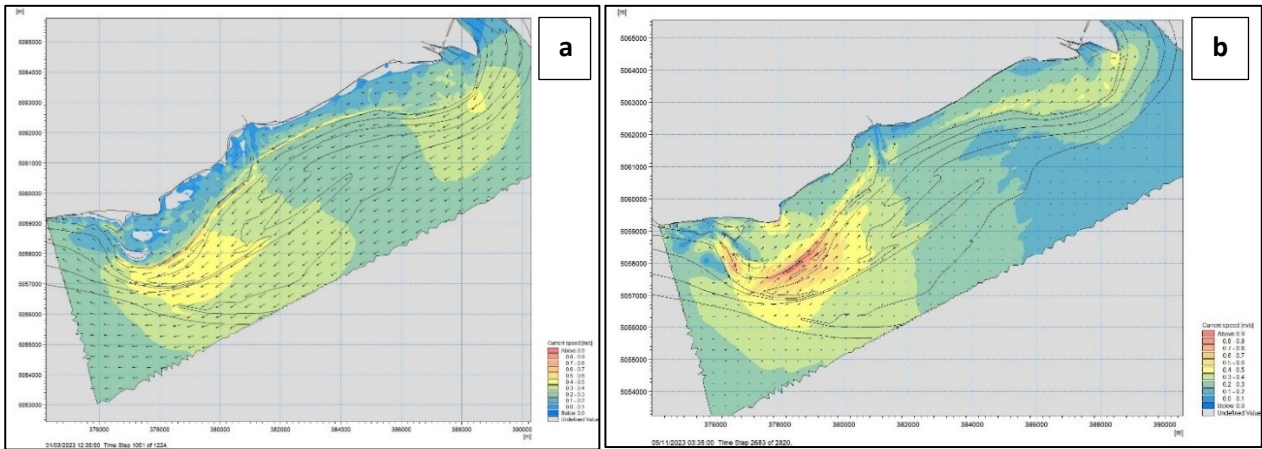


Figure 99 Currents at the apex of the (a) Bora and (b) Sirocco storm event in winter 2023.

Both storm events generate the maximum bed shear stress in the same bathymetric range, from -1 m to -3 m (maximum values around -2 m), that represents the longshore transport pathway. Sediment transport processes in the shallow waters are still active in not-extreme conditions (Figure 90Figure 91), during which the anti-clockwise tide is the dominant forcing in the formation of coastal currents capable of transporting the sediment resuspended by the waves. Along the littoral drift pathway, ENE waves are slightly more effective comparing extreme storm events (Figure 89), in particular from the Isonzo river mouth to the half of the MMB, but become dominant if we take into account standard conditions (Figure 93), conditions that are much more frequent throughout the year. The models, therefore, confirm the sedimentological and geochemical evidence, as well as the bibliographic data. Furthermore, Bora storms are able to generate a significant excess of critical bed shear stress in the seabed within -5 m on the deep terrace of the D-MMB, in particular in the south-west sector. Here, BSS exceeds the critical value for suspension even during non-extreme ENE events, indicating that the morpho-sedimentary processes may be active for most of the time.

The area of the deep terrace, consisting of sands but slightly finer, less selected and, above all, richer in Hg than the MMB and the deep bars that bord it respectively to the northwest and southeast, leads us to hypothesize that the currents coming from the north-east could play a decisive role in the transport and selection of the sediments along the littoral drift pathway. The coarser sediments (medium sands) are probably selected and transported within -3 m while the finer ones (fine and very fine sands) are transported to greater depths, on the deep terrace, where the capability of the littoral currents to produce a net sediment suspension decreases due to the depth with a consequent increase in THg concentrations because of its affinity to fine and very fine sands (Figure 100a).

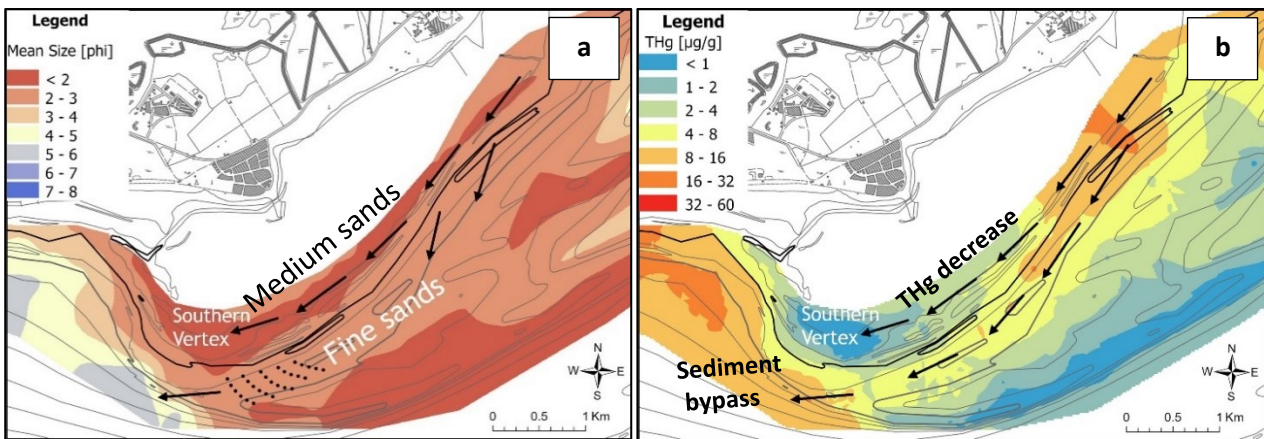


Figure 100 Sediment-transport dynamics of the MMB sector of the littoral drift pathway: (a) detail of the Mz and (b) on the THg concentration.

Moreover, these mechanisms may explain the anomalously high THg concentrations in the coastal sector in front of Grado. Here, in fact, the medium-high THg indicate an Isonzo origin, although this zone is physically separated from the Isonzo delta by the MMB and the D-MMB (Figure 100b). The deep terrace becomes a bypass area for the fine and very fine sands and, therefore, for the Hg which can thus reach the area facing the beaches of Grado.

6.2.3 The Deep Mula Muggia Bank

The deep sedimentary body of the MMB represents both a geomorphological and sedimentological anomaly. Morphologically it can be divided into two parts, the deep terrace and the two deep bars, which present similar but different sedimentological characteristics (Figure 101).

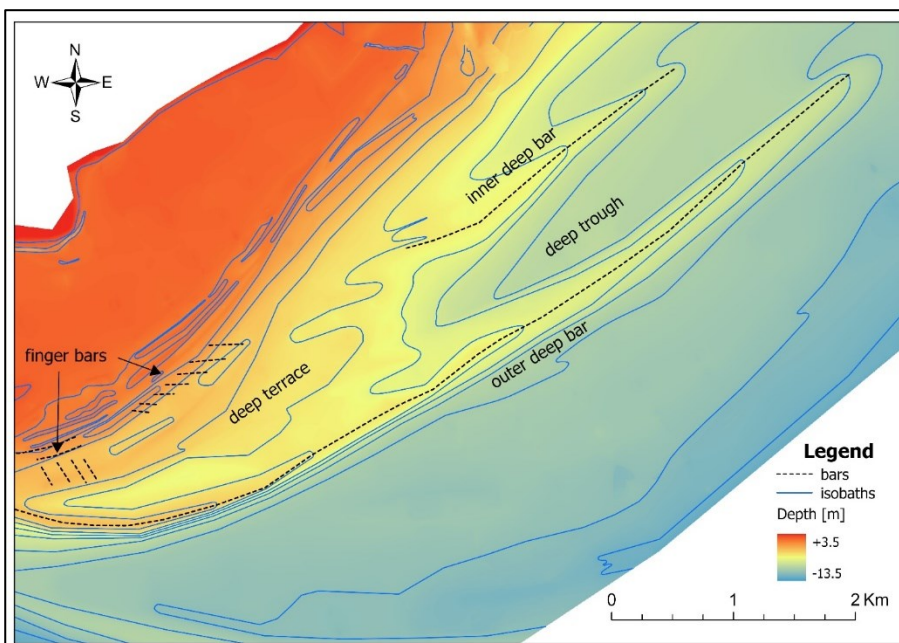


Figure 101 Digital terrain model of the Deep Mula Muggia Bank.

The deep terrace is characterized by finer sediments (Mz of 1.9-2.7 ϕ) compared to the deep bars, in particular the external one where rather coarse sediment (Mz of 1.5-1.8 ϕ) are found compared to the depth (from -4.5 to -8.5 m) (Figure 102a).

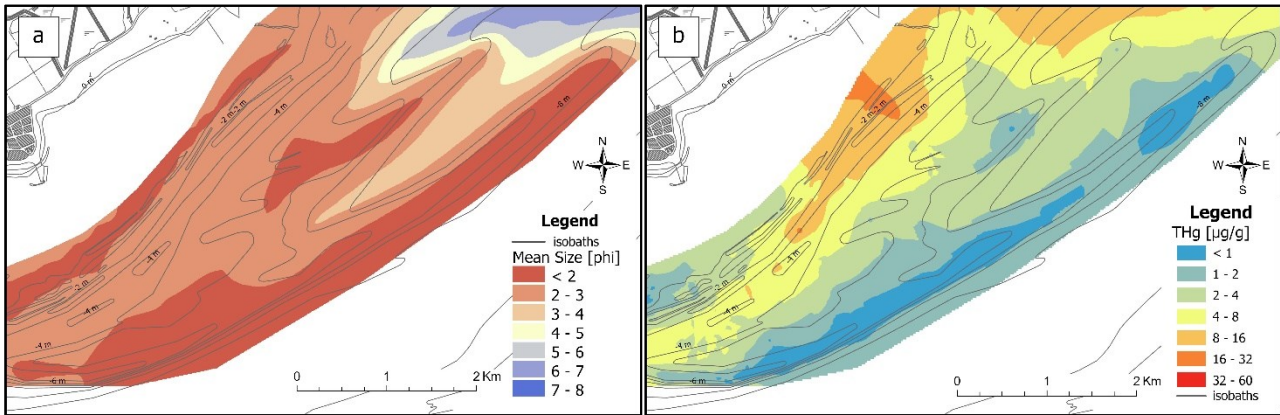


Figure 102 Maps of (a) Mz and (b) THg on the deep-MMB.

The deep terrace, as just described in chapter 6.2.2, is partly influenced by littoral drift that fills the area mainly with fine and very fine sand sediments characterized by moderate-to-high THg. During both extreme and not-extreme ENE wave conditions, sediments may be resuspended and transported throughout the deep terrace.

The south-western area of the deep terrace is characterized by the presence of a set of finger bars. Finger bars have often been identified in microtidal environments (Bruner and Smosna, 1989; Falqués et al., 2021; Garnier et al., 2012; Gelfenbaum and Brooks, 1997, 2003; Niedoroda, 1972; Niedoroda and Tanner, 1970) such as the northern Adriatic Sea. Although the formation mechanism is not yet completely clear, a fundamental role seems to derive from the refraction of waves due to the shoaling (Niedoroda and Tanner, 1970). The bars, in fact, maintain an inclination of 50-70° (clockwise) with respect to the contour of the MMB (Figure 39), showing important feedback from wave shoaling. Moreover, also longshore currents seem to be implicated in the formation of such bars (Falqués et al. 1996, 1993) that are often correlated with high sediment supply and mobility (Falqués et al., 2012, 2021; Levoy et al., 2013; Ribas et al., 2012; Ribas and Kroon, 2007). Accordingly, as just discussed in the previous chapters (6.2.1 & 6.2.2), the evidence of longshore transport towards the deep terrace and the sink of the F-MMB (Fontolan et al. 2018; Interreg Italy-Croatia CWC 2021) seems to confirm the bibliographical data. The dominance of ENE wave-driven longshore currents, both during extreme storm events and even more in standard conditions, agree with the slightly asymmetry of the finger bars of the deep terrace (Figure 37b), further suggesting east-to-west sediment transport on the area. Despite the supposed predominant role of ENE waves, the mechanism of formation of such structures is not completely depicted and a non-marginal influence may be represented also by the southern waves. Further studies involving detailed bathymetric surveys (MBES) of the entire area and spectral analysis of the wave climate could help to more deeply understand the dynamics of formation of these structures.

In addition to the deep terrace, two sandy bars are evident on the D-MMB with a direction of 50°N that are 3 km (the inner one) and 8 km long (the outer one), the latter constituting the outer flank of the D-MMB. The vergence of these structures is opposite to that of the littoral drift, having a tip directed towards the northeast. The sedimentological characteristics of the deep bars, in particular of the outer one, are different compared to the deep terrace. The sediments are coarser (M_z of 1.5 to 1.8 ϕ) and, above all, the THg concentration is very low, less than 0.25 $\mu\text{g/g}$ (THg up to 29.3 $\mu\text{g/g}$ on the deep terrace). The geomorphological anomaly of the deep bars is, therefore, parallelly correlated to the grain size anomaly: in fact, in the northern Adriatic, at depths between -4.5 and -8.5 m, finer sediments and higher concentrations of mud are usually present. By considering the overall geomorphological, sedimentological and granulometric characteristics of the deep bars, two possible evolutionary scenarios are identified: (1) a substantial morpho-sedimentological stability of the structures, with minimal to zero sedimentation rates at least in the last 500 years, i.e. after the opening of the Idrija mine; or (2) the presence of forcing such as to reshape the landforms, able to select only the medium sands and erode/inhibit the deposition of cinnabar grains. Although plausible, the hypothesis (2) is unlikely since the bars have been geomorphologically stable for over 50 years (since 1968). Therefore, the hypothesis (1) that they are relict bedforms on which the deposition of fine matter coming from the Isonzo is obliterated by the southern waves is much more reliable. Especially on the north-eastern tip of the bars, the achievement of the critical shear stress for the resuspension of the sediments is rather limited compared to that for the movement of the sediments for bed load even during storm surge events (Figure 85-Figure 88). It is therefore assumed that during storm events, any fraction of mud deposited, minimal but not zero especially in the samples closest to the river mouth (samples G82 and G87), is removed from the sediments, while the coarse component remains substantially stable. The models of non-extreme wave conditions show an even smaller excess of BSS, which is nearly negligible in the case of ENE waves. (Figure 90). The hydrodynamic conditions are, in all likelihood, capable of keeping the structure unchanged, avoiding the accumulation of mud and preserving the morpho-sedimentological characteristics of the bars.

To the north-east of the D-MMB extends the area belonging to the Isonzo prodelta, governed by dynamics linked to fluvial sediment supply and therefore characterized by fine sediments, with M_z greater than 4 ϕ . The border with the D-MMB presents rather accentuated gradients of M_z . The transition between the two environments is rather rapid in the area between the Primero Inlet and the inner deep bar while in the deep trough area it is much more progressive, as it happens for the bathymetry (Figure 64). The bimodality of sample G81 and the poor and very poor sorting of samples G80, G81 and G94, which are even more poorly sorted if we consider the NSr, suggest the presence of the mixing of sediment sources on the deep trough and on the tip of the inner deep bar. In fact, the NSr highest values are distributed in this area, highlighting the separation between the residual environment of the D-MMB and the prodeltaic one, evidencing the area in which the mixing of sedimentary sources occurs. Here, the southern waves do not seem totally able of

inhibiting the fine sedimentation coming from the river, and the low bed shear stress values even during the southern storms seem to confirm this hypothesis. The hydrodynamic models show that in this area the BSS appears to be slightly lower than the deep external bar, probably due to the damping generated by the bar itself, reducing the capability to completely resuspend and erode the mud deposited during river floods (Figure 87).

6.2.4 Front of Mula Muggia Bank & High Intertidal Bank

The most dynamic part of the whole study area is the westernmost part of the MMB, composed of the F-MMB and the HIB. The secular evolutionary trend of the F-MMB has been an almost steady westward migration at rates around 12.6 m/y in the last two centuries (Bezzi et al., 2021a; Fontolan et al., 2018; Interreg Italy-Croatia CWC, 2021), as can be seen from (Figure 17). An intertidal bank (HIB) was formed in the last 2 decades, while for 2 centuries the entire MMB was submerged. The first topographic evidence of the HIB is provided by the 2019 survey, evidence also confirmed by satellite photos. Nowadays, the bathymetric and aerial photogrammetric surveys of the F-MMB and the HIB respectively show that the first is undergoing a reduction of the progradation rates while the second is getting wider and longer.

The F-MMB has undergone a clear decrease in sedimentation rates in the period 2019-2023 compared to the period 2011-2019, equally distributed across all 13 profiles considered (Figure 56), maintaining the trend of progressive reduction in the sedimentation rate from the north towards the south. In the first six profiles from the north (transects 1F to 6F), since 2019, an accretive trend has been maintained although less accentuated, while in the southern profiles (7F to 13F) an erosive trend has been established (Figure 103).

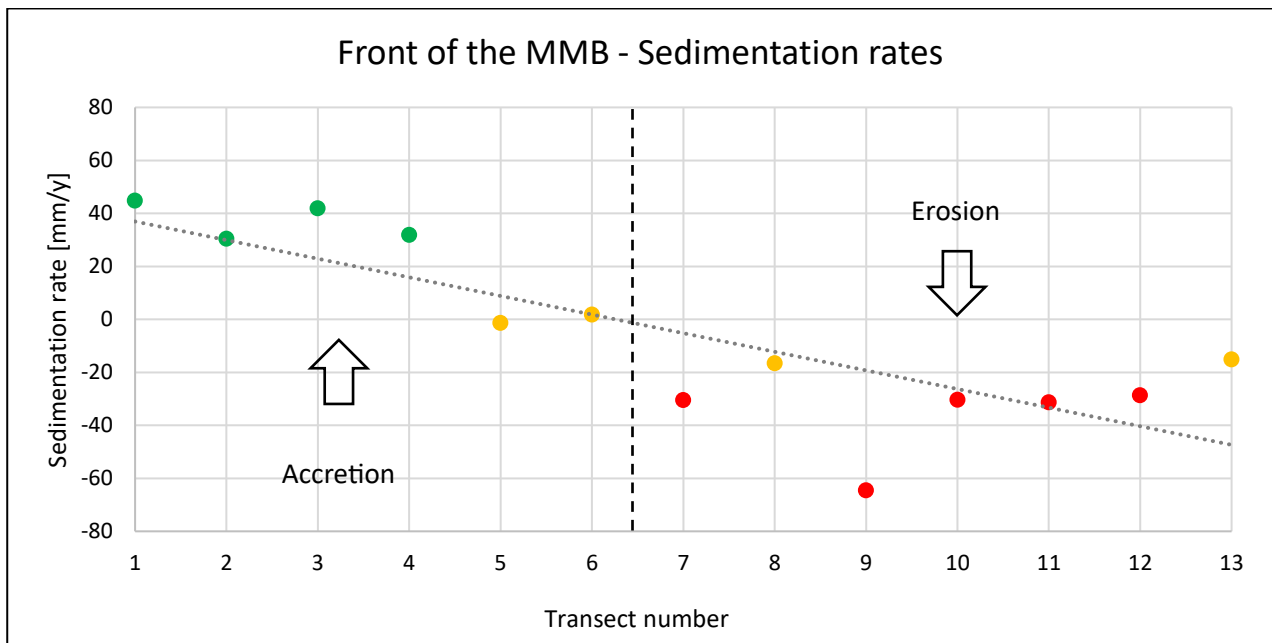


Figure 103 Sedimentation rates of the F-MMB.

On the contrary, the HIB grew both in width in its southernmost part, i.e. near the southern vertex of MMB, and in length towards the north-east, where it also widened due to the formation of a new sand bar (Figure 104). The width of the bank increased by 60 to 100 m in four years, with a rate of 15-25 m/y, and the length by almost 300 m, with a rate of 75 m/y.

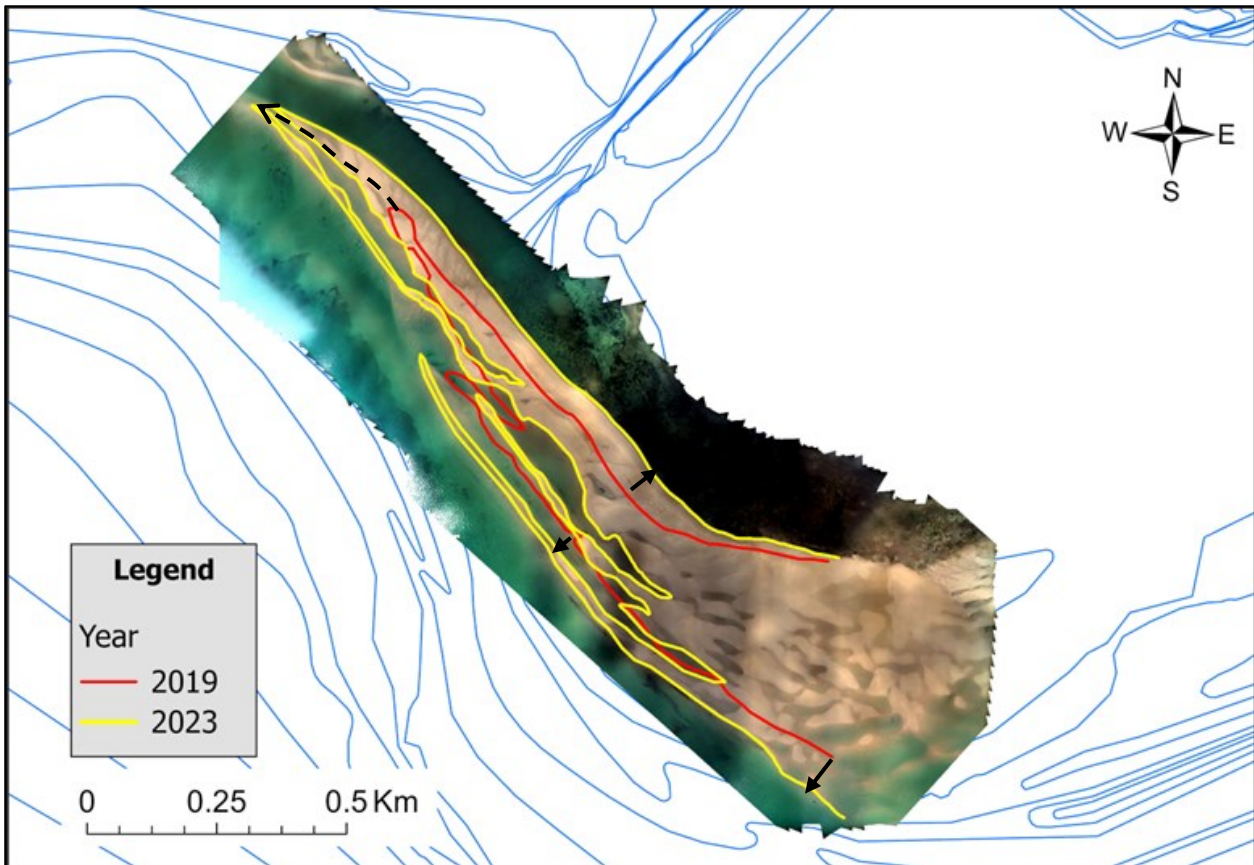


Figure 104 HIB evolution between 2019 and 2023: black arrows represent the bank widening while dotted arrow indicates the elongation towards the north-west.

Part of the evolutionary process of the HIB involves the bank's retreat with annual rates ranging between 2.8 and 17.9 m/y, as previously highlighted in Chapter 6.2.1. The height of the HIB, slightly less than a meter, ensures that the HIB is mainly subjected to significant winnowing during high spring tides and storm surges. For this reason, it is hypothesized that southern storm events have a greater impact on the bank's retreat. In fact, southerly storm events are characterized by high storm surge, greater than +50 cm, which, added to tide and wave set up, can lead to a total level greater than +100 cm and extreme values greater than +150 cm. On the contrary, north-easterly events are instead characterized by negative surges. The two events analyzed confirm the trend: ENE storm in winter 2023 reached a maximum of +0.37 m while the autumn southern storm reached a maximum of +1.36 m, almost one meter more. Given that the HIB reaches a maximum elevation of 0.9 m, it is almost always submerged during southern storm surges also due to the contribution to the water level from the wave set-up. On the other hand, during Bora winter storm part of the HIB was often emerged even taking into account wave set-up and run-up as highlighted by the map in Figure 86 representing the time above critical bed shear stress during ENE storm event. The comparison of the two

extreme events shows how the southern Sirocco waves are the most dominant agent on the HIB (Figure 89), and the BSS generated by southern waves during the storm event is directed parallel to the retreat of the HIB. The impact of southern wave motion on the HIB is even more evident when considering non-extreme conditions. Under these conditions, ENE waves generate a very limited, if not negligible, excess of BSS in the higher areas (Figure 90), whereas southern waves are always capable of inducing transport, aided by the increase in water level caused by southern winds (Figure 91). The implications of storm events in the retreat of the HIB are similar to the rollover of a barrier island under the effect of overwash, even though its occurrence is frequent due to the limited height of the bank. The retreat of the HIB is higher in the central part and lesser on the extremes. The direction of the edge of bank seems to have an implication in the rate of retreat. In fact, the extremes are directed almost east-west ($280-290^{\circ}\text{N}$) while the central part is directed as the F-MMB ($\approx 320^{\circ}\text{N}$). Moreover, there are some other aspects that may affect the rate of retreat. The southern end of the HIB, i.e. at the southern vertex of the MMB, is wider (450 m) than on the west (80-130 m). This may lead to a greater wave energy dissipation and, therefore, a reduced possibility to rollover. On the other hand, on the northern tip of the HIB, the "Brambati" channel acts as a barrier for the landward migration of bank, even if the bank has shown to be able to make the channel migrate northward anyway. The models of the southern storm events confirmed that, showing an average current direction around $180-200^{\circ}\text{N}$. Moreover, the excess of BSS is higher on the tip of HIB compared to the southern vertex, both during extreme (Figure 87) and not-extreme events (Figure 91), possibly leading to a greater retreat in that area.

If, therefore, the evolution of the F-MMB indicates a reduction in the rate of progradation of whole MMB, on the other hand the growth of the HIB denotes a continuity of the area as a sedimentary depocentre. In this context, two morpho-sedimentary processes can be hypothesized. Firstly, the transgression of the sandy bars in the shallower part of the bathymetric profiles may be attributable to an active rollover process within -2 m in favor of the growth of intertidal landforms. This process may cause the southern half of the F-MMB (profiles 7F - 13F) to be eroded while the HIB becomes increasingly wider. Secondly, in the northwestern sector, both the seabed of the F- MMB and the HIB have an accretionary regime, indicating the fundamental activity of the littoral drift as a sediment transport agent. The morpho-sedimentological evidence and the models provide useful information for the interpretation of the forcings acting on the area. Following the littoral drift from east to west, the grain size gradients and THg concentration have a common trend. In fact, up to the southern vertex, the gradients of coarsening, positive sorting, and reduction in THg are identified. On the other hand, from the vertex to the tip of the HIB, the sands become finer, the THg concentration increases while the sorting gradient remains slightly positive, leading to more sorted sediments (Figure 105).

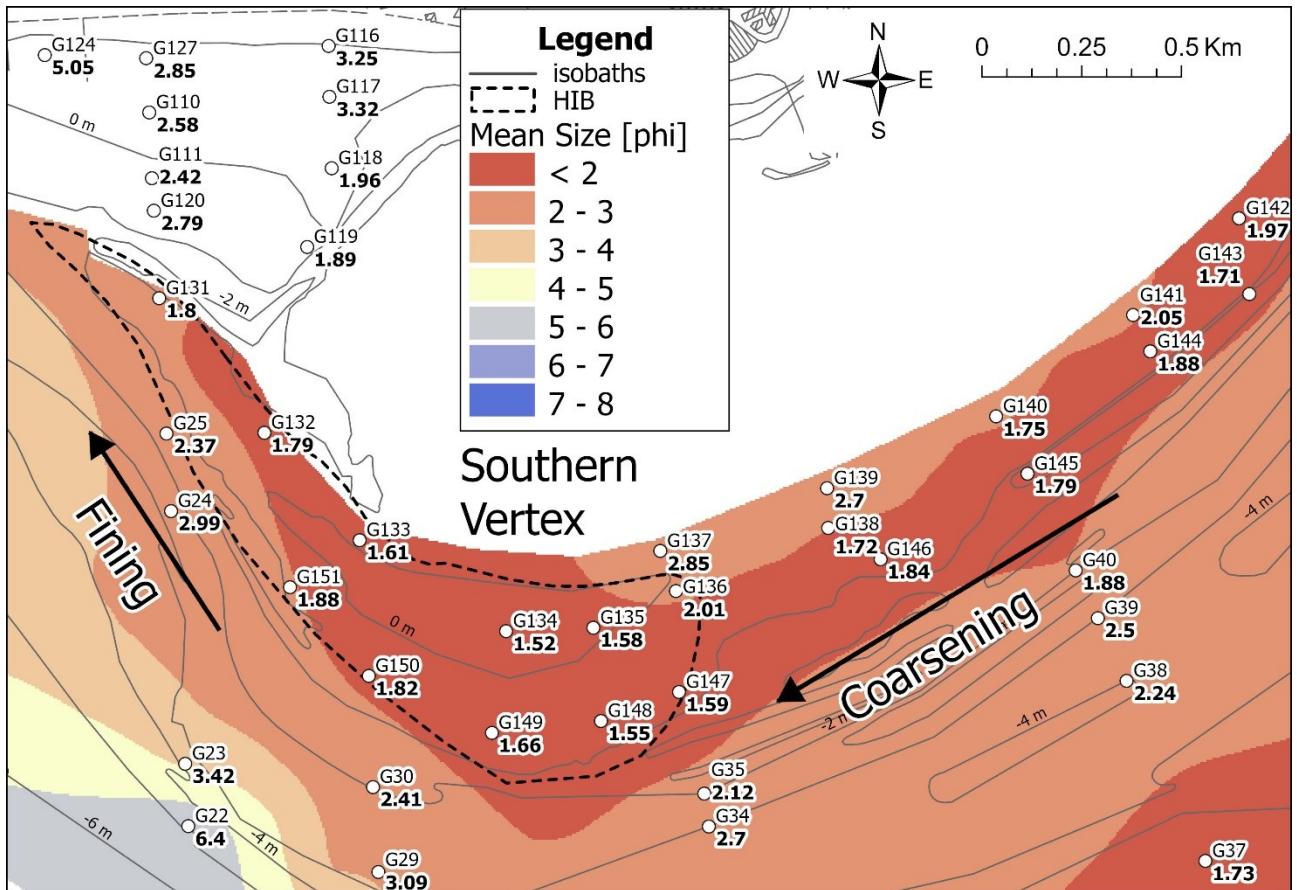


Figure 105 Granulometric gradients on the HIB.

By correlating these sedimentary characteristics with the numerical elaborations of the models we can identify the southern vertex of the MMB as the point where the maximum wave energy is focused during southerly storm events. In fact, the models indicate the southern vertex as the area in which the direction of the currents and bed shear stress changes, moving from vectors opposite the littoral drift to the east, to vectors towards the north-west downstream of the summit (Figure 106).

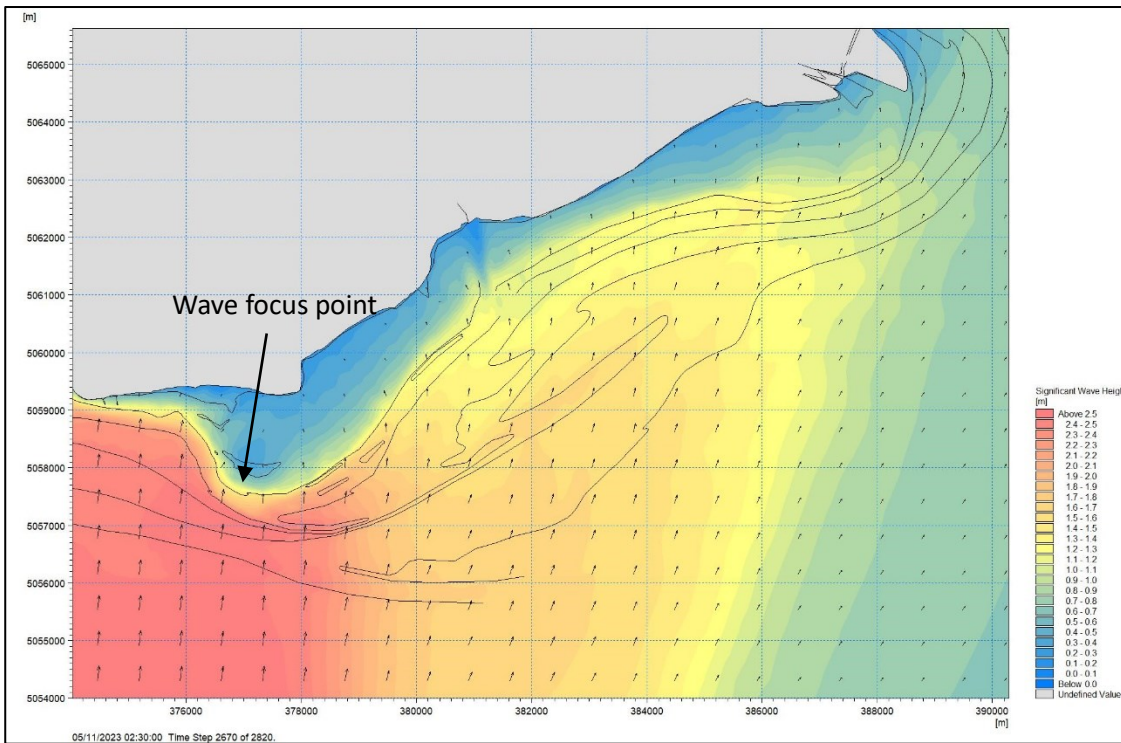


Figure 106 Significant wave height during the apex of the Sirocco waves during storm multi-event of autumn 2023.

On the contrary, ENE waves generate lesser BSS on the HIB and the F-MMB, especially towards northwest (Figure 107). The low sea level caused by Bora winds keeps a large part of the HIB exposed, preventing it from being involved in sediment transport processes.

From the southern vertex towards northwest, the HIB narrows progressively, and the sediment become progressively finer and richer in THg, indicating a reduction in wave energy. This area, together with the northern part of the F-MMB where profiles 1F-6F are located, results bathymetrically protected from Bora waves and dominated by southerly waves both in storm and standard wave conditions, as highlighted by the maps of Figure 89 and Figure 93. Here, the geomorphological and sedimentary characteristics, consistent with models, indicate a predominant transport direction towards the northwest, with the formation of a set of longitudinal bars aligned locally with the longshore drift.

On the western side of the F-MMB, there is an additional set of finger bars. Unlike the finger bars on the deep terrace, where the Bora wave effect prevails, these forms in the F-MMB area among the southern sector dominated by ENE waves and the northern sector dominated by southern waves (Figure 107). Additionally, these forms are not located on a flat area but on a steeper seabed, with depths decreasing from south to north, making it difficult to identify a common symmetry for all the bars (Figure 37c). However, the counterclockwise inclination of these forms, approximately 70° relative to the contour lines of the F-MMB, highlights the refractive effect due to shoaling, which in this case aligns with both the southern and ENE waves. Finally, these forms indicate a high sediment transport, confirmed by the accumulation trends observed in transects 1F-6F (Table 6) and the outward extension of the contour lines.

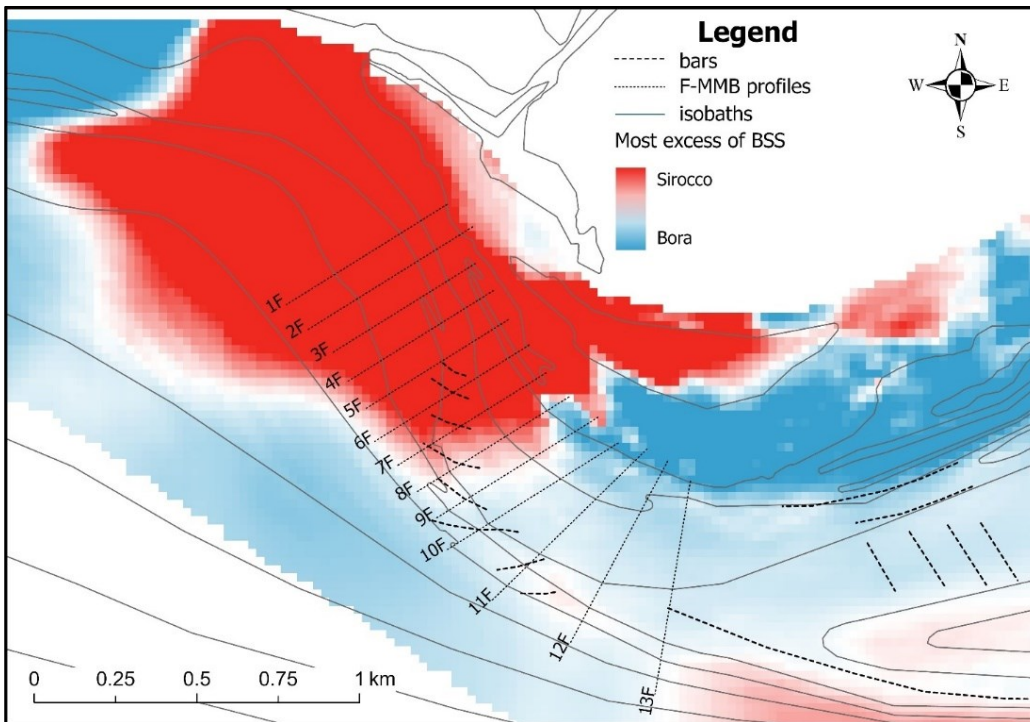


Figure 107 Time of exceedance of critical BSS: zoom on the F-MMB.

It can therefore be assumed that waves coming from the south are able to produce two main effects in the area of the F-MMB.

1. They contribute to the sedimentary transport phenomena of the littoral drift towards the north-west on the F-MMB and on the tip of the HIB, with the implication of the formation of both deep (-4 m) and intertidal (-1 m – 0 m) transvers bars. Moreover, sediment transport is also underlined by the migration of the north-western tip of the HIB over time together with the rollover phenomenon. This migration is quite evident (75 m/y) and has almost led to the occlusion of the artificial channel which border the Grado Pineta shoreline. Furthermore, this migration appears to have accelerated over time, probably due to the greater volume of sediment available on the HIB.
2. They generate cross-shore transport in the southern vertex area, enhancing the effect of rollover in favor of deposition on the HIB, with consequent migration of the longitudinal bars towards the shore (northeast). This mechanism could explain the formation and the expansion of the HIB in the last two decades.

This last aspect could have a strong implication on reducing the secular trend of westward migration of the MMB. The deceleration of the westward migration may be due to a set of factors, such as: the sea level rise, the reduction of longshore sediment transport, the variation in the wave climate and the bathymetric characteristics of the seabed. Sea level has been increasing over the years but has not undergone a significant change in last two decades.

As regards sediment transport, the sedimentary budget of the Isonzo delta and the growth of the HIB itself seem to indicate substantial stability in the sediment availability. The wave data recorded both by the DWRG wave buoys don't evidence a significant variation in the wave climate able over the years such as to be able to generate an evident morpho-sedimentological variation. However, although the wave climate in the northern Adriatic has remained rather stable over time, the constant migration of the MMB towards the west has led the F- MMB to be subject to an increasingly intense attack by the Sirocco waves due to the progressive reduction of the protection offered by the Istrian peninsula. In this context it is probable that the sediment transport towards northeast led by southern waves began long before the emersion of the HIB.

In conclusion, it is assumed that the sediments transported by the littoral drift to the seabed in front of the HIB (profiles 7F-13F) are partly transported towards the north-east and deposited on the HIB itself, and partly towards the north-west generating a positive balance on the north-western area of the F-MMB (Figure 108). In this context, the rise in sea level continuously generates new accommodation space in the HIB area, giving continuity to the ongoing process. This process can also explain the reduction in the migration rates of the F-MMB since part of the sediments made available by the littoral drift are not transported to the seabed towards the west, but towards the land to form and expand the area of the HIB.

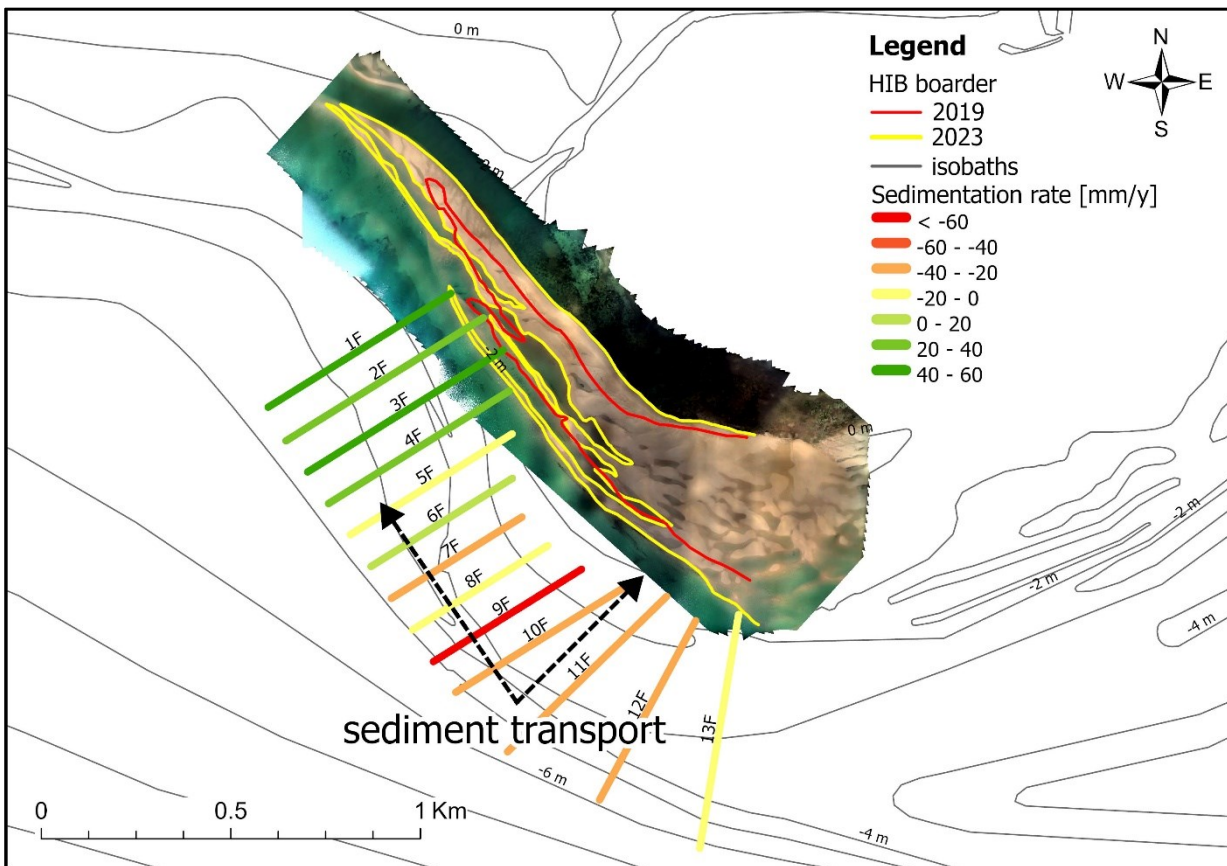


Figure 108 Sediment transport dynamics on the F-MMB.

6.3 Natural dynamics vs urban planning: conflicts and perspectives

The coasts of Grado have experienced significant tourist and economic development over the past two centuries, with the adoption of a backshore defense policy that has rigidified the coastal system, reducing its natural ability to adapt and migrate in response to climate change. To limit the anthropogenic impact on the ecosystem, a conservation program was initiated, leading to the creation of the Natura 2000 protected areas. Consequently, the Grado coastline needs to be maintained for multi-purpose use (McLachlan et al., 2013), balancing recreation and environmental conservation. Integrating morphosedimentary characteristics with the land use designations of coastal elements, whether for tourism or environmental conservation, can provide a useful management tool (Figure 109).

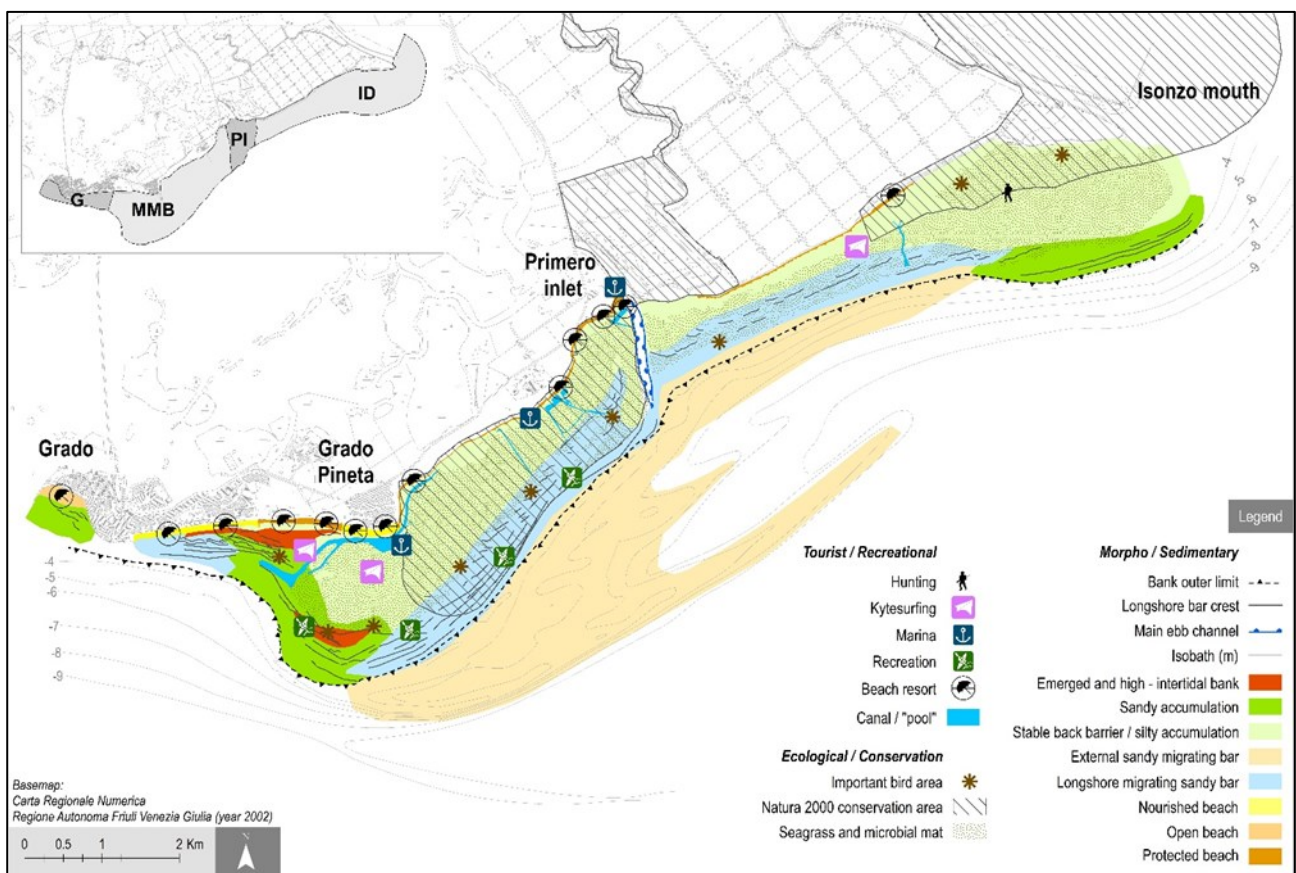


Figure 109 Zoning map with the different morphosedimentary areas and the most important tourist/recreational, ecological, and conservation values, relevant for multi-purpose coastal planning. (Bezzi et al., 2021a)

The zoning aims to synthesize natural dynamics, uses and conflicts and create a baseline for future management guidelines. The map emphasizes how coastal areas have been developed without considering their inherent characteristics. In the absence of Integrated Coastal Zone Management or coordinated coastline management guidelines, the building of beach resorts and facilities occurred even in unsuitable areas located on fetch-limited beaches faced by very shallow waters and a silty seabed (backbarrier area). Despite the sheltered position during extreme storms and "acqua alta", some of these beaches are being eroded, and in the absence of post-storm natural constructive processes, they require periodic sand replenishment. Local coastal tourism is primarily focused on beaches that are managed as private properties

under state concession and are fully equipped with numerous facilities (walkways, beach umbrellas, toilets, showers, and kiosks), leaving little space for free and natural areas. This model implies a lack of acceptance of the specific characteristics of the sites (particularly the backbarrier area) among stakeholders and fosters conflict. At the same time, a variety of touristic uses (small boat docks and kitesurfing, for example) can conflict with the need for nature conservation needs (silty seabed with seagrass meadows, tidal flats used as roosts by birds). However, in certain locations, the large size and dynamism of natural landforms have grown prominent in relation to the needs of seaside tourism, raising serious concerns for the future of these areas. The westernmost part of the MMB, in particular, is viewed as a threat to touristic activities due to the ongoing rapid extension toward the west of the shallow water with silty deposition in the nearshore and the current infilling of the navigation canal. However, in last years this trend seems to be slowing down in favor of the vertical growth of the shoals of HIB, often frequented by unorganized but intense tourist use (bathing, recreational fishing of edible bivalves and kitesurfing). Our analysis, as well as the zoning scheme shown in Figure 109, can be used as a basis to guide future planning of the Grado coastal area, to reduce SLR impact and minimize or eliminate the major conflict that exists between coastal morphodynamics, tourist/recreational beach use, and conservation needs. The backbarrier area and the longshore migrating sandbars have the natural potential to safeguard human settlements and infrastructures while also providing a variety of natural co-benefits such as habitat conservation, carbon sequestration, tourism opportunities, education, and research (Sutton-Grier et al., 2015). This area can be vulnerable to medium and long-term forcing (SLR), which cause the sandbanks to rollover the stable silty backbarrier, a natural ramp for the accommodation of future transgressive bodies. For this reason, the primary concerns are the preservation of the sediment source (the Isonzo River) and the natural ability of the longshore transport to distribute the sand along the littoral toward the west. Proper control of hydraulic interventions in the drainage basin and monitoring of the river's sediment supply, will be required. Simultaneously, hard defense structures should be avoided unless they are limited to reinforcing those already in place to defend the hinterland. The presence of consistent sandy accumulation areas would favor soft shore protection solutions (Goudas et al., 2003) that aim to manage sediments within the coastal system to balance deposition and erosion in adjacent cells (Bezzi et al., 2021b; Bonaldo et al., 2019; Fontolan et al., 2015, 2007). The areas with the highest rates of accretion might exhibit particularly favorable grain size characteristics, being among the coarsest and best-sorted sands in the entire coastal sector. This feature is often crucial for ensuring the longevity of nourishment operations (CERC 1984; James 1975; Krumbain 1957). Once sediment compatibility is established by considering both grain size and geochemical characteristics, overabundant sediments in accumulation areas can be managed as a temporary reservoir for beach re-nourishment. The use of small periodic, scheduled dredging and nourishment is preferable, with a source-to-sink approach that mimics the natural bypass corridor between the barred shoreface updrift and downdrift to the Primero inlet. This approach is favored here as deficit areas are of modest size and are mainly fetch-limited beaches, thus highly conservative.

7 Conclusions

The Grado coast is characterized by the presence of two sedimentary bodies: to the east is the deltaic feature of the Isonzo River, from which a longshore transport corridor extends westward; to the west is the Mula di Muggia sandbank, the main final area of deposition of the riverine inputs. The Mula di Muggia Bank (MMB) is a complex sedimentary body approximately 7-8 km long and over 3 km wide. The MMB essentially consists of a vast, flat backbarrier area bordered by a series of longitudinal sandbars that extend seaward to the upper shoreface limit (-3/-4 m) beyond which a deep sedimentary relict body of probable deltaic origin develops (Brambati, 1985; Marocco, 1989). Over the last two centuries, the MMB has shown a near-constant westward migration, creating critical situations for the nearby beaches, which are heavily used for tourism purposes.

The results of this PhD project allow to elucidate the intricate morphodynamics of this area by integrating data from various sources. This will provide a foundation for future precise planning and reassessment of coastal management decisions, ensuring a balance between environmental conservation and tourism.

The multidisciplinary approach employed was based on the acquisition and elaboration of bathymetric data, aerial photogrammetry, and sediment samples. These datasets were processed to obtain (i) a digital models of the seabed, from which the geomorphological set-up and sediment budgets of the most dynamic areas were derived; (ii) a distribution maps of grain-size parameters, obtained using a semi-automatic method developed during this thesis (the SAIM method); (iii) a distribution map of total mercury concentration in the sediments showing a contamination in much of the study area; and (iv) wave patterns and hydrodynamic models of major storm surges as well as more standard conditions.

In order to obtain a precise sedimentological map in this specific context characterized by a complex bathymetry with the presence of very long and narrow structures, a new semi-automatic interpolation method (SAIM) was developed. The methodology is based on the use of automatic geostatistical interpolation methods actively assisted by expert judgment. With the SAIM approach, it was possible to reduce the interpolation error by about 50%, even compared to the most refined automatic geostatistical procedures, especially in the more morphologically complex areas. The SAIM method has therefore proven to be quite effective in overcoming some common limitations in the creation of sedimentological maps from sediment samples related to the time-consuming and expensive process of data acquisition, which often lead to sparse and not properly spaced datasets. The distribution maps obtained with SAIM were successively analyzed along with other methodologies to gain insights into the morphodynamics of the area.

The combination of sedimentological, geochemical characteristics, and the results of hydrodynamic models allow to define the morphodynamic set-up of the area recognizing different areas of remarkable significance: the river delta, the deep part of the MMB (D-MMB), the front of the MMB (F-MMB) and the high intertidal bank (HIB).

The primary role of the sediment supply from the Isonzo River is verified: although the deltaic area shows a feeble accretionary trend and a significant reduction in the sedimentation rate compared to the past decades, probably correlated with the achievement of a new stability condition (Bezzi et al., 2021a), it continues to play a crucial role in the active morphodynamics of the MMB, which rely on significant sediment supply. Sediments are markedly linked to the river supply, as testified by the distribution of THg, whose contamination is linked to the last 500 years of mining activity at Idrija, located in the drainage basin of the Isonzo River (Covelli et al. 1999; Gosar et al. 1997). Above-natural mercury concentrations (THg > 1 µg/g) are found in the seabed of most of the Grado coastline, transported by the east-to-west longshore currents along the littoral drift pathway. Such longshore corridor consists in a series of longitudinal sandy bars that extends up to -4 m, in which mercury have been proven to be concentrated mainly in fine and very fine sands. Westward coarsening and sorting gradients, as well as the dominance of the Bora wave-driven currents resulted from the simulations with MIKE21 spectral waves and hydrodynamic modules confirm the role of the littoral drift pathway, providing information about the transport and selection mechanisms.

Seawards from the littoral drift corridor, the deep part of the MMB seems to be only partially morphodynamically active, limited to the deep terrace area. Here the role of the longshore drift is highlighted by the presence of significant amount of fine and very fine sands with moderate-to-high concentration of THg (from 1 to 30 µg/g), slightly asymmetrical finger bars, and Bora wave-driven currents capable of resuspending sediments even under non-extreme conditions. Conversely, the deep bars consist of medium sands (Mz of 1.5-1.8 φ), homogeneous in mean size along the structures and almost mercury free (THg < 1 µg/g). Moreover, the hydrodynamic conditions simulated by models predict minimal sediment resuspension only during extreme events, especially from the SSW, exceeding the critical shear stress threshold for a minimal amount of time. The combination of these characteristics highlights the relict nature of these forms, which will need to be further investigated in the future.

Finally, the westernmost area of the MMB, consisting of the F-MMB and a recently formed HIB (during the last two decades), presents several indicators of accretion and adaptation to the evolutionary context due to climate change. Although the F-MMB as a whole has shown a reduction in the accretionary regime compared to the past and a consequent reduction in the long-term westward migration, the sediment budget is still positive, and due to sediment transport from southeast to northwest. In this process, both the presence of additional northward finger bars and hydrodynamic models would emphasize the dominance of southern wave motion, which is significantly more intense in this sector. The importance of southern waves is further highlighted by the morpho-sedimentological characteristics of the HIB. The largest part of the HIB coincides with the southern apex of the MMB, a strong outward extension characterized morphologically by both landward retreat due to rollover and seaward expansion for a total widening of 15-25 m/y, and sedimentologically by the coarsest sediments of the entire area (except for the relict deep bars) with a drastic

reduction in THg concentrations due to the absence of fine and very fine sands. From the southern vertex, a more tapered part of the bank extends northwest, consisting of a series of longitudinal bars. Here, alongside a rollover retreat rate of up to 18 m/y, a growth in the length of these bars towards the northwest of about 75 m/y is evident. The strong accretional tendency of this area is therefore attributable to the combination of high sediment input from westward longshore drift and the effect of reworking, sorting, and transport due to southerly waves.

Overall, the MMB shows a well-marked resilience to SLR compared to most of the urbanized coastal areas worldwide, simultaneously demonstrating a morphological adaptability to marine transgression and an anomalous sediment accumulation capacity. In the absence of direct measurements on the bed load of the Isonzo river, the data and analyses carried out indicate that the river sediment supply is high enough to prevent the establishment of an erosive regime on the Grado coast. Moreover, the physiographic characteristics of the Gulf of Trieste and the morphological set-up of the MMB significantly influence the sediment transport dynamics. For what concerns the active dynamics, the southern vertex of MMB acts as a boundary between the longshore transport dominated by Bora, to the east, and that dominated by Sirocco, to the west. Such dynamics, supported by both model simulations and morpho-sedimentological evidence, emphasizes the importance of auxiliary methodologies in making simulation results more reliable and vice versa.

The morphodynamic analysis of the MMB revealed that, although the bank's migration is viewed as a threat to the management of surrounding tourist beaches, today this trend appears to be declining in favor of the growth of the HIB. In fact, the dominance of Sirocco wave motion in the F-MMB imply a significant sediment transport component towards the shore, leading us to hypothesize a future accretion of the HIB and a natural recharge of the adjacent beaches rather than a westward migration of the MMB with consequent expansion of the back-barrier area. Furthermore, highly accreting areas (e.g. the HIB) can be managed as a temporary reservoir for beach re-nourishment using a source-to-sink technique that simulates the natural bypass corridor of tidal inlets.

As a final remark, Grado's coastline system, which combines areas designated for environmental preservation and tourism/recreation, has become more rigid due to urban growth, making it less adaptable to climate change. Understanding morpho-sedimentary dynamics is crucial for recognizing ongoing processes, reducing the threat posed by SLR. Accurate monitoring of the morphodynamics of the coastal banks is essential to potentially adjust actions and management strategies. The abundance of sediments is a significant asset and provides a tangible opportunity to mitigate the threat of SLR. While erosion and sand loss are severe global issues for the tourism industry, the rapid morphological changes, and the management of large volumes of moving sediments in this area represent both a challenge and an opportunity.

8 Bibliography

- Aagaard, T., 2014. Sediment supply to beaches: Cross-shore sand transport on the lower shoreface. *J Geophys Res Earth Surf* 119, 913–926. <https://doi.org/10.1002/2013JF003041>
- Aagaard, T., Davidson-Arnott, R., Greenwood, B., Nielsen, J., 2004. Sediment supply from shoreface to dunes: linking sediment transport measurements and long-term morphological evolution. *Geomorphology* 60, 205–224. <https://doi.org/10.1016/J.GEOMORPH.2003.08.002>
- Agus, S.B., Siregar, V.P., Susilo, S.B., Sangadji, M.S., Tasirileleu, G.F., Budi, P.S., 2021. Mapping of shallow water bathymetry and reef geomorphology using Sentinel-2 satellite imagery in Genteng Besar and Genteng Kecil Island, Kepulauan Seribu. Volume 944, Issue 1 944, 2021. <https://doi.org/10.1088/1755-1315/944/1/012048>
- Aiello, G., Sacchi, M., 2022. New morpho-bathymetric data on marine hazard in the offshore of Gulf of Naples (Southern Italy). Volume 111, Issue 3, Pages 2881 - 2908 111, 2881–2908. <https://doi.org/10.1007/s11069-021-05161-2>
- Albertazzi, S., Merlin, O.H., Vitturi, L.M., Molinaroli, E., Pelati, L.T., 1987. Distribution and behaviour of ¹³⁷Cs in nearshore sediments of the northern Adriatic and at the Adige River estuary, northern Italy. *Applied Geochemistry* 2, 357–366. [https://doi.org/10.1016/0883-2927\(87\)90020-5](https://doi.org/10.1016/0883-2927(87)90020-5)
- Amoudry, L.O., Souza, A.J., 2011. Deterministic coastal morphological and sediment transport modeling: A review and discussion. *Reviews of Geophysics* 49. <https://doi.org/10.1029/2010RG000341>
- Anfuso, G., Pranzini, E., Vitale, G., 2011. An integrated approach to coastal erosion problems in northern Tuscany (Italy): Littoral morphological evolution and cell distribution. *Geomorphology* 129, 204–214. <https://doi.org/10.1016/j.geomorph.2011.01.023>
- Anthony, E.J., 2015. Wave influence in the construction, shaping and destruction of river deltas: A review. *Mar Geol* 361, 53–78. <https://doi.org/10.1016/j.margeo.2014.12.004>
- Anthony, E.J., 2005. Beach erosion. *Encyclopedia of Coastal Science*.
- Anthony, E.J., Aagaard, T., 2020. The lower shoreface: Morphodynamics and sediment connectivity with the upper shoreface and beach. *Earth Sci Rev* 210. <https://doi.org/10.1016/j.earscirev.2020.103334>
- Anthony, E.J., Marriner, N., Morhange, C., 2014. Human influence and the changing geomorphology of Mediterranean deltas and coasts over the last 6000 years: From progradation to destruction phase? *Earth Sci Rev* 139, 336–361. <https://doi.org/10.1016/J.EARSCIREV.2014.10.003>
- Antonioli, F., Anzidei, M., Amorosi, A., Lo Presti, V., Mastronuzzi, G., Deiana, G., De Falco, G., Fontana, A., Fontolan, G., Lisco, S., Marsico, A., Moretti, M., Orrù, P.E., Sannino, G.M., Serpelloni, E., Vecchio, A., 2017. Sea-level rise and potential drowning of the Italian coastal plains: Flooding risk scenarios for 2100. *Quat Sci Rev* 158, 29–43. <https://doi.org/10.1016/j.quascirev.2016.12.021>
- Aouiche, I., Daoudi, L., Anthony, E.J., Sedrati, M., Ziane, E., Harti, A., Dussouillez, P., 2015. Anthropogenic effects on shoreface and shoreline changes: Input from a multi-method analysis, Agadir Bay, Morocco. *Geomorphology* 254, 16–31. <https://doi.org/10.1016/j.geomorph.2015.11.013>
- Areggi, G., Pezzo, G., Merryman Boncori, J.P., Anderlini, L., Rossi, G., Serpelloni, E., Zuliani, D., Bonini, L., 2023. Present-Day Surface Deformation in North-East Italy Using InSAR and GNSS Data. *Remote Sens (Basel)* 15. <https://doi.org/10.3390/rs15061704>

- Armaroli, C., Ciavola, P., Caleffi, S., Gardelli, M., 2007. Morphodynamics of nearshore rhythmic forms: an energy-based classification. *World Scientific Pub Co Pte Lt*, pp. 4009–4021.
https://doi.org/10.1142/9789812709554_0337
- Arosio, R., Hopley, B., Wheeler, A.J., Sacchetti, F., Conti, L.A., Furey, T., Lim, A., 2023. Fully convolutional neural networks applied to large-scale marine morphology mapping. *Front Mar Sci* 10.
<https://doi.org/10.3389/fmars.2023.1228867>
- Bagnold, R.A., 1966. *An Approach to the Sediment Transport Problem From General Physics*.
- Bagnold, R.A., 1940. Beach formation by waves: some model experiments in a wave tank. *Journal of the Institution of Civil Engineers* 15, 27–52. <https://doi.org/10.1680/IJOTI.1940.14279>
- Bailard, J.A., 1981. An energetics total load sediment transport model for a plane sloping beach (longshore transport). *J Geophys Res* 86, 10938–10954. <https://doi.org/10.1029/JC086IC11P10938/ABSTRACT>
- Baldoni, A., Melito, L., Marini, F., Galassi, G., Giacomini, P., Filomena, G., Barbizzi, N., Lorenzoni, C., Brocchini, M., 2024. Modeling coastal inundation for adaptation to climate change at local scale: the case of Marche Region (central Italy). *Frontiers in Climate* 6. <https://doi.org/10.3389/fclim.2024.1334625>
- Barrell, J., 1912. Criteria for the recognition of ancient delta deposits. *GSA Bulletin* 23, 377–446.
<https://doi.org/10.1130/GSAB-23-377>
- Battjes, J.A., Janssen, J.P.F.M., 1978. Energy loss and set-up due to breaking of random waves, in: *Coastal Engineering*.
- Baux, N., Murat, A., Faivre, Q., Lesourd, S., Poizot, E., Méar, Y., Brasselet, S., Dauvin, J.-C., 2019. Sediment dynamic equilibrium, a key for assessing a coastal anthropogenic disturbance using geochemical tracers: Application to the eastern part of the Bay of Seine. *Cont Shelf Res* 175, 87–98.
<https://doi.org/10.1016/j.csr.2019.02.002>
- Baux, N., Murat, A., Poizot, E., Méar, Y., Gregoire, G., Lesourd, S., Dauvin, J.C., 2022. An innovative geostatistical sediment trend analysis using geochemical data to highlight sediment sources and transport. *Comput Geosci* 26, 263–278. <https://doi.org/10.1007/S10596-021-10123-5/METRICS>
- Bell, F.G., Bullock, S.E.T., Halbich, T.F.J., Lindsay, P., 2001. Environmental impacts associated with an abandoned mine in the Witbank Coalfield, South Africa. *Int J Coal Geol* 45, 195–216.
- Bell, F.G., Stacey, T.R., Genske, D.D., Steffan, T.R.S., Robertson, K., 2000. Mining subsidence and its effect on the environment: some differing examples. *Cases and solutions Environmental Geology* 40.
- Bertotti, L., Cavaleri, L., Tesaro, N., 1996. Long term wave hindcast in the Adriatic Sea. *Il Nuovo Cimento* 19, 91–108.
- Besset, M., Anthony, E.J., Bouchette, F., 2019. Multi-decadal variations in delta shorelines and their relationship to river sediment supply: An assessment and review. *Earth Sci Rev* 193, 199–219.
<https://doi.org/10.1016/J.EARSCIREV.2019.04.018>
- Bezzi, A., Casagrande, G., Fracaros, S., Martinucci, D., Pillon, S., Sponza, S., Bratus, A., Fattor, F., Fontolan, G., 2021a. Geomorphological changes of a migrating sandbank: Multidecadal analysis as a tool for managing conflicts in coastal use. *Water (Switzerland)* 13. <https://doi.org/10.3390/w13233416>
- Bezzi, A., Pillon, S., Martinucci, D., Fontolan, G., 2018. Inventory and conservation assessment for the management of coastal dunes, Veneto coasts, Italy. *J Coast Conserv* 22, 503–518.
<https://doi.org/10.1007/s11852-017-0580-y>

- Bezzi, A., Pillon, S., Popesso, C., Casagrande, G., Da Lio, C., Martinucci, D., Tosi, L., Fontolan, G., 2021b. From rapid coastal collapse to slow sedimentary recovery: The morphological ups and downs of the modern Po Delta. *Estuar Coast Shelf Sci* 260. <https://doi.org/10.1016/j.ecss.2021.107499>
- Bhattacharya, B., Price, R.K., Solomatine, D.P., 2005. Data-driven modelling in the context of sediment transport. *Physics and Chemistry of the Earth* 30, 297–302. <https://doi.org/10.1016/J.PCE.2004.12.001>
- Bianco, F., Conti, P., García-Ayllon, S., Pranzini, E., 2020. An integrated approach to analyze sedimentary stock and coastal erosion in vulnerable areas: Resilience assessment of san vicenzo's coast (Italy). *Water (Switzerland)* 12. <https://doi.org/10.3390/w12030805>
- Boccotti, P., 1997. A general theory of three-dimensional wave groups part I: the formal derivation, *Ocean Engng.*
- Bockelmann, F.-D., Puls, W., Kleeberg, U., Müller, D., Emeis, K.-C., 2017. Mapping mud content and median grain-size of North Sea sediments - A geostatistical approach. *Mar Geol* 397, 60–71. <https://doi.org/10.1016/j.margeo.2017.11.003>
- Bonaldo, D., Antonioli, F., Archetti, R., Bezzi, A., Correggiari, A., Davolio, S., De Falco, G., Fantini, M., Fontolan, G., Furlani, S., Gaeta, M.G., Leoni, G., Lo Presti, V., Mastronuzzi, G., Pillon, S., Ricchi, A., Stocchi, P., Samaras, A.G., Scicchitano, G., Carniel, S., 2019. Integrating multidisciplinary instruments for assessing coastal vulnerability to erosion and sea level rise: lessons and challenges from the Adriatic Sea, Italy. *J Coast Conserv* 23, 19–37. <https://doi.org/10.1007/s11852-018-0633-x>
- Bowen, A.J., 1980. Simple Models of Nearshore Sedimentation, Beach Profiles and Longshore Bars.
- Brambati, A., 1985. Modificazioni costiere nell'arco lagunare dell'Adriatico Settentrionale. *Antichità Altoadriatiche* 27, 13–47.
- Brambilla, W., Conforti, A., Simeone, S., Carrara, P., Lanucara, S., De Falco, G., 2019. Data set of submerged sand deposits organised in an interoperable spatial data infrastructure (Western Sardinia, Mediterranean Sea). *Earth Syst Sci Data* 11, 515–527. <https://doi.org/10.5194/ESSD-11-515-2019>
- Bruner, K.R., Smosna, R.A., 1989. The Movement and Stabilization of Beach Sand on Transverse Bars, Assateague Island, Virginia. *J Coast Res* 5, 593–601.
- Caballeria, M., Coco, G., Falqués, A., Huntley, D.A., 2002. Self-organization mechanisms for the formation of nearshore crescentic and transverse sand bars. *J Fluid Mech* 465, 379–410. <https://doi.org/10.1017/S002211200200112X>
- Carbognin, L., Teatini, P., Tomasin, A., Tosi, L., 2010. Global change and relative sea level rise at Venice: What impact in term of flooding. *Clim Dyn* 35, 1055–1063. <https://doi.org/10.1007/s00382-009-0617-5>
- Carter, R.W.G., 1978. Small scale transverse bars in lough neagh, Northern Ireland. Volume 1, Issue 2, Pages 205 - 209 1, 205–209.
- Casagrande, G., Bezzi, A., Fracaros, S., Martinucci, D., Pillon, S., Salvador, P., Sponza, S., Fontolan, G., 2023. Quantifying Transgressive Coastal Changes Using UAVs: Dune Migration, Overwash Recovery, and Barrier Flooding Assessment and Interferences with Human and Natural Assets. *J Mar Sci Eng* 11. <https://doi.org/10.3390/jmse11051044>
- Cavaleri, L., Bajo, M., Barbariol, F., Bastianini, M., Benetazzo, A., Bertotti, L., Chiggiato, J., Davolio, S., Ferrarin, C., Magnusson, L., Papa, A., Pezzutto, P., Pomaro, A., Umgiesser, G., 2019. The October 29, 2018 storm in Northern Italy – An exceptional event and its modeling. *Prog Oceanogr* 178. <https://doi.org/10.1016/j.pocean.2019.102178>

- CERC, 1984. Shore Protection Manual. U.S. Army Corps of Engineers, Vicksburg, Mississippi 39180.
- Chaumillon, E., Bertin, X., Fortunato, A.B., Bajo, M., Schneider, J.L., Dezileau, L., Walsh, J.P., Michelot, A., Chauveau, E., Créach, A., Hénaff, A., Sauzeau, T., Waeles, B., Gervais, B., Jan, G., Baumann, J., Breilh, J.F., Pedreros, R., 2017. Storm-induced marine flooding: Lessons from a multidisciplinary approach. *Earth Sci Rev*. <https://doi.org/10.1016/j.earscirev.2016.12.005>
- Chen, Z., Luo, F., Zhou, G., Zhu, F., Wu, H., Li, R., Zhang, C., 2024. Hydrodynamic modeling study of nature-based hybrid coastal defense strategy applied in salt marsh restoration. *Estuar Coast Shelf Sci* 298. <https://doi.org/10.1016/j.ecss.2024.108666>
- Church, J.A., White, N.J., 2011. Sea-Level Rise from the Late 19th to the Early 21st Century. *Surv Geophys* 32, 585–602. <https://doi.org/10.1007/s10712-011-9119-1>
- Coco, G., Calvete, D., Bryan, K.R., Murray, A.B., 2022. Rhythmic Coastal Landforms, in: *Treatise on Geomorphology*. Elsevier, pp. 544–560. <https://doi.org/10.1016/B978-0-12-818234-5.00133-4>
- Coco, G., Zhou, Z., Van Maanen, B., Olabarrieta, M., Tinoco, R., Townend, I., 2013. Morphodynamics of tidal networks: Advances and challenges. *Mar Geol* 346, 1–16. <https://doi.org/10.1016/j.margeo.2013.08.005>
- Conti, L.A., Araujo, C.A.S., Paolo, F.S., Barcellos, R.L., Rodrigues, M., Mahiques, M.M., Furtado, V. V., 2012. An integrated GIS for sedimentological and geomorphological analysis of a lagoon environment. Barra de Cananéia inlet region, (Southeastern Brazil). *J Coast Conserv* 16, 13–24. <https://doi.org/10.1007/s11852-011-0164-1>
- Coppens, A.B., 1981. Simple equations for the speed of sound in Neptunian waters. *J Acoust Soc Am* 69, 862–863. <https://doi.org/10.1121/1.385486>
- Cornaglia, P., 1889. Delle spiagge. *Accademia Nazionale Lincei att Classe Science Fisiche, Matematiche e Naturali Memorie* 5, 284–304.
- Cornish, V., 1898. On Sea-Beaches and Sandbanks. Source: *The Geographical Journal* 11, 528–543.
- Correggiari, A., Perini, L., Remia, A., Luciani, P., Foglini, F., Grande, V., Moscon, G., Calabrese, L., Lorito, S., 2016. SISTEMA INFORMATIVO per l'utilizzo della risorsa sabbia offshore nei progetti di protezione costiera: geodatabase in_Sand.
- Covelli, S., Faganeli, J., Horvat, M., Brambati, A., 1999. Porewater Distribution and Benthic Flux Measurements of Mercury and Methylmercury in the Gulf of Trieste (Northern Adriatic Sea), *Estuarine, Coastal and Shelf Science*.
- Covelli, S., Fontolan, G., Faganeli, J., Ogrinc, N., 2006. Anthropogenic markers in the Holocene stratigraphic sequence of the Gulf of Trieste (northern Adriatic Sea). *Mar Geol* 230, 29–51. <https://doi.org/10.1016/j.margeo.2006.03.013>
- Covelli, S., Piani, R., Acquavita, A., Predonzani, S., Faganeli, J., 2007. Transport and dispersion of particulate Hg associated with a river plume in coastal Northern Adriatic environments. *Mar Pollut Bull* 55, 436–450. <https://doi.org/10.1016/j.marpolbul.2007.09.006>
- Cowell, P.J., Stive, M.J.F., Niedoroda, A.W., De Vriend, H.J., Swift, D.J.P., Kaminsky, G.M., Capobianco, M., 2003. The Coastal-Tract (Part 1): A Conceptual Approach to Aggregated Modeling of Low-Order Coastal Change. Volume 19, Issue 4, Pages 812 - 827 19, 812–827.
- Davis, J.C., 2002. *Statistics and Data Analysis in Geology*, 3rd ed. John Wiley and Sons, New York.

- Davis, R.A., Fitzgerald, D.M., 2004. *Beaches and Coasts*. Blackwell Science Ltd, Oxford, UK.
- De Falco, G., Antonioli, F., Fontolan, G., Lo Presti, V., Simeone, S., Tonielli, R., 2015. Early cementation and accommodation space dictate the evolution of an overstepping barrier system during the Holocene. *Mar Geol* 369, 52–66. <https://doi.org/10.1016/j.margeo.2015.08.002>
- De Grassi, P., De Grassi, V., 1957. *Memoria Sulle Variazioni Morfologiche dei Litorali Marini Della Laguna di Grado*. A cura dell'Azienda Autonoma di Soggiorno—Grado 1–54.
- Dean, R.G., 1991. Equilibrium Beach Profiles: Characteristics and Applications. *J Coast Res* 7, 53–84.
- Dean, R.G., 1973. Heuristic Models of Sand Transport in the Surf Zone.
- Desio, A., 1922. Le variazioni della foce del fiume Isonzo. *Riv. Geogr. Ital.* 10-11–12, 249–268.
- Diesing, M., Green, S.L., Stephens, D., Lark, R.M., Stewart, H.A., Dove, D., 2014. Mapping seabed sediments: Comparison of manual, geostatistical, object-based image analysis and machine learning approaches. *Cont Shelf Res* 84, 107–119. <https://doi.org/10.1016/j.csr.2014.05.004>
- Diesing, M., Mitchell, P.J., O'keeffe, E., Gavazzi, G.O.A.M., Le Bas, T., 2020. Limitations of Predicting Substrate Classes on a Sedimentary Complex but Morphologically Simple Seabed. *Remote Sens (Basel)* 12. <https://doi.org/10.3390/rs12203398>
- Dorigo L., 1965. *La Laguna di Grado e le Sue Foci*. Ricerche e Rilievi Idrografici. Magistrato Alle Acque-Ufficio Idrografico 1–231.
- Duman, M., Duman, Ş., Lyons, T.W., Avci, M., Izdar, E., Demirkurt, E., 2006. Geochemistry and sedimentology of shelf and upper slope sediments of the south-central Black Sea. *Mar Geol* 227, 51–65. <https://doi.org/10.1016/j.margeo.2005.11.009>
- Eaton, R.O., 1950. Littoral processes on sandy coasts. *Coastal Engineering Proceedings* 1, 15. <https://doi.org/10.9753/icce.v1.15>
- Egiazaroff, I. V., 1965. Calculation of Nonuniform Sediment Concentrations. *Journal of Hydraulic Engineering* 91, 225–247.
- EGMS, 2022. *End-to-end implementation and operation of the European Ground Motion Service (EGMS) - Product User Manual*.
- Eldeberky, Y., Battjes, J.A., 1996. Spectral modeling of wave breaking: Application to Boussinesq equations. *J Geophys Res Oceans* 101, 1253–1264. <https://doi.org/10.1029/95JC03219>
- Emery, A.R., Hodgson, D.M., Barlow, N.L.M., Carrivick, J.L., Cotterill, C.J., Mellett, C.L., Booth, A.D., 2019. Topographic and hydrodynamic controls on barrier retreat and preservation: An example from Dogger Bank, North Sea. *Mar Geol* 416. <https://doi.org/10.1016/j.margeo.2019.105981>
- EPA, 2007. *EPA Method 7473 (SW-846): Mercury in Solids and Solutions by Thermal Decomposition, Amalgamation, and Atomic Absorption Spectrophotometry*.
- Falqués, A., Coco, G., Huntley, D.A., 2000. A mechanism for the generation of wave-driven rhythmic patterns in the surf zone. *J Geophys Res Oceans* 105, 24071–24087. <https://doi.org/10.1029/2000jc900100>
- Falqués, A., Iranzo, V., Montoto, A., 1993. Resonance of longshore currents under topographic forcing. *Physics of Fluids A* 5, 3071–3084. <https://doi.org/10.1063/1.858717>
- Falqués, A., Montoto, A., Iranzo, V., Falqués, A., Montoto, A., Iranzo, V., 1996. Bed-flow instability of the longshore current. *CSR* 16, 1927–1964. [https://doi.org/10.1016/0278-4343\(96\)00031-3](https://doi.org/10.1016/0278-4343(96)00031-3)

- Falqués, A., Ribas, F., Mujal-Colilles, A., Puig-Polo, C., 2021. A New Morphodynamic Instability Associated With Cross-Shore Transport in the Nearshore. *Geophys Res Lett* 48. <https://doi.org/10.1029/2020GL091722>
- Falqués, A., Van Den Berg, N., Ribas, F., Caballeria, M., 2012. What determines the wavelength of self-organized shoreline sand waves?, in: *Coastal Engineering*. pp. 1–10. <https://doi.org/10.9753/icce.v33.sediment.6>
- Ferrarin, C., Bajo, M., Benetazzo, A., Cavaleri, L., Chiggiato, J., Davison, S., Davolio, S., Lionello, P., Orlić, M., Umgiesser, G., 2021. Local and large-scale controls of the exceptional Venice floods of November 2019. *Prog Oceanogr* 197. <https://doi.org/10.1016/j.pocean.2021.102628>
- Ferrarin, C., Lionello, P., Orlić, M., Raicich, F., Salvadori, G., 2022. Venice as a paradigm of coastal flooding under multiple compound drivers. *Sci Rep* 12. <https://doi.org/10.1038/s41598-022-09652-5>
- FitzGerald, D.M., Fenster, M.S., Argow, B.A., Buynevich, I. V., 2008. Coastal impacts due to sea-level rise. *Annu Rev Earth Planet Sci* 36, 601–647. <https://doi.org/10.1146/ANNUREV.EARTH.35.031306.140139/1>
- Flemming, B.W., 2000. A revised textural classification of gravel-free muddy sediments on the basis of ternary diagrams. *Cont Shelf Res* 20, 1125–1137. [https://doi.org/10.1016/S0278-4343\(00\)00015-7](https://doi.org/10.1016/S0278-4343(00)00015-7)
- Floreani, F., Pavoni, E., Gosar, M., Covelli, S., 2023. Evasion of Gaseous Elemental Mercury from Forest and Urban Soils Contaminated by Historical and Modern Ore Roasting Processes (Idrija, Slovenia). *Atmosphere (Basel)* 14, 1036. <https://doi.org/10.3390/ATMOS14061036/S1>
- Fontolan, G., Bezzi, A., Casagrande, G., Fracaros, S., Popesso, C., Spadotto, S., Favaro, M., Papa, A., 2023a. Real-time monitoring system and an early warning system implemented. Report D 5.4.3_Part B_ Stream project.
- Fontolan, G., Bezzi, A., Martinucci, D., Pillon, S., Popesso, C., Rizzetto, F., 2015. Sediment budget and management of the Veneto beaches, Italy: an application of the Littoral Cells Management System (SICELL). *Centre Francais du Littoral*, pp. 47–50. <https://doi.org/10.5150/cmcm.2015.010>
- Fontolan, G., Bezzi, A., Martinucci, D., Pillon, S., Popesso, C., Sponza, S., Ulliani, A., Bosa, S., Pascolo, S., Lubrano, F., Petti, M., 2017. Studio di assetto morfologico ambientale della laguna di Marano e Grado.
- Fontolan, G., Bratus, A., Bieker, F., Colombetta, L., Gallitelli, D., Lipizer, M., Sgambati, F., Bezzi, A., Casagrande, G., Fracaros, S., Martinucci, D., Pillon, S., Popesso, C., Sponza, S., et al., 2023b. Piano Coste—Accordo attuativo di collaborazione per lo studio e monitoraggio morfo-sedimentologico dello stato dei litorali della regione Friuli Venezia Giulia finalizzato alla gestione integrata della zona costiera in applicazione alla convenzione quadro tra la Regione Autonoma Friuli Venezia Giulia e l'Università degli Studi di Trieste (DGR 264/2014).
- Fontolan, G., Fattor, F., Bezzi, A., Bratus, A., Casagrande, G., Martinucci, D., Pillon, S., Tondello, M., 2018. Studio di assetto morfologico e ambientale del Banco della Mula di Muggia. Trieste.
- Fontolan, G., Pillon, S., Delli Quadri, F., Bezzi, A., 2007. Sediment storage at tidal inlets in northern Adriatic lagoons: Ebb-tidal delta morphodynamics, conservation and sand use strategies. *Estuar Coast Shelf Sci* 75, 261–277. <https://doi.org/10.1016/j.ecss.2007.02.029>
- Fracaros, S., Bezzi, A., Casagrande, G., Pillon, S., Martinucci, D., Sponza, S., Fontolan, G., Bratus, A., 2021. Application of a semi-automatic method for sedimentological mapping, in: Vlahović, I., Matešić, D.

(Eds.), 36th International Meeting of Sedimentology. Croatian Geological Society, Dubrovnik, HR, pp. 554–554.

- French, J., Payo, A., Murray, B., Orford, J., Eliot, M., Cowell, P., 2016. Appropriate complexity for the prediction of coastal and estuarine geomorphic behaviour at decadal to centennial scales. *Geomorphology* 256, 3–16. <https://doi.org/10.1016/J.GEOMORPH.2015.10.005>
- Friedman, G.M., Sanders, J.E., 1978. Principles of sedimentology, Earth Surface Processes. John Wiley & Sons, Ltd. <https://doi.org/10.1002/ESP.3290040317>
- Friedrichs, C.T., Aubrey, D.G., Speer, P.E., 1990. Impacts of relative sea-level rise on evolution of shallow estuaries, in: Coastal and Estuaries Studies. pp. 105–122. <https://doi.org/10.1029/ce038p0105>
- Gaida, T.C., Snellen, M., van Dijk, T.A.G.P., Simons, D.G., 2019. Geostatistical modelling of multibeam backscatter for full-coverage seabed sediment maps. *Hydrobiologia* 845, 55–79. <https://doi.org/10.1007/s10750-018-3751-4>
- Galloway, D.L., Erkens, G., Kuniansky, E.L., Rowland, J.C., 2016. Preface: Land subsidence processes. *Hydrogeol J* 24, 547–550. <https://doi.org/10.1007/s10040-016-1386-y>
- Galloway, W.E., 1975. Process framework for describing the morphologic and stratigraphic evolution of deltaic depositional systems.
- Galloway, W.E., Hobday, D.K., 2012. Terrigenous clastic depositional systems: applications to fossil fuel and groundwater resources. Springer Science & Business Media.
- Garnier, R., Medina, R., Pellon, E., Falqués, A., Turki, I., 2012. Intertidal finger bars at El Puntal spit, Bay of Santander, Spain, in: 33rd Conference of Coastal Engineering. American Society of Civil Engineering, Santander, pp. 1–8.
- Gatto, P., Carbognin, L., 1981. The lagoon of venice: Natural environmental trend and man-induced modification. *Hydrological Sciences Bulletin* 26, 379–391. <https://doi.org/10.1080/02626668109490902>
- Gelfenbaum, G., Brooks, G.R., 2003. The morphology and migration of transverse bars off the west-central Florida coast. *Mar Geol* 200, 273–289. [https://doi.org/10.1016/S0025-3227\(03\)00187-7](https://doi.org/10.1016/S0025-3227(03)00187-7)
- Gelfenbaum, G., Brooks, G.R., 1997. Long-term observations of migrating shore-normal bars, in: Thornton, E.B. (Ed.), Proceedings of the 1997 Coastal Dynamics Conference. ASCE, Reston, VA, United States, pp. 654–663.
- Giardino, A., Schrijvershof, R., Nederhoff, C.M., de Vroeg, H., Brière, C., Tonnon, P.K., Caires, S., Walstra, D.J., Sosa, J., van Verseveld, W., Schellekens, J., Sloff, C.J., 2018. A quantitative assessment of human interventions and climate change on the West African sediment budget. *Ocean Coast Manag* 156, 249–265. <https://doi.org/10.1016/j.ocecoaman.2017.11.008>
- Gonçalves, J.A., Henriques, R., 2015. UAV photogrammetry for topographic monitoring of coastal areas. *ISPRS Journal of Photogrammetry and Remote Sensing* 104, 101–111. <https://doi.org/10.1016/j.isprsjprs.2015.02.009>
- Goovaerts, P., 1997. Geostatistics for Natural Resources Evaluation. Oxford University Press, New York.
- Gordini, E., Caressa, S., Marocco, R., 2003. Nuova carta morfo-sedimentologica del Golfo di Trieste (Da Punta Tagliamento alla foce dell'Isonzo). *Gortania Atti Mus. Friul. Stor. Nat.* 25, 5–29.

- Gordini, E., Zuliani, D., Deponte, M., Cotterle, D., Visnovich, G., Fabris, P., 2013. Intervento urgente di protezione civile in comune di grado di ripascimento spiaggia e sistemazione opere di difesa lungo la linea di costa - Indagini geofisiche/geognostiche - Rapporto finale. Sgonico (TS), Italy.
- Gosar, M., Pirc, S., Bidovec, M., 1997. JOURNAL OF GEOCHEMICAL EXPLORATION ELSEVIER Mercury in the Idrijca River sediments as a reflection of mining and smelting activities of the Idrija mercury mine, Journal of Geochemical Exploration.
- Goud, M.R., Aubrey, D.G., 1985. Theoretical and observational estimates of nearshore bedload transport rates. *Mar Geol* 64, 91–111. [https://doi.org/10.1016/0025-3227\(85\)90162-8](https://doi.org/10.1016/0025-3227(85)90162-8)
- Goudas, C., Katsiaris, G., May, V., Karambas, T. (Eds.), 2003. *Soft Shore Protection, Coastal Systems and Continental Margins*. Springer Netherlands, Dordrecht. <https://doi.org/10.1007/978-94-010-0135-9>
- Govers, G., 1987. Initiation of motion in overland flow. *Sedimentology* 34, 1157–1164. <https://doi.org/10.1111/J.1365-3091.1987.TB00598.X>
- Gregory, J.M., Griffies, S.M., Hughes, C.W., Lowe, J.A., Church, J.A., Fukimori, I., Gomez, N., Kopp, R.E., Landerer, F., Cozannet, G. Le, Ponte, R.M., Stammer, D., Tamisiea, M.E., van de Wal, R.S.W., 2019. Concepts and Terminology for Sea Level: Mean, Variability and Change, Both Local and Global. *Surv Geophys*. <https://doi.org/10.1007/s10712-019-09525-z>
- Griggs, G., Reguero, B.G., 2021. Coastal adaptation to climate change and sea-level rise. *Water* (Switzerland). <https://doi.org/10.3390/w13162151>
- Guillén, J., Simarro, G., Calvete, D., Ribas, F., Fernández-Mora, A., Orfila, A., Falqués, A., De Swart, R., Sancho-García, A., Durán, R., 2024. Sediment leakage on the beach and upper shoreface due to extreme storms. *Mar Geol* 468, 107207. <https://doi.org/10.1016/j.margeo.2023.107207>
- Hallermeier, R.J., 1981. A profile zonation for seasonal sand beaches from wave climate. *Coastal Engineering* 4, 253–277. [https://doi.org/10.1016/0378-3839\(80\)90022-8](https://doi.org/10.1016/0378-3839(80)90022-8)
- Hasan, R.C., Ierodiaconou, D., Monk, J., 2012. Evaluation of Four Supervised Learning Methods for Benthic Habitat Mapping Using Backscatter from Multi-Beam Sonar. *Remote Sensing* 2012, Vol. 4, Pages 3427-3443 4, 3427–3443. <https://doi.org/10.3390/RS4113427>
- Hasselmann, K., 1974. On the spectral dissipation of ocean waves due to white capping. *Boundary Layer Meteorol* 6, 107–127.
- Hasselmann, S., Hasselmann, K., Allender, J.H., Barnett, T.P., 1985. Computations and parameterizations of the nonlinear energy transfer in a gravity-wave spectrum. Part II: Parameterizations of the nonlinear energy transfer for application in wave models. *J Phys Oceanogr* 15, 1378–1391. [https://doi.org/doi:10.1175/1520-0485\(1985\)015<1378:CAPOTN>2.0.CO;2](https://doi.org/doi:10.1175/1520-0485(1985)015<1378:CAPOTN>2.0.CO;2)
- Himmelstoss, E.A., Henderson, R.E., Kratzmann, M.G., Farris, A.S., 2021. *Digital Shoreline Analysis System (DSAS) version 5.1 user guide*.
- Hinton, C.L., Nicholls, R.J., 2007. Shoreface morphodynamics along the Holland coast. Volume 274, Pages 93 - 101 274, 93–101. <https://doi.org/10.1144/GSL.SP.2007.274.01.10>
- Holthuijsen, L.H., Booij, N., Herbers, T.H.C., 1989. A prediction model for stationary, short-crested waves in shallow water with ambient currents. *Coastal Engineering* 13, 23–54. [https://doi.org/10.1016/0378-3839\(89\)90031-8](https://doi.org/10.1016/0378-3839(89)90031-8)

- Holzer, T.L., Johnson, A.I., 1985. Land subsidence caused by ground water withdrawal in urban areas. *GeoJournal* 11, 245–255.
- Ierodiaconou, D., Monk, J., Rattray, A., Laurenson, L., Versace, V.L., 2011. Comparison of automated classification techniques for predicting benthic biological communities using hydroacoustics and video observations. *Cont Shelf Res* 31, S28–S38. <https://doi.org/10.1016/J.CSR.2010.01.012>
- Innangi, S., Innangi, M., Di Febraro, M., Di Martino, G., Sacchi, M., Tonielli, R., 2022. Continuous, High-Resolution Mapping of Coastal Seafloor Sediment Distribution. *Remote Sens (Basel)* 14, 1268. <https://doi.org/10.3390/RS14051268/S1>
- INTERREG II, 2001. Progetto di Monitoraggio Dell’alto-Adriatico-Relazione Conclusiva, Luglio 1998–Giugno 2001. Trieste.
- Interreg Italy-Croatia CWC, 2021. Report on Pilot Areas—Geomorphological Maps. [WWW Document]. https://www.italy-croatia.eu/documents/279156/0/3.2_RDV_D3.2.1__Pilot+areas+geomorphological+map_rev.pdf/02261cd1-a210-280e-bba4-6a6aebec7f97?t=1614604207922.
- Ippen, A.T., Eagleson, P.S., 1955. A study of sediment sorting by waves shoaling on a plane beach, in: *Beach Erosion Board Technical Memorandum*. U.S. Army Corps of Engineers.
- Jacobs, Walter., 2011. Sand-mud erosion from a soil mechanical perspective. [s.n.].
- James, W.R., 1975. Techniques in Evaluating Suitability of Borrow Material for Beach Nourishment. Technical Manual No. 60. Coastal Engineering Reserch Center, U.S. Army, Corps of Engineers, Fort Belvoir, Va. 22060.
- Janssen, P.A.E.M., 1991. Quasi-linear theory of wind-wave generation applied to wave forecasting. *J. PHYSICAL OCEANOGRAPHY* 21, 1631–1642. [https://doi.org/10.1175/1520-0485\(1991\)021<1631:QLTOWW>2.0.CO;2](https://doi.org/10.1175/1520-0485(1991)021<1631:QLTOWW>2.0.CO;2)
- Janssen, P.A.E.M., 1989. Wave-Induced Stress and the Drag of Air Flow over Sea Waves. *J Phys Oceanogr* 19, 745–754. [https://doi.org/10.1175/1520-0485\(1989\)019<0745:wisatd>2.0.co;2](https://doi.org/10.1175/1520-0485(1989)019<0745:wisatd>2.0.co;2)
- Janušaitė, R., Jukna, L., Jarmalavičius, D., Pupienis, D., Žilinskas, G., 2023. A novel gis-based approach for automated detection of nearshore sandbar morphological characteristics in optical satellite imagery. *Volume 13, Issue 11* 13. <https://doi.org/10.3390/rs13112233>
- Jenness, J., 2006. Topographic Position Index (TPI) v. 1.2.
- Jerosch, K., 2013. Geostatistical mapping and spatial variability of surficial sediment types on the Beaufort Shelf based on grain size data. *Journal of Marine Systems* 127, 5–13. <https://doi.org/10.1016/j.jmarsys.2012.02.013>
- Johnson, H.K., Kofoed-Hansen, H., 2000. Influence of Bottom Friction on Sea Surface Roughness and Its Impact on Shallow Water Wind Wave Modeling. Horsholm, Denmark. [https://doi.org/doi.org/10.1175/1520-0485\(2000\)030<1743:IOBFOS>2.0.CO;2](https://doi.org/doi.org/10.1175/1520-0485(2000)030<1743:IOBFOS>2.0.CO;2)
- Kamphuis, J.W., Hall, K.R., 1983. Cohesive Material Erosion by Unidirectional Current. *Journal of Hydraulic Engineering* 109, 49–61.
- Kandrot, S., Hayes, S., Holloway, P., 2022. Applications of Uncrewed Aerial Vehicles (UAV) Technology to Support Integrated Coastal Zone Management and the UN Sustainable Development Goals at the Coast. *Estuaries and Coasts* 45, 1230–1249. <https://doi.org/10.1007/S12237-021-01001-5/FIGURES/3>

- Katopodes, N.D., 2019. Gravity Waves. *Free-Surface Flow*: 122–186. <https://doi.org/10.1016/B978-0-12-815487-8.00003-2>
- Khabidov, A., 2001. Transverse Bars Formation on a Tideless Beach. *Coastal Dynamics 2001* 666–672. [https://doi.org/10.1061/40566\(260\)68](https://doi.org/10.1061/40566(260)68)
- Khomsin, Mukhtasor, Pratomo, D.G., Suntoyo, 2021. The Development of Seabed Sediment Mapping Methods: The Opportunity Application in the Coastal Waters, in: *IOP Conference Series: Earth and Environmental Science*. IOP Publishing Ltd. <https://doi.org/10.1088/1755-1315/731/1/012039>
- Kinsela, M.A., Hanslow, D.J., Carvalho, & R.C., Linklater, & M., Ingleton, T.C., Morris, B.D., Allen, K.M., Sutherland, M.D., Woodroffe, C.D., 2022. Mapping the Shoreface of Coastal Sediment Compartments to Improve Shoreline Change Forecasts in New South Wales, Australia. *Estuaries and Coasts* 45, 1143–1169. <https://doi.org/10.1007/s12237-020-00756-7>
- Klemas, V. V., 2015. Coastal and Environmental Remote Sensing from Unmanned Aerial Vehicles: An Overview. <https://doi.org/10.2112/JCOASTRES-D-15-00005.1> 31, 1260–1267. <https://doi.org/10.2112/JCOASTRES-D-15-00005.1>
- Komar, P.D., 1976. *Beach processes and sedimentation*. Prentice-Hall, Eaglewood Cliffs, N.J.
- Komen, G.J., Cavaleri, L., Donelan, M., Hasselmann, K., Hasselmann, S., Janssen, P.A.E.M., 1994. *Dynamics and Modelling of Ocean Waves*. *Dynamics and Modelling of Ocean Waves*. <https://doi.org/10.1017/CBO9780511628955>
- Konicki, K.M., Holman, R.A., 2000. The statistics and kinematics of transverse sand bars on an open coast. *Mar Geol* 169, 69–101. [https://doi.org/10.1016/S0025-3227\(00\)00057-8](https://doi.org/10.1016/S0025-3227(00)00057-8)
- Konicki, K.M., Holman, R.A., 1997. Transverse Bars in Duck, North Carolina. *Proceedings of the Coastal Engineering Conference 3*, 3588–3599. <https://doi.org/10.1061/9780784402429.277>
- Koop, L., Snellen, M., Simons, D.G., 2021. An object-based image analysis approach using bathymetry and bathymetric derivatives to classify the seafloor. *Geosciences (Switzerland)* 11, 1–26. <https://doi.org/10.3390/geosciences11020045>
- Kruit, C., 1954. Proposal for a descriptive classification of sediments in stereomicroscopic studies. unpublished.
- Krumbein, W.C., 1957. A method for specification of sand for beach fills. Technical memorandum No. 102. United States. Beach Erosion Board. Engineer Research and Development Center (U.S.), Washington, DC.
- Krumbein, W.C., 1934. Size frequency distributions of sediments. *J Sediment Petrol* 4, 65–77.
- Laporte-Fauret, Q., Marieu, V., Castelle, B., Michalet, R., Bujan, S., Rosebery, D., 2019. Marine Science and Engineering Low-Cost UAV for High-Resolution and Large-Scale Coastal Dune Change Monitoring Using Photogrammetry. *J Mar Sci Eng* 7. <https://doi.org/10.3390/jmse7030063>
- Lark, R.M., Dove, D., Green, S.L., Richardson, A.E., Stewart, H., Stevenson, A., 2012. Spatial prediction of seabed sediment texture classes by cokriging from a legacy database of point observations. *Sediment Geol* 281, 35–49. <https://doi.org/10.1016/J.SEDGEO.2012.07.009>
- Lark, R.M., Marchant, B.P., Dove, D., Green, S.L., Stewart, H., Diesing, M., 2015. Combining observations with acoustic swath bathymetry and backscatter to map seabed sediment texture classes: The

empirical best linear unbiased predictor. *Sediment Geol* 328, 17–32.
<https://doi.org/10.1016/j.sedgeo.2015.07.012>

Leont'yev, I.O., 2014. Calculation of longshore sediment transport. *Oceanology (Wash D C)* 54, 205–211.
<https://doi.org/10.1134/S0001437014020131>

Levoy, F., Anthony, E.J., Monfort, O., Robin, N., Bretel, P., 2013. Formation and migration of transverse bars along a tidal sandy coast deduced from multi-temporal Lidar datasets. *Mar Geol* 342, 39–52.
<https://doi.org/10.1016/J.MARGEO.2013.06.007>

Li, T., Sun, G., Yang, C., Liang, K., Ma, S., Huang, L., Luo, W., 2019. Source apportionment and source-to-sink transport of major and trace elements in coastal sediments: Combining positive matrix factorization and sediment trend analysis. *Science of the Total Environment* 651, 344–356.
<https://doi.org/10.1016/j.scitotenv.2018.09.198>

Lionello, P., Cavaleri, L., Nissen, K.M., Pino, C., Raicich, F., Ulbrich, U., 2012. Severe marine storms in the Northern Adriatic: Characteristics and trends. *Physics and Chemistry of the Earth* 40–41, 93–105.
<https://doi.org/10.1016/j.pce.2010.10.002>

Longdill, P.C., Healy, T.R., Black, K.P., Mead, S.T., 2007. Integrated Sediment Habitat Mapping for Aquaculture Zoning. *J Coast Res SI*, 173–179.

Longhorn, R.A., 2005. Coastal spatial data infrastructure, in: Bartlett, D.J., Smith, J. (Jennifer L. (Eds.), *GIS for Coastal Zone Management*. CRC Press, United States of America, pp. 1–15.

Lorenzo-Trueba, J., Ashton, A.D., 2014. Rollover, drowning, and discontinuous retreat: Distinct modes of barrier response to sea-level rise arising from a simple morphodynamic model. *J Geophys Res Earth Surf* 119, 779–801. <https://doi.org/10.1002/2013JF002941>

Lundblad, E.R., Wright, D.J., Miller, J., Larkin, E.M., Rinehart, R., Naar, D.F., Donahue, B.T., Anderson, S.M., Battista, T., 2006. A benthic terrain classification scheme for American Samoa. *Marine Geodesy* 29, 89–111. <https://doi.org/10.1080/01490410600738021>

Mantz, P.A., 1977. Incipient transport of fine grains and flakes by fluids-extended shield diagram. *Journal of the Hydraulics Division* 103.

Marocco, R., 1989. Lineamenti geomorfologici della costa e dei fondali del Golfo di Trieste e considerazioni sulla loro evoluzione tardo-quadernaria. *Int J Speleol* 18, 87–110.

Maselli, V., Trincardi, F., 2013. Man made deltas. *Scientific Reports* 2013 3:1 3, 1–7.
<https://doi.org/10.1038/srep01926>

Masselink, G., Hughes, M., Knight, J., 2014. Introduction to coastal processes & geomorphology, second edition. *Introduction to Coastal Processes and Geomorphology, Second Edition* 1–416.
<https://doi.org/10.4324/9780203785461/INTRODUCTION-COASTAL-PROCESSES-GEOMORPHOLOGY-GERD-MASSSELINK-MICHAEL-HUGHES-JASPER-KNIGHT>

McBreen, F., Wilson, J.G., Mackie, A.S.Y., Nic Aonghusa, C., 2008. Seabed mapping in the southern Irish Sea: Predicting benthic biological communities based on sediment characteristics, in: *Hydrobiologia*. pp. 93–103. <https://doi.org/10.1007/s10750-008-9341-0>

McBride, R.A., Byrnes, M.R., Hiland, M.W., 1995. Geomorphic response-type model for barrier coastlines: a regional perspective. *Mar Geol* 126, 143–159. [https://doi.org/10.1016/0025-3227\(95\)00070-F](https://doi.org/10.1016/0025-3227(95)00070-F)

- McLachlan, A., Defeo, O., Jaramillo, E., Short, A.D., 2013. Sandy beach conservation and recreation: Guidelines for optimising management strategies for multi-purpose use. *Ocean Coast Manag* 71, 256–268. <https://doi.org/10.1016/j.ocecoaman.2012.10.005>
- McLaren, P., Bowles, D., 1985. The effects of sediment transport on grain-size distributions. *J Sediment Petrol* 55, 457–470. <https://doi.org/10.1306/212F86FC-2B24-11D7-8648000102C1865D>
- McManus, J., 2002. Deltaic responses to changes in river regimes. *Mar Chem* 79, 155–170. [https://doi.org/10.1016/S0304-4203\(02\)00061-0](https://doi.org/10.1016/S0304-4203(02)00061-0)
- Meilianda, E., Huhn, K., Alfian, D., Bartholomä, A., 2015. Variability of surface sediment re-distribution in the high-energy coastal shelf environment at German bight, North Sea.
- Mel, R.A., Coraci, E., Morucci, S., Crosato, F., Cornello, M., Casaioli, M., Mariani, S., Carniello, L., Papa, A., Bonometto, A., Ferla, M., 2023. Insights on the Extreme Storm Surge Event of the 22 November 2022 in the Venice Lagoon. *J Mar Sci Eng* 11, 1750. <https://doi.org/10.3390/jmse11091750>
- Messaros, R.C., Rosati, J.D., Buonaiuto, F., Rasmussen, C., Vega, A.M., Bocamazo, L., 2018. Assessing the Coastal Resilience of Manasquan Inlet to Sea Bright, New Jersey: Regional Sediment Budget 1992–2003. *J Coast Res.* <https://doi.org/10.2112/JCOASTRES-D-17-00067.1>
- Miller, M.C., Mccavet, I.N., Komar, U.D., 1977. Threshold of sediment motion under unidirectional currents. *Sedimentology* 24, 507–527.
- Molinaroli, E., Sarretta, A., Ferrarin, C., Masiero, E., Specchiulli, A., Guerzoni, S., 2014. Sediment grain size and hydrodynamics in Mediterranean coastal lagoons: Integrated classification of abiotic parameters. *Journal of Earth System Science* 123, 1097–1114.
- Neder, C., Sahade, R., Abele, D., Pesch, R., Jerosch, K., 2020. Default Versus Configured-Geostatistical Modeling of Suspended Particulate Matter in Potter Cove, West Antarctic Peninsula. *Fluids* 5, 1–22. <https://doi.org/10.3390/fluids5040235>
- Nicholls, R.J., 1995. Coastal Megacities and Climate Change. *GeoJournal* 37, 369–379.
- Niedoroda, A.W., 1972. Waves, Current, Sediments and Sand Bars Associated with Low Energy Coastal Environments. *Gulf Coast Association Geological Society Trans.* 22, 229–239.
- Niedoroda, A.W., Swift, D.J.P., Hopkins, T.S., Ma, C.M., 1984. Shoreface Morphodynamics on Wave-Dominated Coasts. *Developments in Sedimentology* 39, 331–354. [https://doi.org/10.1016/S0070-4571\(08\)70153-5](https://doi.org/10.1016/S0070-4571(08)70153-5)
- Niedoroda, A.W., Tanner, W.F., 1970. Preliminary study of transverse bars. *Mar Geol* 9, 41–62. [https://doi.org/10.1016/0025-3227\(70\)90079-4](https://doi.org/10.1016/0025-3227(70)90079-4)
- Nienhuis, J.H., Lorenzo-Trueba, J., 2019. Can Barrier Islands Survive Sea-Level Rise? Quantifying the Relative Role of Tidal Inlets and Overwash Deposition. *Geophys Res Lett* 46, 14613–14621. <https://doi.org/10.1029/2019GL085524>
- Nota, D.J.G., 1958. Sediments of the western Guiana shelf. Report of Orinoco shelf expedition. Volume 2. *Mededelingen van de Landbouwhogeschool te Wageningen/Nederland* 58, 1–98.
- Osborne, P.D., Simpson, D.P., 2005. Cross-shore variation of grain size on beaches. *Encyclopedia of Coastal Science.*
- Otvos, E.G., 2018. Coastal barriers, northern Gulf - Last Eustatic Cycle; genetic categories and development contrasts. A review. *Quat Sci Rev* 193, 212–243. <https://doi.org/10.1016/J.QUASCIREV.2018.04.001>

- Palmer, K., Watson, C., Fischer, A., 2019. Non-linear interactions between sea-level rise, tides, and geomorphic change in the Tamar Estuary, Australia. *Estuar Coast Shelf Sci* 225. <https://doi.org/10.1016/j.ecss.2019.106247>
- Park, N.W., Jang, D.H., 2014. Comparison of geostatistical kriging algorithms for intertidal surface sediment facies mapping with grain size data. *The Scientific World Journal* 2014. <https://doi.org/10.1155/2014/145824>
- Patsch, K., Griggs, G., 2008. A sand budget for the Santa Barbara Littoral Cell, California. *Mar Geol* 252, 50–61. <https://doi.org/10.1016/j.margeo.2008.01.013>
- Pavoni, E., Petranich, E., Floreani, F., Bezzi, A., Makdoud, M., Fracaros, S., Fontolan, G., Covelli, S., 2023a. Occurrence and speciation of mercury in the recent sediments of the western coastal area of the Gulf of Trieste (northern Adriatic Sea): is the legacy of historical mining still present?, in: *The Geoscience Paradigm: Resources, Risks and Future Perspectives*. Potenza.
- Pavoni, E., Petranich, E., Signore, S., Fontolan, G., Bezzi, A., Covelli, S., 2023b. Fluxes of settling sediment particles and associated mercury in a coastal environment contaminated by past mining (Gulf of Trieste, northern Adriatic Sea). *J Soils Sediments* 23, 4098–4109. <https://doi.org/10.1007/s11368-023-03451-9>
- Pavoni, E., Petranich, E., Signore, S., Fontolan, G., Covelli, S., 2021. The legacy of the idrija mine twenty-five years after closing: Is mercury in the water column of the gulf of trieste still an environmental issue? *Int J Environ Res Public Health* 18. <https://doi.org/10.3390/ijerph181910192>
- Pellón, E., Garnier, R., Medina, R., 2014. Intertidal finger bars at El Puntal, Bay of Santander, Spain: Observation and forcing analysis. *Earth Surface Dynamics* 2, 349–361. <https://doi.org/10.5194/ESURF-2-349-2014>
- Perini, L., Calabrese, L., Luciani, P., 2020. Mareggiate e impatti sulla costa. Aggiornamento dei dati al 2020, degli indicatori e analisi delle tendenze. Obiettivo di Direzione 3: Contributo al Piano sui cambiamenti climatici. Settore geologico e dei suoli; Macroattività 3.4 SGSS –RER.
- Petti, M., Bosa, S., Pascolo, S., 2018. Lagoon Sediment Dynamics: A Coupled Model to Study a Medium-Term Silting of Tidal Channels. *Water (Basel)* 10. <https://doi.org/10.3390/w10050569>
- Petti, M., Pascolo, S., Bosa, S., Bezzi, A., Fontolan, G., 2019. Tidal Flats Morphodynamics: A new Conceptual Model to Predict Their Evolution over a Medium-Long Period. *Water (Basel)* 11. <https://doi.org/10.3390/W11061176>
- Pilkey, O.H., Cooper, J.A.G., 2014. Are natural beaches facing extinction? <https://doi.org/10.2112/SI70-073.1> 70, 431–436. <https://doi.org/10.2112/SI70-073.1>
- Poizot, E., Méar, Y., 2010. Using a GIS to enhance grain size trend analysis. *Environmental Modelling and Software* 25, 513–525. <https://doi.org/10.1016/J.ENVSOF.2009.10.002>
- Pomaro, A., Cavaleri, L., Lionello, P., 2017. Climatology and trends of the Adriatic Sea wind waves: analysis of a 37-year long instrumental data set. *International Journal of Climatology* 37, 4237–4250. <https://doi.org/10.1002/joc.5066>
- Pomaro, A., Cavaleri, L., Papa, A., Lionello, P., 2018. Data Descriptor: 39 years of directional wave recorded data and relative problems, climatological implications and use. *Sci Data* 5. <https://doi.org/10.1038/sdata.2018.139>

- Pouzet, P., Idier, D., 2024. A composite approach to document a century of overwash events in a high tide environment of southern Brittany, France. *Estuar Coast Shelf Sci* 298. <https://doi.org/10.1016/j.ecss.2024.108626>
- Psuty, N.P., Schmelz, W.J., Spahn, A., Greenberg, J., 2016. Geotemporal vectors of coastal geomorphological change interacting with National Park Service management policy at Great Kills Park, Gateway National Recreation Area, USA. *Geomorphology* 252, 5–16. <https://doi.org/10.1016/j.geomorph.2015.05.023>
- Rafati, Y., Hsu, T.J., Calantoni, J., Puleo, J., 2022. Entrainment and Transport of Well-Sorted and Mixed Sediment Under Wave Motion. *J Geophys Res Oceans* 127. <https://doi.org/10.1029/2022JC018686>
- RAFVG, 2019. Piano Regolatore Portuale del Porto di Monfalcone, Variante Localizzata. Studio Meteomarinario.
- RAFVG, 1986. Caratteristiche chimico-fisiche e biologiche dei corpi idrici superficiali e profondi della regione (Allegato 5).
- Ribas, F., De Swart, H.E., Calvete, D., Falqués, A., 2012. Modeling and analyzing observed transverse sand bars in the surf zone. *J Geophys Res Earth Surf* 117. <https://doi.org/10.1029/2011JF002158>
- Ribas, F., de Swart, H.E., Calvete, D., Falqués, A., 2011. Modeling waves, currents and sandbars on natural beaches: The effect of surface rollers. *Journal of Marine Systems* 88, 90–101. <https://doi.org/10.1016/J.JMARSYS.2011.02.016>
- Ribas, F., Falqués, A., Montoto, A., 2003. Nearshore oblique sand bars. *J Geophys Res Oceans* 108. <https://doi.org/10.1029/2001jc000985>
- Ribas, F., Kroon, A., 2007. Characteristics and dynamics of surfzone transverse finger bars. *J Geophys Res Earth Surf* 112, 3028. <https://doi.org/10.1029/2006JF000685>
- Ritchie, A.C., Warrick, J.A., East, A.E., Magirl, C.S., Stevens, A.W., Bountry, J.A., Randle, T.J., Curran, C.A., Hilldale, R.C., Duda, J.J., Gelfenbaum, G.R., Miller, I.M., Pess, G.R., Foley, M.M., Mccoy, R., Ogston, A.S., 2018. Morphodynamic evolution following sediment release from the world's largest dam removal. *Sci Rep* 8. <https://doi.org/10.1038/s41598-018-30817-8>
- Roberts, H., Brooks, T., 2018. *Sediment budget analysis: practitioner guide*. Horizon House, Deanery Road, Bristol, BS1 5AH.
- Rosati, J.D., 2005. Concepts in sediment budgets. *J Coast Res.* <https://doi.org/10.2112/02-475A.1>
- Rosati, J.D., Walton, T.L., Bodge, K., 2002. Longshore Sediment Transport, in: Walsh, M.J. (Ed.), *Coastal Engineering Manual*. Department of the Army, Washington, DC, pp. 1–113.
- Rubin, Z.K., Kondolf, G.M., Carling, P.A., 2015. Anticipated geomorphic impacts from Mekong basin dam construction. *International Journal of River Basin Management* 13, 105–121. <https://doi.org/10.1080/15715124.2014.981193>
- Ruessink, B.G., Wijnberg, K.M., Holman, R.A., Kuriyama, Y., van Enckevort, I.M.J., 2003. Intersite comparison of interannual nearshore bar behavior. *J Geophys Res Oceans* 108. <https://doi.org/10.1029/2002jc001505>
- Ruggiero, P., Kaminsky, G.M., Gelfenbaum, G., Cohn, N., 2016. Morphodynamics of prograding beaches: A synthesis of seasonal- to century-scale observations of the Columbia River littoral cell. *Mar Geol* 376, 51–68. <https://doi.org/10.1016/J.MARGE0.2016.03.012>

- Ruiz De Alegría-Arzaburu, A., David Gracia-Barrera, A., Kono-Martínez, T., Coco, G., 2022. Subaerial and upper-shoreface morphodynamics of a highly-dynamic enclosed beach in NW Baja California. *Geomorphology* 413, 108336. <https://doi.org/10.1016/j.geomorph.2022.108336>
- Sabatier, F., Maillet, G., Provansal, M., Fleury, T.J., Suanez, S., Vella, C., 2006. Sediment budget of the Rhône delta shoreface since the middle of the 19th century. *Mar Geol* 234, 143–157. <https://doi.org/10.1016/j.margeo.2006.09.022>
- Sanders, J.E., Kumar, N., 1975. Evidence of Shoreface Retreat and In-Place “Drowning” During Holocene Submergence of Barriers, Shelf off Fire Island, New York. *GSA Bulletin* 86, 65–76. [https://doi.org/10.1130/0016-7606\(1975\)86<65:EOSRAI>2.0.CO;2](https://doi.org/10.1130/0016-7606(1975)86<65:EOSRAI>2.0.CO;2)
- Sarretta, A., Pillon, S., Molinaroli, E., Guerzoni, S., Fontolan, G., 2010. Sediment budget in the Lagoon of Venice, Italy. *Cont Shelf Res* 30, 934–949. <https://doi.org/10.1016/j.csr.2009.07.002>
- Seymour, R.J., 2005a. Longshore sediment transport. *Encyclopedia of Coastal Science*.
- Seymour, R.J., 2005b. Cross-shore sediment transport. *Encyclopedia of Coastal Science*.
- Shen, S.-L., Wu, H.-N., Cui, Y.-J., Yin, Z.-Y., 2014. Long-term settlement behaviour of metro tunnels in the soft deposits of Shanghai. *Tunnelling and Underground Space Technology* 40, 309–323. <https://doi.org/10.1016/j.tust.2013.10.013>
- Shepard, F.P., 1952. Revised nomenclature for depositional coastal features. *Am Assoc Pet Geol Bull* 36, 1902–1912.
- Shepard, F.P., 1950. Beach cycles in southern California, in: *Beach Erosion Board (Technical Memo 20)*. U.S. Army Corps of Engineering, Washington DC.
- Sielski, L.H., Angulo, R.J., Souza, M.C., Veiga, F.A., 2017. A low-cost approach to improve sediment mapping in shallow marine environment: A case study on the inner continental shelf of Parana, Southern Brazil, in: *2017 IEEE/OES Acoustics in Underwater Geosciences Symposium (RIO Acoustics)*. IEEE, pp. 1–6. <https://doi.org/10.1109/RIOAcoustics.2017.8349745>
- Sponza, S., Salvador, P., Fracaros, S., 2023. Interaction between coastal fisheries and wintering seabirds along the coasts of Friuli Venezia Giulia, in: *XXI Convegno Italiano Di Ornitologia*. Varese.
- Stive, M.J.F., de Vriend, H.J., 1995. Modelling shoreface profile evolution. *Mar Geol* 126, 235–248. [https://doi.org/10.1016/0025-3227\(95\)00080-I](https://doi.org/10.1016/0025-3227(95)00080-I)
- Stramondo, S., Bozzano, F., Marra, F., Wegmuller, U., Cinti, F.R., Moro, M., Saroli, M., 2008. Subsidence induced by urbanisation in the city of Rome detected by advanced InSAR technique and geotechnical investigations. *Remote Sens Environ* 112, 3160–3172. <https://doi.org/10.1016/j.rse.2008.03.008>
- Sutton-Grier, A.E., Wowk, K., Bamford, H., 2015. Future of our coasts: The potential for natural and hybrid infrastructure to enhance the resilience of our coastal communities, economies and ecosystems. *Environ Sci Policy*. <https://doi.org/10.1016/j.envsci.2015.04.006>
- Swift, D.J.P., Niederoda, A.W., Vincent, C.E., Hopkins, T.S., 1985. Barrier island evolution, middle Atlantic shelf, U.S.A. Part I: Shoreface dynamics. *Mar Geol* 63, 331–361. [https://doi.org/10.1016/0025-3227\(85\)90089-1](https://doi.org/10.1016/0025-3227(85)90089-1)
- Syvitski, J.P.M., Saito, Y., 2007. Morphodynamics of deltas under the influence of humans. *Glob Planet Change* 57, 261–282. <https://doi.org/10.1016/j.gloplacha.2006.12.001>

- Thom, B.G., Hall, W., 1991. Behaviour of beach profiles during accretion and erosion dominated periods. *Earth Surf Process Landf* 16, 113–127. <https://doi.org/10.1002/ESP.3290160203>
- Tillmann, T., Wunderlich, J., 2013. Barrier rollover and spit accretion due to the combined action of storm surge induced washover events and progradation: Insights from ground-penetrating radar surveys and sedimentological data. *J Coast Res* 65, 600–605. <https://doi.org/10.2112/si65-102.1>
- Tosi, L., Teatini, P., Strozzi, T., Carbognin, L., Brancolini, G., Rizzetto, F., 2010. Ground surface dynamics in the northern Adriatic coastland over the last two decades, in: *Rendiconti Lincei*. pp. 115–129. <https://doi.org/10.1007/s12210-010-0084-2>
- Trobec, A., Busetti, M., Zgur, F., Baradello, L., Babich, A., Cova, A., Gordini, E., Romeo, R., Tomini, I., Poglajen, S., Diviacco, P., Vrabec, M., 2018. Thickness of marine Holocene sediment in the Gulf of Trieste (northern Adriatic Sea). *Earth Syst Sci Data* 10, 1077–1092. <https://doi.org/10.5194/essd-10-1077-2018>
- Udden, J.A., 1914. Mechanical composition of clastic sediments. *Geol Soc Am Bull* 25, 655–744. <https://doi.org/10.1130/GSAB-25-655>
- Umgiesser, G., Bajo, M., Ferrarin, C., Cucco, A., Lionello, P., Zanchettin, D., Papa, A., Tosoni, A., Ferla, M., Coraci, E., Morucci, S., Crosato, F., Bonometto, A., Valentini, A., Orlić, M., Haigh, I.D., Nielsen, J.W., Bertin, X., Fortunato, A.B., Pérez Gómez, B., Alvarez Fanjul, E., Paradis, D., Jourdan, D., Pasquet, A., Murre, B., Tintoré, J., Nicholls, R.J., 2021. The prediction of floods in Venice: Methods, models and uncertainty (review article). *Natural Hazards and Earth System Sciences*. <https://doi.org/10.5194/nhess-21-2679-2021>
- Van Maanen, B., Nicholls, R.J., French, J.R., Barkwith, A., Bonaldo, D., Burningham, H., Murray, A.B., Payo, A., Sutherland, J., Thornhill, G., Townend, I.H., Van Der Wegen, M., Walkden, M.J.A., 2016. Simulating mesoscale coastal evolution for decadal coastal management: A new framework integrating multiple, complementary modelling approaches. *Geomorphology* 256, 60–80. <https://doi.org/10.1016/j.geomorph.2015.10.026>
- Van Rijn, L.C., 2020. Critical bed-shear stress for mud-sand beds.
- Van Rijn, L.C., 2011. Coastal erosion and control. *Ocean Coast Manag* 54, 867–887. <https://doi.org/10.1016/j.ocecoaman.2011.05.004>
- Van Rijn, L.C., 1993. Principles of sediment transport in rivers, estuaries and coastal seas. www.aquapublications.nl.
- Walbridge, S., Slocum, N., Pobuda, M., Esri, D.J.W., 2018. Unified Geomorphological Analysis Workflows with Benthic Terrain Modeler. *Geosciences (Basel)* 8. <https://doi.org/10.6084/m9.figshare.5946463>
- Ward, I., Larcombe, P., 2008. Determining the preservation rating of submerged archaeology in the post-glacial southern North Sea: A first-order geomorphological approach. *Environmental Archaeology* 13, 59–83. <https://doi.org/10.1179/174963108x279229>
- Ware, S., Downie, A.L., 2020. Challenges of habitat mapping to inform marine protected area (MPA) designation and monitoring: An operational perspective. *Mar Policy* 111. <https://doi.org/10.1016/j.marpol.2019.103717>
- Watson, S.J., Neil, H., Ribó, M., Lamarche, G., Strachan, L.J., MacKay, K., Wilcox, S., Kane, T., Orpin, A., Nodder, S., Pallentin, A., Steinmetz, T., 2020. What We Do in the Shallows: Natural and Anthropogenic

Seafloor Geomorphologies in a Drowned River Valley, New Zealand. *Front Mar Sci* 7.
<https://doi.org/10.3389/fmars.2020.579626>

Weiss, A., 2001. Topographic position and landforms analysis, in: ESRI User Conference.

Wentworth, C.K., 1922. A Scale of Grade and Class Terms for Clastic Sediments. *J Geol* 30, 377–392.
<https://doi.org/10.1086/622910>

Wright, L.D., 1995. Morphodynamics of inner continental shelves, 1st ed, (No Title). CRC-Press.

Wright, L.D., Short, A.D., Green, M.O., 1985. Short-term changes in the morphodynamic states of beaches and surf zones: An empirical predictive model. *Mar Geol* 62, 339–364. [https://doi.org/10.1016/0025-3227\(85\)90123-9](https://doi.org/10.1016/0025-3227(85)90123-9)

Yaiche Temam, I., Bouhmadouche, M., Hemdane, Y., Kessali, N., Amiri, H., 2024. Analysis of the hydrosedimentary circulation in the mouth of dominated wave environment using grain size analysis, wave/current modeling and image processing case of the principal Rivers in Zemmouri bay. *Model Earth Syst Environ*. <https://doi.org/10.1007/s40808-024-02007-1>

Yamashita, S., Naruse, H., Nakajo, T., 2018. Reconstruction of sediment-transport pathways on a modern microtidal coast by a new grain-size trend analysis method. *Prog Earth Planet Sci* 5.
<https://doi.org/10.1186/S40645-018-0166-9>

Yavuz, H., 2004. An estimation method for cover pressure re-establishment distance and pressure distribution in the goaf of longwall coal mines. *International Journal of Rock Mechanics & Mining Sciences* 41, 193–205. [https://doi.org/10.1016/S1365-1609\(03\)00082-0](https://doi.org/10.1016/S1365-1609(03)00082-0)

Young, I.R., 1999. Wind generated ocean waves, 1st ed. Elsevier.

Zananiri, I., Vakalas, I., 2019. Geostatistical mapping of marine surficial sediment types in the Northern Aegean Sea using indicator kriging. *Geo-Marine Letters* 39, 363–376. <https://doi.org/10.1007/s00367-019-00581-3>

Zanchettin, D., Bruni, S., Raicich, F., Lionello, P., Adloff, F., Androsov, A., Antonioli, F., Artale, V., Carminati, E., Ferrarin, C., Fofonova, V., Nicholls, R.J., Rubinetti, S., Rubino, A., Sannino, G., Spada, G., Thiéblemont, R., Tsimplis, M., Umgiesser, G., Vignudelli, S., Wöppelmann, G., Zerbini, S., 2021. Sea-level rise in Venice: Historic and future trends (review article). *Natural Hazards and Earth System Sciences*.
<https://doi.org/10.5194/nhess-21-2643-2021>





Zhengfu, B., Inyang, H.I., Daniels, J.L., Frank, O., Sue, S., 2010. Environmental issues from coal mining and their solutions. *Mining science and technology* 20, 215–223. [https://doi.org/10.1016/S1674-5264\(09\)60187-3](https://doi.org/10.1016/S1674-5264(09)60187-3)

9 Acknowledgements

Vorrei innanzitutto ringraziare la mia famiglia. Mamma, Papà, Rossi, i nonni Graziella, Noemi, Angilin e Sergio, gli zii Linduta e Adri e i cugini Esty, Frenchi e Giulo: senza di voi non sarei qui e non avrei potuto intraprendere questo percorso. Ringrazio di cuore il prof. Fontolan e, con lui Annelore, Chiara, Giulia*, Davide, Paolo, Sebastian*, Simone e Stefano per avermi supportato, sopportato e integrato nel Coastal group non solo come studente, ma come compagno di avventura. Ringrazio i colleghi e compagni dottorandi di UNITS e tutte le persone con cui mi è capitato di collaborare, in particolare Antonio per avermi approcciato allo “Italico Naviglio” ancora in tempi di tesi magistrale. Ringrazio Raffa, Isaac e tutti gli amici di Terzo e Aquileia; i Moni; la Directory e la DCC; il Bianco, Gubb e Berna. Uno speciale ringraziamento al Possa perché, povero, lo disturbo quasi ogni giorno. Feh, ti ringrazio infinitamente: sei, probabilmente, la persona che più mi ha fatto maturare in questi anni. E infine ci sei tu, Lollo (e famiglia), perché, come i famigliari, mi sei sempre stato vicino, fin da quando ero piccino.

Article

Geomorphological Changes of a Migrating Sandbank: Multidecadal Analysis as a Tool for Managing Conflicts in Coastal Use

Annelore Bezzi ^{1,*}, Giulia Casagrande ¹, Saverio Fracaros ¹, Davide Martinucci ¹, Simone Pillon ¹, Stefano Sponza ¹, Antonio Bratus ², Fabrizio Fattor ² and Giorgio Fontolan ^{1,3,*}

¹ Department of Mathematics and Geosciences, University of Trieste, Via E. Weiss 1, 34128 Trieste, Italy; gcasagrande@units.it (G.C.); saverio.fracaros@phd.units.it (S.F.); dmartinucci@units.it (D.M.); spillon@units.it (S.P.); sponza@units.it (S.S.)

² Autonomous Region of Friuli Venezia Giulia, Geological Survey, Via S. Anastasio 3, 34132 Trieste, Italy; antonio.bratus@regione.fvg.it (A.B.); fabrizio.fattor@regione.fvg.it (F.F.)

³ National Interuniversity Consortium for Marine Sciences, CoNISMa, Piazzale Flaminio 9, 00196 Rome, Italy

* Correspondence: bezzi@units.it (A.B.); fontolan@units.it (G.F.)

Abstract: While beach erosion and sand loss are typically of great concern to the tourism industry, managing rapid morphological changes linked to large amounts of moving sediments is the challenge facing Grado, an important seaside resort in the northern Adriatic, Italy. The cause of the unusual management conflict is the presence of the Mula di Muggia Bank, a nearshore depositional system made up of relict and active migrating sandbanks extending up to 2 km seawards from the touristic beachfront. A reconstruction of the morpho-sedimentary evolution of the coastal system over a 200-year period was done using a large dataset which includes historical cartography, topographic maps, aerial photos and topo-bathymetric surveys. The results show the growth of a significant urban development aimed at creating a tourist destination by occupying the waterfront along fetch-limited coastal tracts with very shallow water and scarce hydrodynamics. Furthermore, a number of sandy dynamic landforms (longshore migrating bars, a bypass corridor, an ebb-tidal delta) and accumulation zones attest to a sediment excess which can be mostly attributed to the eastern river supplies. The progressive constant migration rate of 12.6 my^{-1} allowed the bank to induce the expansion of the low-energy silty backbarrier environment, characterised by abundant seagrass meadows a short distance directly in front of the tourist beaches of Grado. As a result of historical analysis and more current observations, areas with diverse morphosedimentary features and with varying tourist/recreational, ecological, and conservation values have been identified. These can be considered as basic units for future accurate planning and re-evaluation of coastal management choices to balance environmental protection and tourist use. A soft coastal defence approach is proposed which includes either the preservation of specific environments or the proper use of excess sand for beach nourishment via periodic dredging or sediment bypassing.

Keywords: sandbank; migration; barrier; backbarrier; shoreline analysis; historical evolution; coastal zone management



Citation: Bezzi, A.; Casagrande, G.; Fracaros, S.; Martinucci, D.; Pillon, S.; Sponza, S.; Bratus, A.; Fattor, F.; Fontolan, G. Geomorphological Changes of a Migrating Sandbank: Multidecadal Analysis as a Tool for Managing Conflicts in Coastal Use. *Water* **2021**, *13*, 3416. <https://doi.org/10.3390/w13233416>

Academic Editor:
Miguel Ortega-Sánchez

Received: 26 October 2021
Accepted: 30 November 2021
Published: 3 December 2021

Publisher's Note: MDPI stays neutral with regard to jurisdictional claims in published maps and institutional affiliations.



Copyright: © 2021 by the authors. Licensee MDPI, Basel, Switzerland. This article is an open access article distributed under the terms and conditions of the Creative Commons Attribution (CC BY) license (<https://creativecommons.org/licenses/by/4.0/>).

1. Introduction

Coastal systems are the most densely populated locations on the planet, as well as the most vulnerable to sea-level rise (SLR) caused by global warming. Continued accelerated global SLR, along with potential increases in the frequency and intensity of extreme sea-level events [1,2], will cause rapid coastal changes in many parts of the world. Even currently, erosion, drowning and increased vulnerability involve sedimentary bodies such as beaches, coastal dunes, barrier island systems and deltas. The transgressive trend is exacerbated by the simultaneous severe anthropogenic influence on sediment supply and

transport, as well as on coastal dynamics and subsidence [3–13]. In light of the environmental, socioeconomic, and cultural values of coastal areas, the coastal response and adaptation capability to relative SLR are not uniform and assume considerable local variation, making comprehension and prediction one of the most important and debated topics in scientific literature, i.e., [14,15]. The definition of the temporal scale is critical for assessing coastal evolution and distinguishing coastal change caused by episodic, seasonal, or long-term processes [16,17]. A multidecadal analysis of the shoreline is a basic requirement for coastal management and one of the classic geomorphological methodologies [18–23]. Shoreline analysis is typically performed using historical databases, aerial photos, and maps, which are then supplemented with GPS surveys and high-resolution remote sensing methodologies [17,19–21]. Long-term series are not always available due to the lack of historical institutional databases for coastal monitoring, such as those in the United States [19,24], Belgium [25], or the Netherlands [26]. At the same time, the integration of heterogeneous databases poses problems due to differing levels of accuracy and precision of survey measurements and is heavily dependent on the correct choice of a shoreline proxy indicator [27].

Even more complex is the issue that arises when dealing with bathymetric data, which typically represents the basis for a more complete morphological analysis and sediment-budget approach [22,28–34]. The qualitative-quantitative analysis of historical and recent data should also include a more thorough examination of the morphological elements and their evolution [18,35,36] completed by the analysis of territorial development [23,36,37], which will allow both to have a pertinent geomorphological framework and assess the anthropogenic influence on coastal evolution.

In this work we analyse the Mula di Muggia Bank (hereinafter MMB), a nearshore depositional system made up of active and relict sandbanks that extends up to 2 km seawards from the touristic beachfront of Grado (northern Adriatic, Italy). While erosion and sand loss are always key issues for the tourism business [38–43], managing rapid morphological changes linked to large quantities of moving sediments is the challenge here. The reconstruction of the morphological evolution over a 200-year period, combined with an overview of the most significant anthropogenic changes, addresses the need to develop an adequate knowledge base for effective future planning and re-evaluation of coastal management decisions to balance environmental protection and tourist use.

2. Study Area

2.1. Geographic Setting

The study area, entirely included in the Municipality of Grado, is located between the Grado inlet and the mouth of the Isonzo River, in the Gulf of Trieste, northern Adriatic, Italy (Figure 1). It represents the easternmost part of the system of barrier islands bordering the Grado Lagoon and is nearly entirely devoted to tourism and agriculture. Grado is a tourist town with approximately 8000 inhabitants, which more than triples during the summer season; the number of nights spent in tourist accommodation is ca. 1.4 million per year [44].

Seaward, a wide system of intertidal and subtidal sand bars extends until a depth of 3 m. Their morphology was first mapped and described by [45] and, more recently, by [46–49]. From the planimetric view, the belt of multiple sandy bars forms two arcuate triangular shapes (the MMB and the delta complex of the Isonzo River), which extend up to 2 km seawards, and converge towards a landward central point, ideally represented by the tidal inlet of Primero. Overall, these morphological systems represent an anomaly in the regular bathymetric trend of the northern Adriatic and the Gulf of Trieste, with a strong extroflexion of the nearshore contour lines, corresponding to high sediment thicknesses (up to 8 m) deposited during the Holocene, following the Last Glacial Maximum [50].

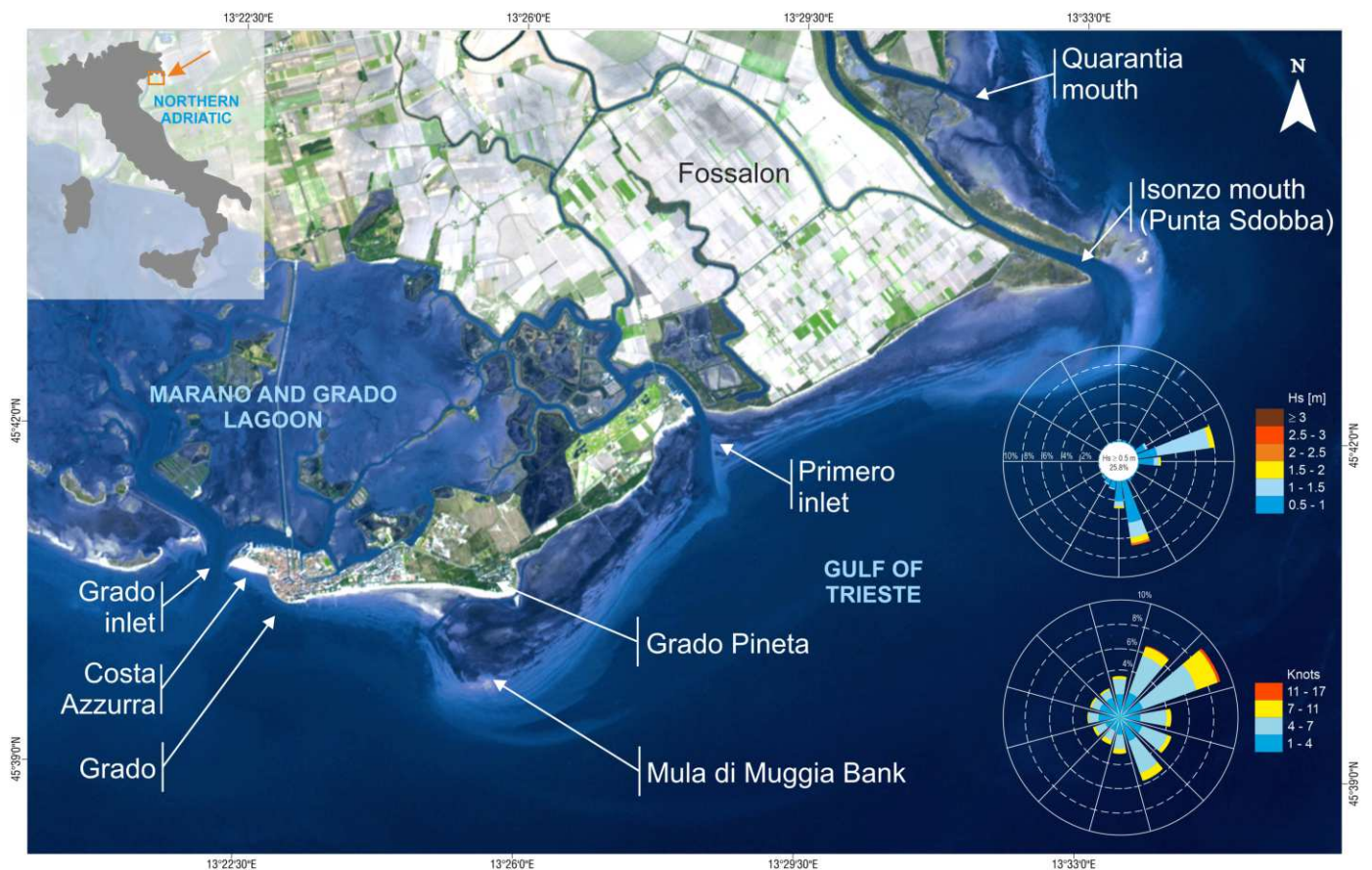


Figure 1. Overview of the study area (Basemap: Landsat, in false-colour, wind and wave roses redrawn from [51]).

A large part of the MMB, as well as the mouth of the Isonzo River, are currently part of the Natura 2000 network (Special Areas of Conservation and Special Protection Area IT 3330006 and IT 3330005). The Autonomous Region of Friuli-Venezia Giulia has added both sites to its list of regional geosites.

The Isonzo River is the principal sediment source in the area. The drainage basin of the Isonzo has a total extension of 3452 km², with major tributaries (the Natisone—Torre and Vipacco Rivers). The average annual flow rate at the river mouth is 196.8 m³ s⁻¹, ranging monthly from 43.1 to 665.9 m³ s⁻¹ [52]. The 18–19 November 1940 flood reached 4400 m³ s⁻¹, flooding 350 hectares of crops on Isola Morosini, not far from the river mouth [53]. Despite the lack of data, the torrential regime of the river, which collects and discharges the waters from the southern slope of the Julian Alps, and the extremely high rainfall of its Prealps catchment (mean yearly rainfall between 2700 and 3200 mm) support the hypothesis of the significant potentiality of solid river discharge. Instead, extensive anthropogenic modification (afforestation, river damming, and river-bed sand mining) has been blamed for a significant decrease in fluvial sediment load over the last century, according to some authors [54,55]. The decline is not directly measured but is confirmed by the evidence of morphological changes to the river bed [55].

2.2. Oceanographic and Meteorological Forcing

The wind climate of the northern Adriatic is characterised by the predominance of winds from the first quadrant, primarily from the ENE direction (the Bora) either in terms of frequency or strength [51,56]. South-easterly winds (the Scirocco) with a longer geographic fetch (more than 800 km) are also significant. Tides in the Gulf of Trieste are semi-diurnal with a mean range of 76 cm [57], a mean spring-tide range of 105 cm, and a mean neap tide of 22 cm [58]. The combination of spring tides, seiches, south-easterly winds, and low atmospheric pressure can result in an exceptional rise in sea level (known as “acqua alta”),

which reached 194 cm over the Venice benchmark on 4 November 1966. Due to the Bora and the Scirocco winds, the wave regime is typically bimodal. According to data recorded at the wave buoy OGS-DWRG1 (located at the coordinates 13.24° E, 45.56° N, −16 m depth), the mean significant wave height (H_s) is less than 0.5 m. Events with H_s greater than 0.5 m account for 25% of the overall record, with prevailing waves from the SE (10.7%) and ENE (10.5%). The Scirocco has the highest recorded waves, with $H_s = 4.4$ m [51]. The yearly wave energy for the northern Adriatic area is $15.61 \text{ m}^2 \text{ s}^2$ [59]. Forced by the prevailing Bora winds, short waves act along the coastal area of Grado inducing a longshore drift directed westward from the Isonzo River to Grado.

3. Materials and Methods

To conduct this study, a large dataset was collected, analysed and critically selected, including data of various origins. Historical cartography (from 1798 to 1830), topographic maps (from 1869 to 2003), aerial photos (from 1954 to 2019) and nautical map ((1927) or topo-bathymetric surveys (from 1968 to 2019) were used to recognize the landforms, identify anthropogenic changes, and interpret the morpho-sedimentary processes. A part of the collected data was used to map the landform changes over time, to identify some geomorphological indicators and to support the quali-quantitative analysis.

According to the quality and reliability of the sources, we followed two different approaches. The first approach involved historical cartography: earlier depictions of the area were frequently inaccurate, and in some cases completely fictitious. After careful comparison between them, the chosen maps had to represent plausible morphological elements that were recognisable over time. The second approach concerned the correlation of recent data. The availability of different types of information over a long period of time raises the question of how the data should be associated. For this reason, the available materials we chose had to be relative to the same year (for example, aerial photos and topo-bathymetric surveys from 2007), or could be comparable in a very limited time span (for example, aerial photos from 1978 and topo-bathymetric surveys from 1985), or were of the same type (for example, photointerpretation data).

To evaluate the morphological changes of the MMB, a topo-bathymetric survey was carried out in 2019. A double sampling approach was chosen: we replicated the profiles placed at the same points in 1968 to have the best-matched data possible, while for the most dynamic areas such as bars, troughs, and channels, a higher density acquisition was performed for better reconstruction. All the specific information about the survey methodology and detailed results are reported in [60]. Table 1 summarises the entire dataset, including the cartographic databases consulted on the internet [61,62].

Table 1. Summary of the entire dataset used for elaboration. A, B, C, D refer to the use of the data or the type of results obtained: (A) basemap, also consulted for information on anthropogenic changes; (B) consulted for the morphological and sedimentological interpretation; (C) cartographic restitution of the interpreted morphologies and sedimentology; (D) reference period of the multidecadal evolution (see Section 4.2).

Survey Year	Type of Source Data	References	Type of Resulting Data			
			A	B	C	D
1798–1805	historical map	Kriegskarte von Zach		•		
1822–1824	historical map	Carta di cabotaggio del mare Adriatico, Istituto Geografico Militare di Milano	•		•	I
1830	historical map	Franzische Landesaufnahme [61]	•		•	I
1869–1887	topographic map	Franzisco—Josephinische Landesaufnahme [61]		•		II
1894	topographic map	Topographische Karte, Militärgeographisches Institut	•		•	II
1915–1917	topographic map	Grado, F. 40II.S.E. della Carta d'Italia, Istituto Geografico Militare, 1917 Punta Sdobba, F. 40III.S.O. della Carta d'Italia, Istituto Geografico Militare, 1915		•		III
1927	nautical map	Marina di Grado, Istituto Idrografico della Marina, 1928 (survey 1927)			•	III
1938	topographic map	Grado, F. 40II.S.E. della Carta d'Italia, Istituto Geografico Militare Punta Sdobba, F. 40III.S.O. della Carta d'Italia, Istituto Geografico Militare	•		•	III
1949	topographic map	Grado, F. 40II.S.E. della Carta d'Italia, Istituto Geografico Militare Foce dell'Isonzo, F. 40III.S.O. della Carta d'Italia, Istituto Geografico Militare	•	•		IV
1954	aerial photos	GAI (Gruppo Aereo Italiano)			•	IV
1959	topographic map	Foce dell'Isonzo, F. 40III.S.O. della Carta d'Italia, Istituto Geografico Militare	•	•		V
1968	topo-bathymetric survey	Consiglio Nazionale delle Ricerche (CNR) Project "Studio del regime dei litorali"			•	V
1972–1973	sedimentological survey	Consiglio Nazionale delle Ricerche (CNR) Project "Regime e Conservazione dei litorali italiani", 1970–1975 [54]		•		V
1974	topographic map	Carta Tecnica Regionale (CTR)—Regione Autonoma Friuli Venezia Giulia, flight 1974, published in 1978	•	•		V
1978	aerial photos	Consiglio Nazionale delle Ricerche (CNR)—Project "Dinamica dei litorali", 1975–1980			•	V
1985	topo-bathymetric survey	Regione Autonoma Friuli Venezia Giulia, 1985 [54]			•	VI
1985	sedimentological survey	Regione Autonoma Friuli Venezia Giulia, 1985 [54]			•	VI
1990	topographic map	Carta Tecnica Numerica Regionale (CTNR)—Regione Autonoma Friuli Venezia Giulia, flight 1990, published in 1993	•	•		VI
2003	topographic map	Carta Tecnica Numerica Regionale (CTNR)—Regione Autonoma Friuli Venezia Giulia—aggiornamento generale anno 2003	•	•		VI
2007	digital orthophoto	Available on Geoportale Nazionale [62]			•	VI
2007	topo-bathymetric survey	MIUR FISR—Project "Vector" (coordinated by CoNISMa—Consorzio Nazionale Interuniversitario per le Scienze del Mare), 2006–2009			•	VI
2018	digital ortophotos	Lidar surveys—true orthophoto of the Regione Autonoma Friuli Venezia Giulia, 2017–2020	•	•		VII
2019	topo-bathymetric survey	University of Trieste, Interreg Project Italy-Croatia "Change We Care" [60]			•	VII
2019	digital orthophotos (UAV survey)	University of Trieste, Interreg Project Italy-Croatia "Change We Care" [60]			•	VII

4. Results

4.1. Morpho-Sedimentary Configuration

Thanks to the most recent topo-bathymetric surveys (2019) and photo interpretation (2018), a detailed geomorphological map was created (Figure 2). The map depicts four distinct zones of environmental and morphological homogeneity: (a) the Grado sector (G sector), which consists of the coastal area facing Grado and is characterised by bathing areas and a medium-gradient seabed (between 0.3 and 0.9%); (b) the Mula di Muggia shoal complex (MMB sector), which has a strongly asymmetric shape and can be identified by the -5 m contour line, and is about 1810 m from the shoreline in the western sector to a maximum of 2705 m in the eastern sector. The bank's apex is defined by barely emerging bars (0.57 m), whereas another emerging bank can be found near the tourist beach; (c) the Primero Inlet area (PI sector), representing the Primero tidal inlet system, which is characterised by the main ebb channel separating the MMB from (d) the Isonzo Delta (ID sector), the river's deltaic complex. Beaches vary in width along the entire coast: the central portion of sectors G and MMB, as well as the entire sector ID, have no or narrow beaches (average value of about 14 m), while the remnant areas have an average value of about 75 m. Behind the beaches, in sector ID, there is a large reclamation agricultural area.

A low-energy silty backbarrier environment with abundant seagrass meadows and microbial mats front the tourism beaches of G, MMB, and the western edge of ID. The shallow seabed is affected by numerous little canals used by small boats, some swimming "pools" and a small marina.

A barrier—upper shoreface system confines the backbarrier system to the sea between 300 and 1300 m from the shoreline. This is shown by an intertidal sandbank and a barred shoreface which indicate the sandy masses currently being transported longshore to the southwest. (Figure 3). The barrier system includes the emerging bars of the apex of the MMB that partially obstruct the marina's access canal in front of the Grado Pineta promontory. The bathymetric surveys were used to estimate the outer limit of this very dynamic zone, corresponding to a mean depth value of 2.7 m. A series of crests and troughs may be seen offshore, overstepping the limit of the bank in a relatively flat area that morphologically resembles a terrace (see section A–A1 in Figure 2). These forms can be identified in the MMB zone between -4 m and -6 m and have been recognised as finger bars [63–66] after both an aerial photo and topo-bathymetric examination. Other elongated sandy relict bodies of unknown origin (the external bars in Figure 2) lie within a depth of 9 m, as also indicated by [49,50,67].

The PI sector has a distinct main ebb channel and a marginal channel, as well as evidence of a sediment bypass corridor connecting the updrift and downdrift flanks, following the main longshore drift.

The easternmost sector is the active sedimentary lobe of the Isonzo delta, nourished by the sediment supplied by the river at Punta Sdobba. The topographic profile (section B–B1 in Figure 2) is represented by the flat depositional delta front and the concave featureless transition from the delta front to the prodelta.

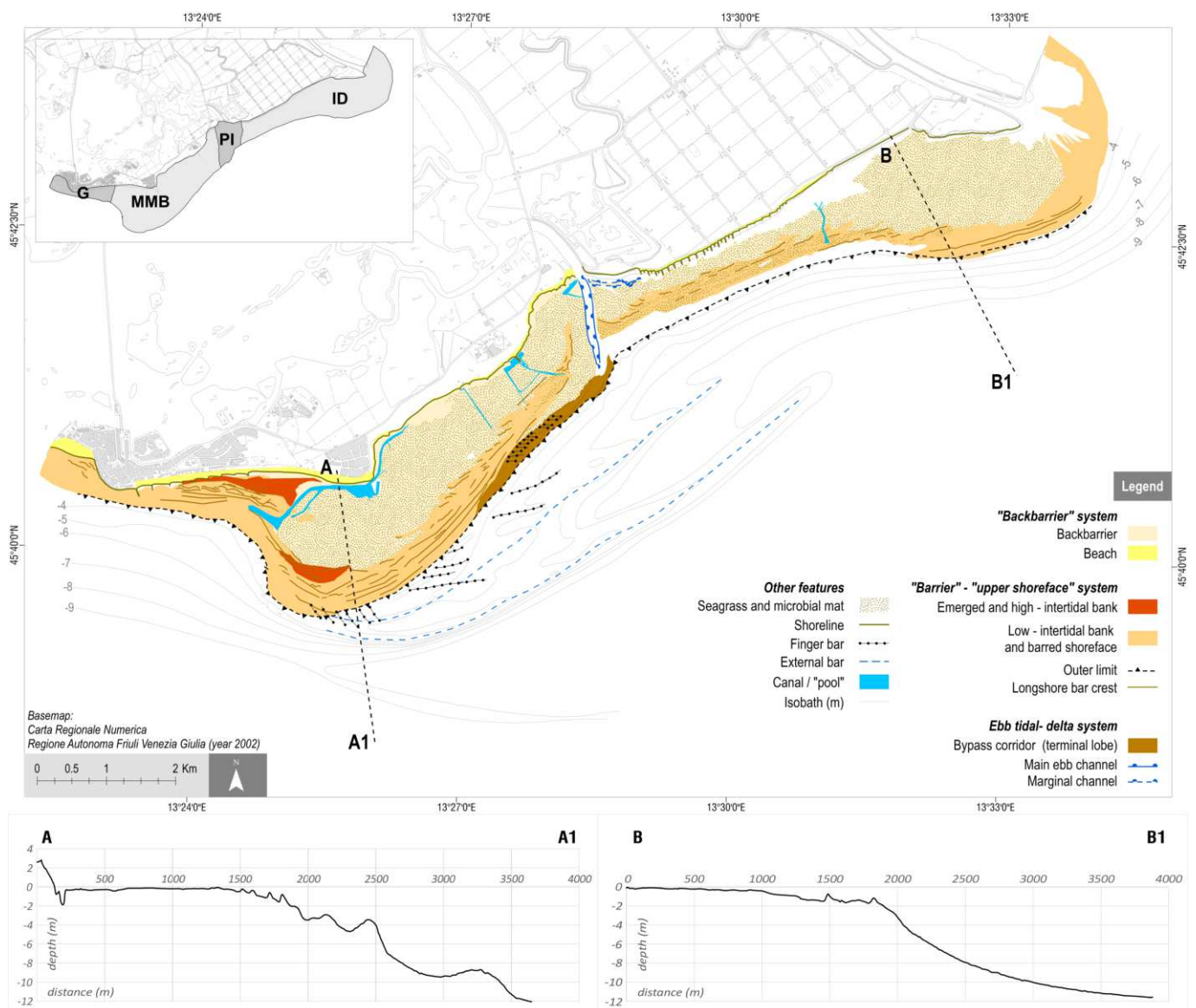


Figure 2. Geomorphological map of the coastal area including the Grado (G), Mula di Muggia (MMB), Primero inlet (PI) and Isonzo Delta (ID) sectors.

A sedimentological map, derived from the available sedimentological data, is proposed to complete the morpho-sedimentary frame (Figure 4; after [54]). The sedimentological evidence mirrors the morphological evidence and can be summarised as follows:

- Fine sand ($2 < Mz < 3 \text{ phi}$) is the most common sediment type of the beaches as a result of natural wave dynamics along this fetch-limited and protected shoreline.
- Very fine sand ($3 < Mz < 4 \text{ phi}$) occurs on the artificial beach between Grado and Grado Pineta, as well as on the barred shoreface in front of it, replaced by coarse silt from -3 m seawards.
- An inversion of the normal coast-to-sea transition (seaward fining) occurs in the coastal tract, which is seaward limited by the sandbanks (MMB and ID). Here, the finest sediments ($>3.5 \text{ phi}$, but mostly medium and fine silt) dominate the intertidal flat facing the shoreline, confirming the backbarrier characteristics of the area. Seaward, the sediments with the coarsest Mz ($<2.5 \text{ phi}$) follow the bar and trough zone close to the outer limit of the bank and upper shoreface, identifying this zone as the most dynamic and exposed to wave action. Here the western longshore is active, and longshore elongated bars are the dominant landforms.

- The seaward limit of the littoral sand prism can be identified between -5 and -6 m in the ID zone, while on the seabed of the MMB a vast zone of pure, fine sand extends up to $-7/-8$ m, corresponding to east-oriented sand bars, the origin of which is still unknown.

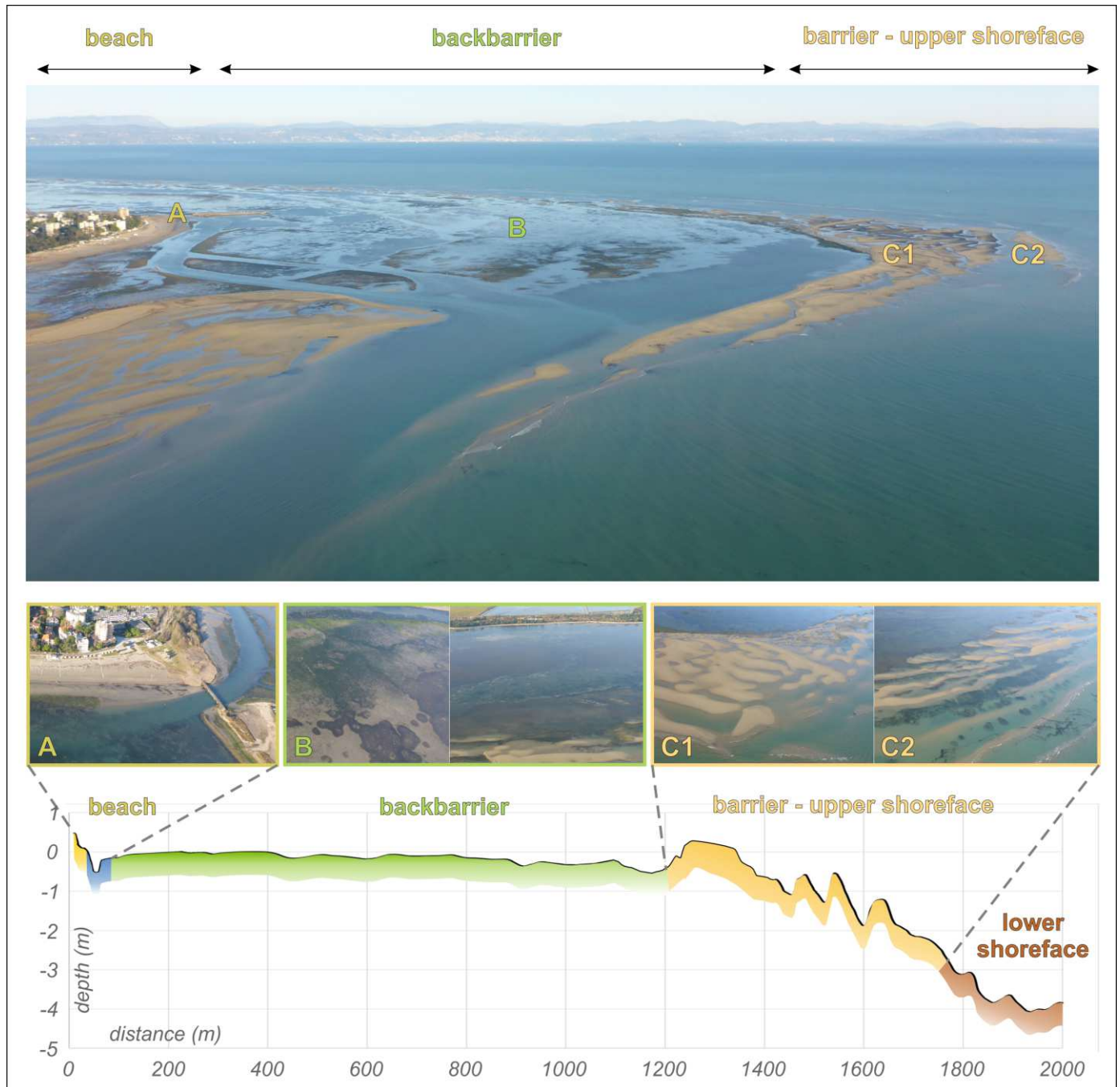


Figure 3. Morpho-bathymetric structure of the Mula di Muggia Bank. The barrier (C1) and the longshore bars (C2) migrate westward (from the top to the bottom of the upper image), thus obstructing the canal that crosses the backbarrier (B). The canal is the sole route for small boats to traverse the shallow silty zone toward the coastline (A) and the Grado Pineta marina.

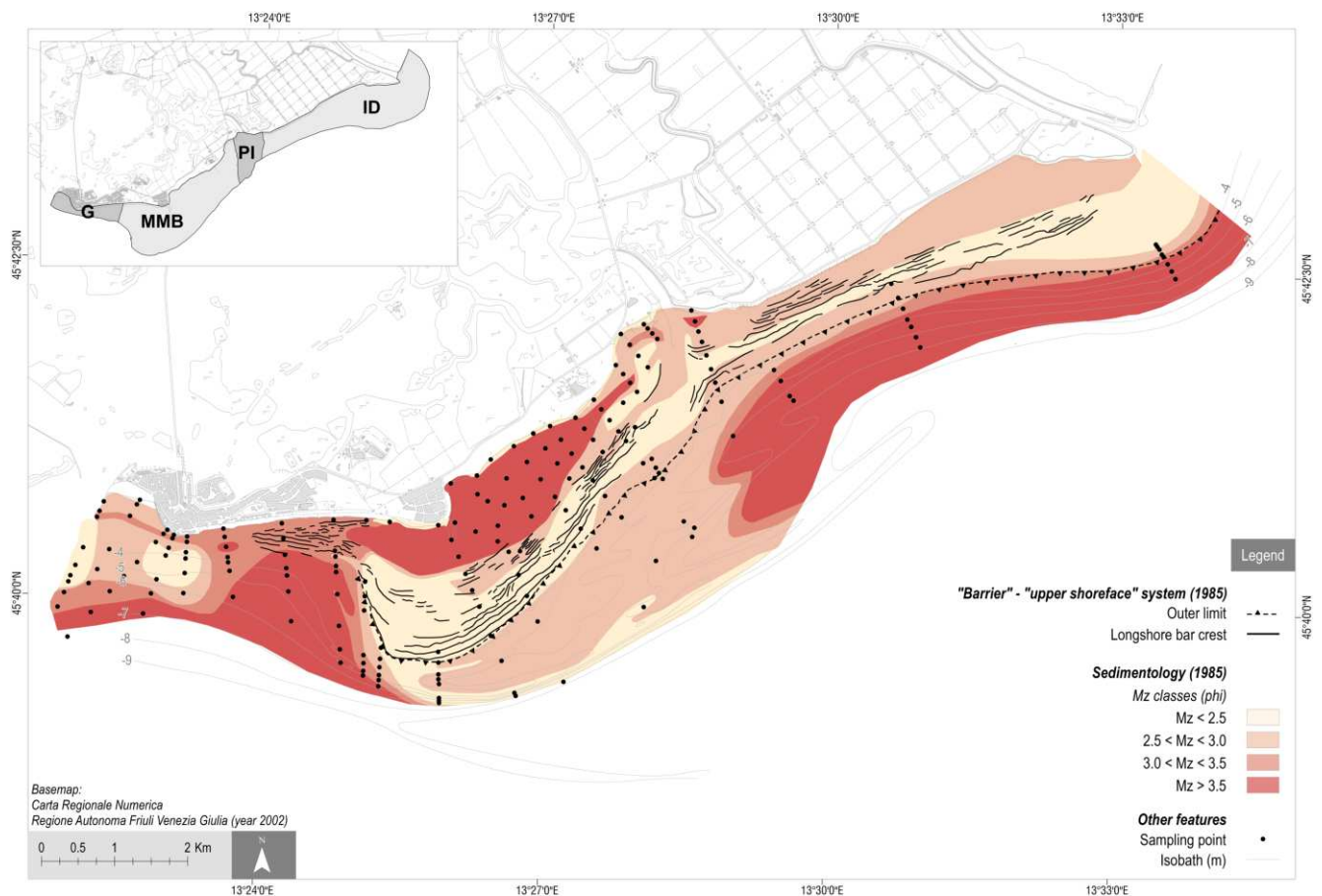


Figure 4. Sedimentological map (mean size, Mz in phi unit) of the beach and shoreface, depicting the longshore moving sand corridor (Mz < 2.5 phi) from the Isonzo River to the Mula di Muggia Bank. Compiled after [54].

4.2. Multi-Decadal Evolution

The analysis of the historical cartography allows for the definition of the evolution of the coastal landforms between Grado and the mouth of the Isonzo River since 1800. It was possible to identify and describe the main characteristics of the MMB such as shape, specific elements, and position, as well as those of the Primero inlet and the Isonzo delta, using cartography available from 1822 to 1949. The first aerial photos and topo-bathymetric surveys, however, did not arrive until 1954, providing greater precision to the identified forms and their evolution, both qualitatively and quantitatively.

According to the available data, the entire period was divided into seven-time intervals, and a summary of the most significant morphological changes and territorial transformations is presented below and in Figures 5 and 6.

4.2.1. First Period (1822–1830)

The first two historical maps are very similar in appearance with regard to the coastline which is mostly natural. Apart from Grado, which was portrayed as a small port settlement, the coast was undeveloped, consisting of a series of barrier islands separated by inlets (Porto di Grado, Rotta dei Moreri and Primero inlets) and characterised by well-developed coastal dunes.

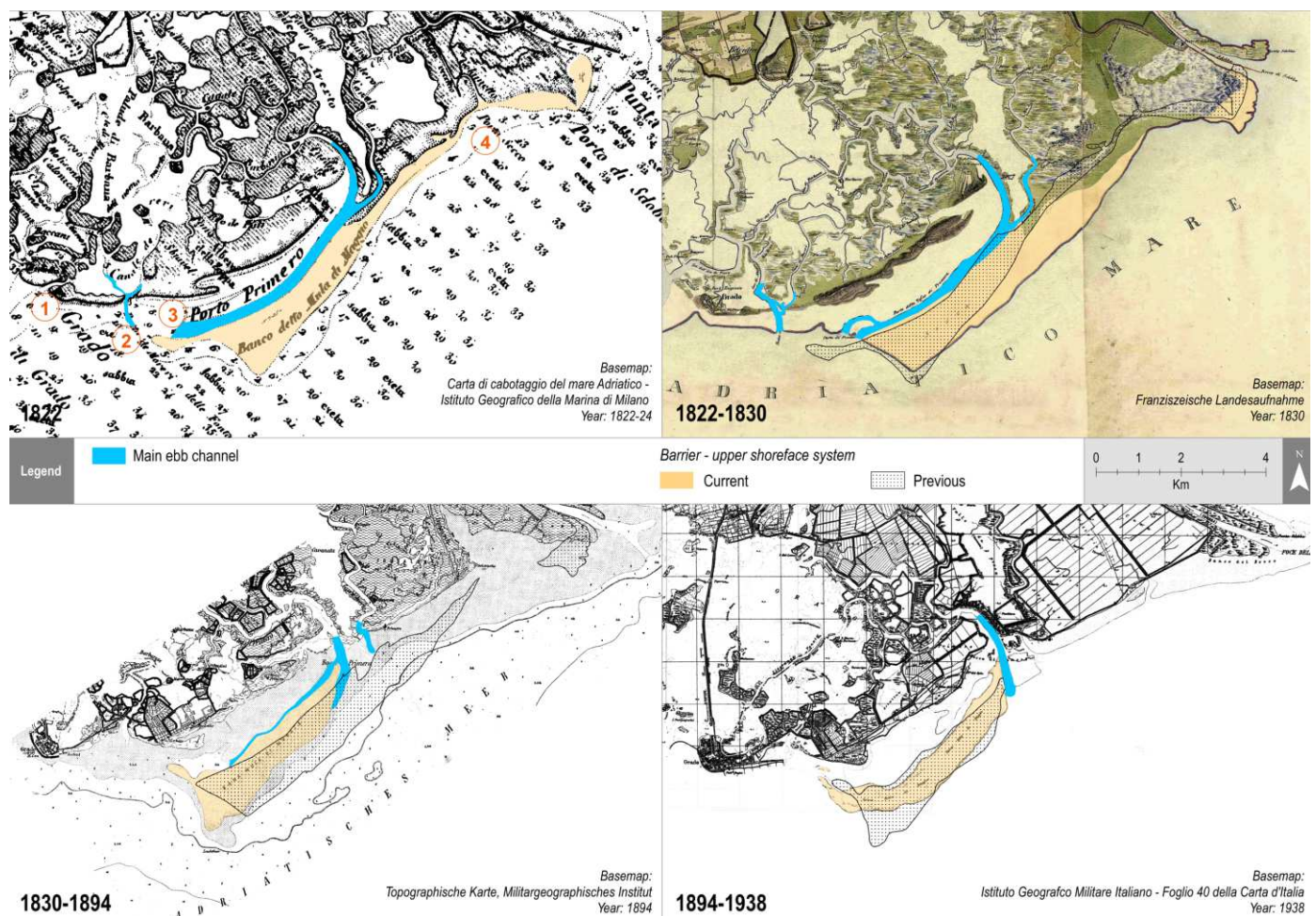


Figure 5. Evolution of the coastal tract in the period from 1822 to 1938, according to historical documents and maps. The main ebb channel of Primero and the barrier—upper shoreface system of the Mula di Muggia Bank are depicted for progressive comparison. Numbers in the oldest map refer to the following locations: 1—Porto di Grado, 2—Rotta dei Moreri, 3—Porto Primero, 4—Porto Secco, mouth of the Isonzo Vecchio.

The MMB was depicted as a northeast–southwest elongated sandy shoal in continuity with the eastern sand shoals extending up to the mouth of the Isonzo (Sdobba). Parallel to the coastline and seaward limited by the bank, the Primero channel (named Porto Primero) was lengthened by 5 km with a seaward decreasing depth from 5.8 m to 1.3 m.

The morphological configuration of the area suggested a longshore transport from east to west, fed by the Isonzo River. The narrow channel of the old Isonzo (Isonzo Vecchio) that served as the river’s main branch until the first half of the 1600s [68] is clearly evident between the Primero channel and the mouth of the Isonzo. The mouth of the Isonzo Vecchio is referred to as the Porto Secco in the oldest map.

4.2.2. Second Period (1830–1894)

Since 1830 a significant erosion phase of the coast has begun, affecting various sectors of the study area including the Grado beaches and the area around the Primero inlet. As a result of the retreating shoreline, a new breach of the Primero channel formed, leading directly into the sea in a north–south direction. Meanwhile, the MMB has migrated landward and westward. During this time, the coast began to be artificially stabilised by inlet closures (e.g., Rotta dei Moreri) and fish farm embankments in the Grado lagoon. The first beach resort in Grado is marked on the 1894 map.

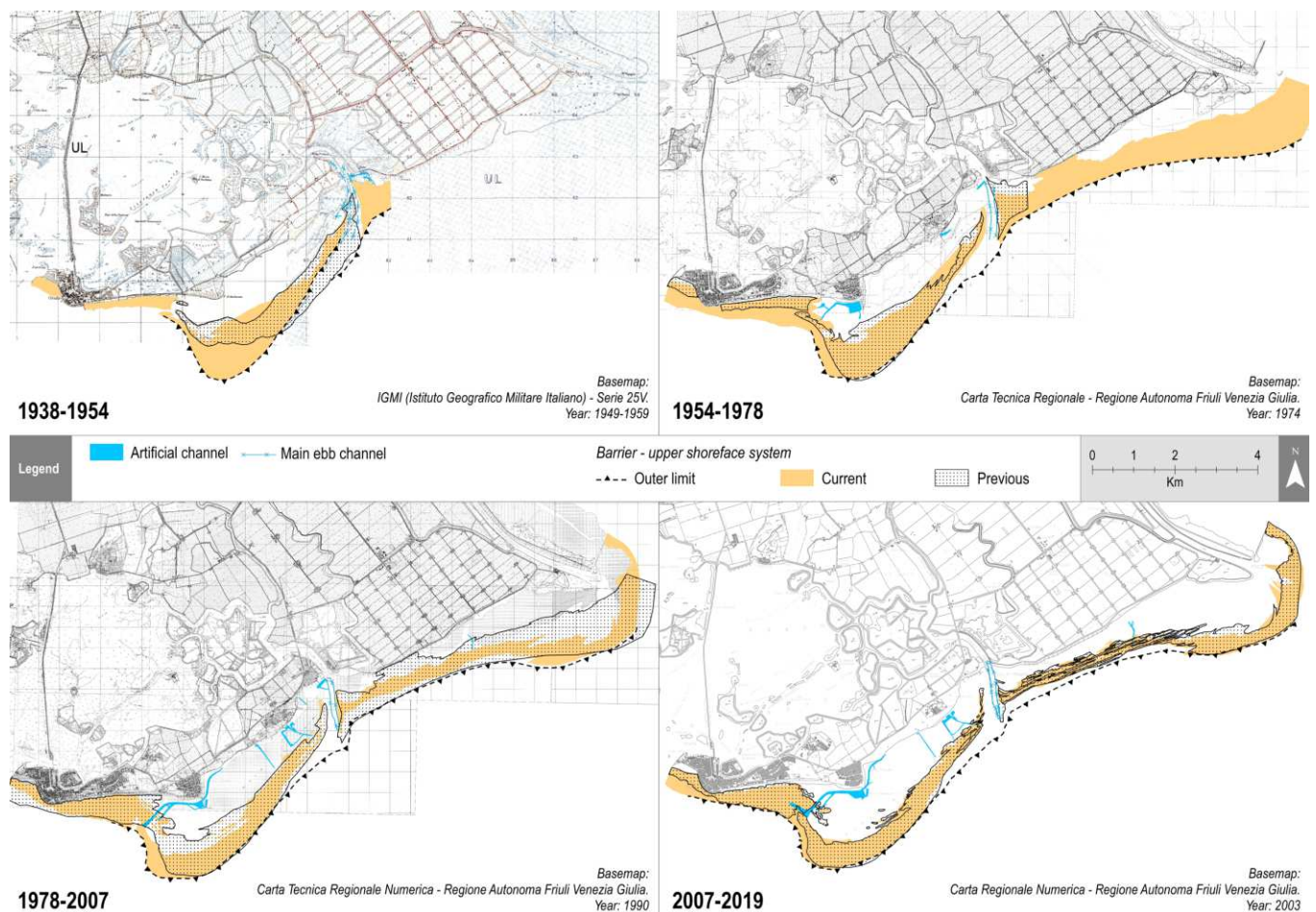


Figure 6. Evolution of the coastal tract in the period from 1838 to 2019, according to historical documents and maps. The main ebb channel of Primero, the canals and barrier—upper shoreface system of the Mula di Muggia Bank are depicted for progressive comparison.

4.2.3. Third Period (1894–1938)

The MMB continued to migrate landward and westward, apparently reducing its extent. However, we assumed that this modification is due to a different interpretation compared to the previous cartography, i.e., only the most emerged part of the bank has been mapped. The most notable coastal engineering works have been carried out since 1927 with the construction of the Bocca di Grado jetties (between 1927 and 1934) and the first phase of the tourist-seaside development of the city with the creation, from Grado toward the east of an artificial beach protected by groins. The necessary sand was extracted from coastal dunes on the barrier island between the current Grado Pineta and the mouth of Primero [45]. Concurrently, reclamation works on the lagoon lands behind the littoral up to Fossalon commenced with landfilling, mechanical drainage, and seaward embankments. According to the 1927 nautical map, the newly breached Primero channel became the main channel of the inlet, while the old one lost its hydraulic efficiency and began to silt up. Following a flood breach in 1896, a new mouth branch of the Isonzo (known as the Quarantia mouth) opened to the north [45], which grew in importance over time, quickly becoming the most important branch [68] until 1937, when it was artificially and definitively closed [45]. The 1927 nautical chart provides the first detailed bathymetry of the western side of the bank, allowing for the description of the submerged morphology of the area.

4.2.4. Fourth Period (1938–1954)

Because of the interception of longshore sedimentary transport caused by the jetties built to stabilise the Grado inlet, a new beach developed in front of the historic centre of Grado, while the eastern beach was artificially completed with sand (around 90,000 m³) mined from the fronting sandy shoals. The first aerial photos (1954) and the first morphological analysis [45] enable us to observe in greater detail the MMB landforms by distinguishing the wide strip of active parallel sandy bars that migrate westward following the longshore transport. During this time, extensive reclamation between the Grado Pineta promontory and the mouth of the Isonzo was completed, with the direct result of reducing the extent of the Primero lagoon basin.

4.2.5. Fifth Period (1954–1978)

The availability of aerial photos (1978) and the 1968 topo-bathymetric survey allowed for a more accurate description of the MMB morphology, with evidence of a terrace-like bare flat with a series of sand bars on a seaward slope. During this time, the outer limit (−2.7 m) remained almost unchanged in the eastern sectors and at the apex of the bank, but the western sections continued to migrate westward. A low energy, silty backbarrier environment with large seagrass meadows may be seen behind the active barred area. Along the coast, urban and tourism development continued: the new coastal town of Grado Pineta was created, along with a groin, a small marina, little canals and a few “swimming pools” on the shallow seabed. The development of the latter resulted in a significant change in the hydraulic circulation of the backbarrier area.

4.2.6. Sixth Period (1978–2007)

The apex and eastern limit of the MMB remained almost unchanged, while the growth and migration of additional sand bars proceeded on the western margin. The topmost partially emerging bar assumed a nearly N-S direction, resulting in partial occlusion of the newly dug channel in front of the Grado Pineta promontory. This canal was constructed in the 1980s to improve water circulation in the backbarrier. Grado’s eastern beach began to be directly influenced by the migration of the MMB with the extension of submerged sandbanks, which isolated 800 m of beach from wave action, favouring the sedimentation of fine sediments. At the Primero inlet, a clear ebb-tidal delta structure is recognisable, with evidence of a sediment bypass corridor connecting the updrift and downdrift flanks, following the main longshore drift. Seagrasses colonised vast stretches of the backbarrier, indicating a newly stabilised, low-energy environment. An increase in seagrass extension also occurred between the Primero inlet and the mouth of the Isonzo, occupying the calm runnels and troughs of the depositional multi-barred upper shoreface which is constantly nourished by the river sediments.

4.2.7. Seventh Period (2007–2019)

The Costa Azzurra beach accretion, which had mostly occurred throughout the fourth period, slowed during this time. The eastern boundary of the MMB, as well as the apical part, remained fairly unchanged but the sandbanks continued to spread to the west. The emergent bar from the previous time period expanded, moving to the northwest and isolating a new section of the tourist beach. Bars and troughs between Primero and the mouth of the Isonzo River were preserved, showing evidence of migration towards the west in the direction of the prevailing longshore currents.

4.3. The Bank Migration

According to the available historical and modern documentation, the MMB system has been preserved for more than a century, albeit with a significant migration to the west due to longshore drift.

Data from photointerpretation and historical cartography from 1830 to 2019, in particular, allowed us to recognize the bank’s external limit planimetrically and detail the

progressive migration westward of the sandy bars that form it (Figure 7). The limit of the bank was already mapped in the cartographic documents, while in aerial photographs it was recognisable by easily distinguished morphological elements such as sand bars or wave breaking lines (see Section 4.1). The numbered vectors in the map of Figure 7 depict the maximum shift of the western limit of the MMB between succeeding data, indicating a constant trend over time with a rate of around 12.6 my^{-1} . Landward, the progressive western migration and extension of the intertidal sandy bars take place in front of the beach, creating a progressively wider shallow nearshore zone.

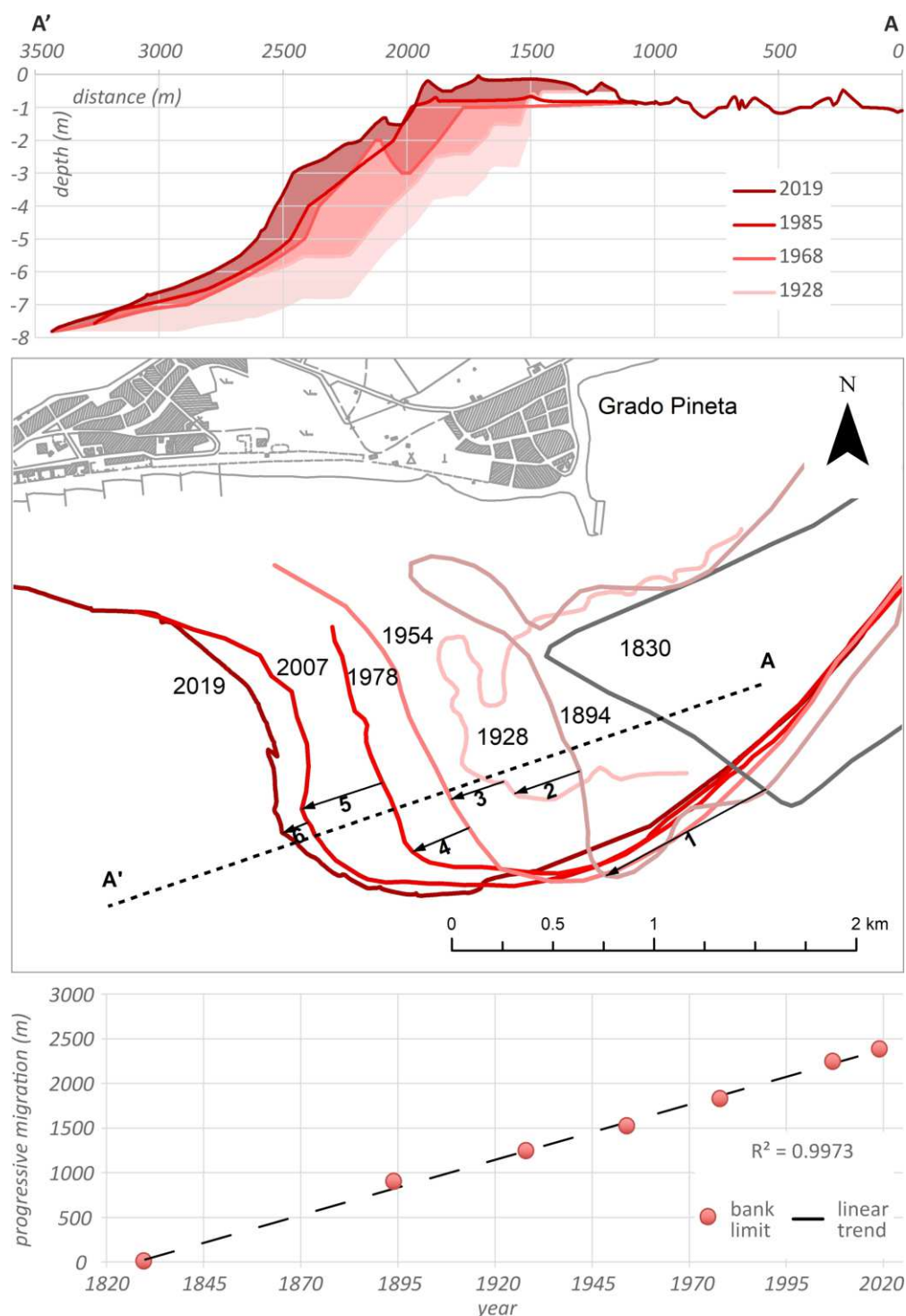


Figure 7. Detail of the bank migration analysed on the western front.

Bathymetric data, on the other hand, have provided a cross-sectional view of the migration process (Figure 7), revealing a progradation involving the shoreface until the -8m depth. The upper part of the profile envelope depicts an aggradation process that leads to an elevation near the emersion at the top of the bank, as well as a recent proclivity to rollover.

5. Discussion and Conclusions

5.1. The Sedimentary Surplus Anomaly and the Role of the Isonzo River

The gathered and analysed data allowed for two major outcomes: on the one hand, the multidecadal analysis highlighted the evolution of the MMB and adjacent coasts over time, beginning with the earliest and most likely cartographic representations and progressing to modern high-resolution surveys; on the other hand, it was possible to describe the evolution of coastal landforms in relation to contemporary anthropogenic and tourist development.

Our work emphasises the importance of data obtained from historical maps, documents and orthophotos, in supporting proper coastal planning. The research has revealed the presence of a unique coastline system, a mosaic of natural and human-made landscapes, each with its own dynamism and physical characteristics. The MMB represents a morphological oddity if compared to the rest of the Adriatic: the presence of a vast system of submerged sandy shoals that created a wave dissipative domain has resulted in the beaches along the coast taking on the characteristics of “fetch limited beaches” (low wave energy) and having an anomalous appearance (very low elevation and slope, flat morphology, reduced carrying capacity).

Despite forcing factors such as the SLR and anthropogenic effect, the sandbank system has been documented in its overall shape since the early 1800s and has been preserved over time, conserving its overall structure, although with significant dynamism. The role of the Isonzo sedimentary depocenter in the constructive processes is supported by locally documented evolution: until 1950, the erosive phase of the barrier islands coincided with the shift of the mouth of the Isonzo to the eastern Gulf of Trieste, and since the mouth was brought back to Sdobba, the erosive effects on the coast appear to have been reduced.

The preservation of this system is in opposition to the prevalence of erosive behaviours on Italian beaches [69–71], erosion that appears to make exceptions where the coastline benefits from active riverine sedimentation or cannibalisation by deltaic dismantling [34,37,72–75]. The sedimentary budget will require future investigation but the geomorphological signals are unmistakably indicative of a notable sediment contribution by the Isonzo River, as follows:

- the current presence of vast sandy shoals at the mouth of the Isonzo;
- the wide area of sandy accumulation with emerging banks in front of the Grado beach.
- the ebb-tidal delta with a volume between 600,000 and 850,000 m^3 at the Primero inlet which can be considered in equilibrium with its hydraulic cross-section and tidal prism [59]. The full development of the ebb-tidal delta, which can be temporally placed between 1949 [58] and 1995 [59], indicates a very rapid growth which can be attributed to a sediment flux from east to west greater than 60,000 $\text{m}^3 \text{y}^{-1}$, calculated according to the Tidal Inlet Reservoir Model [76].

Furthermore, the reduction in sediment mining on the Isonzo riverbed, as well as an increase in the frequency of flood events can play in favour of a recent increase in the river sediment supply to the coast. Finally, artificial basins can change their function over time, and after a specific filling threshold has been reached, they can become “permeable” to solid transport. This is the case with the Crois dam on the Torre torrent, a tributary of the Isonzo, which was rapidly filled thanks to a solid annual supply of 40,000–50,000 m^3 [77] and no longer serves as a barrier to river sediment transport to the mouth.

5.2. The Conflict between Natural Dynamics and Poor Urban Planning

The vast majority of the coastal territory between Grado and the Primero inlet was rapidly urbanised in two phases, the first towards the end of the 19th century and the second in the 1960s, to promote the growth of tourism. According to historical archives, new beaches were artificially formed using replenishment sands obtained from the neighbouring seabed [45]. The rest of the area, from Primero to Isonzo, was largely utilised for agricultural purposes. As a result of this rapid coastal development, a strong backshore defence policy (“keep the line”) has been adopted, leading to a rigid system with no degrees of freedom in terms of possible beach migration to the hinterland. Despite the touristic development, many of the coastal area’s natural elements have been preserved, leading to the implementation of a conservation program that includes the creation of the Natura 2000 protected areas. Consequently, the Grado coastline needs to be maintained for multi-purpose use [78], balancing recreation and environmental conservation.

As a result of the historical analysis and more recent data collection, areas with varied morphosedimentary characteristics and with distinct tourist/recreational, ecological, and conservation values have been identified on a map (Figure 8).

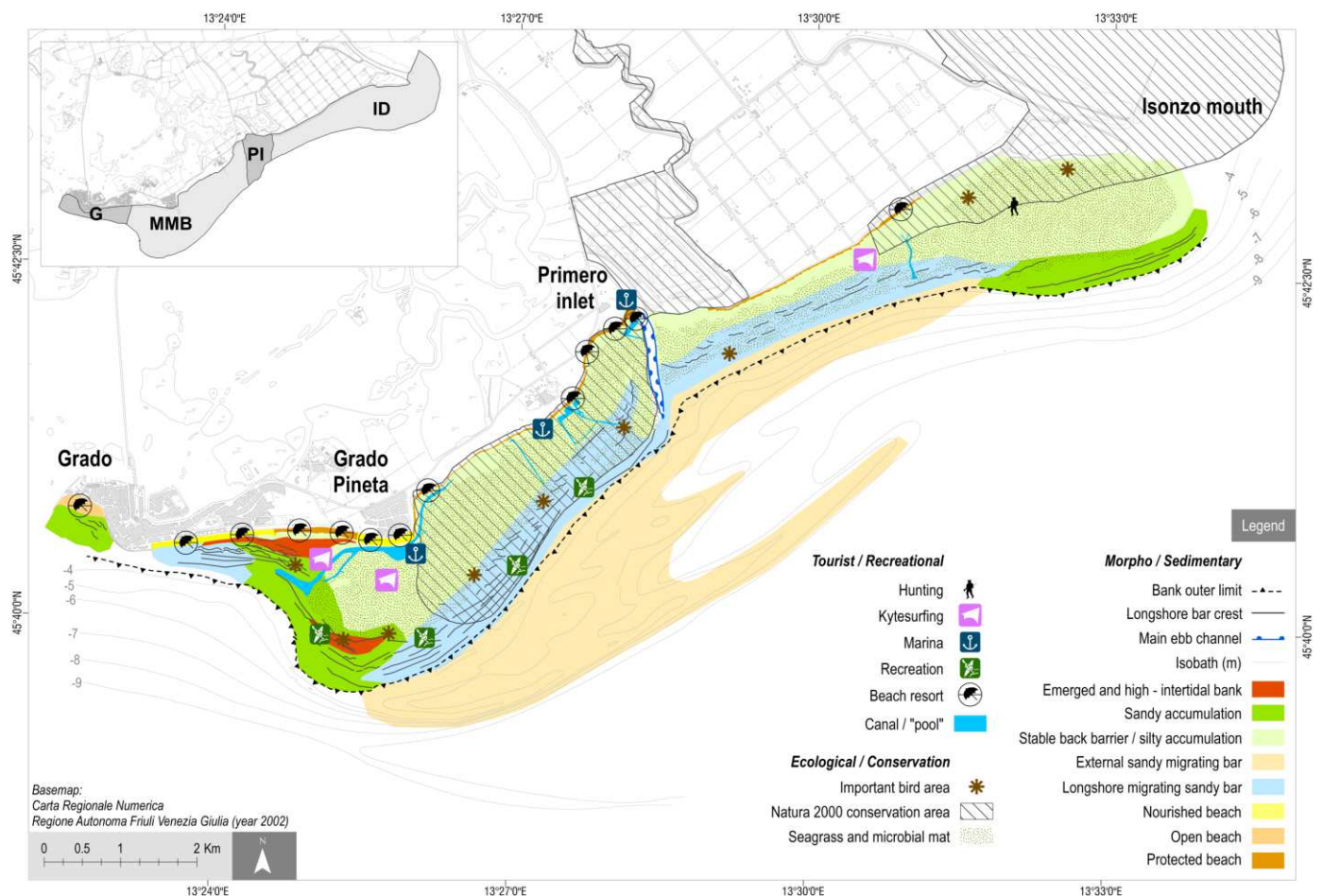


Figure 8. Zoning map with the different morphosedimentary areas and the most important tourist/recreational, ecological, and conservation values, relevant for multi-purpose coastal planning.

The zoning aims to synthesise natural dynamics, uses and conflicts and create a baseline for future management guidelines. The map emphasises how coastal areas have been developed without considering their inherent characteristics. In the absence of Integrated Coastal Zone Management or coordinated coastline management guidelines, the building of beach resorts and facilities occurred even in unsuitable areas located on fetch-limited beaches faced by very shallow waters and a silty seabed (backbarrier area).

Despite the sheltered position during heavy storms and “*acqua alta*”, some of these beaches are being eroded, and in the absence of post-storm natural constructive processes, they require periodic sand replenishment. Local coastal tourism is primarily focused on beaches that are managed as private properties under state concession and are fully equipped with numerous facilities (walkways, beach umbrellas, toilets, showers, and kiosks), leaving little space for free and natural areas. This model implies a lack of acceptance of the specific characteristics of the sites (particularly the backbarrier area) among stakeholders and fosters conflict. At the same time, a variety of touristic uses (small boat docks and kitesurfing, for example) can conflict with the need for nature conservation needs (silty seabed with seagrass meadows, tidal flats used as roosts by birds).

However, in certain locations, the large size and dynamism of natural landforms have grown prominent in relation to the needs of seaside tourism, raising serious concerns for the future of these areas. The westernmost part of the migrating bars, in particular, is viewed as a threat to touristic activities due to the ongoing rapid extension toward the west of the shallow water with silty deposition in the nearshore and the current infilling of the navigation canal. At the same time, longshore migrating sandy bars are being frequented by unorganized but intense tourist use (bathing, recreational fishing of edible bivalves and kitesurfing).

5.3. Perspectives of Proper Coastal Management

Our analysis, as well as the zoning scheme shown in Figure 8, can be used as a basis to guide future planning of the Grado coastal area, to reduce SLR impact and minimise or eliminate the major conflict that exists between coastal morphodynamics, tourist/recreational beach use, and conservation needs.

The backbarrier area and the longshore migrating sandbars have the natural potential to safeguard human settlements and infrastructures while also providing a variety of natural co-benefits such as habitat conservation, carbon sequestration, tourism opportunities, education, and research [79]. This area can be vulnerable to medium and long-term forcing (SLR), which can cause the sandbanks to rollover the stable silty backbarrier, a natural ramp for the accommodation of future transgressive bodies.

For this reason, the primary concerns are the preservation of the sediment source (the Isonzo River) and the natural ability of the longshore transport to distribute the sand along the littoral toward the west. Proper control of hydraulic interventions in the drainage basin and monitoring of the river’s sediment supply, will be required. Simultaneously, hard defence structures should be avoided unless they are limited to reinforcing those already in place to defend the hinterland.

The presence of consistent sandy accumulation areas would favour soft shore protection solutions [80] that aim to manage sediments within the coastal system to balance deposition and erosion in adjacent cells [31–33,59]. Once sediment compatibility is established, overabundant sediments in accumulation areas can be managed as a temporary reservoir for beach re-nourishment. The use of small periodic, scheduled dredging and nourishment is preferable, with a source-to-sink approach that mimics the natural by-pass corridor between the barred shoreface updrift and downdrift to the Primero inlet. This approach is favoured here as deficit areas are of modest size and are mainly fetch-limited beaches, thus highly conservative.

As a final remark, correct monitoring of the morphodynamics of the coastal banks needs to be ensured to possibly re-direct the actions and planned management.

The abundance of sediments represents a source of great wealth as well as a concrete possibility to counter the SLR threat. While erosion and loss of sand are serious global issues for the tourism industry, the rapid morphological changes and the management of large quantities of moving sediments here represent a challenge as well as an opportunity.

Author Contributions: Conceptualization, A.B. (Annelore Bezzi), G.C. and G.F.; methodology, S.P. and D.M.; validation, A.B. (Annelore Bezzi) and G.F.; investigation, A.B. (Annelore Bezzi), S.F., G.C., S.P., D.M., A.B. (Antonio Bratus) and S.S.; resources, F.F.; writing—original draft preparation, A.B.

(Annelore Bezzi), G.C. and G.F.; writing—review and editing, A.B. (Annelore Bezzi), G.C., D.M. and G.F.; supervision, G.F. and F.F.; project administration, A.B. (Antonio Bratus) and G.F.; funding acquisition, A.B. (Antonio Bratus) and G.F. All authors have read and agreed to the published version of the manuscript.

Funding: The research was funded by the 2014–2020 INTERREG VA Italy–Croatia CBC Programme, project ID 10043385 “Change We care”. It also received financial support from the Regione Autonoma Friuli Venezia Giulia—Direzione centrale difesa dell’ambiente, energia e sviluppo sostenibile, through institutional partnership contracts “PR Mula di Muggia” and “PR Coste FVG”.

Institutional Review Board Statement: Not applicable.

Informed Consent Statement: Not applicable.

Data Availability Statement: Not applicable.

Acknowledgments: This work is dedicated to our colleague and friend Ruggero Marocco, who sadly passed away. Ruggero was a great lover and connoisseur of the Grado territory, and he has always supported and assisted us in our coastal studies. He must be credited as the inspiration for this work.

Conflicts of Interest: The authors declare no conflict of interest.

References

- Church, J.A.; Clark, P.U.; Cazenave, A.; Gregory, J.M.; Jevrejeva, S.; Levermann, A.; Merrifield, M.A.; Milne, G.A.; Nerem, R.S.; Nunn, P.D.; et al. Sea level change. In *Climate Change 2013: The Physical Science Basis. Contribution of Working Group I to the Fifth Assessment Report of the Intergovernmental Panel on Climate Change*; Stocker, T.F., Qin, D., Plattner, G.-K., Tignor, M., Allen, S.K., Boschung, J., Nauels, A., Xia, Y., Bex, V., Midgley, P.M., Eds.; Cambridge University Press: Cambridge, UK; New York, NY, USA, 2013. Available online: https://www.ipcc.ch/site/assets/uploads/2018/02/WG1AR5_Chapter13_FINAL.pdf (accessed on 26 October 2021).
- Oppenheimer, M.; Glavovic, B.C.; Hinkel, J.; van de Wal, R.; Magnan, A.K.; Abd-Elgawad, A.; Cai, R.; Cifuentes-Jara, M.; DeConto, R.M.; Ghosh, T.; et al. Sea level rise and implications for low-lying islands, coasts and communities. *IPCC Special Report on the Ocean and Cryosphere in a Changing Climate*. Pörtner, H.-O., Roberts, D.C., Masson-Delmotte, V., Zhai, P., Tignor, M., Poloczanska, E., Mintenbeck, K., Alegría, A., Nicolai, M., Okem, A., et al., Eds.; 2019. Available online: <https://www.ipcc.ch/srocc/chapter/chapter-4-sea-level-rise-and-implications-for-low-lying-islands-coasts-and-communities/> (accessed on 26 October 2021).
- Anthony, E.J.; Marriner, N.; Morhange, C. Human influence and the changing geomorphology of Mediterranean deltas and coasts over the last 6000 years: From progradation to destruction phase? *Earth-Sci. Rev.* **2014**, *139*, 336–361. [[CrossRef](#)]
- Besset, M.; Anthony, E.J.; Bouchette, F. Multi-decadal variations in delta shorelines and their relationship to river sediment supply: An assessment and review. *Earth-Sci. Rev.* **2019**, *193*, 199–219. [[CrossRef](#)]
- McManus, J. Deltaic responses to changes in river regimes. *Mar. Chem.* **2002**, *79*, 155–170. [[CrossRef](#)]
- Maselli, V.; Trincardi, F. Man made deltas. *Sci. Rep.* **2013**, *3*, 1926. [[CrossRef](#)]
- Stutz, M.L.; Pilkey, O.H. The relative influence of humans on barrier islands: Humans versus geomorphology. In *Humans as Geologic Agents*; Ehlen, J., Haneberg, W.C., Larson, R.A., Eds.; Geological Society of America: Boulder, CO, USA, 2005; Volume 16. [[CrossRef](#)]
- FitzGerald, D.M.; Fenster, M.S.; Argow, B.A.; Buynevich, I.V. Coastal impacts due to sea-level rise. *Ann. Rev. Earth Plan. Sci.* **2008**, *36*, 601–647. [[CrossRef](#)]
- McBride, R.A.; Anderson, J.B.; Buynevich, I.V.; Cleary, W.; Fenster, M.S.; FitzGerald, D.M.; Harris, M.S.; Hein, C.J.; Klein, A.H.F.; Liu, B.; et al. 10.8 Morphodynamics of barrier systems: A synthesis. In *Treatise on Geomorphology*; Shroder, J.F., Ed.; Academic Press: New York, NY, USA, 2013; Volume 10, pp. 166–244. [[CrossRef](#)]
- FitzGerald, D.M.; Hein, C.J.; Hughes, Z.; Kulp, M.; Georgiou, I.; Miner, M. Runaway barrier island transgression concept: Global case studies. In *Barrier Dynamics and Response to Changing Climate*; Moore, L.J., Murray, A.B., Eds.; Springer: Cham, Switzerland, 2018; pp. 3–56. [[CrossRef](#)]
- De la Vega-Leinert, A.C.; Nichols, R.J. Potential implications of sea-level rise for Great Britain. *J. Coast. Res.* **2008**, *24*, 342–357. [[CrossRef](#)]
- Martínez, M.L.; Hesp, P.A.; Gallego-Fernández, J.B. Coastal dunes: Human impact and need for restoration. In *Restoration of Coastal Dunes*; Martínez, M.L., Gallego-Fernández, J.B., Hesp, P.A., Eds.; Springer: Berlin/Heidelberg, Germany, 2013; pp. 1–14. [[CrossRef](#)]
- Psuty, N.P.; Silveira, T.M. Global climate change: An opportunity for coastal dunes?? *J. Coast. Conserv.* **2010**, *14*, 153–160. [[CrossRef](#)]
- Leatherman, S. Barrier dynamics and landward migration with Holocene sea-level rise. *Nature* **1983**, *301*, 415–417. [[CrossRef](#)]
- Cooper, J.A.G.; Masselink, G.; Coco, G.; Short, A.D.; Castelle, B.; Rogers, K.; Anthony, E.; Green, A.N.; Kelley, J.T.; Pilkey, O.H.; et al. Sandy beaches can survive sea-level rise. *Nat. Clim. Chang.* **2020**, *10*, 993–995. [[CrossRef](#)]

16. Cooper, J.A.G.; Green, A.N.; Loureiro, C. Geological constraints on mesoscale coastal barrier behavior. *Glob. Planet. Chang.* **2018**, *168*, 15–34. [[CrossRef](#)]
17. Zhang, K.; Douglas, B.; Leatherman, S. Do storms cause long-term beach erosion along the U.S. East Barrier Coast? *J. Geol.* **2002**, *110*, 493–502. [[CrossRef](#)]
18. McBride, R.A.; Byrnes, M.R.; Hiland, M.W. Geomorphic response-type model for barrier coastlines: A regional perspective. *Mar. Geol.* **1995**, *126*, 143–159. [[CrossRef](#)]
19. Hapke, C.J.; Himmelstoss, E.A.; Kratzmann, M.G.; List, J.H.; Thieler, E.R. *National Assessment of Shoreline Change: Historical Shoreline Change along the New England and Mid-Atlantic Coasts*; Open-File Report 2010-1118; U.S. Geological Survey: Reston, VA, USA, 2011; 57p. Available online: <https://pubs.usgs.gov/of/2010/1118/> (accessed on 26 October 2021).
20. Morton, R.A. Historical changes in the Mississippi-Alabama barrier-island chain and the roles of extreme storms, sea level, and human activities. *J. Coast. Res.* **2008**, *24*, 1587–1600. [[CrossRef](#)]
21. Simeoni, U.; Fontolan, G.; Tessari, U.; Corbau, C. Domains of spit evolution in the Goro area, Po Delta, Italy. *Geomorphology* **2007**, *86*, 332–348. [[CrossRef](#)]
22. Kaminsky, G.M.; Ruggiero, P.; Buijsman, M.C.; McCandless, D.; Gelfenbaum, G. Historical evolution of the Columbia River littoral cell. *Mar. Geol.* **2010**, *273*, 96–126. [[CrossRef](#)]
23. Kombiadou, K.; Matias, A.; Ferreira, Ó.; Carrasco, A.R.; Costas, S.; Plomaritis, T. Impacts of human interventions on the evolution of the Ria Formosa barrier island system (S. Portugal). *Geomorphology* **2019**, *343*, 129–144. [[CrossRef](#)]
24. Ruggiero, P.; Kratzmann, M.G.; Himmelstoss, E.A.; Reid, D.; Allan, J.; Kaminsky, G. *National Assessment of Shoreline Change: Historical Shoreline Change along the PACIFIC Northwest Coast*; Open-File Report 2012-1007; U.S. Geological Survey: Reston, VA, USA, 2013; 62p.
25. Lebbe, L.; Van Meir, N.; Viaene, P. Potential implications of sea-level rise for Belgium. *J. Coast. Res.* **2008**, *24*, 358–366. [[CrossRef](#)]
26. Guillen, J.; Stive, M.J.F.; Capobianco, M. Shoreline evolution of the Holland coast on a decadal scale. *Earth Surf. Process. Landf.* **1999**, *24*, 517–536. [[CrossRef](#)]
27. Ruggiero, P.; Kaminsky, G.M.; Gelfenbaum, G. Linking proxy-based and datum-based shorelines on high-energy coastlines: Implications for shoreline change analyses. *J. Coast. Res.* **2003**, *38*, 57–82.
28. Rosati, J.D. Concepts in sediment budgets. *J. Coast. Res.* **2005**, *21*, 307–322. [[CrossRef](#)]
29. Hapke, C.J.; Lentz, E.E.; Gayes, P.T.; McCoy, C.A.; Hehre, R.; Schwab, W.C.; Williams, S.J. Review of sediment budget imbalances along Fire Island, New York: Can nearshore geologic framework and patterns of shoreline change explain the deficit? *J. Coast. Res.* **2010**, *26*, 510–522. [[CrossRef](#)]
30. Byrnes, M.R.; Rosati, J.D.; Griffee, S.F.; Berlinghoff, J.L. Historical sediment transport pathways and quantities for determining an operational sediment budget: Mississippi Sound Barrier Islands. *J. Coast. Res.* **2013**, *63*, 166–183. [[CrossRef](#)]
31. Fontolan, G.; Bezzi, A.; Martinucci, D.; Pillon, S.; Popesso, C.; Rizzetto, F. Sediment budget and management of the Veneto beaches, Italy: An application of the modified Littoral Cells Management System (SICELL). In Proceedings of the Coastal and Maritime Mediterranean Conference CM2, Ferrara, Italy, 25–27 November 2015; pp. 47–50.
32. Bonaldo, D.; Antonioli, F.; Archetti, R.; Bezzi, A.; Correggiari, A.; Davolio, S.; De Falco, G.; Fantini, M.; Fontolan, G.; Furlani, S.; et al. Integrating multidisciplinary instruments for assessing coastal vulnerability to erosion and sea level rise: Lessons and challenges from the Adriatic Sea, Italy. *J. Coast. Conserv.* **2019**, *23*, 19–37. [[CrossRef](#)]
33. Pranzini, E.; Cinelli, I.; Cipriani, L.E.; Anfuso, G. An integrated coastal sediment management plan: The example of the Tuscany region (Italy). *J. Mar. Sci. Eng.* **2020**, *8*, 33. [[CrossRef](#)]
34. Bezzi, A.; Pillon, S.; Popesso, C.; Casagrande, G.; Da Lio, C.; Martinucci, D.; Tosi, L.; Fontolan, G. From rapid coastal collapse to slow sedimentary recovery: The morphological ups and downs of the modern Po Delta. *Estuar. Coast. Shelf Sci.* **2021**, *260*, 107499. [[CrossRef](#)]
35. Rosati, J.D.; Stone, G.W. Geomorphologic evolution of barrier islands along the northern U.S. Gulf of Mexico and implications for engineering design in barrier restoration. *J. Coast. Res.* **2009**, *251*, 8–22. [[CrossRef](#)]
36. Acuña-Piedra, J.F.; Quesada-Román, A. Multidecadal biogeomorphic dynamics of a deltaic mangrove forest in Costa Rica. *Ocean. Coast. Manag.* **2021**, *211*, 105770. [[CrossRef](#)]
37. Alberico, I.; Cavuoto, G.; Di Fiore, V.; Punzo, M.; Tarallo, D.; Pelosi, N.; Ferraro, L.; Marsella, E. Historical maps and satellite images as tools for shoreline variations and territorial changes assessment: The case study of Volturno Coastal Plain (Southern Italy). *J. Coast. Conserv.* **2018**, *22*, 919–937. [[CrossRef](#)]
38. Parsons, G.R.; Powell, M. Measuring the cost of beach retreat. *Coast. Manag.* **2001**, *29*, 91–103.
39. Pranzini, E.; Williams, A.T. (Eds.) *Coastal Erosion and Protection in Europe*; Routledge: London, UK; New York, NY, USA, 2013; 457p.
40. Alexandrakis, G.; Manasakis, C.; Kampanis, N.A. Valuating the effects of beach erosion to tourism revenue. A management perspective. *Ocean Coast. Manag.* **2015**, *111*, 1–11. [[CrossRef](#)]
41. Becken, S.; 2016 Climate Change Impacts on Coastal Tourism. CoastAdapt Impact Sheet 6, National Climate Change Adaptation Research Facility, Gold Coast. Available online: https://coastadapt.com.au/sites/default/files/factsheets/T312_7_Coastal_Tourism.pdf (accessed on 26 October 2021).
42. Thinh, N.A.; Thanh, N.N.; Tuyen, L.T.; Hens, L. Tourism and beach erosion: Valuing the damage of beach erosion for tourism in the Hoi An World Heritage site, Vietnam. *Environ. Dev. Sustain.* **2019**, *21*, 2113–2124. [[CrossRef](#)]

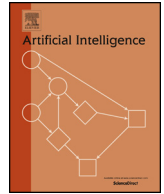
43. Arabadzhyan, A.; Figini, P.; García, C.; González, M.M.; Lam-González, Y.E.; Carmelo, J.L. Climate change, coastal tourism, and impact chains—A literature review. *Curr. Issues Tour.* **2021**, *24*, 2233–2268. [CrossRef]
44. Città di Grado—Presenza di Turisti. Available online: <https://www.comunegrado.it/amministrazione-trasparente/507-informazioni-ambientali/fattori-inquinanti/presenza-di-turisti> (accessed on 26 October 2021).
45. De Grassi, P.; De Grassi, V. *Memoria Sulle Variazioni Morfologiche dei Litorali Marini Della Laguna di Grado*; A cura dell’Azienda Autonoma di Soggiorno—Grado: Grado, Italy, 1957; 54p. (In Italian)
46. Marocco, R. Lineamenti geomorfologici della costa e dei fondali del Golfo di Trieste e considerazioni sulla loro evoluzione tardo-quadernaria. *Int. J. Speleol.* **1989**, *18*, 87–110. (In Italian) [CrossRef]
47. Gatto, F.; Marocco, R. Caratteri morfologici ed antropici della Laguna di Grado (Alto Adriatico). *Gortania Atti Mus. Friul. Stor. Nat.* **1992**, *14*, 19–42. (In Italian)
48. Gordini, E.; Caressa, S.; Marocco, R. Nuova carta morfo-sedimentologica del Golfo di Trieste (Da Punta Tagliamento alla foce dell’Isonzo). *Gortania Atti Mus. Friul. Stor. Nat.* **2003**, *25*, 5–29. (In Italian)
49. Marocco, R.; Figus, B. Banchi sommersi della Mula di Muggia, Trezza Grande e Trezza Piccola. In *Geositi del Friuli Venezia Giulia*; Cucchi, F., Finocchiaro, F., Muscio, G., Eds.; Regione Autonoma Friuli Venezia Giulia, Tipografia Arti Grafiche Friulane: Udine, Italy, 2009; pp. 304–305. (In Italian)
50. Trobec, A.; Buseti, M.; Zgur, F.; Baradello, L.; Babich, A.; Cova, A.; Gordini, E.; Romeo, R.; Tomini, I.; Poglajen, S.; et al. Thickness of marine Holocene sediment in the Gulf of Trieste (Northern Adriatic Sea). *Earth Syst. Sci. Data* **2018**, *10*, 1077–1092. [CrossRef]
51. Regione Autonoma Friuli Venezia Giulia—Autorità di Sistema Portuale del Mare Adriatico Orientale. Piano Regolatore Portuale del Porto di Monfalcone, Variante Localizzata. Studio Meteorologico. Progettisti: Modimar, SJS Engineering, Archest. 2019. Available online: https://www.regione.fvg.it/rafvfg/export/sites/default/RAFVG/ambiente-territorio/pianificazione-gestione-territorio/FOGLIA9/allegati/Allegato_33_alla_Delibera_2066-2019.pdf (accessed on 26 October 2021).
52. INTERREG II. *Progetto di Monitoraggio Dell’alto-Adriatico-Relazione Conclusiva, Luglio 1998–Giugno 2001*; Direzione Regionale dell’Ambiente, Laboratorio di Biologia Marina: Trieste, Italy, 2001; 112p. (In Italian)
53. Regione Autonoma Friuli Venezia Giulia. Progetto CAMIS—Attività Coordinate Per la Gestione del Fiume Isonzo. Studio Morfologico del Fiume Isonzo. Relazione Generale. 2014. Available online: http://www.camisproject.eu/modules/uploader/uploads/system_menu/files_sys/studio-morfologico-art-prima-fase_copy1.pdf (accessed on 26 October 2021).
54. Regione Autonoma Friuli Venezia Giulia. *Studio Sedimentologico e Marittimo Costiero dei Litorali del Friuli Venezia Giulia, Ipotesi di Intervento Per il Recupero Ambientale e la Valorizzazione Della Fascia Costiera*; Brambati, A., Ed.; Regione Autonoma Friuli Venezia Giulia, Direzione Regionale dei Lavori Pubblici, Servizio dell’Idraulica: Trieste, Italy, 1985; 665p. (In Italian)
55. Siche, I.; Arnaud-Fassetta, G. Anthropogenic activities since the end of the Little Ice Age: A critical factor driving fluvial changes on the Isonzo River (Italy, Slovenia). *Méditerranée* **2014**, *122*, 183–199. [CrossRef]
56. Bezzi, A.; Pillon, S.; Martinucci, D.; Fontolan, G. Inventory and conservation assessment for the management of coastal dunes, Veneto coasts, Italy. *J. Coast. Conserv.* **2018**, *22*, 503–518. [CrossRef]
57. Petti, M.; Pascolo, S.; Bosa, S.; Bezzi, A.; Fontolan, G. Tidal flats morphodynamics: A new conceptual model to predict their evolution over a medium-long period. *Water* **2019**, *11*, 1176. [CrossRef]
58. Dorigo, L. *La Laguna di Grado e le Sue Foci. Ricerche e Rilievi Idrografici*; Magistrato Alle Acque-Ufficio Idrografico: Venezia, Italy, 1965; 231p. (In Italian)
59. Fontolan, G.; Pillon, S.; Delli Quadri, F.; Bezzi, A. Sediment storage at tidal inlets in northern Adriatic lagoons: Ebb-tidal delta morphodynamics, conservation and sand use strategies. *Estuar. Coast. Shelf Sci.* **2007**, *75*, 261–277. [CrossRef]
60. Interreg Italy-Croatia Change We Care. Report on Pilot Areas—Geomorphological Maps. Activity 3.2, Task 3.2.1, Version 1.0, Delivery Date 30 June 2020. Available online: https://www.italy-croatia.eu/documents/279156/0/3.2_RDV_D3.2.1_Pilot+areas+geomorphologi-cal+map_rev.pdf/02261cd1-a210-280e-bba4-6a6aebec7f97?t=1614604207922 (accessed on 26 October 2021).
61. Arcanus Maps—Europe in the XIX Century. Available online: <https://maps.arcanum.com/en/> (accessed on 26 October 2021).
62. Geoportale Nazionale—Servizio di Consultazione WMS. Available online: <http://www.pcn.minambiente.it/mattm/servizio-wms/> (accessed on 26 October 2021).
63. Falques, A.; Ribas, F.; Calvete, D. Rhythmic Shoreline Features. 2019. Available online: http://www.coastalwiki.org/wiki/Rhythmic_shoreline_features#cite_ref-G_17-0 (accessed on 26 October 2021).
64. Niedoroda, A.W.; Tanner, W.F. Preliminary study of transverse bars. *Mar. Geol.* **1970**, *9*, 41–62. [CrossRef]
65. Gelfenbaum, G.; Gregg, B. The morphology and migration of transverse bars off the west-central Florida coast. *Mar. Geol.* **2003**, *200*, 273–289. [CrossRef]
66. Ribas, F.; Kroon, A. Characteristics and dynamics of surfzone transverse finger bars. *J. Geophys. Res.* **2007**, *112*, F03028. [CrossRef]
67. Trincardi, F.; Correggiari, A.; Cattaneo, A.; Remia, A.; Taviani, M.; Angeletti, L.; Fogliani, F.; Campiani, E. *Carta Geologica dei Mari Italiani Alla Scala 1:250,000 Foglio NL 33—Venezia*; ISPRA: Roma, Italy, 2011. (In Italian)
68. Desio, A. Le variazioni della foce del fiume Isonzo. *Riv. Geogr. Ital.* **1922**, *10-11-12*, 249–268. (In Italian)
69. GNRAC. Lo stato dei litorali italiani. *Studi Costieri* **2006**, *10*, 3–172. (In Italian)
70. Anfuso, G.; Martinez-del-Pozo, J.A.; Rangel-Buitrago, N. Morphological cells in the Ragusa littoral (Sicily, Italy). *J. Coast. Conserv.* **2013**, *17*, 369–377. [CrossRef]
71. Semeoshenkova, V.; Newton, A. Overview of erosion and beach quality issues in three Southern European countries: Portugal, Spain and Italy. *Ocean Coast. Manag.* **2015**, *118 Pt A*, 12–21. [CrossRef]

72. Bellotti, P. Il modello morfo-sedimentario dei maggiori delta tirrenici italiani. *Boll. Soc. Geol. Ital.* **2000**, *119*, 777–792. (In Italian)
73. Pranzini, E. Updrift river mouth migration on cusped deltas: Two examples from the coast of Tuscany (Italy). *Geomorphology* **2001**, *38*, 125–132. [[CrossRef](#)]
74. Alberico, I.; Amato, V.; Aucelli, P.P.C.; D'Argenio, B.; Di Paola, G.; Pappone, G. Historical shoreline evolution and recent shoreline trends of Sele plain coastline (southern Italy). The 1870–2009 time window. *J. Coast. Res.* **2011**, *28*, 1638–1647. [[CrossRef](#)]
75. Bezzi, A.; Casagrande, G.; Martinucci, D.; Pillon, S.; Del Grande, C.; Fontolan, G. Modern sedimentary facies in a progradational barrier-spit system: Goro lagoon, Po delta, Italy. *Estuar. Coast. Shelf Sci.* **2019**, *227*, 106323. [[CrossRef](#)]
76. Kraus, N.C. *Reservoir Model for Calculating Natural Sand Bypassing and Change in Volume of Ebb-Tidal Shoals, Part I: Description*; ERDC/CHL CHETN IV-39; US Army Corps of Engineers, Engineer Research and Development Center, Coastal and Hydraulics Laboratory: Vicksburg, MS, USA, 2002; 14p. Available online: <https://apps.dtic.mil/sti/pdfs/ADA588874.pdf> (accessed on 26 October 2021).
77. Regione Autonoma Friuli Venezia Giulia. Indirizzi per l'Individuazione dei Corsi d'Acqua, o di Tratti dei Medesimi, nei Quali è Necessaria l'Esecuzione Degli Interventi di Manutenzione Degli Alvei che Prevedono l'Estrazione ed Asporto di Materiale Litoide. Aggiornamento. 2013. Available online: http://mtom.regione.fvg.it/storage/2013_676/Allegato%201%20alla%20Delibera%20676-2013.pdf (accessed on 26 October 2021). (In Italian).
78. McLahlan, A.; Defeo, O.; Jaramillo, E.; Short, A.D. Sandy beach conservation and recreation: Guidelines for optimising management strategies for multi-purpose use. *Ocean Coast. Manag.* **2013**, *71*, 256–268. [[CrossRef](#)]
79. Sutton-Grier, A.E.; Wowk, K.; Bamford, H. Future of our coasts: The potential for natural and hybrid infrastructure to enhance the resilience of our coastal communities, economies and ecosystems. *Environ. Sci. Policy* **2015**, *51*, 137–148. [[CrossRef](#)]
80. Goudas, C.; Katsiaris, G.; May, V.; Karambas, T. (Eds.) *Soft Shore Protection. An Environmental Innovation in Coastal Engineering*; Springer: Dordrecht, The Netherlands, 2003; 398p. [[CrossRef](#)]



Contents lists available at ScienceDirect

Artificial Intelligence

journal homepage: www.elsevier.com/locate/artint

On the robustness of sparse counterfactual explanations to adverse perturbations



Marco Virgolin^{a,*}, Saverio Fracaros^b

^a Evolutionary Intelligence Group, Centrum Wiskunde & Informatica, Science Park 123, 1098 XG Amsterdam, the Netherlands

^b Department of Mathematics and Geosciences, University of Trieste, via Weiss 2, 34128 Trieste, Italy

ARTICLE INFO

Article history:

Received 8 April 2022

Received in revised form 25 November 2022

Accepted 12 December 2022

Available online 16 December 2022

Keywords:

Counterfactual explanation

Explainable machine learning

Explainable artificial intelligence

Robustness

Uncertainty

ABSTRACT

Counterfactual explanations (CEs) are a powerful means for understanding how decisions made by algorithms can be changed. Researchers have proposed a number of desiderata that CEs should meet to be practically useful, such as requiring minimal effort to enact, or complying with causal models. In this paper, we consider the interplay between the desiderata of *robustness* (i.e., that enacting CEs remains feasible and cost-effective even if adverse events take place) and *sparsity* (i.e., that CEs require only a subset of the features to be changed). In particular, we study the effect of addressing robustness separately for the features that are recommended to be changed and those that are not. We provide definitions of robustness for sparse CEs that are workable in that they can be incorporated as penalty terms in the loss functions that are used for discovering CEs. To carry out our experiments, we create and release code where five data sets (commonly used in the field of fair and explainable machine learning) have been enriched with feature-specific annotations that can be used to sample meaningful perturbations. Our experiments show that CEs are often not robust and, if adverse perturbations take place (even if not worst-case), the intervention they prescribe may require a much larger cost than anticipated, or even become impossible. However, accounting for robustness in the search process, which can be done rather easily, allows discovering robust CEs systematically. Robust CEs make additional intervention to contrast perturbations much less costly than non-robust CEs. We also find that robustness is easier to achieve for the features to change, posing an important point of consideration for the choice of what counterfactual explanation is best for the user. Our code is available at: <https://github.com/marcovirgolin/robust-counterfactuals>.

© 2022 The Author(s). Published by Elsevier B.V. This is an open access article under the CC BY license (<http://creativecommons.org/licenses/by/4.0/>).

1. Introduction

Modern Artificial Intelligence (AI) systems often rely on machine learning models such as ensembles of decision trees and deep neural networks [1–3], which contain from thousands to billions of parameters. These large models are appealing because, under proper training and regularization regimes, they are often unmatched by smaller models [4,5]. However, as large models perform myriads of computations, it can be very difficult to interpret and predict their behavior. Because of this, large models are often called *black-box models*, and ensuring that their use in high-stakes applications (e.g., of medicine and finance) is fair and responsible can be challenging [6,7].

* Corresponding author.

E-mail address: marco.virgolin@cwi.nl (M. Virgolin).

The field of eXplainable AI (XAI) studies methods to dissect and analyze black-box models [8,9] (as well as methods to generate interpretable models when possible [10]). Famous methods of XAI include feature relevance attribution [11, 12], explanation by analogy with prototypes [13,14], and, of focus in this work, *counterfactual explanations*. Counterfactual explanations enable to reason by contrast rather than by analogy, as they show in what ways the input given to a black-box model needs to be changed for the model to make a different decision [15,16]. A classic example of counterfactual explanation is: “Your loan request has been rejected. If your salary was 60 000\$ instead of 50 000\$ and your debt was 2500\$ instead of 5000\$, your request would have been approved.” A user who obtains an unfavorable decision can attempt to overturn it by intervening according to the counterfactual explanation.

Normally, the search of counterfactual explanations is formulated as an optimization problem (see Sec. 2.1 for a formal description). Given the feature values that describe the user as starting point, we seek the minimal changes to those feature values that result in a point for which the black-box model makes a different (and oftentimes, a specific favorable) decision. We wish the changes to be minimal for two reasons: one, to learn about the behavior of the black-box model for a neighborhood of data points, e.g., to assess its fairness (although this is not guaranteed in general, see e.g., [17]); two, in the hope that putting the counterfactual explanation into practice by means of real-life intervention will require minimal effort too. For counterfactual explanations to be most useful, more desiderata than requiring minimal feature changes may need to be taken into account (see Sec. 9) [18].

In this paper, we consider a desideratum that can be very important for the usability of counterfactual explanations: *robustness to adverse perturbations*. By adverse perturbations we mean changes in feature values that happen due to unforeseen circumstances beyond the user’s control, making reaching the desired outcome no longer possible, or requiring the user to put more effort than originally anticipated. These unforeseen circumstances can have various origins, e.g., time delays, measurement corrections, biological processes, and so on. For example, if a counterfactual explanation for improving a patient’s heart condition prescribes lowering the patient’s blood pressure, the chosen treatment may need to be employed for longer, or even turn out to be futile, if the patient has a genetic predisposition to resist that treatment (for more examples, see Sec. 5.1 and choices made in the coding of our experiments, in `robust_cfe/dataproc.py`).

We show that, if adverse perturbations might happen, one can and *should* seek counterfactual explanations that are robust to such perturbations. A particular novelty of our work is that we distinguish between whether perturbations impact the features that counterfactual explanations prescribe to *change* or *keep as they are* (note that some features may be irrelevant and can be changed differently than how prescribed by a counterfactual explanation, we address this in Sec. 2.3). This is because counterfactual explanations are normally required to be *sparse* in terms of the intervention they prescribe (i.e., only a subset of the features should be changed), for better usability (see Sec. 2.1). As it will be shown, making this discrimination allows to improve the effectiveness and efficiency with which robustness can be accounted for. Consequently, one might need to consider carefully which counterfactual explanation to pursue, based on whether they are robust to features to change or keep as they are.

In summary, this paper makes the following contributions:

1. We propose two workable definitions of robustness of counterfactual explanations that concern, respectively, the features prescribed to be changed and those to be kept as they are;
2. We release code to support further investigations, where five existing data sets are annotated with perturbations and plausibility constraints that are tailored to the features and type of user seeking recourse;
3. We provide experimental evidence that accounting for robustness is important to prevent adverse perturbations from making it very hard or impossible to achieve recourse through counterfactual explanations, when adverse perturbations are sampled from a distribution (i.e., they are not necessarily worst-case ones);
4. We show that robustness for the features to change is far more reliable and computationally efficient to account for than robustness for the features to keep as they are;
5. Additionally, we propose a simple but effective genetic algorithm that outperforms several existing gradient-free search algorithms for the discovery of counterfactual explanations. The algorithm supports plausibility constraints and implements the proposed definitions of robustness.

2. Preliminaries

In the following, we introduce preliminary concepts for reasoning about robustness of counterfactual explanations in a sparse sense. In particular, we (i) describe the problem statement of searching for counterfactual explanations, (ii) present the notions of perturbation and robustness in general terms, and (iii) introduce the definitions of \mathcal{C} and \mathcal{K} , which are sets that partition the features of a counterfactual explanation. The following Secs. 3 and 4 will then present the main contribution of this paper: notions of robustness that are tailored to sparse counterfactual explanations, i.e., specific to \mathcal{C} and \mathcal{K} .

2.1. Problem statement

Let us assume we are given a point $\mathbf{x} = (x_1, \dots, x_d)$, where d is the number of features. Each feature takes values either in (a subset of) \mathbb{R} , in which case we call it a *numerical* feature, or in (a subset of) \mathbb{N} , in which case we call it a *categorical*

feature. For categorical features, we use natural numbers as a convenient way to identify their categories, but disregard ordering. For example, for the categorical feature *gender*, 0 might mean *male*, 1 might mean *female*, and 2 might mean *non-binary*. Thus, $\mathbf{x} \in \mathbb{R}^{d_1} \times \mathbb{N}^{d_2}$, where $d_1 + d_2 = d$.

A *counterfactual example*¹ for a point \mathbf{x} is a point $\mathbf{z} \in \mathbb{R}^{d_1} \times \mathbb{N}^{d_2}$ such that, given a classification (black-box) machine learning model $f : \mathbb{R}^{d_1} \times \mathbb{N}^{d_2} \rightarrow \{c_1, c_2, \dots\}$ (c_i is a decision or *class*), $f(\mathbf{z}) \neq f(\mathbf{x})$. We wish \mathbf{z} to be *close* to \mathbf{x} under a meaningful distance function δ that is problem-specific and meets several desiderata (see Sec. 9). For example, commonly-used distances that are capable of handling both numerical and categorical features are variants of Gower's distance [19] (see Eq. (9) and, e.g., [20] for a variant thereof). Often, when dealing with more than two classes, we also impose $f(\mathbf{z}) = t$, i.e., the *target* class we desire \mathbf{z} to be. Other times, we wish to find a *set* of counterfactual examples $\{\mathbf{z}_1, \dots, \mathbf{z}_k\}$, possibly of different classes, to obtain multiple means of recourse or simply gain information on the decision boundary of f nearby \mathbf{x} (e.g., to explain f 's local behavior) [15,21,22].

For the sake of readability, we provide formal definitions only for the case when all features are numerical (i.e., $\mathbf{x} \in \mathbb{R}^d, d_1 = d, d_2 = 0$). For completeness, we include explanations of how to deal with categorical features in the running text. Furthermore, we assume feature independence. While this assumption is rarely entirely met in real-world practice, it is commonly done in literature due to the lack of causal models (e.g., only four works consider causality in Sec. 9), and allows us to greatly simplify the introduction of the concepts hereby presented. We discuss the limitations that arise from this assumption in Sec. 8.

A counterfactual *explanation* is represented by a description of how \mathbf{x} needs to be changed to obtain \mathbf{z} . In other words, a counterfactual explanation is a prescription on what interventions should be made to *reach* the respective counterfactual example. For example, under the assumption of independence and all-numerical features, the difference $\mathbf{z} - \mathbf{x}$ is typically considered the counterfactual explanation for how to reach \mathbf{z} from \mathbf{x} . What particular form counterfactual explanations take is not crucial to our discourse, and we will use $\mathbf{z} - \mathbf{x}$ for simplicity.

We proceed by considering the following traditional setting where, for simplicity of exposition and without loss of generality, we will assume that features are pre-processed so that a difference in one unit in terms of feature i is equivalent to a difference in one unit in feature j (i.e., the user's effort is commensurate across different features). Alternatively, one can account for this in the computation of the distance (see, e.g., Eq. (9)). We seek the (explanation relative to an) *optimal* \mathbf{z}^* with:

$$\mathbf{z}^* \in \operatorname{argmin}_{\mathbf{z}} \delta(\mathbf{z}, \mathbf{x})$$

$$\text{with } \delta(\mathbf{z}, \mathbf{x}) := \|\mathbf{z} - \mathbf{x}\|_1 + \lambda \|\mathbf{z} - \mathbf{x}\|_0 \quad (1)$$

and subject to $f(\mathbf{z}) = t$ and $\mathbf{z} - \mathbf{x} \in \mathcal{P}$.

In other words, δ is a linear combination, weighed by λ , of the sum of absolute distances between the feature values of \mathbf{x} and \mathbf{z} , and the count of feature values that are different between \mathbf{x} and \mathbf{z} . Note that \mathbf{z}^* needs not be unique, i.e., multiple optima may exist. Moreover, the difference $\mathbf{z} - \mathbf{x}$ must abide to some plausibility constraints specified in a collection \mathcal{P} . We model plausibility constraints as a set of specifications, each relative to a feature i , concerning whether $z_i - x_i$ is allowed to be > 0 , < 0 , and $\neq 0$, i.e., a feature can increase, decrease, or change at all (for categorical features, we only consider the latter). For example for a private individual who wishes to be granted a loan, one of such constraints may specify that they cannot reasonably intervene to change the value of a currency (such a feature is called *mutable but not actionable*), i.e., counterfactual explanations must have $z_i - x_i = 0$, for i representing currency value. Similarly, the individual's age may increase but not decrease, i.e., $z_i - x_i > 0$, for i representing age.

We particularly consider the $L1$ -norm (i.e., the term $\|\cdot\|_1$ of δ in Eq. (1)) because it is reasonable to think that, for independent features, the total *cost* of intervention (i.e., the effort the user must put) is the sum of the costs of intervention for each feature separately, and that these costs grow linearly. Some works (e.g., [20,23]) choose the $L2$ -norm ($\|\cdot\|_2$, also known as Euclidean norm) instead of the $L1$ -norm; the definitions of robustness given in this paper can be easily adapted for the $L2$ -norm. Regarding the $L0$ -norm (i.e., the term $\|\cdot\|_0$ of δ in Eq. (1)), this term explicitly promotes a form of sparsity, as it seeks to minimize how many features have a different value between \mathbf{z} and \mathbf{x} . This is desirable because, oftentimes, the user can only reasonably focus on, and intervene upon, a limited number of features (even if this amounts to a larger total cost in terms of $L1$ compared to intervention on *all* the features) [24].

2.2. Perturbations & robustness

Unforeseen circumstances (e.g., inflation) might lead to more or different intervention to be needed, compared to what was originally prescribed by a counterfactual explanation (e.g., increase savings by 1000 \$ to be granted credit access). Thus, instead of reaching \mathbf{z} as intended by the counterfactual explanation, a different point \mathbf{z}' is obtained. Note that while the effects of unforeseen circumstances can impact feature values, the circumstances themselves need not be encoded as feature values. In fact, we will only focus on the extent by which feature values may be perturbed by such circumstances.

¹ Many authors use \mathbf{x}' to represent a counterfactual example for \mathbf{x} , instead of \mathbf{z} . We chose \mathbf{z} not to overload the notation with superscripts later on in the manuscript, for readability.

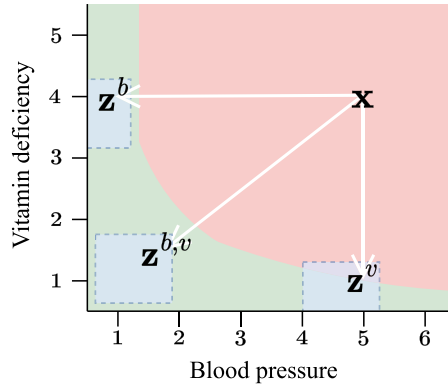


Fig. 1. Example of considering robustness to perturbations when seeking counterfactual examples. The red and green areas respectively represent *high risk* and *low risk* classifications of a cardiac condition according to a model f . The patient, represented by \mathbf{x} , is at high risk. Three possible counterfactual examples are shown for different interventions (white arrows): \mathbf{z}^b for treating blood pressure, \mathbf{z}^v for treating vitamin deficiency, and $\mathbf{z}^{b,v}$ for treating both. We assume to know the maximal extent of perturbation (under reasonable risk) for blood pressure and vitamin deficiency due to natural physiological events. This allows us to define the blue areas surrounding each counterfactual example. Perturbations \mathbf{w} to one of the counterfactual examples can lead to any other point in the blue area. \mathbf{z}^v is the best of the three in terms of proximity to \mathbf{x} but its blue area partly overlaps with the red area. This means that there exist \mathbf{w} such that $\mathbf{z}^v + \mathbf{w}$ leads to a point in the red area, invalidating the counterfactual explanation. In such cases, it is important to estimate if additional intervention is possible so that \mathbf{z}^v can still be reached, and at what cost. (For interpretation of the colors in the figure(s), the reader is referred to the web version of this article.)

Let us define the vector $\mathbf{w} = \mathbf{z} - \mathbf{z}'$ as a *perturbation* for the counterfactual example \mathbf{z} . We assume that perturbations that impact feature i are sampled from some distribution $P(w_i)$ and we are interested in controlling for, or *being robust to*, large magnitude perturbations that have reasonable risk. For example for normally-distributed perturbations, we might want to consider the values that can be sampled at the 95th or 99th percentile. We will therefore assume that we can define a vector $\mathbf{p} = (p_1^{(-)}, p_1^{(+)}, \dots, p_d^{(-)}, p_d^{(+)})$ where $p_i^{(-)} \leq 0$ and $p_i^{(+)} \geq 0$ represent, respectively, the smallest negative and largest positive perturbations that can reasonably happen to the i^{th} feature. For example, if the i^{th} feature represents the blood pressure of a patient, then $p_i^{(-)}$ tells by how much the blood pressure might lower at most (e.g., as a consequence of dehydration) and $p_i^{(+)}$ tells by how much the blood pressure might raise at most (e.g., as a consequence of anti-inflammatory drug intake). Clinicians may be able to define this information from their experience or retrieve it from medical literature. In general, the magnitudes of $p_i^{(-)}, p_i^{(+)}$ need not be the same, i.e., $|p_i^{(-)}| \neq |p_i^{(+)}|$. Note that for an i^{th} feature that is categorical, decreases or increases $p_i^{(-)}, p_i^{(+)}$ as explained for numerical features are no longer meaningful. For categorical features, we will assume that \mathbf{p} contains elements that represent what categorical perturbations are possible for that feature, i.e., p_i will be a set of indices that represent categories.

Under the problem setting we considered in Sec. 2.1, perturbations that may impact a counterfactual explanation define a *box* (hyper-rectangle) of all possible points \mathbf{z}' that can be reached from \mathbf{z} due to perturbations. An example is illustrated in Fig. 1. We define the concept of **p-neighborhood** of \mathbf{z} as follows:

Definition 1. (p-neighborhood** and **p-neighbors** of a counterfactual example)** Given a model f , a point \mathbf{x} , a respective counterfactual example \mathbf{z} , and a vector of possible perturbations \mathbf{p} , the **p-neighborhood** of \mathbf{z} is the set:

$$N := \left\{ \mathbf{z}' \mid z'_i \in [z_i + p_i^{(-)}, z_i + p_i^{(+)}] \right\}. \tag{2}$$

A point $\mathbf{z}' \in N$ such that $\mathbf{z}' \neq \mathbf{z}$ is called a **p-neighbor** of \mathbf{z} .

Not all perturbations are problematic. Our goal is to study robustness to *adverse* perturbations, i.e., those for which $f(\mathbf{z} + \mathbf{w}) = f(\mathbf{z}') \neq t$. In other words, we wish to seek counterfactual examples \mathbf{z} that have no (or the fewest possible) **p-neighbors** for which perturbations can cause the classification performed by f to be different from t . When that happens, we say that the counterfactual explanation has been *invalidated* by the perturbation. However, it may be the case that invalidation is not *permanent*: there may still exist intervention (i.e., a new counterfactual explanation) that adheres to the constraints in \mathcal{P} and allows us to overcome invalidation. Therefore, in this work, we will seek to discover counterfactual explanations that are *robust* in the sense that (i) if invalidated, additional intervention remains possible, (ii) the cost of additional intervention is small.

Unforeseenly, if f is assumed to be a general model (e.g., not necessarily a linear one), then the following argument holds.

Proposition 1. For a general f , information on the classification of a \mathbf{p} -neighbor (e.g., that $f(\mathbf{z}') = f(\mathbf{z})$ for \mathbf{z}' on the boundary of N) provides no information about the classification of another \mathbf{p} -neighbor (e.g., that $f(\mathbf{z}') \neq f(\mathbf{z}'')$ for \mathbf{z}'' in the interior of N).

Proof. We cannot preclude that the model f is, for example, a neural network. Under the universal approximation theorem [25], f may represent any function. Thus, f may represent a Swiss cheese-like function, where for example $f(\mathbf{z}') \neq f(\mathbf{z}'')$ with $\mathbf{z}'' := \mathbf{z}' + \mathbf{e}$ and $\mathbf{e} = (\varepsilon_1, \dots, \varepsilon_d)$ different from the zero-vector, however small $|\varepsilon_i|, \forall i$. \square

This proposition means that if no information on, e.g., regularity or smoothness of f is available, then we must check each and every \mathbf{p} -neighbor \mathbf{z}' of \mathbf{z} to assess whether some of them may invalidate the explanation, i.e., $\exists \mathbf{z}'$ such that $f(\mathbf{z}') \neq t$. Checking all neighbors is typically not feasible, e.g., as soon as some of the features are real valued. Thus, the best one can do is to take an approximate approach. For example, a Monte-Carlo sampling approach can be used where a batch of random points within N is considered, hoping that the batch is representative of all points in N . As we will show in the next sections, a better strategy can be designed if sparsity is considered.

We conclude this section by noting that perturbations, as described so far, are *absolute*, i.e., independent of the starting point \mathbf{x} , the counterfactual in consideration \mathbf{z} , or the intervention entailed by the counterfactual explanation $\mathbf{z} - \mathbf{x}$. Perturbations to feature i might however depend on x_i and z_i , i.e., be sampled from a distribution $P(w_i|x_i, z_i)$. For example, due to market fluctuations, a return on investment may be smaller than anticipated by 5% of the expected value. Such type of *relative* perturbations entail different \mathbf{p} -neighborhoods for different \mathbf{x} and \mathbf{z} . For simplicity and without loss of generality, we will proceed by assuming that perturbations can only be absolute. We explain how we also included *relative* perturbations in the annotations used for our experiments in Sec. 5.

2.3. Sparsity, features in \mathcal{C} and \mathcal{K}

We use the form of sparsity mentioned in Sec. 2.1 to partition the features into two sets. As mentioned before, sparsity is an important desideratum because it may not be reasonable to expect that the user can realistically intervene on, and keep track of, *all* the features to achieve recourse. Given a specific counterfactual explanation \mathbf{z} for the point \mathbf{x} , we call the set containing the (indices of the) features whose values should *change* $\mathcal{C} = \{i \in \{1, \dots, d\} \mid z_i \neq x_i\}$, and its complement, i.e., the set of the (indices of the) features whose values should be *kept as they are*, $\mathcal{K} = \{i \in \{1, \dots, d\} \mid z_i = x_i\}$. Typically, because a sufficiently large λ is used, or because of the plausibility constraints specified in \mathcal{P} , $\mathcal{K} \neq \emptyset$.

Note that the proposed partitioning between \mathcal{C} and \mathcal{K} implicitly assumes that all features are relevant to the counterfactual explanation. If certain features are irrelevant, perturbations to those features will have no effect on f 's decision, and thus those features need not be accounted for when assessing robustness. This means that accounting for irrelevant features makes assessing robustness more computationally expensive than needed. However, as f is considered a black-box, we cautiously assume that all features are relevant for assessing robustness.

We will proceed by accounting for perturbations and respective robustness separately for features in \mathcal{C} and \mathcal{K} . Accounting for robustness separately is important because, as we will show, assessing robustness for features in \mathcal{C} can be done far more efficiently and be more effective than for features in \mathcal{K} . Knowing this, if multiple counterfactual explanations can be found, the user may want to choose the counterfactual explanation that fits him/her best based on the robustness it exhibits in terms of \mathcal{C} and \mathcal{K} . In the next section, we present our first notion of robustness, which concerns \mathcal{C} .

3. Robustness for \mathcal{C}

We begin by focusing on the features that the counterfactual explanation instructs to change, i.e., the features (whose indices are) in \mathcal{C} . Recall that we assume that a vector of maximal perturbation magnitudes \mathbf{p} can be defined. This leads us to the following definition.

Definition 2. (*C-perturbation*) Given a point \mathbf{x} , a respective counterfactual example \mathbf{z} , and the vector of maximal magnitude perturbations \mathbf{p} , a *C-perturbation* for the counterfactual explanation $\mathbf{z} - \mathbf{x}$ is a vector

$$\mathbf{w}^c = (w_1^c, \dots, w_d^c), \text{ where} \tag{3}$$

$$\begin{cases} p_i^{(-)} \leq w_i^c \leq p_i^{(+)} & \text{if } i \in \mathcal{C}, \\ w_i^c = 0 & \text{otherwise, i.e., } i \notin \mathcal{C} \end{cases} \tag{4}$$

and such that $\exists i : w_i^c > 0$, i.e., \mathbf{w}^c is not the zero-vector.

In other words, a \mathcal{C} -perturbation is a perturbation that acts only on features in \mathcal{C} , and at least on one of such features. Next, we use the concept of \mathcal{C} -perturbations to introduce the one of \mathcal{C} -setbacks.

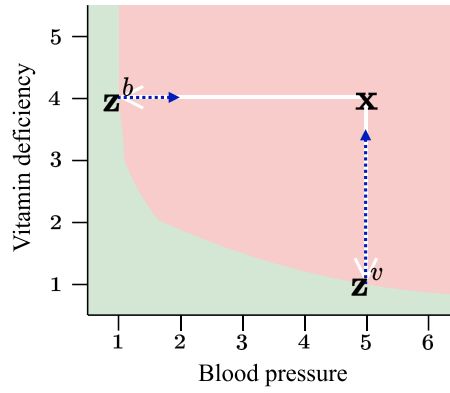


Fig. 2. Example of C -setbacks. The red and green areas represent *high risk* and *low risk* classifications of a cardiac condition according to a model f . The patient, represented by \mathbf{x} , is at high risk. Two treatments are possible but cannot be administered jointly due to drug incompatibility, hence sparsity of intervention is needed (only one of the two treatments can be pursued). The closest (and thus optimal) counterfactual example is \mathbf{z}^v and concerns treating vitamin deficiency (white arrow pointing down). Another counterfactual example is \mathbf{z}^b and concerns treating blood pressure (white arrow pointing left). Maximal C -setbacks are shown for both counterfactual examples (blue dashed segments). The setbacks can make both counterfactual examples invalid. However, the counterfactual examples can still be reached with additional intervention (treatment administration). Indeed, if one accounts for the possibility that maximal C -setbacks may take place, then the total cost (original intervention + additional intervention to remedy the perturbation, i.e., $3 + 2.5$) to reach \mathbf{z}^v becomes larger than the total cost to reach \mathbf{z}^b (i.e., $4 + 1$).

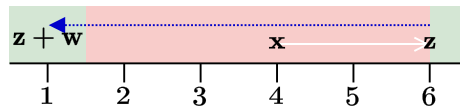


Fig. 3. One-dimensional example of how a C -setback can be advantageous if the magnitude of perturbation exceeds the magnitude of intervention.

Definition 3. (C -setback) A C -setback for the counterfactual explanation $\mathbf{z} - \mathbf{x}$ is a C -perturbation such that

$$\begin{cases} p_i^{(-)} \leq w_i^c \leq 0 & \text{if } z_i - x_i > 0 \\ 0 \leq w_i^c \leq p_i^{(+)} & \text{if } z_i - x_i < 0 \\ w_i^c = 0 & \text{otherwise, i.e., } i \notin C. \end{cases} \tag{5}$$

We denote C -setbacks with $\mathbf{w}^{c,s}$.

In words, a C -setback is a C -perturbation where each and every element of the perturbation $w_i^{c,s}$ is of opposite sign to the counterfactual explanation $z_i - x_i$. We can interpret the meaning of C -setbacks $\mathbf{w}^{c,s}$ as vectors that *push the user away from \mathbf{z} and back towards \mathbf{x}* along the direction of intervention. Furthermore, we call a *maximal C -setback*, denoted by $\mathbf{w}_{\max}^{c,s}$, C -setback whose elements that correspond to features in C have maximal magnitude, i.e., $w_i^{c,s} = p_i^-$ if $z_i - x_i > 0$ and $w_i^{c,s} = p_i^+$ if $z_i - x_i < 0$. An example is given in Fig. 2.

C -setbacks are arguably more interesting than C -perturbations because C -setbacks are the subset of these perturbations that plays against the user. In fact, certain C -perturbations might be advantageous, enabling to reach \mathbf{z} with less intervention than originally provisioned (i.e., when the sign of w_i^c and that of $z_i - x_i$ matches). To account for robustness, we are interested in understanding whether perturbations can prevent us to reach \mathbf{z} , hence we will proceed by focusing exclusively on C -setbacks.

It is important to note that even C -setbacks can be advantageous if one allows their perturbations to be of larger magnitude than intervention, i.e., if $|w_i^{c,s}| > |z_i - x_i|$ is allowed ([26] discuss this aspect in detail). In a nutshell, if $|w_i^{c,s}| > |z_i - x_i|$, then a C -setback can lead to a point that “precedes” \mathbf{x} in terms of the direction of intervention. For that point, the intervention may be less costly than the one that was originally planned or entirely not needed because the point is of the target class (see, e.g., Fig. 3). Advantageous situations are not interesting for robustness and counterfactual explanations that can be overturned by perturbations may well not be interesting to pursue. We therefore consider any C -setback to have elements capped by $|w_i^{c,s}| \leq |z_i - x_i|$.

Perhaps the most interesting scenario for considering C -setbacks is when dealing with \mathbf{z}^* , since a counterfactual example that is optimal (i.e., one minimizes Eq. (1)) is an ideal outcome. The following simple result holds for \mathbf{z}^* :

Proposition 2. For any C -setback $\mathbf{w}^{c,s}$ of \mathbf{z}^* (such that $|w_i^{c,s}| \leq |z_i^* - x_i|$ for all i), $f(\mathbf{z}^* + \mathbf{w}^{c,s}) \neq t$.

Proof. We use *reduction ad absurdum*. Let us assume the opposite of what was said in Proposition 2, i.e., there exists $\mathbf{w}^{c,s}$ such that $f(\mathbf{z}^* + \mathbf{w}^{c,s}) = t$. Let $\mathbf{z}' := \mathbf{z}^* + \mathbf{w}^{c,s}$, and so $f(\mathbf{z}') = t$. By construction of $\mathbf{w}^{c,s}$, $\delta(\mathbf{z}', \mathbf{x}) = \delta(\mathbf{z}^* + \mathbf{w}^{c,s}, \mathbf{x}) < \delta(\mathbf{z}^*, \mathbf{x})$. In other words, \mathbf{z}' is of the target class and is closer to \mathbf{x} than \mathbf{z}^* is. This contradicts the fact that \mathbf{z}^* is optimal. \square

Now, because of Proposition 2, we are *guaranteed* that if a \mathcal{C} -setback $\mathbf{w}^{c,s}$ happens to \mathbf{z}^* , the resulting point will no longer be classified as t . Intuitively, this is a natural consequence of the fact that optimal counterfactual examples lay on the border of the decision boundary as otherwise they would not be optimal. Also, since \mathbf{z}^* is optimal, the respective L_0 component for the distance between \mathbf{x} and \mathbf{z}^* is minimal, i.e., all features in \mathcal{C} and thus in $\mathbf{w}^{c,s}$ are relevant for the classification. Given the premises just made, it becomes important to understand whether invalidation to \mathbf{z}^* can be averted with additional intervention and, if so, whether the cost of such intervention can be minimized.

It is important to note that invalidation of a counterfactual explanation due to a \mathcal{C} -setback can always be averted, i.e., additional intervention to reach the intended z_i for all $i \in \mathcal{C}$ is always possible. To see this, consider the fact that the intervention entailed by the counterfactual explanation $\mathbf{z} - \mathbf{x}$ must adhere to the plausibility constraints specified in \mathcal{P} (else, $\mathbf{z} - \mathbf{x}$ would not be a possible counterfactual explanation). Since \mathcal{C} -setbacks are aligned with the direction of the original intervention, the point $\mathbf{z} + \mathbf{w}^{c,s} - \mathbf{x}$, which is in between \mathbf{x} and \mathbf{z} , must meet \mathcal{P} . It therefore suffices to apply additional intervention along the originally-intended direction to recover the desired counterfactual example. Under the L_1 -norm (as per the choice of δ in Eq. (1)), the cost associated with the additional intervention needed to overcome a \mathcal{C} -setback $\mathbf{w}^{c,s}$ is simply $\|\mathbf{w}^{c,s}\|_1$.

Since invalidation due to \mathcal{C} -setbacks can be dealt with additional intervention, and since one can reasonably assume that the user keeps track of how the value of x_i changes for $i \in \mathcal{C}$ over the course of intervention (otherwise, (s)he would not know when to stop the intervention), it follows that there is no necessity for counterfactual examples to be far from the decision boundary in terms of their features in \mathcal{C} . (Note that this is in contrast with prior work on aspects of robustness for counterfactuals, where the possibility of additional intervention is not considered and counterfactual examples are required to be far from the decision boundary in terms of all of their features; see Sec. 9.) Thus, rather than seeking counterfactual examples that are not invalidated by \mathcal{C} -setbacks, we seek counterfactual examples for which the additional intervention that is needed to contrast \mathcal{C} -setbacks is minimal. To this end, we can use Proposition 2 in order to seek counterfactual examples that are optimal (i.e., require minimum intervention cost) when the additional cost to contrast maximal \mathcal{C} -setbacks $\mathbf{w}_{\max}^{c,s}$ is factored in. In the following definition, to highlight that \mathcal{C} -setbacks depend on the specific \mathbf{z} and \mathbf{x} (as they determine \mathcal{C}) and avoid confusion, we use the function notation $W_{\max}^{c,s}(\mathbf{z}, \mathbf{x})$ in place of $\mathbf{w}_{\max}^{c,s}$.

Definition 4. (*Optimal counterfactual example under \mathcal{C} -setbacks*) Given a model f , a point \mathbf{x} , and a vector \mathbf{p} , we call a point $\mathbf{z}^{*,c}$ such that

$$\mathbf{z}^{*,c} - W_{\max}^{c,s}(\mathbf{z}^{*,c}, \mathbf{x}) \in \operatorname{argmin}_{(\mathbf{z} - W_{\max}^{c,s}(\mathbf{z}, \mathbf{x}))} \delta(\mathbf{z} - W_{\max}^{c,s}(\mathbf{z}, \mathbf{x}), \mathbf{x}), \quad (6)$$

an *optimal counterfactual example under \mathcal{C} -setbacks*.

This definition gives us a way to seek a (multiple may exist) counterfactual explanation that entails minimal intervention cost when accounting for maximal \mathcal{C} -setbacks. Indeed, it suffices to equip a given search algorithm with Eq. (6), i.e., perform the following steps: (1) for any \mathbf{z} to be evaluated, compute the respective $\mathbf{w}_{\max}^{c,s}$, (2) instead of computing $\delta(\mathbf{z}, \mathbf{x})$, compute $\delta(\mathbf{z} - \mathbf{w}_{\max}^{c,s}, \mathbf{x})$, and (3) at the end of the search, return the point that minimizes such distance, i.e., $\mathbf{z}^{*,c}$.

Performing the computations just mentioned takes linear time in the number of features ($O(d)$) because we only need to build $\mathbf{w}_{\max}^{c,s}$ (step 1 above) and subtract it from \mathbf{z} prior to computing δ (step 2 above) for any given \mathbf{z} (f should still be evaluated on \mathbf{z}). This is relatively fast (as demonstrated in B.3.2), especially compared to the situation described in Sec. 2.2, where one would need to use f to predict the class of a number of neighbors of \mathbf{z} . Note also that in Eq. (6) setbacks are subtracted from counterfactual examples when computing δ , to account for the fact that the cost should increase (recall the construction of \mathcal{C} -setbacks in Definition 3).

4. Robustness for \mathcal{K}

We now consider \mathcal{K} , i.e., the set concerning the features that should be kept to their current value. Mirroring the notion of \mathcal{C} -perturbation (Definition 2), we can define a \mathcal{K} -perturbation to be a vector \mathbf{w}^k such that $p_i^{\{-\}} \leq w_i^k \leq p_i^{\{+\}}$ if $i \in \mathcal{K}$ and $w_i^k = 0$ if $i \notin \mathcal{K}$. Similarly, we can cast the concept of neighborhood from Definition 1 to consider only \mathcal{K} -perturbations, leading to:

Definition 5. (*\mathcal{K} -neighborhood and \mathcal{K} -neighbors of a counterfactual example*) Given a model f , a point \mathbf{x} , a respective counterfactual example \mathbf{z} , and a vector of possible perturbations \mathbf{p} , the \mathcal{K} -neighborhood of \mathbf{z} under \mathbf{p} is the set:

$$K := \left\{ \mathbf{z}' \mid \begin{array}{l} z'_i \in [z_i + p_i^{\{-\}}, z_i + p_i^{\{+\}}], \text{ if } i \in \mathcal{K} \\ z'_i = z_i \text{ otherwise} \end{array} \right\}. \quad (7)$$

A point $\mathbf{z}' \in K$ such that $\mathbf{z}' \neq \mathbf{z}$ is called a \mathcal{K} -neighbor of \mathbf{z} .

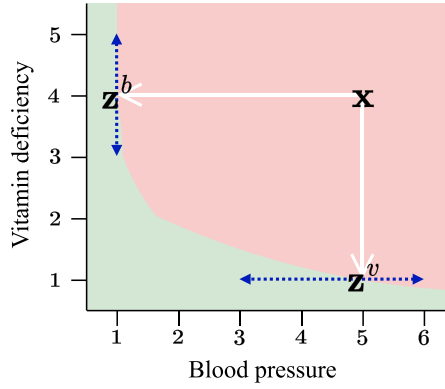


Fig. 4. Example of \mathcal{K} -perturbations. The counterfactual example \mathbf{z}^v is vulnerable to \mathcal{K} -perturbations because these can lead to the red area; the same is not true for \mathbf{z}^b . If it is not plausible to reduce blood pressure, then \mathcal{K} -perturbations to \mathbf{z}^v can lead to permanent invalidity. Else, they can be resolved with additional intervention, in terms of blood pressure.

For a categorical feature $i \in \mathcal{K}$, the neighborhood can be built by swapping z_i with one of the possibilities listed in $p_i \in \mathbf{p}$, where p_i will be a set containing categories perturbations can lead to.

Next, we use K to define the concept of vulnerability to \mathcal{K} -perturbations:

Definition 6. (*Vulnerability to \mathcal{K} -perturbations*) Given a model f , a point \mathbf{x} , and a vector \mathbf{p} , a counterfactual example \mathbf{z} is vulnerable to \mathcal{K} -perturbations if $\exists \mathbf{z}' \in N(\mathbf{z}, \mathbf{p})$ such that $f(\mathbf{z}') \neq f(\mathbf{z})$.

Informally, this definition says that \mathbf{z} is vulnerable to \mathcal{K} -perturbations if the decision boundary surrounding \mathbf{z} is not sufficiently loose with respect to the features in \mathcal{K} . Fig. 4 shows an example. The reason why vulnerability to \mathcal{K} -perturbations is particularly important is that, differently from the case of \mathcal{C} -perturbations, a \mathcal{K} -perturbation can invalidate the counterfactual explanation *permanently*. In fact, a \mathcal{K} -perturbation changes \mathbf{z} along a different direction than the one of intervention. Thus, a \mathcal{K} -perturbation can lead to a point \mathbf{z}' from which there exists no plausible intervention to reach the originally-intended \mathbf{z} from.

For example, consider the feature i to represent *inflation* as a mutable but not actionable feature, i.e., a feature that can be changed (e.g., by global market trends) but not by the user. \mathcal{P} will state that no (user) intervention can exist to change i , i.e., \mathcal{P} imposes $z_i - x_i = 0$. However, an unforeseen circumstance such as the financial crisis of 2008 may lead to a large inflation increase ($p_i^+ > 0$). Consequently, it may become impossible for the user to obtain the desired loan, e.g., because the bank does not hand out certain loans when the inflation is too high.

Now, recall that the reason why Definition 4 can be used for the case of \mathcal{C} -perturbations is that Proposition 2 holds, i.e., there cannot exist points of class t between \mathbf{x} and an optimal counterfactual example \mathbf{z}^* . The same does not hold for \mathcal{K} -perturbations, i.e., since the features in \mathcal{K} are orthogonal to the direction of intervention, it can happen that the maximal perturbation to a feature $i \in \mathcal{K}$ leads to a point \mathbf{z}' for which $f(\mathbf{z}') = t$, while a non-maximal perturbation to the same feature can lead to a point \mathbf{z}'' for which $f(\mathbf{z}'') \neq t$. Thus, checking for maximal perturbations is no longer sufficient: we must check instead for all points in the \mathcal{K} -neighborhood K .

As mentioned in Sec. 2.2, checking each and every point in a neighborhood may not be feasible. Thus, we propose to approximate the assessment of how \mathcal{K} -robust (i.e., non-vulnerable to perturbations in \mathcal{K}) counterfactual explanations can be, with Monte-Carlo sampling. Let $\mathbf{1}_{f(\mathbf{z})} : K \rightarrow \{0, 1\}$ be the indicator function that returns 1 for \mathcal{K} -neighbors that share the same class of \mathbf{z} (i.e., $f(\mathbf{z})$), and 0 for those that do not. Taken a random sample of m \mathcal{K} -neighbors, we define the following score:

$$\mathcal{K}\text{-robustness score}(\mathbf{z}, m) = \frac{1}{m} \sum_{i=1}^m \mathbf{1}_{f(\mathbf{z})}(\mathbf{z}'_i). \tag{8}$$

We remark that even if \mathcal{K} -robustness score(\mathbf{z}, m) = 1, we are not guaranteed that \mathbf{z} is \mathcal{K} -robust, because the score is an approximation. Still, this score can be used to determine which counterfactual examples are preferable to pursue in that they are associated with a smaller risk that adverse perturbations will invalidate them (permanently or not).

5. Experimental setup

In this section, we firstly describe the preparation of the data sets used in our experiments. Secondly, we describe the search algorithms considered for finding near-optimal counterfactual explanations. Lastly, we describe the loss function considered, as well as how to incorporate the proposed notions of robustness into it.

Table 1

Considered data sets, where n and d (resp., d_2) indicate the number of observations and features (only categorical) after pre-processing. The column t is the target class for the (simulated) user. Plausib. constr. reports the number of plausibility constraints that allow features to only increase (\geq), remain equal ($=$), and decrease (\leq). The column Perturb. reports the number of perturbations concerning numerical (N) and categorical (C) features. Finally, Acc._{rf} and Acc._{nn} report the average (across five folds) test accuracy of the random forest and neural network models.

Data set (abbrev.)	n	d	d_2	Classes	User	t	Plausib. constr.	Perturb.	Acc. _{rf}	Acc. _{nn}
Credit risk (Cre)	1000	20	6	High, low	Individual	Low	$\geq:3, =:8, \leq:0$	N:6, C:0	0.76	0.75
Income (Inc)	1883	12	7	High, low	Individual	High	$\geq:2, =:3, \leq:0$	N:4, C:4	0.83	0.82
House price (Hou)	506	13	1	High, low	Municipality	Low	$\geq:0, =:3, \leq:1$	N:11, C:0	0.93	0.93
Productivity (Pro)	1196	12	5	High, med., low	Company	High	$\geq:0, =:0, \leq:0$	N:5, C:2	0.79	0.70
Recidivism risk (Rec)	2000	10	6	High, low	Inmate	Low	$\geq:2, =:2, \leq:0$	N:3, C:2	0.80	0.78

Table 2

Examples of perturbations that we manually annotated on the considered data sets. We take relative perturbations (those with %) with respect to the value of the feature in the intended counterfactual example \mathbf{z} in consideration by the search algorithm.

D.set	Feature	Decrease	Increase	Note
		or Categories		
Cre	Savings	10%	10%	Might happen to save less or more relative to what intended.
Inc	Marital status	{single, married, widowed, ...}		Unforeseen change due to, e.g., proposal, divorce, death.
Hou	Crime rate	1%	5%	Relative, might increase more than decrease.
Pro	Overtime	3	3	Up to 3 more or less days of overtime might be needed.
Rec	Age	0	2	Judicial system delays for up to 2 years.

5.1. Data sets

Table 1 summarizes the data sets we consider. For each data set, we make an assumption on the type of user who seeks recourse, e.g., the user could be a private individual seeking to increase their income, or a company seeking to improve the productivity of its employees. Based on this, we manually define the target class t , the set of plausibility constraints \mathcal{P} on what interventions are reasonably plausible, and the collection \mathbf{p} of maximal magnitudes from which perturbations can be sampled (we will consider uniform and normal distributions). We named the data sets in Table 1 to represent their purpose. Originally, *Credit risk* (abbreviated to Cre) is known as *South German Credit Data* [27], which is a recent update that corrects inconsistencies in the popular *Statlog German Credit Data* [28]. *Income* (Inc) is often called *Adult* or *Census income* [29,30]. *Housing price* (Hou) is also known as *Boston housing* [31] and is often used for research on fairness and interpretability because one of its features raises ethical concerns [32]. *Productivity* (Pro) concerns the productivity levels of employees producing garments [33]. Lastly, *Recidivism* (Rec) is a data set collected by an investigation of ProPublica about possible racial bias in the commercial software COMPAS, which intends to estimate the risk that an inmate will re-offend [34]. Examples of recent works on fair and explainable machine learning that adopted (some of) these data sets are [20,35–40].

We pre-process the data sets similarly to how done often in the literature. This includes, e.g., removal of redundant features and of observations with missing values, and limiting the number of observations considered for Rec. Regarding our annotations for the perturbations, numerical features can have perturbations that increase or decrease the feature value, in absolute or relative terms; we compute relative perturbations with respect to \mathbf{z} . For example, for the numerical feature *capital-gain* of Inc, we assume that perturbations can happen that lead up to a relative 5% increase or 10% decrease of that feature, based on the value to achieve for that feature. For categorical features, we define only absolute perturbations, i.e., possible changes of category are not conditioned to the current category. The choices we made to build \mathbf{p} are subjective, we elaborate on this in Sec. 8. We sample the amount of perturbation using a uniform or normal distribution, as indicated in Sec. 7. Table 2 shows some examples of maximal perturbations we annotated. As mentioned before, we also define plausibility constraints \mathcal{P} for each data set. Each constraint is specific to a feature. For an i^{th} numerical feature, possible constraints are $z_i - x_i \geq 0$, $z_i - x_i \leq 0$, $z_i - x_i = 0$, and *none*. For an i^{th} categorical feature, possible constraints are $z_i = x_i$ and *none*. Full details about our pre-processing and definition of \mathbf{p} and \mathcal{P} are documented in the form of comments in our code, in `robust_cfe/dataproc.py`.

5.2. Black-box models

We consider random forest and neural networks (with standard multi-layer perceptron architecture) as black-box machine learning models f . We use Scikit-learn’s implementations [41]. We assume that we can only access the predictions of f , and no other information such as model parameters or gradients. Our experiments are repeated across a stratified five-fold cross-validation, and each model is obtained by grid-search hyper-parameter tuning. Once trained, the models obtain test accuracy varying from 70% to more than 90% on average across the different data sets, i.e., meaningful decision boundaries are learned. See Appendix A for details on hyper-parameter tuning, and the accuracy of the models on the different data sets. For the discovery of counterfactual examples, we consider observations \mathbf{x} such that $f(\mathbf{x}) \neq t$, from the test sets of the cross-validation.

Table 3

Settings of the considered counterfactual search algorithms. For NeMe, we only set the maximum number of iterations to 100 to achieve commensurate runtimes to those of CoGS (other settings are default). For DiCE, we consider two configurations (“a” and “b”). The loss used (except for DiCE a) is Eq. (9).

CoGS		DiCE (a, b)	
Setting	Value	Setting	Value
Population size	1000	Method	Genetic
Num. generations	100	Total CEs	a : 20, b : 100
Tournament size	2	Max. iterations	a : 500, b : 100
$Smut$	25%	Loss weights	a : Default, b : 0.5 prox., 0.5 spars., 0 div.

GrSp		LORE	
Setting	Value	Setting	Value
Num. in layer	2000	Population size	1000
First radius	0.1	Num. generations	10
Decrease radius	10	Discrete use probabilities	False
Sparse	True	Continuous function estim.	False

5.3. Counterfactual search algorithms

To provide experimental results concerning robustness (Sec. 7), we firstly seek a counterfactual search algorithm that performs best overall among several candidates. To that end, we consider and benchmark the following algorithms from the literature, that can operate upon black-box f : *Diverse Counterfactual Explanations* (DiCE) [22], *Growing Spheres* (GrSp) [23], *Local Rule-based Explanations* (LORE) [20,42], and the *Nelder-Mead method* (NeMe) [43,44]. Furthermore, we devise our own algorithm, a genetic algorithm that we name *Counterfactual Genetic Search* (CoGS).²

The settings used for the algorithms are reported in Table 3. We describe the algorithms below. Note that all of the algorithms are heuristics with no guarantee of discovering optimal (i.e., minimal distance) counterfactual examples, given the nature of the search problem (general, black-box f).

5.3.1. DiCE

DiCE is actually a library that includes three algorithms: random sampling, KD-tree search (i.e., a fast-retrieval data structure built upon the points in the training set), and a genetic algorithm. Of the three, we consider the latter because it performed substantially better in preliminary experiments (and simply refer to it by DiCE). DiCE is configured to return a collection of counterfactual examples rather than a single one. However, three of the other algorithms we consider return a single counterfactual example. Thus, to compare the algorithms on an equal footing, we set DiCE to return a single counterfactual example too. We achieve this by ranking each counterfactual example in the collection according to the loss function in consideration (explained below, see Sec. 5.4), and picking the best-ranking point. We will further consider two different configurations of DiCE:

- *Configuration “a”* uses the default settings except for allowing for a longer number of iteration, to match the same computational budget given to the other algorithms.
- *Configuration “b”* uses custom settings that are aligned to be similar to those used for CoGS, since both DiCE and CoGS are genetic algorithms.

5.3.2. GrSp

GrSp is a greedy algorithm that iteratively samples neighbors of the starting point \mathbf{x} within spheres (i.e., in an L_2 sense) that have increasing radius, until counterfactual examples are found. GrSp includes feature selection to promote sparsity. Unforeseenly, GrSp can only handle numerical features. To be able to use GrSp in our comparison, we let GrSp operate on categorical features as if they were numerical ones (categories are encoded as integers). At the end of the optimization, we transform numerical values back to categories by rounding. Note that this is sub-optimal because an artificial ordering is introduced between categories.

5.3.3. LORE

LORE works by generating a neighborhood around \mathbf{x} with random search or with a genetic algorithm, finding multiple counterfactual explanations at different distance. We consider the variant that adopts the genetic algorithm, because it performed substantially better in preliminary experiments. After the neighborhood is determined, LORE fits a decision tree

² <https://github.com/marcovirgolin/cogs>.

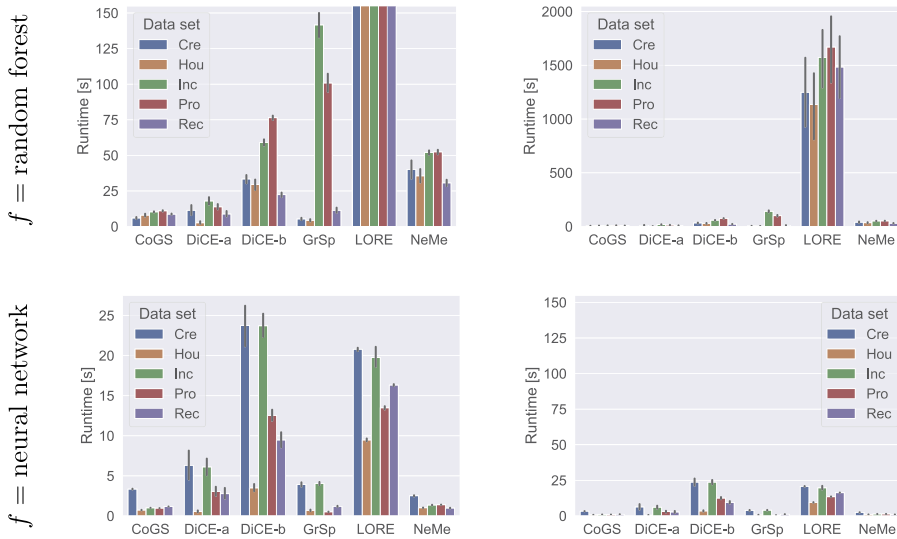


Fig. 5. Runtimes (means and 95% confidence intervals) of the counterfactual search algorithms for the considered data sets and black-boxes (random forest and neural network). The right plots are zoomed-out versions of the left ones.

upon it. Since each path from the root of the decision tree to a leaf represents a classification rule (e.g., “AGE >= 3.4 & SALARY_CATEGORY = HIGH → t”), LORE essentially returns multiple counterfactual explanations expressed as rules. To be able to compare with the other algorithms (which return a single counterfactual example), we build one counterfactual example \mathbf{z} by taking the shortest rule returned by LORE, and applying the rule to the starting point \mathbf{x} (e.g., using the rule above, we set the \mathbf{x} 's age and salary to 3.4 and high, respectively).

We found (confirmed by a discussion with the authors) that applying LORE's rules may result in points that are not actually classified as t . When that happens, we perform up to 15 attempts at generating a counterfactual example from the (shortest returned) rule, by focusing on numerical features that are prescribed to be $>$, \geq (or $<$, \leq) than a certain value. In particular, in applying such part of the rule to \mathbf{x} , we add (or subtract) to the prescribed value a term ϵ , which is initially set to 10^{-3} and is doubled at every attempt. Moreover, since we found LORE to be computationally expensive to run (see Fig. 5), we used a fraction of the computation budget allowed for the other algorithms (see Table 3).

5.3.4. NeMe

NeMe is a classic simplex-based algorithm for gradient-free optimization. Like GrSp, also NeMe cannot naturally handle categorical features. Thus, we use the same approximation used for GrSp, i.e., encode categories with integers, let NeMe treat categories as numerical values, and map such values back to integers (and thus categories) by rounding at the end. We use SciPy's implementation with default parameters [45].

5.3.5. CoGS

We design CoGS as a relatively standard genetic algorithm, adapted for the search of points neighboring \mathbf{x} (especially in terms of the L_0 -norm). CoGS operates as follows. First, an initial population of candidate solutions is generated by sampling feature values uniformly within an interval for numerical features, and from the possible categories for categorical features. These intervals can be specified or taken automatically from the training set. With probability of $2/d$ (d being the total number of features), the feature value of a candidate solution is copied from \mathbf{x} rather than sampled. Every iteration of the algorithm (in the jargon of evolutionary computation, generation), offspring solutions are produced from the current population by crossover and mutation. Following this, survival of the fittest is applied to form the population for the next generation.

Our version of crossover produces two offspring solutions by simply swapping the feature values of two random parents, uniformly at random. Our version of mutation produces one offspring solution from one parent solution by randomly altering its feature values. A feature value is altered with probability of $1/d$ (else, it is left untouched). If the feature to alter is categorical, then the category is swapped with another category, uniformly at random. If the feature to alter is numerical, firstly a random number r is sampled uniformly at random between $-s_{mut}/2$ and $+s_{mut}/2$, where $s_{mut} \in (0, 1]$ is a hyper-parameter that represents the maximal extent of allowed mutations; secondly, the original feature value is changed by adding $r \times (\max_i - \min_i)$, where \max_i and \min_i are, respectively, the maximum and minimum values that are possible for that feature.

After crossover and mutation, the quality (fitness) of offspring solutions is evaluated using the loss function (Eq. (9)) as fitness function (minimization is sought). Finally, we use tournament selection [66]) to form the population for the next generation.

We set CoGS to allow for plausibility constraints (\mathcal{P}) to be specified. If plausibility constraints are used, then mutation is restricted to plausible changes (e.g., the feature that represents age can only increase). If mutation makes a numerical feature obtain a value bigger than \max_i (resp., smaller than \min_i), then the value of that feature is set to \max_i (resp., \min_i).

CoGS is written in Python, and relies heavily on NumPy [67] for speeding up key computations. For example, the population is encoded as a NumPy matrix, and crossover and mutation are implemented with matrix operations.

5.4. Loss

We use the following loss to drive the search of counterfactual examples (where $f(\mathbf{z})$ and t are treated as integers):

$$\frac{1}{2}\gamma(\mathbf{z}, \mathbf{x}) + \frac{1}{2} \frac{\|\mathbf{z} - \mathbf{x}\|_0}{d} + \|f(\mathbf{z}) - t\|_0, \text{ where} \quad (9)$$

$$\gamma(\mathbf{z}, \mathbf{x}) = \frac{1}{d} \left(\sum_i^{d_1} \frac{|z_i - x_i|}{\max_i - \min_i} + \sum_j^{d_2} \|z_j - x_j\|_0 \right). \quad (10)$$

The function γ in the equation above is Gower's distance [19,46], where features indexed by i are numerical and those indexed by j are categorical (with values treated as integers); the maximal and minimal values of a numerical feature, \max_i and \min_i , can be taken from the (training) data set or, as done in our case, are provided as extra annotations of the data sets. The term $\|\mathbf{z} - \mathbf{x}\|_0/d$ promotes sparsity of intervention and, like Gower's distance, ranges from zero to one. The third and last term requires the execution of the machine learning model f , and simply returns zero when $f(\mathbf{z}) = t$ and one when $f(\mathbf{z}) \neq t$.

5.4.1. Incorporating robustness in the loss

To seek robust counterfactual examples, we make use of the notions described in Sec. 3 and Sec. 4. When optimizing for robustness to perturbations concerning \mathcal{C} , we use Definition 4, i.e., maximal \mathcal{C} -setbacks are computed on the fly for the candidate \mathbf{z} and their contribution is used to update the contribution of γ to the loss function. When optimizing for robustness to perturbations concerning \mathcal{K} , we compute the \mathcal{K} -robustness score with Eq. (8) and add $\frac{1}{2}(1 - \mathcal{K}\text{-robustness score})$ to the loss. In the results presented below, we use $m = 64$ to compute the \mathcal{K} -robustness score; an analysis on the impact of m is provided in B.3.

6. Preliminary results: choosing a suitable counterfactual search algorithm

This section reports on the benchmarking of the considered search algorithms, to identify an overall best. We repeat the execution of each algorithm five times and consider the best-found counterfactual example out of the five repetitions. We search for a counterfactual example for each \mathbf{x} in the test sets from the five cross-validation, for \mathbf{x} such that $f(\mathbf{x}) \neq t$. Since LORE takes much longer to execute than the other algorithms (see Fig. 5), we perform three repetitions instead of five, and consider only the first five \mathbf{x} in each test set of the five folds. Since only DiCE and CoGS support plausibility constraints, we do not use plausibility constraints in this comparison (a comparison between DiCE and COGS under plausibility constraints is provided in Appendix B.1).

6.1. Runtimes

Fig. 5 shows the runtime of the algorithms across the different data sets, irrespective of whether they succeed or fail to find a counterfactual example, i.e., a point for which f predicts t . The experiments were run on a cluster where the computing nodes can have slightly different CPUs, thus we invite to consider the order of magnitude of the runtimes rather than the exact numbers. The figure shows that, using random forest, CoGS and DiCE (configuration a) are the fastest algorithms (or, at least, have fastest implementations), but GrSp and NeMe are competitive. LORE is much slower to execute than the other algorithms. When using a neural network, inference times are generally faster, and CoGS, DiCE-a, GrSp and NeMe are competitive.

6.2. Success in discovering counterfactual examples

Table 4 shows the frequency with which the counterfactual search algorithms succeed in finding a counterfactual example, i.e., a point for which f predicts t . CoGS and the two variants of DiCE succeed systematically, whereas the other algorithms do not. GrSp performs third-best overall. In particular, GrSp always finds counterfactual examples on Hou, which is a data set with a single categorical feature. Since GrSp is intended to operate solely with numerical features, this result nicely supports the hypothesis that GrSp works well when (almost all) features are numerical. Although LORE supports both numerical and categorical features, it does not perform better than GrSp on most data sets; at least for the limited number of runs conducted with LORE due to excessive runtime, as explained before. Lastly, NeMe often performs substantially worse than all other algorithms.

Table 4

Mean \pm standard deviation across five cross-validation folds of the frequency with which the counterfactual search algorithms succeed in finding a counterfactual example. Plausibility constraints are not considered here because not all algorithms support them.

	Alg.	Cre	Inc	Hou	Pro	Rec
$f = \text{random forest}$	CoGS	1.00	1.00	1.00	1.00	1.00
	DiCE-a	1.00	1.00	1.00	1.00	1.00
	DiCE-b	1.00	1.00	1.00	1.00	1.00
	GrSp	0.46 \pm 0.11	0.89 \pm 0.06	1.00	0.86 \pm 0.04	0.30 \pm 0.15
	LORE	0.56 \pm 0.20	0.20 \pm 0.13	0.68 \pm 0.20	0.24 \pm 0.20	0.60 \pm 0.38
	NeMe	0.08 \pm 0.03	0.05 \pm 0.02	0.04 \pm 0.05	0.03 \pm 0.01	0.14 \pm 0.02
$f = \text{neural network}$	CoGS	1.00	1.00	1.00	1.00	1.00
	DiCE-a	1.00	1.00	1.00	1.00	1.00
	DiCE-b	1.00	1.00	1.00	1.00	1.00
	GrSp	0.87 \pm 0.07	0.25 \pm 0.04	1.00	0.51 \pm 0.12	0.49 \pm 0.10
	LORE	0.52 \pm 0.20	0.28 \pm 0.16	0.68 \pm 0.10	0.76 \pm 0.23	0.84 \pm 0.23
	NeMe	0.14 \pm 0.07	0.11 \pm 0.03	0.09 \pm 0.01	0.11 \pm 0.04	0.51 \pm 0.03

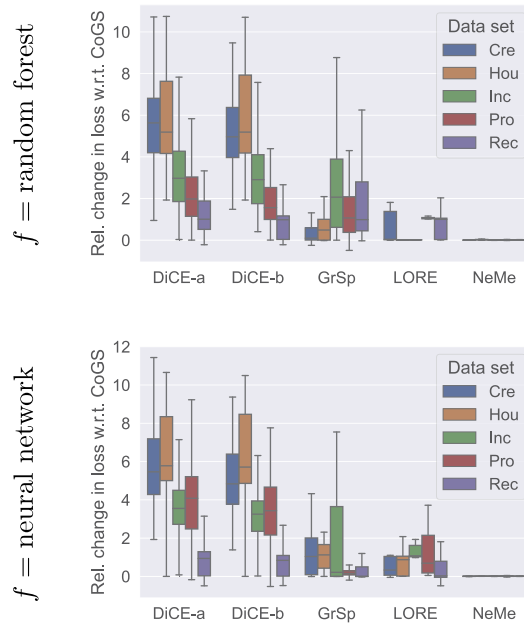


Fig. 6. Boxplots of relative change in loss with respect to CoGS for GrSp, LORE, and NeMe, on the different data sets and black-boxes, for success cases.

6.3. Quality of discovered counterfactual examples

As last part in our benchmarking effort, we consider what algorithm manages to produce near-optimal counterfactual examples (i.e., those with smallest loss). In particular, we report the relative change in loss for the best-found counterfactual example with respect to the loss obtained by CoGS, only for success cases. Since we consider only successes, the last term of the loss (Eq. (9)) is always null, i.e., $\|f(\mathbf{z}) - t\|_0 = 0$. The relative change in loss with respect to CoGS for another algorithm Alg is:

$$\frac{\mathcal{L}_{\text{Alg}}(\mathbf{z}) - \mathcal{L}_{\text{CoGS}}(\mathbf{z})}{\mathcal{L}_{\text{CoGS}}(\mathbf{z})}.$$

Fig. 6 shows the relative change in loss of DiCE, GrSp, LORE, and NeMe with respect to CoGS. DiCE, GrSp and LORE typically (but not always) find points that have larger loss than those found by CoGS. NeMe performs very similarly to CoGS, however NeMe seldom succeeds (cf. Table 4). This suggests that NeMe can explore a small neighborhood of \mathbf{x} particularly well, but fails if counterfactual examples are relatively distant from \mathbf{x} .

Table 5

Mean \pm standard deviation of the frequency with which the best-found (among five search repetitions) counterfactual example when not accounting for robustness is accidentally robust w.r.t. \mathcal{C} or \mathcal{K} . For numerical features, we consider them to match in value if they are within a tolerance level (Tol.) of 1%, 5% or 10% of the range for that feature.

	Robustness	Tol.	Cre	Inc	Hou	Pro	Rec
$f = \text{random forest}$	Only \mathcal{C}	1%	0.40 \pm 0.06	0.02	0.76 \pm 0.10	0.53 \pm 0.05	0.27 \pm 0.06
		5%	0.42 \pm 0.07	0.04 \pm 0.02	0.84 \pm 0.09	0.57 \pm 0.06	0.37 \pm 0.07
		10%	0.43 \pm 0.07	0.05 \pm 0.02	0.85 \pm 0.09	0.58 \pm 0.06	0.40 \pm 0.09
	Only \mathcal{K}	1%	0.37 \pm 0.01	0.06 \pm 0.02	0.33 \pm 0.24	0.26 \pm 0.05	0.04 \pm 0.04
		5%	0.44 \pm 0.03	0.40 \pm 0.08	0.63 \pm 0.17	0.37 \pm 0.06	0.08 \pm 0.03
		10%	0.46 \pm 0.04	0.58 \pm 0.07	0.67 \pm 0.16	0.46 \pm 0.07	0.12 \pm 0.02
	Both \mathcal{C}, \mathcal{K}	1%	0.23 \pm 0.04	0.00	0.21 \pm 0.21	0.19 \pm 0.06	0.03 \pm 0.03
		5%	0.27 \pm 0.03	0.00	0.54 \pm 0.21	0.26 \pm 0.05	0.06 \pm 0.04
		10%	0.30 \pm 0.05	0.00	0.60 \pm 0.19	0.34 \pm 0.06	0.08 \pm 0.04
$f = \text{neural network}$	Only \mathcal{C}	1%	0.25 \pm 0.12	0.01 \pm 0.01	0.96 \pm 0.02	0.87 \pm 0.05	0.50 \pm 0.08
		5%	0.27 \pm 0.12	0.02 \pm 0.01	0.97 \pm 0.02	0.89 \pm 0.05	0.56 \pm 0.05
		10%	0.29 \pm 0.11	0.02 \pm 0.01	0.97 \pm 0.02	0.89 \pm 0.05	0.57 \pm 0.04
	Only \mathcal{K}	1%	0.13 \pm 0.07	0.35 \pm 0.02	0.07 \pm 0.05	0.08 \pm 0.06	0.01
		5%	0.26 \pm 0.08	0.52 \pm 0.03	0.80 \pm 0.12	0.42 \pm 0.19	0.01 \pm 0.01
		10%	0.39 \pm 0.02	0.70 \pm 0.04	0.93 \pm 0.04	0.58 \pm 0.14	0.02 \pm 0.02
	Both \mathcal{C}, \mathcal{K}	1%	0.02 \pm 0.02	0.00	0.07 \pm 0.05	0.06 \pm 0.06	0.00 \pm 0.01
		5%	0.06 \pm 0.03	0.00	0.69 \pm 0.09	0.38 \pm 0.18	0.01 \pm 0.01
		10%	0.12 \pm 0.08	0.00	0.93 \pm 0.04	0.52 \pm 0.14	0.01 \pm 0.02

6.4. Conclusion of benchmarking

The results show that, overall, CoGS performs best. DiCE (in particular, DiCE-a) is the closest competitor in terms of speed and success rates, but the algorithm finds counterfactual examples that are substantially more distant from \mathbf{x} (i.e., have larger loss) than those found by CoGS. GrSp has good runtime and generally finds closer counterfactual examples (i.e., lower loss) than DiCE, but it remains inferior to CoGS, both in terms of distance (loss) and success rate. LORE has worse success rate than GrSp, and NeME worse of all. Therefore, we use CoGS for the following experiments on robustness.

We remark that DiCE, like CoGS, supports the specification of plausibility constraints. We show that CoGS performs better than DiCE also under plausibility constraints in Appendix B.1.

7. Experimental results: robustness

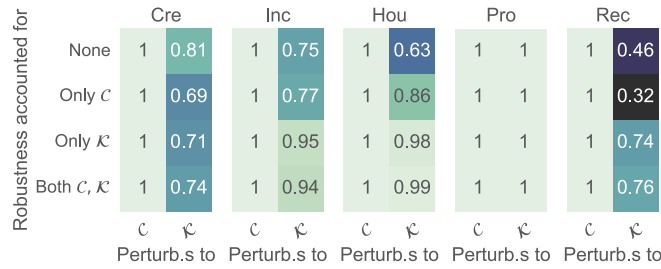
We proceed with presenting the experimental results regarding robustness to perturbations in \mathcal{C} , \mathcal{K} , and jointly. We focus on results that allow us to answer what we believe to be important research questions: (RQ1) *Do we need to account for robustness to discover robust counterfactual examples?* (RQ2) *Does a lack of robustness compromise the feasibility of correcting perturbations with additional intervention?* (RQ3) *Are robust counterfactual explanations advantageous in terms of additional intervention cost?* These questions are addressed, in order, in the next subsections. Because of space limitations, a number of additional results is reported in Appendix B, including runtime taken to account for robustness w.r.t. \mathcal{C} and \mathcal{K} , and the effect of varying m when computing the \mathcal{K} -robustness score. We now account for plausibility constraints \mathcal{P} in all of the following experiments. We remark that in all our experiments, CoGS always succeeded in discovering a counterfactual example for which f predicts t , except for having a mean success rate of 99% (st.dev. of 1%) on the Rec data set when f is implemented as a neural network.

7.1. (RQ1) Do we need to account for robustness to discover robust counterfactual examples?

Table 5 shows the frequency with which robust counterfactual examples are discovered accidentally. To realize this, we compare the best-found counterfactual example that is discovered by CoGS when robustness is *not* accounted for, and the one that is found when \mathcal{C} - or \mathcal{K} -robustness is accounted for (as indicated in Sec. 5.4.1). We take the frequency by which the two match as indication of whether robust counterfactual examples can be discovered by accident. Since numerical feature values may differ only slightly between two best-found counterfactual examples, we consider the values to match if they are sufficiently close to each other, according to a tolerance level of 1%, 5%, or 10% of the range of that feature. As reasonable to expect, the results show that the larger the tolerance level, the more a \mathbf{z}^* discovered when not accounting for robustness matches the respective one that is discovered when accounting for robustness. In general, the result depends on the data set in consideration, and also (albeit arguably less so) on whether random forest or a neural network is used as black-box model f .

For brevity, we now focus on the tolerance level of 5% and random forest. On Inc, best-found counterfactual examples rarely match with those discovered when accounting for \mathcal{C} -robustness (4% on average for the tolerance of 5%), while the

Uniformly-distributed perturbations, $f = \text{random forest}$



Normally-distributed perturbations, $f = \text{random forest}$

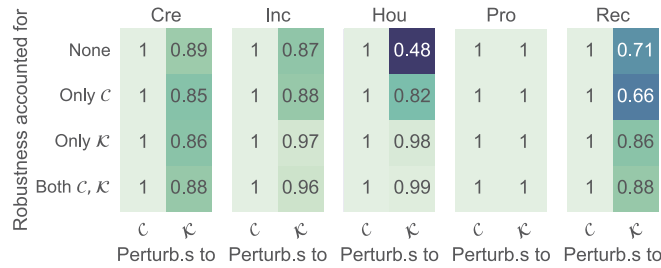


Fig. 7. Mean frequency with which a plausible additional intervention exists, to contrast the perturbations and reach the intended counterfactual example (uniformly-distributed categorical changes and normally- or uniformly-distributed numerical changes, $f = \text{random forest}$). Darker colors represent worse cases.

vice versa happens on Hou (84% on average for the same tolerance). For \mathcal{K} -robustness like for \mathcal{C} -robustness, the result depends on the data set. Importantly, the data sets where the frequencies are high for \mathcal{C} -robustness and \mathcal{K} -robustness are not necessarily the same. On Inc, best-found counterfactual examples are rarely optimal under \mathcal{C} -setbacks, but can often match with counterfactual examples discovered when penalizing low \mathcal{K} -robustness scores (40% on average for the tolerance of 5%). This should not be surprising because \mathcal{C} - and \mathcal{K} -robustness are orthogonal to each other under the assumption of feature independence. The last row shows how often best-found counterfactual examples happen to be both robust to perturbations to \mathcal{C} and \mathcal{K} . The frequencies are clearly always lower than for the previous triplets of rows. Hou is the only data set for which the frequency of discovering a counterfactual example that happens to be both robust w.r.t. \mathcal{C} and \mathcal{K} by chance is relatively large (e.g., above 50% for the tolerance of 5%).

When using the neural network instead of random forest, the trends mentioned before remain the same, but the specific magnitudes can differ. For example, the accidental discovery of robust counterfactual examples w.r.t. \mathcal{C} and/or \mathcal{K} is lower on Cre with the neural network compared to random forest, but the opposite holds for Hou (with some exceptions, e.g., the tolerance level of 1% when both \mathcal{C} - and \mathcal{K} -robustness are sought).

Overall, this result indicates that, except for lucky cases (e.g., Hou with f being the neural network), it is unlikely to discover robust counterfactual examples by chance. Hence, if one wishes to achieve robustness, the search must be explicitly instructed to that end. In the next sections, we investigate whether achieving robustness can actually be important.

7.2. (RQ2) Does a lack of robustness compromise the feasibility of correcting perturbations with additional intervention?

At this point, current works on the robustness of counterfactual explanations typically consider the extent by which robustness helps preventing the invalidation of counterfactual explanations (see Sec. 9). In other words, they consider whether the point \mathbf{z}' that is given by perturbing the best-found counterfactual example is still classified as t . For completeness, we report on this in B.2. Current works do not, however, consider whether an additional intervention that allows to correct the perturbation and obtain t might exist.

Figs. 7 and 8 show the frequency with which achieving the intended counterfactual explanation remains possible after random perturbations take place. The frequency is computed by applying, for each counterfactual explanation outcome of the search, 100 perturbations that are sampled uniformly at random from the categorical possibilities for categorical features, and normally (with st.dev. of 0.1) or uniformly within the numerical intervals for numerical features, as defined in p. We note that similar results are obtained between choosing random forest or a neural network as f .

As expected, it is always possible to contrast \mathcal{C} -setbacks, because these happen along the direction of intervention. Instead, perturbations concerning \mathcal{K} can lead to a \mathbf{z}' such that no further plausible intervention exists to reach the originally intended counterfactual example. We do not report a result for perturbations concerning both \mathcal{C} and \mathcal{K} at the same time

Uniformly-distributed perturbations, $f =$ neural network



Normally-distributed perturbations, $f =$ neural network



Fig. 8. Mean frequency with which a plausible additional intervention exists, to contrast the perturbations and reach the intended counterfactual example (uniformly-distributed categorical changes and normally- or uniformly-distributed numerical changes, $f =$ neural network). Darker colors represent worse cases.

because, by construction, it is the same as the result for perturbations concerning only \mathcal{K} . Like for the results of Sec. 7.1, the extent by which perturbations to \mathcal{K} reduce the possibility for additional intervention depends on the data set. On Pro, all perturbations can be contrasted by an additional intervention because there are no plausibility constraints (see Table 1). Conversely, on Rec, perturbations to \mathcal{K} can often make it impossible to reach the originally-intended counterfactual example, unless \mathcal{K} -robustness is accounted for. In fact, accounting for \mathcal{K} -robustness generally improves the chances that additional intervention is possible, at times substantially (e.g., on Inc, Hou, and Rec). Cre represents the only exception to this, as accounting for \mathcal{K} -robustness performs similar (or sometimes worse) than accounting for none. This suggests that the decision boundary learned by f on this data set may not be very smooth, making the use of the \mathcal{K} -robustness score a too coarse approximation to be helpful. Generally, accounting for perturbations to \mathcal{C} alone does not help achieving substantial robustness to perturbations to \mathcal{K} , except for on Hou. This suggests that, on Hou, f learns decision boundaries that incorporate interesting interactions between certain features. Importantly, accounting for \mathcal{C} -robustness together with accounting for \mathcal{K} -robustness does not substantially compromise the gains obtained by accounting for \mathcal{K} -robustness alone, even though perturbations to \mathcal{C} always admit additional intervention. Overall, these results show that accounting for robustness can be crucial to ensure that, if perturbations happen, additional intervention to obtain t remains possible.

7.3. (RQ3) Are robust counterfactual explanations advantageous in terms of additional intervention cost?

We present the following results in terms of a *relative cost*, namely, the ratio between the cost of intervention to reach the intended \mathbf{z} when random perturbations take place (i.e., initial the cost of reaching \mathbf{z} from \mathbf{x} plus the cost of reaching \mathbf{z} from the perturbed \mathbf{z}'), and the *ideal cost*, i.e., the cost incurred in complete absence of perturbations (i.e., the cost of reaching \mathbf{z} from \mathbf{x}). We compute this relative cost when the notions of robustness are or are not accounted for. The ideal cost is computed when *not* accounting robustness. The cost is modeled by $\frac{1}{2}\gamma(\mathbf{z}, \mathbf{x}) + \frac{1}{2}\frac{\|\mathbf{z}-\mathbf{x}\|_0}{d}$ (i.e., the first part of Eq. (9)). Moreover, if $f(\mathbf{z}') = t$, we assume no additional intervention to be needed, and thus the additional cost is zero and the relative cost is 1.

Figs. 9 and 10 (for random forest and neural network, respectively) show that when no robustness is accounted for (the left-most triplets of boxes in each plot), the relative cost can become dramatically large. In other words, additional intervention to correct the perturbations can be extremely costly. Whether the relative cost increases mostly due to perturbations to \mathcal{C} (blue boxes) or to \mathcal{K} (orange boxes) depends on the data set. For example, perturbations to \mathcal{K} have the largest effect on Rec, while those to \mathcal{C} have the largest effect on Inc (by far), across types of distribution and types of f . For both the random forest and the neural network, the relative cost ranges from around $5\times$ or $10\times$ the ideal cost, up to over $100\times$ (Inc, perturbations to \mathcal{C}) when not accounting for robustness.

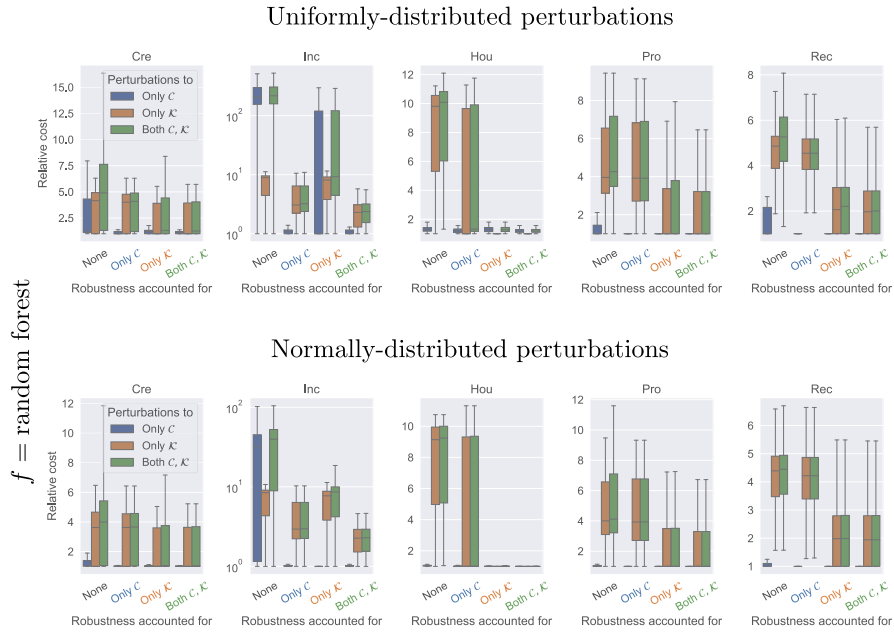


Fig. 9. Cost in terms of different configurations of accounting for robustness and under different perturbations, relative to the ideal cost (with random forest). Due to perturbations, the relative cost for when no notion of robustness is accounted for (label None) is typically much larger than the one for when the right notion of robustness is accounted for (matching color between box and label). The vertical axis for Inc is in logarithmic scale.

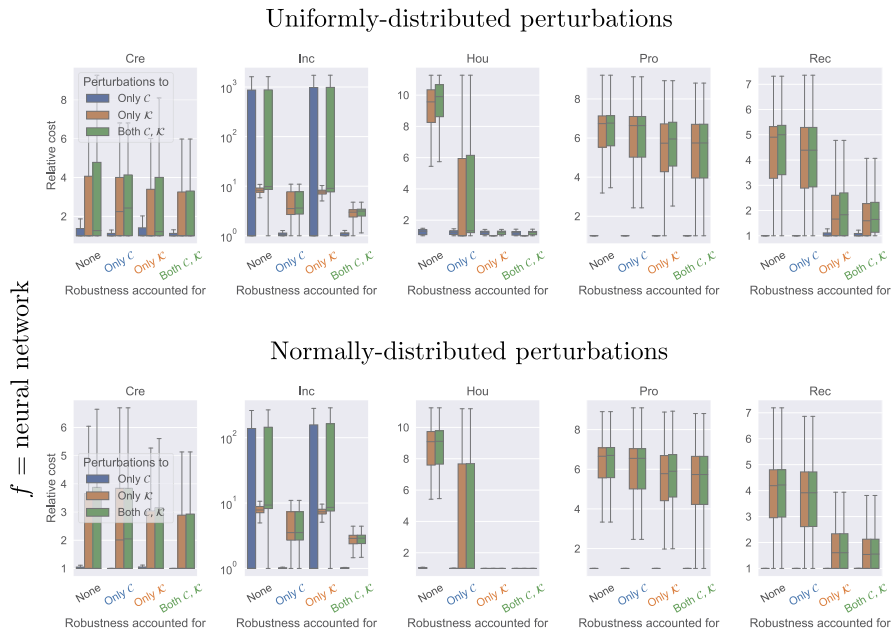


Fig. 10. Cost in terms of different configurations of accounting for robustness and under different perturbations, relative to the ideal cost (with neural network). Due to perturbations, the relative cost for when no notion of robustness is accounted for (label None) is typically much larger than the one for when the right notion of robustness is accounted for (matching color between box and label). The vertical axis for Inc is in logarithmic scale.

When one accounts for the notion of robustness that is meant to deal with the respective type of perturbation, the relative cost often decreases substantially. Accounting for \mathcal{C} -robustness (second blue box from the left in each plot) counters perturbations to \mathcal{C} very well on all the data sets. On Inc in particular, the relative cost improves by two orders of magnitude. As found in Sec. 7.2, accounting for perturbations to \mathcal{K} with the \mathcal{K} -robustness score can remain insufficient, as it can be observed on Cre and Inc for both types of f . Again, this is likely a limitation of using a simple heuristic such as the \mathcal{K} -robustness score to deal with \mathcal{K} -robustness. Accounting for robustness w.r.t. \mathcal{C} (resp., \mathcal{K}) does not, in general, lead to smaller relative cost under perturbations to \mathcal{K} (resp., \mathcal{C}). We confirm this general trend with statistical testing in Appendix C. Lastly,

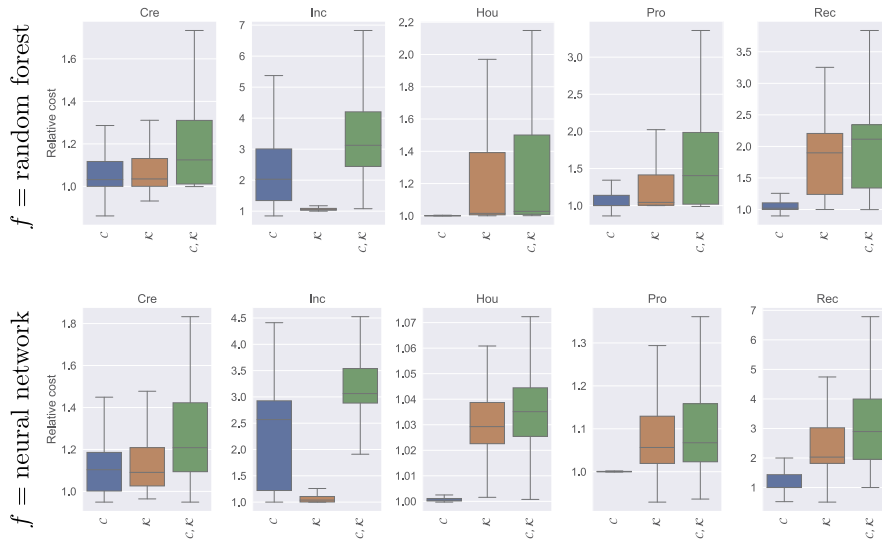


Fig. 11. Cost of accounting for robustness relative to not accounting for robustness (i.e., ideal cost) when no perturbations take place. Note that the (rare) relative costs smaller than 1 are due to a lack of optimality of the search algorithm.

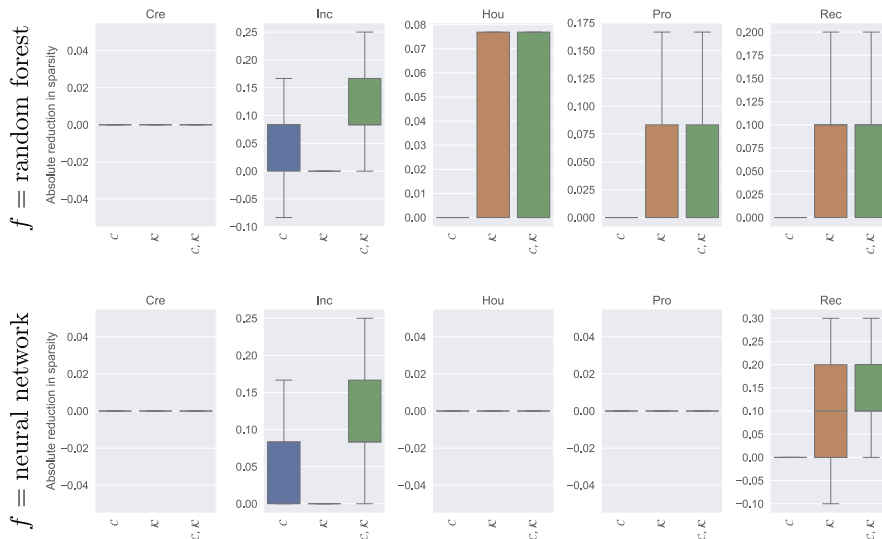


Fig. 12. Reduction in sparsity (relative to the number of features) caused by accounting for robustness. Note the different vertical axes.

accounting for both \mathcal{C} - and \mathcal{K} -robustness (right-most triplets of boxes in each plot) offers protection (lower relative cost) from situations in which both types of perturbations take place. In general across data sets and types of f , the distribution of relative costs for when perturbations to both \mathcal{C} and \mathcal{K} take place and both \mathcal{C} - and \mathcal{K} -robustness are accounted for (right-most green box in each plot) is better than the distribution for when the same perturbations take place but no notion of robustness is accounted for (left-most green box in each plot).

Since the ideal cost is computed when no notion of robustness is accounted for, part of the relative costs for when robustness is accounted for comes from the fact that robust counterfactual examples are generally farther away from \mathbf{x} than non-robust ones. Fig. 11 shows the cost increase that comes solely from accounting for robustness on the considered data sets and types of f , without any perturbation taking place. We remark that values smaller than 1 happen only because the discovered counterfactual examples can be suboptimal. Importantly, we find that the cost when accounting for robustness is between $1\times$ and $7\times$ the ideal cost, i.e., when not accounting for robustness. In general, this is significantly smaller than the increase incurred when perturbations take place and robustness is not accounted for, as reported before (generally between $5\times$ and $10\times$ the ideal cost, with up to $100\times$).

Lastly, Fig. 12 shows what part of the cost increase comes from counterfactuals becoming less sparse. For certain data sets (e.g., Cre for both random forest and neural network), robust counterfactual explanations are as sparse as non-robust ones. In general, however, robust counterfactual explanations tend to be less sparse, depending on the choice of f and the

type of robustness that is accounted for. The reduction in sparsity can be moderate or substantial. For example, less than 10% more of the features need to change to account for \mathcal{K} perturbations on Hou with random forest (i.e., approximately one feature). Instead, up to 30% more of the features need to change to account for \mathcal{K} perturbations on Rec with the neural network (i.e., approximately three features). The fact that sparsity decreases when seeking robust counterfactuals is a natural consequence of adopting a linearization of the objectives (see Sec. 5.4). Thus, the reduction in sparsity can be tackled by tuning the weight attributed to the L_0 -norm in Eq. (9).

These results confirm that even though robust counterfactual explanations are, in principle, more costly to pursue than non-robust ones, if random perturbations take place, robust counterfactual explanations require much less additional intervention than non-robust ones.

8. Discussion

Our experimental results provide a positive answer to all three research questions. In general, counterfactual explanations are *not* robust, be it in terms of the features whose value is prescribed to be changed (\mathcal{C} -robustness), or those whose value is prescribed to be kept as is (\mathcal{K} -robustness). Moreover, non-robust counterfactual explanations are more susceptible to make it impossible for the user to remedy perturbations by additional intervention, and the cost of additional intervention is larger for non-robust counterfactual explanations than for robust ones. Ultimately, it is clear that accounting for robustness is important.

Our experimental results suggest that accounting for robustness for features in \mathcal{C} tempers perturbations to \mathcal{C} , and similarly, accounting for robustness for features in \mathcal{K} tempers perturbations to \mathcal{K} . Moreover, even though f can learn non-linear feature interactions, accounting for \mathcal{C} (or \mathcal{K}) has limited effect on contrasting perturbations to \mathcal{K} (resp., \mathcal{C}). Only in some cases (e.g., on Hou), robustness w.r.t. \mathcal{C} has substantial repercussions on the effect of perturbations to \mathcal{K} or vice versa.

In addition to this, even if a counterfactual search algorithm does not guarantee that the discovered counterfactual example will be optimal, we experimentally see that incorporating our Definition 4 into the loss (Sec. 5.4.1) produces a strong resilience to additional cost (Sec. 7.3) for perturbations to the features in \mathcal{C} . Besides being effective, implementation of Definition 4 is also efficient (see B.3.2).

What our results also show is that seeking robustness with respect to features in \mathcal{K} is problematic. This is because of Proposition 1 and the fact that features in \mathcal{K} are not aligned with the direction of intervention. Thus, we proposed to control for \mathcal{K} -robustness using an approximation, i.e., the \mathcal{K} -robustness score. We found that seeking counterfactual examples that maximize the \mathcal{K} -robustness score are often but not always sufficient to obtain a good resilience to perturbations to the features in \mathcal{K} . Moreover, the \mathcal{K} -robustness score requires to sample (and evaluate with f) multiple points, which is far more expensive than computing Definition 4. Therefore, future work should consider whether a better method can be used than the \mathcal{K} -robustness score. For example, if information on f is available, that information may be used to provide guarantees on the neighborhood of \mathbf{z} (see, e.g., Theorem 2 in [40] for linear f).

The assumption that features are independent is simplistic but often made in literature, because only a small number of works assume a causal model is available (e.g., [47,48]). Under the assumption of feature independence, as done here, one models the neighborhood of a counterfactual example with a box (under L_1) or a hyper-sphere (under L_2). However, if certain features have a causal dependency on other features, this neighborhood morphs into other, possibly very complex shapes (e.g., when this dependency is not linear). Importantly, if feature i depends on j , then one cannot change j without having that i implicitly changes too. Similarly, a perturbation happening to j would implicitly alter i . As our framework currently assumes independence, it is important to study to what extent separation between \mathcal{C} and \mathcal{K} remains possible and meaningful. For many real-world problems, it is reasonable to expect that there exist groups of features that are truly independent from other groups of features. Thus, the study of robustness for \mathcal{C} and \mathcal{K} could be carried out at a higher level, i.e., of feature groups in future work.

There is a number of further aspects worth mentioning when one wishes to implement a research work like on counterfactual explanations into practice, including this work. For example, we use the L_1 -norm within Gower's distance to measure intervention cost. In fact, literature works typically choose one distance measure (e.g., ours, or Gower's with L_2 -norm instead, or other variants, see Sec. 9). Of course, a realistic implementation of intervention cost may need to be more refined, e.g., by mixing different types of norms. Similarly, one might wish to use different distributions to sample meaningful perturbations (as opposed to only uniform or only normal as done in our synthetic experiments), and different functions to define the maximal extent of perturbation, which may e.g., account for the distribution of feature values. For example, for denser areas of feature i , p_i^+ and p_i^- should be smaller than for less dense areas. Other desiderata may need to be included when seeking counterfactuals in practice (see, e.g., [49,50]), including accounting for multiple types of robustness of the same time, such as those related to uncertainties of f [51,52]

Lastly, we made subjective choices to define perturbations (\mathbf{p}) and plausibility constraints (\mathcal{P}) in the data sets. We made these choices as best as we could, based on reading the meta-information in web sources and the papers that describe the data sets. We have no doubt that domain experts would make much better choices than ours. Nevertheless, we argue that this is not an important limitation because, as long as the community agrees that our choices are reasonable, they suffice to provide a sensible test bed for benchmarking robustness. Hopefully, other researchers will find our annotations to be useful for future experiments on the robustness of counterfactual explanations. Similarly, we hope that other researchers will find CoGS to be an interesting algorithm to benchmark against.

9. Related work

A number of works in literature propose several new desiderata that are largely orthogonal to our notions of robustness but can be important to enhance the practical usability of counterfactual explanations. For example, Dandl et al. [49] consider, besides proximity of \mathbf{z} to \mathbf{x} according to different distances, whether other training points \mathbf{x}' are sufficiently close to \mathbf{z} for it to reasonably belong to the training data distribution. A similar desideratum is considered in [21] and [53]; the latter work employs neural autoencoders to that end. [54] remarks the importance of sparsity for explanations, with the concepts of *pertinent negatives* (the minimal features that should be different to (more) confidently predict the given class) and *pertinent positives* (the minimal features that help correctly identifying the class). Laugel et al. [36,50] require that \mathbf{z} can always be reached from a training point \mathbf{x}' without having to cross the decision boundary of f , for \mathbf{z} not to be the result of an artifact in the decision boundary of f . In [47] and [22], counterfactual explanations are studied through the lens of causality. For recent surveys on counterfactual explanations, the reader is referred to [55,16,56].

We now focus on works that deal with some notion of robustness and/or perturbations explicitly. Artelt et al. [57] present theoretical results on the effect of perturbations (e.g., under linear f), evaluate the effect of different type of perturbations (Gaussian, uniform, masking) with three classifiers, and find that counterfactual explanations that obey plausibility constraints are more robust than counterfactual explanations that do not. Differently from us, Artelt et al. do not consider sparsity and do not optimize for robustness. The work by Karimi et al. [48] extends [47] to consider possible uncertainties in causal modeling. In [17], it is shown that a malicious actor can, in principle, jointly optimize small perturbations and the model f such that, when applying the perturbations to points of a specific group (e.g., white males), the respective counterfactual explanations are much less costly than normal (in fact, counterfactual explanations are conceptually similar to adversarial examples, see, e.g., [58–60]). Some works consider forms of robustness of counterfactual explanations with respect to changes of f (e.g., whether \mathbf{z} is still classified as t if f' is used instead of f) [51,61] or updates to f (e.g., after data distribution shift of temporal or geospatial nature) [62,52]. In [63], robustness of counterfactual explanations is studied in the context of differentially-private support vector machines. Dominguez et al. [40] consider whether counterfactual explanations remain valid in presence of uncertainty on \mathbf{x} , and also account for causality. We also note that Dominguez et al. consider a neighborhood of uncertainty around \mathbf{x} which is akin to Definition 1; in fact, such sort of neighborhoods is common tools in post-hoc explanation methods, e.g., the Anchor explainer by [64] seeks representative points for a class by assessing that the prediction of f for the points in their neighborhood is the same. Zhang et al. [65] propose a counterfactual search method based on linear programming that works for neural networks with ReLU activations; this work can be seen through the lens of robustness in that the method produces *regions* of points that share the desired class. Finally, contemporary to our work, Fokkema et al. [26] provide important theoretical results that counterfactual explanations (and other XAI methods such as feature attribution ones) can be dramatically different when small perturbations are applied to the starting point \mathbf{x} (or, in general, point to explain).

To the best of our knowledge, there exists no other work prior to ours that attempts to exploit sparsity when assessing robustness, although sparsity is an important property for counterfactual explanations. Moreover, existing works typically consider whether robustness helps preventing counterfactual explanations from becoming invalid, while we further consider that additional intervention may be possible, and assess the associated cost.

10. Conclusion

Counterfactual explanations can help us understand how black-box AI systems reach certain decisions, as well as what intervention is possible to alter such decisions. For counterfactual explanations to be most useful in practice, we studied how they can be made *robust* to adverse perturbations that may naturally happen due to unforeseen circumstances, to ensure that the intervention they prescribe remains valid, and potential additional intervention cost that may be needed remains limited. We presented novel notions of robustness, which concern adverse perturbations to the features that a counterfactual explanation prescribes to change (\mathcal{C} -robustness) and to keep as they are (\mathcal{K} -robustness), respectively. We have annotated five existing data sets with reasonable perturbations and plausibility constraints and developed a competitive counterfactual search algorithm to search for (robust) counterfactual explanations. Our experimental results show that, most often than not, counterfactual explanations do not happen to be robust by accident. Consequently, if adverse perturbations take place, counterfactual explanations may require a much larger cost to be realized than anticipated, or even make it impossible for the user to achieve recourse. Our definitions of robustness can be incorporated in the search process, and robust counterfactual explanations can be discovered. We have shown that \mathcal{C} -robustness can be accounted for efficiently and effectively, while the same is not always true for \mathcal{K} -robustness. This aspect should be taken into account when choosing what counterfactual explanation is best for the user. Overall, robust counterfactual explanations are resilient against invalidation and require much smaller additional intervention to contrast perturbations.

Declaration of competing interest

The authors declare that they have no known competing financial interests or personal relationships that could have appeared to influence the work reported in this paper.

Table A.1

Hyper-parameter settings considered for tuning random forest.

Name	Options
No. trees	{50, 500}
Min. samples split	{2, 8}
Max. features	$\{\sqrt{d}, d\}$

Table A.2

Hyper-parameter settings considered for tuning the neural network.

Name	Options
Learning rate	{0.0001, 0.01}
Max. iterations	{200, 1000}
Solver	{Adam, SGD}

Table A.3Test accuracy of hyper-parameter-tuned random forests acting as black-box models f for the considered data sets across five-fold cross-validation.

Fold	Cre	Inc	Hou	Pro	Rec
0	0.71	0.86	0.93	0.79	0.80
1	0.78	0.82	0.90	0.77	0.82
2	0.78	0.79	0.91	0.78	0.78
3	0.74	0.82	0.91	0.82	0.77
4	0.76	0.83	0.97	0.78	0.80
Avg.	0.76	0.83	0.93	0.79	0.80

Table A.4Test accuracy of hyper-parameter-tuned neural networks acting as black-box models f for the considered data sets across five-fold cross-validation.

Fold	Cre	Inc	Hou	Pro	Rec
0	0.74	0.83	0.94	0.62	0.78
1	0.78	0.82	0.93	0.70	0.79
2	0.73	0.80	0.91	0.69	0.75
3	0.78	0.82	0.91	0.77	0.78
4	0.74	0.82	0.96	0.72	0.79
Avg.	0.75	0.82	0.93	0.70	0.78

Data availability

The data is available at the github repository linked in the abstract.

Acknowledgements

We thank dr. Stef C. Maree for insightful early discussions. This work made use of the Dutch national e-infrastructure with the support of the SURF Cooperative using grant no. EINF-2512. Funding: This publication is part of the project Robust Counterfactual Explanations (with project number EINF-2512) of the research program Computing Time on National Computer Facilities which is (partly) financed by the Dutch Research Council (NWO).

Appendix A. Hyper-parameter optimization of random forest and neural network

To obtain a black-box model f for a given cross-validation fold, we train a random forest model or a neural network (a multi layer perceptron for classification) optimized with grid-search hyper-parameter tuning (with five-fold cross-validation on the training set). The hyper-parameter settings we considered are listed in Tables A.1 and A.2, all other being Scikit-learn's default (v. 1.0.1). For random forest, we one-hot encode categorical features when training and querying the random forest model (see the code `robust_cfe/blackbox_with_preproc.py`). For the neural network, we additionally scale numerical features to have mean of zero and standard deviation of one.

The performance of tuned random forest on all folds is shown in Table A.3, the respective one for the neural network is shown in Table A.4.

Table B.1

Mean \pm standard deviation across five cross-validation folds of the frequency with which CoGS and the two variants of DiCE succeed in finding a counterfactual example under plausibility constraints.

	Alg.	Cre	Inc	Hou	Pro	Rec
$f = \text{r.f.}$	CoGS	1.00	1.00	1.00	1.00	1.00
	DiCE-a	1.00	1.00	1.00	1.00	0.99 ± 0.06
	DiCE-b	1.00	1.00	1.00	0.20 ± 4.00	1.00 ± 0.05
$f = \text{n.n.}$	CoGS	1.00	1.00	1.00	1.00	1.00 ± 0.04
	DiCE-a	1.00	1.00 ± 0.04	1.00	1.00	1.00
	DiCE-b	1.00	1.00	1.00	1.00	0.80 ± 4.00

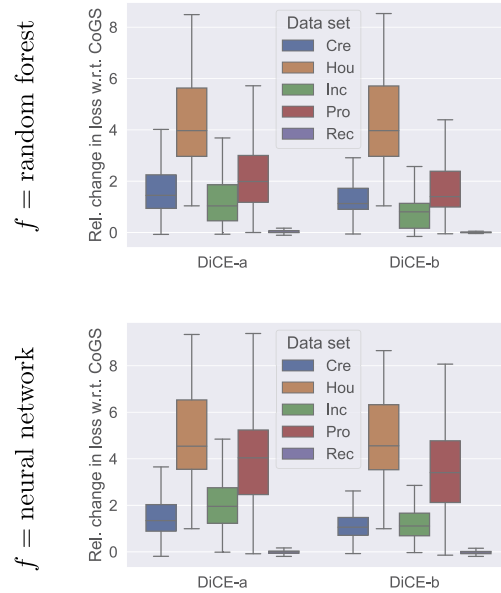


Fig. B.1. Boxplots of relative change in loss with respect to CoGS for the two variants of DiCE when using plausibility constraints, on the different data sets and black-boxes, for success cases.

Appendix B. Additional results

We provide additional results. These are (i) a further comparison between DiCE and CoGS when plausibility constraints are enforced, (ii) the (possibly non-permanent) invalidity caused by perturbations, as typically done in the literature of robustness, (iii) and effect of increasing m for the computation of the \mathcal{K} -robustness score.

B.1. DiCE vs. CoGS with plausibility constraints

Table B.1 shows the average and the standard deviation of the success rate (how many times a counterfactual of the desired class is found) for the two variants of DiCE and of CoGS when plausibility constraints are active. The algorithms are comparable in that they succeed in most cases. However, DiCE-b can perform substantially worse in two cases, i.e., data set Pro when using the random forest, and data set Rec when using the neural network.

Lastly, Fig. B.1 shows the relative change in loss obtained by the algorithms. As it can be seen, DiCE comes close to the performance of CoGS only on Rec. Thus, overall, CoGS remains superior to DiCE also when plausibility constraints are enforced.

We attribute this to the fact that, differently from CoGS, DiCE is inherently designed to discover a diverse set of counterfactuals instead of a single and closest-possible counterfactual.

B.2. Invalidity of counterfactual explanations

We now show whether the fact that best-found counterfactual explanations are typically not robust is associated with a greater chance that perturbations can make them invalid, i.e., such that $f(\mathbf{z}') \neq t$ where \mathbf{z}' is the point to which \mathbf{z}^* is shifted by the perturbation. Here, we do not consider whether additional intervention may or may not be possible. Fig. B.2 shows the average frequency with which perturbations cause invalidity. The frequencies are computed by applying, to each

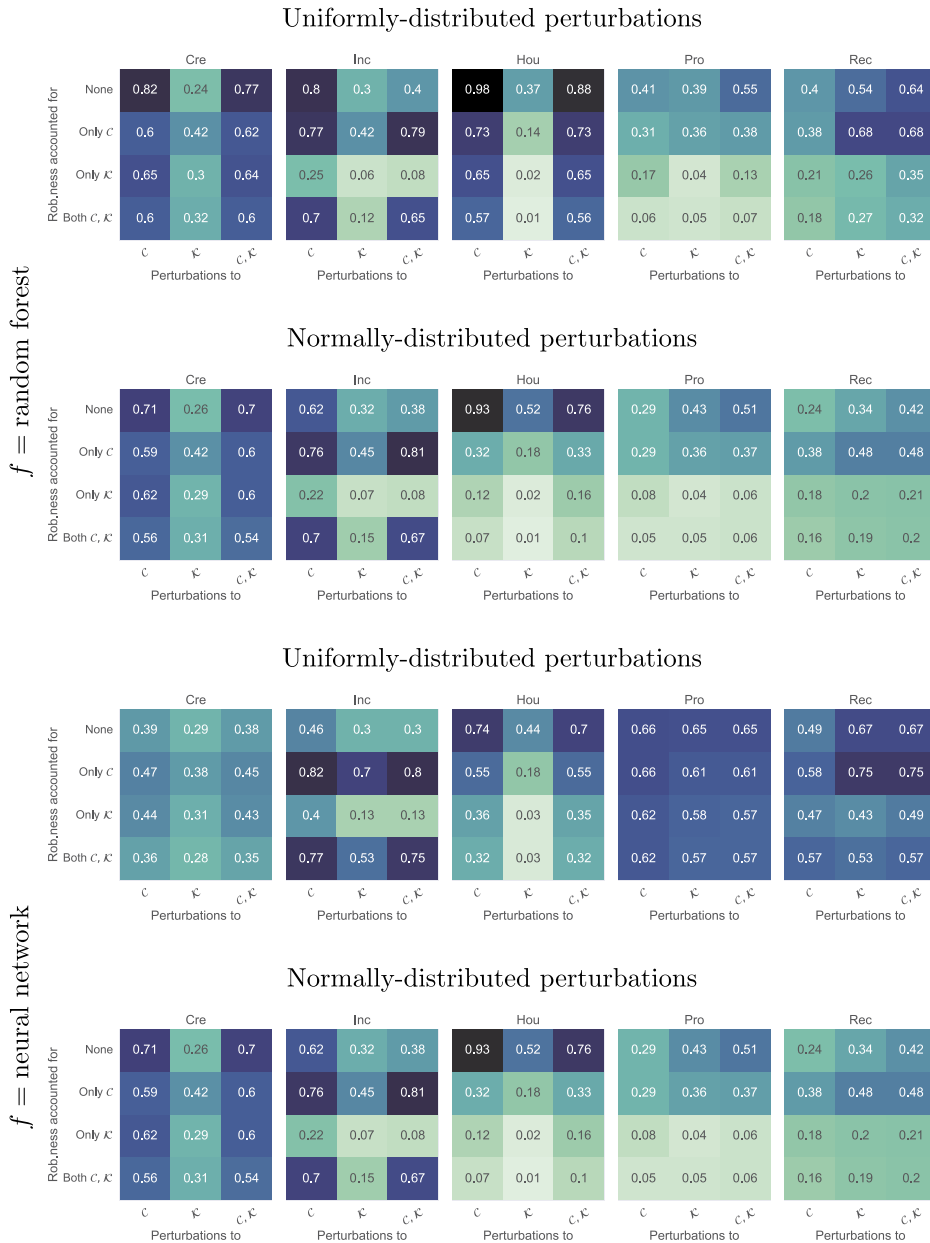


Fig. B.2. Mean frequency of invalidity of counterfactual explanations under different types of perturbations and when accounting for different types of robustness. Darker colors represent worse scenarios, i.e., larger average invalidity.

discovered counterfactual example, 100 perturbations that are sampled uniformly at random for categorical features (from the categorical possibilities) and uniformly or normally (with st.dev. of 0.1) for numerical features (within the numerical intervals). The figure shows that when no notion of robustness is accounted for, perturbations generally have a larger chance of causing invalidity of the counterfactual explanation.

Regarding perturbations to (features in) \mathcal{C} (i.e., \mathcal{C} -setbacks), recall that accounting for the respective notion of robustness is intended to provide counterfactual explanations with minimal additional intervention cost, the maximal \mathcal{C} -setback were to happen. Ideally, the returned counterfactual example should still be optimal, i.e., as near to \mathbf{x} as possible, which means that the example is on the border of the decision boundary of f . Thus, under optimality guarantees, $f(\mathbf{z}^* + \mathbf{w}^{\mathcal{C},s}) \neq t$ (Proposition 2); This means that any \mathcal{C} -setback should result in invalidity (i.e., all entries for perturbations to \mathcal{C} should report 1). This does not always happen in Fig. B.2 because CoGS does not guarantee to discover optimal counterfactual examples and, thus, in many cases the returned example is not on the boundary, and the \mathcal{C} -setback is too small to cross the boundary. The frequency of this phenomenon depends on the data set. Also, while accounting for robustness w.r.t. \mathcal{C} should not, in theory, decrease invalidity rate but only make additional intervention less costly, as confirmed in Sec. 7.3),

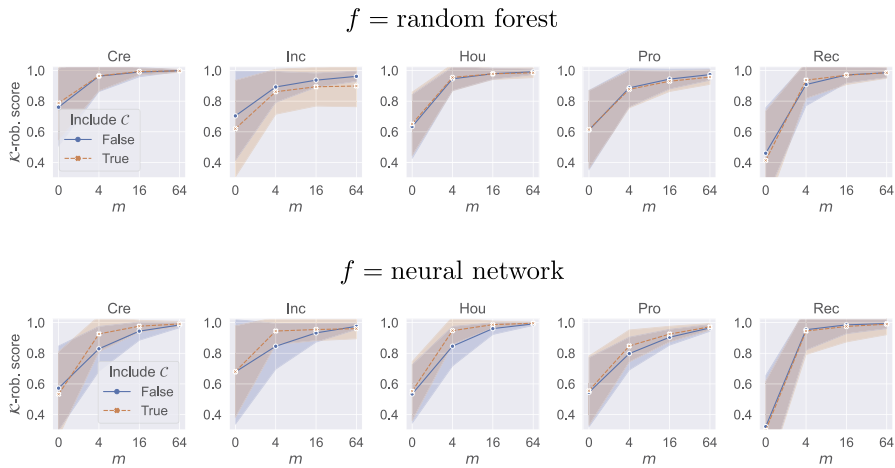


Fig. B.3. Approximated ground-truth \mathcal{K} -robustness scores (using 1000 samples) for increasing m , to determine what value of m is needed for good robustness to perturbations to \mathcal{K} . Shaded areas represent standard deviations.

we find that accounting for robustness w.r.t. \mathcal{C} lowers invalidity rate on Hou (e.g., most evident for both types of f with normally-distributed perturbations).

When \mathcal{K} -robustness is accounted for, the best-found counterfactual explanation is supposed to be in a region such that the decision boundary is relatively loose with respect to the features in \mathcal{K} . Consequently, accounting for \mathcal{K} -robustness *should*, in fact, counter invalidity, as we do not wish risking that it becomes impossible to carry out additional intervention due to the plausibility constraints. The figure shows that, in general, there can be a substantial gain in lowering invalidity by accounting for \mathcal{K} -robustness. At times, accounting for \mathcal{K} -robustness allows to reach almost zero invalidity, see the cell that corresponds to robustness for \mathcal{K} and perturbations to \mathcal{K} , on Inc, Hou, and Pro, for both types of f and sampling distributions. However, it is not always the case that \mathcal{K} -robustness helps, due to the heuristic nature of the \mathcal{K} -robustness score: see, e.g., Cre.

Lastly, we observe that the frequency of invalidity can raise when both notions of robustness are accounted for at the same time (e.g., on Inc for uniformly-distributed perturbations when using the neural network). Note that this is not necessarily a problem because invalidity from perturbations to \mathcal{C} is expected to be high, as the goal of robustness w.r.t. \mathcal{C} is to be able to minimize additional intervention cost.

B.3. Setting m for \mathcal{K} -robustness

We report results on setting the hyper-parameter m for computing \mathcal{K} -robustness scores (see Eq. (8)). In particular, we run CoGS accounting for \mathcal{K} -robustness in the loss function, for $m \in \{0, 4, 16, 64\}$. Note that using $m = 0$ corresponds to *not* accounting for \mathcal{K} -robustness.

B.3.1. Achieved \mathcal{K} -robustness

We consider how increasing m improves \mathcal{K} -robustness, using an approximated *ground-truth*. We approximate the ground-truth of the true \mathcal{K} -robustness by calculating the \mathcal{K} -robustness score over 1000 samples over the counterfactual example discovered using a specific m .

Fig. B.3 shows the results obtained for this experiment. We also consider the case in which \mathcal{C} -robustness is accounted for. If \mathcal{K} -robustness is not accounted for ($m = 0$), then the (approximated ground-truth) \mathcal{K} -robustness of the discovered counterfactual examples can be quite low, see, e.g., Rec for random forest (score approximately of 0.4) and neural network (score below 0.4). As soon as a few samples are considered ($m = 4$), the \mathcal{K} -robustness increases substantially (see, e.g., Cre). Further increasing m has diminishing returns (note that m is increased exponentially). Accounting for \mathcal{C} -robustness is largely orthogonal, meaning, it has no effect in terms of \mathcal{K} -robustness.

B.3.2. Additional required runtime

Fig. B.4 shows the additional runtime incurred between runs of CoGS that account for some notion of robustness and runs that do not account for it, in particular for increasing m in the calculation of the \mathcal{K} -robustness score. The figure shows that accounting for \mathcal{C} -robustness comes at no significant extra cost in runtime. This follows from the fact that we can use Definition 4 and thus only need to compute the maximal \mathcal{C} -setback. Conversely, accounting for \mathcal{K} -robustness can come at a relatively large additional cost in runtime, which appears to be linear in m (note that m grows exponentially in the plots). Fortunately, the experimental results of B.3 suggest that small values of m are often sufficient to obtain good \mathcal{K} -robustness scores.

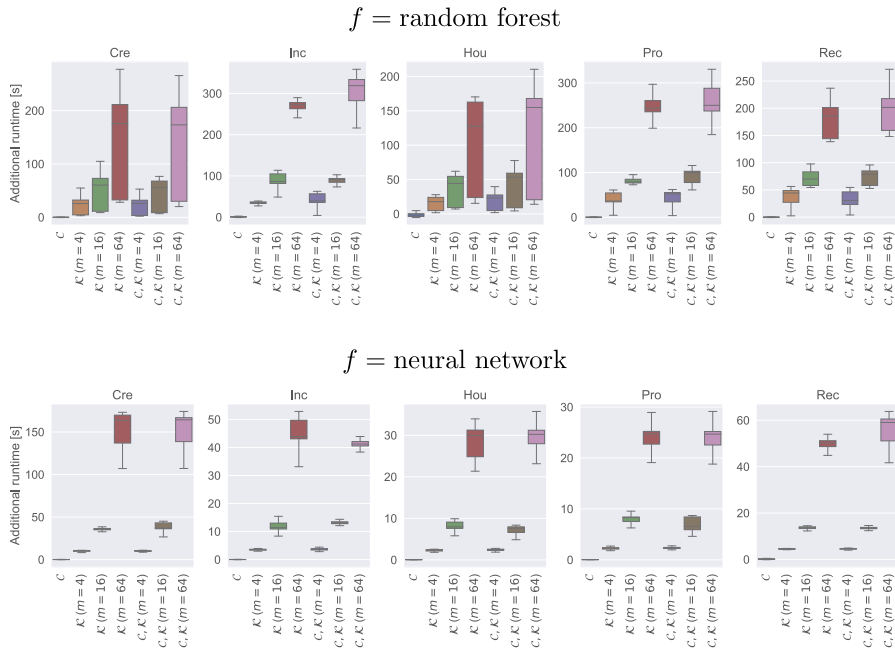


Fig. B.4. Additional runtime of CoGS for different configurations of accounting for robustness with respect to the runtime when not accounting for robustness.

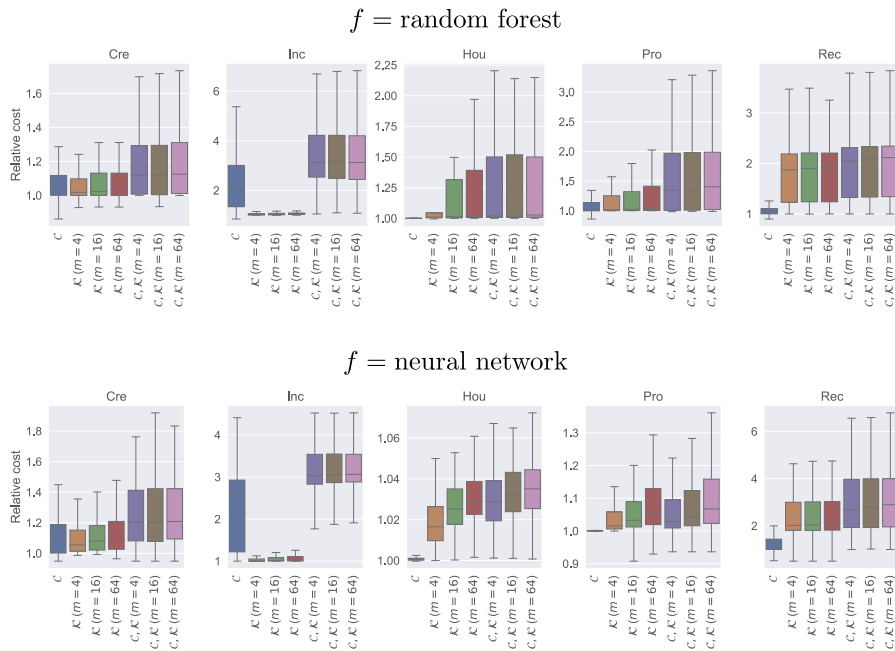


Fig. B.5. Cost of accounting for robustness relative to not accounting for robustness (i.e., ideal cost) when no perturbations take place for different values of m . Note that the (rare) relative costs smaller than 1 are due to a lack of optimality of the search algorithm.

B.3.3. Additional cost from accounting for robustness

Fig. B.5 expands on the results reported in Fig. 11 by including different values of m . We do not find major differences based on the setting of m for computing the \mathcal{K} -robustness score, except for the tails of the respective distributions on Hou, and slightly less so on Pro (for both types of f). Accounting for C - and \mathcal{K} -robustness at the same time leads to larger costs than accounting for only one of the two, as it is reasonable to expect. On average, the cost that comes from accounting for robustness alone is limited (up to $6.5\times$ the ideal cost, see Inc), especially in light of the results found for

Table C.1

Result of pairwise comparison on the effect of accounting for different types of robustness for data set Cre under different perturbations (both random forest and neural network, both uniform and normal sampling distributions). The displayed p -values are obtained with the Mann-Whitney U test under Holm-Bonferroni correction and post Kruskal-Wallis test rejecting the null hypothesis with p -value $\ll 0.01$.

Cre, perturbations to \mathcal{C}				
Robustness	None	Only \mathcal{C}	Only \mathcal{K}	Both \mathcal{C}, \mathcal{K}
None	1.000	0.000	0.000	0.000
Only \mathcal{C}	0.000	1.000	0.000	0.125
Only \mathcal{K}	0.000	0.000	1.000	0.000
Both \mathcal{C}, \mathcal{K}	0.000	0.125	0.000	1.000
Cre, perturbations to \mathcal{K}				
Robustness	None	Only \mathcal{C}	Only \mathcal{K}	Both \mathcal{C}, \mathcal{K}
None	1.000	0.520	0.000	0.000
Only \mathcal{C}	0.520	1.000	0.000	0.000
Only \mathcal{K}	0.000	0.000	1.000	0.912
Both \mathcal{C}, \mathcal{K}	0.000	0.000	0.912	1.000
Cre, perturbations to \mathcal{C} and \mathcal{K}				
Robustness	None	Only \mathcal{C}	Only \mathcal{K}	Both \mathcal{C}, \mathcal{K}
None	1.000	0.000	0.000	0.000
Only \mathcal{C}	0.000	1.000	0.000	0.000
Only \mathcal{K}	0.000	0.000	1.000	0.003
Both \mathcal{C}, \mathcal{K}	0.000	0.000	0.003	1.000

Table C.2

Result of pairwise comparison on the effect of accounting for different types of robustness for data set Inc under different perturbations (both random forest and neural network, both uniform and normal sampling distributions). The displayed p -values are obtained with the Mann-Whitney U test under Holm-Bonferroni correction and post Kruskal-Wallis test rejecting the null hypothesis with p -value $\ll 0.01$.

Inc, perturbations to \mathcal{C}				
Robustness	None	Only \mathcal{C}	Only \mathcal{K}	Both \mathcal{C}, \mathcal{K}
None	1.000	0.000	0.000	0.000
Only \mathcal{C}	0.000	1.000	0.000	0.000
Only \mathcal{K}	0.000	0.000	1.000	0.000
Both \mathcal{C}, \mathcal{K}	0.000	0.000	0.000	1.000
Inc, perturbations to \mathcal{K}				
Robustness	None	Only \mathcal{C}	Only \mathcal{K}	Both \mathcal{C}, \mathcal{K}
None	1.000	0.000	0.000	0.000
Only \mathcal{C}	0.000	1.000	0.000	0.000
Only \mathcal{K}	0.000	0.000	1.000	0.000
Both \mathcal{C}, \mathcal{K}	0.000	0.000	0.000	1.000
Inc, perturbations to \mathcal{C} and \mathcal{K}				
Robustness	None	Only \mathcal{C}	Only \mathcal{K}	Both \mathcal{C}, \mathcal{K}
None	1.000	0.000	0.000	0.000
Only \mathcal{C}	0.000	1.000	0.000	0.000
Only \mathcal{K}	0.000	0.000	1.000	0.000
Both \mathcal{C}, \mathcal{K}	0.000	0.000	0.000	1.000

when perturbations take place, described in Sec. 7.3 (additional intervention due to perturbations can lead to $100\times$ times larger costs for non-robust counterfactual explanations, see Inc on Fig. 9).

Appendix C. Statistical significance

We report the statistical significance for the results displayed in Sec. 7.3. For each data set and type of perturbation, we perform the Kruskal-Wallis tests (since we cannot assume normality) to determine whether significant differences are present between the relative cost induced by applying the different notion of robustness. In all cases, the outcome of the test is that significant differences are present (p -value $\ll 0.01$). Next, we perform post-hoc pairwise comparisons with the Mann-Whitney-U test to assess whether one notion of robustness protects from the considered perturbation significantly differently than another. The result of the pairwise comparison analysis is shown in Tables C.1 to C.5.

Table C.3

Result of pairwise comparison on the effect of accounting for different types of robustness for data set Hou under different perturbations (both random forest and neural network, both uniform and normal sampling distributions). The displayed p -values are obtained with the Mann-Whitney U test under Holm-Bonferroni correction and post Kruskal-Wallis test rejecting the null hypothesis with p -value $\ll 0.01$.

Hou, perturbations to \mathcal{C}				
Robustness	None	Only \mathcal{C}	Only \mathcal{K}	Both \mathcal{C}, \mathcal{K}
None	1.000	0.000	0.000	0.000
Only \mathcal{C}	0.000	1.000	0.261	0.006
Only \mathcal{K}	0.000	0.261	1.000	0.083
Both \mathcal{C}, \mathcal{K}	0.000	0.006	0.083	1.000
Hou, perturbations to \mathcal{K}				
Robustness	None	Only \mathcal{C}	Only \mathcal{K}	Both \mathcal{C}, \mathcal{K}
None	1.000	0.000	0.000	0.000
Only \mathcal{C}	0.000	1.000	0.000	0.000
Only \mathcal{K}	0.000	0.000	1.000	0.070
Both \mathcal{C}, \mathcal{K}	0.000	0.000	0.070	1.000
Hou, perturbations to \mathcal{C} and \mathcal{K}				
Robustness	None	Only \mathcal{C}	Only \mathcal{K}	Both \mathcal{C}, \mathcal{K}
None	1.000	0.000	0.000	0.000
Only \mathcal{C}	0.000	1.000	0.000	0.000
Only \mathcal{K}	0.000	0.000	1.000	0.008
Both \mathcal{C}, \mathcal{K}	0.000	0.000	0.008	1.000

Table C.4

Result of pairwise comparison on the effect of accounting for different types of robustness for data set Pro under different perturbations (both random forest and neural network, both uniform and normal sampling distributions). The displayed p -values are obtained with the Mann-Whitney U test under Holm-Bonferroni correction and post Kruskal-Wallis test rejecting the null hypothesis with p -value $\ll 0.01$.

Pro, perturbations to \mathcal{C}				
Robustness	None	Only \mathcal{C}	Only \mathcal{K}	Both \mathcal{C}, \mathcal{K}
None	1.000	0.000	0.000	0.000
Only \mathcal{C}	0.000	1.000	0.000	0.008
Only \mathcal{K}	0.000	0.000	1.000	0.000
Both \mathcal{C}, \mathcal{K}	0.000	0.008	0.000	1.000
Pro, perturbations to \mathcal{K}				
Robustness	None	Only \mathcal{C}	Only \mathcal{K}	Both \mathcal{C}, \mathcal{K}
None	1.000	0.000	0.000	0.000
Only \mathcal{C}	0.000	1.000	0.000	0.000
Only \mathcal{K}	0.000	0.000	1.000	0.760
Both \mathcal{C}, \mathcal{K}	0.000	0.000	0.760	1.000
Pro, perturbations to \mathcal{C} and \mathcal{K}				
Robustness	None	Only \mathcal{C}	Only \mathcal{K}	Both \mathcal{C}, \mathcal{K}
None	1.000	0.000	0.000	0.000
Only \mathcal{C}	0.000	1.000	0.000	0.000
Only \mathcal{K}	0.000	0.000	1.000	0.014
Both \mathcal{C}, \mathcal{K}	0.000	0.000	0.014	1.000

On Cre under \mathcal{K} -perturbations (middle part of Table C.1), accounting for robustness w.r.t. \mathcal{C} is not significantly different than not accounting for any notion of robustness (p -value = 0.52 > 0.01); similarly, accounting for robustness w.r.t. \mathcal{K} induces the same relative cost as accounting for robustness w.r.t. both \mathcal{C} and \mathcal{K} . On Hou under \mathcal{C} -perturbations (top part of Table C.3), accounting for \mathcal{C} is not significantly different than accounting for \mathcal{K} (p -value = 0.52 > 0.01), while accounting for \mathcal{K} is not significantly different than accounting for both \mathcal{C} and \mathcal{K} (p -value = 0.083 > 0.01). When perturbations happen to both \mathcal{C} and \mathcal{K} on Pro and Rec (bottom part of respective tables), accounting for \mathcal{K} is not significantly different than accounting for both \mathcal{C} and \mathcal{K} (p -value = 0.014 > 0.01 and p -value = 0.271 > 0.01, respectively). In general, the results match what can be seen in Figs. 9 and 10. Also, we note that in the majority of the cases, accounting for one notion of robustness is significantly different than accounting for another (or for none).

Table C.5

Result of pairwise comparison on the effect of accounting for different types of robustness for data set Rec under different perturbations (both random forest and neural network, both uniform and normal sampling distributions). The displayed p -values are obtained with the Mann-Whitney U test under Holm-Bonferroni correction and post Kruskal-Wallis test rejecting the null hypothesis with p -value $\ll 0.01$.

Rec, perturbations to \mathcal{C}				
Robustness	None	Only \mathcal{C}	Only \mathcal{K}	Both \mathcal{C}, \mathcal{K}
None	1.000	0.000	0.000	0.000
Only \mathcal{C}	0.000	1.000	0.000	0.000
Only \mathcal{K}	0.000	0.000	1.000	0.115
Both \mathcal{C}, \mathcal{K}	0.000	0.000	0.115	1.000
Rec, perturbations to \mathcal{K}				
Robustness	None	Only \mathcal{C}	Only \mathcal{K}	Both \mathcal{C}, \mathcal{K}
None	1.000	0.000	0.000	0.000
Only \mathcal{C}	0.000	1.000	0.000	0.000
Only \mathcal{K}	0.000	0.000	1.000	0.651
Both \mathcal{C}, \mathcal{K}	0.000	0.000	0.651	1.000
Rec, perturbations to \mathcal{C} and \mathcal{K}				
Robustness	None	Only \mathcal{C}	Only \mathcal{K}	Both \mathcal{C}, \mathcal{K}
None	1.000	0.000	0.000	0.000
Only \mathcal{C}	0.000	1.000	0.000	0.000
Only \mathcal{K}	0.000	0.000	1.000	0.271
Both \mathcal{C}, \mathcal{K}	0.000	0.000	0.271	1.000

References

- [1] J.H. Friedman, Greedy function approximation: a gradient boosting machine, *Ann. Stat.* 29 (2001) 1189–1232.
- [2] G. Ke, Q. Meng, T. Finley, T. Wang, W. Chen, W. Ma, Q. Ye, T.-Y. Liu, LightGBM: a highly efficient gradient boosting decision tree, *Adv. Neural Inf. Process. Syst.* 30 (2017) 3146–3154.
- [3] Y. LeCun, Y. Bengio, G. Hinton, Deep learning, *Nature* 521 (7553) (2015) 436–444.
- [4] M. Belkin, D. Hsu, S. Ma, S. Mandal, Reconciling modern machine-learning practice and the classical bias–variance trade-off, *Proc. Natl. Acad. Sci.* 116 (32) (2019) 15849–15854.
- [5] P. Nakkiran, G. Kaplun, Y. Bansal, T. Yang, B. Barak, I. Sutskever, Deep double descent: where bigger models and more data hurt, *J. Stat. Mech. Theory Exp.* 2021 (12) (2021) 124003.
- [6] B. Goodman, S. Flaxman, European Union regulations on algorithmic decision-making and a “right to explanation”, *AI Mag.* 38 (3) (2017) 50–57.
- [7] A. Jobin, M. Ienca, E. Vayena, The global landscape of AI ethics guidelines, *Nat. Mach. Intell.* 1 (9) (2019) 389–399.
- [8] A. Adadi, M. Berrada, Peeking inside the black-box: a survey on eXplainable Artificial Intelligence (XAI), *IEEE Access* 6 (2018) 52138–52160.
- [9] R. Guidotti, A. Monreale, S. Ruggieri, F. Turini, F. Giannotti, D. Pedreschi, A survey of methods for explaining black box models, *ACM Comput. Surv.* 51 (5) (2018) 1–42.
- [10] C. Rudin, Stop explaining black box machine learning models for high stakes decisions and use interpretable models instead, *Nat. Mach. Intell.* 1 (5) (2019) 206–215.
- [11] M.T. Ribeiro, S. Singh, C. Guestrin, “Why should I trust you?” explaining the predictions of any classifier, in: *Proceedings of the 22nd ACM SIGKDD International Conference on Knowledge Discovery and Data Mining*, 2016, pp. 1135–1144.
- [12] S.M. Lundberg, S.-I. Lee, A unified approach to interpreting model predictions, in: *Advances in Neural Information Processing Systems*, 2017, pp. 4768–4777.
- [13] B. Kim, R. Khanna, O.O. Koyejo, Examples are not enough, learn to criticize! Criticism for interpretability, in: *Advances in Neural Information Processing Systems*, vol. 29.
- [14] C. Chen, O. Li, D. Tao, A. Barnett, C. Rudin, J.K. Su, This looks like that: deep learning for interpretable image recognition, in: H. Wallach, H. Larochelle, A. Beygelzimer, F. d’Alché-Buc, E. Fox, R. Garnett (Eds.), *Advances in Neural Information Processing Systems*, vol. 32, 2019.
- [15] S. Wachter, B. Mittelstadt, C. Russell, Counterfactual explanations without opening the black box: automated decisions and the GDPR, *Harv. J. Law Technol.* 31 (2017) 841.
- [16] I. Stepin, J.M. Alonso, A. Catala, M. Pereira-Fariña, A survey of contrastive and counterfactual explanation generation methods for explainable artificial intelligence, *IEEE Access* 9 (2021) 11974–12001.
- [17] D. Slack, S. Hilgard, H. Lakkaraju, S. Singh, Counterfactual explanations can be manipulated, *arXiv preprint*, arXiv:2106.02666.
- [18] S. Barocas, A.D. Selbst, M. Raghavan, The hidden assumptions behind counterfactual explanations and principal reasons, in: *Proceedings of the 2020 Conference on Fairness, Accountability, and Transparency*, 2020, pp. 80–89.
- [19] J.C. Gower, A general coefficient of similarity and some of its properties, *Biometrics* (1971) 857–871.
- [20] R. Guidotti, A. Monreale, S. Ruggieri, D. Pedreschi, F. Turini, F. Giannotti, Local rule-based explanations of black box decision systems, *arXiv preprint*, arXiv:1805.10820.
- [21] S. Sharma, J. Henderson, J. Ghosh, CERTIFAI: a common framework to provide explanations and analyse the fairness and robustness of black-box models, in: *Proceedings of the AAAI/ACM Conference on AI, Ethics, and Society*, 2020, pp. 166–172.
- [22] R.K. Mothilal, A. Sharma, C. Tan, Explaining machine learning classifiers through diverse counterfactual explanations, in: *Proceedings of the 2020 Conference on Fairness, Accountability, and Transparency*, 2020, pp. 607–617.

- [23] T. Laugel, M.-J. Lesot, C. Marsala, X. Renard, M. Detyniecki, Comparison-based inverse classification for interpretability in machine learning, in: *International Conference on Information Processing and Management of Uncertainty in Knowledge-Based Systems*, Springer, 2018, pp. 100–111.
- [24] M.T. Keane, B. Smyth, Good counterfactuals and where to find them: a case-based technique for generating counterfactuals for explainable AI (XAI), in: *International Conference on Case-Based Reasoning*, Springer, 2020, pp. 163–178.
- [25] K. Hornik, M. Stinchcombe, H. White, Multilayer feedforward networks are universal approximators, *Neural Netw.* 2 (5) (1989) 359–366.
- [26] H. Fokkema, R. de Heide, T. van Erven, Attribution-based explanations that provide recourse cannot be robust, arXiv preprint, arXiv:2205.15834.
- [27] U. Grömping, South German credit data: correcting a widely used data set, report 4/2019, Reports in Mathematics, Physics and Chemistry, Department II, Beuth University of Applied Sciences Berlin, 2019, <https://archive.ics.uci.edu/ml/datasets/South+German+Credit+%28UPDATE%29>.
- [28] H. Hofmann, Statlog German credit data, [https://archive.ics.uci.edu/ml/datasets/Statlog+\(German+Credit+Data\)](https://archive.ics.uci.edu/ml/datasets/Statlog+(German+Credit+Data)), 1994.
- [29] R. Kohavi, B. Becker, Census income, <https://archive.ics.uci.edu/ml/datasets/adult>, 1996.
- [30] R. Kohavi, Scaling up the accuracy of naive-Bayes classifiers: a decision-tree hybrid, in: *Proceedings of the Second International Conference on Knowledge Discovery and Data Mining*, vol. 96, 1996, pp. 202–207.
- [31] D. Harrison Jr., D.L. Rubinfeld, Hedonic housing prices and the demand for clean air, *J. Environ. Econ. Manag.* 5 (1) (1978) 81–102.
- [32] M. Carlisle, Racist data destruction?, <https://medium.com/@docintangible/racist-data-destruction-113e3eff54a8>, 2019.
- [33] A.A. Imran, M.S. Rahim, T. Ahmed, Mining the productivity data of the garment industry, *Int. J. Bus. Intell. Data Min.* 19 (3) (2021) 319–342.
- [34] J. Larson, S. Mattu, L. Kirchner, J. Angwin, How we analyzed the COMPAS recidivism algorithm, <https://www.propublica.org/article/how-we-analyzed-the-compas-recidivism-algorithm>, 2016.
- [35] M. Kearns, S. Neel, A. Roth, Z.S. Wu, Preventing fairness gerrymandering: auditing and learning for subgroup fairness, in: *International Conference on Machine Learning*, PMLR, 2018, pp. 2564–2572.
- [36] T. Laugel, M.-J. Lesot, C. Marsala, X. Renard, M. Detyniecki, The dangers of post-hoc interpretability: unjustified counterfactual explanations, arXiv preprint, arXiv:1907.09294.
- [37] F. Ding, M. Hardt, J. Miller, L. Schmidt, Retiring adult: new datasets for fair machine learning, in: *Thirty-Fifth Conference on Neural Information Processing Systems*, 2021.
- [38] W. La Cava, J.H. Moore, Genetic programming approaches to learning fair classifiers, in: *Proceedings of the 2020 Genetic and Evolutionary Computation Conference, GECCO '20*, Association for Computing Machinery, New York, NY, USA, 2020, pp. 967–975.
- [39] M. Virgolin, A. De Lorenzo, F. Randone, E. Medvet, M. Wahde, Model learning with personalized interpretability estimation (ml-pie), in: *Proceedings of the Genetic and Evolutionary Computation Conference Companion, GECCO '21*, Association for Computing Machinery, New York, NY, USA, 2021, pp. 1355–1364.
- [40] R. Dominguez-Olmedo, A.H. Karimi, B. Schölkopf, On the adversarial robustness of causal algorithmic recourse, in: *Proceedings of the 39th International Conference on Machine Learning*, vol. 162, PMLR, 2022, pp. 5324–5342.
- [41] F. Pedregosa, G. Varoquaux, A. Gramfort, V. Michel, B. Thirion, O. Grisel, M. Blondel, P. Prettenhofer, R. Weiss, V. Dubourg, J. Vanderplas, A. Passos, D. Cournapeau, M. Brucher, M. Perrot, E. Duchesnay, Scikit-learn: machine learning in Python, *J. Mach. Learn. Res.* 12 (2011) 2825–2830.
- [42] R. Guidotti, A. Monreale, F. Giannotti, D. Pedreschi, S. Ruggieri, F. Turini, Factual and counterfactual explanations for black box decision making, *IEEE Intell. Syst.* 34 (6) (2019) 14–23.
- [43] J.A. Nelder, R. Mead, A simplex method for function minimization, *Comput. J.* 7 (4) (1965) 308–313.
- [44] F. Gao, L. Han, Implementing the Nelder-Mead simplex algorithm with adaptive parameters, *Comput. Optim. Appl.* 51 (1) (2012) 259–277.
- [45] P. Virtanen, R. Gommers, T.E. Oliphant, M. Haberland, T. Reddy, D. Cournapeau, E. Burovski, P. Peterson, W. Weckesser, J. Bright, S.J. van der Walt, M. Brett, J. Wilson, K.J. Millman, N. Mayorov, A.R.J. Nelson, E. Jones, R. Kern, E. Larson, C.J. Carey, Í. Polat, Y. Feng, E.W. Moore, J. VanderPlas, D. Laxalde, J. Perktold, R. Cimrman, I. Henriksen, E.A. Quintero, C.R. Harris, A.M. Archibald, A.H. Ribeiro, F. Pedregosa, P. van Mulbregt, SciPy 1.0 Contributors, SciPy 1.0: fundamental algorithms for scientific computing in Python, *Nat. Methods* 17 (2020) 261–272.
- [46] M. D’Orazio, Distances with mixed type variables some modified Gower’s coefficients, arXiv preprint, arXiv:2101.02481.
- [47] A.-H. Karimi, J. Von Kügelgen, B. Schölkopf, I. Valera, Algorithmic recourse under imperfect causal knowledge: a probabilistic approach, arXiv preprint, arXiv:2006.06831.
- [48] A.-H. Karimi, B. Schölkopf, I. Valera, Algorithmic recourse: from counterfactual explanations to interventions, in: *Proceedings of the 2021 ACM Conference on Fairness, Accountability, and Transparency, FAccT '21*, Association for Computing Machinery, New York, NY, USA, 2021, pp. 353–362.
- [49] S. Dandl, C. Molnar, M. Binder, B. Bischl, Multi-objective counterfactual explanations, in: *International Conference on Parallel Problem Solving from Nature*, Springer, 2020, pp. 448–469.
- [50] T. Laugel, M.-J. Lesot, C. Marsala, X. Renard, M. Detyniecki, Unjustified classification regions and counterfactual explanations in machine learning, in: *Joint European Conference on Machine Learning and Knowledge Discovery in Databases*, Springer, 2019, pp. 37–54.
- [51] M. Pawelczyk, K. Broelemann, G. Kasneci, On counterfactual explanations under predictive multiplicity, in: *Conference on Uncertainty in Artificial Intelligence*, PMLR, 2020, pp. 809–818.
- [52] K. Rawal, E. Kamar, H. Lakkaraju, Algorithmic recourse in the wild: understanding the impact of data and model shifts, arXiv preprint, arXiv:2012.11788.
- [53] A. Van Looveren, J. Klaise, Interpretable counterfactual explanations guided by prototypes, arXiv preprint, arXiv:1907.02584.
- [54] A. Dhurandhar, P.-Y. Chen, R. Luss, C.-C. Tu, P. Ting, K. Shanmugam, P. Das, Explanations based on the missing: towards contrastive explanations with pertinent negatives, in: *Advances in Neural Information Processing Systems*, vol. 31.
- [55] S. Verma, J. Dickerson, K. Hines, Counterfactual explanations for machine learning: a review, arXiv preprint, arXiv:2010.10596.
- [56] A.-H. Karimi, G. Barthe, B. Schölkopf, I. Valera, A survey of algorithmic recourse: contrastive explanations and consequential recommendations, *ACM Computing Surveys (CSUR)*.
- [57] A. Artelt, V. Vaquet, R. Velioglu, F. Hinder, J. Brinkrolf, M. Schilling, B. Hammer, Evaluating robustness of counterfactual explanations, in: *IEEE Symposium Series on Computational Intelligence*, IEEE, 2021, pp. 01–09.
- [58] M. Pawelczyk, C. Agarwal, S. Joshi, S. Upadhyay, H. Lakkaraju, Exploring counterfactual explanations through the lens of adversarial examples: a theoretical and empirical analysis, arXiv preprint, arXiv:2106.09992.
- [59] V. Ballet, X. Renard, J. Aigrain, T. Laugel, P. Frossard, M. Detyniecki, Imperceptible adversarial attacks on tabular data, arXiv preprint, arXiv:1911.03274.
- [60] T. Freiesleben, The intriguing relation between counterfactual explanations and adversarial examples, *Minds Mach.* (2021) 1–33.
- [61] A. Ferrario, M. Loi, The robustness of counterfactual explanations over time, *IEEE Access*.
- [62] A. Ferrario, M. Loi, A series of unfortunate counterfactual events: the role of time in counterfactual explanations, arXiv preprint, arXiv:2010.04687.
- [63] R. Mochaourab, S. Sinha, S. Greenstein, P. Papapetrou, Robust counterfactual explanations for privacy-preserving SVM, in: *International Conference on Machine Learning (ICML 2021)*, Workshop on Socially Responsible Machine Learning, 2021.
- [64] M.T. Ribeiro, S. Singh, C. Guestrin, Anchors, High-precision model-agnostic explanations, in: *Proceedings of the AAAI Conference on Artificial Intelligence*, vol. 32, 2018.
- [65] X. Zhang, A. Solar-Lezama, R. Singh, Interpreting neural network judgments via minimal, stable, and symbolic corrections, in: *Advances in Neural Information Processing Systems*, vol. 31.

Appendix references

- [66] B.L. Miller, D.E. Goldberg, Genetic algorithms, tournament selection, and the effects of noise, *Complex Syst.* 9 (3) (1995) 193–212.
- [67] C.R. Harris, K.J. Millman, S.J. van der Walt, R. Gommers, P. Virtanen, D. Cournapeau, E. Wieser, J. Taylor, S. Berg, N.J. Smith, R. Kern, M. Picus, S. Hoyer, M.H. van Kerkwijk, M. Brett, A. Haldane, J.F. del Río, M. Wiebe, P. Peterson, P. Gérard-Marchant, K. Sheppard, T. Reddy, W. Weckesser, H. Abbasi, C. Gohlke, T.E. Oliphant, Array programming with NumPy, *Nature* 585 (7825) (2020) 357–362.

Article

Quantifying Transgressive Coastal Changes Using UAVs: Dune Migration, Overwash Recovery, and Barrier Flooding Assessment and Interferences with Human and Natural Assets

Giulia Casagrande ^{1,2,*}, Annelore Bezzi ¹, Saverio Fracaros ¹, Davide Martinucci ^{1,2}, Simone Pillon ¹, Paolo Salvador ³, Stefano Sponza ¹ and Giorgio Fontolan ^{1,2}

¹ Coastal Group, Department of Mathematics and Geosciences, University of Trieste, Via E. Weiss 1, 34128 Trieste, Italy; bezzi@units.it (A.B.); saverio.fracaros@phd.units.it (S.F.); dmartinucci@units.it (D.M.); spillon@units.it (S.P.); sponza@units.it (S.S.); fontolan@units.it (G.F.)

² National Interuniversity Consortium for the Marine Sciences (CoNISMA), Piazzale Flaminio 9, 00196 Rome, Italy

³ Department of Life Sciences, University of Trieste, Via L. Giorgieri 10, 34127 Trieste, Italy; paolo.salvador@units.it

* Correspondence: gcasagrande@units.it

Abstract: The advantages derived from the use of Uncrewed Aerial Vehicles (UAVs) are well-established: they are cost-effective and easy to use. There are numerous environmental applications, particularly when monitoring contexts characterized by rapid morphological changes and high rates of sediment transport, such as coastal areas. In this paper, three different case studies of survey and monitoring with high resolution and accuracy obtained through the use of UAVs are presented; these concern transgressive coastal sites. Results allow for the definition and quantification of coastal landforms and processes, including: (i) The anatomy of a parabolic dune and the rate of landward migration that could interfere with a tourist settlement; (ii) The mode and timing of morphological recovery and realignment of a barrier island overwashed by storm surge episodes; and (iii) The potential flood risk of a progradational spit that is a nesting site of a species of migratory breeding birds of conservation concern. The results demonstrate and confirm that, through a good coupling of drone-sensed quality data and accurate topographic control, quantitative estimates that are useful in assessing the impacts of natural processes involving both human and natural assets can be obtained.

Keywords: coastal monitoring; dune migration; washover; flood risk; barrier island; Piscinas dunefield; Marano and Grado Lagoon; *Sternula albifrons*; UAV survey



Citation: Casagrande, G.; Bezzi, A.; Fracaros, S.; Martinucci, D.; Pillon, S.; Salvador, P.; Sponza, S.; Fontolan, G. Quantifying Transgressive Coastal Changes Using UAVs: Dune Migration, Overwash Recovery, and Barrier Flooding Assessment and Interferences with Human and Natural Assets. *J. Mar. Sci. Eng.* **2023**, *11*, 1044. <https://doi.org/10.3390/jmse11051044>

Academic Editors: Maria Alicandro, Sara Zollini and Donatella Dominici

Received: 8 March 2023

Revised: 29 April 2023

Accepted: 9 May 2023

Published: 13 May 2023



Copyright: © 2023 by the authors. Licensee MDPI, Basel, Switzerland. This article is an open access article distributed under the terms and conditions of the Creative Commons Attribution (CC BY) license (<https://creativecommons.org/licenses/by/4.0/>).

1. Introduction

Along with providing essential ecosystem services such as shoreline protection, improved water quality, fishing resources, and food and habitat for wildlife, coastal zones attract people due to the diversity of leisure activities available [1].

By their nature, coastal environments change rapidly in response to waves, currents, winds, and tides and necessitate frequent and precise geomorphological monitoring [2]. Direct observation, instrumental measurements, or imaging can be used in the short or medium term to monitor the various compartments, such as the nearshore, which includes the shoreface, the beach, and the coastal dunes. The main aim is to assess the modifications induced by sediment transport, which impact coastal landforms, habitats, and human goods [2]. This is crucial in transgressive contexts (such as shoreline retreat, washover, blowout, or transgressive dunefields), which can be induced and/or worsened by the accelerating global sea-level rise [3,4].

As coastal environments are constantly changing, so are the technologies and techniques used to map and monitor them [5]. Since the 2000s, aerial photos captured by

Uncrewed Aerial Vehicles (UAVs) have made coastal monitoring increasingly more affordable and efficient (see review articles of [5–10]). Ref. [11] highlighted that UAV remote sensing technology could possibly serve as the answer to the monitoring objectives that are essential for an efficient coastal management.

The advantages of UAV remote sensing technology for coastal mapping include automated surveys, high repeatability, minimal preparation, quick responses to extreme events, high measurement efficiency, and the generation of Digital Surface Models (DSMs) with high resolution and accuracy or point cloud by Structure for Motion (SfM) photogrammetry [11–14].

Low-cost investigations of vegetation, morphological, and sedimentological changes on beaches, coastal dunes, and estuarine mudflats or tidal flats using photogrammetry via UAVs supported by ground control points (GCPs) show the applicability of UAV remote sensing technology to the study of multiscale geomorphological dynamics caused by erosion, sedimentation, and other processes [12,15–17]. Furthermore, an increasing number of publications are reporting the use of UAVs in the monitoring and evaluation of the physical environment, which affects habitat and, as a result, species, [8,18] establishing it as an indispensable tool in this field.

For an understanding of a wide range of coastal processes at diverse geographical and temporal scales and site-specific demands, a set of case studies covering distinct and expert ways of data collection and processing is crucial.

This work presents the findings of three separate case studies of UAV monitoring in extremely dynamic coastal settings using aerial images and detailed topography to gather exact information on morphology, sediment budget, and plant cover. In the first case study, we attempted to describe the architecture of a parabolic dune and calculate the rate of movement of its active lobes, as well as the associated sand drift risk, in a typical transgressive aeolian setting. In the second case, the investigations assessed the mode and timing of morphological recovery and realignment following storm surge overwashing on a highly dynamic sandy barrier island. Finally, in order to evaluate the possible flood risk that would imperil a nesting colony site of a species of migratory breeding birds of conservation concern, we acquired the micro-topography of a progradational spit and put it in relation to tide level measurements.

The goal of examining these various scenarios is to demonstrate how drone surveys, whose instrumental performance and timing have greatly improved over time, can deliver accurate, high-quality site data even in very dynamic environments, especially when more information is associated with them that can aid in understanding the processes at work. This information can support the assessment of fundamental coastal management issues and the correlated geohazards, ecosystem restoration, and species conservation.

2. Study Areas and Background

This study deals with the monitoring of three study cases in Italy (Figure 1), which represent different sedimentary environments and processes: (i) The transgressive parabolic dune of Piscinas in Sardinia; (ii) A washover fan in Martignano island; and (iii) A prograding spit in Tratauri bank, both of which evolve along the barrier island system of the Marano and Grado Lagoon (MGL) in the northern Adriatic Sea.

2.1. The Transgressive Parabolic Dune of Piscinas

Coastal transgressive dune systems are large-scale, mobile, partially vegetated dune complexes that can decouple from the backshore and migrate inland [19]. Coastal transgressive dunes require abundant sediment and wind energy over century-to-millennial timescales to develop the complicated cut-and-fill sequences seen in mature systems. Control factors such as a high sediment supply, climatic conditions (e.g., arid or semi-arid), vegetation disturbance, and strong wave and wind energy have all been taken into account by [4,19]. Good examples of Pleistocene and Holocene transgressive dunefields have been documented worldwide along strandplain coastlines (e.g., [20–24]). Contemporary active

transgressive dunefields are found on many of the world's coasts [23,25–28] and are often well-developed in areas with significant wind energy.

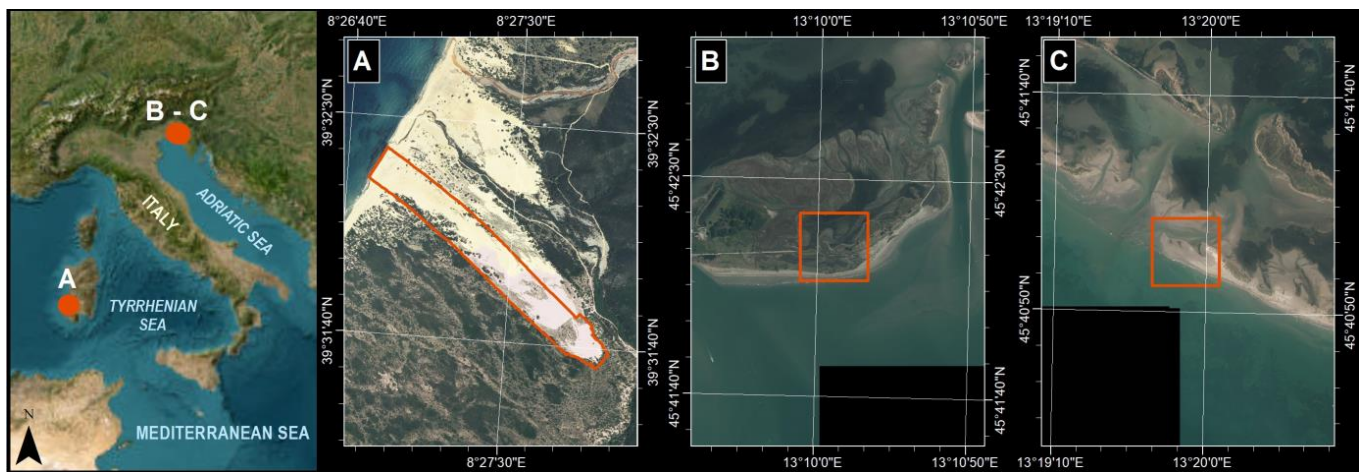


Figure 1. Location of the study sites. In the red boxes: (A) the main transgressive parabolic dune of Piscinas; (B) the washover fan induced by a storm event in 2013 along the Martignano barrier island; (C) the prograding spit, at the western end of the Tratauri bank, and one of the most frequented nesting sites of the Little Tern and Oystercatcher. While A is located in the west coast of Sardinia, both B and C are located along the barrier island system of the Marano and Grado Lagoon.

Parabolic dunes are a common type of transgressive landform. These dunes are typically U-shaped or V-shaped, with two trailing ridges extending from short to elongated. The trailing ridges have a deflation basin upwind that ends in a U- or V-shaped depositional lobe [29–31] and a precipitation ridge (namely slipface). They can be nested or overlap, exhibiting multiple formation episodes. The shape, slope, and type of terrain over which the dunes move, the type and density of vegetation, and the speed and direction of the wind all affect the rates of migration or advancement of these dunes.

The west coast of Sardinia hosts the only examples of active transgressive parabolic dunes in Italy, where they are exposed to strong winds from the northwest. Aeolian activity was significant also in the past, as testified by the extensive outcrop of Middle and Upper Pleistocene aeolianites all along the west coasts [32–34].

The monitored dune is the main parabolic dune of Piscinas (Figure 1A). Here, the wind regime is typically bimodal: winds from the 290°–330° direction (the Mistral) are predominant, either in terms of frequency or strength. The Sirocco winds, from 120°–150° are subordinate [35]. The dune of Piscinas, along with the Monte Arcuentu, are included in the Zone of Special Conservation and Zone of Special Protection (ITB040031), inside the EU Natura 2000 Network. This area is very rich in several species of animals, vegetation, and habitat [36], enhancing its naturalistic value.

2.2. The Dynamic Barrier Islands of the Marano and Grado Lagoon

Barrier islands are important landforms that protect the inland, bays, and estuaries from sea storms; they can be found on about 12% of the world's coasts [37] and are notable for their highly dynamic evolution. Transgressive processes, such as landward migration as a result of relatively rapid sea level rise or continuous storms, are typical modes of barrier evolution. The most common storm-related phenomenon is washover, which occurs when the wave run-up level and/or storm surge level (water level above predicted tide) exceeds the beach crest height, causing water and sediment to move landward [38]. The result is the formation of sand bodies toward the lagoon or the protected bay, with the washover fan being the most common. Washover fans can evolve through processes of channel fill, fan deposition, and subsequent salt marsh colonization by vegetation [39,40], or aeolian deflation and reworking. In this way, washover processes are the primary mechanism

by which barriers can increase in width and migrate landward [41–43]. In addition to transgressive processes, progradational trends can coexist on barrier islands thanks to sediment supply and longshore transport prominence [44–48]. Longshore constructive processes result in spit lengthening, nearshore bar welding, and breach closure or inlet migration [48,49]. Spit progradation occurs at different speeds and modes of berm accretion [50]; depressions between newly formed barriers can evolve into parallel swales or enclosed cat's-eye ponds [51,52]. Barrier islands have a notable naturalistic value for their vegetation richness and because they are the ideal habitat for many bird species, both resident and migratory [53]. New washover deposits are ecologically important as they increase habitat diversity and sustain more or less endangered species of birds [54–57].

The MGL is located in the northern Adriatic Sea, between the mouths of the Tagliamento and Isonzo rivers, covering an area of around 160 km². The lagoon is protected from the sea by a system of low-elevation sandy barrier islands and sand banks, that are constantly and rapidly evolving [58,59]. These landforms are periodically overwashed and breached by storm events, but they are also characterized by significant longshore transport and consequent rapid spit construction and progradation. The local wind climate is affected by the strong wind from the ENE (the Bora), which is predominant in frequency and strength [60,61]. The Sirocco wind is also statistically significant but subordinate in terms of strength. Tides are semi-diurnal with a mean range of 76 cm [62], and a mean spring-neap tide range of 105 and 22 cm, respectively [63]. An unusual rise in sea level may result from a confluence of spring tides, seiches, southerly winds, and low atmospheric pressure (known as “acqua alta”). Due to the Bora and the Sirocco winds, the wave regime is typically bimodal. According to data recorded at the wave buoy OGS-DWRG1 (located offshore at the coordinates 13.24° E, 45.56° N, –16 m depth), the mean significant wave height (Hs) is less than 0.5 m. Events with Hs greater than 0.5 m account for 25% of the overall record, with prevailing waves from the SE (10.7%) and ENE (10.5%). The Sirocco has the highest recorded waves, with Hs = 4.4 m [60]. The yearly wave energy flux for the northern Adriatic area is 1.95 kW/m, calculated using 11 years (1999–2006 and 2009–2013) of tri-hourly wave data from the Ancona buoy (Rete Ondametrica Nazionale, RON network). The longshore drift is directed from the Isonzo River mouth toward west.

The MGL has a great naturalistic value, both for the mosaic of habitats and for the richness of species. It is the Zone of Special Conservation and Zone of Special Protection inside the EU Natura 2000 Network, according to the European Directives 92/43/CEE and 2009/147/CE. More than 300 bird species are observed, of which 126 are nesting, probable, or confirmed. At a national level, it is one of the most relevant sites in the Adriatic for resting and wintering of water birds [64].

The barrier islands are the most important and preferred nesting site of the Little Tern (*Sternula albifrons*), whose typical habitat is the exposed sand substrate with scarce vegetation cover [65,66]. This species nests in the MGL barrier islands and, in recent years, within some fish farms in the lagoon basin, but its overall population is declining, falling from 250 pairs observed in 1984 [67] to 112–129 pairs in 2022 [68].

For our specific analysis, two cases were selected along the barrier island system of MGL, as indicated in Figure 1: a washover fan created by a storm event in 2013 on the Martignano barrier island (Box B) and a prograding spit at the western end of the Tratauri bank (Box C). To date, this is the only frequented nesting site of the Little Tern (*Sternula albifrons*) along the coastline.

3. Materials and Methods

Over a seven-year period, UAV surveys were conducted on three distinct environments (Figure 1) that reflect specific sedimentary dynamics in transgressive domains: a parabolic migrating dune in Piscinas, Sardinia; a washover fan in Martignano barrier island, MGL; and a prograding spit in Tratauri bank, MGL.

The UAV surveys in Piscinas were meant to assess the migration of the parabolic dune after the winter season and describe its current state; the surveys in Martignano and

the Tratauri Bank were designed to evaluate the post-storm evolution of a washover and determine the microtopography to support nesting bird monitoring.

Despite the advancement of technology during the timeframe in question and the deployment of various aircraft models, a common protocol for all the surveys can be defined, as is detailed below. Each UAV survey was carefully planned, checking out the regulated or prohibited fly zones and calculating the best UAV flight paths. The flight lines were designed to be orthogonal to the symmetry axis of every area captured by the photos. To achieve high accuracy in the georeferenced photogrammetric model, a large number of GCPs were positioned on the ground during each survey, materialized with 50 × 50 cm plastic square targets, and printed with coded symbols to aid recognition on photographs during data processing. All the GCPs were georeferenced with centimetre-level accuracy in the specific coordinate system (WGS84 UTM 32 North or WGS84 UTM 33 North, depending on the site), using a GNSS (Global Navigation Satellite System) Stonex S9III NRTK (Network Real Time Kinematic) receiver (Manufacturer: Stonex Srl, Paderno Dugnano, Italy) connected through GSM (Global System for Mobile Communications) to the HxGN SmartNet reference station network for real-time GNSS correction. For the conversion of ellipsoidal heights into orthometric ones, referring to the National vertical datum (IGM42 by Military Geographic Institute), the corresponding GK2 IGMI grids were used.

Following each flight, the photographs were downloaded to the ground station to be checked for quality (focusing, contrast, blurring, etc.). At the end of each survey day, a quick low-resolution photogrammetric model was created to check for photograph orientation issues and coverage gaps. This check was performed to ensure that no areas were overlooked and to determine whether the flight should be repeated. The photogrammetric models were processed using the SfM algorithm with Agisoft Metashape Professional v.1.7 software. The final products were: a point cloud (sparse cloud and dense cloud), a mesh, a textured mesh, a DSM, contours, and an orthomosaic. The characteristics of each survey, including the type of drone and sensor used, flight plans, GCPs, acquired surfaces, errors, resolution, and accuracy of the main outputs, are summarized in Table 1.

Table 1. For each study site, the table reports the year of the UAV survey with the main characteristics of the cameras and flight plan, acquisition details, and output resolution. Manufacturer information of UAVs and cameras: Dji (Manufacturer: DJI, Shenzhen, China); Neutech (Manufacturer: Neutech, Mogliano Veneto, Italy); Sony (Manufacturer: Sony Group, Tokyo, Japan).

Acquisition year	Piscinas			Martignano		Tratauri
	2014	2015	2016	2018	2021	2014
Type of UAV	Neutech NT4-contra	Neutech NT4-contra	Neutech NT6	Dji Phantom 4	Dji Phantom 4 Pro	Neutech NT4-contra
Camera model	Sony NEX-7 (20 mm)	Sony NEX-7 (20 mm)	Sony ILCE-5000 (20 mm)	Dji FC6310 (8.8 mm)	Dji FC6310 (8.8 mm)	Sony NEX-7 (20 mm)
Average flight height from the ground (m)	95	106	160	77	27	67
Image acquisition overlap (%)	70	70	80	80	80	70
Image acquisition sidelap (%)	70	70	70	80	80	80
Useful Photographs Acquired (number)	3911	445	281	785	1497	167
Surveyed GCPs (number)	291	58	37	46	12	20
RMSE (Root Mean Square Error) XYZ on the GCPs (cm)	2.5~3.8	2 ~2.6	0.6	2.2	3.8	4.8
Surveyed area (m ²)	65 × 10 ⁴	12 × 10 ⁴	29 × 10 ⁴	55 × 10 ⁴	15.7 × 10 ⁴	8 × 10 ⁴
Orthophoto GSD (Ground Sampling Distance) (cm/pix)	1.5~2	1.8~2	3	2	1.5	2
DSM (Digital Surface Model) GSD (cm/pix)	3~4	3.6~4	6	4	3	4

In Piscinas, the first survey, conducted in November 2014, before the beginning of the winter season, covered the entire area of the parabolic dune, while the second, conducted in May 2015, in the middle of the spring season and theoretically after the strong winds period, focused on monitoring the migrating lobes. Unfortunately, during the survey days, strong Mistral winds blew, and only some lobes were acquired. The photogrammetric models were loaded and analysed in ESRI ArcGIS v.10.8. DSMsoD (Digital Surface Models of Difference) were created utilizing the DSMs of the two surveys to assess the erosional and depositional effects of the aeolian transport. To estimate sand displacements, 10 profiles were extracted from the DSMs of the three compared lobes.

Three UAV surveys were conducted on the Martignano barrier island between 2016 and 2021 (Table 1) to determine the evolution of a washover. The surveys were compared to other available orthophotos from 2010 (courtesy of the Friuli Venezia Giulia Civil Protection Dept.) and 2014 (courtesy of the Friuli Venezia Giulia Region, AGEA flight) to provide a complete evolutionary picture of the area, which allowed us to quickly map the structure of the washover after its creation. After being processed with SfM algorithms, each spatial dataset was loaded into ESRI ArcGIS for spatial analysis and sedimentary volume estimates. Because the resulting 2021 DSM is influenced by dense and abundant vegetation and a lower number of GCPs, it was not used to calculate the sedimentary budget and DSMoD for the entire washover system. Instead, two cross-sections were extracted from all three years DSMs in the central and less vegetated sectors, one nearly parallel to the main axis of the washover and the other parallel to the shoreline, to better emphasize the topographic evolution of the area and to make volumetric estimates of the collected sediments. However, the cross-section parallel to the axis of the washover was manually corrected by filtering the vegetation signal to prevent volumetric computation errors almost exclusively in the 2021 DSM.

About 8×10^4 m² of the westernmost prograding spit on the Tratauri bank has been surveyed using UAV to provide supporting data for the monitoring of the most important waterbird breeding populations of conservation concern in the MGL. The bird monitoring was carried out by the Department of Mathematics and Geosciences at the University of Trieste in collaboration with the Biodiversity Service of Friuli Venezia Giulia Region in accordance with Habitat Directive 92/43/CEE and Birds Directive 2009/147/CE. Five bird censuses were conducted between May and July 2014 to monitor the Little Tern nesting colony: on 15 May, 21 May, 3 June, 24 June, and 9 July. A NRTK GNSS receiver was used to determine the position and elevation above m.s.l. (National datum IGM 42) of the nesting site. In order to also know the morphological evolution of the site, the previous shoreline position was digitized on the available aerial orthophotos taken in 2012 (courtesy of the Friuli Venezia Giulia Civil Protection Dept.), 2011, and 2014 (courtesy of the Friuli Venezia Giulia Region, AGEA flights), and the morphology and distribution of plant cover were observed. The UAV-obtained DSM was compared to the maximum tide levels recorded by the Grado tide gauge (courtesy of the Istituto Superiore per la Protezione e la Ricerca Ambientale) during each time interval between two consecutive nesting censuses. The DSM was classified according to altitude ranges, and the position of the nests compared to different elevation areas, for assessing their vulnerability to inundation.

4. Results

4.1. Piscinas

Orthophotos and DSM from the 2014 survey were used to describe the morphological characteristics of the main parabolic dune. The dune was aligned with the prevailing direction of the Mistral wind and extended in an elongated shape for about 2 km inland from the shore. In addition, the landform varied largely in elevation, starting from approximately 1.5 m above m.s.l. near the shore to a maximum height of almost 113 m near the southernmost portion of the dune. It includes five large sandy accumulations shaped like depositional lobes, which are typical of parabolic dunes (Figure 2). This information allowed us to classify the Piscinas dune as a multilobed parabolic dune. Each lobe had an

upwind surface with an average slope of 5° to 8° , often ending in a small flat stretch (the crest) and terminating with a short, steeply inclined surface (from 15° for the first lobe to over 30° for the last lobe) that constitutes the precipitation ridge (slipface).

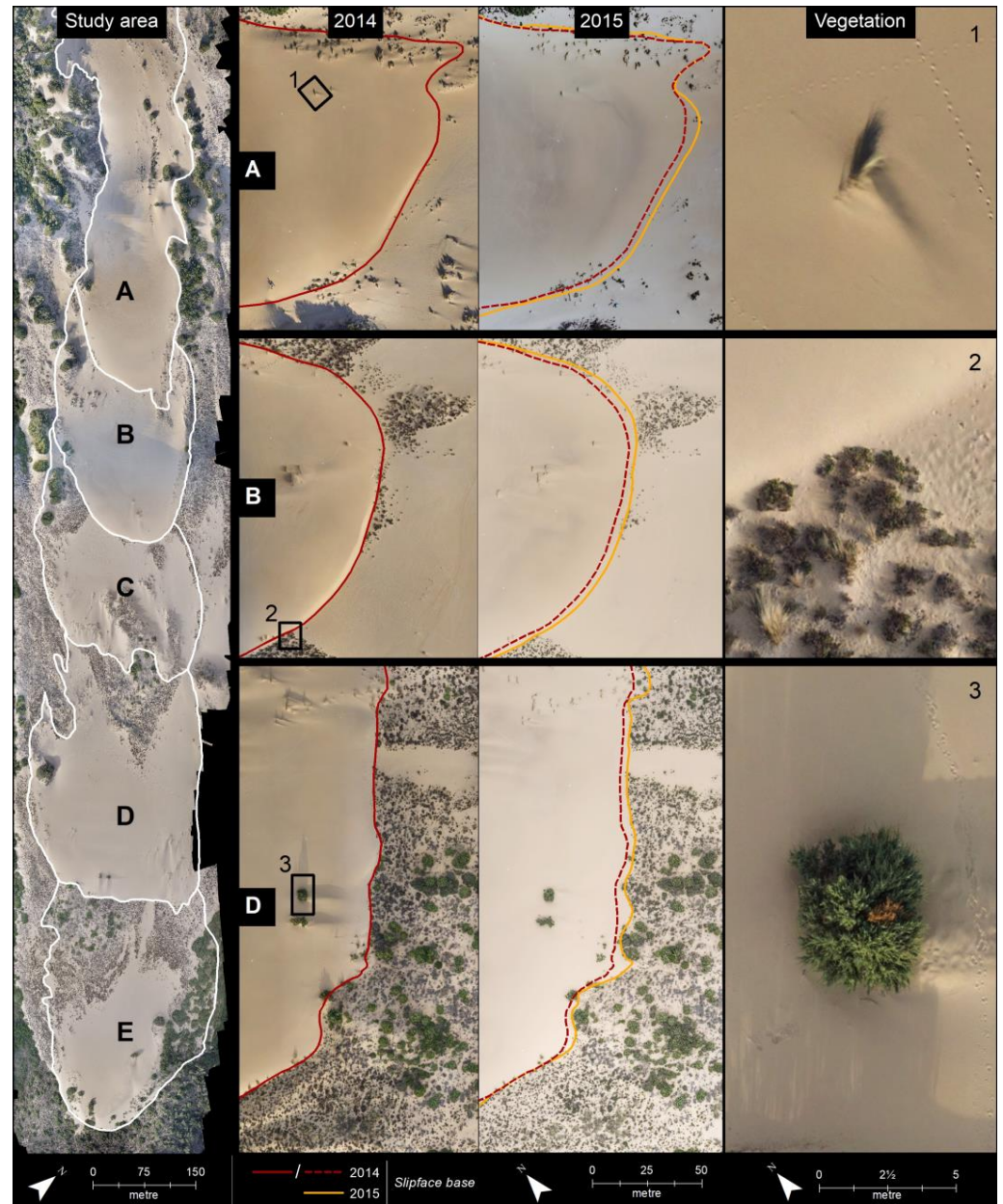


Figure 2. The main parabolic dune of Piscinas. On the left is the UAV orthophoto of 2014, with the representation of the five lobes ((A–E), white lines). In the middle, a comparison of the three monitored lobes (surveys of 2014 and 2015) with the representation of the migration that occurred after 6 months. Zoom boxes on the right allow to appreciate the different types of vegetation identified (box 1: Marram grass; box 2: bushes; box 3: arboreal shrubs). See the text for major details.

Each aeolian sub-environment was recognized using either the accurate topographic data or the various types of vegetation, easily identified thanks to the remarkable resolution (right side of Figure 2): (1) the Marram grass characteristic of active areas with continuous aeolian deposition, which was frequently detectable in the lateral margins of the lobes or near the crest (i.e., lobe A in Figure 2); (2) the bushes of the downwind area, typical of the areas with low wind energy (i.e., lobe B in Figure 2); and (3) the stabilizing arboreal shrubs,

which were typical of the inactive trailing ridge and the current cover surrounding the dune (i.e., lobe D in Figure 2).

Since each lobe was completely unvegetated, they have been recognised as active fronts of the parabolic dune’s migration. Table 2 provides a summary of some data about the length and elevations of lobes.

Table 2. Topographic and migration lobe parameters. The length of the lobes is the distance between the end of the precipitation ridge of the previous lobe and the end of the precipitation ridge of the current lobe. The length of the first lobe is measured from the backshore to the end of the precipitation ridge of the same lobe.

Lobe	Max Length (m)	Elevation (m above m.s.l.)	Cross-Section	Mean Dune Displacement in 6 Months (m)	Mean Lobe Displacement in 6 Months (m)
A	790	From 4.5 to 56.5	1	3	4.3
			2	4	
			3	6	
B	220	From 38 to 71	4	2.5	2.5
			5	3	
			6	2	
C	195	From 53.5 to 83	-	-	-
D	340	From 69 to 104	7	1	3.4
			8	6	
			9	3	
			10	3.5	
E	330	From 65 to 108	-	-	-

The second UAV survey permitted the acquisition of data for assessing the morphological changes of three of the five lobes after six winter months of aeolian activity (Figure 3). Figure 3 reports three examples of the 10 cross-sections extracted from the DSMs to analyse the topographic variations of the three lobes. The accuracy of the surveys can be observed in these profiles, where spikes indicating the vegetation are identical in both years. As expected, the wind deflation affected the stoss side of the lobes, especially along the profile of Lobe B, whereas deposition of the eroded sand occurred on the lee side, from the crest to the whole downwind side. The process induced a dune migration, quantified for each lobe as an average rate (Table 2) obtained by the sections presented in Figure 3: rates are higher in the central profiles, indicating a tendency of the lobes to migrate in a parabolic shape. The migration rate was not uniform across the whole dune: Lobe A migrates 4 m in 6 months, Lobe B migrates 2.5 m in 6 months, and Lobe D migrates 3.4 m in 6 months. The amounts of sand involved in the migration was calculated from the DMSoD (Figure 3) and was likewise substantial: 2145 m³ for Lobe A, 1801 m³ for Lobe B, and 3781 m³ for Lobe D.

4.2. Martignano Barrier Island (Marano and Grado Lagoon)

By comparing the collected orthophotos (Figure 4), it is possible to reconstruct the main morphological changes of the Martignano barrier island between 2010 and 2021, focusing on the shoreline position, emerging areas with stable vegetation or with bare sand (with significant and recent sand deposition), intertidal salt marshes, pioneer beach vegetation, and foredune vegetation.

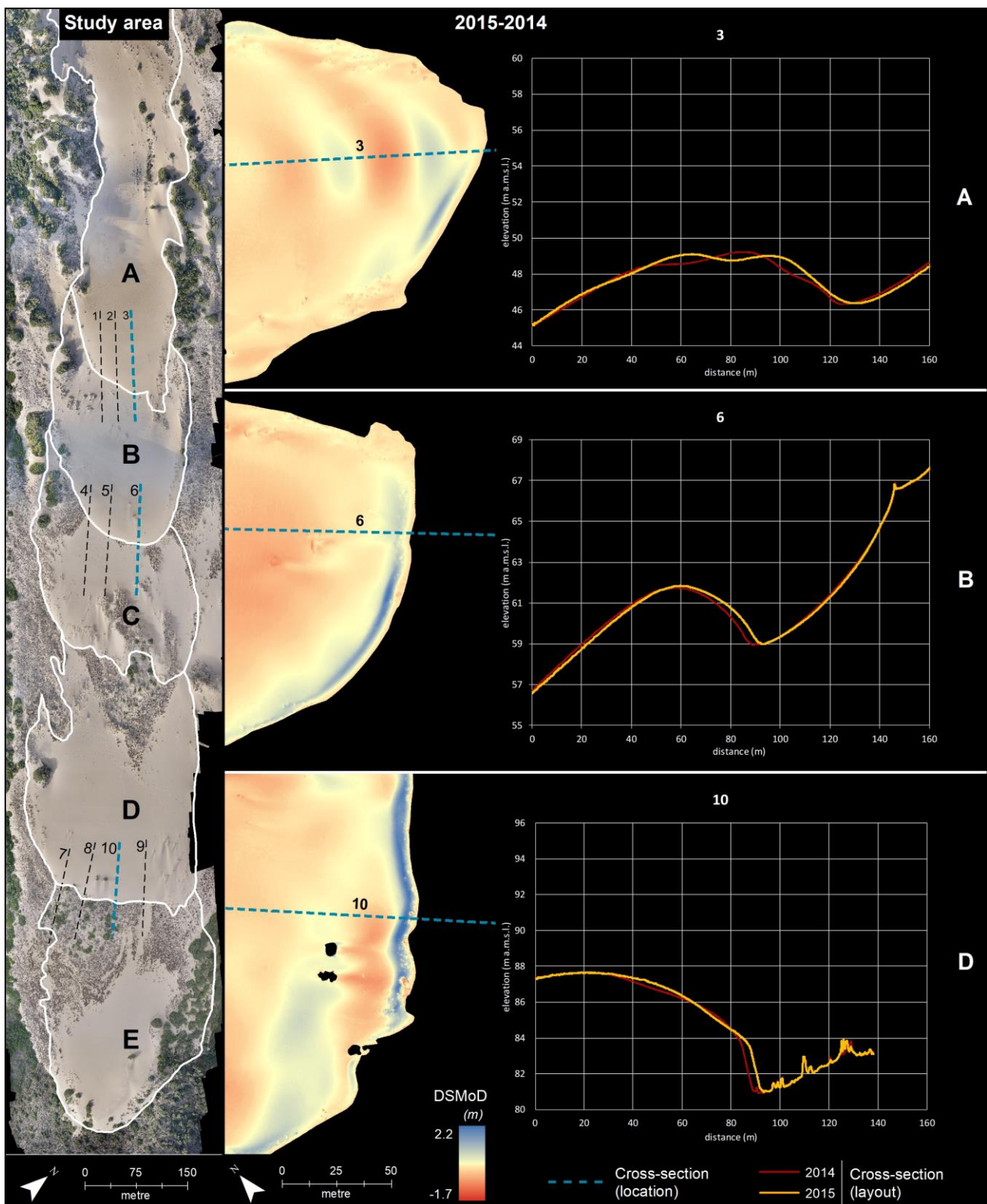


Figure 3. The morphological changes observed in the main parabolic dune of Piscinas after the six months of monitoring. On the left, the representation of the five lobes and the position of the extracted cross-sections; the blue ones were selected for comparison. In the middle, DSMoD of the three monitored lobes (A, B and D) with the selected cross-section. On the right, the extracted cross-sections representing the morphological variation of the monitored lobes between the two surveys.

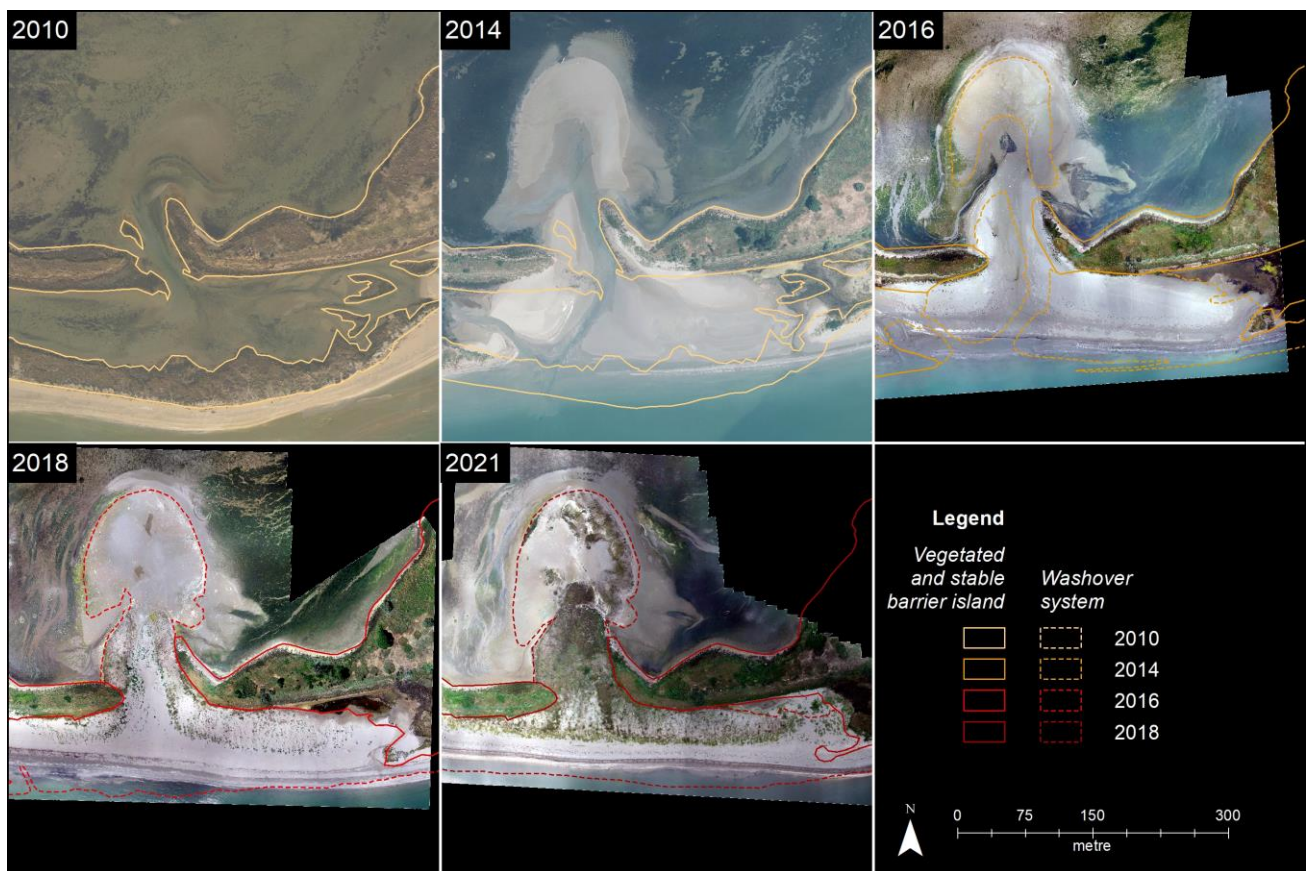


Figure 4. Evolution of the Martignano washover between 2010 and 2021. In each orthophoto, the edges of vegetated and stable barrier island, as well as the washover system, has been mapped for the current year, and overlapped with the previous one.

In 2010, a composite system with two barrier islands, one more active seaward and one stabilized landward, was observed. The latter exhibited relict landforms: a breach and a poorly evident older washover fan. The 2014 orthophoto reveals that a significant breach has occurred, resulting in the formation of a washover structure involving both the barrier island and consisting of a washover mouth (approximately 350 m wide), a sedimentary overflow, a washover channel, and a washover fan approximately in the same position as the relict one. According to the orientation of the washover system and wave data analysis [69], the breach was most likely caused by the impact of two severe storms: the first on 31 October 2012, with $H_s = 4.10$ m from the SE, and the second on 11 February 2013, with $H_s = 3.77$ m from the SE. The entire washover system extended approximately 340 m inland from the shoreline, which has receded approximately 80 m since 2010. The 2016 drone orthophoto shows the washover mouth and channel partially filled with sediment but still connected to the fan. Only a small part of the ancient barrier facing the sea has survived to the east, while the rest has been entirely eroded. The shoreline has been rectified and has retreated a maximum of 30 m since 2014. In 2018, the vegetation started to develop at the mouth and backshore. The washover channel, which was filled with sand but not jet vegetated, is still recognizable. In 2021, the vegetation totally stabilized the areas previously occupied by the mouth and the washover, while the washover fan preserved the whole configuration with rare pioneer plants that have begun to colonise the peripheral intertidal sectors. The photo also depicts the formation of vegetation typical of the foredunes on the backshore. Since 2010, the shoreline has moved more than 100 m landward.

The DSM created thanks to the UAV 2016 and 2018 surveys, as well as the DSMoD between these two years, permits the quantifying of the progressive rapid filling of the

area of the washover mouth and the suture of the beach system (Figure 5). Positive values to the south (in green), in the zone corresponding to the previous washover mouth, indicate sedimentation up to 0.80 m thick, whereas the fan sector can be considered stable. Comparing the topographic profiles obtained from the surveys' DSM (2016, 2018, and 2021) confirms these findings (Figure 5). The DSM profile A-A' reveals that in 2016, there were two steps flanked by a channel in the fan area (between 0 m and 110 m distance), which were most likely caused by the two different storm events that resulted in the superimposition of the washover fan. While the inner portion of the washover fan has stayed unchanged over the years, the channel has progressively filled (e.g., at the progressive 100 m, there is a vertical increment of 0.13 m between 2016 and 2018, as well as between 2018 and 2021). The majority of the deposition happened along the beach between 2016 and 2018, regenerating the foredune, with an estimated volume of 78.1 m³/m of sand, corresponding to a sedimentation rate of 13.3 cm/y. The isolated spikes depicted in the 2018 profile represent the plant grown on the washover system. The peak pattern of the 2021 profile makes this trend much clearer, confirming the resuture of the washover mouth, the spread of vegetation, and the system's current stability. Compared from 2016–2018, sedimentation rates from 2018–2021 have decreased to 2.7 cm/year with the highest rate on the lee side of the foredune. The B-B' profile is consistent with the A-A' profile, showing the total closing of the washover mouth in 2018 as well as the formation of extensive vegetation cover that consolidated the landform in the same year.

4.3. Tratauri Sand Bank (Marano and Grado Lagoon)

In 2014, a colony of Little Tern (*Sternula albifrons*) established itself and nested on the western 450-m-long end of the Tratauri bank, together with two nests of Eurasian Oystercatcher (*Haematopus ostralegus*) and one nest of Kentish Plover (*Charadrius alexandrinus*) [70]. According to field surveys and comparisons of drone orthophotos and traditional aerial photos, the nesting site is the terminal part of a newly formed spit that grew to the northwest 350 m from 2011 to 2014 at a rate of 116 m/y (Figure 6A). At the time of the monitoring, the spit still had poor maturity characteristics for at least a kilometre: mostly bare sand, a flat shape, and a maximum elevation of just over a metre above m.s.l. (Figure 6B).

Seaward, the beach exhibits the typical wave-dominated features, such as the beach face and the berm. Landward, a small step connects the bank to vast intertidal sandy or muddy flats leading to the lagoon. The scarce and discontinuous vegetation has a low degree of complexity, being of the pioneer type; only the association of *Cakiletea maritima* is prevalent.

The five censuses conducted on the site allowed for the observation of several nesting phases: the first on 14 May and the last on 9 July 2014. The number and spatial distribution of nests have changed over time. The number of nests reached a maximum on June 3 with 55 nests and then decayed rapidly. Spatially, the colony was mainly located on the landward side of the spit, ultimately being moved eastward (Figure 7). Despite the fact that the temporal evolution of the nests' number could be considered natural (with an increase, a maximum, and a decrease phase), a very low reproductive success has been observed during the census. Analysing the microtopography on the 0.10-m-classified DSM, we can put the position of the nests in relation to the micro-relief. The choice of the nest sites appears not to be completely influenced by the elevation above m.s.l. (Figure 7). Most of the nests are located on elevations that are not directly affected by high water levels during the time considered; many nests are found on the landward side of the bank, which appears to be the lowest and thus most vulnerable to high tides but is better protected from waves. By classifying the nests according to the different tidal maximum levels for each time interval between one avifauna census and the next, we can finally assess which positions may have been at risk of flooding (see the histogram in Figure 7).

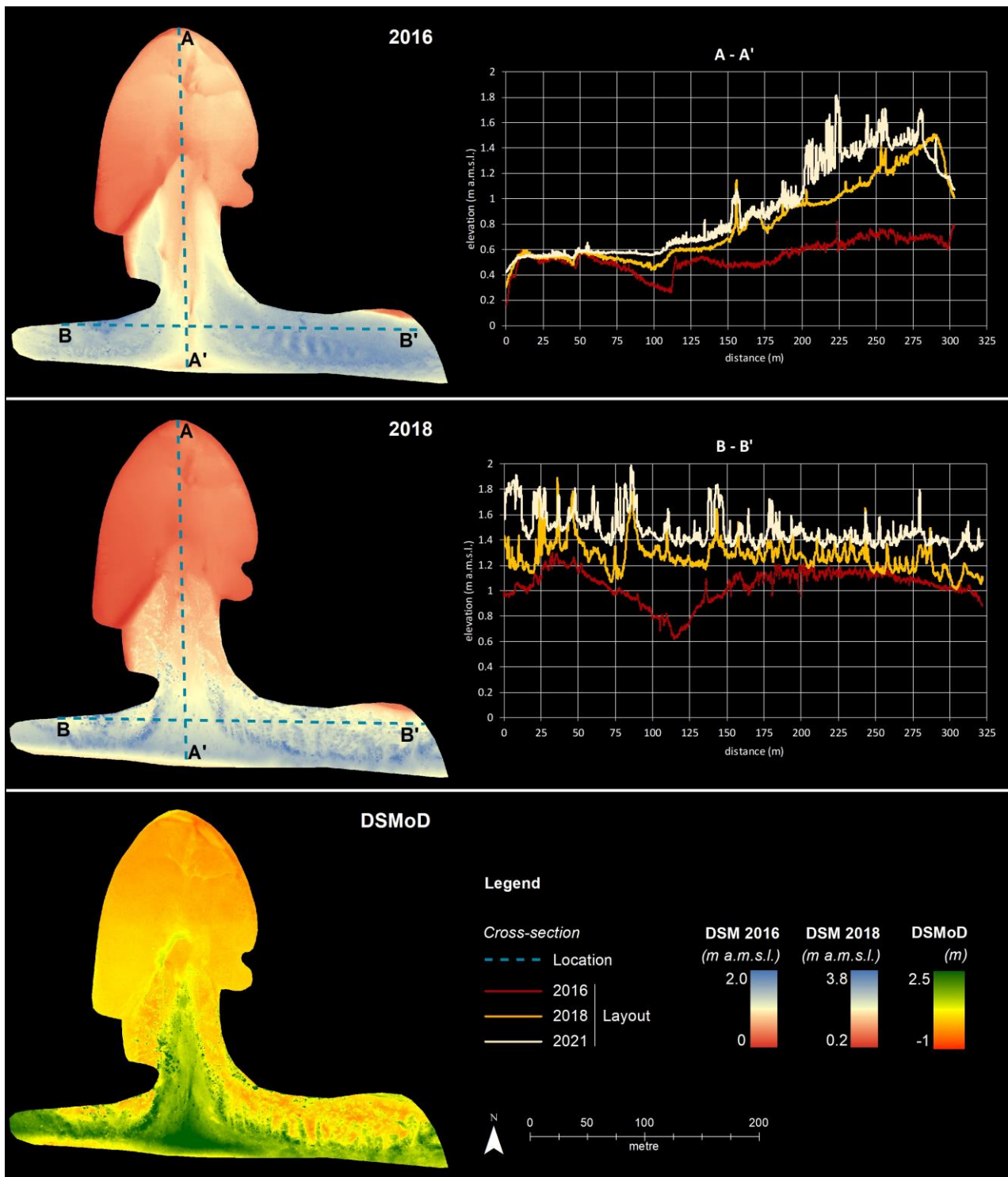


Figure 5. Topographical changes of the Martignano washover. On the left column, the DSM of 2016 and 2018, and the DSMoD relative to the comparison between the two years. On the right column, the cross-extracted sections A-A' and B-B', reporting the changing elevation of the complete dataset, including the 2021 survey.

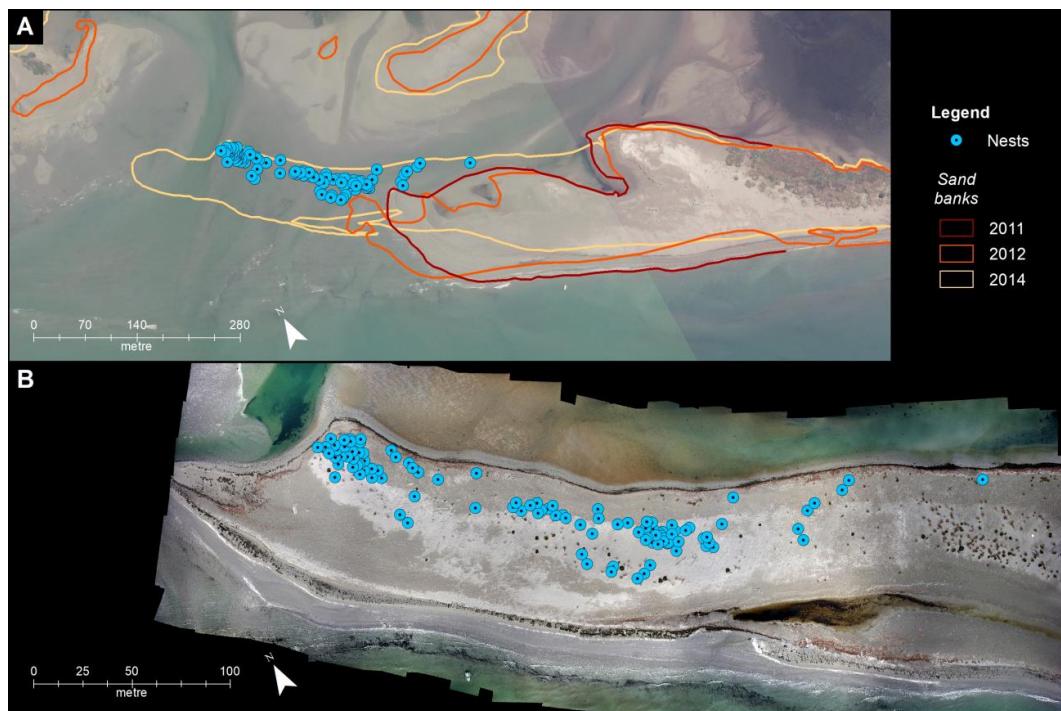


Figure 6. (A) Morphological evolution and spit migration of the Tratauri bank from 2011–2014 (basemap = 2011 orthophoto); (B) Orthophoto derived from drone survey carried out in 2014 along the western tip of the bank occupied by the nests of Little Terns (*Sternula albifrons*).

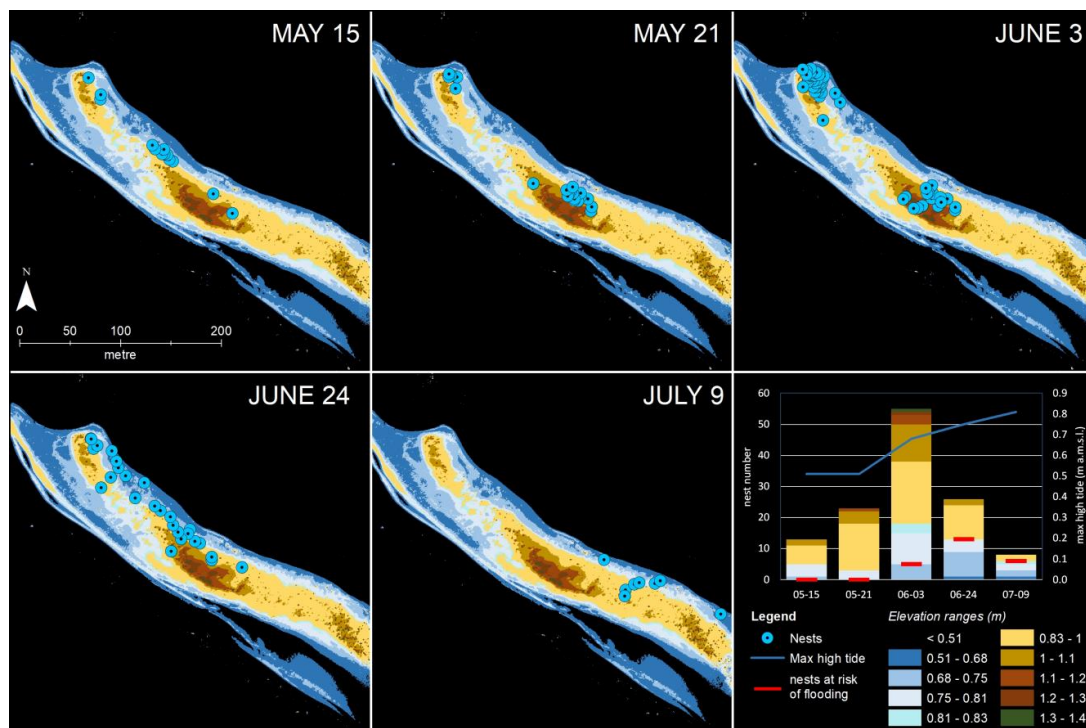


Figure 7. Distribution of the nests of the Little Tern on the Tratauri bank at the different census surveys in 2014. The histogram represents the evolution of the nests' number over time. For each census date, nests are classified according to elevation classes using the same colour in the maps and histogram; the red line on the histogram represents the division between nests at high risk of flooding (below the line) and "safe" nests (above the line).

5. Discussion

5.1. *The Transgressive Dune Anatomy and Migration*

The findings of the UAV surveys allow us to classify the Piscinas dune as a parabolic multilobate aeolian dune with five distinct depositional lobes. Our work concentrates on some of the active lobes, identifying source zones and deposition zones along a typical source-to-sink pathway. Currently, over each observed lobe, the onshore Mistral winds that affect the area are topographically accelerated along the stoss slope, thus eroding the surface and transporting the sand through the crest into the precipitation ridge and beyond it. This mechanism of deflation and deposition by wind, here precisely detected by UAV monitoring, is extensively reported in the literature (e.g., [71–73]), and it results in the landward migration of the lobes. The origin of the available sediment could be explained by the cannibalization of the Quaternary aeolianites that constitute the oldest transgressive dunes [35]. In fact, generally, cannibalization of old dunes is prevalent, especially when newer dunes migrate across relict dunes [30]. Thanks to the UAV surveys, we registered a migration rate between 2.5 and 4.3 m per six months of monitoring. These values are higher than the 1.6 m per year reported by [35] as the result of monitoring the final lobe only (lobe E), although comparable with those reported by other authors under similar environmental conditions (e.g., [74,75]).

As demonstrated in this case study, UAV surveys permit the acquisition of information on dune migration and pathways. As a consequence, it is possible to make assessments on potential sand drift hazards. This assessment furnishes, in a unique case at the national level, an evaluation of the potential risk due to the presence of the natural elements of the SIC area and, particularly, the touristic resort about 300 m beyond the terminal lobe. Indeed, considering (i) an average migration rate of 3.4 m per six months; (ii) this rate can be approximated to an annual rate because of the monitoring period (during the winter and spring seasons the winds are the strongest); and (iii) the distance of the resort, the touristic site can be reached by the terminal lobe at least in 88 years. Monitoring dune migration is essential to prevent sand invasion. Due to the fact that only six months of monitoring were done, our approach produced a first estimation. In similar circumstances, longer-term monitoring would be more effective over the course of a few years or more in order to assess the seasonality of the wind climate, as well as the variability in sand drift potential at the yearly scale.

In general, where settlements, tourism facilities, or natural protected areas are adjacent to transgressive dunefields, knowledge of dune morphodynamics and potential risk due to sand drift is necessary. The magnitude of the migration rate and the volume of sediment involved aid in determining appropriate specific mitigation actions or adaptation policies in order to prevent habitat loss and disruptions to human assets.

5.2. *The Washover Formation and Recovery*

The case of Martignano Island represents an example of monitoring storm effects and subsequent natural recovery processes. Given the capacity to generate both DSMs and orthophotos, the series of UAV surveys over time supported by previous data enables not only the qualitative and quantitative detection and evaluation of morphological and ecological changes but also the computation of sedimentary budgets.

Because we began monitoring this site well after the storm that caused the washover, we have only been able to quantify the first stages of evolution in terms of evolutionary mapping rather than sedimentary volumes. A shorter interval monitoring frequency, on the other hand, would not have resulted in more information about the evolution of washover in its complexity. We also noticed that the lower number of GCPs in the 2021 survey compared to previous ones, as well as their concentration in the central part of the study area, caused elevation error propagation at the DSM's edges. As a result, the comparison area is limited to the error-free central sector, confirming the importance of maintaining a consistent pattern of GCP positioning during monitoring to produce reliable results.

Despite these limitations, this work allows us to interpret important aspects of the dynamics of the Martignano barrier island, which can be used to assess its resilience to storms and the transgressive process associated with global sea level rise. We were able to deduce that the island breach occurred between 2012 and 2013, at the same location as a previous breach, indicating the presence of an erosive hot spot, thanks to the availability of wave recordings and aerial photos. The absence of human physical constraints in this small section of the barrier island allowed for the rapid formation of a new sand body landward (the washover fan). The shallow depth of the backbarrier wetlands, which provides a small accommodation space for the sedimentary supply from the beach, aided this. As several authors [38,45,76] have pointed out, these sandy deposits can represent a remarkably important part of the barrier island in terms of sedimentary budget and extent, allowing the barrier to be preserved during transgressive trends. The sandy structure of the washover fan currently exists as a relict landform in the backbarrier area; this condition has allowed the generation of a new habitat suitable as foraging sites for populations of the Greater Flamingo (*Phoenicopterus roseus*), as discovered by [57], demonstrating the importance of episodic events, such as storm surges, in generating new landforms and habitats that can support biodiversity in lagoon ecosystems.

Furthermore, the sediment budget of $101.4 \text{ m}^3/\text{m}$, which correspond to a sedimentation rate of $6.9 \text{ cm}/\text{year}$ for the entire surveyed time span on the A-A' cross-section (Figure 5), along with the full morphological recovery of the washover channel in 8 years before being vegetated in 2021, leads to the conclusion that the area is affected by a significant sedimentary supply. The existence of a consistent longshore sediment transport is confirmed if we take into account that the barrier island did not fragment after the event and that the beach and foredunes have recovered. This supports a previous study of the nearby Sant'Andrea tidal inlet [77] and shows that there is an ongoing process of sediment bypass from the Sant'Andrea ebb-tidal delta.

5.3. The Spit Evolution and Inundation Risk for Avifauna

This case study emphasizes the importance of combining wildlife data with geomorphological observations, especially in highly dynamic coastal environments where UAV surveys are currently the best option for mapping small areas with high resolution and accuracy. Thanks to the rapid natural formation of new emerging sandy bodies (prograding spits), the Tratauri bank (barrier islands of the MGL) provides a resource for the Little Tern as an alternative nesting site to the adjacent beaches, which are fully exploited for beach tourism. Indeed, the search for new habitats has become an essential but highly uncertain issue [78] at the worldwide level because of the increasing anthropization of the beaches [79] in the 19th and 20th centuries, which caused the distribution and abundance of these birds to decrease significantly. Theoretically, the relative remoteness of the location and the existence of protection regulations are variables that support the reproductive success of the Tratauri Bank; other factors, most notably predation, work against it. Our findings demonstrate that the nesting colonies have selected a location whose genesis is very recent (within the last two years), located a few centimetres above the high tide level, and highly floodable during severe tides, storms, or high water. Due to the rising spring tides in the study year, the risk of nest flooding rose during the nesting and breeding seasons.

The accuracy and resolution of the UAV survey appear to be acceptable in light of the slight differences in elevation detected in the nesting region, although accuracy is still contingent on the setup of enough ground control points and the precise nest's location. The need for such high resolution, high elevation accuracy, and a specific time for surveying excludes the possibility of using other remote sensing techniques such as satellites or LIDAR (Laser Imaging Detection and Ranging) surveys at the regional level. Another factor that influences the choice of the most pertinent mode of survey is the colony disturbance brought on by direct ground observations and/or by the UAV, which varies for each bird species and depends on many factors related to the aircraft model and overflight modes [80]. In any case, the rapidity of the survey, both via direct ground and by UAV,

represents a condition that can restrict the disturbance. In terms of timing, a survey at the start of the breeding season in the areas considered most suitable for nesting allows for the optimization of two aspects: the need to check the morphological changes brought on by the wave's action during the winter and the avoidance of colony overflight during the reproductive phase.

The availability of such a micro-topographic model can be a valid tool to be used for conservation and management purposes: to know the precise characteristics of the areas chosen by the bird species, to assess the flooding risks, and eventually to take protection measurements.

6. Conclusions

This work presents three case studies in which coastal dynamics play an important role, with implications for the environment and human issues. UAV monitoring with high resolution and accuracy allows for the detection of quantitative geomorphological effects of varying origin (wind, storms, waves) in areas where regular institutional monitoring surveys (aerial or LIDAR) or satellite data are not available or have insufficient resolution. Ad hoc UAV surveys allow us to capture high-quality images that are relatively simple to elaborate in order to obtain quantitative data on various aspects: a digital terrain model and terrain description to generate geomorphological maps; an assessment of plant cover as an indicator of sediment movement or stability; a quantification of morphological changes; and sediment budget in the short or medium term to identify and analyse processes in place.

The assessment of sand drift in an aeolian transgressive dunefield is the most important result in the first analysed case (Piscinas). The Piscinas dune was identified as a parabolic multilobate aeolian dune with five distinct depositional lobes distinguished by source and deposition zones along a typical source-to-sink pathway. The dune is moving landward, and a risk assessment of sand drift into the Natura2000 protected area and tourism resort was completed. Integration with climate models as a basis for future appropriate, specific mitigation actions, or adaptation policies could be the next step.

The main result of the second case (Martignano Island) was the assessment of the barrier island's resilience capacity to transgressive phenomena. The entity of washover deposit as a result of storm impacts, as well as the progressive post-storm beach recovery and suture of the barrier island, were detected and quantified. The data indicate that the beach-dune system with vegetation recovered completely in eight years, with a mean accumulation of 101.4 m³/m of sediments along the breaching axis.

The third case (Tratauri barrier island) demonstrates how the UAV-acquired micro-topography could represent a low-impact approach for developing a risk assessment for the flooding of bird nests in newly formed coastal sectors.

The naturally high dynamics of the examined coastal environments can be a risk factor and a point of contention between human use and nature preservation. This work lays the groundwork for the development of a protocol that allows for the understanding and acceptance of the results obtained from these technologies in order to provide useful information to decision-makers for future coastal management. This is made possible by aerial drone acquisitions and the characterization of ongoing physical processes.

Author Contributions: Conceptualization, G.C., A.B., S.S. and G.F.; methodology, validation, formal analysis, G.C., A.B., S.F., D.M., S.P., P.S. and S.S.; investigation, G.C., A.B., S.F., D.M., S.P., P.S., S.S. and G.F.; data elaboration, D.M., S.P., P.S. and S.S.; writing—original draft preparation, G.C. and A.B.; writing—review and editing, G.C., A.B., S.F., D.M., S.P., P.S., S.S. and G.F.; supervision, G.F.; project administration, funding acquisition, G.F. and S.S. All authors have read and agreed to the published version of the manuscript.

Funding: This research was funded by Italian Ministry of Education, University and Research CNR Flagship Project RITMARE, and by Regione Friuli Venezia Giulia, projects “PR-AVIFAUNA-2020”, “PR-COSTEREGFVG-2019” and “PR-SAPRFONTOLAN”. This study was carried out within the consortium iNEST (Interconnected North-Est Innovation Ecosystem) funded by the European Union Next-GenerationEU (Piano Nazionale di Ripresa e Resilienza (PNRR)—Missione 4 Componente 2, Investimento 1.5—D.D. 1058 23/06/2022, ECS_00000043). This manuscript reflects only the Authors’ views and opinions.

Institutional Review Board Statement: Not applicable.

Informed Consent Statement: Not applicable.

Data Availability Statement: Data are available to the corresponding author upon request.

Acknowledgments: We’d like to thank Giovanni De Falco, Simone Simeone, and Alessandro Conforti of IAS CNR Oristano for their support during the surveys in Sardinia. Sara Menon and Chiara Popesso are fully acknowledged for their technical assistance in the field and lab activities.

Conflicts of Interest: The authors declare no conflict of interest.

References

1. Leven, L.A.; Boesch, D.F.; Covich, A.; Dahm, C.; Erséus, C.; Ewel, K.C.; Kneib, R.T.; Moldenke, A.; Palmer, M.A.; Shelgrove, P.; et al. The function of marine critical zone transition zones and the importance of sediment biodiversity. *Ecosystems* **2001**, *4*, 430–451. [[CrossRef](#)]
2. Morang, A.; Gorman, L.T. Monitoring coastal geomorphology. In *Encyclopedia of Coastal Science*; Schwartz, M.L., Ed.; Encyclopedia of Earth Science Series; Springer: Dordrecht, The Netherlands, 2005; pp. 447–458.
3. Cazenave, A.; Cozannet, G.L. Sea level rise and its coastal impacts. *Earth’s Future* **2014**, *2*, 15–34. [[CrossRef](#)]
4. Hesp, P.A.; DaSilva, M.; Miot da Silva, G.; Bruce, D.; Keane, R. Review and direct evidence of transgressive aeolian sand sheet and dunefield initiation. *Earth Surf. Process. Landf.* **2022**, *47*, 2660–2675. [[CrossRef](#)]
5. Guan, S.; Sirianni, H.; Wang, G.; Zhu, Z. sUAS Monitoring of Coastal Environments: A Review of Best Practices from Field to Lab. *Drones* **2022**, *6*, 142. [[CrossRef](#)]
6. Klemas, V.V. Coastal and environmental remote sensing from unmanned aerial vehicles: An overview. *J. Coast. Res.* **2015**, *31*, 1260–1267. [[CrossRef](#)]
7. Adade, R.; Aibinu, A.M.; Ekumah, B.; Asaana, J. Unmanned Aerial Vehicle (UAV) applications in coastal zone management—A review. *Environ. Monit. Assess.* **2021**, *193*, 154. [[CrossRef](#)] [[PubMed](#)]
8. Kandrot, S.; Hayes, S.; Holloway, P. Applications of Uncrewed Aerial Vehicles (UAV) Technology to Support Integrated Coastal Zone Management and the UN Sustainable Development Goals at the Coast. *Estuaries Coast.* **2022**, *45*, 1230–1249. [[CrossRef](#)]
9. Yang, Z.; Yu, X.; Dedman, S.; Rosso, M.; Zhu, J.; Yang, J.; Xia, Y.; Tian, Y.; Zhang, G.; Wang, J. UAV remote sensing applications in marine monitoring: Knowledge visualization and review. *Sci. Total Environ.* **2022**, *838*, 155939. [[CrossRef](#)]
10. Jessin, J.; Heinzlief, C.; Long, N.; Serre, D. A Systematic Review of UAVs for Island Coastal Environment and Risk Monitoring: Towards a Resilience Assessment. *Drones* **2023**, *7*, 206. [[CrossRef](#)]
11. Gonçalves, J.A.; Henriques, R. UAV photogrammetry for topographic monitoring of coastal areas. *ISPRS J. Photog. Remote Sens.* **2015**, *104*, 101–111. [[CrossRef](#)]
12. Laporte-Fauret, Q.; Marieu, V.; Castelle, B.; Michalet, R.; Bujan, S.; Rosebery, D. Low-cost UAV for high-resolution and large-scale coastal dune change monitoring using photogrammetry. *J. Mar. Sci. Eng.* **2019**, *7*, 63. [[CrossRef](#)]
13. Casella, E.; Drechsel, J.; Winter, C.; Benninghoff, M.; Rovere, A. Accuracy of sand beach topography surveying by drones and photogrammetry. *Geo-Mar. Lett.* **2020**, *40*, 255–268. [[CrossRef](#)]
14. Pinton, D.; Canestrelli, A.; Moon, R.; Wilkinson, B. Estimating ground elevation in coastal dunes from high-resolution UAV-LIDAR Point Clouds and Photogrammetry. *Remote Sens.* **2023**, *15*, 226. [[CrossRef](#)]
15. Brunetta, R.; Duo, E.; Ciavola, P. Evaluating short-term tidal flat evolution through UAV surveys: A case study in the Po Delta (Italy). *Remote Sens.* **2021**, *13*, 2322. [[CrossRef](#)]
16. Jaud, M.; Grasso, F.; Le Dantec, N.; Verney, R.; Delacourt, C.; Ammann, J.; Deloffre, J.; Grandjean, P. Potential of UAVs for monitoring mudflat morphodynamics (application to the Seine Estuary, France). *ISPRS Int. J. Geo Inf.* **2016**, *5*, 50. [[CrossRef](#)]
17. Suo, C.; McGovern, E.; Gilmer, A. Coastal dune vegetation mapping using a multispectral sensor mounted on an UAS. *Remote Sens.* **2019**, *11*, 1814. [[CrossRef](#)]
18. Habel, J.C.; Teucher, M.; Ulrich, W.; Bauer, M.; Rödder, D. Drones for butterfly conservation: Larval habitat assessment with an unmanned aerial vehicle. *Landsc. Ecol.* **2016**, *31*, 2385–2395. [[CrossRef](#)]
19. Hesp, P.A. Conceptual models of the evolution of transgressive dune field systems. *Geomorphology* **2013**, *199*, 138–149. [[CrossRef](#)]
20. Clarke, M.; Rendell, H.; Tastet, J.-P.; Clave, B.; Masse, L. Late-Holocene sand invasion and North Atlantic storminess along the Aquitaine coast, Southwest France. *Holocene* **2002**, *12*, 231–238. [[CrossRef](#)]

21. Barbosa, L.M.; Dominguez, J.M.L. Coastal dune fields at the São Francisco River strandplain, Northeastern Brazil: Morphology and environmental controls. *Earth Surf. Proc. Land* **2004**, *29*, 443–456. [[CrossRef](#)]
22. Clarke, M.L.; Rendell, H.M. Effects of storminess, sand supply and the North Atlantic Oscillation on sand invasion and coastal dune accretion in western Portugal. *Holocene* **2006**, *16*, 341–355. [[CrossRef](#)]
23. Tsoar, H.; Levin, N.; Porat, N.; Maia, L.P.; Herrmann, H.J.; Tatumi, S.H.; Claudino-Sales, V. The effect of climate change on the mobility and stability of coastal sand dunes in Ceará state (NE Brazil). *Quat. Res.* **2009**, *71*, 217–226. [[CrossRef](#)]
24. Clemmensen, L.B.; Murray, A.; Heinemeier, J.; de Jong, R. The evolution of Holocene coastal dunefields, Jutland, Denmark: A record of climate change over the past 5000 years. *Geomorphology* **2009**, *105*, 303–313. [[CrossRef](#)]
25. Hunter, R.E.; Richmond, B.M.; Alpha, T.R. Storm-controlled oblique dunes of the Oregon coast. *Geol. Soc. Am. Bull.* **1983**, *94*, 1450. [[CrossRef](#)]
26. Illenberger, W.K.; Rust, I.C. A sand Budget for the Alexandria coastal dunefield, South Africa. *Sedimentology* **1988**, *35*, 513–521. [[CrossRef](#)]
27. Fryberger, S.G.; Krystinik, L.F.; Schenk, C.J. Tidally flooded back-barrier dunefield, Guerrero Negro area, Baja California, Mexico. *Sedimentology* **1990**, *37*, 23–43. [[CrossRef](#)]
28. Muckersie, C.; Shepherd, M.J. Dune phases as time-transgressive phenomena, Manawatu, New Zealand. *Quat. Int.* **1995**, *26*, 61–67. [[CrossRef](#)]
29. Pye, K.; Tsoar, H. *Aeolian Sand and Sand Dunes*; Springer: Berlin/Heidelberg, Germany, 1990; 458p.
30. Hesp, P. Dune coasts. In *Treatise on Estuarine and Coastal Science*; Wolanski, E., McLusky, D., Eds.; Academic Press: Cambridge, MA, USA, 2011; Chapter 3.02, pp. 193–221.
31. Hesp, P.A.; Walker, I.J. Coastal dunes. In *Treatise on Geomorphology*; Shroder, J., Lancaster, N., Sherman, D.J., Baas, A.C.W., Eds.; Elsevier: San Diego, CA, USA, 2013; Volume 11, pp. 328–355.
32. Palmerini, V.; Ulzega, A. Sedimentologia e geomorfologia del settore costiero tra la foce del Rio Piscinas e Capo Pecora (Sardegna sud-occidentale). *Rend. Sem. Fac. Sc. Univ. Cagliari* **1969**, *39*, 313–350.
33. Annino, E.; Barca, S.; Costamagna, L.G. Lineamenti stratigrafico-strutturali dell'Arburese (Sardegna sud-occidentale). *Rend. Sem. Fac. Sc. Univ. Cagliari* **2000**, *70*, 403–426.
34. Andreucci, S.; Clemmensen, L.B.; Pascucci, V. Transgressive dune formation along a cliffed coast at 75 Ka in Sardinia, western Mediterranean: A record of sea-level fall and increased windiness. *Terra Nova* **2010**, *22*, 424–433. [[CrossRef](#)]
35. Pitzalis, A. Dinamica geomorfologica del sistema dunare di Piscinas-Scivu (Sardegna sud-occidentale). In *Dune di Piscinas-Monte Arcuentu*; Schenk, H., Ulzega, A., Eds.; Amministrazione Provinciale di Cagliari: Cagliari, Italy, 2002; pp. 5–19.
36. Schenk, H.; Ulzega, A. *Dune di Piscinas—Monte Arcuentu*; Amministrazione Provinciale di Cagliari: Cagliari, Italy, 2002; pp. 1–60.
37. Pilkey, O.H.; Fraser, M.E. *A Celebration of the World's Barrier Islands*; Columbia University Press: New York, NY, USA, 2003; 400p.
38. Donnelly, C.; Kraus, N.; Larson, M. State of knowledge on measurement and modeling of coastal overwash. *J. Coast. Res.* **2006**, *22*, 965–991. [[CrossRef](#)]
39. Elliott, H.R.T. Siliciclastic shorelines. In *Sedimentary Environments and Facies*, 2nd ed.; Reading, H.G., Ed.; Blackwell Scientific Publications: Oxford, UK, 1986; pp. 155–188.
40. Rodriguez, A.B.; Yu, W.; Theuerkauf, E.J. Abrupt increase in washover deposition along a transgressive barrier island during the late nineteenth century acceleration in sea-level rise. In *Barrier Dynamics and Response to Changing Climate*; Moore, L., Murray, A., Eds.; Springer: Cham, Switzerland, 2018; pp. 121–145.
41. Hosier, P.E.; Cleary, W.J. Cyclic geomorphic patterns of washover on a barrier island in southeastern North Carolina. *Environ. Geol.* **1977**, *2*, 23–31. [[CrossRef](#)]
42. Leatherman, S.P.; Zaremba, R.E. Overwash and aeolian processes on a U.S. northeast coast barrier. *Sediment. Geol.* **1987**, *52*, 183–206. [[CrossRef](#)]
43. Oertel, G.F. The barrier island system. *Mar. Geol.* **1985**, *63*, 1–18. [[CrossRef](#)]
44. Hayes, M.O.; Ruby, C.H. Barriers of Pacific Alaska. In *Geology of Holocene Barrier Island Systems*; Davis, R.A., Jr., Ed.; Springer: Berlin/Heidelberg, Germany, 1994; pp. 395–433.
45. Morton, R.A. Texas barriers. In *Geology of Holocene Barrier Island Systems*; Davis, R.A., Jr., Ed.; Springer: Berlin/Heidelberg, Germany, 1994; pp. 75–114.
46. Garrison, J.R.; Williams, J.; Potter Miller, S.; Weber, E.T.; McMechan, G.; Zeng, X. Ground-penetrating radar study of North Padre Island: Implications for barrier island internal architecture, model for growth of progradational microtidal barrier islands, and Gulf of Mexico sea-level cyclicity. *J. Sedim. Res.* **2010**, *80*, 303–319. [[CrossRef](#)]
47. Bezzi, A.; Casagrande, G.; Martinucci, D.; Pillon, S.; del Grande, C.; Fontolan, G. Modern sedimentary facies in a progradational barrier-spit system: Goro Lagoon, Po Delta, Italy. *Estuar. Coast. Shelf Sci.* **2019**, *227*, 106323. [[CrossRef](#)]
48. Bezzi, A.; Casagrande, G.; Fracaros, S.; Martinucci, D.; Pillon, S.; Sponza, S.; Bratus, A.; Fattor, F.; Fontolan, G. Geomorphological changes of a migrating sandbank: Multidecadal analysis as a tool for managing conflicts in coastal use. *Water* **2021**, *13*, 3416. [[CrossRef](#)]
49. Popesso, C.; Pacheco, A.; Ferreira, Ó.; Fontolan, G. Evolution of a relocated inlet migrating naturally along an open coast. *J. Coast. Res.* **2016**, *75*, 233–237. [[CrossRef](#)]
50. Hine, A.C. Mechanisms of berm development and resulting beach growth along a barrier spit complex. *Sedimentology* **1979**, *26*, 333–351. [[CrossRef](#)]

51. Otvos, E.G. Beach ridges—Definitions and significance. *Geomorphology* **2000**, *32*, 83–108. [[CrossRef](#)]
52. Davis, R.A.; Yale, K.E.; Pekala, J.M.; Hamilton, M.V. Barrier island stratigraphy and Holocene history of west-central Florida. *Mar. Geol.* **2003**, *200*, 103–123. [[CrossRef](#)]
53. Moore, F.R.; Kerlinger, P.; Simons, T.R. Stopover on a Gulf Coast barrier island by spring trans-Gulf migrants. *Wilson Bull.* **1990**, *102*, 487–500.
54. Godfrey, P.J.; Godfrey, M.M. The role of overwash and inlet dynamics in the formation of salt marshes on North Carolina barrier islands. In *Ecology of Halophytes*; Reimold, R.J., Queen, W.H., Eds.; Academic Press: Cambridge, MA, USA, 1974; pp. 407–427.
55. Conner, W.H.; Day, J.W.; Baumann, R.H.; Randall, J.M. Influence of hurricanes on coastal ecosystems along the northern Gulf of Mexico. *Wetl. Ecol. Manag.* **1989**, *1*, 45–56. [[CrossRef](#)]
56. Withers, K. Shorebird use of coastal wetland and barrier island habitat in the Gulf of Mexico. *Sci. World Jour.* **2002**, *2*, 514–536. [[CrossRef](#)] [[PubMed](#)]
57. Salvador, P.; Bezzi, A.; Martinucci, D.; Sponza, S.; Fontolan, G. Circular bedforms due to pit foraging of Greater Flamingo *Phoenicopterus Roseus* in a back-barrier intertidal habitat. *Diversity* **2022**, *14*, 788. [[CrossRef](#)]
58. Brambati, A.; De Muro, S.; Marocco, R.; Selivanov, A. barrier island evolution in relation to the sea-level changes: The example of the Grado Lagoon (northern Adriatic Sea, Italy). *Boll. Geof. Teor. Appl.* **1998**, *39*, 145–161.
59. Fontolan, G.; Pillon, S.; Bezzi, A.; Villalta, R.; Lipizer, M.; Triches, A.; D’Aietti, A. Human impact and the historical transformation of saltmarshes in the Marano and Grado Lagoon, northern Adriatic Sea. *Estuar. Coast. Shelf Sci.* **2012**, *113*, 41–56. [[CrossRef](#)]
60. Regione Autonoma Friuli Venezia Giulia-Autorità di Sistema Portuale del Mare Adriatico Orientale. Piano Regolatore Portuale Del Porto Di Monfalcone, Variante Localizzata. Studio Meteomarinario. Progettisti: Modimar, SJS Engineering, Archest. 2019. Available online: https://www.regione.fvg.it/rafvfg/export/sites/default/RAFVG/ambiente-territorio/pianificazione-gestione-territorio/FOGLIA9/allegati/Allegato_33_alla_Delibera_2066-2019.pdf (accessed on 21 January 2023).
61. Bezzi, A.; Pillon, S.; Martinucci, D.; Fontolan, G. Inventory and conservation assessment for the management of coastal dunes, Veneto coasts, Italy. *J. Coast Conserv.* **2018**, *22*, 503–518. [[CrossRef](#)]
62. Petti, M.; Pascolo, S.; Bosa, S.; Bezzi, A.; Fontolan, G. Tidal flats morphodynamics: A new conceptual model to predict their evolution over a medium-long period. *Water* **2019**, *11*, 1176. [[CrossRef](#)]
63. Dorigo, L. *La Laguna di Grado e le Sue Foci. Ricerche e Rilievi Idrografici*; Magistrato alle Acque—Ufficio Idrografico: Venice, Italy, 1965; 231p.
64. Cosolo, M.; Sponza, S.; Fattori, U. *La Laguna di Marano e Grado: Un Mosaico di Biodiversità—Un Patrimonio da Preservare*; Regione Autonoma Friuli Venezia Giulia: Udine, Italy, 2015; 52p.
65. Scarton, F.; Valle, R.; Borella, S. Il Fraticello (*Sterna albifrons*) nidificante in Laguna di Venezia: Anni 1989–1993 (Vertebrata, Aves). *Lav. Soc. Ven. Sc Nat.* **1995**, *20*, 81–87.
66. Scarton, F.; Baldin, M.; Valle, R. L’avifauna acquatica nidificante nelle barene artificiali della Laguna di Venezia. *Boll. Mus. Civ. Stor. Nat. Venezia* **2009**, *60*, 127–141.
67. Utmar, P. *La consistenza e tendenza delle popolazioni nidificanti oggetto di ricerca per conto degli osservatori faunistici anni 1987–1997*; Technical Report, Regione Autonoma Friuli Venezia Giulia: Gorizia, Italy, 1997.
68. Sponza, S.; Salvador, P. *Monitoraggio e Gestione di Alcune Specie di Uccelli Acquatici Nidificanti di Interesse Comunitario (Ciconiformi, Falacrocoracidi e Caradriformi) Nella Zona Costiera del Friuli Venezia Giulia. Relazione Finale—Stagione Riproduttiva 2002*; Technical Report; Regione Autonoma Friuli Venezia Giulia: Trieste, Italy, 2022.
69. Pomaro, A.; Cavaleri, L.; Papa, A.; Lionello, P. 39 years of directional wave recorded data and relative problems, climatological implications and use. *Sci. Data* **2018**, *5*, 180139. [[CrossRef](#)] [[PubMed](#)]
70. Regione Autonoma Friuli Venezia Giulia. *Monitoraggio delle Specie di Ciconiformi, Falacrocoracidi e Caradriformi Nidificanti Nella Zona Costiera del Friuli Venezia Giulia, SIC IT3340006 Carso Triestino e Goriziano, ZPS IT3341002 Aree Carsiche Della Venezia Giulia, SIC e ZPS IT3330006 Valle Cavanata e Banco Della Mula di Muggia, SIC e ZPS IT3320037 Laguna di Marano e Grado*; Technical Report; Regione Autonoma Friuli Venezia Giulia: Trieste, Italy, 2015.
71. Hesp, P.; Hyde, R. Flow dynamics and geomorphology of a trough blowout. *Sedimentology* **1996**, *43*, 505–525. [[CrossRef](#)]
72. Fraser, G.S.; Bennett, S.W.; Olyphant, G.A.; Bauch, N.J.; Ferguson, V.; Gellasch, C.A.; Millard, C.L.; Mueller, B.; O’Malley, P.J.; Way, J.N.; et al. Windflow circulation patterns in a coastal dune blowout, south coast of Lake Michigan. *J. Coast. Res.* **1998**, *14*, 451–460.
73. Pease, P.; Gares, P. The influence of topography and approach angles on local deflections of airflow within a coastal blowout. *Earth Surf. Process. Land.* **2013**, *38*, 1160–1169. [[CrossRef](#)]
74. Lindhorst, S.; Betzler, C. The climate-archive dune: Sedimentary record of annual wind intensity. *Geology* **2016**, *44*, 711–714. [[CrossRef](#)]
75. Costas, I.; Reimann, T.; Tsukamoto, S.; Ludwig, J.; Lindhorst, S.; Frechen, M.; Hass, H.C.; Betzler, C. Comparison of OSL ages from young dune sediments with a high-resolution independent age model. *Quat. Geochronol.* **2012**, *10*, 16–23. [[CrossRef](#)]
76. Hudock, J.W.; Flaig, P.P.; Wood, L.J. Washover Fans: A modern geomorphologic analysis and proposed classification scheme to improve reservoir models. *J. Sedim. Res.* **2014**, *84*, 854–865. [[CrossRef](#)]
77. Popesso, C. *Evolution and Stability of Tidal Inlets: A Comparison between Two Natural Cases along Human-Affected Coastlines*. Ph.D. Thesis, University of Trieste, Trieste, Italy, 2016.
78. Catry, T.; Ramos, J.A.; Catry, I.; Allen-Revez, M.; Grade, N. Are salinas a suitable alternative breeding habitat for Little Terns *Sterna Albifrons*? *Ibis* **2004**, *146*, 247–257. [[CrossRef](#)]

79. Tucker, G.M.; Heath, M.F. *Birds in Europe: Their Conservation Status*; Birdlife Conservation Series n. 3; Birdlife International: Cambridge, UK, 1994; 600p.
80. Mapes, K.L.; Pricope, N.G.; Baxley, J.B.; Schaale, L.E.; Danner, R.M. Thermal imaging of beach-nesting bird habitat with unmanned aerial vehicles: Considerations for reducing disturbance and enhanced image accuracy. *Drones* **2020**, *4*, 12. [[CrossRef](#)]

Disclaimer/Publisher's Note: The statements, opinions and data contained in all publications are solely those of the individual author(s) and contributor(s) and not of MDPI and/or the editor(s). MDPI and/or the editor(s) disclaim responsibility for any injury to people or property resulting from any ideas, methods, instructions or products referred to in the content.



36TH



IAS

DU
BROV
NIK

MEETING OF SEDIMENTOLOGY

ABSTRACTS BOOK



12-16 June 2023, DUBROVNIK, CROATIA

36th International Meeting of Sedimentology
June 12–16, 2023, Dubrovnik, Croatia

ABSTRACTS BOOK



Organized by:

Croatian Geological Society (HGD) and International Association of Sedimentologists (IAS)

**Organizing Committee**

Lara Wacha, *chair*, Croatian Geological Survey, Zagreb
Katarina Gobo, University of Zagreb, Faculty of Science
Nikolina Ilijanić, Croatian Geological Survey, Zagreb
Tvrtko Korbar, Croatian Geological Survey, Zagreb
Marijan Kovačić, University of Zagreb, Faculty of Science
Duje Kukoč, Croatian Geological Survey, Zagreb
Borna Lužar-Oberiter, University of Zagreb, Faculty of Science
Maja Martinuš, University of Zagreb, Faculty of Science
Slobodan Miko, Croatian Geological Survey, Zagreb
Davor Pavelić, University of Zagreb, Faculty of Mining, Geology and Petroleum Engineering
Kristina Pikelj, University of Zagreb, Faculty of Science
Igor Vlahović, University of Zagreb, Faculty of Mining, Geology and Petroleum Engineering

Scientific Committee

Igor Vlahović, *president*, University of Zagreb, Croatia
Nevena Andrić Tomašević, Karlsruhe Institute of Technology, Germany
Bruno Campo, University of Bologna, Italy
Sonia Campos Soto, Complutense University of Madrid, Spain
Luca Caracciolo, FAU Erlangen-Nürnberg, Germany
Blanka Cvetko Tešović, University of Zagreb, Croatia
Shahin E. Dashtgard, Simon Fraser University, Canada
Andrea Di Capua, National Research Council – IGAG, Italy
Goran Durn, University of Zagreb, Croatia
Gianluca Frijia, University of Ferrara, Italy
Massimiliano Ghinassi, University of Padova, Italy
Luis Gibert Beotas, University of Barcelona, Spain
Bosiljka Glumac, Smith College, USA
Antun Husinec, St. Lawrence University, USA
Stuart Jones, Durham University, UK
Tvrtko Korbar, Croatian Geological Survey, Croatia
Marijan Kovačić, University of Zagreb, Croatia
Juan Carlos Laya, Texas A&M University, USA
Marta Marchegiano, University of Granada, Spain
Cole McCormick, Pennsylvania State University, USA
Mardi McNeil, Geoscience Australia, Australia
Theresa Nohl, University of Vienna, Austria
Shuxin Pan, PetroChina – NWGI, China
Guido Pastore, University of Milano–Bicocca, Italy
Maximiliano Paz, University of Saskatchewan, Canada
Daniel A. Petráš, Czech Geological Survey, Czech Republic
Miquel Poyatos-Moré, Universitat Autònoma of Barcelona, Spain
Joanna Pszonka, Polish Academy of Sciences – MEERI, Poland
John J.G. Reijmer, Vrije Universiteit Amsterdam, The Netherlands
Valentina Marzia Rossi, National Research Council – IGG, Italy
Arnoud Sloodman, Colorado School of Mines, USA
Miroslaw Slowakiewicz, University of Warsaw, Poland
Thomas Steuber, Khalifa University of Science and Technology, Abu Dhabi, UAE
Finn Surlyk, University of Copenhagen, Denmark
Michal Šujan, Comenius University in Bratislava, Slovakia
Romain Vaucher, University of Geneva, Switzerland
Alan Vranjković, INA Oil Company, Croatia
Lara Wacha, Croatian Geological Survey, Croatia
Guodong Wang, PetroChina, China
Pujun Wang, Jilin University, China
Valentin Zuchuat, RWTH Aachen University, Germany
Nadja Zupan Hajna, Research Centre of the Slovenian Academy of Sciences and Arts, Slovenia

Publisher: Croatian Geological Society (HGD)

For the publisher: Slobodan Miko

Editors: Igor Vlahović and Darko Matešić

Language Editor: Julie Robson (Scotland, United Kingdom)

Digital layout: Laser Plus d.o.o

Cover design: Ana Badrić

eISBN: 978-953-6907-79-3

Theme 16. Techniques and technologies in sedimentology**General Session**

Oral presentation

Application of a semi-automatic method for sedimentological mapping

Saverio Fracaro¹, Annelore Bezzi², Giulia Casagrandè, Simone Pillo³, Davide Martinucci,
Stefano Sponza, Giorgio Fontolan³, Antonio Bratuš

¹University of Trieste, Department of Mathematics and Geosciences, Trieste, Italy

²Autonomous Region of Friuli Venezia Giulia, Geological Survey, Trieste, Italy









³National Interuniversity Consortium for Marine Sciences, CoNISMa, Rome, Italy

saverio.fracaros@phd.units.it

Sedimentological maps, which are useful for understanding sediment dynamics, modelling sediment transport, and supporting sediment management, are important components in analysing coastal environments. Usually, sedimentological maps are based on the collection of superficial samples with different spatial distributions; however, the density of sampling is often low due to the need for optimising time and cost. A low sampling density may not be an issue to map coasts with standard bathymetry and seaward-fining sediment distribution but become critical in the presence of bathymetric anomalies. In fact, both sedimentological and morphological settings are the result of the coastal processes, and in these cases, even advanced automatic interpolation techniques cannot produce maps that properly represent the sedimentological signature of the morphological set-up. The presence of relict landforms, the Isonzo River sediment supply, and the westward littoral drift make the littoral of Grado (North Adriatic Sea, Italy) a good example of such an anomalous coast. Here, the morphological and sedimentological settings, coupled with a sparse and irregular sampling distribution, make an experienced assessment necessary to identify and solve critical issues in the sedimentological maps obtained through automatic algorithms. To construct more reliable maps of the study area, we propose a semi-automatic method based on four steps: (1) identify the incongruities of the automatic models by a match with the landforms; (2) draw polylines between samples to manually force the direction of interpolation; (3) generate simulated samples on the polylines in order to (4) interpolate both collected and simulated samples. In the study area, this approach was able to effectively represent the sedimentary anomalies caused by relict and active morphologies, both interpolating current samples and re-analysing old data with different sampling distribution. Each grain-size parameter distribution can be modelled using this technique, which can also be applied in other fields. The main benefits of this method are its ability to (1) increase useful data density without spending too much time on sediment sampling, (2) re-analyse old data, and (3) tune models only where they are unreliable.

Article

Remote Measurement of Tide and Surge Using a Deep Learning System with Surveillance Camera Images

Gaetano Sabato ¹, Giovanni Scardino ¹, Alok Kushabaha ^{1,2,*}, Giulia Casagrande ³, Marco Chirivì ⁴,
Giorgio Fontolan ³, Saverio Fracaros ³, Antonio Luparelli ⁴, Sebastian Spadotto ³
and Giovanni Scicchitano ¹

¹ Department of Earth and Geoenvironmental Sciences, University of Bari, Via Orabona 4, 70125 Bari, Italy

² Istituto Universitario di Studi Superiori (IUSS)—School for Advanced Studies, Piazza della Vittoria 15, 27100 Pavia, Italy

³ Department of Mathematics, Informatics and Geosciences, University of Trieste, Via Weiss 2, 34128 Trieste, Italy

⁴ CETMA (Centro di Ricerca Europeo di Tecnologie Design e Materiali), S.S.7 Km.706 + 030 c/o Cittadella della Ricerca, 72100 Brindisi, Italy

* Correspondence: alok.kushabaha@iusspavia.it

Abstract: The latest progress in deep learning approaches has garnered significant attention across a variety of research fields. These techniques have revolutionized the way marine parameters are measured, enabling automated and remote data collection. This work centers on employing a deep learning model for the automated evaluation of tide and surge, aiming to deliver accurate results through the analysis of surveillance camera images. A mode of deep learning based on the Inception v3 structure was applied to predict tide and storm surges from surveillance cameras located in two different coastal areas of Italy. This approach is particularly advantageous in situations where traditional tide sensors are inaccessible or distant from the measurement point, especially during extreme events that require accurate surge measurements. The conducted experiments illustrate that the algorithm efficiently measures tide and surge remotely, achieving an accuracy surpassing 90% and maintaining a loss value below 1, evaluated through Categorical Cross-Entropy Loss functions. The findings highlight its potential to bridge the gap in data collection in challenging coastal environments, providing valuable insights for coastal management and hazard assessments. This research contributes to the emerging field of remote sensing and machine learning applications in environmental monitoring, paving the way for enhanced understanding and decision-making in coastal regions.

Keywords: deep learning; tide; storm surge; coastal monitoring; convolutional neural network



Citation: Sabato, G.; Scardino, G.; Kushabaha, A.; Casagrande, G.; Chirivì, M.; Fontolan, G.; Fracaros, S.; Luparelli, A.; Spadotto, S.; Scicchitano, G. Remote Measurement of Tide and Surge Using a Deep Learning System with Surveillance Camera Images. *Water* **2024**, *16*, 1365. <https://doi.org/10.3390/w16101365>

Academic Editor: Jianjun Ni

Received: 10 April 2024

Revised: 30 April 2024

Accepted: 10 May 2024

Published: 11 May 2024



Copyright: © 2024 by the authors. Licensee MDPI, Basel, Switzerland. This article is an open access article distributed under the terms and conditions of the Creative Commons Attribution (CC BY) license (<https://creativecommons.org/licenses/by/4.0/>).

1. Introduction

The rise in global mean sea level, attributed to human-induced climate change [1], is resulting in a global escalation in the frequency of coastal flooding, with a multitude of negative impacts for coastal communities, public safety, and economies [2].

The components of flooding include astronomical and meteorological water levels. The astronomical water level is determined by the tidal cycle, which is primarily caused by the gravitational attraction between the Moon and the Earth. Tides follow a regular pattern and can cause a periodic rise and fall in the water level along coastlines. On the other hand, meteorological water levels are influenced by weather events such as storms, heavy rainfall, or strong winds. These factors can lead to a temporary increase in water level in coastal areas, known as “storm surge”. Storm surge can significantly contribute to coastal flooding during extreme weather events. Both of these components can result in an elevation of the water level and contribute to flooding in coastal areas. It is important to consider both factors when evaluating and managing the risk of flooding [3].

Tidal patterns have significant impacts on various aspects of human life and the ecosystem [4]. The positive outcomes of tides include preserving the marine ecosystem, facilitating fishing and harvesting [5], controlling pollution, generating power, and influencing weather circulation [6]. Tides play a vital role in many coastal ecosystems: they influence the habitats, aid in reproductive activities, and support the food chain [7]. In fishing, tides are used to catch fish and harvest seafood, optimizing economic returns [8]. Additionally, they contribute to the generation of renewable energy through tidal energy, harnessing hydraulic forces [9]. Tidal currents impact the circulation of weather, leading to the creation of more favorable climate conditions and contributing to the balance of global temperatures. [10]. They also play a vital role in the movement of sediment along the beach. Phases of high and low tide influence the deposition of sand, gravel, and other particles on the beach [11]. Understanding tides offers opportunities for their optimal utilization in modern society [12].

Significant emphasis must be placed on coastal protection measures in response to storms and the ensuing storm surge.

A storm surge is an anomalous increase in water levels caused by a storm that exceeds the expected astronomical tide. It represents the fluctuation in water level directly influenced by the storm's presence [13].

The primary driver behind storm surges comes from the powerful winds associated with cyclones [14]. The wind patterns surrounding the cloud-free area of a cyclone's 'eye' are determined by a cyclonic circulation through diabatically produced potential vorticity (PV) anomalies in the lower-mid troposphere [15,16]. In offshore areas, this circulation remains largely undisturbed, resulting in minimal signs of storm surge [17]. When the hurricane approaches nearshore areas, the cyclonic circulation is influenced by seabed friction [18], determining the water flow inland [19]. Regarding coastal protection and emergency management, it is important to emphasize that the storm surge can penetrate far inland from the coastline [20,21].

To capture the characteristics of forcing during extreme events and the resulting impacts on the coastal environment, a combination of direct methods (e.g., wave buoys, tide gauges, LiDAR surveys) and indirect methods (e.g., webcam or satellite images) have long been utilized. In recent times, the popularity of indirect methods has increased significantly due to their ability to analyze large volumes of data using artificial intelligence techniques.

Machine learning and deep learning [22], two branches of artificial intelligence [23], are proving to be versatile tools in the examination of coastal environments [24]. This, in turn, can facilitate the informed and sustainable planning and management of coastal regions [25]. Such efforts contribute to safeguarding marine ecosystems and enhancing the tourism appeal of beaches [26]. Machine and deep learning enable the analysis of beach areas through the processing of satellite imagery [27] or footage from surveillance cameras [28]. For instance, machine learning algorithms can be employed to recognize and categorize various aspects of coastal landscapes, such as beach morphology, that are influenced by tides and currents [29]. Additionally, deep learning facilitates the creation of specialized algorithms tailored to the detection of specific coastal features, enhancing the precision and efficiency of monitoring and analysis systems [30]. This, in turn, positively influences beach management by enabling a more precise evaluation of a beach's condition and a more timely response to potential emergencies [31].

In this study, we present the results of experiments conducted using an algorithm for automated tide and surge measurement from images captured by a surveillance camera system. Once an image is acquired and submitted to the system, the algorithm is capable of providing the corresponding tidal height and, consequently, the surge [28]. These results are highly useful in areas where the tide sensor is remotely located, necessitating time corrections [32], and in situations of extreme events, such as Mediterranean Hurricanes, where surge measurement becomes valuable.

The tool presented in this paper represents an upgrade of the Convolutional Neural Network (CNN) for Tide Assessment developed in LEUCOTEA [28]. The forecasts pro-

duced by neural networks were compared to the observational data derived from tide gauge records. The previous code was written in MATLAB and used the GoogLeNet model [33]. This latest update is translated into Python [34] and is based on the Inception V3 model developed by Google [35].

The employment of a comprehensive observational system spanning multiple platforms provides the opportunity for real-time feedback on the occurrence of oceanic and atmospheric events. Moreover, this approach would enable the execution of analyses that are typically reliant on in situ sensors [36], thereby circumventing logistical challenges and facilitating the seamless creation of information databases [37].

The paper was organized as follows:

- Section 2 contains the methodology section, where the study areas, datasets, and deep learning models are reported;
- Section 3 presents the results and discussion, including predictions and hyperparameters;
- Section 4 contains the conclusions.

2. Methodology

In this section, we present a detailed overview of the methodologies and techniques employed in this study. We outline the specific approaches adopted for the remote measurement of tides and surges, as well as details of the deep learning system utilized for analysis. Additionally, we discuss the preprocessing steps applied to the surveillance camera images and the training procedures undertaken to optimize the performance of the model. The following subsections provide a comprehensive overview of the methodologies used in this research endeavor.

2.1. Data Acquisition and Territorial Framework

In the preliminary step, the process begins by choosing a coastal region for investigation and assembling a pertinent set of images to effectively portray the entire spectrum of potential tidal values. A substantial quantity of images is essential for conducting a thorough analysis. In our case, we chose two locations in Italy, and the model was trained and tested using images from surveillance cameras.

2.1.1. Site 1: Santa Lucia

The first site is Santa Lucia, located on the Maddalena peninsula in the municipality of Siracusa (SR), southeastern Sicily (Figure 1a). It features numerous distinct characteristics, various residential settlements, several commercial activities, as well as areas of natural and archaeological interest. In 2004, the Plemmirio Marine Protected Area was established to safeguard the surrounding marine environment and its abundant marine fauna. The management of the Marine Area provided the images from the surveillance camera.

The coastal region of south-eastern Sicily extends over approximately 300 km and is experiencing significant erosion, with the shoreline retreating at a rate of about 5 m/year [38]. This region has faced severe storms over the past few decades, experiencing waves that have reached approximately 6 m in height and storm surges surpassing 1 m [39]. The examined coastal region displays a mix of small rocky headlands and low-lying beach systems, often adjacent to coastal lagoons. The impacts of numerous tsunamis have been recorded by studying accumulations of boulders [40,41], high-energy deposits [42], and the stratigraphy of the lagoon areas [43,44]. Furthermore, the region has also been impacted by severe storms, resulting in the displacement of boulders and cobbles along the coastline [40]. Similar to other Mediterranean coastal areas, these storm occurrences have undergone impacts similar to those witnessed in past extreme marine events, such as tsunamis.

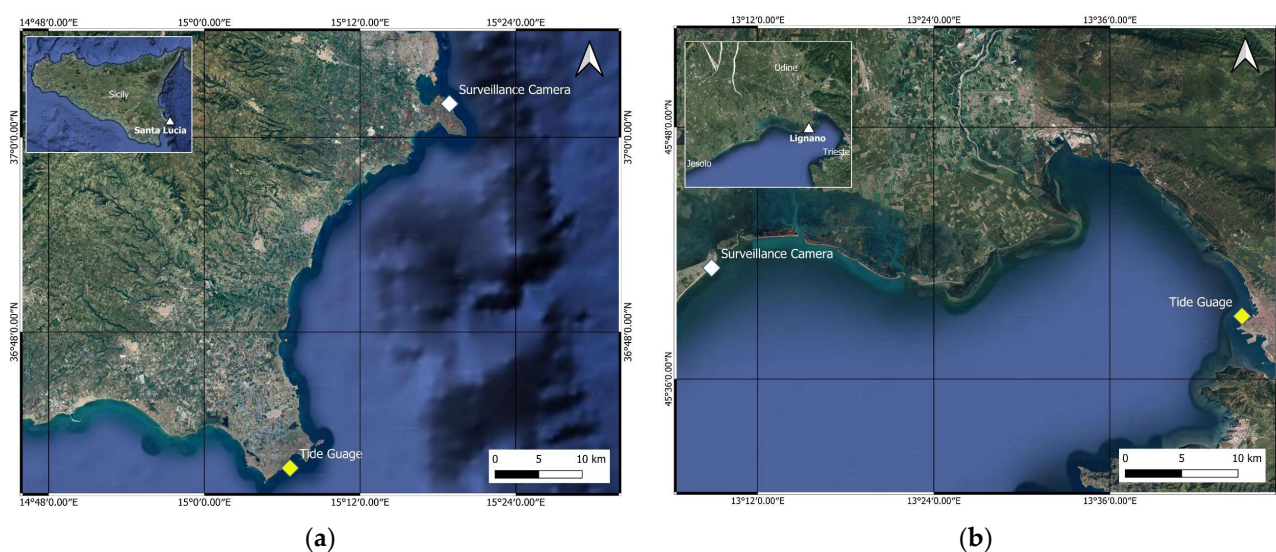


Figure 1. Study areas with surveillance camera locations: (a) site 1—Santa Lucia; (b) site—2 Lignano.

We also conducted an analysis using data recorded by the Catania wave buoy from the National Wave Network (Rete Ondametrica Nazionale (RON)). The most powerful storm in southeastern Sicily since 1990 was identified, characterized by a substantial wave height (H_s) of around 6.2 m and a peak period (T_p) of 11.3 s. Several medicanes, or Mediterranean hurricanes, have affected the coasts of south-eastern Sicily, and in recent decades, these events have had a greater impact compared to typical seasonal storms. Between 2014 and 2023, ten cyclones passed in the Ionian Sea, with four of them—Qendresa in 2014, Zorbas in 2018, Apollo in 2021, and Helios in 2023 [45]—strongly impacting the coast of south-eastern Sicily. While the Ionian Sea is not typically prone to the formation of tropical cyclones, medicanes result from a process known as Tropical Transition (TT), where an extratropical system transforms into a tropical system or induces a hybrid cyclone [46,47]. However, some studies suggest that climate change may alter medicanes in the future, potentially reducing their frequency but intensifying their impact [48]. Nevertheless, in the Ionian basin, except for 2019, a medicanne has crossed the region each year since 2014.

2.1.2. Site 2: Lignano Sabbiadoro

The second site is Lignano Sabbiadoro, a municipality located in the Friuli Venezia Giulia region (Figure 1b). Here, the images, acquired from a webcam placed on the roof of a restaurant overlooking the sea, were provided by the Panomax portal (<https://lignano.panomax.com/> (accessed on 4 May 2023)) for tourism in the Friuli Venezia Giulia Region. Despite only having around 7000 inhabitants, it is one of the most important seaside resorts in the Northern Adriatic Sea, with around 3.5 million visitors (ISTAT, 2019). Lignano is located on the peninsula made up of the eastern lobe of the Tagliamento river delta and separates the Adriatic Sea from the Marano and Grado lagoon. The coast, conventionally divided from the Tagliamento river mouth (to the south) to the Lignano inlet (to the north) into the three sectors of Riviera, Pineta and Sabbiadoro, is made up of a single sandy beach approximately 8 km long. The beach has a curvilinear shape: from south to north, the direction rotates progressively clockwise from around 10° N to 45° N at the locality of Sabbiadoro, where the webcam is located, and then rotates in the opposite direction near the tidal inlet. The width of the beach varies from 23 m to 181 m. The seabed facing Sabbiadoro beaches is characterized by the presence of the ebb tidal delta of the Lignano inlet, whose morphological high is evident up to 1600 m from the shoreline, beyond which the depth progressively increases from 2 to 10 m in 1500 m, resulting in an average slope of 3.2‰ [49].

The sediment budget of the shoreface in Sabbiadoro has been positive over the last 20 years [49], although the beach has shown an erosive trend partly compensated by

nourishments and partly by the attempt to protect the beach using seasonal barriers made up of plastic bags filled with sand taken in situ.

The tides in the Northern Adriatic Sea are semi-diurnal, with average mean spring tide and mean neap tide ranges of 78 cm, 105 cm [50], and 22 cm [51], respectively.

The local wind climate is affected by two main winds, “Bora” and “Sirocco”. Although the Bora wind (from ENE) is predominant in terms of frequency and strength [52,53], the Sirocco wind (coming from the SSE) is statistically significant, although it holds a subordinate position in terms of strength.

The wave regime tends to exhibit a bimodal pattern due to the prevailing wind conditions. As per data collected from the wave buoy OGS DWRG1 (positioned offshore at coordinates 13.24 E, 45.56 N; 16 m depth), the average significant wave height (H_s) remains below 0.5 m. Instances of H_s exceeding 0.5 m make up 25% of the entire dataset, with prevailing waves originating from the SE (10.7%) and ENE (10.5%). The Sirocco wind contributes to the highest recorded waves, reaching an H_s of 4.4 m [53]. The simultaneous influence of spring tides, seiches, winds, and low atmospheric pressure has the potential to cause a significant elevation in sea level, resulting in a locally recognized surge referred to as “acqua alta”.

The storm surges in the Northern Adriatic Sea are mainly related to the Sirocco and secondly to the Bora due to their different fetches. Considering the beach of Lignano, the fetch of the Bora is around 50 km while the Sirocco acts along the entire Adriatic basin for around 800 km, being able to produce greater and more persistent storm surges at the end of the basin [54].

Extreme storm events in the northern Adriatic have been the subject of multiple studies, most of which are associated with the city of Venice due to its important artistic and cultural heritage. The major extreme events were recorded between late October and December (1966, 1979, 2018, and 2019), while the 1986 event occurred in February [55]. Cavaleri et al. [56] studied the event of 29 October 2018, identifying extreme storm surge values above 150 cm, limited by the out-of-phase astronomical tide, and assuming that much more catastrophic consequences would occur in the case of concomitant in-phase factors. Moreover, the authors observed a significant increase in the nearshore sea level associated with the wave set-up and surface wind stress, caused by the progressive decrease in depth shoreward. Ferrarin et al. [57] analyzed the meteorological characteristics of the November 2019 event, comparing it with previous extreme events in 1966, 1979, and 2018. Unlike previous events, characterized by high storm surges associated with a low astronomical tidal range, the 2019 event showed how the in-phase concomitance of even non-extreme factors can lead to an exceptional rise in sea level. Mel et al. [58] analyzed the event at the end of November 2022, associated with a persistent low pressure over central Italy which generated both Sirocco winds along the Adriatic and Bora winds over the northern Adriatic, causing storm surges of 173 cm (refer to the Punta della Salute gauge datum, ZMPS) and wave heights of up to 4.5 m at the CNR platform, located 12 m offshore from the Venice lagoon.

The barrier islands of the adjacent Marano and Grado lagoon were also affected by such extreme events, and were frequently overwashed and breached with the formation of multiple washover fans [59].

2.2. Creation of the Dataset

The dataset creation constitutes the initial step and is essential for training the Convolutional Neural Network (CNN). This task is typically performed manually by the research team. In our case, we tested the system using two different datasets of images during significant meteorological events. In each frame, a value was assigned based on the real data recorded during the event from the tide gauge sensors. Starting from the historical data that were acquired, the overall range of tidal values in the considered area is divided into intervals, with each representing a membership class. The amplitude value must be as representative as possible of the event type to consider the excursion values of the

site. For site 1, a minimum value of -81.4 cm and a maximum value of 89.9 cm were considered, while for site 2, a minimum value of -20 cm and a maximum value of 145 cm were considered. The image datasets were split into groups based on the membership class of the corresponding tidal value. To address class imbalances (Figure 2), a function was implemented to calculate the respective weights for each class. These weights were then converted into a dictionary where the keys represent the unique classes in the training data and the values correspond to the class weights. This approach helps prevent the model from being overly influenced by more represented classes at the expense of less represented ones. The characteristics of each dataset are listed in Table 1.

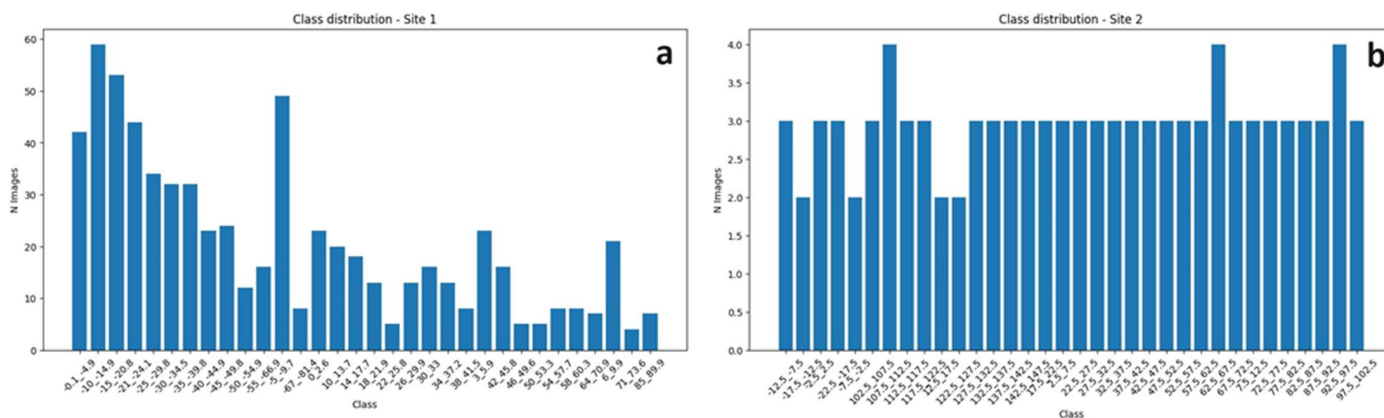


Figure 2. Dataset class distribution: (a) Santa Lucia; (b) Lignano Sabbiadoro.

Since there were no sensors at the specific sites, the nearest ones were used, and all corrections for tidal lag were applied: in the case of Santa Lucia, Capo Passero’s (SR) tide gauge was used, while Trieste’s tide gauge was used for Lignano. For Santa Lucia, the images of the impact of the cyclone Helios (8–11 February 2023) were analyzed (Figure 3a). In the case of Lignano, a severe storm surge that occurred between 21 November and 23 November 2022 was analyzed (Figure 3b).

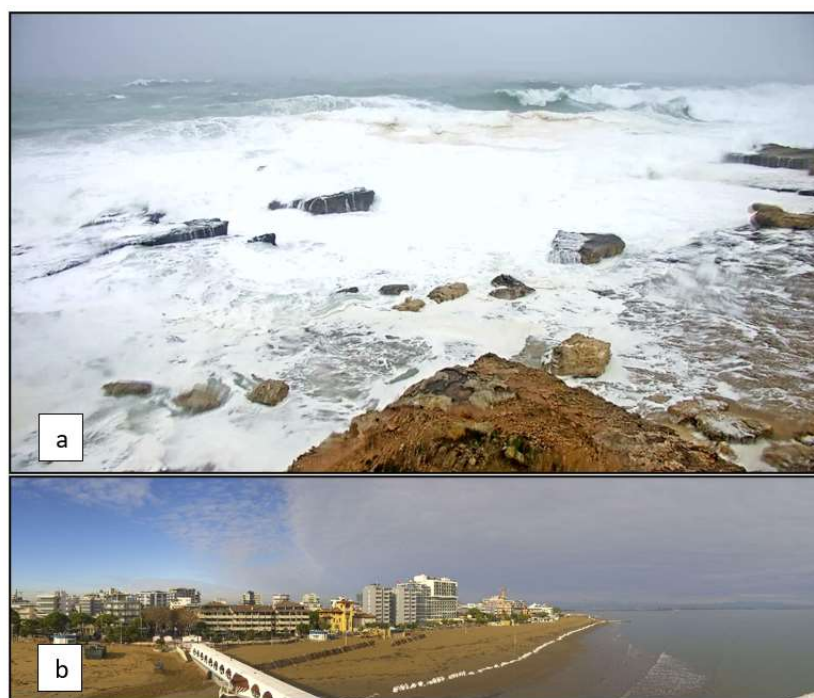


Figure 3. Images extracted from the surveillance cameras in the following areas: (a) Santa Lucia; (b) Lignano Sabbiadoro.

Table 1. Dataset and site information.

Name Dataset	Basement	N° Imgs	Train	Test	N° Classes	Site	Coordinates UTM Wgs84
Santa Lucia	Rock	3.266	2.605	661	32	Santa Lucia (SR), Italy	37°02′03.19″ N 15°18′54.41″ E
Lignano	Sand	430	248	101	34	Lignano Sabbiadoro (UD), Italy	45°41′18.36″ N 13°08′51.08″ E

2.3. Installation and Requirements

It is necessary to set up the entire script by creating an environment with the necessary and suitable requirements for its proper functioning. The open-source TensorFlow 2 library was used for model training [60]. For convenience and to ensure a better performance, we proceeded to install the system on the Google Collaboratory platform, which temporarily provides high-performance workstations [61].

In our case, the features provided by the Google Colab workstation were as follows:

- CPU: Intel Xeon 2.00 GHz (×2)
- GPU: NVIDIA Tesla T4 16 GB
- Driver Version: 525.85.12
- CUDA Version: 12.0
- RAM: 12.7 GB

2.4. Training Model Process and Testing

We opted for the Inception v3 model as our foundation, a convolutional neural network specifically designed for image analysis and object detection [35]. Originally developed as a module for GoogLeNet, it is the third iteration of Google’s Inception Convolutional Neural Network. Similar to how ImageNet serves as a classified visual object database [62], Inception assists in object classification within the realm of computer vision. The Inception v3 architecture has found widespread use across various applications [63], and is frequently employed in a “pre-trained” state from ImageNet. One notable application lies within the life sciences field, where it contributes to leukemia research [64–66].

The next step involves training our dataset to enable the system to recognize high tides based on previously organized classes. The images were automatically resized to a dimension of 224 × 224 pixels, and augmentation techniques, including rescale, horizontal and vertical flip, width and height shift, and zoom, were applied. The duration of the computational processes relies on several factors, chiefly the computational capacity. Given that the training of models encompasses CNN and image processing procedures, substantial resource utilization is expected, particularly involving the CPU, GPU, and RAM. We delegated the training to the GPU instead of the CPU, which has specialized functional units such as the ‘tensor core’ and parallel computing, thereby speeding up processing times [67]. The configuration of hyperparameters represents the second factor affecting both the time required and the accuracy achieved by the trained model [68]. Hyperparameters in a deep learning model are not learned directly through the training process; instead, they are selected manually by the user or through automated hyperparameter search techniques. These parameters play a pivotal role in controlling the model’s behavior during training and influencing its generalization capabilities. Examples of hyperparameters include the learning rate, the number of epochs, and the batch size.

Optimal hyperparameter selection is essential to ensure a deep learning model achieves strong generalization capabilities without succumbing to issues like overfitting or underfitting [69]. The hyperparameters used were chosen after repeated fine-tuning and they are as follows: batch Size = 8, Starting LR = 0.003, Epochs = 35.

Image analysis follows a step-by-step procedure incorporating three layers: convolutional layers, pooling layers, and fully connected layers. Two-dimensional convolutional layers are employed to process two-dimensional signals, like images. These layers apply

a convolution kernel to the image, executing convolutions at each position between the kernel and the corresponding image segment. The kernel then shifts by a set number of pixels, referred to as the stride. It is important to consider the stride value, as a small stride can lead to redundant information. To control the output size, zero padding is introduced, which adds a border of zeros (of size l) around the image. The convolutional operations are complemented by an activation function known as the Rectified Linear Unit (ReLU), which is typically applied as an activation layer. This is a common activation function in deep learning neural networks that introduces non-linearity, facilitating the learning of complex models. The advantages of ReLU include its simplicity and computational efficiency, its ability to mitigate the vanishing gradient problem in deep neural networks, and the promotion of sparsity in the representation of outputs, which can be beneficial in certain contexts [70].

Moreover, to normalize each activation across different channels, a cross-channel normalization operation was employed. It improves model performance by ensuring a consistent scale of features, expediting convergence during training, enhancing stability, and acting as an implicit regularization. This process contributes to more efficient and robust model learning [71]. The CNN architecture also incorporates pooling layers, which serve to reduce the dimensionality of the input by subsampling, either through mean-pooling or max-pooling applied to patches of the image. Much like convolutional layers and pooling layers, these work on different parts of the image and incorporate a stride parameter. In the context of this specific deep learning network, 2D max-pooling layers were employed, extracting the maximum values from within the patches [72]. To handle inputs with the same height and width, depth concatenation layers were employed, which concatenate the inputs along the third dimension, representing the channels. The CNN concludes with a fully connected layer, establishing connections between each element of the preceding layer and every element within the softmax layer. The softmax layer, which estimates relative probabilities, is instrumental in determining the ultimate and most probable value. The structural framework of the deep neural network is crafted around Inception modules [33].

The Inception V3 model was trained using a deep learning technique called “transfer learning” [73]. This involves using a pre-trained deep learning model on a large dataset and updating the last layers of the model on a specific dataset of interest [74]. This approach allows the knowledge gained during the pre-training of the model to improve the model’s ability to generalize to new data [75]. These modules enable the network to select from various convolutional filter sizes within each block, enhancing its flexibility and adaptability.

The original architecture of Inception v3 was modified to tailor it to this application; the last layer was removed, and a Global Average 2D pooling layer was implemented to allow the CNN to better adapt to the specific case study. This is a special layer employed in Convolutional Neural Networks to compress the input tensor space. Unlike traditional pooling layers with fixed-size windows, Global Average Pooling calculates the average of all values in the feature map, generating a single mean value for each channel. This process reduces the spatial dimensions of the feature map while preserving crucial information about the features. The use of this layer is often considered to reduce the number of parameters in the model, prevent overfitting, and improve generalization. Additionally, it makes the network less sensitive to variations in the position and size of objects in images. Our modified architecture has 313 layers, of which 184 are trainable.

During the training process, the CNN was trained using 70% of the available images for training purposes and the remaining 30% for validation, which is considered by the literature as the optimal partition of the dataset for training these types of CNNs [35,76].

Figure 4 shows the training curves for the model in both case studies.

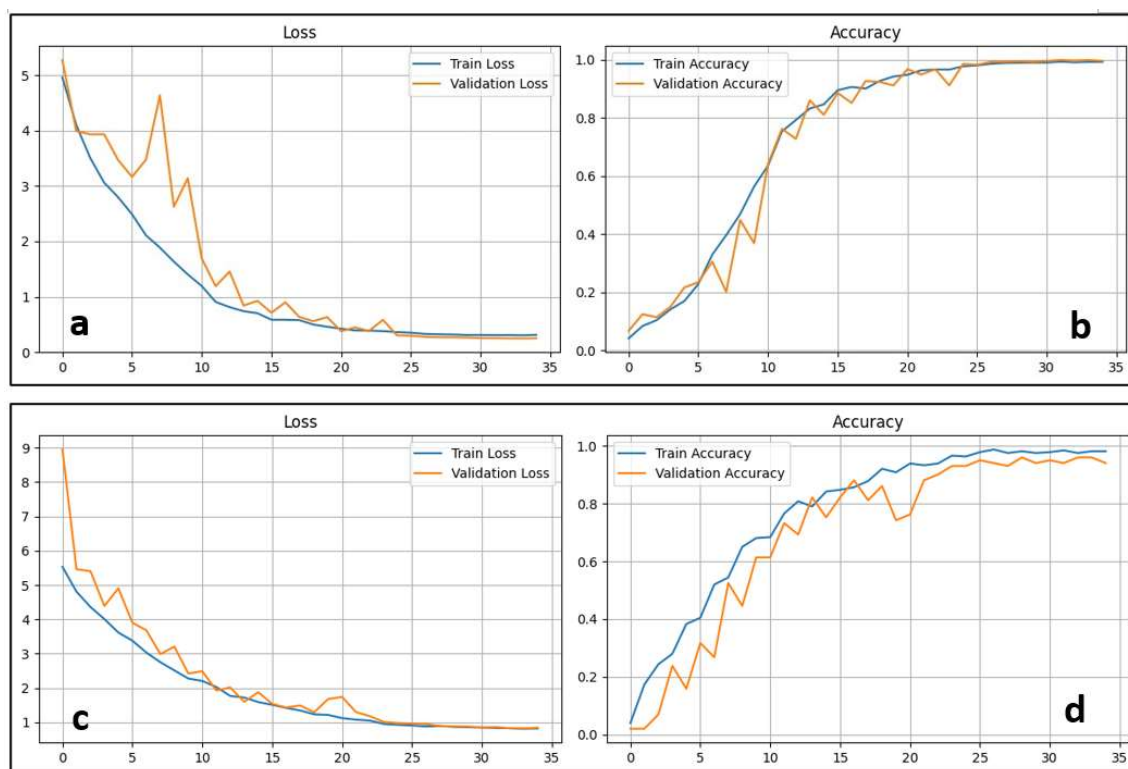


Figure 4. Training curves produced by machine learning model: (a) loss values for Santa Lucia; (b) accuracy values for Santa Lucia; (c) loss values for Lignano Sabbiadoro; (d) accuracy values for Lignano Sabbiadoro.

3. Results and Discussion

The CNN outputs deliver the probabilities corresponding to tide classes linked to a specific video frame captured by the webcams. In Figure 5a,b, the probabilities of tide classes related to a given image are illustrated. To depict tide phases across a continuous temporal spectrum, various snapshots were automatically extracted from the video recordings, with tide classes assigned to each image. The CNN achieved an accuracy exceeding 90%, and the Categorical Cross-Entropy Loss function yielded a value below 1 at the conclusion of the iterations. Detailed results can be found in Table 2. The evaluation of the CNN output metrics involved the examination of the confusion matrix (depicted in Figure 6a,b), which illustrates the relationship between predicted classes (CNN output) and true classes (spatial reference from field surveys). The confusion matrix stands as a commonly employed metric in the domain of classification problem-solving. Its versatility extends to both binary and multiclass classification scenarios. This matrix furnishes a tabulated representation of counts stemming from predicted and actual values [77].

Table 2. Results from training.

Location	Accuracy	Loss
Santa Lucia	99.55%	0.25
Lignano	94.06%	0.88

As tide classes are mutually exclusive and encompass all potential tide phases, the most probable predicted class was chosen as a dependable representation of tide values. It is worth noting that during storms and medicanes, exceptional values may arise, wherein predicted classes may be linked to higher values than those typically associated with common tide phases.

In addition to considering the accuracy and loss metrics mentioned above, F1 scores in the various classes are presented below for a deeper understanding of the performance of the CNN model. The F1 score combines accuracy and recall through its harmonic mean and offers insight into the model's effectiveness in handling class imbalances [78].

In both cases, the obtained weighted average is significantly higher, over 90%, indicating a good overall performance for all classes.

In particular, for the Santa Lucia site, the F1 scores show a weighted average of 0.9955. Most of the classes in this series achieve perfect scores (1.0). There is a slight decrease in the F1 score for class 2 (0.9709) and class 20 (0.9286). Although these scores are slightly lower than the results obtained by the other classes, they are still considered good and indicate the substantial ability of the model to correctly classify images belonging to the respective classes.

For the Lignano site, the weighted average is 0.9339. Specifically, classes 0 and 9 show lower F1 scores (0.5), suggesting difficulty in accurately predicting these particular tidal classes. This could be attributed to their limited representation in the training data. In contrast, many other classes, such as 2, 4, 5, and 6, achieve perfect scores (1.0), highlighting the excellent performance of the model within these tidal classes. Other classes, such as 1, 3, 24, 25, and 27, show moderate F1 scores ranging from (0.8 to 0.8571), indicating areas where improvements can be made.

Overall, the F1 scores for both sites demonstrate the effectiveness of the model in accurately classifying tidal heights into different categories, revealing areas of strength and scope for additional improvement.

The widespread use of deep learning models integrated with monitoring sensors, and they are becoming a low-cost tool for engineering and oceanographic studies [4,79–81]. On the other hand, using surveillance cameras allows for an increase in the density of data in coastal areas without monitoring stations. Remote sensing data combined with machine learning models have usually been applied to obtain physical features of the coastal areas, like water depth [82,83], storm surge [10,11,84], and hydrological parameters [85]. To date, few studies have focused on the assessment of meteo-marine parameters through deep learning and video monitoring [86–88]. Here, classification techniques using the Inception V3 model allowed us to obtain new observations of tide phases characterizing sandy and rocky coasts.

In summary, the outcomes of the study are influenced by factors such as image quality and landscape complexity. Convolutional neural networks (CNNs) have shown impressive effectiveness in classifying data across diverse applications, but it is important to note that using CNNs requires substantial computational resources. However, the advantages include the high precision in image classification, demonstrated by the elevated F1 scores at specific sites. The efficiency of CNNs is notable due to their parallel processing, making them suitable for large datasets. Additionally, CNNs automate image identification and classification, reducing the need for human intervention, and their customization feature allows for adaptation to specific application requirements through fine-tuning with representative image data.

However, from the evidence, it can be concluded that training the model is sufficient to implement and correlate it to the new environment. Training is necessary only once, after which it will be possible to perform classification of all the images that are inserted to recognize the tide height.

Using a temporal denomination for the images, it is possible to recreate the time-sheet of the extreme event to provide a better understanding of its temporal progression (Figure 7) and also for potential comparison with real data. Regarding Lignano, the images do not

cover the entire 24 h period as the camera does not record during the night. One of the benefits of using systems like this is that they can reduce the workload of the operator, who has to manually analyze and view the images, and obtain almost instantaneous results. This approach could be relevant for the study of extreme events and for measuring hydrodynamic parameters in order to model the high frequency in the coastal dynamic. Similar approaches to the high-frequency dynamic are also applied to predict coastal changes, like shoreline movements [89], sea surface temperature changes [90], and tropical cyclone forecasting [91,92].

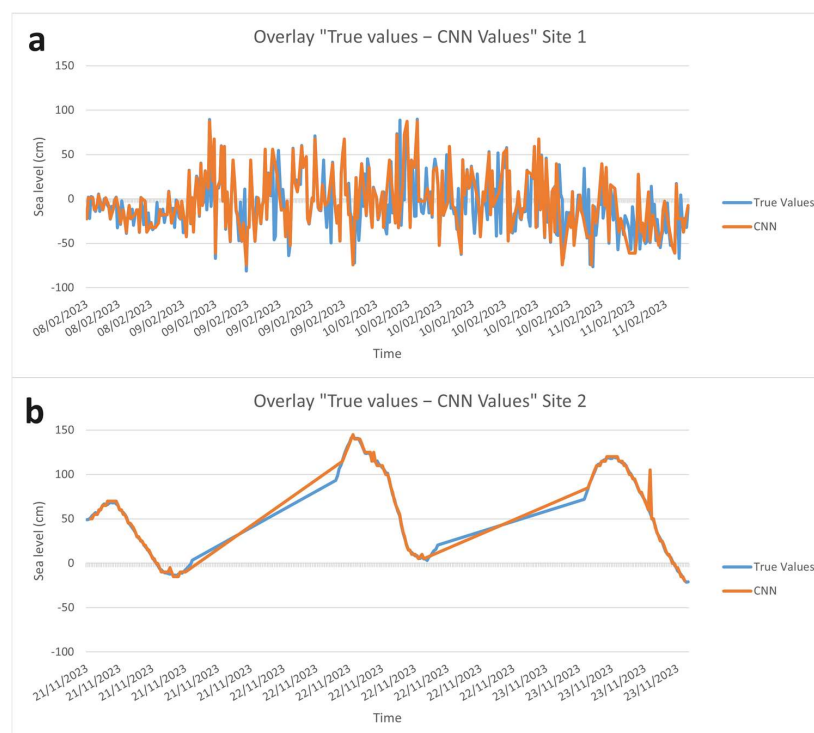


Figure 7. Comparison between extracted tide values using CNN and observed values through tide gauge from different locations (a) Santa Lucia and (b) Lignano Sabbiadoro.

The field of application is diverse and could be of interest for those institutions that deal with the research and monitoring of beaches. Classification techniques could be integrated with segmentation techniques for beach monitoring [93–95] in order to obtain a reliable assessment of sedimentary balance.

4. Conclusions

In this study, we introduced a deep learning-based system for the automatic measurement and classification of tides in surveillance camera images. Deep learning techniques offer a cost-effective solution for coastal monitoring by increasing the availability of data that are sparsely distributed along coastlines. Furthermore, video footage serves as a valuable resource for gaining insights into high-energy occurrences, exemplified by the impact of Helios in southeastern Sicily in February 2023. Leveraging convolutional neural networks (CNN) in these scenarios enables the evaluation of hydrodynamic characteristics such as storm surge, which are challenging to assess in the field during actual events.

Accumulating a significant volume of data is essential for the development of prediction models that forecast the intensity of future extreme marine events. The application of deep learning in coastal monitoring facilitates the expansion of available datasets, thus proving valuable in this context.

The findings suggest that, even with a limited test dataset, the algorithm is capable of accurately recognizing the value of the tide or the relative surge during extreme events. The

trained models achieved accuracy values exceeding 90% and a loss below 1. The generated confusion matrices also exhibited excellent results, with predicted values rarely deviating from the reference diagonal. Furthermore, by comparing the time-series of actual values with those predicted by the CNN for the two intense weather events, it is evident that the curves follow very similar patterns.

The precision of the outcomes relies on multiple factors, encompassing image quality and the intricacy of objects within the images. Overall, convolutional neural networks have proven highly effective in tasks involving classification and measurement across diverse applications. The incorporation of deep learning technology could yield even more advantages. Introducing such a system would offer the chance to receive instantaneous feedback on the consequences of atmospheric events in real-time. In addition, it would empower remote analysis, eliminating the necessity of in-person visits. This not only addresses logistical challenges but also facilitates the establishment of comprehensive databases of information. Utilizing systems like this could also alleviate the workload of operators who would otherwise need to manually analyze and review images, enabling almost instantaneous results.

Author Contributions: G.S. (Gaetano Sabato): conceptualization, methodology, software, validation, data curation, writing—original draft, visualization. G.S. (Giovanni Scardino): conceptualization, methodology, validation and review. A.K.: software, data curation and review. G.C.: data curation, writing. M.C.: methodology, software, writing and review. G.F.: writing and review, conceptualization and founding. S.F.: data curation, writing. A.L.: methodology, software, validation and review. S.S.: data curation. G.S. (Giovanni Scicchitano): conceptualization, review, supervision, validation and founding. All authors have read and agreed to the published version of the manuscript.

Funding: This research has been funded by the PRIN 2022 PNRR project titled “ARCHIMEDE-MultidisciplinARy approaCH to better define vulnerabllity and hazard of MEDicanEs along the Ionian coasts of Sicily” (CUP H53D23011380001, Principal Investigator Prof. G. Scicchitano). Part of this study was funded by the consortium iNEST (Interconnected North-Est Innovation Ecosystem) funded by the European Union Next-GenerationEU (Piano Nazionale di Ripresa e Resilienza (PNRR)-Missione 4 Componente 2, Investimento 473 1.5-D.D. 1058 23/06/2022, ECS_00000043).

Data Availability Statement: Name of the code/library: tide_measurement-using-Mechine-Learning-Model-inception-V3; Contact e-mail and phone number: alok.kushabaha@iusspavia.it/0805442604; Hardware requirements: CPU: Intel Xeon 2.00 GHz (x2), GPU: NVIDIA Tesla T4 16GB, Driver Version: 525.85.12, CUDA Version: 12.0, RAM: 12.7 GB; Program language: Python (3.10 version); Software required: Google Colaboratory, Jupiter Notebook; Program size: 803 MB; The source codes are available for downloading at the link: https://github.com/alokkush2024/tide_measurement-using-Mechine-Learning-Model-inception-V3-/tree/tide_measurement_code (accessed on 9 January 2024).

Acknowledgments: This research is part of the activities conducted under the RIPARTI project, specifically the LEUCOTEIA initiative (CUP: B83C22004070002), led by Giovanni Scicchitano from the Department of Earth and Environmental Sciences at the University of Bari “Aldo Moro”. This research was supported by the Civil Protection of the Autonomous Region of Friuli Venezia Giulia as part of a collaboration with the Department of Mathematics, Informatics, and Geosciences at the University of Trieste.

Conflicts of Interest: The authors declare no conflicts of interest.

References

1. Lee, H.; Calvin, K.; Dasgupta, D.; Krinner, G.; Mukherji, A.; Thorne, P.W.; Trisos, C.; Romero, J.; Aldunce, P.; Barrett, K.; et al. IPCC, 2023: *Climate Change 2023: Synthesis Report. Contribution of Working Groups I, II and III to the Sixth Assessment Report of the Intergovernmental Panel on Climate Change*; Core Writing Team, Lee, H., Romero, J., Eds.; First Intergovernmental Panel on Climate Change (IPCC); IPCC: Geneva, Switzerland, 2023. [CrossRef]
2. Intergovernmental Panel On Climate Change (IPCC). *Climate Change 2022—Impacts, Adaptation and Vulnerability: Working Group II Contribution to the Sixth Assessment Report of the Intergovernmental Panel on Climate Change*, 1st ed.; Cambridge University Press: Cambridge, UK, 2023. [CrossRef]
3. Chaumillon, E.; Bertin, X.; Fortunato, A.B.; Bajo, M.; Schneider, J.; Dezileau, L.; Walsh, J.P.; Michelot, A.; Chauveau, E.; Créach, A.; et al. Storm-induced marine flooding: Lessons from a multidisciplinary approach. *Earth-Sci. Rev.* **2017**, *165*, 151–184. [CrossRef]

4. Jones, O.; Barker, N. Tides, coasts and people: Culture, ecology and sustainability. In *Littoral 2010—Adapting to Global Change at the Coast: Leadership, Innovation, and Investment*; EDP Sciences: Cambridge, UK, 2011. [CrossRef]
5. Bezerra, D.M.M.; Nascimento, D.M.; Ferreira, E.N.; Rocha, P.D.; Mourão, J.S. Influence of tides and winds on fishing techniques and strategies in the Mamanguape River Estuary, Paraíba State, NE Brazil. *An. Acad. Bras. Ciências* **2012**, *84*, 775–788. [CrossRef]
6. Purnaini, R.; Purwono, S. Tidal Influence on water quality of Kapuas Kecil River downstream. *E3S Web Conf.* **2018**, *31*, 04006. [CrossRef]
7. GSGislasson & Associates Ltd. British Columbia Seafood Sector and Tidal Water Recreational Fishing: A Strengths, Weaknesses, Opportunities, and Threats Assessment. Technical Report: British Columbia Canada, 2004. Available online: https://www.for.gov.bc.ca/hfd/library/documents/bib105375_sum.pdf (accessed on 20 January 2024).
8. U.S. Department of Energy, Office of Efficiency & Renewable Energy. Powering the blue economy: Exploring opportunities for marine renewable energy in maritime markets. In *Chapter 4—Offshore Marine Aquaculture*; 2019. Available online: <https://www.energy.gov/sites/prod/files/2019/03/f61/73355.pdf> (accessed on 15 February 2024).
9. Hafner, M.; Luciani, G. (Eds.) *The Palgrave Handbook of International Energy Economics*; Springer International Publishing: Cham, Switzerland, 2022. [CrossRef]
10. Müller, M.; Haak, H.; Jungclaus, J.H.; Sündermann, J.; Thomas, M. The effect of ocean tides on a climate model simulation. *Ocean Model.* **2010**, *35*, 304–313. [CrossRef]
11. Webb, P. Introduction to Oceanography. 2023. Available online: <http://rwu.pressbooks.pub/webboceanography> (accessed on 7 April 2024).
12. Hicks, S.D. Understanding Tides. Technical Report, U.S. Department of Commerce National Oceanic and Atmospheric Administration National Ocean Service, 2006; 66p. Available online: https://tidesandcurrents.noaa.gov/publications/Understanding_Tides_by_Steacy_finalFINAL11_30.pdf (accessed on 15 February 2024).
13. Von Storch, H.; Woth, K. Storm surges: Perspectives and options. *Sustain. Sci.* **2008**, *3*, 33–43. [CrossRef]
14. Bullock, J.A.; Haddow, G.D.; Coppola, D.P. 3-Hazards. In *Homeland Security*, 2nd ed.; Bullock, J.A., Haddow, G.D., Coppola, D.P., Eds.; Butterworth-Heinemann: Oxford, UK, 2018; pp. 45–66. [CrossRef]
15. Oddo, P.; Bonaduce, A.; Pinardi, N.; Guarnieri, A. Sensitivity of the Mediterranean Sea level to atmospheric pressure and free surface elevation numerical formulation in NEMO. *Geosci. Model Dev.* **2014**, *7*, 3001–3015. [CrossRef]
16. Rooney, A. *Hurricane! Nature's Fury E-Book Series*; Britannica Digital Learning: Chicago, IL, USA, 2012; 32p.
17. Idier, D.; Bertin, X.; Thompson, P.; Pickering, M.D. Interactions between mean sea level, tide, surge, waves and flooding: Mechanisms and contributions to sea level variations at the coast. *Surv. Geophys.* **2019**, *40*, 1603–1630. [CrossRef]
18. Miles, T.; Seroka, G.; Glenn, S. Coastal ocean circulation during hurricane Sandy. *J. Geophys. Res. Ocean.* **2017**, *122*, 7095–7114. [CrossRef]
19. Mulligan, R.P.; Walsh, J.P.; Wadman, H.M. Storm surge and surface waves in a shallow lagoonal estuary during the crossing of a hurricane. *J. Waterw. Port Coast. Ocean Eng.* **2015**, *141*, A5014001. [CrossRef]
20. Ren, H.; Dudhia, J.; Li, H. The size characteristics and physical explanation for the radius of maximum wind of hurricanes. *Atmos. Res.* **2022**, *277*, 106313. [CrossRef]
21. Nott, J. *Extreme Events: A Physical Reconstruction and Risk Assessment*; Cambridge University Press: Cambridge, UK, 2006.
22. Shinde, P.P.; Shah, S. A Review of Machine Learning and Deep Learning Applications. In Proceedings of the 2018 Fourth International Conference on Computing Communication Control and Automation (ICCCUBEA), Pune, India, 16–18 August 2018; pp. 1–6. [CrossRef]
23. Ongsulee, P. Artificial intelligence, machine learning and deep learning. In Proceedings of the 15th International Conference on ICT and Knowledge Engineering (ICT&KE), Bangkok, Thailand, 22–24 November 2017. [CrossRef]
24. Pourzangbar, A.; Jalali, M.; Brocchini, M. Machine learning application in modelling marine and coastal phenomena: A critical review. *Front. Environ. Eng.* **2023**, *2*, 1235557. [CrossRef]
25. Moksness, E.; Dahl, E.; Støttrup, J. *Integrated Coastal Zone Management*; John Wiley & Sons: Hoboken, NJ, USA, 2009. [CrossRef]
26. Northrop, E.; Schuhmann, P.; Burke, L.; Fyall, A.; Alvarez, S.; Spenceley, A.; Becken, S.; Kato, K.; Roy, J.; Some, S.; et al. Opportunities for Transforming Coastal and Marine Tourism—Towards Sustainability, Regeneration and Resilience. Technical Report Commissioned by High Level Panel for a Sustainable Ocean Economy (Oceanpanel.org), 2022; 135p. Available online: https://oceanpanel.org/wp-content/uploads/2022/06/22_REP_HLP-Tourism_v6.pdf (accessed on 6 January 2024).
27. Choung, Y.-J.; Jung, D. Comparison of machine and deep learning methods for mapping sea farms using high-resolution satellite image. *J. Coast. Res.* **2021**, *114*, 420–423. [CrossRef]
28. Scardino, G.; Scicchitano, G.; Chirivì, M.; Costa, P.J.M.; Luparelli, A.; Mastronuzzi, G. Convolutional neural network and optical flow for the assessment of wave and tide parameters from video analysis (LEUCOTE): An innovative tool for coastal monitoring. *Remote Sens.* **2022**, *14*, 2994. [CrossRef]
29. Tsiakos, C.-A.D.; Chalkias, C. Use of machine learning and remote sensing techniques for shoreline monitoring: A review of recent literature. *Appl. Sci.* **2023**, *13*, 3268. [CrossRef]
30. Dang, K.B.; Dang, V.B.; Ngo, V.L.; Vu, K.C.; Nguyen, H.; Nguyen, D.A.; Nguyen, T.D.L.; Pham, T.P.N.; Giang, T.L.; Nguyen, H.D.; et al. Application of deep learning models to detect coastlines and shorelines. *J. Environ. Manag.* **2022**, *320*, 115732. [CrossRef]
31. Merz, B.; Kuhlicke, C.; Kunz, M.; Pittore, M.; Babeyko, A.; Bresch, D.N.; Domeisen, D.I.V.; Feser, F.; Koszalka, I.; Kreibich, H.; et al. Impact forecasting to support emergency management of natural hazards. *Rev. Geophys.* **2020**, *58*, e2020RG000704. [CrossRef]

32. Meli, M.; Olivieri, M.; Romagnoli, C. Sea-level change along the Emilia-Romagna coast from tide gauge and satellite altimetry. *Remote Sens.* **2020**, *13*, 97. [CrossRef]
33. Szegedy, C.; Liu, W.; Jia, Y.; Sermanet, P.; Reed, S.; Anguelov, D.; Erhan, D.; Vanhoucke, V.; Rabinovich, A. Going deeper with convolutions. *arXiv* **2014**, arXiv:1409.4842.
34. Ozgur, C.; Colliau, T.; Rogers, G.; Hughes, Z. MatLab vs. Python vs. R. *J. Data Sci.* **2021**, *15*, 355–372. [CrossRef]
35. Szegedy, C.; Vanhoucke, V.; Ioffe, S.; Shlens, J.; Wojna, Z. Rethinking the inception architecture for computer vision. *arXiv* **2015**, arXiv:1512.00567.
36. Pytharouli, S.; Chaikalis, S.; Stiros, S.C. Uncertainty and bias in electronic tide-gauge records: Evidence from collocated sensors. *Measurement* **2018**, *125*, 496–508. [CrossRef]
37. Ganti, V.; Gehrke, J.; Ramakrishnan, R. Mining very large databases. *Computer* **1999**, *32*, 38–45. [CrossRef]
38. Anzidei, M.; Scicchitano, G.; Scardino, G.; Bignami, C.; Tolomei, C.; Vecchio, A.; Serpelloni, E.; De Santis, V.; Monaco, C.; Milella, M.; et al. Relative sea-level rise scenario for 2100 along the coast of South Eastern Sicily (Italy) by InSAR data, satellite images and high-resolution topography. *Remote Sens.* **2021**, *13*, 1108. [CrossRef]
39. Anzidei, M.; Scicchitano, G.; Tarascio, S.; De Guidi, G.; Monaco, C.; Barreca, G.; Mazza, G.; Serpelloni, E.; Vecchio, A. Coastal retreat and marine flooding scenario for 2100: A case study along the coast of Maddalena peninsula (Southeastern Sicily). *Geogr. Fis. Din. Quat.* **2018**, *41*, 5–16.
40. Scicchitano, G.; Pignatelli, C.; Spampinato, C.R.; Piscitelli, A.; Milella, M.; Monaco, C.; Mastronuzzi, G. Terrestrial laser scanner techniques in the assessment of tsunami impact on the Maddalena peninsula (South-Eastern Sicily, Italy). *Earth Planets Space* **2012**, *64*, 8. [CrossRef]
41. Nandasena, N.A.K.; Scicchitano, G.; Scardino, G.; Milella, M.; Piscitelli, A.; Mastronuzzi, G. Boulder displacements along rocky coasts: A new deterministic and theoretical approach to improve incipient motion formulas. *Geomorphology* **2022**, *407*, 108217. [CrossRef]
42. Scardino, G.; Rizzo, A.; De Santis, V.; Kyriakoudi, D.; Rovere, A.; Vacchi, M.; Torrisi, S.; Scicchitano, G. Insights on the origin of multiple tsunami events affected the archaeological site of Ognina (South-Eastern Sicily, Italy). *Quat. Int.* **2022**, *638–639*, 122–139. [CrossRef]
43. De Martini, P.M.; Barbano, M.S.; Smedile, A.; Gerardi, F.; Pantosti, D.; Del Carlo, P.; Pirrotta, C. A unique 4000 year long geological record of multiple tsunami inundations in the Augusta bay (Eastern Sicily, Italy). *Mar. Geol.* **2010**, *276*, 42–57. [CrossRef]
44. De Martini, P.M.; Barbano, M.S.; Pantosti, D.; Smedile, A.; Pirrotta, C.; Del Carlo, P.; Pinzi, S. Geological evidence for paleotsunamis along eastern Sicily (Italy): An Overview. *Nat. Hazards Earth Syst. Sci.* **2012**, *12*, 2569–2580. [CrossRef]
45. D’Adderio, L.P.; Panegrossi, G.; Dafis, S.; Rysman, J.-F.; Casella, D.; Sanò, P.; Fucello, A.; Miglietta, M.M. Helios and Juliette: Two falsely acclaimed medicanes. *Preprint* **2023**. [CrossRef]
46. Bentley, A.M.; Keyser, D.; Bosart, L.F. A dynamically based climatology of subtropical cyclones that undergo tropical transition in the North Atlantic basin. *Mon. Weather. Rev.* **2016**, *144*, 2049–2068. [CrossRef]
47. Flaounas, E.; Davolio, S.; Raveh-Rubin, S.; Pantillon, F.; Miglietta, M.M.; Gaertner, M.A.; Hatzaki, M.; Homar, V.; Khodayar, S.; Korres, G.; et al. Mediterranean cyclones: Current knowledge and open questions on dynamics, prediction, climatology and impacts. *Weather Clim. Dyn.* **2022**, *3*, 173–208. [CrossRef]
48. Romera, R.; Gaertner, M.A.; Sánchez, E.; Domínguez, M.; González-Alemán, J.J.; Miglietta, M.M. Climate change projections of medicanes with a large multi-model ensemble of regional climate models. *Glob. Planet. Chang.* **2017**, *151*, 134–143. [CrossRef]
49. Fontolan, G.; Bratus, A.; Bieker, F.; Colombetta, L.; Gallitelli, D.; Lipizer, M.; Sgambati, F.; Bezzi, A.; Casagrande, G.; Fracaros, S.; et al. Piano Coste—Accordo attuativo di collaborazione per lo studio e monitoraggio morfo-sedimentologico dello stato dei litorali della regione Friuli Venezia Giulia finalizzato alla gestione integrata della zona costiera in applicazione alla convenzione quadro tra la Regione Autonoma Friuli Venezia Giulia e l’Università degli Studi di Trieste (DGR 264/2014). 2023. Unpublished Technical Report.
50. Petti, M.; Pascolo, S.; Bosa, S.; Busetto, N. The tidal prism as a dynamic response of a nonlinear harmonic system. *Phys. Fluids* **2023**, *35*, 017124. [CrossRef]
51. Dorigo. La Laguna di Grado e le sue foci. Ricerche e rilievi idrografici. *Uff. Idrogr. Del Magistr. Alle Acque* **1965**, *155*, 231.
52. Bezzi, A.; Pillon, S.; Martinucci, D.; Fontolan, G. Inventory and conservation assessment for the management of coastal dunes, Veneto coasts, Italy. *J. Coast. Conserv.* **2018**, *22*, 503–518. [CrossRef]
53. Regione Autonoma Friuli Venezia Giulia. Piano Regolatore Portuale Del Porto Di Monfalcone Variante Localizzata. Studio Meteomarinario. Progettisti: Modimar, SJS Engineering, Archest. Technical Report, 2019. Available online: https://www.regione.fvg.it/rafvfg/export/sites/default/RAFVG/ambiente-territorio/pianificazione-gestione territorio/FOGLIA9/allegati/Allegato_33_alla_Delibera_2066-2019.pdf (accessed on 26 November 2023).
54. Lionello, P.; Cavaleri, L.; Nissen, K.M.; Pino, C.; Raicich, F.; Ulbrich, U. Severe marine storms in the northern Adriatic: Characteristics and trends. *Phys. Chem. Earth Parts A/B/C* **2012**, *40–41*, 93–105. [CrossRef]
55. Umgiesser, G.; Bajo, M.; Ferrarin, C.; Cucco, A.; Lionello, P.; Zanchettin, D.; Papa, A.; Tosoni, A.; Ferla, M.; Coraci, E.; et al. The prediction of floods in Venice: Methods, models and uncertainty (review article). *Nat. Hazards Earth Syst. Sci.* **2021**, *21*, 2679–2704. [CrossRef]

56. Cavaleri, L.; Bajo, M.; Barbariol, F.; Bastianini, M.; Benetazzo, A.; Bertotti, L.; Chiggiato, J.; Davolio, S.; Ferrarin, C.; Magnusson, L.; et al. The October 29, 2018 storm in Northern Italy—An exceptional event and its modeling. *Prog. Oceanogr.* **2019**, *178*, 102178. [[CrossRef](#)]
57. Ferrarin, C.; Bajo, M.; Benetazzo, A.; Cavaleri, L.; Chiggiato, J.; Davison, S.; Davolio, S.; Lionello, P.; Orlić, M.; Umgiesser, G. Local and large-scale controls of the exceptional Venice floods of November 2019. *Prog. Oceanogr.* **2021**, *197*, 102628. [[CrossRef](#)]
58. Mel, R.A.; Coraci, E.; Morucci, S.; Crosato, F.; Cornello, M.; Casaioli, M.; Mariani, S.; Carniello, L.; Papa, A.; Bonometto, A.; et al. Insights on the extreme storm surge event of the 22 November 2022 in the Venice Lagoon. *J. Mar. Sci. Eng.* **2023**, *11*, 1750. [[CrossRef](#)]
59. Casagrande, G.; Bezzi, A.; Fracaros, S.; Martinucci, D.; Pillon, S.; Salvador, P.; Sponza, S.; Fontolan, G. Quantifying transgressive coastal changes using UAVs: Dune migration, overwash recovery, and barrier flooding assessment and interferences with human and natural assets. *J. Mar. Sci. Eng.* **2023**, *11*, 1044. [[CrossRef](#)]
60. Abadi, M.; Agarwal, A.; Barham, P.; Brevdo, E.; Chen, Z.; Citro, C.; Corrado, G.S.; Davis, A.; Dean, J.; Devin, M.; et al. TensorFlow: Large-Scale Machine Learning on Heterogeneous Distributed Systems. 2015. Available online: <http://download.tensorflow.org/paper/whitepaper2015.pdf> (accessed on 5 March 2024).
61. Carneiro, T.; Medeiros Da Nóbrega, R.V.; Nepomuceno, T.; Bian, G.-B.; De Albuquerque, V.H.C.; Filho, P.P.R. Performance analysis of google laboratory as a tool for accelerating deep learning applications. *IEEE Access* **2018**, *6*, 61677–61685. [[CrossRef](#)]
62. Yu, Z.; Dong, Y.; Cheng, J.; Sun, M.; Su, F. Research on face recognition classification based on improved GoogleNet. *Secur. Commun. Netw.* **2022**, *2022*, 7192306. [[CrossRef](#)]
63. Warkar, K.V.; Pandey, A.B. A survey on multiclass image classification based on Inception-v3 transfer learning model. *Int. J. Res. Appl. Sci. Eng. Technol.* **2021**, *9*, 169–172. [[CrossRef](#)]
64. Anilkumar, K.K.; Manoj, V.J.; Sagi, T.M. Automated detection of leukemia by pretrained deep neural networks and transfer learning: A comparison. *Med. Eng. Phys.* **2021**, *98*, 8–19. [[CrossRef](#)]
65. Mulya, R.F.; Utami, E.; Ariatmanto, D. Classification of acute lymphoblastic leukemia based on white blood cell images using inceptionv3 model. *J. RESTI (Rekayasa Sist. Dan Teknol. Inf.)* **2023**, *7*, 947–952. [[CrossRef](#)]
66. Ramaneswaran, S.; Srinivasan, K.; Vincent, P.M.D.R.; Chang, C.-Y. Hybrid Inception v3 XGBoost model for acute lymphoblastic leukemia classification. *Comput. Math. Methods Med.* **2021**, *2021*, 2577375. [[CrossRef](#)]
67. Raihan, M.A.; Goli, N.; Aamodt, T. Modeling deep learning accelerator enabled GPUs. IEEE International Symposium on Performance Analysis of Systems and Software (ISPASS). *arXiv* **2019**, arXiv:1811.08309.
68. Yang, L.; Shami, A. On hyperparameter optimization of machine learning algorithms: Theory and practice. *Neurocomputing* **2020**, *415*, 295–316. [[CrossRef](#)]
69. Zhang, H.; Zhang, L.; Jiang, Y. Overfitting and underfitting analysis for deep learning based end-to-end communication systems. In Proceedings of the 11th International Conference on Wireless Communications and Signal Processing (WCSP), Xi'an, China, 23–25 October 2019; pp. 1–6. [[CrossRef](#)]
70. Agarap, A.F. Deep learning using rectified linear units (ReLU). *arXiv* **2019**, arXiv:1803.08375.
71. Shanker, M.; Hu, M.Y.; Hung, M.S. Effect of data standardization on neural network training. *Omega* **1996**, *24*, 385–397. [[CrossRef](#)]
72. Gholamalinezhad, H.; Khosravi, H. Pooling methods in deep neural networks, a review. *arXiv* **2020**, arXiv:2009.07485.
73. Han, D.; Liu, Q.; Fan, W. A new image classification method using CNN transfer learning and web data augmentation. *Expert Syst. Appl.* **2018**, *95*, 43–56. [[CrossRef](#)]
74. Zhuang, F.; Qi, Z.; Duan, K.; Xi, D.; Zhu, Y.; Zhu, H.; Xiong, H.; He, Q. A comprehensive survey on transfer learning. *arXiv* **2020**, arXiv:1911.02685.
75. Shin, H.-C.; Roth, H.R.; Gao, M.; Lu, L.; Xu, Z.; Nogues, I.; Yao, J.; Mollura, D.; Summers, R.M. Deep convolutional neural networks for computer-aided detection: CNN architectures, dataset characteristics and transfer learning. *IEEE Trans. Med. Imaging* **2016**, *35*, 1285–1298. [[CrossRef](#)]
76. Götz, T.I.; Göb, S.; Sawant, S.; Erick, X.F.; Wittenberg, T.; Schmidkonz, C.; Tomé, A.M.; Lang, E.W.; Ramming, A. Number of necessary training examples for neural networks with different number of trainable parameters. *J. Pathol. Inform.* **2022**, *13*, 100114. [[CrossRef](#)]
77. Kulkarni, A.; Chong, D.; Batarseh, F.A. 5-Foundations of data imbalance and solutions for a data democracy. In *Data Democracy. At the Nexus of Artificial Intelligence, Software Development, and Knowledge Engineering*; Batarseh, F.A., Yang, R., Eds.; Academic Press: Cambridge, MA, USA, 2020; pp. 83–106. [[CrossRef](#)]
78. Huang, H.; Xu, H.; Wang, X.; Silamu, W. Maximum F1-score discriminative training criterion for automatic mispronunciation detection. *IEEE/ACM Trans. Audio Speech Lang. Process.* **2015**, *23*, 787–797. [[CrossRef](#)]
79. Yin, L.; Wang, L.; Li, T.; Lu, S.; Tian, J.; Yin, Z.; Li, X.; Zheng, W. U-Net-LSTM: Time Series-Enhanced Lake Boundary Prediction Model. *Land* **2023**, *12*, 1859. [[CrossRef](#)]
80. Sabato, G.; Scardino, G.; Kushabaha, A.; Chirivi, M.; Luparelli, A.; Scicchitano, G. Automatic Seagrass Banquettes Detection from Surveillance Camera Images with Detectron2. *Geogr. Fis. E Din. Quat.* **2023**, *45*, 229–235. [[CrossRef](#)]
81. Ibaceta, R.; Almar, R.; Catalán, P.A.; Blenkinsopp, C.E.; Almeida, L.P.; Cienfuegos, R. Assessing the Performance of a Low-Cost Method for Video-Monitoring the Water Surface and Bed Level in the Swash Zone of Natural Beaches. *Remote Sens.* **2018**, *10*, 49. [[CrossRef](#)]

82. Al Najar, M.; Thoumyre, G.; Bergsma, E.; Almar, R.; Benshila, R.; Wilson, D. Satellite Derived Bathymetry Using Deep Learning. *Mach. Learn.* **2023**, *112*, 1107–1130. [[CrossRef](#)]
83. Zhou, G.; Su, S.; Xu, J.; Tian, Z.; Cao, Q. Bathymetry Retrieval From Spaceborne Multispectral Subsurface Reflectance. *IEEE J. Sel. Top. Appl. Earth Obs. Remote Sens.* **2023**, *16*, 2547–2558. [[CrossRef](#)]
84. Chen, W.; Liu, W.; Liang, H.; Jiang, M.; Dai, Z. Response of Storm Surge and M2 Tide to Typhoon Speeds along Coastal Zhejiang Province. *Ocean Eng.* **2023**, *270*, 113646. [[CrossRef](#)]
85. Zhang, K.; Li, Y.; Yu, Z.; Yang, T.; Xu, J.; Chao, L.; Ni, J.; Wang, L.; Gao, Y.; Hu, Y.; et al. Xin'anjiang Nested Experimental Watershed (XAJ-NEW) for Understanding Multiscale Water Cycle: Scientific Objectives and Experimental Design. *Engineering* **2022**, *18*, 207–217. [[CrossRef](#)]
86. Andriolo, U.; Mendes, D.; Taborda, R. Breaking Wave Height Estimation from Timex Images: Two Methods for Coastal Video Monitoring Systems. *Remote Sens.* **2020**, *12*, 204. [[CrossRef](#)]
87. Callens, A.; Morichon, D.; Liria, P.; Epelde, I.; Lique, B. Automatic Creation of Storm Impact Database Based on Video Monitoring and Convolutional Neural Networks. *Remote Sens.* **2021**, *13*, 1933. [[CrossRef](#)]
88. Davidson, M.A.; Aarninkhof, S.G.J.; Van Koningsveld, M.; Holman, R.A. Developing Coastal Video Monitoring Systems in Support of Coastal Zone Management. *J. Coast. Res.* **2006**, *39*, 49–56.
89. Calkoen, F.; Luijendijk, A.; Rivero, C.R.; Kras, E.; Baart, F. Traditional vs. Machine-Learning Methods for Forecasting Sandy Shoreline Evolution Using Historic Satellite-Derived Shorelines. *Remote Sens.* **2021**, *13*, 934. [[CrossRef](#)]
90. Xiao, C.; Chen, N.; Hu, C.; Wang, K.; Xu, Z.; Cai, Y.; Xu, L.; Chen, Z.; Gong, J. A Spatiotemporal Deep Learning Model for Sea Surface Temperature Field Prediction Using Time-Series Satellite Data. *Environ. Model. Softw.* **2019**, *120*, 104502. [[CrossRef](#)]
91. Giffard-Roisin, S.; Yang, M.; Charpiat, G.; Kumler Bonfanti, C.; Kégl, B.; Monteleoni, C. Tropical Cyclone Track Forecasting Using Fused Deep Learning from Aligned Reanalysis Data. *Front. Big Data* **2020**, *3*, 1. [[CrossRef](#)]
92. Jiang, G.-Q.; Xu, J.; Wei, J. A Deep Learning Algorithm of Neural Network for the Parameterization of Typhoon-Ocean Feedback in Typhoon Forecast Models. *Geophys. Res. Lett.* **2018**, *45*, 3706–3716. [[CrossRef](#)]
93. Diakogiannis, F.I.; Waldner, F.; Caccetta, P.; Wu, C. ResUNet-a: A Deep Learning Framework for Semantic Segmentation of Remotely Sensed Data. *ISPRS J. Photogramm. Remote Sens.* **2020**, *162*, 94–114. [[CrossRef](#)]
94. Sabato, G.; Scardino, G.; Kushabaha, A.; Chirivi, M.; Luparelli, A.; Scicchitano, G. Deep Learning-Based Segmentation Techniques for Coastal Monitoring and Seagrass Banquette Detection. In Proceedings of the 2023 IEEE International Workshop on Metrology for the Sea; Learning to Measure Sea Health Parameters (MetroSea), La Valletta, Malta, 4–6 October 2023; pp. 524–527.
95. Yang, T.; Jiangde, S.; Hong, Z.; Zhang, Y.; Han, Y.; Zhou, R.; Wang, J.; Yang, S.; Tong, X.; Kuc, T. Sea-Land Segmentation Using Deep Learning Techniques for Landsat-8 OLI Imagery. *Mar. Geod.* **2020**, *43*, 105–133. [[CrossRef](#)]

Disclaimer/Publisher's Note: The statements, opinions and data contained in all publications are solely those of the individual author(s) and contributor(s) and not of MDPI and/or the editor(s). MDPI and/or the editor(s) disclaim responsibility for any injury to people or property resulting from any ideas, methods, instructions or products referred to in the content.